Investigation and Optimization of Connections in Timber Assemblies Subjected to Blast Loading

by

Christian Viau

Thesis submitted to the University of Ottawa

in partial fulfillment of the requirements for the degree of

Doctor of Philosophy

in Civil Engineering

Under the auspices of the Ottawa-Carleton Institute for Civil Engineering



uOttawa

Department of Civil Engineering

Faculty of Engineering

University of Ottawa

© Christian Viau, Ottawa, Canada, 2020

Abstract

The majority of research on high strain-rate effects in timber structures has been limited to the study of the load-bearing members in isolation. Limited work has been conducted on timber connections and full-scale timber assemblies under blast loading, and these have generally been constrained to qualitative observations. In North America, the increasing prevalence of mid- and high-rise timber structures makes them susceptible to blast effects. In addition, questions remain on how to design and optimize these timber assemblies, including the connections, against blast loads, due in part to the limitations on comprehensive design provisions.

The effects of far-field blast explosions were simulated using the University of Ottawa shock tube. A total of fifty-eight dynamic tests were conducted on connection-level and full-scale specimens. The research program aimed to investigate the behaviour of heavy-timber connections when subjected to simulated blast loads. The experimental results showed that connections with a main failure mechanism consisting of wood crushing experienced significant increases in dynamic peak load when compared to the static peak load. In contrast, connections where steel yielding and rupturing occurred experienced no statistically significant increase in dynamic peak load. Full-scale glulam specimens with bolted connections designed to yield via wood crushing and bolt bending performed better than those with overdesigned connections. Bolted connections which failed in splitting led to premature failure of the glulam assembly. Reinforcement with self-tapping screws allowed these bolted joints to fail in a combination of bolt yielding and wood crushing, and provided more ductility when compared to unreinforced specimens. Specially designed energy-absorbing connections significantly increased the energy dissipation capabilities of the timber assemblies. The basis of these connections was to allow for connection yielding while delaying failure of the wood member. This was achieved via elastoplastic connection behaviour, which effectively limited the load imparted onto the wood member. Based on the experimental results, limitations in the current Canadian blast provisions were highlighted and discussed. A two-degree-of-freedom blast analysis software was developed and validated using full-scale and connection-level experimental results and was found to adequately capture the system response with reasonable accuracy. Sensitivity analyses regarding the applicability of using single-degree-of-freedom analysis were presented and discussed.

Acknowledgements

I would be lying if I said I knew what I was getting myself into when I was persuaded into doing a Ph.D. over four years ago. It took me nearly quitting the program—a couple of times—to realize that I had made the right decision. The end product is hours upon hours of devotion towards contributing to my field, while satisfying my curiosity for learning and absorbing new information. This effort could not have been achieved without the help of many individuals.

Foremost, I want to thank Dr. Ghasan Doudak for his continued guidance, encouragement, and support during the course of this research project. Thanks to your mentorship and trust, I was able to develop as a researcher and gain the confidence necessary to lead independent research efforts and make difficult decisions. I look forward to continued collaborations with you… and more of your award-winning ribs.

To my friends and colleagues, I cannot thank you enough for your assistance and comradery. Special thanks go out to Dr. Daniel Lacroix and Dr. Eric Jacques for their technical assistance with the shock tube, experimental test setups, and analytical work, as well as friendship. I look forward to collaborating with the both of you in the near future. To Dr. Gamal Elnabelsya and Dr. Muslim Majeed, thank you for all the help and guidance provided during my time in the lab. To Mr. Luc Cloutier and Ms. Paula Oppici, thank you for your administrative assistance and moral support. To those whom helped me in the lab, please know that this thesis could not have been completed without your help: Antoine Bérubé, Andrew McGrath, Damian Oliveira, Laith Gharaibeh, and Gladys Thelohan. Thank you all so much.

To my partner Mario, I am forever grateful of your love, patience, and support. Thank you for putting up with me working late in the lab, listening to my spiels about obscure research-related topics which I simply *had* to share with you, and my tendency to panic when things do not go as planned. I love you so much.

Finalement, un grand merci à ma famille, Andrée, Robert, et Charles, pour votre aide, encouragement et amour inconditionnel. To Carmela and Jacques, thank you so much for accepting me into your lives, and for hosting us each week for supper; it is something I always look forward to. I love you all, je vous aime tous!

Table of Contents

Abstract ii
Acknowledgements iii
Table of Contents iv
List of Tables xii
List of Figures xiv
Symbols and Notations xxiv
Chapter 1 - Introduction 1
1.1 Research Needs 1
1.2 Research Objectives 3
1.3 Methodology and Scope of Research 4
1.4 Structure of Thesis 4
Chapter 2 - Literature Review 6
2.1 General 6
2.2 Wood as an Engineering Material 6
2.2.1 Properties of Wood 6
2.2.2 Engineered Wood Products 7
2.3 Dowel-Type Wood Connections 9
2.3.1 European Yield Model 9
2.3.2 Brittle Failure Modes in the Parallel- and Perpendicular-to-Grain Directions 11
2.4 Ductility in Timber Connections and Structures 13
2.5 Blast Loading 16
2.5.1 Blast Wave Characteristics 16
2.5.2 Dynamic Analysis for Blast 18

2.6 Behaviour of Timber Under Impact Loading 21
2.7 Behaviour of Timber Elements and Assemblies Subjected to Blast Loading 22
2.7.1 Light-Frame Wood Stud Walls Subjected to Blast Loading 22
2.7.2 Glulam Subjected to Blast Loading 23
2.7.3 Cross-Laminated Timber Subjected to Blast Loading 25
2.8 Performance of Connections Under Blast Loading 27
2.8.1 Timber Connections Under High Strain-Rates 27
2.8.2 Timber Connections Under Blast Loading 29
2.8.3 Blast Energy-Absorbing Connections and Systems 31
2.9 Summary 33
Chapter 3 - Experimental Program 34
3.1 General 34
3.2 Description of Test Specimens and Connections 38
3.2.1 CLT Bearing Connections and Specimens 38
3.2.2 Bolted Glulam Connections and Specimens 40
3.2.3 Energy-Absorbing Connections 43
3.3 Material Characterization of Glulam and CLT Members 46
3.4 Static Connection-Level Testing of CLT Bearing Connections 47
3.5 Static Connection-Level Testing of Bolted Glulam Connections 48
3.5.1 Embedment Strength Tests 48
3.5.2 Bolt Bending Tests 48
3.5.3 Single-Bolt Joint Tests 49
3.6 Static Connection-Level Testing of Energy-Absorbing Connections 50

3.7 Dynamic Testing 51
3.7.1 Description of Test Setups 53
3.7.2 Measuring Methods and Equipment 59
Chapter 4 - Experimental Results 60
4.1 General 60
4.2 Static Test Results 60
4.2.1 Characterization of Timber Members 60
4.2.2 CLT Bearing Connections 60
4.2.3 Bolted Glulam Connections 63
4.2.4 Energy-Absorbing Connections 66
4.3 Dynamic Test Results 68
4.3.1 CLT Bearing Connections Specimens 68
4.3.2 Full-Scale CLT Specimens 76
4.3.3 Full-Scale Glulam Specimens 86
Chapter 5 - Analytical Modelling and Results 100
5.1 General 100
5.2 Model Description 100
5.3 Resistance Curves 104
5.4 Inelastic Blast Analysis Software – *BlasTDOF* 105
5.4.1 Input Modules 106
5.4.2 Dynamic Analysis Module 109
5.4.3 Output Module 112
5.5 Analytical Modelling Results 113

Chapter 6 - Discussion 120
6.1 Behaviour of CLT Assemblies with Bearing Connections 120
6.1.1 Connections Under Dynamic Loading 120
6.1.2 Effect of Axial Restraint on the Connection Response 123
6.1.3 CLT Assemblies Under Dynamic Loading 124
6.1.4 Energy Dissipation in CLT Bearing Connections 125
6.2 Glulam Assemblies with Bolted Connections 128
6.2.1 General Behaviours and Failure Modes 128
6.2.2 Perpendicular-to-Grain Splitting 130
6.2.3 Use of Self-Tapping Screws to Prevent Splitting Failure 132
6.2.4 Energy Dissipation in Glulam Bolted Connections 133
6.3 Behaviour of Timber Assemblies with Energy-Absorbing Connections 136
6.3.1 Proposed Capacity-Based Blast Design Philosophy 136
6.3.2 Comparisons with Typical CLT and Glulam Connections 140
6.3.3 Assemblies Subjected to Multiple Blast Loads and Replaceability of EACs 143
6.4 Analytical Modelling 145
6.4.1 TDOF Versus SDOF 145
6.4.2 Sensitivity Analyses for SDOF and TDOF Modelling 147
6.4.3 SDOF Analysis using Composite Resistance Curves 152
Chapter 7 - Blast Design Considerations 155
7.1 Overview 155
7.2 Design of Bolted Connections Based on CSA S850 Code Provisions 156
7.3 Proposed Approach for the Design of Optimized Bolted Connections 159

Chapter 8 - Conclusions and Recommendations 162
8.1 General 162
8.2 Conclusions 162
8.3 Recommendations for Future Research Work 163
References 166
Appendix A – Test Results of Connection-Level CLT Specimens 174
Connection-level Specimen C1 175
Connection-level Specimen C2 177
Connection-level Specimen C3 179
Connection-level Specimen C4 181
Connection-level Specimen C5 183
Connection-level Specimen C6 185
Connection-level Specimen C7 186
Connection-level Specimen C8 188
Connection-level Specimen C9 190
Connection-level Specimen C10 192
Connection-level Specimen C11 194
Connection-level Specimen C12 196
Connection-level Specimen C13 198
Connection-level Specimen C14 200
Connection-level Specimen C15 202
Connection-level Specimen C16 204
Appendix B – Test Results of Full-Scale CLT Specimens 206
Specimen CLT1 207

Specimen CLT2 210
Specimen CLT3 213
Specimen CLT4 216
Specimen CLT5 219
Specimen CLT6 223
Specimen CLT7 227
Specimen CLT8 231
Specimen CLT9 235
Specimen CLT10 239
Specimen CLT11 243
Specimen CLT12 247
Specimen CLT13 251
Specimen CLT14 – Shot #1 255
Specimen CLT14 – Shot #2 258
Specimen CLT14 – Shot #3 261
Specimen CLT14 – Shot #4 265
Specimen CLT15 – Shot #1 269
Specimen CLT15 – Shot #2 272
Specimen CLT15 – Shot #3 275
Specimen CLT15 – Shot #4 279
Appendix C – Test Results of Full-Scale Glulam Specimens 283
Specimen G1 284
Specimen G2 287

Specimen G3 290
Specimen G4 293
Specimen G5 297
Specimen G6 301
Specimen G7 305
Specimen G8 309
Specimen G9 313
Specimen G10 317
Specimen G11 321
Specimen G12 325
Specimen G13 329
Specimen G14 333
Specimen G15 – Shot #1 337
Specimen G15 – Shot #2 340
Specimen G16 – Shot #1 344
Specimen G16 – Shot #2 347
Specimen G16 – Shot #3 350
Specimen G16 – Shot #4 353
Specimen G16 – Shot #5 356
Specimen G16 – Shot #6 359
Specimen G16 – Shot #7 362
Specimen G17 366
Specimen G18 370

Specimen G19 – Shot #1..... 374

Specimen G19 – Shot #2..... 377

Appendix D – Derivation of Dynamic Resistance..... 381

Appendix E – Derivation of Stiffness Expression for Beams with Rotational Springs..... 389

List of Tables

Table 2.1: EYM Failure Modes and Unit Lateral Yielding Resistances (CSA, 2019) 10

Table 3.1: Summary of Test Matrix for Connection-Level Specimens 36

Table 3.2: Summary of Test Matrix for Dynamic Full-Scale Specimens 37

Table 3.3: CLT Bearing Connection Details 38

Table 3.4: Bolted Glulam Connection Details 41

Table 3.5: Summary of Preliminary Analytical Modelling for EACs 44

Table 4.1: Summary of Static Connection-Level Testing on CLT Bearing Connections 61

Table 4.2: Summary of Static Connection-Level Testing on Single-Bolt Connections 65

Table 4.3: Summary of Static Connection-Level Testing on Energy-Absorbing Connections 66

Table 4.4: Summary of Dynamic Connection-Level Testing 74

Table 4.5: Summary of Dynamic Testing on Full-Scale CLT Specimens 85

Table 4.6: Summary of Dynamic Testing on Full-Scale Glulam Specimens 98

Table 5.1: Summary of TDOF Prediction Accuracies for Each Full-Scale Assembly Type 114

Table 5.2: Summary of All TDOF Modelling Predictions for the Validation of *BlasTDOF* 115

Table 6.1: Results for T-Test Analyses for CLT Bearing Connections 122

Table 6.2: Effect of Connections and Failure Sequence on Work Done by CLT Assemblies ... 127

Table 6.3: Comparison of Wood Crushing for Unreinforced and Reinforced Specimens 133

Table 6.4: Effect of Connections and Failure Sequence on Work Done by Glulam Assemblies136

Table 6.5: Effect of Overstrength Factor on Work Done by Energy-Absorbing Assemblies 140

Table 6.6: Summary of SDOF Prediction Accuracies for Various Failure Sequences 147

Table 6.7: Sensitivity Analyses 149

Table 7.1: Summary of Design Parameters for Glulam Beams 155

List of Figures

Figure 2.1: Effect of Load Duration on Bending Strength (Liska, 1950) 7

Figure 2.2: Brock Commons Tallwood House (courtesy of naturallywood.com, 2017) 8

Figure 2.3: Examples of CLT and Glulam 9

Figure 2.4: Potential Brittle Failure Modes (CSA, 2019) 11

Figure 2.5: Placement of Dowels in the Perpendicular-to-Grain Direction (CSA, 2019) 12

Figure 2.6: Monotonically Tested Specimens (Lam, et al., 2008) 14

Figure 2.7: Application of the Concept of Overstrength for Ductile Timber Assemblies (adapted from Jorissen and Fragiacomo, 2011) 15

Figure 2.8: Typical Pressure-Time History of a Blast Wave (PDC, 2008) 16

Figure 2.9: Cantilever Beam Discretized into Three Beam Elements (Paz and Leigh, 2006) 20

Figure 2.10: Dynamic Failure Modes of Beams and Columns (Lacroix and Doudak, 2018a) 24

Figure 2.11: CLT Structures Prior to Live Blast Testing (Weaver, et al., 2017) 26

Figure 2.12: Representative Failure Modes of 3-Ply CLT Panels (Poulin, et al., 2017) 27

Figure 2.13: Tested Joint Configurations (Girhammar and Andersson, 1988) 28

Figure 2.14: Examples of Retrofitted Stud Wall End Connections (Viau and Doudak, 2016a) .. 30

Figure 3.1: CLT Bearing Connections 39

Figure 3.2: Examples of Connection-Level and Full-Scale CLT Specimens 40

Figure 3.3: Bolted Connection Reinforcements 42

Figure 3.4: Full-Scale Glulam Specimen with Bolted Connections 43

Figure 3.5: Energy-Absorbing Connections 45

Figure 3.6: Moisture Content Measuring Equipment 46

Figure 3.7: Static Connection-Level Test Setup for CLT Bearing Connections 47
Figure 3.8: Embedment Strength Test Setup 48
Figure 3.9: Bolt Bending Test Setup 49
Figure 3.10: Single-Bolt Joint Test Setup 49
Figure 3.11: EAC Static Test Setup 50
Figure 3.12: Shock Tube Test Apparatus 52
Figure 3.13: Dynamic Connection-Level Test Setup 54
Figure 3.14: Connection-Level Specimen with Axial Restraint 55
Figure 3.15: Side Sketch of Dynamic Full-Scale Test Setup for CLT 56
Figure 3.16: CLT EAC (yellow) Bearing on Support Bracket (black) 57
Figure 3.17: Side Sketch of Dynamic Full-Scale Test Setup for Glulam 58
Figure 3.18: Glulam EAC (yellow) Bearing on Load Cell (green) 58
Figure 3.19: Strain Gauge Application 59
Figure 4.1: Experimental Static Load-Displacement Curves for CLT Bearing Connections 62
Figure 4.2: Representative Static Behaviour of CLT Bearing Connections 62
Figure 4.3: Results of Embedment and Bolt Bending Tests 63
Figure 4.4: Obtaining Mechanical Properties of Bolted Connections 64
Figure 4.5: Experimental Static Load-Displacement Curves for Single-Bolt Joints 65
Figure 4.6: Representative Static Behaviour of Single-Bolt Connections 66
Figure 4.7: Experimental Static Load-Displacement Curves for 7/8” Deep EACs 67
Figure 4.8: Representative States of Energy-Absorbing Connections 67
Figure 4.9: Representative Damage Levels for Wood Crushing and ML24Z Angle Yielding 68

Figure 4.10: Typical Results of Dynamic Connection-Level Testing on CLT Bearing Connections (Results from Test C11) 75

Figure 4.11: Typical Results of Dynamic Full-Scale Testing on CLT and Glulam Specimens (Results from Test G16-4) 99

Figure 5.1: Two-Degree-of-Freedom Idealization of a Timber Assembly 102

Figure 5.2: Member Properties Tab 106

Figure 5.3: Connection Properties Tab 107

Figure 5.4: Blast Loading Tab 108

Figure 5.5: Summary of *BlasTDOF* Dynamic Analysis Algorithm 111

Figure 5.6: Analysis Results Tab 112

Figure 5.7: Representative Resistance Curves for Timber Members and Connections 114

Figure 5.8: Displacement Prediction Results for Validation of TDOF Model 116

Figure 5.9: Experimental Displacements and Predictions for the Validation of *BlasTDOF* 117

Figure 5.10: System Resistance Prediction Results for Validation of TDOF Model 119

Figure 6.1: Representative Dynamic Behaviour of Connections 121

Figure 6.2: Experimental Static and Dynamic Load-Displacement Curves 122

Figure 6.3: Effect of Axial Restraint on Dynamic Load-Displacement Curve for ML24Z Angles 124

Figure 6.4: Typical ML24Z Connection Damage in CLT Assemblies 125

Figure 6.5: Effect of Connection Design of Specimens Subjected to Similar Blast Loads 127

Figure 6.6: Representative Dynamic Failure Modes of Glulam Beams 129

Figure 6.7: Representative Bolted Connection Yielding and Wood Crushing in Glulam Beams 129

Figure 6.8: Representative Splitting Failure in Glulam Beams 130

Figure 6.9: Bolt Yielding and Wood Crushing in Specimens Failing in Splitting 131

Figure 6.10: Glulam Specimens with STS Reinforcement 132

Figure 6.11: Possible Failure Modes and Failure Sequences for 2x1 Bolted Joints 134

Figure 6.12: Possible Failure Modes and Failure Sequences for Overdesigned Bolted Joints... 135

Figure 6.13: Failure Sequence Parameters and Energy Dissipation in Timber Connections 137

Figure 6.14: Failure Sequence Parameters and Energy Dissipation in Optimized Connections 139

Figure 6.15: Normalized Load-Displacement Curves of Various Connections Relative to Yield 141

Figure 6.16: Effect of Connections on Damage Reduction in Wood Members 142

Figure 6.17: Effect of Multiple Shots on Glulam and CLT Specimens..... 143

Figure 6.18: Process of EAC Replacement Following a Blast Test 144

Figure 6.19: Experimental Displacements Versus SDOF Predictions..... 146

Figure 6.20: Inputs for Sensitivity Analyses..... 148

Figure 6.21: Results of Sensitivity Analyses for Predictions of Maximum Mid-Span Deflection 151

Figure 6.22: Generation of the Composite Resistance Curve for CLT14-3 using *BlasTDOF* ... 153

Figure 6.23: Experimental Displacements Versus SDOF Predictions using Composite Resistance Curves 154

Figure 7.1: Predictions of Splitting Capacities 157

Figure 7.2: Behaviour of Glulam Assembly Designed According to CSA S850 (2012) 158

Figure 7.3: Load-Displacement Curves of Tested Bolted Connections 161

Figure A.1: Load-Displacement Relationship of Specimen C1 Left-Support Joint 175

Figure A.2: Specimen C1 Before and After Testing..... 175

Figure A.3: Damage in Specimen C1 After Testing 176
Figure A.4: Load-Displacement Relationship of Specimen C2 Right-Support Joint 177
Figure A.5: Specimen C2 Before and After Testing 177
Figure A.6: Damage in Specimen C2 After Testing 178
Figure A.7: Load-Displacement Relationship of Specimen C3 Right-Support Joint 179
Figure A.8: Specimen C3 Before and After Testing 179
Figure A.9: Damage in Specimen C3 After Testing 180
Figure A.10: Load-Displacement Relationship of Specimen C4 Left-Support Joint 181
Figure A.11: Specimen C4 Before and After Testing 181
Figure A.12: Screw Failure in Left Support Block of Specimen C4 After Testing 182
Figure A.13: Load-Displacement Relationship of Specimen C5 Right-Support Joint 183
Figure A.14: Specimen C5 Before and After Testing 183
Figure A.15: Screw Failure in Specimen C5 After Testing 184
Figure A.16: Load-Displacement Relationship of Specimen C6 Right-Support Joint 185
Figure A.17: Dynamic Test Results for Specimen C7 186
Figure A.18: Documentation of Damage for Specimen C7 187
Figure A.19: Dynamic Test Results for Specimen C8 188
Figure A.20: Documentation of Damage for Specimen C8 189
Figure A.21: Dynamic Test Results for Specimen C9 190
Figure A.22: Documentation of Damage for Specimen C9 191
Figure A.23: Dynamic Test Results for Specimen C10 192
Figure A.24: Documentation of Damage for Specimen C10 193
Figure A.25: Dynamic Test Results for Specimen C11 194

Figure A.26: Documentation of Damage for Specimen C11 195
Figure A.27: Dynamic Test Results for Specimen C12 196
Figure A.28: Documentation of Damage for Specimen C12 197
Figure A.29: Dynamic Test Results for Specimen C13 198
Figure A.30: Documentation of Damage for Specimen C13 199
Figure A.31: Dynamic Test Results for Specimen C14 200
Figure A.32: Documentation of Damage for Specimen C14 201
Figure A.33: Dynamic Test Results for Specimen C15 202
Figure A.34: Documentation of Damage for Specimen C15 203
Figure A.35: Dynamic Test Results for Specimen C16 204
Figure A.36: Documentation of Damage for Specimen C16 205
Figure B.1: Dynamic Test Results for Specimen CLT1 208
Figure B.2: Documentation of Damage for Specimen CLT1 209
Figure B.3: Dynamic Test Results for Specimen CLT2 211
Figure B.4: Documentation of Damage for Specimen CLT2 212
Figure B.5: Dynamic Test Results for Specimen CLT3 214
Figure B.6: Documentation of Damage for Specimen CLT3 215
Figure B.7: Dynamic Test Results for Specimen CLT4 217
Figure B.8: Documentation of Damage for Specimen CLT4 218
Figure B.9: Dynamic Test Results for Specimen CLT5 220
Figure B.10: Documentation of Damage for Specimen CLT5 222
Figure B.11: Dynamic Test Results for Specimen CLT6 224
Figure B.12: Documentation of Damage for Specimen CLT6 226

Figure B.13: Dynamic Test Results for Specimen CLT7 228
Figure B.14: Documentation of Damage for Specimen CLT7 230
Figure B.15: Dynamic Test Results for Specimen CLT8 232
Figure B.16: Documentation of Damage for Specimen CLT8 234
Figure B.17: Dynamic Test Results for Specimen CLT9 236
Figure B.18: Documentation of Damage for Specimen CLT9 238
Figure B.19: Dynamic Test Results for Specimen CLT10 240
Figure B.20: Documentation of Damage for Specimen CLT10 242
Figure B.21: Dynamic Test Results for Specimen CLT11 244
Figure B.22: Documentation of Damage for Specimen CLT11 246
Figure B.23: Dynamic Test Results for Specimen CLT12 248
Figure B.24: Documentation of Damage for Specimen CLT12 250
Figure B.25: Dynamic Test Results for Specimen CLT13 252
Figure B.26: Documentation of Damage for Specimen CLT13 254
Figure B.27: Dynamic Test Results for Test CLT14-1 256
Figure B.28: Documentation of Damage for Test CLT14-1 257
Figure B.29: Dynamic Test Results for Test CLT14-2 259
Figure B.30: Documentation of Damage for Test CLT14-2 260
Figure B.31: Dynamic Test Results for Test CLT14-3 262
Figure B.32: Documentation of Damage for Test CLT14-3 264
Figure B.33: Dynamic Test Results for Test CLT14-4 266
Figure B.34: Documentation of Damage for Test CLT14-4 268
Figure B.35: Dynamic Test Results for Test CLT15-1 270

Figure B.36: Documentation of Damage for Test CLT15-1 271
Figure B.37: Dynamic Test Results for Test CLT15-2 273
Figure B.38: Documentation of Damage for Test CLT15-2 274
Figure B.39: Dynamic Test Results for Test CLT15-3 276
Figure B.40: Documentation of Damage for Test CLT15-3 278
Figure B.41: Dynamic Test Results for Test CLT15-4 280
Figure B.42: Documentation of Damage for Test CLT15-4 282
Figure C.1: Dynamic Test Results for Specimen G1 285
Figure C.2: Documentation of Damage for Specimen G1 286
Figure C.3: Dynamic Test Results for Specimen G2 288
Figure C.4: Documentation of Damage for Specimen G2 289
Figure C.5: Dynamic Test Results for Specimen G3 291
Figure C.6: Documentation of Damage for Specimen G3 292
Figure C.7: Dynamic Test Results for Specimen G4 294
Figure C.8: Documentation of Damage for Specimen G4 296
Figure C.9: Dynamic Test Results for Specimen G5 298
Figure C.10: Documentation of Damage for Specimen G5 300
Figure C.11: Dynamic Test Results for Specimen G6 302
Figure C.12: Documentation of Damage for Specimen G6 304
Figure C.13: Dynamic Test Results for Specimen G7 306
Figure C.14: Documentation of Damage for Specimen G7 308
Figure C.15: Dynamic Test Results for Specimen G8 310
Figure C.16: Documentation of Damage for Specimen G8 312

Figure C.17: Dynamic Test Results for Specimen G9 314
Figure C.18: Documentation of Damage for Specimen G9 316
Figure C.19: Dynamic Test Results for Specimen G10 318
Figure C.20: Documentation of Damage for Specimen G10 320
Figure C.21: Dynamic Test Results for Specimen G11 322
Figure C.22: Documentation of Damage for Specimen G11 324
Figure C.23: Dynamic Test Results for Specimen G12 326
Figure C.24: Documentation of Damage for Specimen G12 328
Figure C.25: Dynamic Test Results for Specimen G13 330
Figure C.26: Documentation of Damage for Specimen G13 332
Figure C.27: Dynamic Test Results for Specimen G14 334
Figure C.28: Documentation of Damage for Specimen G14 336
Figure C.29: Dynamic Test Results for Test G15-1 338
Figure C.30: Documentation of Damage for Test G15-1 339
Figure C.31: Dynamic Test Results for Test G15-2 341
Figure C.32: Documentation of Damage for Test G15-2 343
Figure C.33: Dynamic Test Results for Test G16-1 345
Figure C.34: Documentation of Damage for Test G16-1 346
Figure C.35: Dynamic Test Results for Test G16-2 348
Figure C.36: Documentation of Damage for Test G16-2 349
Figure C.37: Dynamic Test Results for Test G16-3 351
Figure C.38: Documentation of Damage for Test G16-3 352
Figure C.39: Dynamic Test Results for Test G16-4 354

Figure C.40: Documentation of Damage for Test G16-4 355

Figure C.41: Dynamic Test Results for Test G16-5 357

Figure C.42: Documentation of Damage for Test G16-5 358

Figure C.43: Dynamic Test Results for Test G16-6 360

Figure C.44: Documentation of Damage for Test G16-6 361

Figure C.45: Dynamic Test Results for Test G16-7 363

Figure C.46: Documentation of Damage for Test G16-7 365

Figure C.47: Dynamic Test Results for Specimen G17..... 367

Figure C.48: Documentation of Damage for Specimen G17..... 369

Figure C.49: Dynamic Test Results for Specimen G18..... 371

Figure C.50: Documentation of Damage for Specimen G18..... 373

Figure C.51: Dynamic Test Results for Test G19-1 375

Figure C.52: Documentation of Damage for Test G19-1 376

Figure C.53: Dynamic Test Results for Test G19-2 378

Figure C.54: Documentation of Damage for Test G19-2 380

Figure D.1: Idealized System with External and Internal Forces for the Elastic Range 381

Figure D.2: Simplified Idealized System with External and Internal Forces for the Elastic Range 383

Figure D.3: Simplified Idealized System with External and Internal Forces for the Plastic Range 387

Figure E.1: Uniformly Distributed Beam with Two Rotational End Springs..... 389

Figure E.2: Beam with Two Equal Concentrated Point Loads at Third Spans with Rotational End Springs 395

Symbols and Notations

Acronym	Definition
ANFO	Ammonium nitrate fuel oil
ASTM	American Society for Testing and Materials
CFRP	Carbon fibre-reinforced polymer
CLT	Cross-laminated timber
CNC	Computer numerical control
CoV	Coefficient of variation
CSA	Canadian Standard Association
CSL	Coated structural lumber
DAS	Data acquisition system
DIF	Dynamic increase factor
DoD	Department of Defense
DOF	Degree-of-freedom
EAC	Energy-absorbing connection
EWP	Engineered wood product
EYM	European Yield Model
FEA	Finite element analysis
FJ	Finger joint
FRP	Fibre-reinforced polymer
GFRP	Glass fibre-reinforced polymer
Glulam	Glued-laminated timber
HSS	Hollow structural section
LSL	Laminated strand lumber
LTD	Load-transfer device
LVDT	Linear variable differential transducers
LVL	Laminated veneer lumber
MC	Moisture content
MDOF	Multiple-degree-of-freedom
OSB	Oriented strand board
PSL	Parallel-strand lumber
SAE	Society of Automobile Engineers
SDOF	Single-degree-of-freedom
SHPB	Split-Hopkinson pressure bar
SIF	Strength increase factor
SPF	Spruce-pine-fir
STS	Self-tapping screw
TDOF	Two-degree-of-freedom
TNT	Trinitrotoluene
USAF	United States Airforce
UTM	Universal testing machine

Symbol	Definition
a	Spacing of load-application points
A	Loaded area
$\{A\}$	Acceleration vector
B	Non-dimensional rotational restraint constant
c	Damping coefficient
C_F	Connection failure
C_S	Connection splitting failure
C_Y	Connection yielding
$[C]$	Damping matrix
d	Depth of the timber member
d_f	Dowel diameter
D_{EXP}	Maximum experimental displacement
D_{SDOF}	SDOF-predicted maximum displacement
D_{TDOF}	TDOF-predicted maximum displacement
$\{D\}$	Displacement vector
e_p	Unloaded edge distance
EI	Bending stiffness
$\{F\}$	Force vector
F_{Blast}	Applied blast force
$F(t)$	Forcing function
$F_{u,conn}$	Connection failure load
$F_{u,wood}$	Timber member failure load
$F_{y,conn}$	Connection yield load
$f(x,t)$	Distributed load per unit length as a function of time
f_1 & f_2	Side and main member embedment strength
f_b	Specified strength in bending
f_y	Dowel yield strength
G	Relative density of wood
I^+	Positive impulse
I^-	Negative impulse
I_R	Peak reflected impulse
K	Stiffness
$[K]$	Stiffness matrix
K_D	Load duration modification factor
K_H	Load sharing modification factor
K_{Sb}	Service condition modification factor for bending
K_{SF}	Service condition modification factor for fasteners
K_T	Treatment modification factor
K_L	Lateral stability factor
K_{Load}	Load transformation factor
K_{LM}	Load-mass transformation factor
K_{Mass}	Mass transformation factor
K_R	Resistance transformation factor
$K_r l$	Rotational stiffness

K_X	Curvature factor
K_{Zbg}	Size factor in bending for glulam
L	Clear span
L_{Driver}	Driver length
m	Mass
$\bar{m}(x)$	Distributed mass
$[M]$	Mass matrix
M_r	Static bending capacity
M_{r-D}	Dynamic bending capacity
$n_{columns}$	Number of bolt columns in bolt group
n_{rows}	Number of bolt rows in bolt group
n_{screws}	Number of self-tapping screws
n_u	Unit lateral yield load
$P(t)$	Pressure-time history
P_R	Peak reflected pressure
P_{so}	Peak incident overpressure
P_{max}	Peak joint load
P_{yield}	Yield load
$P_{plateau}$	Average yield plateau load
QS_{rT}	Static splitting capacity
QS_{rT-D}	Dynamic splitting capacity
$R(t)$	Resistance function
R	Resistance
R	Standoff distance
$\{R\}$	Resistance vector
R_{peak}	Peak resistance
Rxn_{peak}	Wood member reaction at failure
S	Section modulus
t	Thickness of the timber member
t_1	Side member thickness
t_2	Main member thickness
t_A	Arrival time of the shock front
t_f	Time to ultimate failure
t_o	Positive phase duration
t_o^-	Negative phase duration
t_{crit}	t critical value for Student's t-test
t_{stat}	t-statistic for Student's t-test
$T_{EXP.}$	Experimental time-to-maximum
T_{TDOF}	TDOF-predicted time-to-maximum
$\ddot{u}(t)$	Acceleration
$\dot{u}(t)$	Velocity
$u(t)$	Displacement
$\{V\}$	Velocity vector
$V(t)$	Dynamic reaction
x_{eq}	Location of equivalent inertial force
W	Charge weight

W_F	Wood failure
Z	Scaled distance
α	Blast waveform parameter
α_u	Overstrength factor for connection failure
α_y	Overstrength factor for connection yielding
Δ	Displacement
Δt	Analysis time step
$\dot{\epsilon}_{\text{average}}$	Average strain-rate
γ	Yield factor
λ	Dowel slenderness ratio
μ_{max}	Maximum ductility ratio
ϕ_b	Resistance factor for bending failure
ϕ_w	Resistance factor for brittle failures
$\phi(x)$	Shape function

Chapter 1 - Introduction

1.1 Research Needs

Recent efforts towards the design and construction of taller wood structures have generated great interest in the use of engineered wood products (EWPs), such as glued-laminated timber (glulam) and cross-laminated timber (CLT). As designers and engineers aim to provide their clients with sustainable, cost-effective, and safe mid- to high-rise structures, an increasing amount of tall timber structures are being built nowadays. Examples of such innovative structures include the Richmond Olympic Oval in Richmond, British Columbia, Canada, the Tianning Temple in Changzhou City, China, as well as the UMass Design Building in Amherst, Massachusetts.

A higher risk of being exposed to the effects of explosions can be associated with such high-profile structures. In response to this need, blast design provisions have been enacted in various countries (e.g. Office of the Deputy Prime Minister, 2004; Unified Facilities Criteria Program, 2008; Unified Facilities Criteria Program, 2009; CSA, 2012). Of particular interest to the current study is the Canadian Standard Association (CSA) blast standard, which addresses blast load design, analysis, and performance requirements (CSA, 2012). The standard contains detailed design provisions for reinforced concrete and structural steel, and relatively limited requirements for timber structures. It should also be noted that the research that laid the foundation for these provisions for timber structures has been based on very limited work, most of which were conducted on small-scale clear specimens (Spencer, 1978; Jansson, 1992). The method by which the current blast standards calculate the dynamic strength is by multiplying the static design strength of a structural element by a strength increase factor (SIF) and a dynamic increase factor (DIF). The SIF brings the design-level strength (usually 5^{th} percentile) to a value corresponding to the average strength, and the DIF modifies the static-level strength for the effect of high strain-rate. The high strain-rate effect is a material property and usually differs for different materials and different failure modes. Recent studies have established appropriate design values for DIF for full-scale visually graded lumber studs (Jacques, et al., 2014), light-frame stud walls (Lacroix and Doudak, 2015; Viau and Doudak, 2016b; Viau and Doudak, 2016a), glulam beams and columns (Lacroix and Doudak, 2018b; Lacroix and Doudak, 2018a), and CLT panels (Poulin, et al., 2017).

A major shortcoming of the blast design standards is the approach to the design of timber connections. For example, the sole provision in the Canadian blast standard (CSA, 2012) for timber connection simply states that "*Connections between structural elements shall be limited to bearing failure in the wood member or connector. The connection shall be designed for forces corresponding to 1.2 times the capacity of the components being considered."* (CSA, 2012). In essence, the connection must be designed to fail in a ductile manner while having a capacity that is 20 % higher than that of the wood element to which it is connected. Although this general statement seems reasonable for structural members that behave in a ductile manner (e.g. structural steel and reinforced concrete), it is not appropriate to require the same sequence of failure in timber structures where member failure is usually brittle. Requiring ductile behaviour in the connections ensures, on the one hand, that in the case of an overloading, catastrophic brittle failure would not occur between structural elements. On the other hand, requiring the connections to be designed for a higher load than the capacity of the structural members shifts the failure to be in the wood element. Also, given the fact that no DIF is established for various connection types, there are no guarantees that the 20 % increase in load is sufficient for the wood member to fully develop its capacity.

Several studies have shown that the design provision for timber connections is overly simplistic and inadequate for the connection design of light-frame stud walls and CLT panels (e.g. Viau and Doudak, 2016a; Côté and Doudak, 2019). Attempts have been made in the literature to enhance the post peak performance of some timber elements using multi-directional fibre-reinforced polymer (FRP) (Lacroix and Doudak, 2018c), however such retrofit techniques are typically still governed by the failure in the wood fibres and although the past-peak performance of the assembly is enhanced, the enhancement is relatively limited. Developing inelastic energy dissipation in the connections goes against the design philosophy outlined in the blast design standard, however, the aforementioned studies on timber connections under blast (Viau and Doudak, 2016a; Côté and Doudak, 2019) have shown indications that this design approach may yield promising results. It should be noted that this philosophy is not entirely new. For example, failure of wood assemblies, such as light-frame and CLT shearwalls specifically, require the failure and energy dissipation to occur in the connections rather than the timber elements. The drawback of such an approach is clearly that if failure occurs in the connection rather than the structural member, it could lead to the system not reaching its ultimate capacity (member strength) or to the possibility of progressive

collapse. It is therefore paramount to consider the post peak behaviour of the connections and to ensure that the ultimate failure does not occur prematurely. Ideally, the connections would yield first, contribute to the dissipation of the energy in the system and reduce the demand on the timber element, but ultimately the timber structural element would reach its ultimate capacity and failure prior to the ultimate failure being reached in the connections.

The current study aims to quantitatively and qualitatively assess the blast performance of timber connections at the component and system levels, through the use of simulated blast waves, in order to develop design provisions for typical and blast-resistant timber connections.

Supplementary to the need for understanding the connection behaviour, the methodology by which designers and engineers must analyze structural systems typically entails either simplified analysis methods or high-fidelity modelling. The former has been shown to be adequate for blast, due to the uncertain nature of the loading, while the latter tends to be computationally expensive, and is only beneficial when complex subsystem interactions and contact explosions are of interest. One additional aim of the current study is to develop and validate a modelling tool which is capable of capturing the effects of realistic boundary conditions as well as strain-rate effects in the timber assembly.

1.2 Research Objectives

The overarching goal of this research project is to investigate the behaviour of heavy-timber connections when subjected to simulated blast loads. More specifically, the goals of this project are to:

1. Investigate the response and failure mode of various heavy-timber connections subjected to static and dynamic loads for the purpose of establishing an appropriate dynamic increase factor;
2. Investigate the behaviour of glulam and CLT members with realistic boundary conditions under simulated blast loads;
3. Design, fabricate, and optimize innovative energy-absorbing connections for heavy-timber members with the emphasis on maximizing energy dissipation;
4. Develop a modelling software and procedure that can be used for timber elements with realistic boundary conditions subjected to blast loads, and;

5. Examine the validity of current blast design requirements for timber members and connections, and provide recommendations where applicable.

1.3 Methodology and Scope of Research

The methodology used to achieve the research objectives is as follows:

- Review of timber properties, key timber connection design provisions and parameters, blast wave characteristics, and dynamic analysis procedures;
- Completion of a detailed literature review of high strain-rate effects on timber members and connections;
- Conduct static and dynamic testing of typical connections in isolation in order to establish their dynamic increase factor (DIF), resistance curve, and failure modes;
- Conduct dynamic testing of full-scale glulam beams and CLT panels with typical connections to establish the performance of the connections in an assembly;
- Design and manufacture connections with optimized blast-resistant behaviour, and;
- Develop and validate a material predictive numerical procedure which takes strain-rate effects and non-idealized boundary conditions into consideration.

The scope of this project is limited to glulam and CLT structural members, which are arguably the most common load-bearing elements used in mid- and high-rise timber structures. Dynamic testing will consist of simulating the effects of far-field blast explosions, which results in planar shock fronts. Typical connections for both glulam and CLT, namely bolts and angles brackets with screw fasteners, are investigated due to their common use in heavy timber construction. More particularly, the bolted connections investigated in this project are limited to slender fasteners that would allow for the development of ductile connections. This is also consistent with the provisions of the Canadian blast design standard (CSA, 2012). Specific limitations of the research are further discussed throughout the thesis as well as in the future recommendation section of Chapter 8.

1.4 Structure of Thesis

Chapter 1 introduces the topic of study and presents the research needs, objectives, methodology, and scope.

Chapter 2 presents background information on timber members, timber connections, and blast loading, as well as a comprehensive literature review on a number of studies that have been performed on the ductility of timber assemblies, high strain-rate effects in timber members and connections, as well as various methodologies for blast analyses.

Chapter 3 presents the experimental program and includes detailed descriptions of the specimens and test setups.

Chapter 4 presents the static and dynamic results for all connection-level and full-scale specimens.

Chapter 5 presents the analytical model developed for the purpose of evaluating the behaviour of timber elements with connections subjected to blast loads. Also presented in this chapter are the modelling results.

Chapter 6 presents the discussion of both the experimental and numerical results. This includes the determination of dynamic increase factors in connections, effect of connections on the response of the timber assembly, and optimization of connections for energy dissipation.

Chapter 7 presents the implications of the Canadian blast standard, including a direct comparison between the provisions found in the code and the observations resulting from experimental testing.

Chapter 8 presents a summary of the most significant research findings and proposes potential future research topics that can build on the current research effort and further contribute to the knowledge base in this area.

Appendix A provides detailed summaries of the connection-level CLT dynamic test results.

Appendix B provides detailed summaries of the full-scale CLT dynamic test results.

Appendix C provides detailed summaries of the full-scale glulam dynamic test results.

Appendix D presents the derivation of the equation for the dynamic resistance of glulam beams and CLT panels using an equivalent single-degree-of-freedom (SDOF) approach.

Appendix E provides the derivations of the equations for beams with semi-rigid rotational end springs under uniformly distributed loading, as well as two concentrated point loads at equal span (four-point bending).

Chapter 2 - Literature Review

2.1 General

Blast events occur suddenly and can have devastating consequence on buildings and their occupants (e.g. Oklahoma City bombing (1995), Texas City Refinery explosion (2005), Lac-Mégantic rail disaster (2014)). Such events have necessitated the development of design standards (Unified Facilities Criteria Program, 2008; ASCE, 2011; CSA, 2012) that provide guidelines to aid in analyzing and designing new and existing structures against blast loads. Due to the majority of past research being conducted on materials with inherent blast resistant properties, such as reinforced concrete and structural steel, the clauses pertaining to these materials are often more developed than those for timber and engineered wood products. The following section presents background information on wood members and connections, and provides an overview on blast loading characteristics and analysis methods. A comprehensive literature review on previous studies relating to ductility in timber assemblies, high strain-rate effects in timber elements and connections, and innovative ductile connections, is also presented.

2.2 Wood as an Engineering Material

2.2.1 Properties of Wood

Wood can be considered as an orthotropic material with properties differing along its longitudinal, radial, and tangential directions (Ross, 2010). Due to the viscoelastic nature of wood, these properties are also affected by various time-dependent variables including rate of loading and load duration. As shown in Figure 2.1, when compared to the standard static testing duration of 10 minutes, a decrease in bending strength, which is logarithmically proportional to the load duration, is found for long-term load durations. Creep effects are generally responsible for the reduction in strength, to an approximate asymptote of 60 % of its standard strength (Ross, 2010; Breyer, et al., 2015).

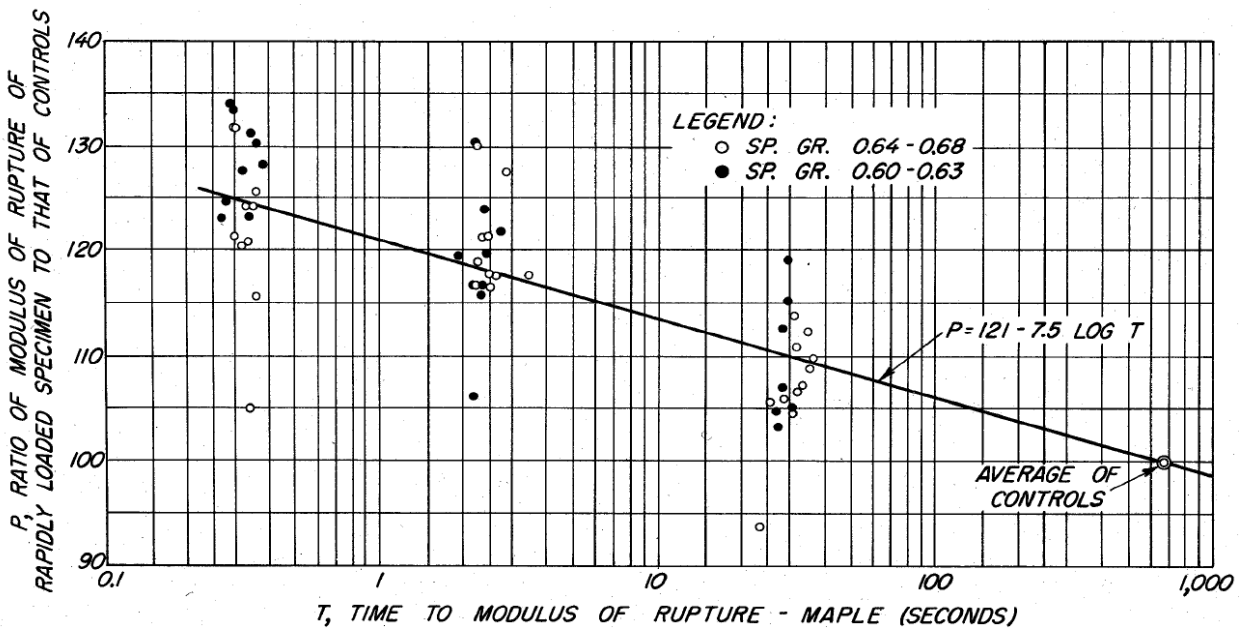


Figure 2.1: Effect of Load Duration on Bending Strength (Liska, 1950)

2.2.2 Engineered Wood Products

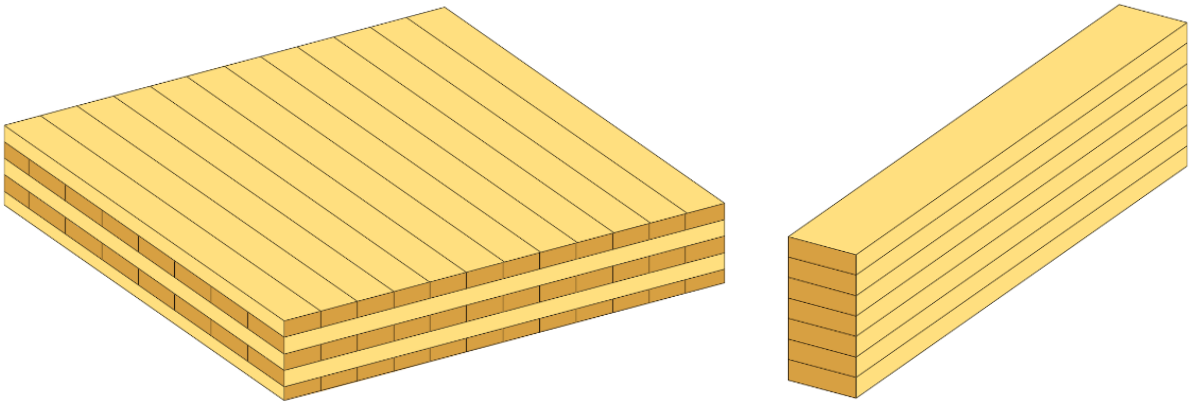
Wood is often used for light-frame construction, which is the status quo for residential structures. However, with recent advancements in manufacturing technologies, creating engineered wood products that have highly controlled and desirable properties is now feasible. These are often used in modern designs, which necessitate spans and heights that are significantly larger than those found in residential construction. A prime example of such a structure is the University of British Columbia *Brock Commons Tallwood House*; an 18-storey timber-concrete hybrid building that is 53 m tall (see Figure 2.2).



Figure 2.2: Brock Commons Tallwood House (courtesy of naturallywood.com, 2017)

Examples of engineered wood products include parallel-strand lumber (PSL), laminated veneer lumber (LVL), oriented strand board (OSB), glued-laminated timber (glulam), and cross-laminated timber (CLT). Glulam and CLT are typically used as gravity load-bearing elements in mid- and high-rise structures, and were therefore selected to be investigated as part of the current study.

Glulam consists of layers of dimensional lumber glued together with a strong adhesive and connected with finger joints to create continuity along the length of the lumber pieces. Under standard test loading duration, the strength of the adhesive used between the laminates and finger joints is always equal to or higher than that of the wood itself. CLT consists of several layers of dimensional lumber stacked crosswise and glued together on their wide face. Typical CLT panels comprise of three and seven layers, although other layups and higher thicknesses can be made available. In terms of behaviour, CLT differs from glulam in that the orthogonal nature of the CLT panels allows for two-way action to develop when supported for that purpose. Additionally, the cross-laminations provide reinforcement against splitting, which is often an issue during connection design (FPInnovations, 2011). Examples of a CLT panel and a glulam beam are shown in Figure 2.3.



(a) CLT Panel (b) Glulam Beam

Figure 2.3: Examples of CLT and Glulam

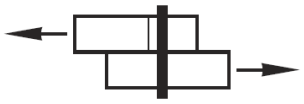
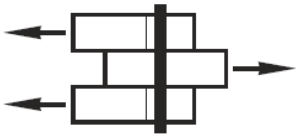
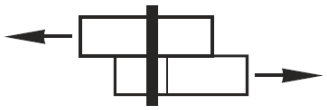
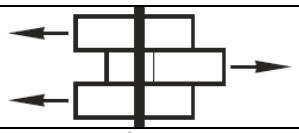
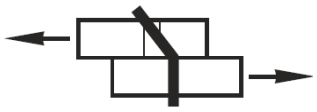
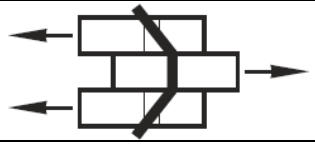
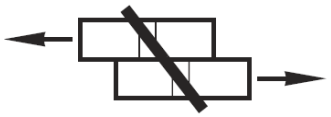
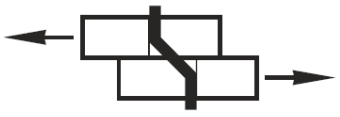
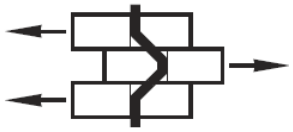
2.3 Dowel-Type Wood Connections

2.3.1 European Yield Model

Many timber design codes (e.g. CEN, 2004b; AWC, 2015; CSA, 2019) utilize connection design equations based on the European Yield Model (EYM) formulas derived by Johansen (1949) to predict the lateral load-carrying capacity of dowelled wood connections. The EYM assumes that failure occurs either in wood crushing or by combination of dowel yielding and wood crushing. Both of these failure modes are considered ductile, and are generally the desired governing mode for timber connections. Failure in timber connections depends on a number of variables, including the relative density of the wood (G), thicknesses of the side and main members (t_1 and t_2), diameter of the fastener (d_f), embedment strength of the side and main members (f_1 and f_2), yield strength of the dowel (f_y), and the overall geometrical configuration of the joint. The number of parameters and their respective variability can present a challenge to designers, as the connections in wood structures are often critical, and must be designed appropriately in order to avoid premature failure (Heine, 2001; Quenneville and Mohammad, 2001; Sawata, 2015).

The yield modes for two- and three-member connections are presented in Table 2.1. Associated with each failure is the equation to determine the load at which the specific yield mode will occur. The letters associated with the equations are consistent with those presented in the Canadian wood design standard (CSA, 2019). For each connection type, the smallest unit lateral yield load (n_u) will correlate to the governing mode to be used in the appropriate design calculations.

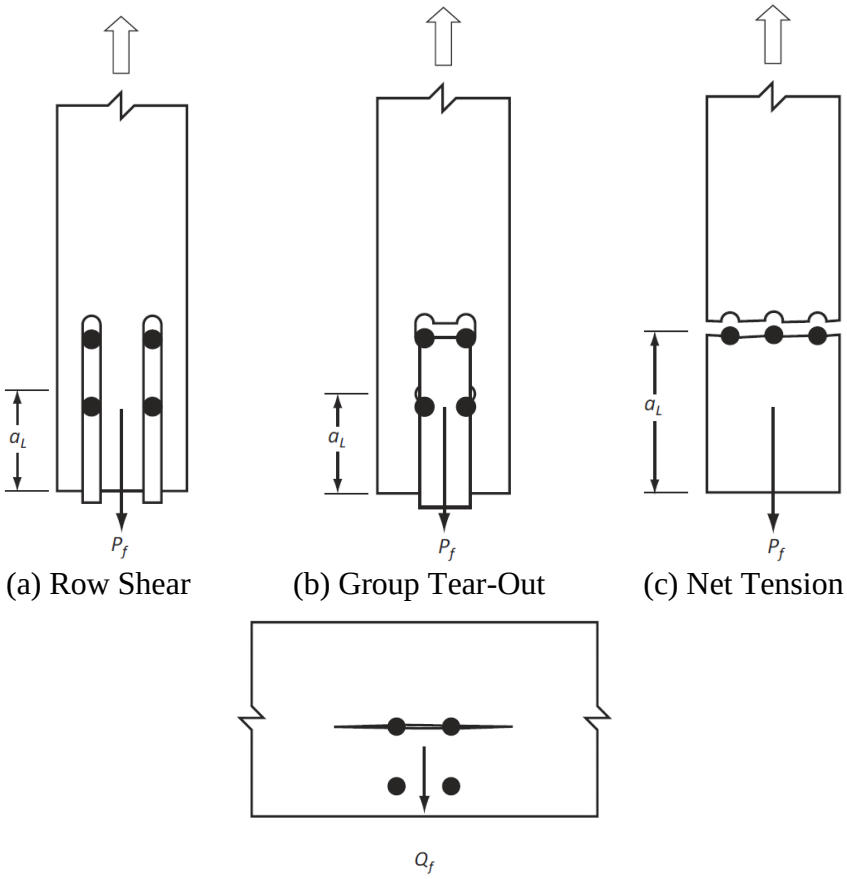
Table 2.1: EYM Failure Modes and Unit Lateral Yielding Resistances (CSA, 2019)

Mode	Visual Representation		Unit Lateral Yielding Resistance (kN)
	Two-Member Connection	Three-Member Connection	
(a)			$f_1 d_f t_1$
(b)		N/A	$f_2 d_f t_2$
(c)	N/A		$\frac{1}{2} f_2 d_f t_2$
(d)			$f_1 d_f^2 \left(\sqrt{\frac{f_2 f_y}{6 f_1 (f_1 + f_2)}} + \frac{t_1}{5 d_f} \right)$
(e)		N/A	$f_1 d_f^2 \left(\sqrt{\frac{f_2 f_y}{6 f_1 (f_1 + f_2)}} + \frac{t_2}{5 d_f} \right)$
(f)		N/A	$\frac{f_1 d_f^2}{5} \left(\frac{t_1}{d_F} + \frac{f_2 t_2}{f_1 d_f} \right)$
(g)			$f_1 d_f^2 \sqrt{\frac{2 f_2 f_y}{3 f_1 (f_1 + f_2)}}$

The current study focusses on the behaviour of three-member connections, as these are most commonly used for glulam members. For those connection configurations, Mode (a) and (c) represent failure modes that are characterized by crushing failure occurring in the side or main member, respectively. Mode (d) represents a failure mode characterized by the formation of a single plastic hinge in the steel dowel occurring in or near the main member. Finally, Mode (g) represents the failure where plastic hinges occur in all members. Based on the above description, it can be noted that small diameter dowels will likely undergo inelastic deformations while stocky dowels will cause crushing of the side or main member. This leaves the designer with different options to control the strength, stiffness, as well as ductility of the connection.

2.3.2 Brittle Failure Modes in the Parallel- and Perpendicular-to-Grain Directions

The theory outlined by Johansen (1949) only considers ductile connection failures. However, it has been shown that the ultimate failure of dowel-type connections may be brittle and characterized by failure in the wood member. The orthogonal nature of wood leads to difference in the failure mode depending on whether the load is applied parallel- or perpendicular-to-grain. Three brittle failure modes can occur in the parallel-to-grain direction, depending on the connection layout and properties of the joint components, while only splitting between the wood fibres can occur in the perpendicular-to-grain direction, as illustrated in Figure 2.4.



(a) Row Shear (b) Group Tear-Out (c) Net Tension

(d) Perpendicular-to-Grain Splitting

Figure 2.4: Potential Brittle Failure Modes (CSA, 2019)

Row-shear failure (Figure 2.4a) is characterized by a shear "plug" failure along the wood grain, whereas group tear-out (Figure 2.4b) involves a combination of row-shear failure along the grain, in tandem with a tension failure occurring in the area between the rows of bolts. Net tension failure (Figure 2.4c) also may occur due to excessive removal of wood material in order to install the bolts.

The ultimate failure of a timber connection loaded in the perpendicular-to-grain direction is that of a fracture in the wood (splitting) at the connections (Figure 2.4d). While strength and ductility in timber can generally be reached if loading is in the compression perpendicular-to-grain direction, its strength is significantly lower, and little-to-no ductility is usually achieved. To minimize the possibility of brittle behaviour, current design provisions impose limitations on the placement of fasteners within the wood members, as a function of the fastener's diameter, d_f. These limitations, however, have shown to not completely eliminate the brittle behaviour (Quenneville and Mohammad, 2001). An example of the minimum spacing, edge, and end distances can be found in Figure 2.5 for an exterior joint (CSA, 2019).

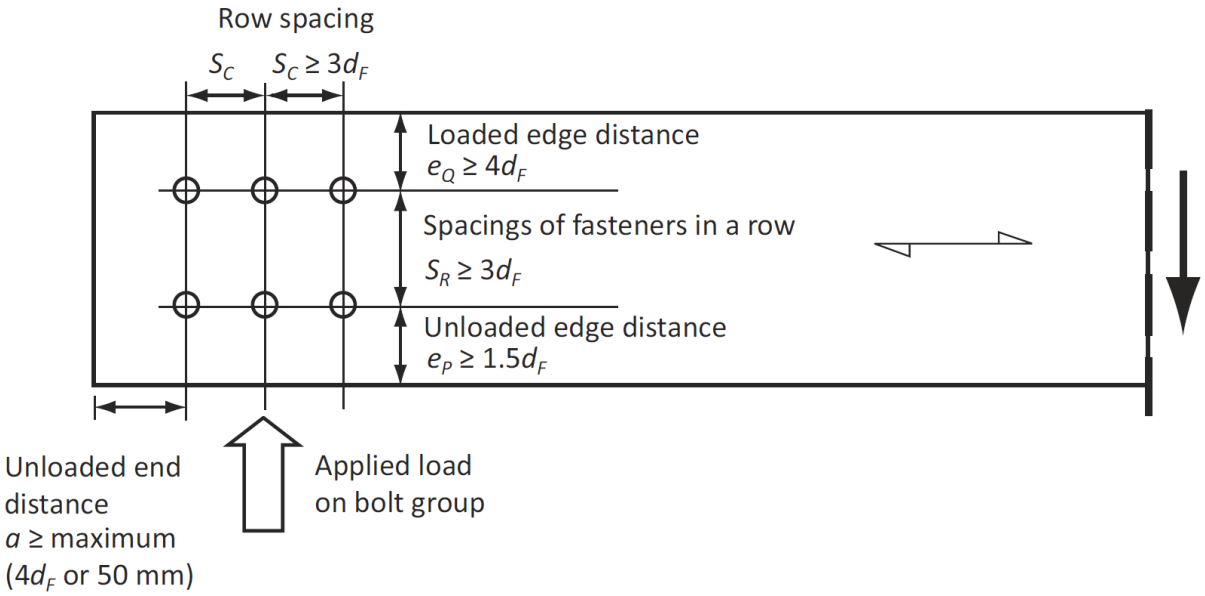


Figure 2.5: Placement of Dowels in the Perpendicular-to-Grain Direction (CSA, 2019)

The minimum required loaded edge distance, e_Q, is meant reduce the possibility for splitting failure and promote ductile failure. Experimental work on timber joints perpendicular-to-grain by Reshke, et al. (2000) and Quenneville and Mohammad (2001) found that the minimum loaded edge distance of four times the fastener diameter does not completely prevent splitting from occurring in the connection and does not ensure ductile joint behaviour. Other studies found correlation between the unloaded edge distance and the strength of a given joint configuration when loaded perpendicular-to-grain (Foschi, 1973; Ehlbeck, et al., 1989). The current splitting capacity equation (Equation 2.1) from CSA (2019) shows that the connection capacity increases as the unloaded edge decreases.

$$QS_{rT} = \phi_w 14t \sqrt{\frac{d - e_p}{1 - \frac{d - e_p}{d}}} (K_D K_{SF} K_T) \qquad \text{Equation 2.1}$$

where ϕ_w is the resistance factor for brittle failures, K_D, K_{SF}, and K_T are the modification factors for load duration, service condition, and treatment, respectively, d is the depth of the timber member, t the thickness of the timber member, and e_p the unloaded edge distance, as per Figure 2.5.

2.4 Ductility in Timber Connections and Structures

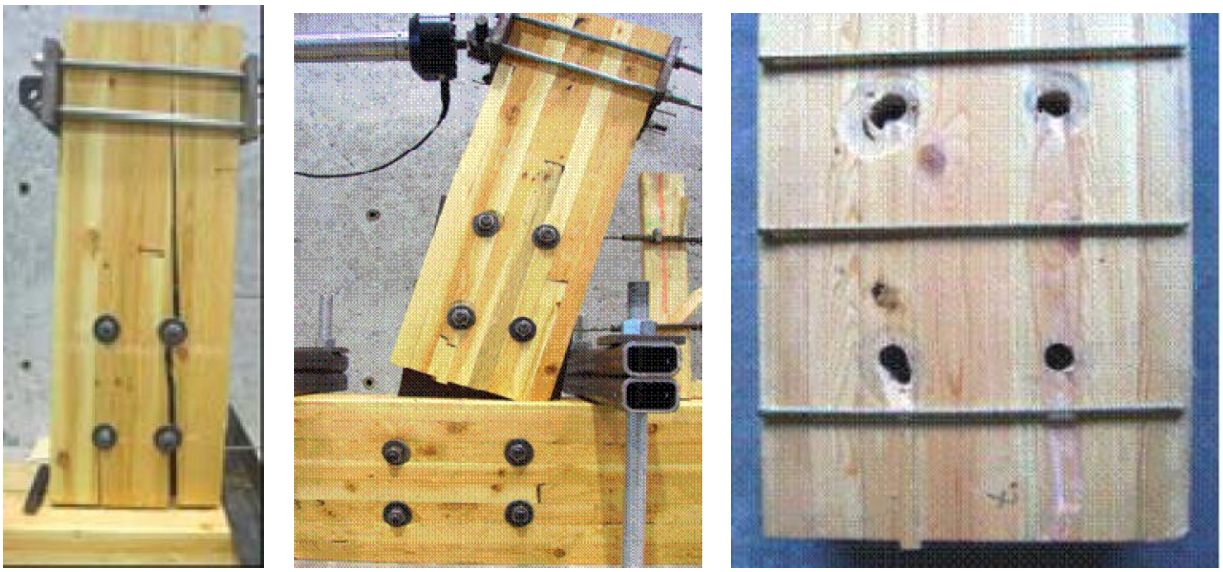
For timber structures, ductile connection behaviour is desired, as it will allow the structure to dissipate energy without resulting in a catastrophic failure (Pirinen, 2014; Mpidi Bita, et al., 2018). Since ductile behaviour of the timber members cannot be ensured due to the brittle nature of the material, ductile connections can be designed to work as structural fuses, effectively failing in a ductile manner prior to failure of the members. This is of particular importance during an extreme loading event, such as an earthquake or a blast, where the structure must rely on inelastic deformations to withstand the loading and allow occupant evacuation.

The main metric indicating whether a dowelled connection will behave in a ductile manner is the slenderness ratio of the dowels, denoted λ, as calculated using Equation 2.2.

$$\lambda = \frac{t}{d_f} \qquad \text{Equation 2.2}$$

where t is the wood member thickness and d_f is the fastener diameter. Jorissen (1998) evaluated the relationship between failure modes and slenderness ratio of perpendicular-to-grain dowelled connections using a constant timber thickness of 24 mm and varying the fastener diameter from 3 mm to 16 mm (corresponding to λ values of 1.5 to 8). It was found that for $\lambda \leq 2.8$, the governing failure mode was that of wood splitting. For the range of $2.8 \leq \lambda \leq 4.2$, the EYM Mode 1 failure governed, and finally, for $\lambda > 4.2$, Mode 3 failure governed the behaviour (Jorissen, 1998). These findings were later corroborated by Mischler, et al. (2000) and Brühl, et al. (2011), who both reported brittle failure when $2 \leq \lambda \leq 3$ and ductile failure when $\lambda \geq 6$.

One technique that has been successfully used to prevent brittle failure in connections is through reinforcement. Various techniques for reinforcing timber joints have been investigated, such as using densification (Blaß and Schädle, 2011; Wang, et al., 2015), and self-tapping screws (Lam, et al., 2008; Wang, et al., 2015). In particular, the use of self-tapping screws (STS) can be easily implemented into any type of dowelled connection with a simple hand drill. By carefully positioning the screws at the critical splitting locations, this can effectively delay the onset of splitting or fracture of the wood due to the confinement effect of the screws. This type of reinforcement is extremely versatile, and can be used to reinforce parallel- and perpendicular-to-grain connections. For perpendicular-to-grain loading, Lam, et al. (2008) investigated the contribution of STS as perpendicular-to-grain reinforcements for bolted glulam connections with slotted steel plates subjected to monotonic and cyclic loading (see Figure 2.6). It was observed that connections reinforced with STS experienced an increase in capacity by a factor of 2 and 1.7 when compared to un-reinforced connections under monotonic and reverse cyclic loading, respectively (Lam, et al., 2008). It is important to note that while STS have shown promising results for the reinforcement of bolted joints, the current Canadian wood design standard (CSA, 2019) does not include provisions for the design of connections using STS fasteners, nor does it contain requirements for using STS to reinforce timber bolted joints.



(a) Unretrofitted (b) Retrofitted (c) Reinforcement Layout

Figure 2.6: Monotonically Tested Specimens (Lam, et al., 2008)

Jorissen and Fragiacomo (2011) discussed the implications of ductility in design of timber structures under static and dynamic loading including earthquakes and impact loads. Following the capacity-based design developed and proposed by Paulay and Priestley (1992), the authors outlined a design procedure for timber assemblies with ductile connections. In essence, the design strength capacity of the ductile element (i.e. the connections) must be less than that of the brittle timber element. To ensure that this occurs, the timber member must be designed using a overstrength factor, which is defined as the ratio between the capacities of the timber member and the connections (Jorissen and Fragiacomo, 2011). This overstrength factor is a function of the variation of strength of both components, and has as purpose to minimize the overlapping areas under the distribution curves for the connection and member resistance (see Figure 2.7). It is therefore imperative that the material variability of both the strength and stiffness be well known. Such basis for design and analysis has recently been considered in the design of CLT shearwalls subjected to in-plane seismic loading (Nolet, et al., 2019), which rely on yielding of ductile wall components, such as hold-downs, to lead to safe response.

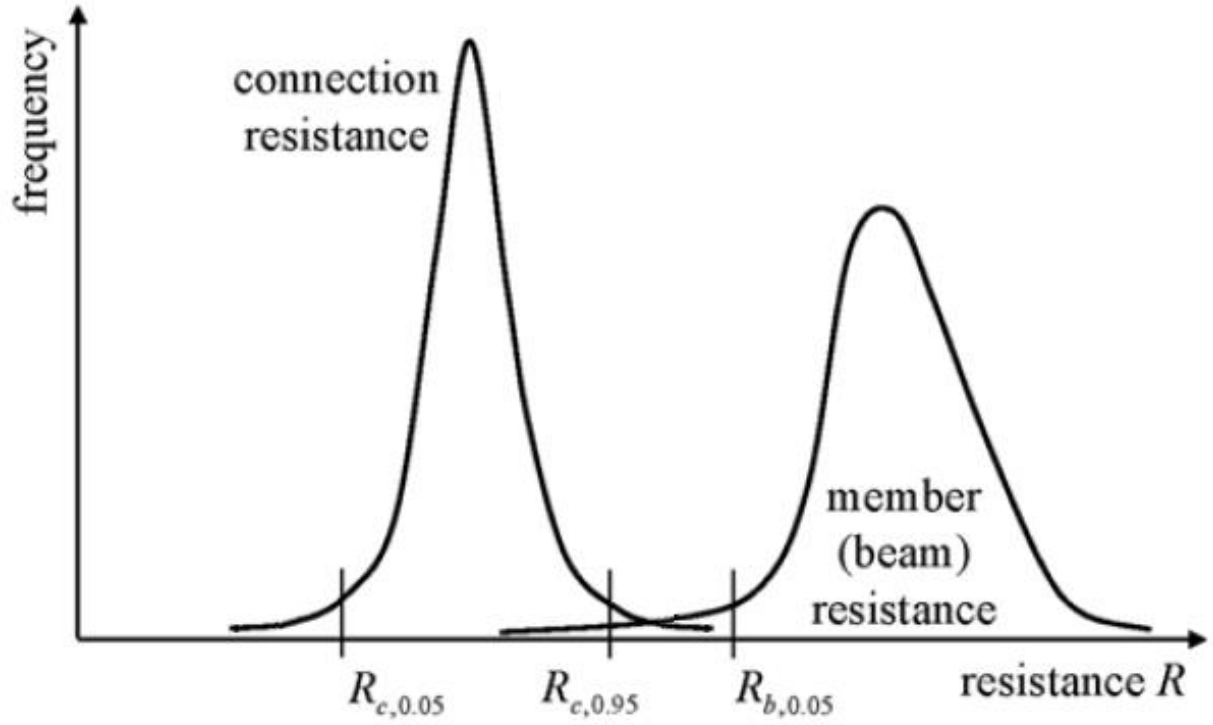


Figure 2.7: Application of the Concept of Overstrength for Ductile Timber Assemblies (adapted from Jorissen and Fragiacomo, 2011)

2.5 Blast Loading

2.5.1 Blast Wave Characteristics

Explosions are characterized by a sudden release of a large quantity of nuclear, physical, or chemical energy (Krauthammer, 2008; Dusenberry, 2010). A large proportion of the existing knowledge base is on physical and chemical explosions, as these are more common than nuclear explosions. Physical explosions occur in situations where no chemical or nuclear reaction is required to generate energy. An example is the sudden rupturing of the tank walls of a container whose content is under high pressure. The expansion of the content stemming from the rupturing of the tank generates a shock wave (Steinfeld and Wormhoudt, 1998). Chemical explosions are a product of either decomposition or combustion reactions. These reactions are exothermic and produce the energy required to create a shock wave (Davis, 1972). Examples of well-known decomposition reactions are those occurring in the detonation of trinitrotoluene (TNT) and ammonium nitrate fuel oil (ANFO). These reactions and associated detonations lead to the creation of shockwaves which tend to propagate in a hemispherical or spherical profile away from the source, depending on whether the explosion occurred from the ground or in the air (Krauthammer, 2008).

Shock waves are characterized through the use of pressure-time histories, which measure the variation in pressure at a certain distance away from the detonation source as a function of time elapsed since detonation. The pressure-time history of a typical shock wave is shown in Figure 2.8.

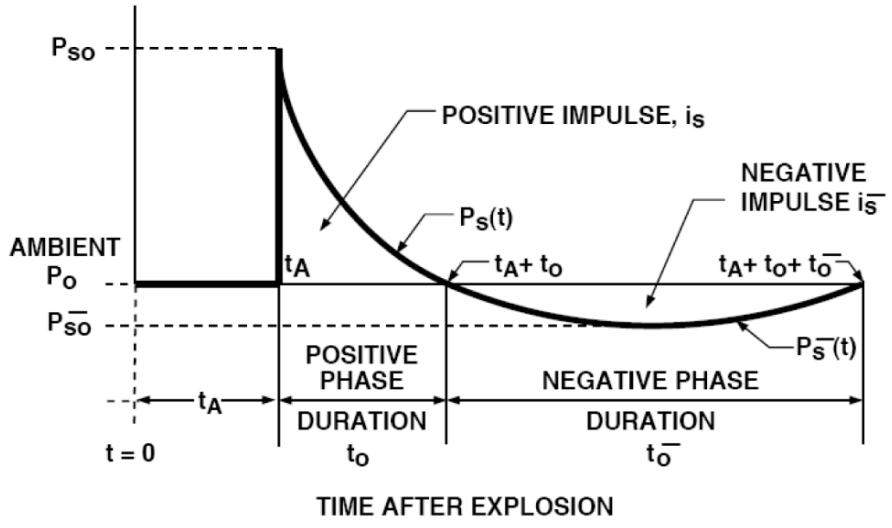


Figure 2.8: Typical Pressure-Time History of a Blast Wave (PDC, 2008)

As the shock wave travels away from the source, a reduction in the pressure and an increase in the overall blast duration takes place. This initial shock front is known as the "positive phase" and will generally have the greatest effect on the structure. Due to the overexpansion of the air particles brought on by the positive phase, a vacuum will be created due to the lower-than-ambient pressure. This is known as the "negative phase," which is generally longer in duration, but typically has much lesser effect on the structure. Oftentimes, designers completely ignore the effects of any other phase besides the initial positive phase (Unified Facilities Criteria Program, 2008; Dusenberry, 2010). This may be adequate for most design cases where the structural element is designed for multidirectional loading (such as a beam-column) but may not be adequate in case of unidirectional loading (such as a design of window anchorage). Following the negative phase, the ambient pressure returns to the pre-blast pressure.

The most utilized method to model the pressure-time history is the modified Friedlander equation (Friedlander, 1946), which is characterized by an instantaneous rise in pressure followed by an exponential decay (Equation 2.3). Another important parameter that must be quantified is the impulse, which can be defined as the area under the pressure-time histories shown in Figure 2.8. The peak positive and negative impulses can be determined by using Equation 2.4 and Equation 2.5, respectively.

$$P(t) = P_{so} e^{-\frac{\alpha t}{t_o}} \left(1 - \frac{t}{t_o}\right) \qquad \text{Equation 2.3}$$

$$I^{+} = \int_{t_A}^{t_A + t_o} P(t) dt \qquad \text{Equation 2.4}$$

$$I^{-} = \int_{t_A + t_o}^{t_A + t_o + t_o^{-}} P(t) dt \qquad \text{Equation 2.5}$$

where P_{so} is the incident peak overpressure, t is the time, t_A is the arrival time of the shock front, t_o is the positive phase duration, t_o^- is the negative phase duration, and α is the blast waveform parameter.

Due to the logistical difficulties and high costs associated with conducting live blast testing on full-scale structures or structural components, it is often desired to carry out experiments using small amounts of explosives. The Hopkinson and Cranz scaling law, presented in Equation 2.6,

allows for scaling of various quantities of explosives at various distances. The scaled distance, *Z*, takes into consideration the weight of the detonated explosive charge, *W*, and the standoff distance, *R*, which is defined as the distance between the charge and the element exposed to the effects of the charge.

$$Z = \frac{R}{W^{1/3}} \qquad \text{Equation 2.6}$$

2.5.2 Dynamic Analysis for Blast

Blast events involve loading durations significantly smaller than those observed during earthquakes and wind loading. The interaction between the shockwave and the structure lasts only a fraction of a second, and generates inertial forces and kinetic energies that must be accounted for in analyses. Minimizing the computational costs while obtaining accurate results presents one of the main challenges in analytical blast research.

High-fidelity modelling techniques, such as finite element analysis (FEA), have been successfully used by researchers to describe and predict the behaviour of various structural elements subjected to blast loading (Jama, et al., 2009; Wu, et al., 2011; Crawford, 2013; Abladey and Braimah, 2014). Examples of the most commonly used FEA software include: ABAQUS (Dassault Systèmes Simulia Corp., 2014), Ansys Autodyn (Ansys, 2019), and LS-DYNA (LSTC, 2015). While developing FEA models using these tools allows for great versatility and flexibility in the material and loading inputs, such information may now be available in the case of blast analysis. Due to the uncertainty associated with such events, especially when characterizing the blast loading, designers typically resort to much simpler analysis, such as the equivalent single-degree-of-freedom (SDOF) method. Since its implementation, a vast number of official documents have been published outlining the methodology (e.g. PDC, 2008; Unified Facilities Criteria Program, 2008). The method consists of transforming an actual structure with distributed properties into an equivalent system, which can be described by a degree-of-freedom (DOF), consisting of a spring to describe the stiffness, and a lumped mass at the DOF. This is done through the use of a mathematically derived transformation factors, which take into account the actual load distribution, boundary conditions, and deflected shape (Biggs, 1964). The general equation for an equivalent SDOF system is shown in Equation 2.7.

$$K_{LM} m\ddot{u}(t) + c\dot{u}(t) + R(u,t) = P_R(t)A \qquad \text{Equation 2.7}$$

where K_{LM} is the load-mass factor, m is the total mass of the system, c is the damping coefficient, $R(u,t)$ is the resistance function of the system, $P_R(t)$ is the reflected pressure, A is the loaded area on which the reflected pressure is enacted, $\ddot{u}(t)$ is the acceleration of the system, and $\dot{u}(t)$ is the velocity of the system. SDOF analysis can be easily implemented and performed using a spreadsheet software, or through the use of available software, such as RCBlast (Jacques, 2014).

In blast analyses, it is often reasonable to neglect damping, due to the fact that the effect of damping on the maximum response is insignificant (Biggs, 1964; Jansson, 1992). Additionally, the resistance function is often used when employing equivalent SDOF analysis since there is no possibility of running the analysis with a negative stiffness, which is typical when softening of the system occurs (PDC, 2008).

One main limitation of SDOF is that it can only capture a single deflected shape, which is usually approximated by a quadratic or sinusoidal equation. Higher order vibrational modes are therefore not captured which can lead to erroneous and unconservative results, depending on the structure. Another limitation is that boundary conditions are typically idealized as being a combination of pinned, fixed, or free. Solutions which consider the case of semi-rigid connections have been published (e.g. Hadianfard and Shekari, 2018), however, these are typically in the form of rotational fixity and do not account for translational flexibility, nor for nonlinear behaviour of the end conditions. Additionally, SDOF models are generally developed for a single failure mode and are not able to capture other structural behaviours. Increasing the number of DOFs would inherently allow for higher order vibration and failure modes to be captured in the response. Additionally, the use of additional DOFs would allow for other system subcomponents to be considered in the analyses, such as end connections.

Whereas SDOF analysis comprises lumping the real structure into a single point of interest, multiple-degree-of-freedom (MDOF) analysis models the real structure as a series of nodal coordinates, each with assigned DOFs. Generally speaking, the higher the number of nodes used to model the structure, the better the approximations of the true dynamic behaviour (Clough and Penzien, 1991). The number of DOFs per node typically ranges from one to three, and are typically connected via massless elements, such as links, springs, and bars. In MDOF models, all member

displacements and/or rotations, masses, and dampers are presumed to be concentrated at the nodes. An example of a MDOF beam model is shown in Figure 2.9, where a cantilever beam is modelled using three beam segments and four discrete nodes, each with two DOFs; one translational and one rotational.

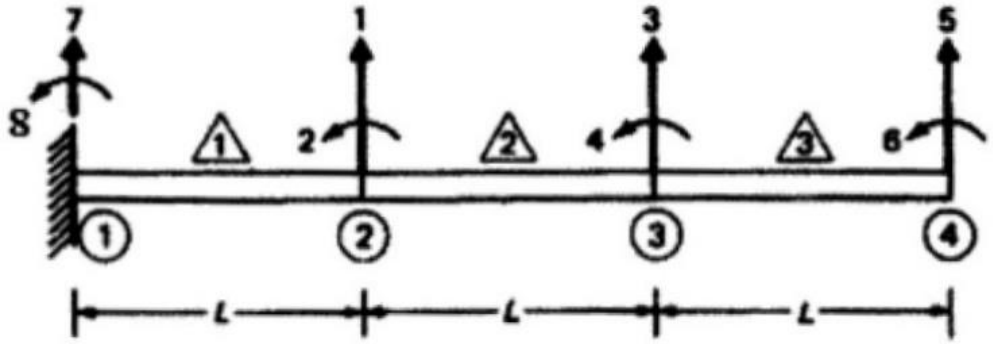


Figure 2.9: Cantilever Beam Discretized into Three Beam Elements (Paz and Leigh, 2006)

Due to the fact that each node requires its own equation of motion, the general equation of the entire system is written in matrix format, as shown in Equation 2.8.

$$[M]\ddot{\boldsymbol{u}} + [C]\dot{\boldsymbol{u}} + [K]\boldsymbol{u} = \boldsymbol{F} \qquad \text{Equation 2.8}$$

where [*M*], [*C*], and [*K*] are the mass, damping, and stiffness matrices of the structure, respectively, $\boldsymbol{F}$ is the force vector, and $\ddot{\boldsymbol{u}}$, $\dot{\boldsymbol{u}}$, and $\boldsymbol{u}$ are the acceleration, velocity, and displacement vectors, respectively. The three matrices are derived based on assumed displacement functions, which are widely available in published literature (Paz and Leigh, 2006; Logan, 2011). The force vector is defined by lumping the distributed force of the incoming blast load onto the discrete nodes, based on tributary area. Finally, the displacement, velocity, and acceleration vectors are the unknowns, which must be solved for each time step. Due to the high numbers of computations required, the use of computerized algorithms can significantly reduce computational time.

MDOF analysis has been successfully used by researchers to model various structural components subjected to blast loads (e.g. El-Dakhakhni, et al., 2009; Park and Krauthammer, 2009; Saatci and Vecchio, 2009; Nassr, et al., 2012; Guner, 2016; Xu, et al., 2017). In general, it was found that MDOF provided an accurate description of the response of structural elements subjected to blast loads, when compared to SDOF, which generally gave conservative predictions. It can therefore be concluded that MDOF can provide good balance between accuracy and computational efficacy when the need for additional DOFs is deemed required.

2.6 Behaviour of Timber Under Impact Loading

A significant portion of the available literature on the topic of high strain-rate effects in wood focused primarily on impact loading. Impact loading typically consists of the physical application of a high magnitude load over an extremely short time duration (e.g. a vehicle crashing into a bollard). Early research was typically conducted on defect-free (i.e. clear) wood specimens. It was later recognized that only full-size samples can be representative of the actual behaviour of timber specimens (Barrett and Lau, 1994).

One of the first studies on the topic of high strain-rate effects was conducted by Liska (1950), where the effects on the apparent compressive and flexural strength of clear wood specimens were investigated. The study reported an increase in the range of 10 % to 40 % in both of these parameters. These results were later corroborated by other studies, which reported a similar increase (Spencer, 1978; Neumann, et al., 2011). Nadeau, et al. (1982) studied the high strain-rate effects including the effects of variability in the sample batch. In order to compare the top and bottom percentile results, half of the test specimens were intentionally notched on the tension side in order to promote crack initiation and propagation. While the strain-rate of the test program was not as high as blast or impact loading, it was determined that only the un-notched specimens experienced an increase in strength (Nadeau, et al., 1982). A study by Jansson (1992) reported similar results, in which the effects of strain-rate was highly dependent on the quality of wood, and that dynamic strength increase was typically found in higher-quality lumber (Jansson, 1992). Whereas aforementioned studies were conducted with clear specimens, the study by Jansson (1992) was conducted with specimens representative of those found in construction. It was observed that specimens with knots and deflects would likely fail in flexural at the zone near the knot. As the time to failure decreased (i.e. the strain-rate increased), the failure modes would also shift from a crack-dependent failure to a brash failure.

Gilbertson and Bulleit (2013) investigated the applicability of Split-Hopkinson pressure bar (SHPB) testing on wood. The authors tested two wood species, one being a low-density soft wood, which is typical in construction. Testing was conducted at strain-rates varying from 70 to 340 s^{-1} along the longitudinal, tangential, and radial directions of the wood fibres. The authors reported a significant increase in compressive strength of the soft wood specimens, by at least a factor of two (Gilbertson and Bulleit, 2013). These results were corroborated by Wouts, et al. (2016), where the

authors again considered quantifying high strain-rate effects as a function of the direction of loading. While the increase in strength in both the longitudinal and transverse directions appeared to be linearly proportional with strain-rate, it was observed that the failure mode in the transverse direction was similar across all strain-rates, whereas it tended to change in the longitudinal direction (Wouts, et al., 2016).

2.7 Behaviour of Timber Elements and Assemblies Subjected to Blast Loading

2.7.1 Light-Frame Wood Stud Walls Subjected to Blast Loading

Blast loading differs from impact loading in terms of strain-rates and impulses enacted onto the structures. While impact loading is typically transmitted via physical media, blast loading involves pressures travelling through a medium, which can lead to complex interactions between the structures and the pressure waves (Braimah, 2013). Early research on the effect of blast loads on timber structures was conducted on model full-scale light-frame homes subjected to nuclear blasts (Kimbell and Fies, 1953; Randall, 1961). These tests were not representative of typical blast explosion, due to the enormous quantity of energy released, and focused rather on the overall behaviour of the structures. The main conclusion was that failure of these structures were heavily dependent on continuity in the systems, and was almost always initiated at the load-bearing studs, hangers, and connections.

Marchand (2002) conducted live-explosive testing on full-scale light-frame wood stud wall structures. The study focused on the overall behaviour of the structures and was limited to qualitative experimental results. Since no in-situ properties of the structural members were measured during testing, published data was used to obtain the strength and stiffness of the specimens in order to conduct a damage assessment in order to develop design provisions and response limits for wood structures (Oswald, 2005). Since then, more detailed holistic studies focusing on the quantification of behaviour and performance of components have been conducted.

Recent research effort at the University of Ottawa Shock Tube Test Facility investigated the behaviour of light-frame wood stud walls subjected to blast loading. Jacques, et al. (2014) conducted static and dynamic testing on thirty studs in isolation, in order to establish a dynamic increase factor (DIF) on the modulus of rupture and modulus of elasticity. The specimens were 8 ft. long visually graded spruce-pine-fir (SPF) 2 x 6 studs. In order to focus on the performance of

the material itself, idealized boundary conditions were used. Statistical analysis showed that while a DIF of 1.41 could be justified for the modulus of rupture, no increase in the modulus of elasticity could be substantiated. Lacroix and Doudak (2015) conducted testing on twenty typical full-scale light-frame stud walls using simply supported boundary conditions. The authors reported a DIF on the modulus of rupture and modulus of elasticity of 1.40 and 1.18, respectively. Observations of sheathing tearing at higher pressures prompted other studies to investigate possible retrofitting techniques for light-frame wood stud walls. Replacing the sheathing with corrugated metal panels and thicker plywood sheathing (Lacroix, et al., 2014), as well as the addition of welded wire mesh between the studs and the outer sheathing (Viau and Doudak, 2016b) showed promising results.

2.7.2 Glulam Subjected to Blast Loading

A study on the behaviour of glulam beams subjected to simulated blast loading was undertaken at the University of Ottawa Shock Tube Testing Facility (Lacroix and Doudak, 2018b). The authors tested a total of thirty-eight beams with three different cross-sections from two glulam manufacturers to destruction under static loading and simulated blast loading. The experimental tests and following analyses yielded a DIF of 1.14 for the strain-rate range of 0.14 to 0.51 s^{-1}, however, this was only applicable when the outer tension laminate of the glulam beam did not include a series of continuous or closely positioned finger joints (FJs) in the high moment region (Lacroix and Doudak, 2018b). When such a finger-joint pattern was present, the authors observed no increase due to high strain-rate effects. With this finding, the authors recommended that a DIF of unity be used if the absence of a continuous finger joint cannot be ensured. Additionally, the authors developed and validated a material predictive SDOF model using the appropriate DIFs.

In a subsequent study by the same authors, the effect of variable axial load on the dynamic response of glulam structural members subjected to combined lateral-blast and axial loading was developed and validated using experimental data for full-scale blast tests on beam and column specimens (Lacroix and Doudak, 2018a). The effect of varying axial load on the response of glulam columns to blast was also investigated. As shown in Figure 2.10, when compared to a failed beam specimen, the damage in the column tended to be more concentrated at the mid-span, with significantly more wrinkling in the fibres observed near the compression face (Lacroix and Doudak, 2018a).



(a) Typical Failed Beam Specimen (b) Typical Failed Column Specimen (c) Close-up of Column Specimen

Figure 2.10: Dynamic Failure Modes of Beams and Columns (Lacroix and Doudak, 2018a)

A SDOF model developed by the authors was capable of predicting the maximum displacement of the columns and time to maximum displacement with reasonable accuracy (Lacroix and Doudak, 2018a).

In an attempt to improve on the brittle failure mode observed in the glulam beams and columns, sixteen retrofitted glulam members of the same size tested statically and dynamically by Lacroix and Doudak (2018a) were investigated (Lacroix and Doudak, 2018c). The specimens were retrofitted with either carbon fibre-reinforced polymer (CFRP) or glass fibre-reinforced polymers (GFRP). Four different retrofit configurations were considered, including GFRP tension reinforcement with and without full-length confinement and U-shaped GFRP and CFRP tension reinforcement with partial-length confinement. Increases in resistance and maximum deflection in the range of 1.35 to 1.66 and 1.3 to 1.62, respectively, were obtained when FRP tension laminates with and without confinement were used. While these increases improved the capacity of the columns, it was deemed necessary to confine the tension laminates, in order to delay or prevent

premature debonding between the FRP and the specimen. An added benefit from the use of FRP was the reduction of debris throw, which previous studies on light-frame wood stud walls deemed problematic (Bogosian and Avanessian, 2004; Viau and Doudak, 2016b).

2.7.3 Cross-Laminated Timber Subjected to Blast Loading

The US Department of Defense (DoD) has recently used CLT as the construction material for the housing of its military personnel (WoodWorks, 2016). Facilities constructed for the DoD must be designed in accordance with UFC 4-010-01 (Unified Facilities Criteria Program, 2012). UFC 4-010-01 contains prescriptive detailing requirements and standoff distances for several types of construction that, if met, exempt designers from having to analyze the building for blast loads. As CLT construction is not addressed by UFC 4-010-01, recent research efforts have been undertaken in order to determine if CLT construction can indeed meet the prescriptive requirements of UFC 4-010-01. Early blast testing on CLT panels was conducted through the use of shock tube simulated blast loads (Lowak, 2015; Lowak, 2016). While the reports themselves are unpublished, it has been reported that a strength increase factor of 1.6, which encompasses both high strain-rate effects and converting design level stress levels to their mean values, was determined by comparing static and dynamic results (USACE, 2015). The authors developed a SDOF model using published design values, and it was found that applying a 0.70 factor on the stiffness would lead to reasonable deflection predictions. Two major limitations of this study include the fact that simply supported boundary conditions were used (USACE, 2015) and that the tested panels were never pushed significantly beyond their elastic limit, thus no post-peak behaviour was observed. To supplement the shock tube results, a series of live blast tests were also conducted (Weaver, et al., 2017). These full-scale structures had a 4.6 m^2 footprint and were two-story high, as shown in Figure 2.11.



Figure 2.11: CLT Structures Prior to Live Blast Testing (Weaver, et al., 2017)

The effect of boundary conditions was not investigated in-depth, as these were typically over-designed steel angles fixed to CLT floors and concrete slab. Weaver, et al. (2018) investigated the effects of axial loading on specimens with identical geometry and dimensions. It was observed that for the same charge quantity and standoff distance tested by Weaver, et al. (2017), the load-bearing CLT panels exhibited less observable damage than those without axial load. This finding is consistent with that observed by Lacroix and Doudak (2018a) for glulam columns subjected to blast loads.

Eighteen simply supported CLT panels were investigated in the shock tube facility and it was reported that a DIF of 1.28 on the resistance and no apparent increase in stiffness were observed (Poulin, et al., 2017). Two resistance material-predictive models that account for high strain-rate effects and the experimentally observed post-peak residual behaviour were developed. During dynamic testing, two predominant failure modes were observed, consisting of flexural failure and rolling shear failure (see Figure 2.12), whereas the governing failure mode observed during static testing was flexure (Poulin, et al., 2017).



(a) Flexural Failure (b) Rolling Shear Failure

Figure 2.12: Representative Failure Modes of 3-Ply CLT Panels (Poulin, et al., 2017)

2.8 Performance of Connections Under Blast Loading

2.8.1 Timber Connections Under High Strain-Rates

While several studies relating to steel connections under blast loads exist (e.g. Karns, et al., 2007; Morrill, et al., 2007; Crawford, et al., 2012; Stoddart, et al., 2014), little work has been done on timber connections subjected to blast loads.

One of the earliest studies regarding the effect of high strain-rates effects on timber connection is that by Girhammar and Andersson (1988), who investigated whether the capacity of nailed timber joints experienced any loading rate effect. The authors tested four timber joint configurations (shown in Figure 2.13) under deformation rates varying from 0.033 mm/sec to 1000 mm/sec. In two of the joint configurations, the load was applied in the parallel-to-grain direction, while the other two in the perpendicular-to-grain direction. Within each group (i.e. parallel and perpendicular), the two joints tested consisted of a thick and thin three-member joint, with all three members being wood-based. The thick joint configuration was chosen in order to promote a failure mode which includes combined wood crushing and nail yielding, whereas the thin joint

configuration was chosen in order to promote a pure wood crushing failure mode (Girhammar and Andersson, 1988). Common wire nails with diameters of 3.4 mm were used throughout testing, correlating to slenderness ratios (λ) of 10 and 5, for the thick member and thin member joints, respectively.

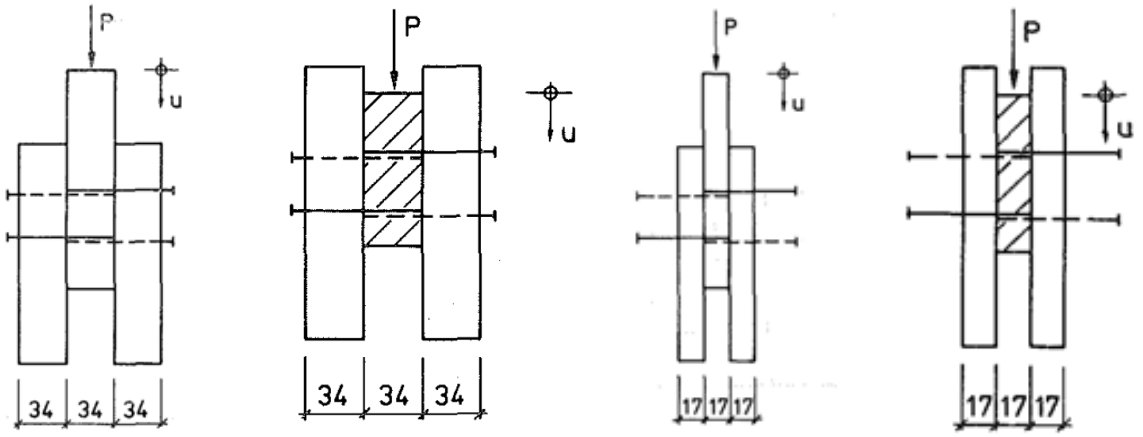


Figure 2.13: Tested Joint Configurations (Girhammar and Andersson, 1988)

The test results showed a proportional increase in the ultimate load capacity and a decrease in the total deformation capacity for all joint configurations as a function of strain-rate. The failure modes were consistent, with the thick member joints failing in combined bending and embedment failure, followed by a brittle splitting failure of the main member, and bearing failure for the thin member joints (Girhammar and Andersson, 1988). Embedment tests in both parallel and perpendicular-to-grain directions were also performed. For parallel-to-grain, the load-deformation relationship is nearly elastic-plastic for low deformation rates, and high deformation rates caused a rapid decrease in the load after maximum load was reached. For the perpendicular-to-grain embedment tests, the load-deformation relationship for all deformation rates was that of linear elastic followed by a reduction in stiffness. The ultimate embedment strength was found to increase as a function of the deformation rate. Tests on the nails themselves showed a slight increase in yield load; however, the authors noted that this increase was significantly lower than that occurring in the wood. On average, an increase in strength by a factor of 1.2, 1.16, and 1.3 were observed for the bearing strength of the wood, thick member joints, and thin member joints, respectively.

Similar tests on two-member nailed joints were conducted by Rosowsky and Reinhold (1999). A 10 mm thick piece of plywood was fastened to a 38 mm thick stud via 2.97 mm diameter power-driven nails. The loading rates varied from 0.0042 mm/sec to 420 mm/sec. When comparing the

mean failure loads, those for the lower rates of loading were comparable, whereas the mean failure load for the highest rate of loading was significantly lower than those observed for the lower rates of loading. The authors attributed this to the shift in failure mode, and concluded that no apparent strain-rate effects were found for such joints. The lack of evidence for strain-rate effects can likely be attributed to the premature failure of the joints, and the fact that the failure mechanisms of crushing of the wood and/or yielding of the nails, similar to that reported by Girhammar and Andersson (1988), could not develop.

A study by Daneff (1997) compared monotonic loading of bolted timber joints at two different loading rates; a slow rate (0.042 mm/sec) and a fast rate (25 mm/sec). The joints in question consisted of two-member wood joints and one ½ in. SAE Grade 2 bolt, correlating to a slenderness ratio of 3. Tests were performed in both parallel- and perpendicular-to-grain directions. In the parallel-to-grain direction, embedment failure in the wood was observed, along with some damage in the washers. Splitting was observed following embedment failure; however, this was more significant when the specimens were loaded at a fast rate. In the perpendicular-to-grain direction, major splitting for both loading rates was observed, with some embedment failure occurring in the side member running parallel to the loading direction. The author concluded that connections exposed to a fast rate of loading exhibit stiffer behaviour and attained higher yield loads than those exposed to a slow rate of loading (Daneff, 1997). The author also recommended that the effect of the slenderness ratio be studied.

2.8.2 Timber Connections Under Blast Loading

During the development of the *Vehicle Bomb Mitigation Guide* (Department of the Air Force, 2006), tests were conducted on coated structural lumber (CSL) and laminated strand lumber (LSL) in part for its use in the retrofitting of temporary shelters for USAF members during overseas operations (Parlin, et al., 2014). Full-scale live blast testing was conducted on CSL shelters where the predominant failure mode was established to be in the wall and roof-to-wall interface (Syron, et al., 2010). This was found to be due to the placement of the FRP reinforcement, which caused failure in the connection. A later study investigated the potential use of laminated-strand lumber (LSL) in order to retrofit the connection zone (Syron, 2010).

Viau and Doudak (2016a) investigated whether typical prescriptive code guidelines for light-frame would perform adequately under blast. Examples of the connections tested are shown in Figure

2.14. The authors concluded that the typical nailed connections, including those designed for high seismic regions, did not allow the studs to develop their full flexural capacity due to a premature failure, and thus resulting in hazardous debris. While significant damage in the joist hanger connections was observed, the studs were able to attain their ultimate flexural resistance. It was concluded that overdesigning the connections based on the stud capacity may not be adequate and that proper understanding of the failure mechanism of the connection must be investigated. Additionally, the authors acknowledged the limitations of SDOF analysis when analyzing the wall behaviour (Viau and Doudak, 2016a).



(a) Joist Hanger (b) Angle

Figure 2.14: Examples of Retrofitted Stud Wall End Connections (Viau and Doudak, 2016a)

An experimental study by Côté and Doudak (2019) investigated the effects of realistic boundary conditions on the behaviour of CLT walls when subjected to simulated out-of-plane blast loads. Simulated blast tests were conducted at the University of Ottawa Shock Tube Test Facility. Configurations with seismic detailing were considered, in order to evaluate whether existing structures that have adequate capacities to resist high seismic loads would also be capable of resisting a blast load while limiting the extent of damage. In addition, typical connections used in construction to resist gravity and lateral loads, as well as connections designed specifically to resist

a given blast load were investigated. The results indicated that the detailing of the connections appears to significantly affect the behaviour of the CLT walls. Self-tapping screws connecting the floor slab to the wall in end grain performed poorly and experienced brittle failure through splitting in the perpendicular-to-grain direction in the CLT. Angle connections, which do not generate perpendicular-to-grain stresses in the CLT, performed well with yielding in the fasteners and/or angle brackets occurring. Significant energy dissipation through yielding of the connections significantly reduced the energy transferred into the CLT panels. The study also concluded that using SDOF modelling in conjunction with the material models proposed by Poulin, et al. (2017) could not accurately capture the behaviour of the system.

Based on the experimental results from Weaver, et al. (2017), Sanborn (2018) investigated the applicability of various SDOF models which could consider the effects of the boundary conditions. Three cases were investigated, namely boundary conditions of pin-pin, fix-pin, and fix-fix. For the simply supported case, the model over-predicted the displacements, whereas it under-predicted the displacements for the fix-fix case. This demonstrates that a better understanding on the behaviour of the boundary conditions is necessary to accurately capture the behaviour. Additionally, while the SDOF model predictions were adequate for CLT panels which exhibited linear-elastic behaviour, the author noted that the models could not accurately predict the CLT panel response where these were loaded beyond their elastic limit (Sanborn, 2018). This is due to the author's use of a linear-elastic resistance curve for the CLT panels, which does not take any post-peak behaviour into consideration, as observed from laboratory results (Poulin, et al., 2017).

2.8.3 Blast Energy-Absorbing Connections and Systems

Whitney (1996) investigated the development of energy-absorbing supports for precast concrete panels using a shock tube. Quarter-, half-, and full-scale tests of the shock-absorbing systems were conducted for a range of pressures and impulses correlating to far-field blast explosions. Static testing was used to determine the best performing shapes, which was determined as being a hexagonal shape connector. The load-deflection relationship of the connector was found to be elastic-plastic, with the yielding plateau providing most of the energy dissipating capacities (Whitney, 1996). Since DIFs for steel typically vary between 1.0 and 1.1, the authors recommended a conservative value of 1.0 for the connector. SDOF analysis was conducted with all of the resistance assumed to be via the shock-absorbing connections, and the mass contribution

from the wall panel. The authors concluded that the use of these connectors is efficient in dissipating energies at high pressures, however, the overall system performance was dictated by the enacted impulse.

Lavarnway and Pollino (2015) investigated the use of various round hollow structural sections (HSS) to be used as sacrificial elements in a blast-resistant assembly. Static testing was performed on the connections, followed by an analytical evaluation using FEA for a wide range of blast scenarios, in order to determine the optimal geometry. The static experimental testing correlated well with the FEA results and verified that a round HSS would be capable of dissipating the energy imparted by a blast load, through the large deformations and strains imposed on the section during loading.

Building on energy dissipating steel connectors, researchers have also looked at filling these connectors with materials containing energy-absorbing properties, such as aluminum foam, honeycomb foam, and polystyrene (Bornstein and Ackland, 2013). One such study by Wang, et al. (2017) investigated the effects of filling two energy-absorbing connectors with two types of aluminum foams. The authors found that the performance of energy-absorbing connectors could be improved by filling aluminum foam and tweaking the geometry of the steel (Wang, et al., 2017). Using aluminum foam was shown to be the most efficient way in increasing the yield load. An additional benefit from the use of the aluminum was densification of the material, which correlated to an increase in load towards the end of the yielding plateau.

Oswald (2018) developed and tested precast concrete panels with steel energy-absorbing connectors with and without aluminum honeycomb inserts, similar to those tested by Whitney (1996). Shock tube testing was conducted on these assemblies with the varying parameters being the thickness of the panels. The author found that the use of energy-absorbing connectors resulted in reduced peak panel displacement and reaction force, in the ranges of 20 – 40 % and 25 – 40 %, respectively. These reductions were highest in the assemblies with thicker panels, due to the fact that the energy absorbed by the connectors was of a larger proportion than that absorbed by the flexural response of the panels (Oswald, 2018).

2.9 Summary

This chapter presented an overview of the knowledge base that currently exists on the behaviour of timber members and connections under static and short-term load duration, their associated advantages and shortcomings in terms of performance and ductility, as well as the current knowledge gaps.

Studies on the topic of blast loads on timber columns and panels generally conclude that timber experience high strain-rate effects, while research on the behaviour of timber connections is lacking. Very few studies have investigated the high strain-rate effects in the connections. This information is of great importance, mainly because connections have the potential to act as structural fuses during extreme loading, but the activation of such fuses depends on precise understanding of their behaviour. As such, investigating the behaviour of various connections in isolation both under static and dynamic loading is paramount.

The concept of using sacrificial building components in blast has been introduced, however, research combining these innovative approaches into heavy-timber structures is not yet explored. The current study aims to investigate the behaviour of various timber connections under simulated blast loads and develop innovative methods of energy dissipations with timber elements, including glulam and CLT.

Chapter 3 - Experimental Program

3.1 General

An experimental program was developed to investigate the response of cross-laminated timber (CLT) and glued-laminated timber (glulam) assemblies, with idealized and realistic boundary connections, subjected to simulated blast loading. The experimental program included the investigation of bearing type CLT connections (flexible and rigid angles), bolted connections used in glulam assemblies, as well as development and testing of energy-absorbing connections (EACs). The experimental program involved the testing of twenty-five static and dynamic connection-level tests in order to determine the properties of the connections. An overview of the connection-level specimens is presented in Table 3.1. In addition, fifteen full-scale CLT specimens and nineteen full-scale glulam specimens were tested under dynamic four-point bending. An overview, summarizing the full-scale specimens' length, end connections, and quantity of shock tube tests to which the specimen was subjected, is presented in Table 3.2.

Three CLT panels were tested with simply supported end conditions in order to characterize the dynamic behaviour of the panels prior to the implementation of end connections. Eight CLT assemblies were tested with typical bearing connection, with varying connection capacities and failure mechanisms. The remaining four CLT assemblies were tested with EACs. Two assemblies were subjected to a single pressure-impulse combination, for the purpose of assessing the energy input correlating to the onset of and flexural failure. Two other assemblies were each exposed to four pressure-impulse combinations of increasing magnitude, in order to investigate whether these panels exhibited loss of strength or stiffness, and to explore the replaceability of the EACs following a blast event. The first shot consisted of an elastic shot, where no damage occurred in both the panel and connections. The second shot consisted of a pressure-impulse combination which is expected to cause flexural failure of the CLT panel, had it been connected with idealized pinned boundary conditions. The third and fourth pressure-impulse combinations were chosen to progressively load the assembly until failure of the panel occurred. The yield load for the EACs varied in order to investigate the effect of various levels of energy dissipation in the connections.

Three glulam beams were tested with simply supported end conditions in order to characterize the dynamic behaviour of the beams prior to the implementation of end connections. Eleven glulam

specimens were tested with bolted connections. These connections consisted of two, four, and six bolts per end, representing a range of connection capacities relative to the beam capacity. The geometry of the bolted connections varied in order to investigate the suitability of code design equations to prevent brittle failure modes (i.e. splitting). This was done by progressively increasing the unloaded edge distance (see Figure 2.5) until splitting governed the overall behaviour of the assembly. These tested bolt configurations were then replicated with the addition of self-tapping screws (STS) in order to investigate their potential in reinforcing the bolted joints against splitting. The remaining five glulam beams were tested with EACs of varying depths, including 7.5”, 5.0”, and 3.75”, representing overdesigned, optimized, and underdesigned EACs for the glulam specimens, respectively. One such specimen equipped with optimized EACs was subjected to a total of seven pressure-impulse combinations of increasing magnitudes until flexural failure of the beam was reached. This was done to investigate whether the beams exhibited loss of strength or stiffness following elastic behaviour, and also to investigate the potential of the EACs to be replaced following a blast event.

Table 3.1: Summary of Test Matrix for Connection-Level Specimens

Specimen Type	Loading Regime	Specimen	Connections Detail
CLT	Static	C1	1 ML24Z Angle (no axial restraint)
		C2	
		C3	
		C4	Thick Angle (6 Screws)
		C5	
		C6	
	Dynamic	C7	1 ML24Z Angle (no axial restraint)
		C8	
		C9	1 ML24Z Angle (axial restraint)
		C10	
		C11	
		C12	2 ML24Z Angle (no axial restraint)
		C13	
		C14	Thick Angle (3 Screws)
		C15	Thick Angle (6 Screws)
		C16	Thick Angle (9 Screws)
Glulam	Static	SB1	1 x 12.7 mm ASTM A307 Bolt 6.4 mm Steel Side Plates 137 mm Wide Glulam Member
		SB2	
		SB3	
EAC		EAC1	7/8” Deep EAC
		EAC2	
		EAC3	
		EAC4	
		EAC5	
		EAC6	

Table 3.2: Summary of Test Matrix for Dynamic Full-Scale Specimens

Specimen Type	Specimen	Specimen Length (m)	End Connections	Number of Tests
CLT	CLT1	2.500	Simply Supported	1
	CLT2	2.500	Simply Supported	1
	CLT3	2.500	Simply Supported	1
	CLT4	2.083	Thick Angle (3 Screws)	1
	CLT5	2.083	Thick Angle (6 Screws)	1
	CLT6	2.083	Thick Angle (9 Screws)	1
	CLT7	2.083	2 ML24Z	1
	CLT8	2.083	3 ML24Z	1
	CLT9	2.083	4 ML24Z	1
	CLT10	2.083	2 ML24Z	1
	CLT11	2.083	3 ML24Z	1
	CLT12	2.083	3.25” Deep EACs	1
	CLT13	2.083	3.25” Deep EACs	1
	CLT14	2.083	3.25” Deep EACs	4
	CLT15	2.083	2.5” Deep EACs	4
Glulam	G1	2.500	Simply Supported	1
	G2	2.500	Simply Supported	1
	G3	2.500	Simply Supported	1
	G4	2.388	B1	1
	G5	2.388	B1	1
	G6	2.388	B2	1
	G7	2.388	B3	1
	G8	2.388	B4	1
	G9	2.388	B5	1
	G10	2.388	B6	1
	G11	2.388	B7	1
	G12	2.388	B8	1
	G13	2.388	B9	1
	G14	2.388	B10	1
	G15	2.500	7.5” Deep EACs	2
	G16	2.500	5.0” Deep EACs	7
	G17	2.500	5.0” Deep EACs	1
	G18	2.500	3.75” Deep EACs	1
	G19	2.500	3.75” Deep EACs	2

3.2 Description of Test Specimens and Connections

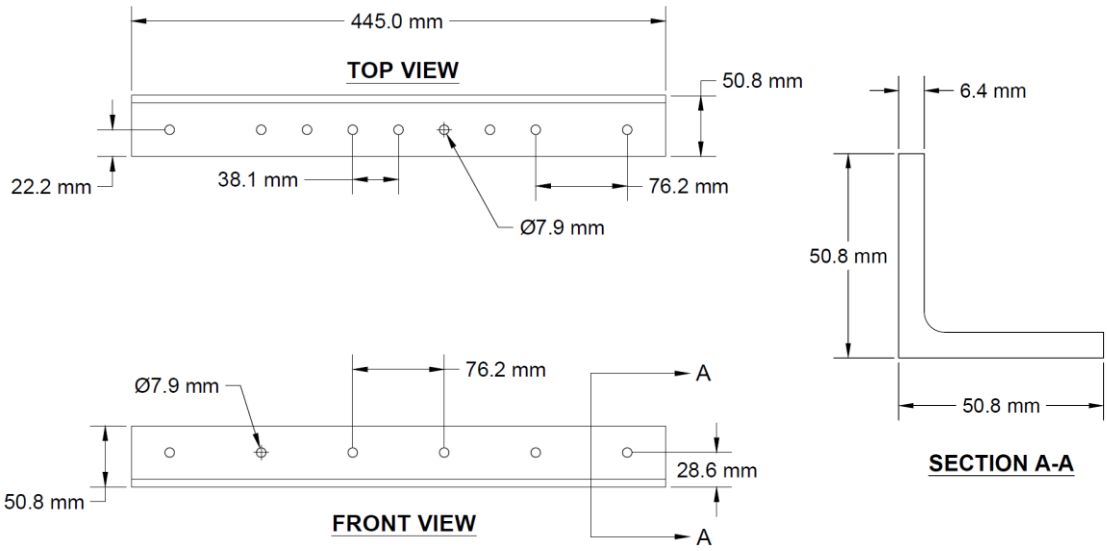
The CLT specimens were obtained from *Nordic Structures*, and consisted of 445 mm wide by 175 mm deep E1 grade panels. The panels consisted of five 35 mm thick laminates and were manufactured in accordance with ANSI/APA PRG 320 (ANSI/APA, 2012). The glulam specimens were also obtained from *Nordic Structures*, and consisted of 137 mm wide by 267 mm deep 24F-1.9E grade spruce-pine-fir members.

3.2.1 CLT Bearing Connections and Specimens

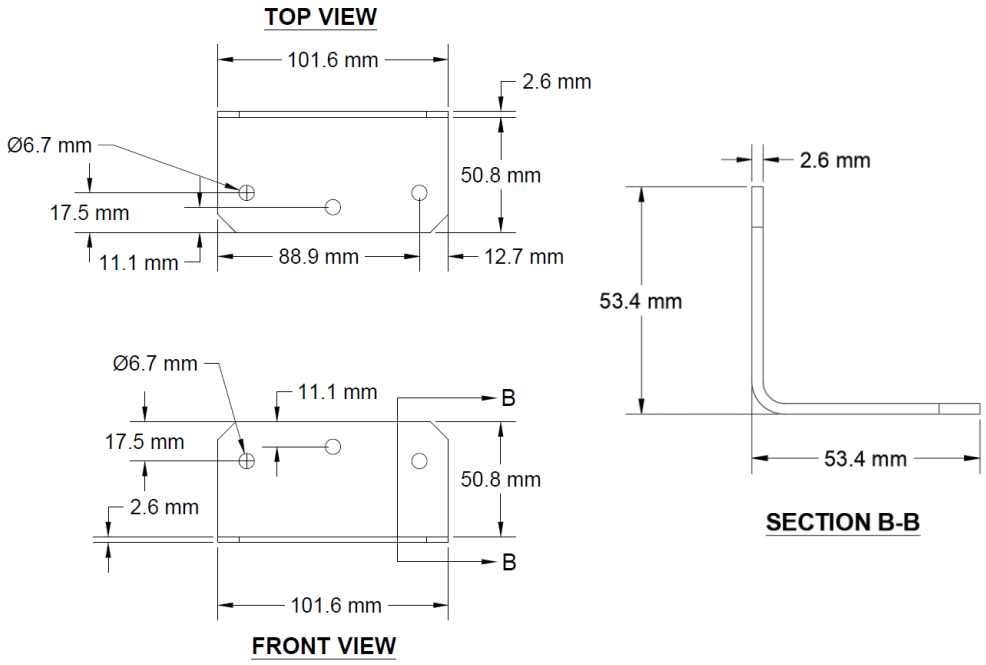
Two types of CLT bearing connections were investigated in the current study, namely a ML24Z angle produced by *Simpson Strong-Tie*, and a manufactured thick angle, as shown in Figure 3.1. Both connections were fastened using *Heco-Topix Tellerkopf* screws, with the quantity of screws depending on the type of connection and required connection capacity. Shown in Table 3.3 are the details for both connections tested. For connections consisting of the ML24Z angles, the designed capacities of the connections were selected by adding or removing angle brackets, each consisting of three screws. For connections with the manufactured thick angle, the design capacity was established by varying the number of screws used in the connection. To maintain a balanced load distribution in the screws, the number of screws was selected to be three, six, or nine screws. Two blocks cut from undamaged CLT panels were connected to the ends of the tested panel, thus simulating the in-plane stiffness of the floor diaphragms above and below a CLT wall panel. Examples of connection-level (thick angle with six screws) and full-scale (three ML24Z angles) specimens are shown in Figure 3.2a and Figure 3.2b, respectively. Each CLT specimen was instrumented on both faces with strain gauges at the mid-span of the panel, in order to measure the compressive and tensile strain in the wood.

Table 3.3: CLT Bearing Connection Details

Connection	**Angle Dimensions**			**Heco-Topix Tellerkopf Dimensions**		
	Width (mm)	Height & Depth (mm)	Thickness (mm)	Total Length (mm)	Threaded Length (mm)	Diameter (mm)
ML24Z	101.6	53.4	2.6	120	100	8.0
Thick Angle	445.0	50.8	6.4			



(a) Sketch of Thick Angle

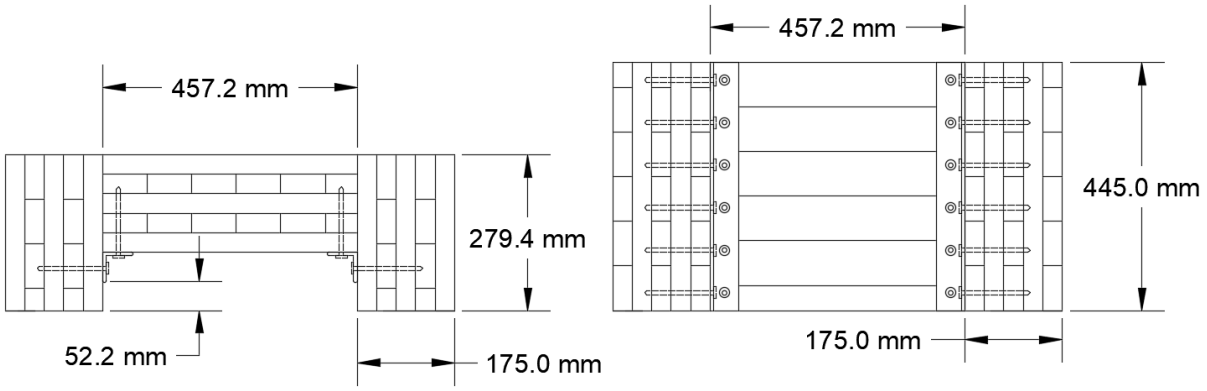


(b) Sketch of ML24Z Angle

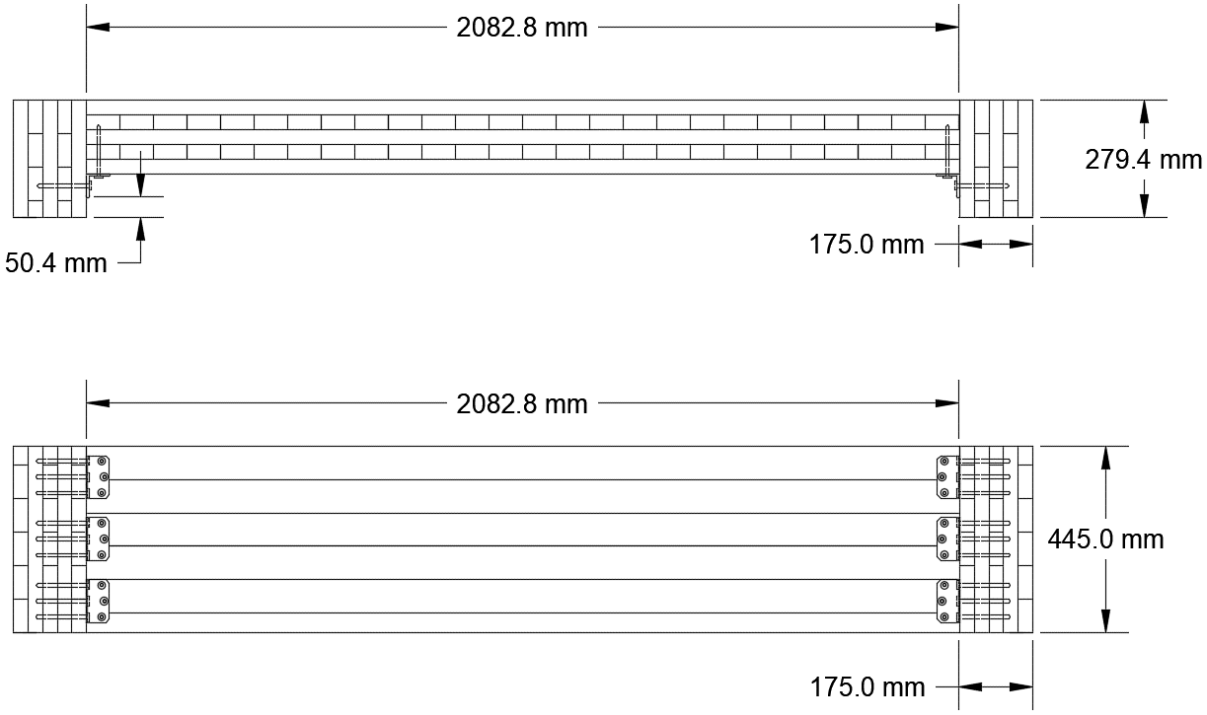


(c) Thick Angle (left) and ML24Z Angle (right)

Figure 3.1: CLT Bearing Connections



(a) Connection-Level CLT Specimen with Thick Angles



(b) Full-Scale CLT Specimen with ML24Z Angles

Figure 3.2: Examples of Connection-Level and Full-Scale CLT Specimens

3.2.2 Bolted Glulam Connections and Specimens

The bolted connections investigated throughout this research program consisted of 12.7 mm diameter 203.2 mm long ASTM A307 bolts within a steel-wood-steel connection with 6.4 mm thick steel side plates. In order to promote bolt yielding, wood crushing, and an overall ductile failure mode, a bolt slenderness ratio of $\lambda = 10.8$ was maintained throughout testing. This approach of using slender bolts is based on the requirements outlined in Eurocode 8 (CEN, 2004a), used to promote ductile behaviour in the bolted connections under seismic loading. Ten bolted connections were investigated, as summarized in Table 3.4.

Table 3.4: Bolted Glulam Connection Details

Connection Configuration	n_{rows}	$n_{columns}$	Unloaded End Distance (mm)	Row Spacing (mm)	Spacing of Fasteners in a Row (mm)	Unloaded Edge Distance (mm)	n_{screws}
B1	2	1	50.8	50.8	N/A	19.1	None
B2						38.1	
B3						76.2	
B4						133.5	
B5						203.2	
B6						76.2	3
B7						133.5	6
B8						203.2	9
B9		2			50.8	19.1	None
B10		3					None

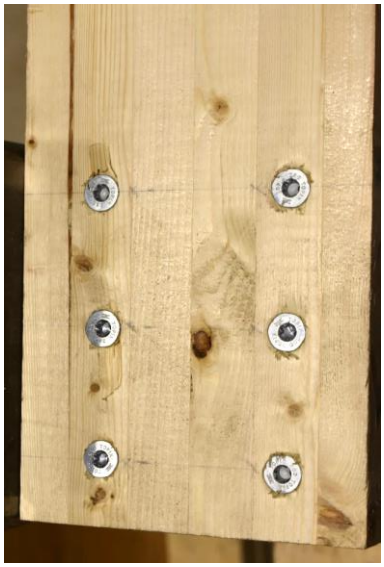
For all bolted connections, the connection geometry met the requirements outlined in CSA O86 (CSA, 2019) for the placement of bolts and dowels in a connection loaded perpendicular-to-grain (see Figure 2.5). The unloaded edge distance, critical when designing against splitting, was varied from a code minimum of 19.1 mm to a maximum of 203.2 mm. This variation would allow for the validation of the current code splitting equation (CSA, 2019), and for the investigation into the capability for self-tapping screws to be used as reinforcement to delay or prevent splitting failure expected in some of the specimens (i.e. B3 – B5). The reinforcement of bolted connections against splitting was accomplished using 8.0 mm diameter *Heco-Topix Countersunk Head* screws, which had a total and threaded length of 260 mm and 252 mm, respectively. The quantity of reinforcing screws was based on the connection geometry and required connection capacity, and was determined based on manufacturer guidelines (Closen, 2014; ETA, 2016). The reinforced connections are shown in Figure 3.3.



(a) Reinforcing Screws with Hand Drill



(b) Connection B6



(c) Connection B7



(d) Connection B8

Figure 3.3: Bolted Connection Reinforcements

The bolt holes were made using a drill press equipped with *Wood Owl* auger bits, as shown in Figure 3.4a. Proper care was taken when positioning the specimen in the drill press in order to minimize deviations in the bolt holes and ensure proper alignment. The side plates were manufactured from two 152x76x6.4 rectangular HSS. The preconceived bolt configurations were drilled through both HSS section walls using computer numerical control (CNC) machining. Afterwards, a plasma cutter was used to split these sections lengthwise in order to create two pairs of side plates with matching bolt holes. The steel side plates were then installed into the glulam beam, as shown in Figure 3.4b.



(a) Drilling Bolt Holes into Glulam Specimen



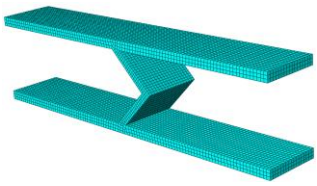
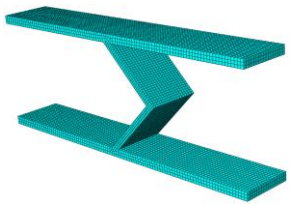
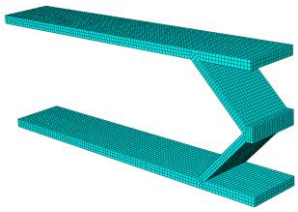
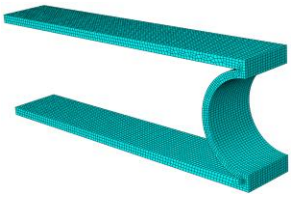
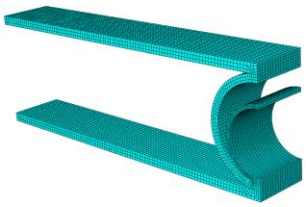
(b) Installation of Bolts and Steel Side Plates

Figure 3.4: Full-Scale Glulam Specimen with Bolted Connections

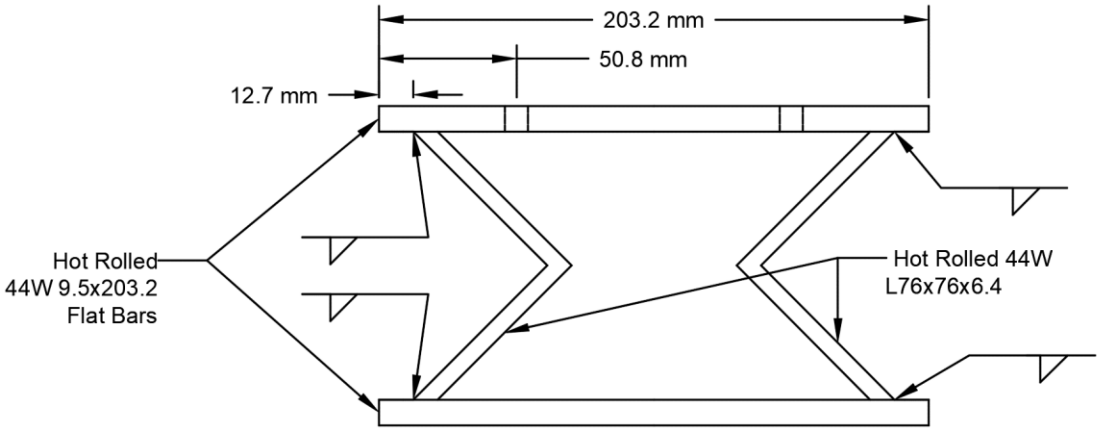
3.2.3 Energy-Absorbing Connections

Various shapes and failure mechanisms were investigated in order to arrive to an optimal energy-absorbing connection (EAC) for the purpose of its implementation within a timber assembly. The work on this connection was conducted synchronously with another study at the University of Ottawa with the aim to investigate several EAC shapes, as shown in Table 3.5. The most suitable configuration from Table 3.5 was selected for the current study based on the shape of the force-displacement curve as well as consistency in performance and repeatability in the results. Emphasis in evaluating the behaviour was put on three important parameters, namely the yield strength, length and slope of the yield plateau, and the total energy dissipated by the connection. The yield strength and the length of the yield plateau can be controlled by changing the thickness and size of the steel sections, respectively.

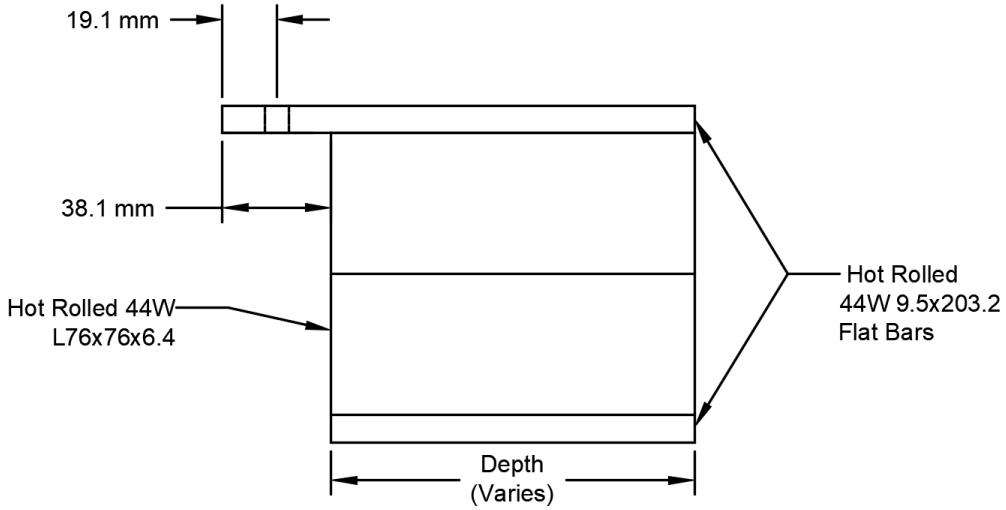
Table 3.5: Summary of Preliminary Analytical Modelling for EACs

Configuration	ABAQUS Modelling Sketches	Parameters Investigated
Double L-Sections		Section thickness Section size Welded or separated sections
		
		
Circular Sections		Section thickness Section diameter Multiple circular sections
		

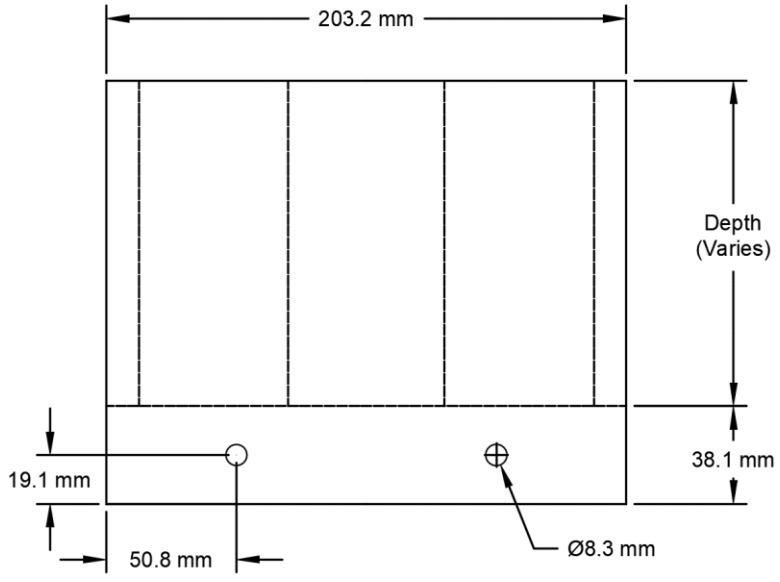
The ease of controlling the yield strength allowed for the customization of the EAC relative to the load-bearing member behaviour. Based on this investigation, the final prototype consisted of two L76x76x6.4 hot-rolled CSA G40.21 44W/300W (CSA, 2013) steel sections welded symmetrically to 9.5 mm thick hot-rolled steel plates of the same steel grade at their top and bottom edges, as shown in Figure 3.5. The EACs were connected to the timber element using the same *Heco-Topix Tellerkopf* screws described in the previous section. The depth of the EACs varied from 63.5 mm to 190.5 mm, depending on the capacity of the timber member to which it would be connected, as well as the desired overstrength safety factor.



(a) Front View



(b) Side View



(c) Top View

Figure 3.5: Energy-Absorbing Connections

3.3 Material Characterization of Glulam and CLT Members

Prior to subjecting the CLT and glulam timber members to dynamic testing, their in-situ density and moisture content were determined. A *Tramex Moisture Encounter Plus* pinless moisture meter (Figure 3.6) was used to measure the moisture content of the timber members at the time of testing. The in-situ density of each dynamic test specimen was determined by measuring their respective volume and weight. This was done in conformance with ASTM D2395 (ASTM, 2017b), specifically using Test Method G for obtaining the density of full-size members.



(a) Moisture Meter (b) Obtaining Readings Prior to Testing

Figure 3.6: Moisture Content Measuring Equipment

3.4 Static Connection-Level Testing of CLT Bearing Connections

Static connection-level tests were performed on CLT panels fastened to CLT blocks of the same width (445 mm) and length of 457.2 mm in order to establish the load-displacement relationship of each joint in isolation. This data was used to quantify high strain-rate effects in these connections. Static testing was performed in conformance with ASTM D7147 (ASTM, 2011), as shown in Figure 3.7.

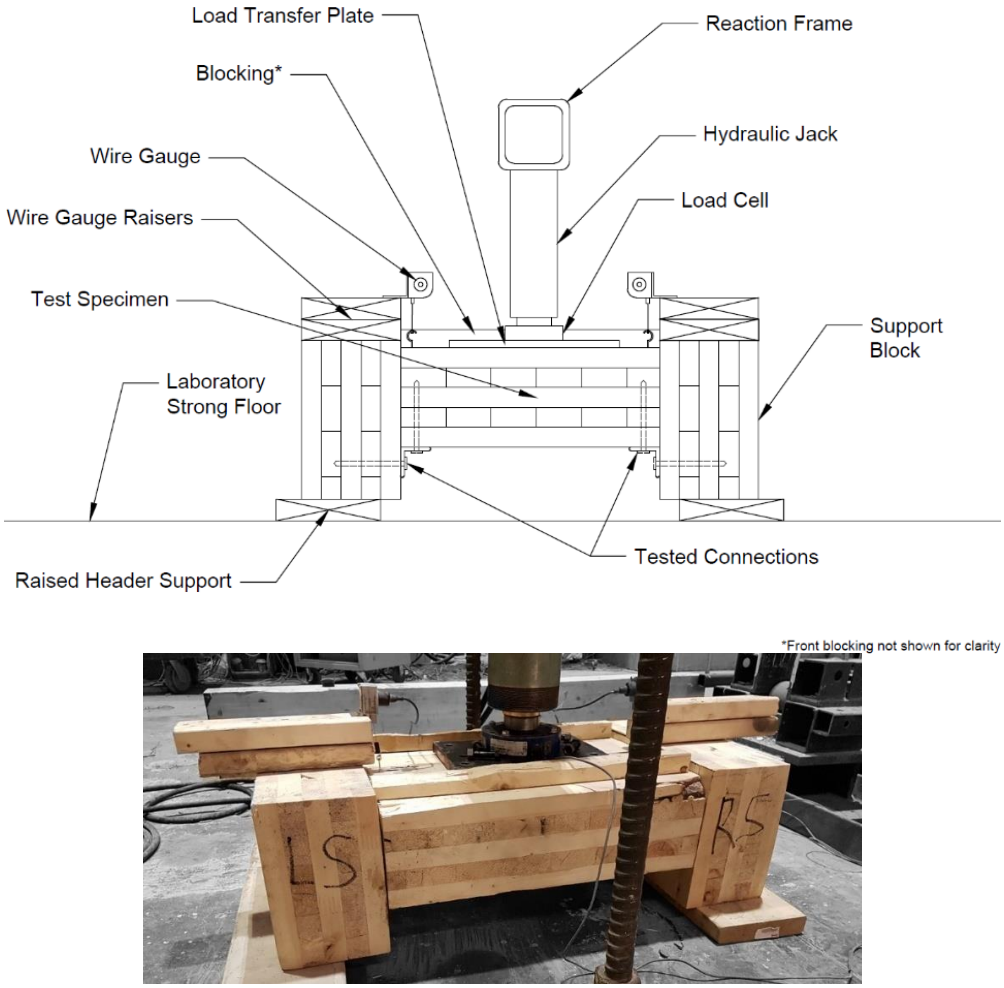


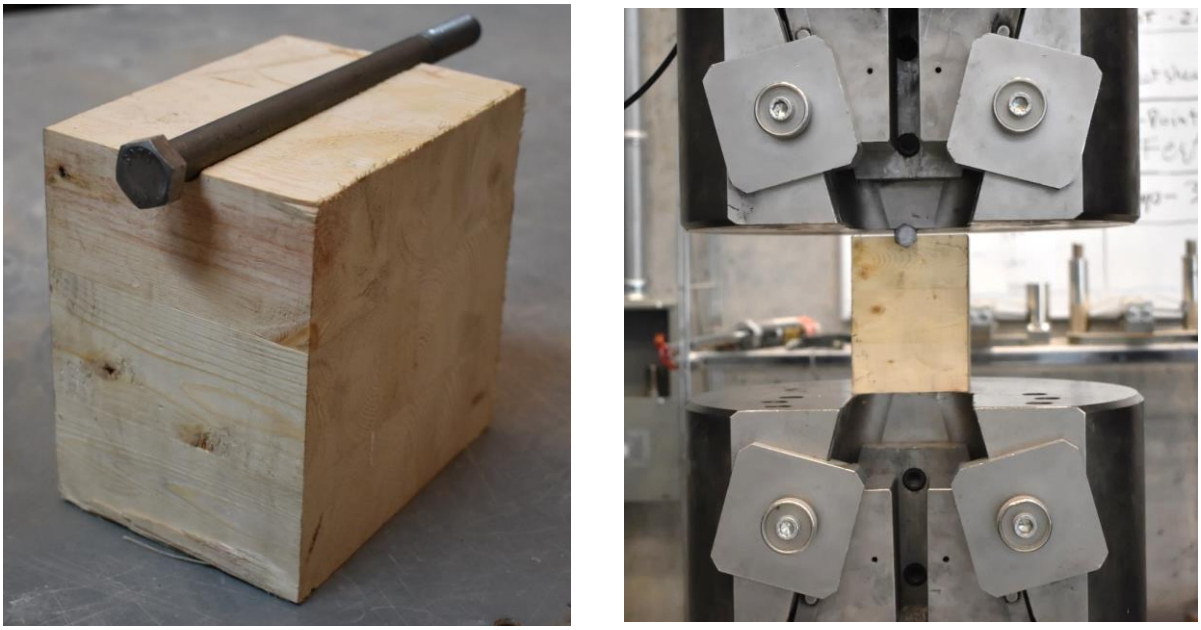
Figure 3.7: Static Connection-Level Test Setup for CLT Bearing Connections

A load cell located at the load application point was used to measure the applied load. Static testing of the connection-level specimens was performed until failure of one of the two joints. The loading rate was such that failure of the joint would occur within five to ten minutes. During the static tests, a data acquisition system (DAS) was used to collect the data at a sampling rate of 10 samples per second. The vertical joint displacements were measured using two wire gauges, each connected to the ends of the intermediate CLT panel.

3.5 Static Connection-Level Testing of Bolted Glulam Connections

3.5.1 Embedment Strength Tests

The embedment strength of ten 12.7 mm diameter bolts was determined using a universal testing machine (UTM) based on ASTM D5764 (ASTM, 2018), as shown in Figure 3.8. For each test, a loading rate of 2 mm/min was used. The joint load and displacement were measured and recorded at a sampling rate of 20 samples per second. The tests were conducted until the joint displacement reached one half of the bolt diameter.



(a) Typical Specimen (b) Test Setup

Figure 3.8: Embedment Strength Test Setup

3.5.2 Bolt Bending Tests

Ten representative 12.7 mm diameter ASTM A307 bolts measuring 203.2 mm in length were subjected to bending tests based on ASTM F1575 (ASTM, 2017a), in order to determine their yield moment. This data would be used to obtain the bolt yield stress, a parameter used in the European Yield Model (EYM) (CSA, 2019). As shown in Figure 3.9, a point load was applied at the centre of the bolt, which had a clear span of 152 mm. A loading rate of 4 mm/min was used. The applied load and bolt displacement were recorded at a sampling rate of 20 samples per second.

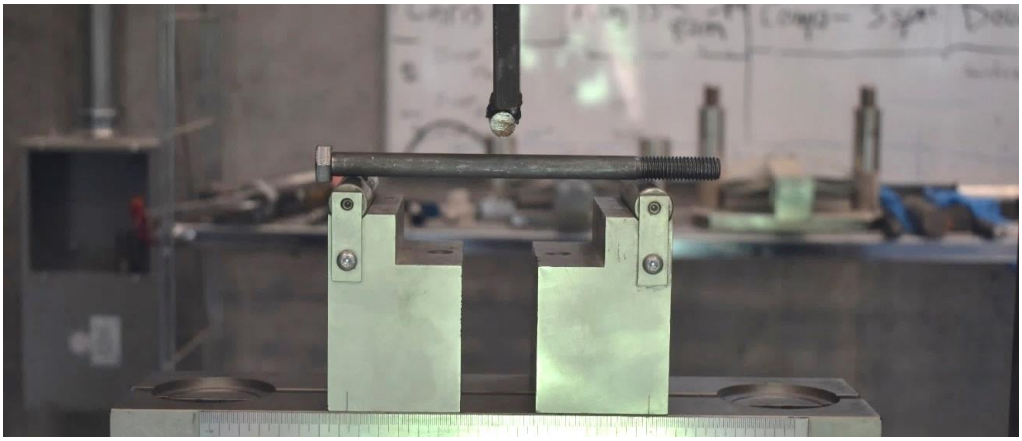


Figure 3.9: Bolt Bending Test Setup

3.5.3 Single-Bolt Joint Tests

The load-displacement relationship of three single-bolt connections, consisting of 12.7 mm diameter bolt in a steel-wood-steel connection identical to those implemented within the full-scale test specimens, was obtained based testing conducted in accordance with ASTM D5652 (ASTM, 2015). As shown in Figure 3.10, the wood portion of the bolted connection was supported directly on the UTM platform, while both steel side plates were loaded at a rate of 4 mm/min. The applied load and joint slip were measured and recorded at a sampling rate of 20 samples per second. A load cell was used to obtain the force reading, while the displacement was recorded using linear variable differential transducers (LVDTs) (not shown in Figure 3.10). The tests were conducted until fracturing of the bolt occurred. These results will be used as inputs in the analytical model.



Figure 3.10: Single-Bolt Joint Test Setup

3.6 Static Connection-Level Testing of Energy-Absorbing Connections

A total of six energy-absorbing connections (EACs) were tested in compression in order to obtain their load-displacement relationship. The obtained results from these connection-level tests were used for the full-scale test EACs by normalizing the data and adjusting for the depths. As shown in Figure 3.11, the EACs were compressed between the top and bottom UTM platforms, at a loading rate of 10 mm/min. This loading rate was chosen in order to reach the final state within ten minutes, but no less than five minutes, in conformance with similar test procedures (e.g. ASTM, 2011; ASTM, 2015). The applied load and EAC displacement were measured and recorded at a sampling rate of 20 samples per second. The tests were conducted until the top and bottom EAC bearing plates came into contact, whereby the test was terminated once the densification reached a load that is roughly twice that of the yield load.

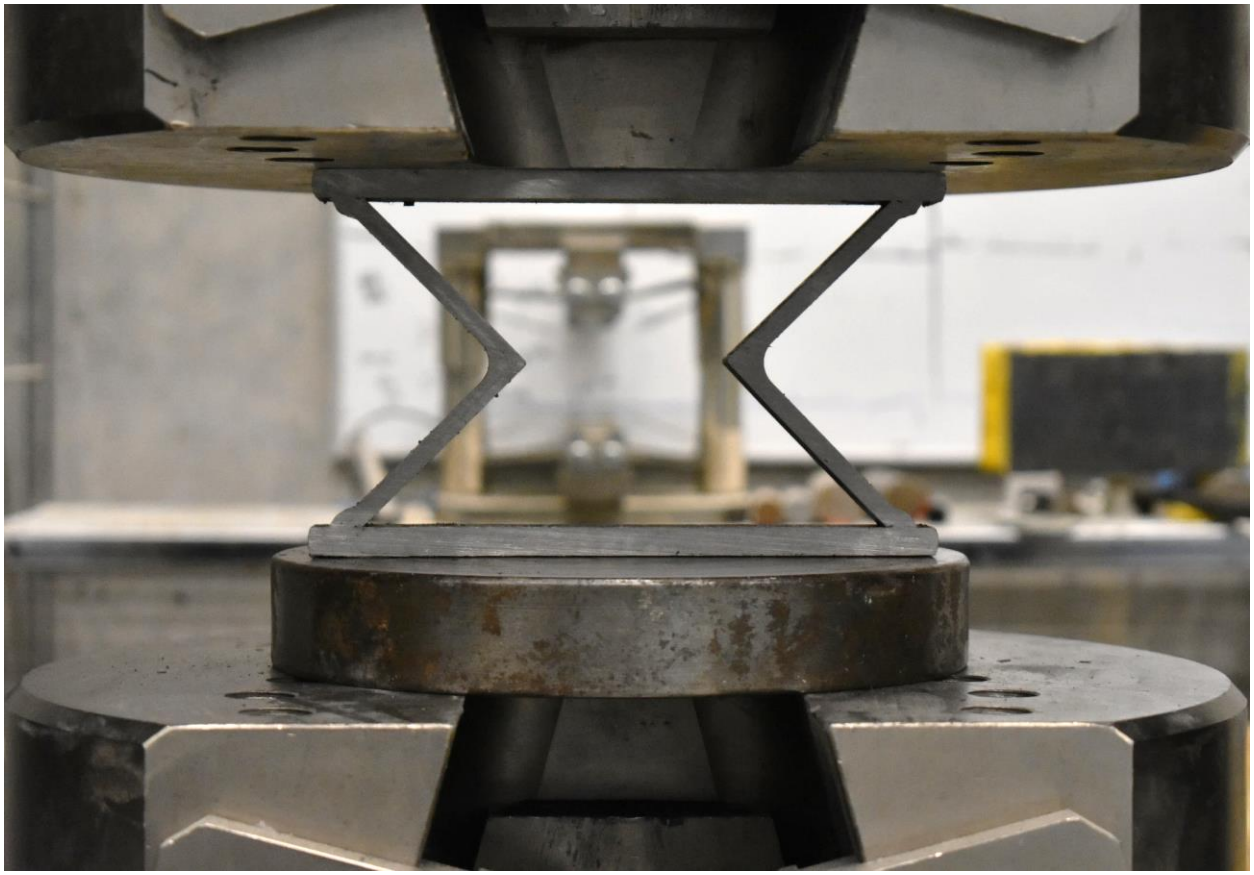


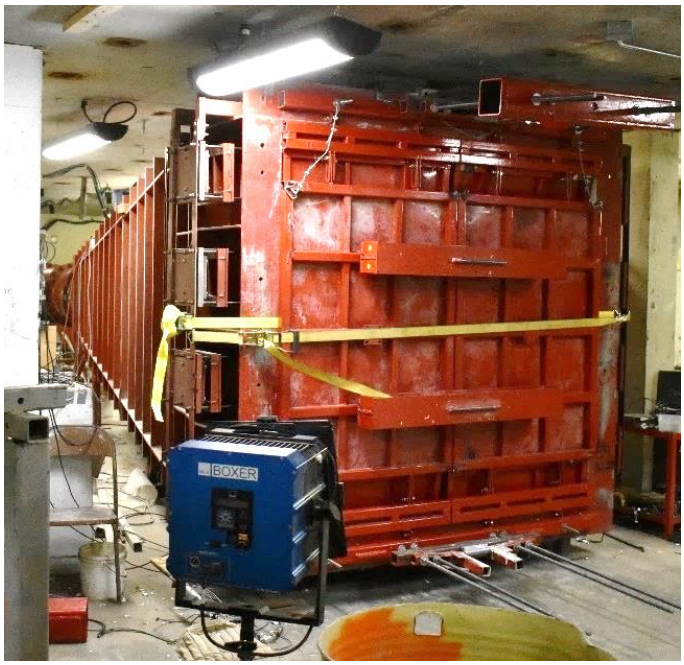
Figure 3.11: EAC Static Test Setup

3.7 Dynamic Testing

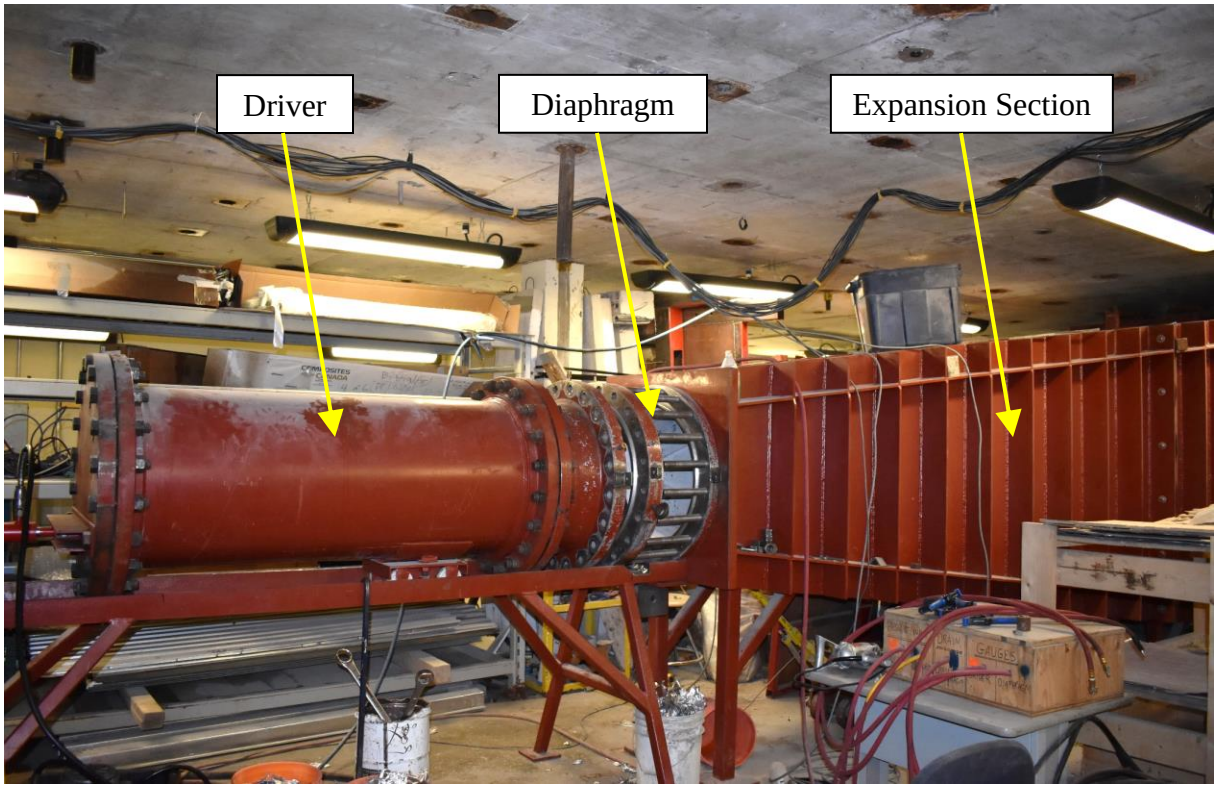
The dynamic testing was performed using the University of Ottawa Shock Tube, a test apparatus capable of producing high strain-rates similar to those observed during far-field blast explosions. The shock tube consists of three main components: the driver section, the diaphragm section, and the expansion section. The mechanism used in the tests is referred to as a double diaphragm firing system, where sheets of aluminum foils are used to separate the three sections. The thicknesses and quantity of aluminum foils are predetermined and depend on the pressure-impulse combination for which the specimen is to be subjected. The peak reflected pressure is controlled by the driver pressure while the peak reflected impulse is controlled by the driver length. The driver length can be adjusted in 305 mm increments from 305 mm (1 ft.) to 5185 mm (17 ft.). Upon the installation of the desired driver length and aluminum foils, compressed air is introduced into the driver and diaphragm section. When the desired driver pressure is attained, the diaphragm is drained (i.e. air is allowed to escape through a control nozzle) until the aluminum foils separating the driver and diaphragm rupture. This subsequently ruptures the other set of foils separating the diaphragm and the expansion section, allowing for the release of the compressed air. This creates a shockwave that travels down the 6096 mm (20 ft.) long expansion section, where it eventually comes into contact with the test specimen. The opening of the expansion section measures 2032 mm x 2032 mm (80 in. x 80 in.), which allows for testing of large- to full-scale specimens. The shock tube is capable of generating positive reflected pressures and impulses up to 100 kPa and 2200 kPa-ms, respectively. Depending on driver pressure and length, the positive phase of the blast wave can vary from 5 ms to 70 ms. A load-transfer device (LTD) was used to collect the pressure generated by the shock tube and transfer it to the test specimen. The LTD consisted of rigid steel panels covering the entire opening of the end frame and was capable of moving freely in the lateral direction up to deflections of 200 mm through the use of slotted hinges. The loading pattern can be chosen as a concentrated point load at mid-span, which was utilized in the connection-level connection tests, or four-point bending capable of transferring the loads as two concentrated point loads at the third spans of the full-scale specimens. The LTD, as well as the overall shock tube apparatus, is shown in Figure 3.12.



(a) Front View – One Point Load



(b) Front View – Two Point Loads



(c) Rear View

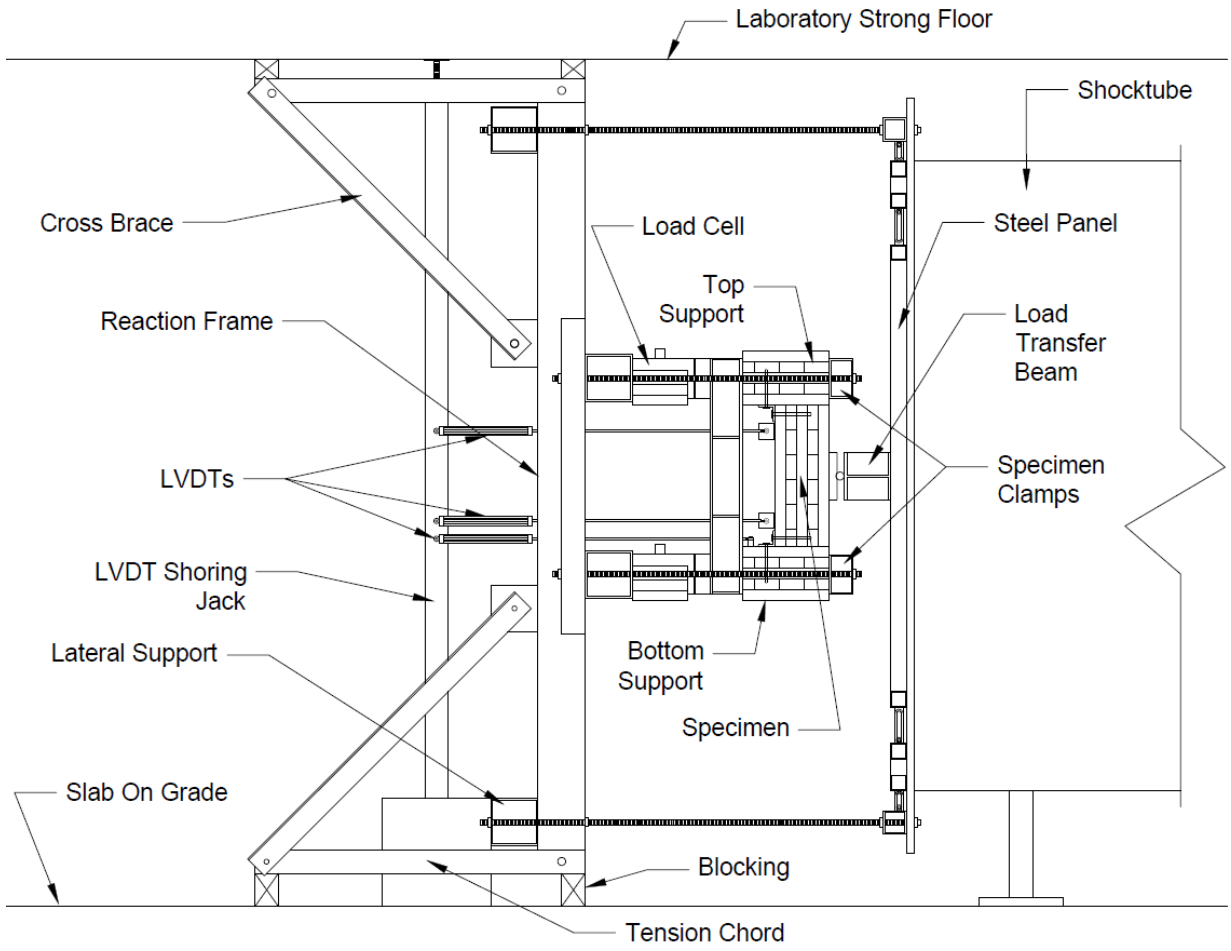
Figure 3.12: Shock Tube Test Apparatus

3.7.1 Description of Test Setups

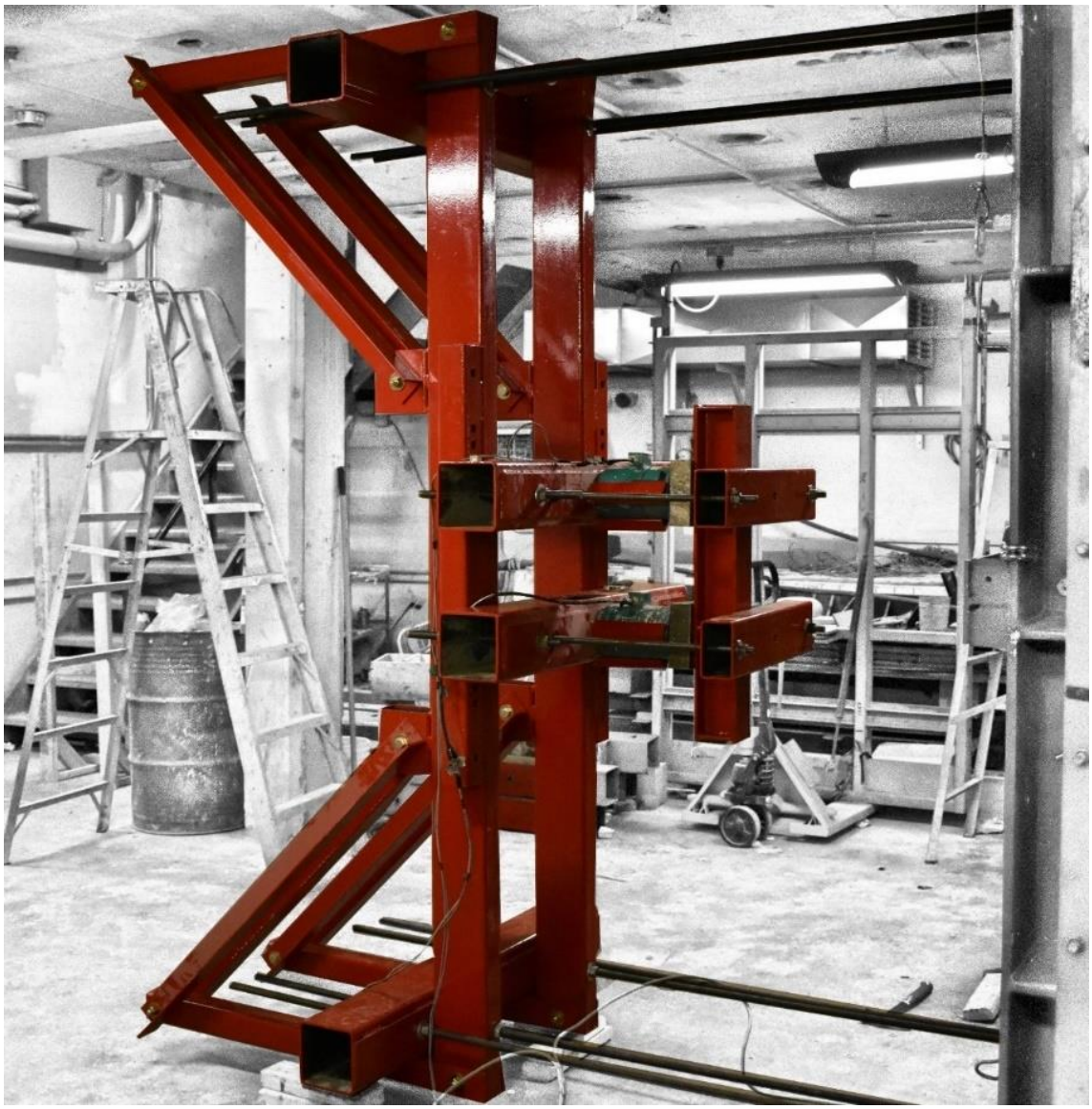
This section describes the test setups for the connection-level and full-scale specimens subjected to blast loading using the shock tube. Four kinds of test setups were used due to the different specimen geometries and end conditions.

3.7.1.1 Connection-Level Test Setup

For the connection-level tests, a load-transfer-device (LTD) with a single load transfer beam positioned at mid-span (see Figure 3.12a) was used to convert the reflected pressure into a concentrated point load applied directly on the specimen. A vertical reaction frame utilizing a combination of flexural and truss elements was designed and constructed to support the connection specimens, as shown in Figure 3.13. In both static and dynamic connection-level tests, identical spans and loading pattern were used in order to facilitate direct comparisons of the results obtained from the two loading types.



(a) Side Sketch



(b) Frontal View Without Specimen

Figure 3.13: Dynamic Connection-Level Test Setup

Conducting experimental research usually entails introducing simplifications that may cause deviation from reality but that makes the behaviour easier to interpret and model. One such idealization is whether to restrain the vertical movement of the supporting blocks under the deformation of the boundary connections. The study by Côté and Doudak (2019) showed that due to deformation in the ML24Z angles, uplift in the support elements was observed. Although noted in the study, no attempt was made to quantify the effect of a potential axial restraint developed due to gravity loads. This effect was investigated in the current study by introducing an axial restraint both at the dynamic connection-level as well as full-scale level. For the former, this was

accomplished using two 1500 kg rated tie-down straps. An example of a connection-level specimen with axial restraint is shown in Figure 3.14. For the latter, an axial restraint was introduced by blocking the top and bottom end blocks to the ceiling and lab floor, respectively.



Figure 3.14: Connection-Level Specimen with Axial Restraint

3.7.1.2 Full-Scale CLT Test Setup

Full-scale dynamic four-point bending tests on CLT assemblies were conducted using an LTD with two transfer beams (see Figure 3.12b) and a test setup specially designed for CLT panels with and without end connections. A clear span of 2235 mm was used for the specimens tested with simply supported boundary conditions whereas a clear span of 2083 mm was used for the specimens with realistic end connections. This is due to geometrical limitations of the shock tube when the boundary connections are added to the assembly. The idealized simply supported boundary conditions consisted of two HSS with welded rollers placed on both sides of the tested specimens. The HSS sections were used to clamp the panels to the shock tube. The HSS members were attached to the end frame with threaded rods and were held in place vertically using shims and adjustable steel column sections. Steel plates were placed at all load application and support points in order to minimize localized crushing of the wood.

Realistic end conditions were implemented using two blocks cut from undamaged CLT panels which were connected to the ends of the tested panel. For the bearing type CLT connections, these were directly connected into both the vertical CLT panel and the horizontal end blocks by means of self-tapping screws. The end blocks were then clamped to the shock tube using HSS sections and steel rods protruding from the shock tube's end frame. For axially unrestrained specimens, the spacing blocks, used to initially position the specimen at the correct alignment, were removed to allow for vertical movement. For axially restrained specimens, the end blocks were shimmed to the slab-on-grade and ceiling. This end condition simulates the in-plane stiffness of the floors above and below the CLT wall. The full-scale test setups for CLT, including simply supported and end connected boundary conditions, is presented in Figure 3.15.

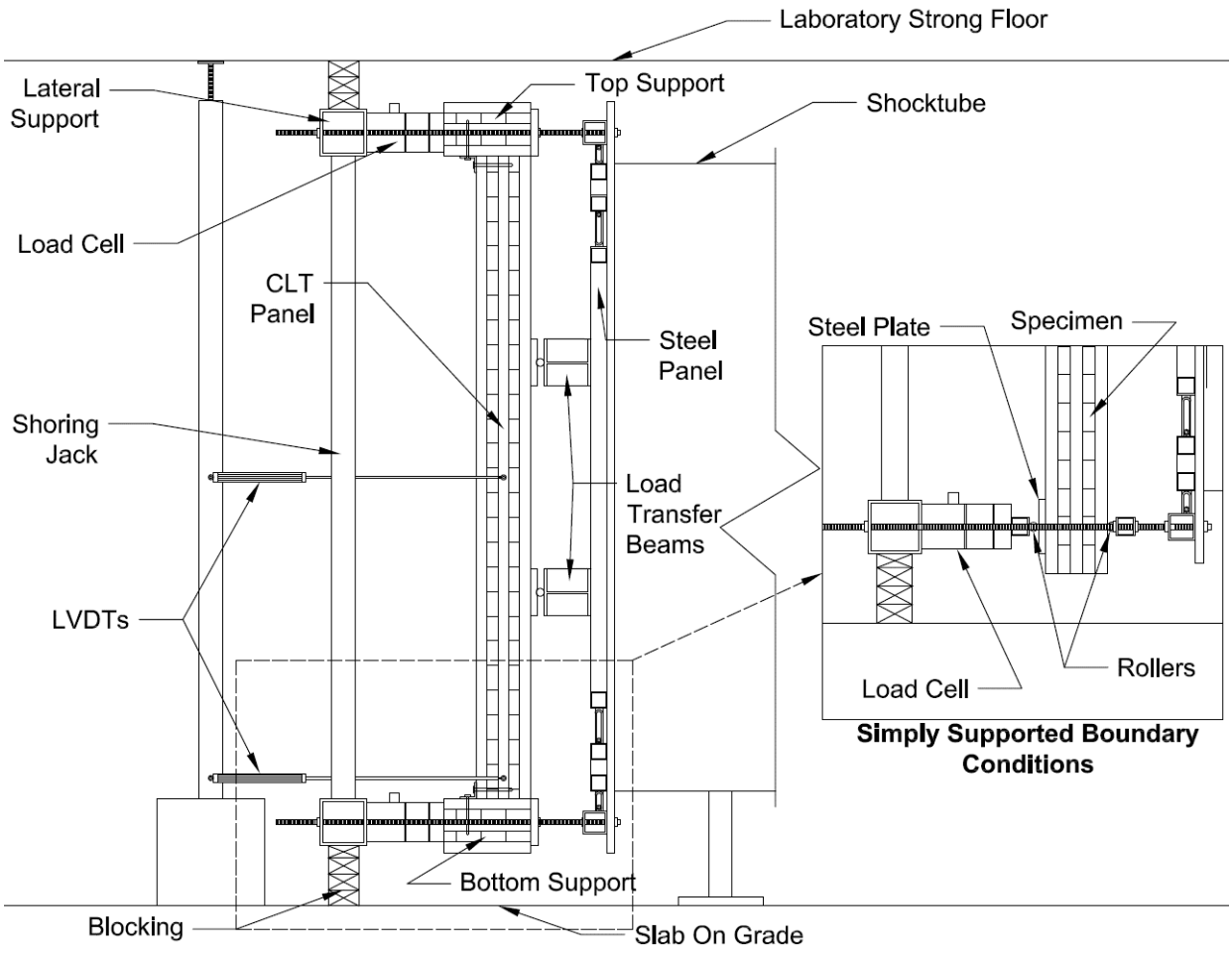


Figure 3.15: Side Sketch of Dynamic Full-Scale Test Setup for CLT

Full-scale CLT specimens with energy-absorbing connections (EACs) required an additional component to the boundary elements. The geometry of the EACs required a bearing surface on

which they would be supported. Stiffened L127x127x9.5 support brackets were designed in order to support the EACs throughout response with minimal deformations. Four 25.4 mm diameter A307 bolts were used to fasten the support brackets to the end blocks, in addition to two self-tapping screws to aid against uplift and overturning of the bracket. Once installed, the EACs were fastened to the stiffened section through 5 mm diameter hex bolts. The support brackets are shown in Figure 3.16.

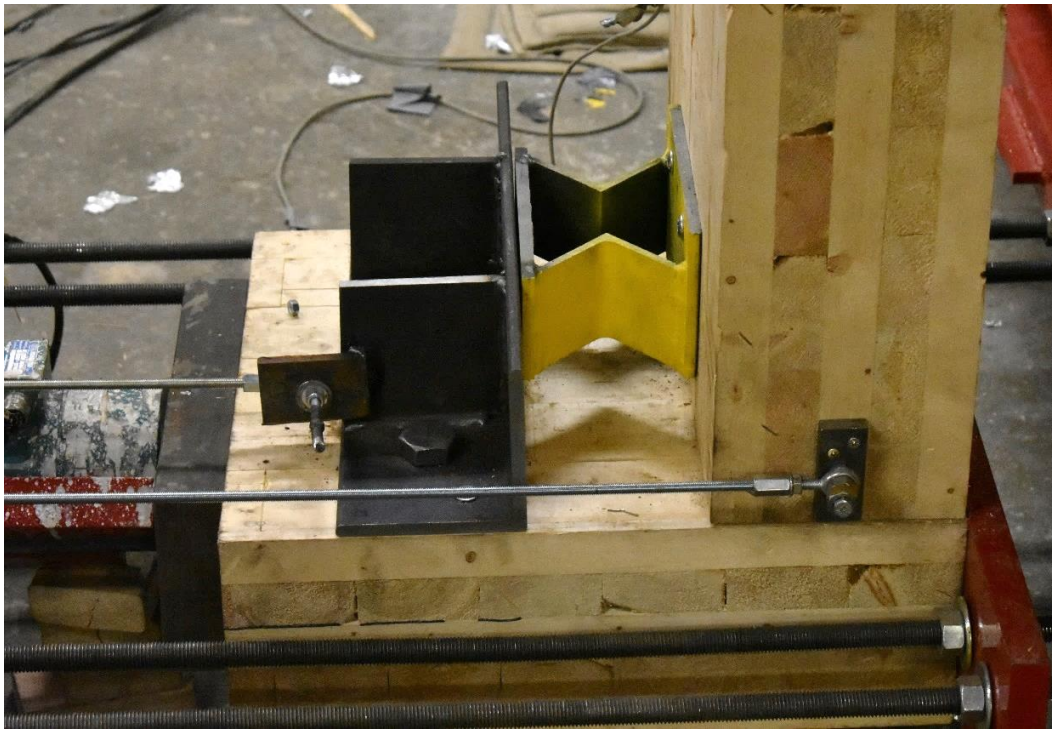


Figure 3.16: CLT EAC (yellow) Bearing on Support Bracket (black)

3.7.1.3 Full-Scale Glulam Test Setup

The load-transfer mechanism used for the dynamic testing of glulam assemblies was identical to that used for the CLT slabs. A clear span of 2235 mm was used for all full-scale specimens. The idealized simply supported boundary conditions were provided by two steel plates and a roller on top of the load cells, as well as another roller placed on the compression side of the glulam beam. Lateral supports were provided at the glulam ends in order to prevent any instabilities during the beams' response to the applied load.

Glulam assemblies with bolted connections had the protruding ends of the steel side plates clamped to the shock tube between thick steel plates and the load cells. The full-scale test setups for glulam, including simply supported and end connected boundary conditions, is presented in Figure 3.17.

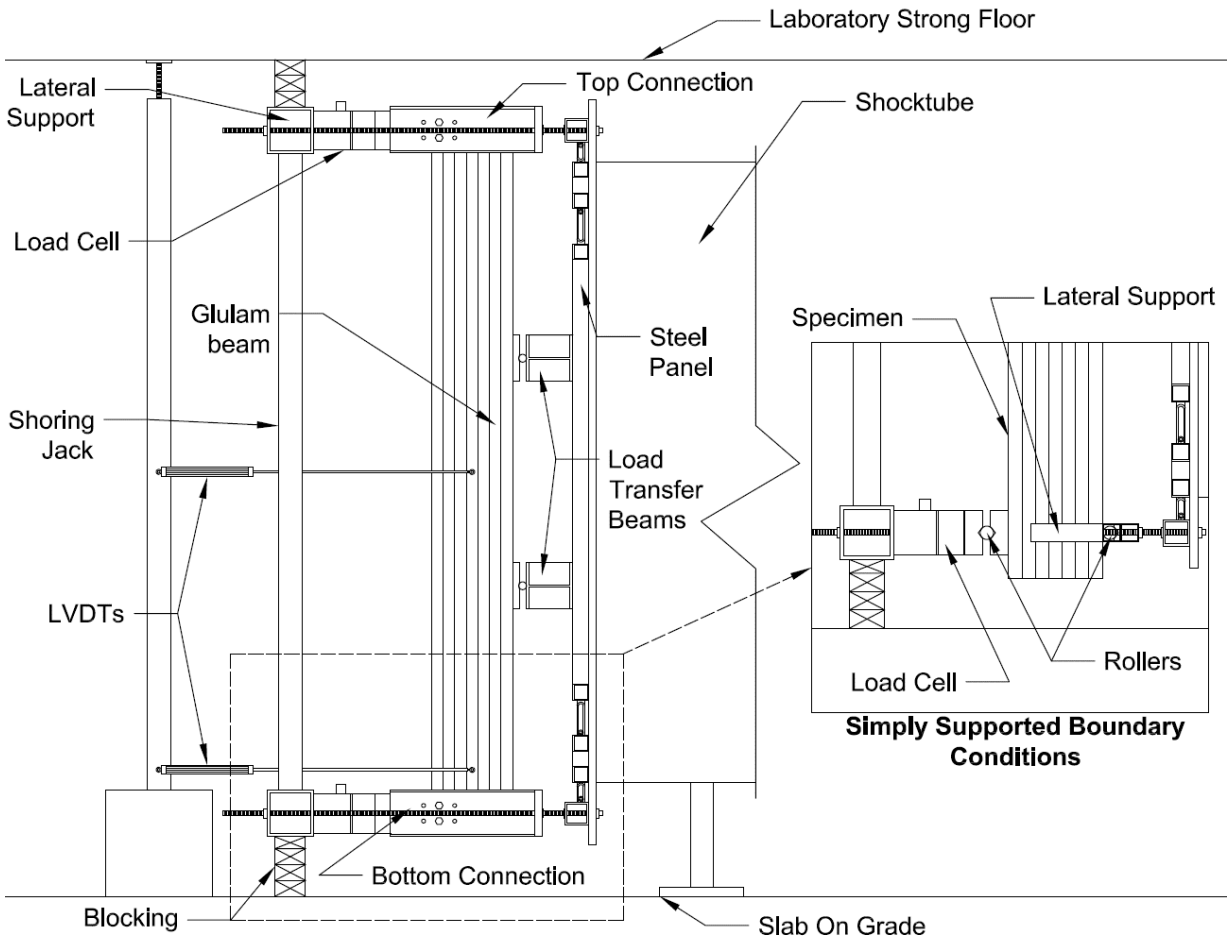


Figure 3.17: Side Sketch of Dynamic Full-Scale Test Setup for Glulam

The EACs used with the glulam specimens were supported directly against the load cells, and the specimens were held in place prior to testing by a supporting roller pressing against the compression face of the beams, and lateral supports were again provided, as shown in Figure 3.18. This method of supporting the ends was made in order to minimize potential slips and interactions with other components.



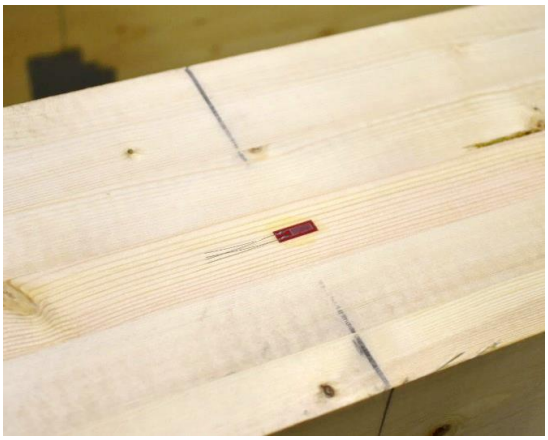
Figure 3.18: Glulam EAC (yellow) Bearing on Load Cell (green)

3.7.2 Measuring Methods and Equipment

The reflected pressure of each test was measured using two dynamic piezoelectric pressure sensors, placed at the bottom and on the side of the shock tube opening. Strain gauges were used at the mid-span tension and compression sides for the full-scale specimens in order to obtain strain data and determine the dynamic failure point for each test. The area where the strain gauges were placed was hand-sanded and thoroughly cleaned. Strong adhesive was then used to glue the strain gauges onto the specimen. The strain gauge was then covered with electrical and duct tape. This process of attaching the strain gauges was repeated for each specimen, and is summarized in Figure 3.19. The strain gauges used were *FLA-6-350-11* general purpose 350-ohm strain gauges, measuring 6.0 mm x 12.5 mm.



(a) Sanding and Cleaning



(b) Gluing of Strain Gauge

Figure 3.19: Strain Gauge Application

Displacement-time histories of the test specimens were obtained using 300 mm stroke linear variable differential transducers (LVDTs). These LVDTs were attached to a steel enclosing bracket, which acted as a protective barrier. The bracket was attached to a steel jack post, thus requiring the displacement of the shock tube to be removed from all measured displacements. Two *Revere Model 92/93* compression load cells were used throughout testing in order to measure the load-time histories. A data acquisition system which recorded data at a sampling rate of 100,000 samples per second was used to collect the information from all the sensors. Additionally, two *Phantom VEO 410L* high-speed cameras recording at 2000 frames per second were connected to the DAS in order to capture the dynamic response of each test, and enables motion analysis of any desired point of interest on the specimens. The recording process was triggered by the pressure wave passing by the pressure sensors.

Chapter 4 - Experimental Results

4.1 General

The experimental results from the static and dynamic testing described in Chapter 3 are presented in this chapter. For the static testing, this includes connection-level testing of cross-laminated timber (CLT) bearing connections, bolted glulam connections, and energy-absorbing connections (EACs). For the dynamic testing, this includes connection-level testing of CLT connections, as well as full-scale testing of CLT and glulam assemblies with idealized and realistic boundary conditions.

4.2 Static Test Results

4.2.1 Characterization of Timber Members

For the CLT panels, the average moisture content was determined to be 13.3 % with a CoV of 0.11 while the average density was found to be 527.9 kg/m^3 with a CoV of 0.01, based on fifteen samples. For the glulam beams, the average moisture content was determined to be 12.8 % with a CoV of 0.10 while the average density was found to be 540.5 kg/m^3 with a CoV of 0.01, based on nineteen samples obtained from the full-scale test specimens.

4.2.2 CLT Bearing Connections

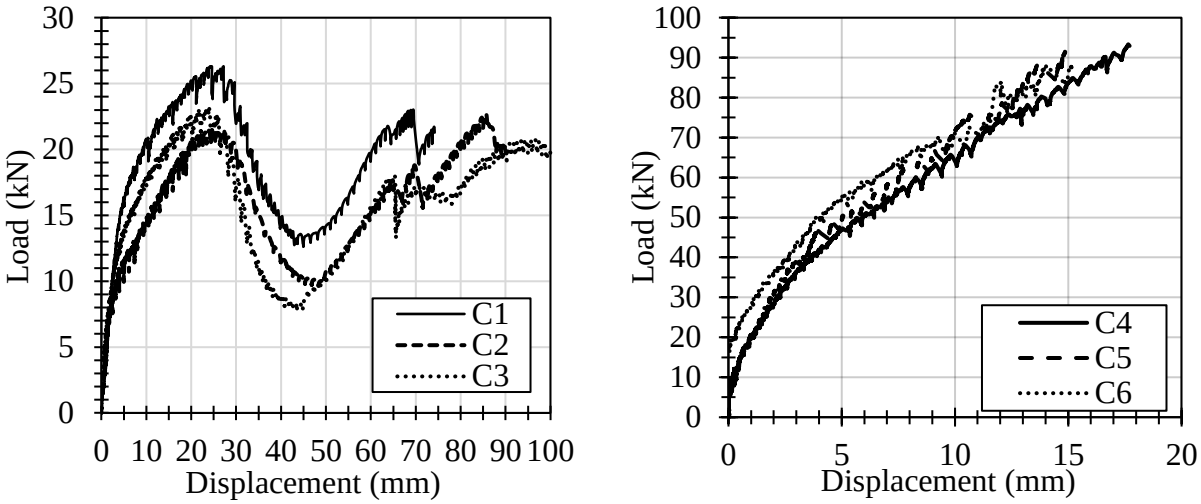
A total of six static connection-level tests for the ML24Z (specimens C1 – C3) and manufactured thick angle (specimens C4 – C6) were conducted. The results are summarized in Table 4.1, which includes the peak joint load (P_{max}), joint displacement at peak load (Δ_{Pmax}), joint displacement correlating to a post-peak load selected at 50 % of the peak load ($\Delta_{50\%}$), as suggested by Lacroix and Doudak (2019), joint displacement at ultimate failure (Δ_f), and time to ultimate failure (t_f). In all tests, no damage to the intermediate panel was observed. No post-peak behaviour was observed for all tests on the thick angle and hence no post-peak data is reported.

Table 4.1: Summary of Static Connection-Level Testing on CLT Bearing Connections

Specimen	P_{max} (kN)	Δ_{Pmax} (mm)	$\Delta_{50\%}$ (mm)	Δ_f (mm)	t_f (min)
C1	26.3	24.6	42.9	74.2	6.5
C2	21.5	25.0	42.6	90.3	7.0
C3	23.2	24.0	34.5	100.0	8.8
Average	*23.7*	*24.5*	*40.0*	*88.2*	*7.9*
CoV	*0.08*	*0.02*	*0.10*	*0.12*	*0.11*
C4	93.4	17.7	-	-	7.7
C5	91.5	14.9	-	-	8.5
C6	89.1	15.2	-	-	5.5
Average	*91.3*	*15.9*	-	-	*7.2*
CoV	*0.02*	*0.08*	-	-	*0.18*

The static load-displacement relationships are presented in Figure 4.1 for all tested CLT bearing connections. The behaviour of the ML24Z angle (Figure 4.1a) shows an initial linear-elastic behaviour followed by drop in stiffness and a shift to a nonlinear behaviour. Past the peak load, the ML24Z angles deformed significantly and created outward forces acting against the support blocks, which in turn caused a separation between the intermediate panel ends and the support blocks. The observed behaviour can be attributed to the absence of axial restraint on the assembly, and correlates to the softening effect in the load-displacement relationship. Significant wood crushing at panel ends was observed due to the perpendicular-to-grain compressive stresses caused by the bending of the ML24Z angles with little to no wood crushing observed around the screws (Figure 4.2a). Following the softening behaviour, the load in the joints continued to increase until rupture of the screws was attained, as shown in Figure 4.2b.

The thick angle connections initially exhibited nonlinear behaviour with early onset of stiffness degradation followed by an almost linear behaviour up to peak load (Figure 4.1b). Little to no angle yielding was observed in all tests on thick angle connections (Figure 4.2c). The ultimate failure of these joints occurred at significantly lower deformation levels when compared to the connection containing the ML24Z angles. The failure mode was observed to be primarily dominated by bending in the screws accompanied by some crushing in the wood, especially near the surface (Figure 4.2d).



(a) ML24Z (b) Thick Angle

Figure 4.1: Experimental Static Load-Displacement Curves for CLT Bearing Connections



(a) Wood Crushing at Panel Ends (ML24Z)



(b) Screw Failure for ML24Z Connections



(c) Lack of Wood Crushing and Angle Bending (Thick Angle)



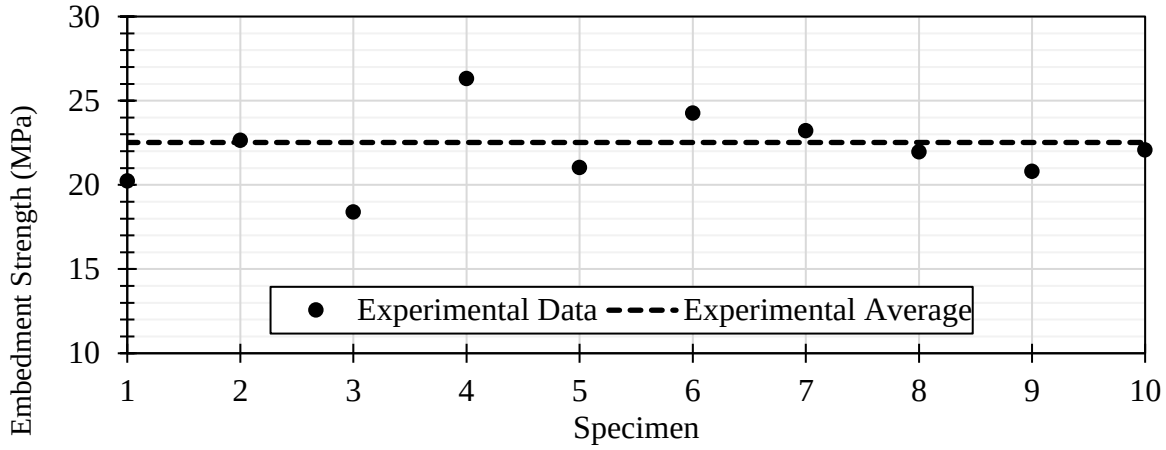
(d) Wood Crushing in Screw Holes of Support Block (Thick Angle)

Figure 4.2: Representative Static Behaviour of CLT Bearing Connections

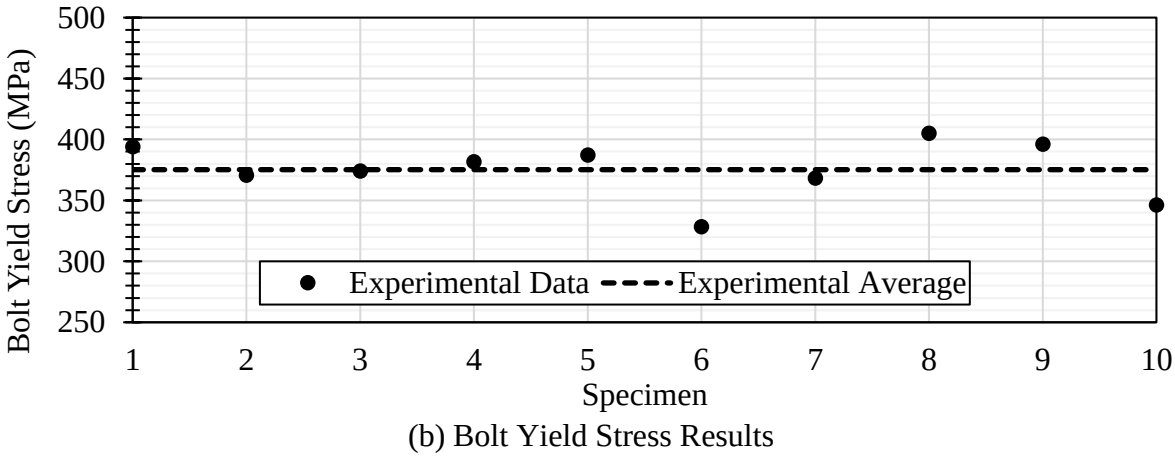
4.2.3 Bolted Glulam Connections

The results presented in this section include the mechanical properties of the tested bolted connections such as the embedment strength, bolt yield stress, and the load-displacement relationship of a single-bolt joint. These parameters would later be used as input in the mechanics-based European Yield Model (EYM) as well as the analytical model used to predict the performance the full-scale glulam assemblies.

Ten embedment tests and ten bolt bending tests were conducted using 12.7 mm diameter A307 bolts. An average embedment strength of 22.1 MPa with a CoV of 0.10 and an average bolt yield stress of 375 MPa with a CoV of 0.06, were obtained. Figure 4.3 presents the results and distribution of the embedment and bolt bending tests along with their respective experimental averages. Typical load-displacement relationship graphs for each test as well as representative failure of embedment and bolt specimens are shown in Figure 4.4.

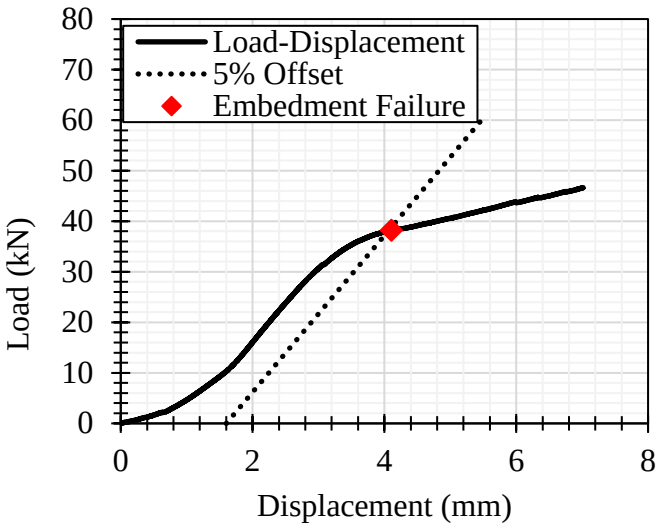


(a) Embedment Strength Results



(b) Bolt Yield Stress Results

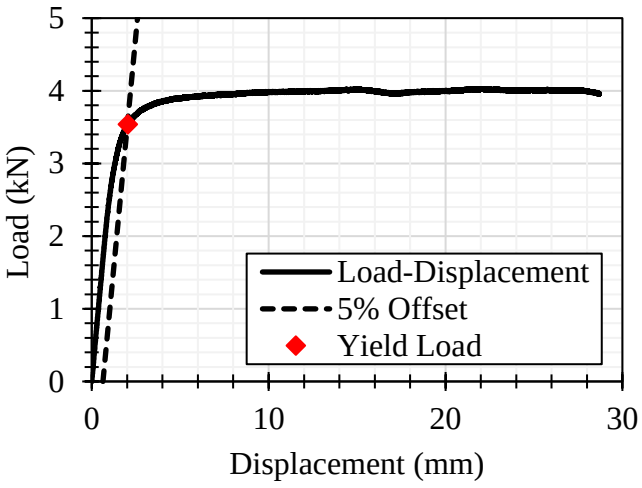
Figure 4.3: Results of Embedment and Bolt Bending Tests



(a) Embedment Strength Test Load-Displacement



(b) Embedment Failure



(c) Bolt Bending Test Load-Displacement



(d) Ongoing Bolt Bending Test

Figure 4.4: Obtaining Mechanical Properties of Bolted Connections

Three single-bolt joints were tested to destruction in order to assess the behaviour of the connections included in the full-scale assemblies. The results are summarized in Table 4.2, which includes the peak joint load (P_{max}), joint displacement at peak load (Δ_{Pmax}), joint displacement correlating to 10 % of the peak load ($\Delta_{10\%}$), joint displacement correlating to 40 % of the peak load ($\Delta_{40\%}$), stiffness of the joint corresponding to a line connecting the 10 % and 40 % points ($K_{10\text{-}40\%}$), stiffness of the joint corresponding to a line connecting the 40 % and 100 % points ($K_{40\text{-}100\%}$), and time to ultimate failure (t_f).

Table 4.2: Summary of Static Connection-Level Testing on Single-Bolt Connections

Specimen	P_{max} (kN)	Δ_{Pmax} (mm)	$\Delta_{10\%}$ (mm)	$\Delta_{40\%}$ (mm)	$K_{10\text{-}40\%}$ (kN/mm)	$K_{40\text{-}100\%}$ (kN/mm)	t_f (min)
SB1	101.1	33.0	1.2	7.8	4.6	2.4	8.5
SB2	97.5	30.9	1.2	7.4	4.7	2.5	8.1
SB3	93.1	34.1	1.5	9.5	3.5	2.3	8.8
Average	*97.2*	*32.7*	*1.3*	*8.2*	*4.3*	*2.4*	*8.5*
CoV	*0.03*	*0.04*	*0.11*	*0.11*	*0.13*	*0.04*	*0.03*

The load-displacement relationships are presented in Figure 4.5 for all single-bolt joint tests. The behaviour of the joints can be described as bilinear. The observed behaviour can be attributed to yielding in the bolts and crushing of the wood fibres, which is typical for bolted connections with slender bolts. In all tests, the ultimate failure was characterized as a sudden shear/tensile fracture of the bolt at the wood-steel shear plane. An example of a failed specimen is shown in Figure 4.6.

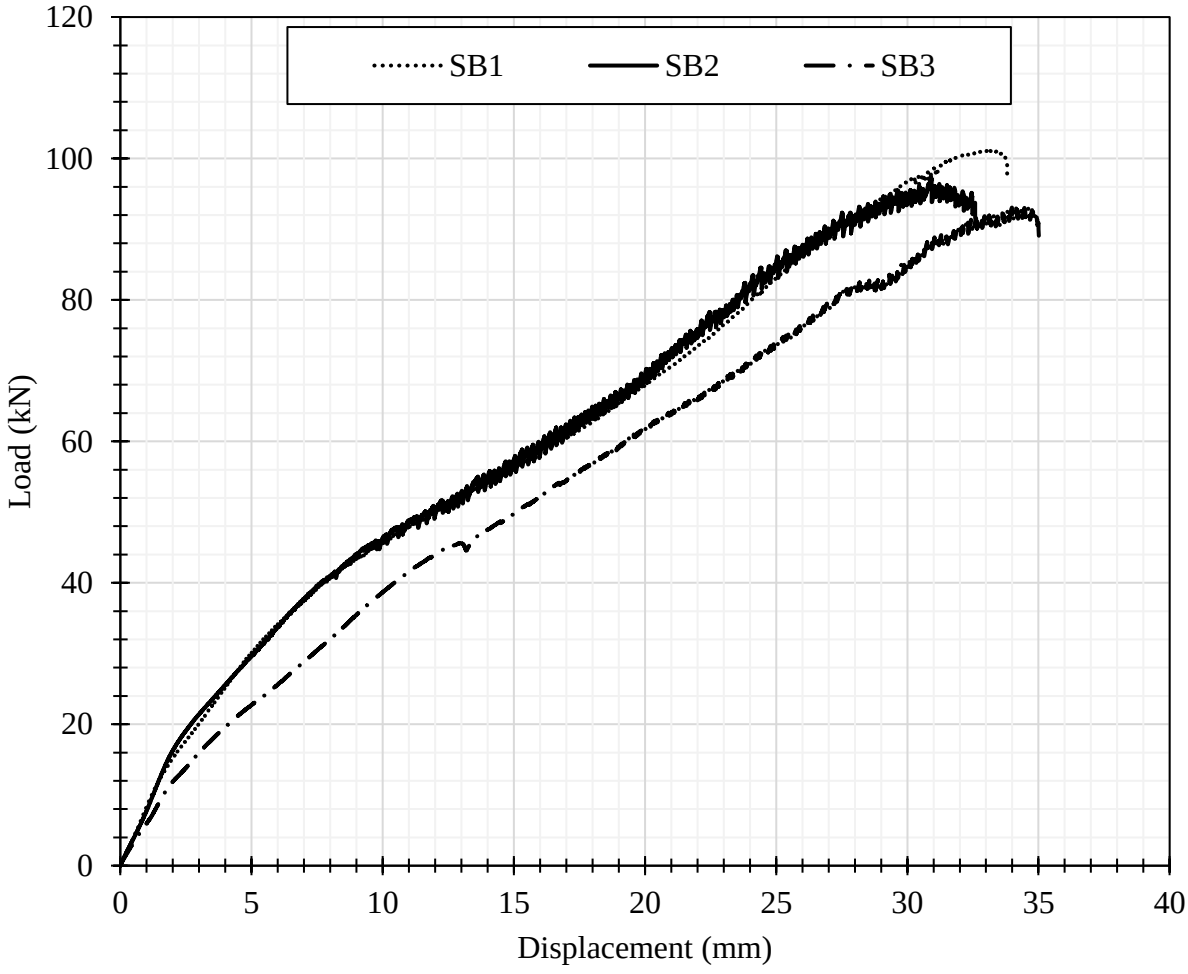


Figure 4.5: Experimental Static Load-Displacement Curves for Single-Bolt Joints



(a) Typical Deformed Bolt Shape (b) Wood Crushing and Bolt Fracturing

Figure 4.6: Representative Static Behaviour of Single-Bolt Connections

4.2.4 Energy-Absorbing Connections

A total of six 22.2 mm (7/8 in.) energy-absorbing connections (EACs) were tested statically in order to obtain their load-displacement relationships. A summary of the results are presented in Table 4.3, which includes the yield load (P_{yield}), joint displacement at yield load (Δ_{yield}), stiffness in the region corresponding to 10 – 40 % of yield load ($K_{10\text{-}40\%}$), average yield plateau load ($P_{plateau}$), displacement correlating to densification of the EAC (Δ_d), and densification stiffness (K_d). Densification is described as the point in the load-displacement relationship, where the top and bottom of the EAC make contact, resulting in a sudden increase in stiffness.

Table 4.3: Summary of Static Connection-Level Testing on Energy-Absorbing Connections

Specimen	**P_{yield} (kN)**	**Δ_{yield} (mm)**	**$K_{10\%\text{-}40\%}$ (kN/mm)**	**$P_{plateau}$ (kN)**	**Δ_d (mm)**	**K_d (kN/mm)**
EAC1	9.7	4.1	3.1	12.7	83.3	15.4
EAC2	8.9	3.2	3.5	12.0	82.0	19.4
EAC3	10.3	3.1	3.6	12.9	81.8	18.5
EAC4	8.8	3.0	2.8	10.9	81.1	15.7
EAC5	8.7	2.9	2.6	10.7	80.5	14.7
EAC6	8.7	3.0	2.6	10.5	81.0	15.0
Average	*9.2*	*3.2*	*3.0*	*11.6*	*81.6*	*16.5*
CoV	*0.07*	*0.12*	*0.13*	*0.08*	*0.01*	*0.11*

The load-displacement relationships are presented in Figure 4.7 for all EAC connection-level tests. The behaviour of the EACs can be described as a trilinear load-displacement curve. An example showing the state of the EACs during all three portions of its behaviour (initial, yield plateau, and densification) is shown in Figure 4.8. Throughout testing, no welding failures occurred. The tests were deemed completed once the EAC experienced a doubling in load relative to the average plateau load.

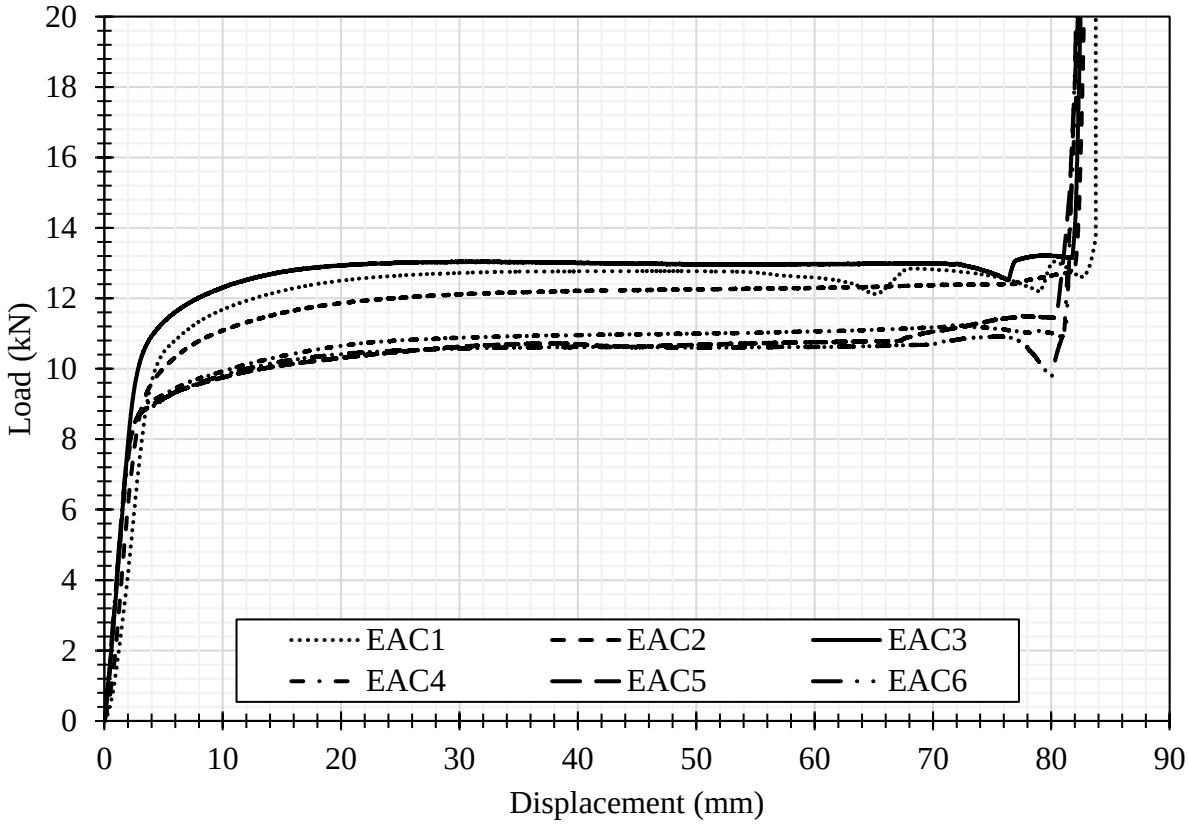


Figure 4.7: Experimental Static Load-Displacement Curves for 7/8" Deep EACs



(a) Initial (b) Yielding (c) Densification

Figure 4.8: Representative States of Energy-Absorbing Connections

4.3 Dynamic Test Results

The following section summarizes the results of fifty-eight dynamic shock tube tests, consisting of ten tests on CLT bearing connections; twenty-one tests on CLT assemblies, and twenty-seven tests on glulam assemblies. Complete test results and observations can be found in Appendices A, B, and C for the connection-level, full-scale CLT, and full-scale glulam specimens, respectively.

4.3.1 CLT Bearing Connections Specimens

All dynamic connection-level tests were conducted with a constant driver length of 9 ft. Each test name reflects the type of test, as well as its numerical sequence (e.g. C7 is a connection-level test and is the seventh to be conducted). All specimens were subjected to a single blast load. Table 4.4 summarizes all dynamic connection-level test results, including the driver pressure, peak reflected pressure, peak reflected impulse, positive phase duration, maximum displacements of each end joints, time-to-maximum displacements, and joint displacements correlating to a post-peak load of 50 % of peak load. Representative damage levels for the ML24Z connections are shown in Figure 4.9, along with the terminologies used to describe each specimen's damage level. Typical results from the dynamic connection-level test are shown in Figure 4.10. These include pressure- and impulse-, displacement-, and load-time histories.



(a) Moderate (b) Heavy (c) Extreme

Figure 4.9: Representative Damage Levels for Wood Crushing and ML24Z Angle Yielding

4.3.1.1 Specimen C7: One ML24Z Angle at Each End without Axial Restraint

A driver pressure of 295.8 kPa was used, which resulted in a peak reflected pressure of 40.3 kPa and a peak reflected impulse of 380.3 kPa-ms over a positive phase of 20.2 ms. For the bottom joint, a peak load of 38.7 kN was measured, correlating to a joint displacement of 44.0 mm. For the top joint, an error in instrumentation meant that no usable data could be recorded.

A significant amount of wood crushing in the intermediate member was observed at both top and bottom joints. Both ML24Z angles underwent a moderate amount of yielding. A slight opening between both end blocks and the intermediate member was observed.

4.3.1.2 Specimen C8: One ML24Z Angle at Each End without Axial Restraint

A driver pressure of 439.9 kPa was used, which resulted in a peak reflected pressure of 55.9 kPa and a peak reflected impulse of 536.3 kPa-ms over a positive phase of 20.2 ms. For the bottom joint, a peak load of 38.9 kN was measured, correlating to a joint displacement of 30.3 mm. A post-peak load above 50 % of peak load was sustained until a joint deformation of 57.7 mm. For the top joint, a peak load of 37.5 kN was measured, correlating to a joint displacement of 36.8 mm. A post-peak load above 50 % of peak load was sustained until a joint deformation of 57.9 mm.

A moderate amount of wood crushing in the intermediate member was observed at both top and bottom joints. Both ML24Z angles underwent a significant amount of yielding. Head failure of the middle screw in the end block was observed in the top joint. A noticeable opening in between both end blocks and the intermediate member was observed, due to lack of axial restraint.

4.3.1.3 Specimen C9: One ML24Z Angle at Each End with Axial Restraint

A driver pressure of 438.5 kPa was used, which resulted in a peak reflected pressure of 53.4 kPa and a peak reflected impulse of 496.6 kPa-ms over a positive phase of 20.6 ms. For the bottom joint, a peak load of 52.3 kN was measured, correlating to a joint displacement of 56.1 mm. A post-peak load above 50 % of peak load was sustained until a joint deformation of 79.2 mm. For the top joint, a peak load of 48.6 kN was measured, correlating to a joint displacement of 49.7 mm. The load was not sufficiently significant to induce post-peak behaviour whereby the load drops below 50 % of peak load in the top joint.

A significant amount of wood crushing in the intermediate member was observed at the bottom joint. The bottom joint ML24Z angle underwent a significant amount of yielding. No noticeable opening in between both end blocks and the intermediate member was observed, due to the axial restraint generated by the straps. The screws connecting the intermediate panel to the end blocks were severely deformed upon removal from the test specimen.

4.3.1.4 Specimen C10: One ML24Z Angle at Each End with Axial Restraint

A driver pressure of 450.2 kPa was used, which resulted in a peak reflected pressure of 59.7 kPa and a peak reflected impulse of 551.6 kPa-ms over a positive phase of 20.6 ms. For the bottom joint, a peak load of 45.4 kN was measured, correlating to a joint displacement of 51.5 mm. The load was not sufficiently significant to induce post-peak behaviour whereby the load drops below 50 % of peak load in the bottom joint. For the top joint, a peak load of 43.5 kN was measured, correlating to a joint displacement of 46.3 mm. A post-peak load above 50 % of peak load was sustained until a joint deformation of 70.4 mm.

A significant amount of wood crushing in the intermediate member was observed at both top and bottom joints. Both ML24Z angles underwent a significant amount of yielding. A slight opening in between both end blocks and the intermediate member was observed. The screws connecting the intermediate panel to the end blocks were severely deformed.

4.3.1.5 Specimen C11: One ML24Z Angle at Each End with Axial Restraint

A driver pressure of 484.7 kPa was used, which resulted in a peak reflected pressure of 59.4 kPa and a peak reflected impulse of 601.9 kPa-ms over a positive phase of 20.0 ms. For the bottom joint, an error in instrumentation made it so that no usable data could be recorded. For the top joint, a peak load of 46.2 kN was measured, correlating to a joint displacement of 39.0 mm. A post-peak load above 50 % of peak load was sustained until a joint deformation of 70.6 mm.

An extreme amount of wood crushing in the intermediate member was observed at the top joint, while significant wood crushing was found in the bottom joint. The ML24Z angles underwent a significant amount of yielding at both top and bottom joints, however, the top angle deformation was most severe. Tilting of the intermediate panel hinted that the top joint attracted more load than the bottom joint, or that the top joint yielded first. From video review, this tilting only occurred near the end of the response of the specimen. No noticeable opening between both end blocks and the intermediate member was observed, due to the axial restraint generated by the straps. The screws connecting the intermediate panel to the end blocks were severely deformed upon removal from the test specimen.

4.3.1.6 Specimen C12: Two ML24Z Angles at Each End without Axial Restraint

A driver pressure of 515.0 kPa was used, which resulted in a peak reflected pressure of 59.9 kPa and a peak reflected impulse of 612.9 kPa-ms over a positive phase of 20.2 ms. For the bottom joint, a peak load of 78.9 kN was measured, correlating to a joint displacement of 31.1 mm. The load was not sufficiently significant to induce post-peak behaviour whereby the load drops below 50 % of peak load in the bottom joint. For the top joint, a peak load of 68.3 kN was measured, correlating to a joint displacement of 24.3 mm. A post-peak load above 50 % of peak load was sustained until a joint deformation of 45.3 mm.

A significant amount of wood crushing in the intermediate member was observed at the top joint, while only noticeable wood crushing was found in the bottom joint. The top joint ML24Z angles underwent a significant amount of yielding, followed by the failure of all six screws which connected the intermediate panel to the top end block. Tilting of the intermediate panel hinted that the top joint attracted more load than the bottom joint or that the top joint yielded first. From video review, this tilting only occurred near the end of the response of the specimen. A significant opening in between both end blocks and the intermediate member was observed, due to lack of axial restraint.

4.3.1.7 Specimen C13: Two ML24Z Angles at Each End without Axial Restraint

A driver pressure of 512.3 kPa was used, which resulted in a peak reflected pressure of 53.8 kPa and a peak reflected impulse of 591.3 kPa-ms over a positive phase of 20.6 ms. For the bottom joint, a peak load of 73.3 kN was measured, correlating to a joint displacement of 23.1 mm. A post-peak load above 50 % of peak load was sustained until a joint deformation of 62.0 mm. For the top joint, a peak load of 62.0 kN was measured, correlating to a joint displacement of 19.5 mm. A post-peak load above 50 % of peak load was sustained until a joint deformation of 45.7 mm.

A significant amount of wood crushing in the intermediate member was observed at both top and bottom joints. All four ML24Z angles underwent a significant amount of yielding. Head failure of the middle screws in the end block of both top joint ML24Z angles was observed. A significant opening in between both end blocks and the intermediate member was observed, due to lack of axial restraint.

4.3.1.8 Specimen C14: Manufactured Thick Angles With 3 Screws Without Axial Restraint

A driver pressure of 313.0 kPa was used, which resulted in a peak reflected pressure of 39.8 kPa and a peak reflected impulse of 390.7 kPa-ms over a positive phase of 20.4 ms. For the bottom joint, a peak load of 50.8 kN was measured, correlating to a joint displacement of 14.3 mm. For the top joint, a peak load of 48.8 kN was measured, correlating to a joint displacement of 16.1 mm. The peak load corresponded to failure of the screws, and therefore no post-peak behaviour was observed.

Significant wood crushing was observed in all six screw holes in the end blocks. For the bottom joint, head failure of the three screws was observed, whereas only two screws failed in the top joint. The remaining top joint screw was severely deformed. Both steel angles showed no sign of damage.

4.3.1.9 Specimen C15: Manufactured Thick Angles With 6 Screws and Without Axial Restraint

A driver pressure of 514.3 kPa was used, which resulted in a peak reflected pressure of 55.2 kPa and a peak reflected impulse of 632.2 kPa-ms over a positive phase of 21.6 ms. For the bottom joint, a peak load of 95.9 kN was measured, correlating to a joint displacement of 12.0 mm. For the top joint, a peak load of 83.4 kN was measured, correlating to a joint displacement of 11.8 mm. The peak load corresponded to failure of the screws, and therefore no post-peak behaviour was observed.

Significant wood crushing was observed in all twelve screw holes in the end blocks. For the bottom joint, head failure of two screws was observed, whereas all six screws failed in the top joint. The remaining bottom joint screws were severely deformed. Both angles showed no sign of damage.

4.3.1.10 Specimen C16: Manufactured Thick Angles With 9 Screws and Without Axial Restraint

A driver pressure of 561.9 kPa was used, which resulted in a peak reflected pressure of 70.7 kPa and a peak reflected impulse of 699.0 kPa-ms over a positive phase of 21.2 ms. For the bottom joint, a peak load of 108.1 kN was measured, correlating to a joint displacement of 10.8 mm. For the top joint, a peak load of 101.9 kN was measured, correlating to a joint displacement of 9.6 mm.

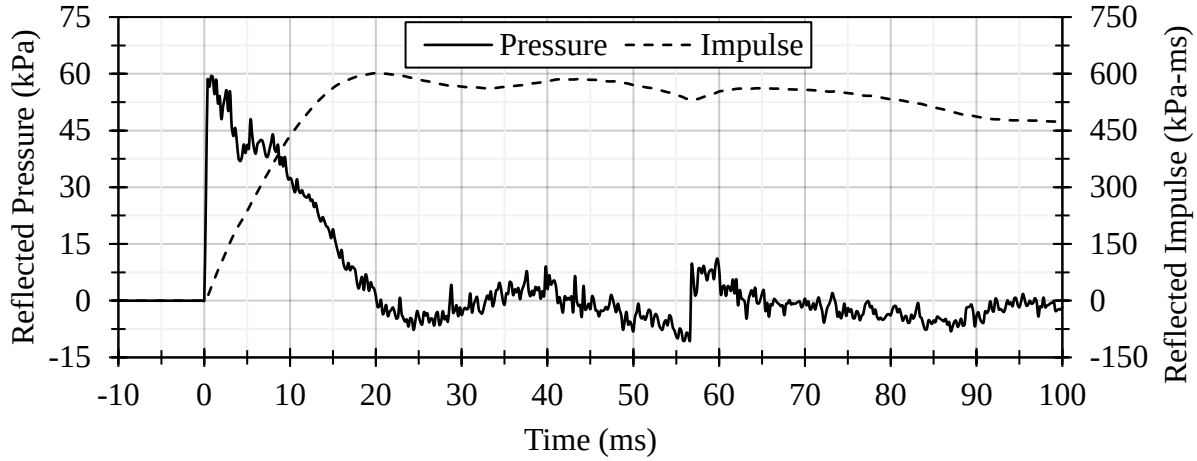
Some wood crushing was observed in all eighteen screw holes in the end blocks, and permanent deflection was apparent. No screw failure was observed, due to the level of the applied load. Both angles showed no sign of damage.

Table 4.4: Summary of Dynamic Connection-Level Testing

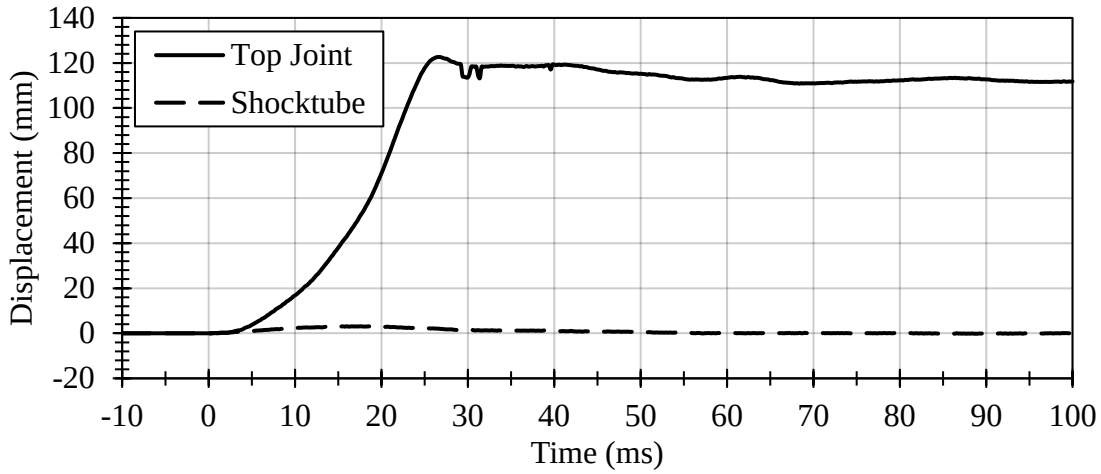
Test Name	Peak Reflected Pressure (kPa)	Peak Reflected Impulse (kPa-ms)	Top Joint				Bottom Joint			
			Peak Load (kN)	Disp. at Peak Load (mm)	Time-to-Peak Load (ms)	Disp. at 50% of Peak Load (mm)	Peak Load (kN)	Disp. at Peak Load (mm)	Time-to-Peak Load (ms)	Disp. at 50% of Peak Load (mm)
C7	40.3	380.3	IE	IE	IE	IE	38.7	44.0	21.6	*
C8	55.9	536.3	37.5	36.8	22.4	57.9	38.9	30.3	22.4	57.7
C9	53.4	496.6	48.6	49.7	21.4	*	52.3	56.1	20.4	79.2
C10	59.7	551.6	43.5	46.3	18.6	70.4	45.4	51.5	18.6	*
C11	59.4	601.9	46.2	39.0	15.2	70.6	IE	IE	IE	IE
C12	59.9	612.9	68.3	24.3	16.4	45.3	78.9	31.1	17.6	*
C13	53.8	591.3	62.0	19.5	14.8	45.7	73.3	23.1	15.8	62.0
C14	39.8	390.7	48.8	16.1	16.2	*	50.8	14.3	13.8	*
C15	55.2	632.2	83.4	11.8	18.2	*	95.9	12.0	15.6	*
C16	70.7	699.0	101.9	9.6	19.6	*	108.1	10.8	18.2	*

IE = instrumentation error, no data recorded.

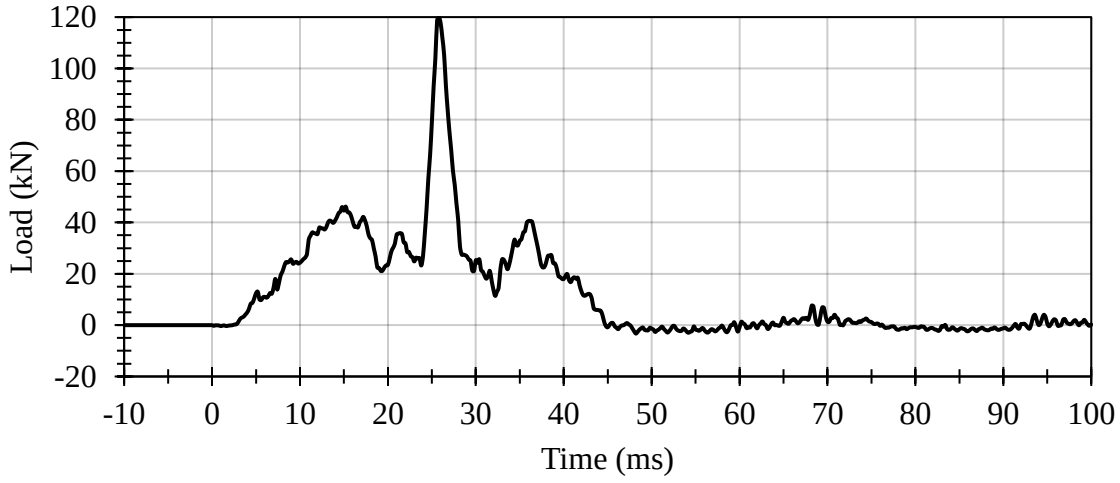
* = no post-peak behaviour / post-peak load never decreased below 50 % of peak load



(a) Pressure- and Impulse-Time Histories



(b) Displacement-Time Histories



(c) Load-Time Histories

Figure 4.10: Typical Results of Dynamic Connection-Level Testing on CLT Bearing Connections (Results from Test C11)

4.3.2 Full-Scale CLT Specimens

This subsection summarizes the results of twenty-one dynamic full-scale tests on fifteen CLT specimens. The boundary conditions varied from idealized simply supported to realistic boundary connections, which includes typical CLT bearing connections and energy-absorbing connections. All dynamic full-scale CLT tests were conducted with a driver length of 9 ft. Each test name reflects the type of test, as well as its numerical sequence. For cases where specimens were exposed to multiple shots, a numerical representation of the order of testing is provided (e.g. CLT14-3 is the fourteenth full-scale CLT specimen to be tested, and at the time of reporting was tested for a total of three times). Table 4.5 summarizes all dynamic full-scale CLT test, the peak reflected pressure, peak reflected impulse, maximum panel dynamic resistance, displacement at maximum resistance, time-to-maximum displacement, initial stiffness, average strain-rate in the panel, and failure mode of the CLT assembly. The average values and their associated coefficient of variation are also given for key properties.

4.3.2.1 Specimen CLT1: Full-scale CLT Panel with Simply Supported Boundary Conditions

A driver pressure of 485.4 kPa was used, which resulted in a peak reflected pressure of 62.5 kPa and a peak reflected impulse of 601.1 kPa-ms over a positive phase of 21.0 ms. A peak dynamic resistance of 159.0 kN was measured, correlating to a mid-span displacement of 31.6 mm. A maximum mid-span displacement of 52.2 mm occurred 25.0 ms after the arrival of the blast wave. The specimen's initial stiffness was determined to be 5.44 kN/mm. The panel suffered minor flexural damage, occurring in the mid-span region at defects on the tension face. Rolling shear was apparent in the transversal laminates, localized mainly in the regions between the end supports and load application points.

4.3.2.2 Specimen CLT2: Full-scale CLT Panel with Simply Supported Boundary Conditions

A driver pressure of 519.2 kPa was used, which resulted in a peak reflected pressure of 62.5 kPa and a peak reflected impulse of 680.4 kPa-ms over a positive phase of 21.2 ms. A peak dynamic resistance of 176.3 kN was measured, correlating to a mid-span displacement of 29.9 mm. A maximum mid-span displacement of 74.7 mm occurred 29.0 ms after the arrival of the blast wave. The specimen's initial stiffness was measured to be 6.00 kN/mm. The panel failed in flexure,

initiated by the failure of a finger joint near the top load application point. Severe rolling shear damage was apparent in the transversal laminates throughout the panel. The second (middle) longitudinal laminate experienced flexural failure as well, however, the applied load was sufficiently high to cause complete failure of all laminates within the specimen.

4.3.2.3 Specimen CLT3: Full-scale CLT Panel with Simply Supported Boundary Conditions

A driver pressure of 550.9 kPa was used, which resulted in a peak reflected pressure of 71.4 kPa and a peak reflected impulse of 658.9 kPa-ms over a positive phase of 20.6 ms. A peak dynamic resistance of 172.0 kN was measured, correlating to a mid-span displacement of 25.3 mm. A maximum mid-span displacement of 146.3 mm occurred 75.0 ms after the arrival of the blast wave. The specimen's initial stiffness was measured to be 5.31 kN/mm. The panel failed completely in flexure, initiated by the failure of a finger joint near the lower load application point. Severe longitudinal and rolling shear damage was apparent throughout the panel. All five laminates failed near the zone of initial flexural failure.

4.3.2.4 Specimen CLT4: Full-scale CLT Panel with Thick Manufactured Angles (3 Screws Each)

A driver pressure of 516.4 kPa was used, which resulted in a peak reflected pressure of 68.4 kPa and a peak reflected impulse of 662.7 kPa-ms over a positive phase of 21.2 ms. A peak dynamic resistance of 82.4 kN was measured, correlating to a mid-span displacement of 22.9 mm. A maximum mid-span displacement of 289.5 mm occurred 92.2 ms after the arrival of the blast wave. The system's initial stiffness was measured to be 2.66 kN/mm. Both end connections experienced failure, in the form of screw shear/tensile failure. The bottom connection failed first and the top shortly after. Significant wood crushing was observed in all six screw holes in the end blocks. The remaining top joint screw was severely deformed. Both angles showed no sign of damage. From video review, the CLT specimen behaved as a rigid body, translating outwards, until striking the blue protective bracket. The CLT panel remained within the elastic region, with no signs of any damage through the panel.

4.3.2.5 Specimen CLT5: Full-scale CLT Panel with Thick Manufactured Angles (6 Screws Each)

A driver pressure of 617.8 kPa was used, which resulted in a peak reflected pressure of 78.3 kPa and a peak reflected impulse of 787.2 kPa-ms over a positive phase of 21.0 ms. A peak dynamic resistance of 151.7 kN was measured, correlating to a mid-span displacement of 39.4 mm. A maximum mid-span displacement of 96.4 mm occurred 32.2 ms after the arrival of the blast wave. The system's initial stiffness was measured to be 4.56 kN/mm. The panel failed in a combination of flexure and rolling shear, initiated by the failure of a knot. Severe rolling shear damage was apparent throughout the panel; however, it was most severe in the upper and lower thirds of the panel. A moderate amount of wood crushing was observed in all twelve screw holes in the end blocks. Most screws had permanent deformations. Both angles showed no sign of damage.

4.3.2.6 Specimen CLT6: Full-scale CLT Panel with Thick Manufactured Angles (9 Screws Each)

A driver pressure of 630.9 kPa was used, which resulted in a peak reflected pressure of 83.6 kPa and a peak reflected impulse of 832.5 kPa-ms over a positive phase of 23.0 ms. A peak dynamic resistance of 163.4 kN was measured, correlating to a mid-span displacement of 37.7 mm. A maximum mid-span displacement of 170.7 mm occurred 63.2 ms after the arrival of the blast wave. The system's initial stiffness was measured to be 4.59 kN/mm. The panel failed in a combination of flexure and rolling shear, initiated by the failure of two finger joints near the lower load application point. Very severe rolling shear damage was apparent throughout the panel. All five laminates failed near the zone of initial flexural failure. A minimal amount of wood crushing was observed in the eighteen screw holes in the end blocks. Most screws were left with little permanent deformations. Both angles showed no sign of damage.

4.3.2.7 Specimen CLT7: Axially Unrestrained Full-scale CLT Panel with 2 ML24Z Angles

A driver pressure of 630.2 kPa was used, which resulted in a peak reflected pressure of 81.5 kPa and a peak reflected impulse of 790.3 kPa-ms over a positive phase of 23.0 ms. A peak dynamic resistance of 139.4 kN was measured, correlating to a mid-span displacement of 39.3 mm. A maximum mid-span displacement of 111.3 mm occurred 36.8 ms after the arrival of the blast wave. The system's initial stiffness was measured to be 4.29 kN/mm. The panel showed signs of minor flexural damage on the tension face, indicating that it was most likely on the onset of failure. Very

minor longitudinal and rolling shear damage was apparent throughout the panel, between the connections and the load application points. A significant amount of wood crushing in the CLT panel was observed at both top and bottom ends, where the ML24Z angles were connected. All four ML24Z angles underwent a significant amount of yielding. The top connection experienced failure of all screws, whereas the bottom connection experienced failure of two screws. A high amount of wood crushing was observed in the end block screw holes. A significant opening between both end blocks and the CLT panel was observed, due to lack of axial restraint.

4.3.2.8 Specimen CLT8: Axially Unrestrained Full-scale CLT Panel with 3 ML24Z Angles

A driver pressure of 626.0 kPa was used, which resulted in a peak reflected pressure of 87.2 kPa and a peak reflected impulse of 816.1 kPa-ms over a positive phase of 23.4 ms. A peak dynamic resistance of 133.6 kN was measured, correlating to a mid-span displacement of 33.3 mm. A maximum mid-span displacement of 193.8 mm occurred 91.6 ms after the arrival of the blast wave. The system's initial stiffness was measured to be 5.17 kN/mm. The panel completely failed in a combination of flexure and rolling shear, initiated by the failure of a finger joint and knot near the top load application point. Severe longitudinal and rolling shear damage was apparent throughout the panel, especially in the top half where flexural failure was initiated. All five laminates were observed to have failed near the zone of initial flexural failure, with the compression face laminates showing signs of compression failure. Some signs wood crushing in the CLT panel was observed at both top and bottom ends, where the ML24Z angles were connected. All six ML24Z angles underwent a minor amount of yielding, more noticeably at the top end block. Minor amounts of wood crushing were observed in the end block screw holes.

4.3.2.9 Specimen CLT9: Axially Unrestrained Full-scale CLT Panel with 4 ML24Z Angles

A driver pressure of 629.5 kPa was used, which resulted in a peak reflected pressure of 87.2 kPa and a peak reflected impulse of 814.6 kPa-ms over a positive phase of 21.4 ms. A peak dynamic resistance of 142.2 kN was measured, correlating to a mid-span displacement of 24.0 mm. A maximum mid-span displacement of 116.3 mm occurred 44.6 ms after the arrival of the blast wave. The system's initial stiffness was measured to be 5.23 kN/mm. The panel failed in a combination of flexure and rolling shear, initiated by the failure of a knot near the top load application point. Severe longitudinal and rolling shear damage was apparent throughout the panel, most severe near the top load application point where flexural failure was initiated. All five laminates failed near

the zone of initial flexural failure. Little-to-no wood crushing in the CLT panel was observed at both top and bottom ends, where the ML24Z angles were connected. All eight ML24Z angles underwent a very minor amount of yielding, more noticeably at the top end block. No noticeable wood crushing was observed in the end block screw holes.

4.3.2.10 Specimen CLT10: Axially Restrained Full-scale CLT Panel with 2 ML24Z Angles

A driver pressure of 617.8 kPa was used, which resulted in a peak reflected pressure of 69.8 kPa and a peak reflected impulse of 624.6 kPa-ms over a positive phase of 21.2 ms. A peak dynamic resistance of 131.7 kN was measured, correlating to a mid-span displacement of 32.3 mm. A maximum mid-span displacement of 85.7 mm occurred 34.6 ms after the arrival of the blast wave. The system's initial stiffness was measured to be 4.35 kN/mm. The panel failed in a combination of flexure and rolling shear, initiated by the failure of a knot near the lower load application point. Severe longitudinal and rolling shear damage was apparent throughout the panel. A noticeable amount of wood crushing in the CLT panel was observed at both top and bottom ends, where the ML24Z angles were connected. All four ML24Z angles underwent a moderate amount of yielding. A moderate amount of wood crushing was observed in all the end block screw holes.

4.3.2.11 Specimen CLT11: Axially Restrained Full-scale CLT Panel with 3 ML24Z Angles

A driver pressure of 631.6 kPa was used, which resulted in a peak reflected pressure of 85.2 kPa and a peak reflected impulse of 823.6 kPa-ms over a positive phase of 22.2 ms. A peak dynamic resistance of 157.3 kN was measured, correlating to a mid-span displacement of 41.8 mm. A maximum mid-span displacement of 102.8 mm occurred 36.6 ms after the arrival of the blast wave. The system's initial stiffness was measured to be 4.68 kN/mm. The panel failed in a combination of flexure and rolling shear, initiated by the failure of a finger joint and knot near the top load application point. Severe longitudinal and rolling shear damage was apparent throughout the panel, most particularly near the top load application point where flexural failure was initiated. All five laminates were observed to have been severely damaged or failed near the zone of initial flexural failure. A moderate amount of wood crushing in the CLT panel was observed at both top and bottom ends, where the ML24Z angles were connected. All six ML24Z angles underwent a moderate amount of yielding, more noticeably at the top end block. A moderate amount of wood crushing was observed in all the end block screw holes.

4.3.2.12 Specimen CLT12: Axially Unrestrained Full-scale CLT Panel with 3.25” Deep EACs

A driver pressure of 750.1 kPa was used, which resulted in a peak reflected pressure of 91.9 kPa and a peak reflected impulse of 961.4 kPa-ms over a positive phase of 22.8 ms. A peak dynamic resistance of 163.9 kN was measured, correlating to a mid-span displacement of 122.5 mm. A maximum mid-span displacement of 140.1 mm occurred 37.8 ms after the arrival of the blast wave. The system’s initial stiffness was measured to be 4.82 kN/mm. The top and bottom EACs were fully deformed and reached densification. This in turn caused the panel to reach a level of damage characterized as onset of flexural failure, where only the leftmost outer laminate failed at a finger joint. Heavy rolling shear was observed in the top and bottom thirds of the panel. No weld failure was observed in the EACs.

4.3.2.13 Specimen CLT13: Axially Unrestrained Full-scale CLT Panel with 3.25” Deep EACs

A driver pressure of 846.0 kPa was used, which resulted in a peak reflected pressure of 107.9 kPa and a peak reflected impulse of 1068.1 kPa-ms over a positive phase of 25.0 ms. A peak dynamic resistance of 157.0 kN was measured, correlating to a mid-span displacement of 124.8 mm. A maximum mid-span displacement of 214.3 mm occurred 56.0 ms after the arrival of the blast wave. The system’s initial stiffness was measured to be 5.14 kN/mm. The top and bottom EACs were fully deformed and reached densification. This in turn caused the panel to fail in a combination of flexure and rolling shear, whereby failure was initiated at the bottom load application point. Two finger joint failures were observed on the tension face. Heavy rolling shear was observed throughout the panel, but was more significant in the lower half of the panel. No weld failure was observed in the EACs.

4.3.2.14 Specimen CLT14: Axially Unrestrained Full-scale CLT Panel with 3.25” Deep EACs

CLT14 was subjected to four different pressure-impulse combinations. For the first shot, a driver pressure of 93.8 kPa was used, which resulted in a peak reflected pressure of 16.9 kPa and a peak reflected impulse of 155.3 kPa-ms over a positive phase of 18.8 ms. A peak dynamic resistance of 41.1 kN was measured, correlating to a mid-span displacement of 10.9 mm. A maximum mid-span displacement of 11.1 mm occurred 25.4 ms after the arrival of the blast wave. The system’s initial

stiffness was measured to be 4.92 kN/mm. The top and bottom EACs, as well as CLT panel all remained elastic and were not damaged by the applied load.

For the second shot, a driver pressure of 252.3 kPa was used, which resulted in a peak reflected pressure of 39.2 kPa and a peak reflected impulse of 328.5 kPa-ms over a positive phase of 20.0 ms. A peak dynamic resistance of 95.0 kN was measured, correlating to a mid-span displacement of 27.5 mm. A maximum mid-span displacement of 27.7 mm occurred 24.4 ms after the arrival of the blast wave. The system's initial stiffness was measured to be 6.76 kN/mm. The top and bottom EACs yielded and were permanently damaged, although not significantly. The CLT panel remained elastic with no signs of damage. The specimen was shored, secured, and the EACs were removed and replaced with new EACs of identical geometries for the next shot.

For the third shot, a driver pressure of 514.3 kPa was used, which resulted in a peak reflected pressure of 76.6 kPa and a peak reflected impulse of 695.2 kPa-ms over a positive phase of 21.4 ms. A peak dynamic resistance of 114.9 kN was measured, correlating to a mid-span displacement of 74.0 mm. A maximum mid-span displacement of 77.0 mm occurred 30.2 ms after the arrival of the blast wave. The system's initial stiffness was measured to be 5.14 kN/mm. The top and bottom EACs yielded significantly and were permanently damaged. The CLT panel remained elastic with no signs of damage. The specimen was shored, secured, and the EACs were removed and replaced with new EACs of identical geometries for the next and final shot.

For the fourth and final shot on CLT14, a driver pressure of 823.9 kPa was used, which resulted in a peak reflected pressure of 97.3 kPa and a peak reflected impulse of 1016.0 kPa-ms over a positive phase of 24.8 ms. A peak dynamic resistance of 165.0 kN was measured, correlating to a mid-span displacement of 123.2 mm. A maximum mid-span displacement of 244.6 mm occurred 79.2 ms after the arrival of the blast wave. The system's initial stiffness was measured to be 4.67 kN/mm. The top and bottom EACs were fully deformed and reached densification. This in turn caused the panel to fail in a combination of flexure and rolling shear, whereby failure was initiated at the top load application point. Three finger joints were observed to be located in the flexural failure zone, possibly influencing the failure to initiate at this location. Heavy rolling shear was observed throughout the panel, but was more significant in the lower half of the panel. All five laminates were observed to have failed near the zone of initial flexural failure. No weld failure was observed in the EACs.

4.3.2.15 Specimen CLT15: Axially Unrestrained Full-Scale CLT Panel with 2.5" Deep EACs

CLT15 was subjected to four different pressure-impulse combinations. For the first shot, a driver pressure of 82.0 kPa was used, which resulted in a peak reflected pressure of 13.9 kPa and a peak reflected impulse of 111.3 kPa-ms over a positive phase of 17.6 ms. A peak dynamic resistance of 16.7 kN was measured, correlating to a mid-span displacement of 8.2 mm. A maximum mid-span displacement of 9.0 mm occurred 25.6 ms after the arrival of the blast wave. Due to the low amount of displacement and load imparted onto the system, the system's initial stiffness could not be determined. The top and bottom EACs, as well as CLT panel all remained elastic and were not damaged by the applied load.

For the second shot, a driver pressure of 279.9 kPa was used, which resulted in a peak reflected pressure of 44.2 kPa and a peak reflected impulse of 396.6 kPa-ms over a positive phase of 20.4 ms. A peak dynamic resistance of 83.4 kN was measured, correlating to a mid-span displacement of 38.2 mm. A maximum mid-span displacement of 38.5 mm occurred 28.6 ms after the arrival of the blast wave. The system's initial stiffness was measured to be 4.65 kN/mm. The top and bottom EACs yielded moderately and were permanently damaged. The CLT panel remained elastic with no signs of damage. The specimen was shored, secured, and the EACs were removed and replaced with new EACs of identical geometries for the next shot.

For the third shot, a driver pressure of 477.8 kPa was used, which resulted in a peak reflected pressure of 65.8 kPa and a peak reflected impulse of 865.8 kPa-ms over a positive phase of 22.0 ms. A peak dynamic resistance of 84.2 kN was measured, correlating to a mid-span displacement of 95.8 mm. A maximum mid-span displacement of 95.8 mm occurred 38.8 ms after the arrival of the blast wave. The system's initial stiffness was measured to be 3.38 kN/mm. The top and bottom EACs yielded significantly and were permanently damaged. Both EACs started undergoing densification. The CLT panel remained elastic with no signs of damage. The specimen was shored, secured, and the EACs were removed and replaced with new EACs of identical geometries for the next and final shot.

For the fourth and final shot on CLT15, a driver pressure of 688.1 kPa was used, which resulted in a peak reflected pressure of 82.0 kPa and a peak reflected impulse of 865.8 kPa-ms over a positive phase of 21.0 ms. A peak dynamic resistance of 165.7 kN was measured, correlating to a

mid-span displacement of 125.1 mm. A maximum mid-span displacement of 172.0 mm occurred 52.8 ms after the arrival of the blast wave. The system's initial stiffness was measured to be 3.56 kN/mm. The top and bottom EACs were fully deformed and reached densification. This in turn caused the panel to fail in a combination of flexure and rolling shear, whereby failure was initiated at the top load application point. Two finger joints were observed to be located in the flexural failure zone, possibly influencing the failure to initiate at this location. Heavy rolling shear was observed throughout the panel, but was more significant in the top half of the panel. All five laminates were observed to have failed near the zone of initial flexural failure. No weld failure was observed in the EACs.

Table 4.5: Summary of Dynamic Testing on Full-Scale CLT Specimens

Test Name	**Boundary Condition**	**P_r (kPa)**	**I_r (kPa-ms)**	**R_{peak} (kN)**	**Δ_{Rpeak} (mm)**	**Δ_{max} (mm)**	**$t_{\Delta max}$ (ms)**	**K_i (kN/mm)**	**$\dot{\epsilon}_{average}$ (s^{-1})**	**Ultimate Failure Mode**
CLT1	Simply Supported	62.5	601.1	159.0	31.6	52.2	25.0	5.44	0.25	W_F
CLT2	Simply Supported	62.2	680.4	176.3	29.9	74.7	29.0	6.00	0.32	W_F
CLT3	Simply Supported	71.4	658.9	172.0	25.3	146.3	75.0	5.31	0.26	W_F
CLT4	Thick Angle (3 Screws)	68.4	662.7	82.4	22.9	289.5	92.2	2.66	IE	C_F
CLT5	Thick Angle (6 Screws)	78.3	787.2	151.7	39.4	96.4	32.2	4.56	0.15	W_F
CLT6	Thick Angle (9 Screws)	83.6	832.5	163.4	37.7	170.7	63.2	4.59	0.26	W_F
CLT7	2 ML24Z	81.5	790.3	139.4	39.3	111.3	36.8	4.29	0.23	C_F
CLT8	3 ML24Z	85.2	823.6	157.3	41.8	102.8	36.6	4.68	0.21	W_F
CLT9	4 ML24Z	87.2	814.6	142.2	24.0	116.3	44.6	5.23	0.24	W_F
CLT10	2 ML24Z	69.8	624.6	131.7	32.3	85.7	34.6	4.35	0.20	W_F
CLT11	3 ML24Z	87.2	816.1	133.6	33.3	193.8	91.6	5.17	0.20	W_F
CLT12	3.25” Deep EACs	91.9	961.4	163.9	122.5	140.1	37.8	4.82	0.27	W_F
CLT13	3.25” Deep EACs	107.9	1068.1	157.0	124.8	214.3	56.0	5.14	0.36	W_F
CLT14-1	3.25” Deep EACs	16.9	155.3	41.1	10.9	11.1	25.4	4.92	0.10	Elastic
CLT14-2	3.25” Deep EACs	39.2	328.5	95.01	27.5	27.7	24.4	6.76	0.10	C_Y
CLT14-3	3.25” Deep EACs	76.6	695.2	114.9	74.0	77.0	30.2	5.14	0.21	C_Y
CLT14-4	3.25” Deep EACs	97.3	1016.0	165.0	123.2	244.6	79.2	4.67	0.40	W_F
CLT15-1	2.5” Deep EACs	13.9	111.3	16.7	8.2	9.0	25.6	-	0.11	Elastic
CLT15-2	2.5” Deep EACs	44.2	396.6	83.4	38.2	38.5	28.6	4.65	0.19	C_Y
CLT15-3	2.5” Deep EACs	65.8	647.3	84.2	95.8	95.8	38.8	3.38	0.18	C_Y
CLT15-4	2.5” Deep EACs	82.0	865.8	165.7	125.1	172.0	52.8	3.56	0.28	W_F
			Averages	**156.8***					**0.23**	
			CoVs	**0.08***					**0.34**	

P_r: Peak reflected pressure **I_r**: Peak reflected impulse **R_{peak}**: Peak resistance **Δ_{Rpeak}**: Displacement at **R_{peak}**
Δ_{max}: Max displacement **$t_{\Delta max}$**: Time-to-**Δ_{max}** **K_i**: Initial system stiffness **$\dot{\epsilon}_{average}$**: Average strain-rate
W_F: Wood failure C_F: Connection failure C_Y: Connection yielding *: Based on W_F

4.3.3 Full-Scale Glulam Specimens

This subsection summarizes the results of twenty-seven dynamic full-scale tests on nineteen glulam specimens. The boundary conditions varied from idealized simply supported to realistic boundary connections, which includes typical bolted connections and energy-absorbing connections. The driver length varied throughout the dynamic full-scale glulam tests, from 9 ft. to 13 ft. Each test name reflects the type of test, as well as its numerical sequence. For cases where specimens were exposed to multiple applied loads, this is followed by a numerical representation of the order of testing (e.g. G16-5 is the third full-scale glulam specimen to be tested, and at the time of report was tested for a total of five times). Table 4.6 summarizes all dynamic full-scale glulam test, including test result information such as the driver length, peak reflected pressure, peak reflected impulse, peak dynamic resistance of the glulam beam, displacement at peak resistance, time-to-peak resistance, maximum beam mid-span displacement, initial system stiffness, average strain-rate in the beam, and failure mode of the glulam assembly. The averages and their associated coefficient of variation are also given for key properties. Typical results from a dynamic full-scale test are shown in Figure 4.11. These include displacement-, strain-, and reaction-time histories.

4.3.3.1 Specimen G1: Full-scale Glulam Beam with Simply Supported Boundary Conditions

A 9 ft. driver with a driver pressure of 461.9 kPa was used, which resulted in a peak reflected pressure of 67.7 kPa and a peak reflected impulse of 637.2 kPa-ms over a positive phase of 26.0 ms. A peak dynamic resistance of 210.6 kN was measured, correlating to a mid-span displacement of 24.4 mm which occurred 13.6 ms after the arrival of the blast wave. A maximum mid-span displacement of 48.5 mm occurred 26.6 ms after the arrival of the blast wave. The specimen's initial stiffness was measured to be 8.58 kN/mm. The glulam specimen experienced flexural failure, with failure occurring at mid-span. From video review, failure was initiated at a knot on the tension face of the beam. No finger joint failure was observed. Flexural damage propagated through the depth until approximately half the depth of the member.

4.3.3.2 Specimen G2: Full-scale Glulam Beam with Simply Supported Boundary Conditions

A 9 ft. driver with a driver pressure of 494.4 kPa was used, which resulted in a peak reflected pressure of 75.0 kPa and a peak reflected impulse of 659.7 kPa-ms over a positive phase of 24.2 ms. A peak dynamic resistance of 214.4 kN was measured, correlating to a mid-span displacement of 23.9 mm which occurred 12.4 ms after the arrival of the blast wave. A maximum mid-span displacement of 76.4 mm occurred 33.2 ms after the arrival of the blast wave. The specimen's initial stiffness was measured to be 9.35 kN/mm. The glulam specimen experienced flexural failure in the constant moment region. Failure was initiated at a knot on the tension face of the beam. A finger joint failure was observed on the tension face. Flexural damage propagated through the depth until approximately three quarters of the member depth.

4.3.3.3 Specimen G3: Full-scale Glulam Beam with Simply Supported Boundary Conditions

A 9 ft. driver with a driver pressure of 534.3 kPa was used, which resulted in a peak reflected pressure of 80.4 kPa and a peak reflected impulse of 724.4 kPa-ms over a positive phase of 25.4 ms. A peak dynamic resistance of 232.0 kN was measured, correlating to a mid-span displacement of 26.8 mm which occurred 12.6 ms after the arrival of the blast wave. A maximum mid-span displacement of 124.2 mm occurred 50.6 ms after the arrival of the blast wave. The specimen's initial stiffness was measured to be 9.87 kN/mm. The glulam specimen experienced flexural failure in the constant moment region. From video review, failure was initiated at a knot on the tension face of the beam. A finger joint failure was observed on the tension face. Flexural damage propagated through the depth the member, almost to the point of the whole member failing in half. The flexural failure in this specimen had noticeably more splintering than the other two simply supported glulam specimens.

4.3.3.4 Specimen G4: Full-scale Glulam Beam with 2x1 Bolted Connections (e_p = 19.1 mm)

A 9 ft. driver with a driver pressure of 548.1 kPa was used, which resulted in a peak reflected pressure of 69.9 kPa and a peak reflected impulse of 735.2 kPa-ms over a positive phase of 25.8 ms. A peak dynamic resistance of 237.4 kN was measured, correlating to a mid-span displacement of 43.4 mm which occurred 18.6 ms after the arrival of the blast wave. A maximum mid-span displacement of 47.5 mm occurred 21.8 ms after the arrival of the blast wave. The system's initial

stiffness was measured to be 6.43 kN/mm. The glulam specimen experienced flexural failure at mid-span. From video review, failure was initiated at a knot on the tension face of the beam. A finger joint failure was observed on the tension face. Significant bolt yielding and wood crushing was observed in the bolted connections. Minor splitting was observed starting from the beam ends through the bolt group, however this split did not propagate beyond the innermost bolt. Upon disassembly of the specimen, all four bolts were observed to have significant yielding and permanent deformations.

4.3.3.5 Specimen G5: Full-scale Glulam Beam with 2x1 Bolted Connections (e_p = 19.1 mm)

A 9 ft. driver with a driver pressure of 559.2 kPa was used, which resulted in a peak reflected pressure of 71.1 kPa and a peak reflected impulse of 720.8 kPa-ms over a positive phase of 25.8 ms. A peak dynamic resistance of 204.0 kN was measured, correlating to a mid-span displacement of 38.6 mm which occurred 15.4 ms after the arrival of the blast wave. A maximum mid-span displacement of 90.5 mm occurred 43.6 ms after the arrival of the blast wave. The system's initial stiffness was measured to be 6.70 kN/mm. The glulam specimen experienced severe flexural failure at mid-span. From video review, failure was initiated at a finger joint on the tension face of the beam. Three finger joint failures were observed on the tension face, with two of them being aligned. Signs of wood compression failure was observed at mid-span on the compression face. Significant bolt yielding and wood crushing was observed in the connections. Minor splitting was observed, however, this was limited to the region between the bolts. Upon disassembly of the specimen, it was observed that all four bolts experienced significant yielding and permanent deformations.

4.3.3.6 Specimen G6: Full-scale Glulam Beam with 2x1 Bolted Connections (e_p = 38.1 mm)

A 9 ft. driver with a driver pressure of 555.7 kPa was used, which resulted in a peak reflected pressure of 73.9 kPa and a peak reflected impulse of 744.1 kPa-ms over a positive phase of 25.4 ms. A peak dynamic resistance of 208.5 kN was measured, correlating to a mid-span displacement of 36.9 mm which occurred 14.6 ms after the arrival of the blast wave. A maximum mid-span displacement of 139.2 mm occurred 68.2 ms after the arrival of the blast wave. The system's initial stiffness was measured to be 7.40 kN/mm. The glulam specimen experienced severe flexural failure at mid-span. From video review, failure was initiated at a finger joint on the tension face of the beam. One finger joint and two partial finger joint failure were observed on the tension face.

Severe wood compression failure was observed near the top load application point on the compression face. Significant bolt yielding and wood crushing was observed in the bolted connections. Upon disassembly of the specimen, all four bolts and bolt holes experienced significant yielding and permanent deformations.

4.3.3.7 Specimen G7: Full-scale Glulam Beam with 2x1 Bolted Connections (e_p = 76.2 mm)

A 9 ft. driver with a driver pressure of 553.0 kPa was used, which resulted in a peak reflected pressure of 70.7 kPa and a peak reflected impulse of 732.6 kPa-ms over a positive phase of 25.2 ms. A peak dynamic resistance of 170.4 kN was measured, correlating to a mid-span displacement of 24.1 mm which occurred 10.2 ms after the arrival of the blast wave. A maximum mid-span displacement of 195.8 mm occurred 54.6 ms after the arrival of the blast wave. The system's initial stiffness was measured to be 6.68 kN/mm. The glulam specimen experienced severe splitting failure at both connections. Following this, the beam was effectively split longitudinally into two separate pieces, which both failed in flexure. Significant wood compression failure was observed at mid-span on the compression face. Noticeable bolt yielding and wood crushing was observed in the bolted connections. Upon disassembly of the specimen, all four bolts and bolt holes experienced a moderate amount of yielding and permanent deformations.

4.3.3.8 Specimen G8: Full-scale Glulam Beam with 2x1 Bolted Connections (e_p = 133.5 mm)

A 9 ft. driver with a driver pressure of 557.1 kPa was used, which resulted in a peak reflected pressure of 72.8 kPa and a peak reflected impulse of 705.7 kPa-ms over a positive phase of 21.0 ms. A peak dynamic resistance of 78.0 kN was measured, correlating to a mid-span displacement of 13.3 mm which occurred 7.2 ms after the arrival of the blast wave. A maximum mid-span displacement of 248.2 mm occurred 82.8 ms after the arrival of the blast wave. The system's initial stiffness was measured to be 6.40 kN/mm. The glulam specimen experienced severe splitting failure at both connections. From video review, splitting failure was initiated at the bottom connection, followed shortly by splitting failure of the top connection. Following this, the beam was effectively split into two separate pieces, which both failed in flexure. Significant wood compression failure was observed at mid-span on the compression face. Very minimal bolt yielding and wood crushing was observed in the bolted connections.

4.3.3.9 Specimen G9: Full-scale Glulam Beam with 2x1 Bolted Connections (e_p = 203.2 mm)

A 9 ft. driver with a driver pressure of 549.5 kPa was used, which resulted in a peak reflected pressure of 69.7 kPa and a peak reflected impulse of 716.0 kPa-ms over a positive phase of 23.0 ms. A peak dynamic resistance of 44.1 kN was measured, correlating to a mid-span displacement of 5.4 mm which occurred 4.8 ms after the arrival of the blast wave. A maximum mid-span displacement of 289.4 mm occurred 52.0 ms after the arrival of the blast wave. The system's initial stiffness was measured to be 8.56 kN/mm. The glulam specimen experienced severe splitting failure at both connections. From video review, splitting failure was initiated at the bottom connection, followed shortly by splitting failure of the top connection. Following this, the beam was effectively split into two separate pieces, which both failed in flexure. Due to the severe nature of the failure mode, significant wood compression failure was observed at mid-span on the compression face. No bolt yielding and wood crushing was observed in the bolted connections, due to the fact that the beam failed very prematurely in splitting.

4.3.3.10 Specimen G10: Full-scale Glulam Beam with 2x1 Reinforced Bolted Connections (e_p = 76.2 mm, 3 STSs per Connection)

A 9 ft. driver with a driver pressure of 552.3 kPa was used, which resulted in a peak reflected pressure of 74.2 kPa and a peak reflected impulse of 738.2 kPa-ms over a positive phase of 26.0 ms. A peak dynamic resistance of 199.0 kN was measured, correlating to a mid-span displacement of 33.8 mm which occurred 13.6 ms after the arrival of the blast wave. A maximum mid-span displacement of 94.3 mm occurred 39.8 ms after the arrival of the blast wave. The system's initial stiffness was measured to be 8.24 kN/mm. Just prior to flexural failure, a small split occurred at the top connection, which propagated to mid-span. This split was limited, however, to a maximum crack width of approximately 3 mm. From video review, flexural failure was initiated at a knot on the tension face of the beam. A finger joint failure was observed on the tension face. The heads of the top connection STSs were slightly embedded into the beam, which may explain to some extent the minor splitting that occurred. The bottom connection did not experience splitting. Significant bolt yielding and wood crushing was observed in the bolted connections. Upon disassembly of the specimen, all four bolts and bolt holes experienced significant yielding and permanent deformations. The top connection split was observed to pass through the whole width of the beam, and was not limited to a superficial check.

4.3.3.11 Specimen G11: Full-scale Glulam Beam with 2x1 Reinforced Bolted Connections (e_p = 133.5 mm, 6 STSs per Connection)

A 9 ft. driver with a driver pressure of 564.7 kPa was used, which resulted in a peak reflected pressure of 73.3 kPa and a peak reflected impulse of 774.6 kPa-ms over a positive phase of 26.0 ms. A peak dynamic resistance of 194.9 kN was measured, correlating to a mid-span displacement of 34.1 mm which occurred 13.2 ms after the arrival of the blast wave. A maximum mid-span displacement of 88.5 mm occurred 30.6 ms after the arrival of the blast wave. The system's initial stiffness was measured to be 6.85 kN/mm. The glulam specimen experienced severe flexural failure at mid-span, along with a minor superficial crack emanating from the top connection. This crack was limited, however, to a width of approximately 1 to 2 mm. From video review, failure was initiated at a knot on the tension face of the beam. No finger joint failure was observed. Significant bolt yielding and wood crushing was observed in the bolted connections. Upon disassembly of the specimen, all four bolts and bolt holes experienced significant yielding and permanent deformations.

4.3.3.12 Specimen G12: Full-scale Glulam Beam with 2x1 Reinforced Bolted Connections (e_p = 203.2 mm, 9 STSs per Connection)

A 9 ft. driver with a driver pressure of 562.6 kPa was used, which resulted in a peak reflected pressure of 74.2 kPa and a peak reflected impulse of 771.1 kPa-ms over a positive phase of 26.6 ms. A peak dynamic resistance of 223.5 kN was measured, correlating to a mid-span displacement of 41.4 mm which occurred 17.8 ms after the arrival of the blast wave. A maximum mid-span displacement of 69.4 mm occurred 47.0 ms after the arrival of the blast wave. The system's initial stiffness was measured to be 6.91 kN/mm. The glulam specimen experienced flexural failure at mid-span. From video review, failure was initiated at a knot and a finger joint on the tension face of the beam. Two finger joint failures were observed on the tension face. Significant bolt yielding and wood crushing was observed in the bolted connections. No splitting failure was observed. Upon disassembly of the specimen, all four bolts experienced significant yielding and permanent deformations, particularly the top connection where damage was most severe. Minor splitting was observed going from bolt to bolt, however, this split did not propagate beyond the region between bolts.

4.3.3.13 Specimen G13: Full-scale Glulam Beam with 2x2 Bolted Connections (e_p = 19.1 mm)

A 9 ft. driver with a driver pressure of 548.1 kPa was used, which resulted in a peak reflected pressure of 71.5 kPa and a peak reflected impulse of 736.0 kPa-ms over a positive phase of 23.8 ms. A peak dynamic resistance of 234.3 kN was measured, correlating to a mid-span displacement of 29.9 mm which occurred 14.0 ms after the arrival of the blast wave. A maximum mid-span displacement of 96.4 mm occurred 52.4 ms after the arrival of the blast wave. The system's initial stiffness was measured to be 8.51 kN/mm. The glulam specimen experienced severe flexural failure at mid-span. From video review, failure was initiated at two knots on the tension face of the beam. A finger joint failure was observed on the tension face. Damage propagation was nearly through the whole depth of the beam. Minor wood compression failure was observed at mid-span on the compression face. Noticeable bolt yielding and wood crushing was observed in the bolted connections. Upon disassembly of the specimen, three of the four bottom connection bolts and bolt holes were moderately yielded and deformed, respectively, whereas three of the four top connections bolts and bolt holes were significantly yielded and deformed, respectively. No splitting was observed in either connection.

4.3.3.14 Specimen G14: Full-scale Glulam Beam with 2x3 Bolted Connections (e_p = 19.1 mm)

A 9 ft. driver with a driver pressure of 563.3 kPa was used, which resulted in a peak reflected pressure of 73.0 kPa and a peak reflected impulse of 761.4 kPa-ms over a positive phase of 25.8 ms. A peak dynamic resistance of 252.4 kN was measured, correlating to a mid-span displacement of 30.5 mm which occurred 13.0 ms after the arrival of the blast wave. A maximum mid-span displacement of 125.2 mm occurred 50.6 ms after the arrival of the blast wave. The system's initial stiffness was measured to be 8.92 kN/mm. The glulam specimen experienced severe flexural failure at mid-span. From video review, failure was initiated at a knot on the tension face of the beam. A finger joint failure was observed on the tension face. Damage propagation was nearly through the whole depth of the beam. No discernible bolt yielding or wood crushing was observed in the bolted connections. Upon disassembly of the specimen, three of the six bolt holes showed very minor sign of wood crushing for both top and bottom connections. Upon removal of the bolts, none of the twelve bolts seemed to have any noticeable permanent deformations. No splitting was observed in either connection.

4.3.3.15 Specimen G15: Full-scale Glulam Beam with 7.5” Deep EACs

G15 was subjected to two different pressure-impulse combinations, both with a 9 ft. driver. For the first shot, a driver pressure of 143.4 kPa was used, which resulted in a peak reflected pressure of 23.5 kPa and a peak reflected impulse of 187.8 kPa-ms over a positive phase of 18.2 ms. A peak dynamic resistance of 83.1 kN was measured, correlating to a mid-span displacement of 10.3 mm which occurred 18.6 ms after the arrival of the blast wave. A maximum mid-span displacement of 10.6 mm occurred 18.0 ms after the arrival of the blast wave. The system’s initial stiffness was measured to be 8.14 kN/mm. The top and bottom EACs, as well as glulam beam all remained elastic and were not damaged by the applied load.

For the second shot, a driver pressure of 536.4 kPa was used, which resulted in a peak reflected pressure of 81.1 kPa and a peak reflected impulse of 726.9 kPa-ms over a positive phase of 26.0 ms. A peak dynamic resistance of 195.8 kN was measured, correlating to a mid-span displacement of 27.9 mm which occurred 12.6 ms after the arrival of the blast wave. A maximum mid-span displacement of 140.0 mm occurred 66.4 ms after the arrival of the blast wave. The system’s initial stiffness was measured to be 7.90 kN/mm. The top and bottom EACs yielded and were permanently damaged, although not significantly. The glulam specimen experienced flexural failure in the constant moment region. From video review, failure was initiated at a knot on the tension face of the beam. No finger joint failure was observed on the tension face. Flexural damage propagated through member depth. No weld failure was observed in the EACs.

4.3.3.16 Specimen G16: Full-scale Glulam Beam with 5” Deep EACs

G16 was subjected to seven different pressure-impulse combinations. For the first shot, a 9 ft. driver with a driver pressure of 532.3 kPa was used, which resulted in a peak reflected pressure of 79.5 kPa and a peak reflected impulse of 713.6 kPa-ms over a positive phase of 26.6 ms. A peak dynamic resistance of 152.5 kN was measured, correlating to a mid-span displacement of 24.5 mm which occurred 11.2 ms after the arrival of the blast wave. A maximum mid-span displacement of 50.3 mm occurred 24.8 ms after the arrival of the blast wave. The system’s initial stiffness was measured to be 7.69 kN/mm. The top and bottom EACs yielded noticeably and were permanently damaged. The glulam beam remained elastic with no signs of damage. The specimen was shored, secured, and the EACs were removed and replaced with new EACs of identical geometries for the next shot.

For the second shot, a 9 ft. driver with a driver pressure of 536.4 kPa was used, which resulted in a peak reflected pressure of 84.5 kPa and a peak reflected impulse of 834.7 kPa-ms over a positive phase of 26.0 ms. A peak dynamic resistance of 159.1 kN was measured, correlating to a mid-span displacement of 28.7 mm which occurred 11.0 ms after the arrival of the blast wave. A maximum mid-span displacement of 68.9 mm occurred 27.0 ms after the arrival of the blast wave. The system's initial stiffness was measured to be 7.55 kN/mm. The top and bottom EACs yielded significantly and were permanently damaged. The glulam beam remained elastic with no signs of damage. The specimen was shored, secured, and the EACs were removed and replaced with new EACs of identical geometries for the next shot.

For the third shot, a 11 ft. driver with a driver pressure of 521.9 kPa was used, which resulted in a peak reflected pressure of 75.0 kPa and a peak reflected impulse of 814.7 kPa-ms over a positive phase of 26.6 ms. A peak dynamic resistance of 150.5 kN was measured, correlating to a mid-span displacement of 25.9 mm which occurred 11.2 ms after the arrival of the blast wave. A maximum mid-span displacement of 61.5 mm occurred 26.4 ms after the arrival of the blast wave. The system's initial stiffness was measured to be 7.52 kN/mm. The top and bottom EACs yielded significantly and were permanently damaged. The glulam beam remained elastic with no signs of damage. The specimen was shored, secured, and the EACs were removed and replaced with new EACs of identical geometries for the next shot.

For the fourth shot, a 11 ft. driver with a driver pressure of 621.2 kPa was used, which resulted in a peak reflected pressure of 77.9 kPa and a peak reflected impulse of 934.0 kPa-ms over a positive phase of 26.8 ms. A peak dynamic resistance of 157.3 kN was measured, correlating to a mid-span displacement of 27.0 mm which occurred 11.0 ms after the arrival of the blast wave. A maximum mid-span displacement of 82.5 mm occurred 29.4 ms after the arrival of the blast wave. The system's initial stiffness was measured to be 7.12 kN/mm. The top and bottom EACs yielded severely and were permanently damaged. By visual inspection, both EACs were near their respective densification limit. The glulam beam remained elastic with no signs of damage. The specimen was shored, secured, and the EACs were removed and replaced with new EACs of identical geometries for the next shot.

For the fifth shot, a 11 ft. driver with a driver pressure of 682.6 kPa was used, which resulted in a peak reflected pressure of 83.8 kPa and a peak reflected impulse of 986.6 kPa-ms over a positive

phase of 27.4 ms. A peak dynamic resistance of 161.0 kN was measured, correlating to a mid-span displacement of 28.3 mm which occurred 11.2 ms after the arrival of the blast wave. A maximum mid-span displacement of 86.8 mm occurred 30.0 ms after the arrival of the blast wave. The system's initial stiffness was measured to be 7.96 kN/mm. The top and bottom EACs yielded severely and were permanently damaged. By visual inspection, both EACs were approaching their respective densification limit. The glulam beam remained elastic with no signs of damage. The specimen was shored, secured, and the EACs were removed and replaced with new EACs of identical geometries for the next shot.

For the sixth shot, a 13 ft. driver with a driver pressure of 647.4 kPa was used, which resulted in a peak reflected pressure of 87.9 kPa and a peak reflected impulse of 1113.9 kPa-ms over a positive phase of 30.8 ms. A peak dynamic resistance of 166.2 kN was measured, correlating to a mid-span displacement of 79.2 mm which occurred 23.2 ms after the arrival of the blast wave. A maximum mid-span displacement of 99.2 mm occurred 31.4 ms after the arrival of the blast wave. The system's initial stiffness was measured to be 7.30 kN/mm. The top and bottom EACs yielded severely and were permanently damaged. By visual inspection, both EACs were very near or had just reached their respective densification limit. The glulam beam remained elastic with no signs of damage. The specimen was shored, secured, and the EACs were removed and replaced with new EACs of identical geometries for the next and final shot.

For the seventh and final shot, a 13 ft. driver with a driver pressure of 812.2 kPa was used, which resulted in a peak reflected pressure of 94.4 kPa and a peak reflected impulse of 1259.6 kPa-ms over a positive phase of 27.6 ms. A peak dynamic resistance of 227.4 kN was measured, correlating to a mid-span displacement of 96.2 mm which occurred 20.8 ms after the arrival of the blast wave. A maximum mid-span displacement of 278.5 mm occurred 41.8 ms after the arrival of the blast wave. The system's initial stiffness was measured to be 7.69 kN/mm. The top and bottom EACs were fully deformed and reached densification. This in turn caused the beam to fail in flexure, whereby failure was initiated at mid-span. Due to the severity of the applied load, the beam was split in half at mid-span in a combination of brash and splintering failure of the wood fibres. No weld failure was observed in the EACs.

4.3.3.17 Specimen G17: Full-scale Glulam Beam with 5” Deep EACs

A 13 ft. driver with a driver pressure of 755.7 kPa was used, which resulted in a peak reflected pressure of 84.9 kPa and a peak reflected impulse of 1199.4 kPa-ms over a positive phase of 28.6 ms. A peak dynamic resistance of 242.0 kN was measured, correlating to a mid-span displacement of 105.9 mm which occurred 23.0 ms after the arrival of the blast wave. A maximum mid-span displacement of 276.2 mm occurred 49.0 ms after the arrival of the blast wave. The system’s initial stiffness was measured to be 8.26 kN/mm. The top and bottom EACs were fully deformed and reached densification. This in turn caused the beam to fail in flexure. The glulam specimen experienced flexural failure in the constant moment region. From video review, failure was initiated at a knot and finger joint on the tension face of the beam. A finger joint failure was observed on the tension face. Flexural damage propagated through the entirety of the member depth. A significant amount of longitudinal shear failure was observed emanating from the flexural failure cracks. The beam had very significant permanent deformations. No weld failure was observed in the EACs.

4.3.3.18 Specimen G18: Full-scale Glulam Beam with 3.75” Deep EACs

A 13 ft. driver with a driver pressure of 640.5 kPa was used, which resulted in a peak reflected pressure of 83.2 kPa and a peak reflected impulse of 1047.7 kPa-ms over a positive phase of 28.0 ms. A peak dynamic resistance of 246.8 kN was measured, correlating to a mid-span displacement of 107.8 mm which occurred 24.0 ms after the arrival of the blast wave. A maximum mid-span displacement of 282.2 mm occurred 50.2 ms after the arrival of the blast wave. The system’s initial stiffness was measured to be 5.66 kN/mm. The top and bottom EACs were fully deformed and reached densification. This in turn caused the beam to fail in flexure. The glulam specimen experienced flexural failure in the constant moment region. From video review, failure was initiated at a knot and finger joint on the tension face of the beam. Two finger joint failures were observed on the tension face. Flexural damage propagated through the entirety of the member depth. A significant amount of longitudinal shear failure was observed emanating from the flexural failure cracks. The beam had very significant permanent deformations. No weld failure was observed in the EACs.

4.3.3.19 Specimen G19: Full-scale Glulam Beam with 3.75” Deep EACs

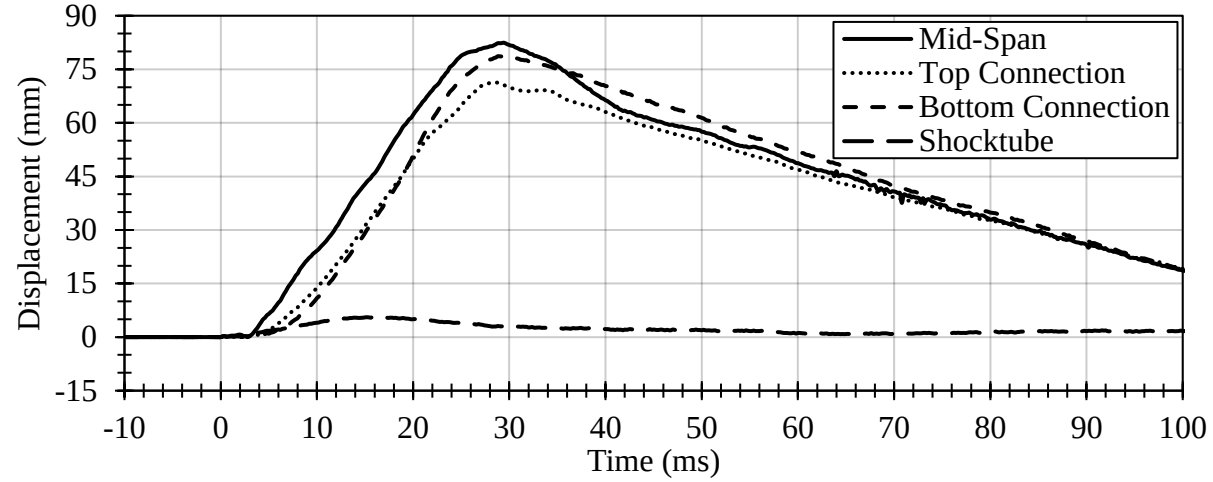
G19 was subjected to two different pressure-impulse combinations with a 13 ft. driver. For the first shot, a driver pressure of 412.3 kPa was used, which resulted in a peak reflected pressure of 58.0 kPa and a peak reflected impulse of 734.6 kPa-ms over a positive phase of 31.4 ms. A peak dynamic resistance of 107.2 kN was measured, correlating to a mid-span displacement of 46.4 mm which occurred 20.6 ms after the arrival of the blast wave. A maximum mid-span displacement of 65.8 mm occurred 34.0 ms after the arrival of the blast wave. The system’s initial stiffness was measured to be 6.08 kN/mm. The top and bottom EACs yielded significantly and were permanently damaged. The glulam beam remained elastic with no signs of damage. The specimen was shored, secured, and the EACs were removed and replaced with new EACs of identical geometries for the next and final shot.

For the second and final shot, a driver pressure of 635.7 kPa was used, which resulted in a peak reflected pressure of 84.4 kPa and a peak reflected impulse of 1033.1 kPa-ms over a positive phase of 28.2 ms. A peak dynamic resistance of 243.7 kN was measured, correlating to a mid-span displacement of 113.3 mm which occurred 25.4 ms after the arrival of the blast wave. A maximum mid-span displacement of 269.8 mm occurred 98.4 ms after the arrival of the blast wave. The system’s initial stiffness was measured to be 5.57 kN/mm. The top and bottom EACs were fully deformed and reached densification. This in turn caused the beam to fail in flexure. The glulam specimen experienced flexural failure in the constant moment region. From video review, failure was initiated at a knot on the tension face of the beam. A finger joint failure was observed on the tension face. Flexural damage propagated through approximately 90 % of the member depth. A significant amount of longitudinal shear failure was observed emanating from the flexural failure cracks. A noticeable amount of wood compression failure was observed at mid-span on the compression face. The beam had very significant permanent deformations. No weld failure was observed in the EACs.

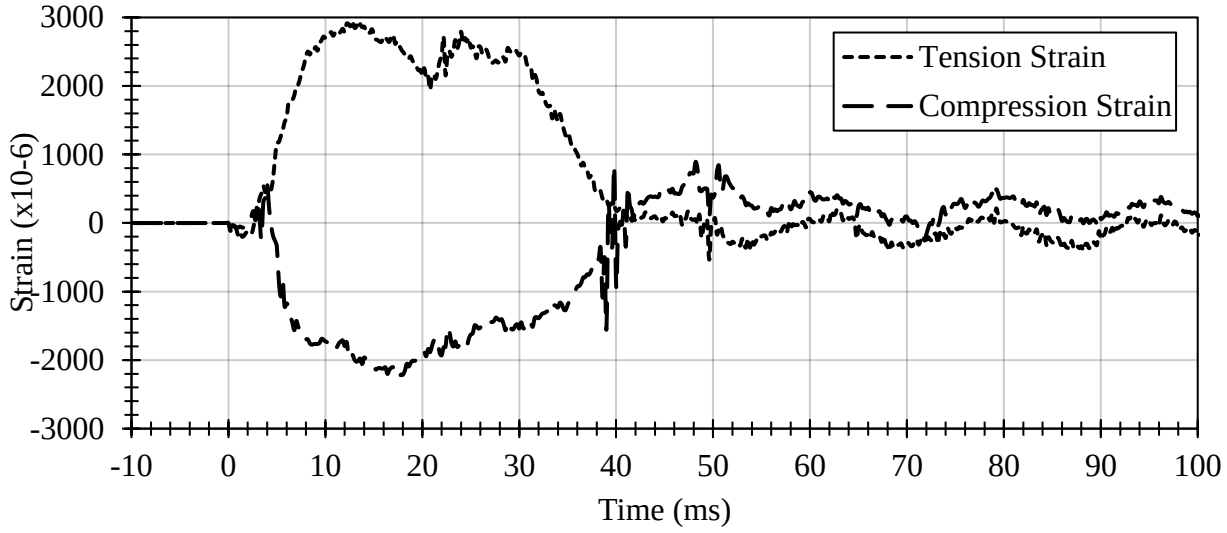
Table 4.6: Summary of Dynamic Testing on Full-Scale Glulam Specimens

Test	**L_{Driver} (ft)**	**Boundary Conditions**	**P_r (kPa)**	**I_r (kPa-ms)**	**R_{peak} (kN)**	**Δ_{Rpeak} (mm)**	**t_{Rpeak} (ms)**	**Δ_{max} (mm)**	**K_i (kN/mm)**	**$\dot{\epsilon}_{average}$ (s^{-1})**	**Ultimate Failure Mode**
G1	9	Simply Supported	67.7	637.2	210.6	24.4	13.6	48.5	8.58	0.43	W_F
G2	9	Simply Supported	75.0	659.7	214.4	23.9	12.4	75.4	9.35	0.37	W_F
G3	9	Simply Supported	80.4	724.4	232.0	26.8	12.6	50.6	9.87	0.51	W_F
G4	9	2x1 Bolts, e_p = 19.1 mm	69.9	735.2	237.4	43.4	18.6	47.5	6.43	0.30	W_F
G5	9	2x1 Bolts, e_p = 19.1 mm	71.1	720.8	204.0	38.6	15.4	90.5	6.70	0.42	W_F
G6	9	2x1 Bolts, e_p = 38.1 mm	73.9	744.1	208.5	36.9	14.6	139.2	7.40	0.41	W_F
G7	9	2x1 Bolts, e_p = 76.2 mm	70.7	732.6	170.4	24.1	10.2	195.8	6.68	0.35	C_F
G8	9	2x1 Bolts, e_p = 133.5 mm	72.8	705.7	78.0	13.3	7.2	248.2	6.40	0.44	C_F
G9	9	2x1 Bolts, e_p = 203.2 mm	69.7	716.0	44.1	5.4	4.8	289.4	8.56	0.34	C_F
G10	9	2x1 Bolts, e_p = 76.2 mm [R]	74.2	738.2	199.0	33.8	13.6	94.3	8.24	0.38	W_F
G11	9	2x1 Bolts, e_p = 133.5 mm [R]	73.3	774.6	194.4	34.1	13.2	88.5	6.85	0.34	W_F
G12	9	2x1 Bolts, e_p = 203.2 mm [R]	74.2	771.1	223.5	41.4	17.8	69.4	6.91	0.30	W_F
G13	9	2x2 Bolts, e_p = 19.1 mm	71.5	736.0	234.3	29.9	14.0	96.4	8.51	0.44	W_F
G14	9	2x3 Bolts, e_p = 19.1 mm	73.0	761.4	252.4	30.5	13.0	125.2	8.92	0.46	W_F
G15-1	9	7.5” Deep EACs	23.5	187.8	83.1	10.3	18.6	10.6	8.14	0.17	Elastic
G15-2	9	7.5” Deep EACs	81.1	726.9	195.8	27.9	12.6	140.0	7.90	0.35	W_F
G16-1	9	5.0” Deep EACs	79.5	713.6	152.5	24.5	11.2	50.3	7.69	0.41	C_Y
G16-2	9	5.0” Deep EACs	84.5	834.7	159.1	28.7	11.0	68.9	7.55	0.40	C_Y
G16-3	11	5.0” Deep EACs	75.0	814.7	150.5	25.9	11.2	61.5	7.52	0.47	C_Y
G16-4	11	5.0” Deep EACs	77.9	934.0	157.3	27.0	11.0	82.4	7.12	0.46	C_Y
G16-5	11	5.0” Deep EACs	83.8	986.6	161.0	28.3	11.2	86.8	7.96	0.38	C_Y
G16-6	13	5.0” Deep EACs	87.9	1113.9	166.1	79.4	23.2	99.2	7.30	0.41	C_Y
G16-7	13	5.0” Deep EACs	94.4	1259.6	227.4	96.2	20.8	278.5	7.69	0.55	W_F
G17	13	5.0” Deep EACs	84.9	1199.4	242.0	105.9	23.0	276.2	8.26	0.47	W_F
G18	13	3.75” Deep EACs	83.2	1047.7	246.8	107.8	24.0	282.2	5.66	0.37	W_F
G19-1	13	3.75” Deep EACs	58.0	734.6	107.2	46.4	20.6	65.8	6.08	0.24	C_Y
G19-2	13	3.75” Deep EACs	84.4	1033.1	243.7	113.3	25.4	269.8	5.57	0.37	W_F
				Averages	**222.9***					**0.39**	
				CoVs	**0.08***					**0.20**	

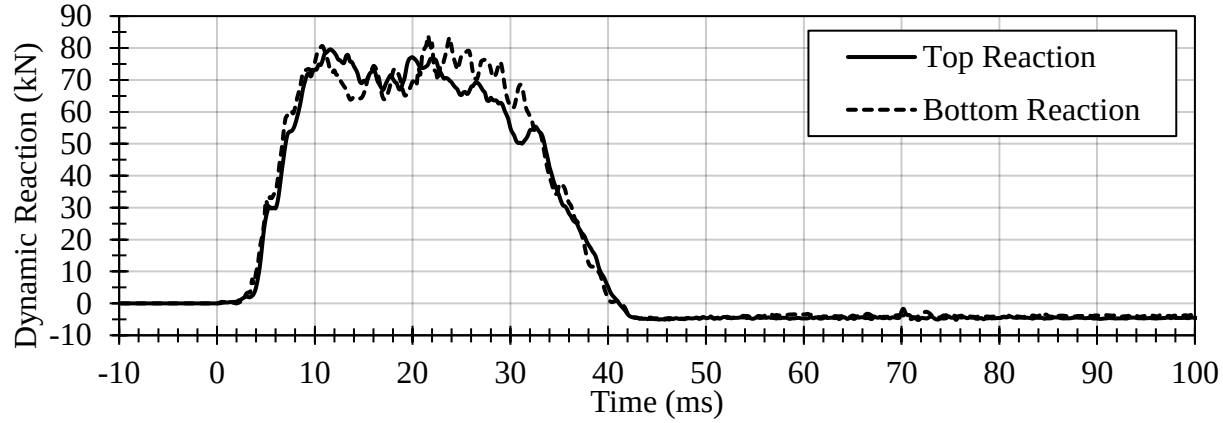
L_{Driver}: Driver length **P_r**: Peak reflected pressure **I_r**: Peak reflected impulse **R_{peak}**: Peak resistance **Δ_{Rpeak}**: Displacement at **R_{peak}**
t_{Rmax}: Time-to-**R_{peak}** **Δ_{max}**: Max displacement **K_i**: Initial system stiffness **$\dot{\epsilon}_{average}$**: Average strain-rate
W_F: Wood failure C_F: Connection failure C_Y: Connection yielding *: Based on W_F



(a) Displacement-Time Histories



(b) Strain-Time Histories



(c) Reaction-Time Histories

Figure 4.11: Typical Results of Dynamic Full-Scale Testing on CLT and Glulam Specimens (Results from Test G16-4)

Chapter 5 - Analytical Modelling and Results

5.1 General

The analytical approach used in the analysis and the key results from the proposed model are presented in this chapter. The majority of studies that used simplified modelling methodologies in blast research, such as single-degree-of-freedom (SDOF) modelling, dealt with idealized boundary conditions (e.g. Jacques, et al., 2012; Poulin, et al., 2017; Lacroix and Doudak, 2018b). Studies investigating structural elements with realistic boundary conditions subjected to blast loads have generally concluded that assuming idealized boundary conditions will often lead to inaccurate predictions when the modelling is limited to SDOF (Viau and Doudak, 2016a; El-Hashimy, et al., 2017; Côté and Doudak, 2019). Without resorting to more resource-intensive finite element analysis (FEA), various methods have been used to model these assemblies effectively. This includes energy methods (e.g. Lavarnway and Pollino, 2015), SDOF analysis with modified resistance curve (e.g. Whitney, 1996; Gagnet, et al., 2017), and two-degree-of-freedom (TDOF) modelling (e.g. Park and Krauthammer, 2009; Jacques and Saatcioglu, 2018). A good balance between simplicity and accuracy can be obtained with TDOF modelling, which consists of lumping the behaviour of each subcomponent (i.e. connections and main load-bearing elements) into equivalent subsystems. This allows for modelling of failure modes, and includes the effects of realistic boundary conditions to be captured by the model.

For the purpose of conducting TDOF analysis, a blast analysis software capable of performing two-degree-of-freedom analysis, titled *BlasTDOF*, was developed.

5.2 Model Description

The wood assembly consisting of a load-bearing timber element, such as a CLT or glulam member, and end connections can be represented as a continuous frame element connected at its ends with translational and rotational springs, as represented in Figure 5.1a. In order to discretize the continuous beam element without resorting to the use of multiple-degree-of-freedom (MDOF) modelling, the equivalent single-degree-of-freedom method (Biggs, 1964) is used to transform the wood member with distributed properties into an equivalent lumped system. This is done through the use of mass, resistance, and load transformation factors, which are obtained by equating the

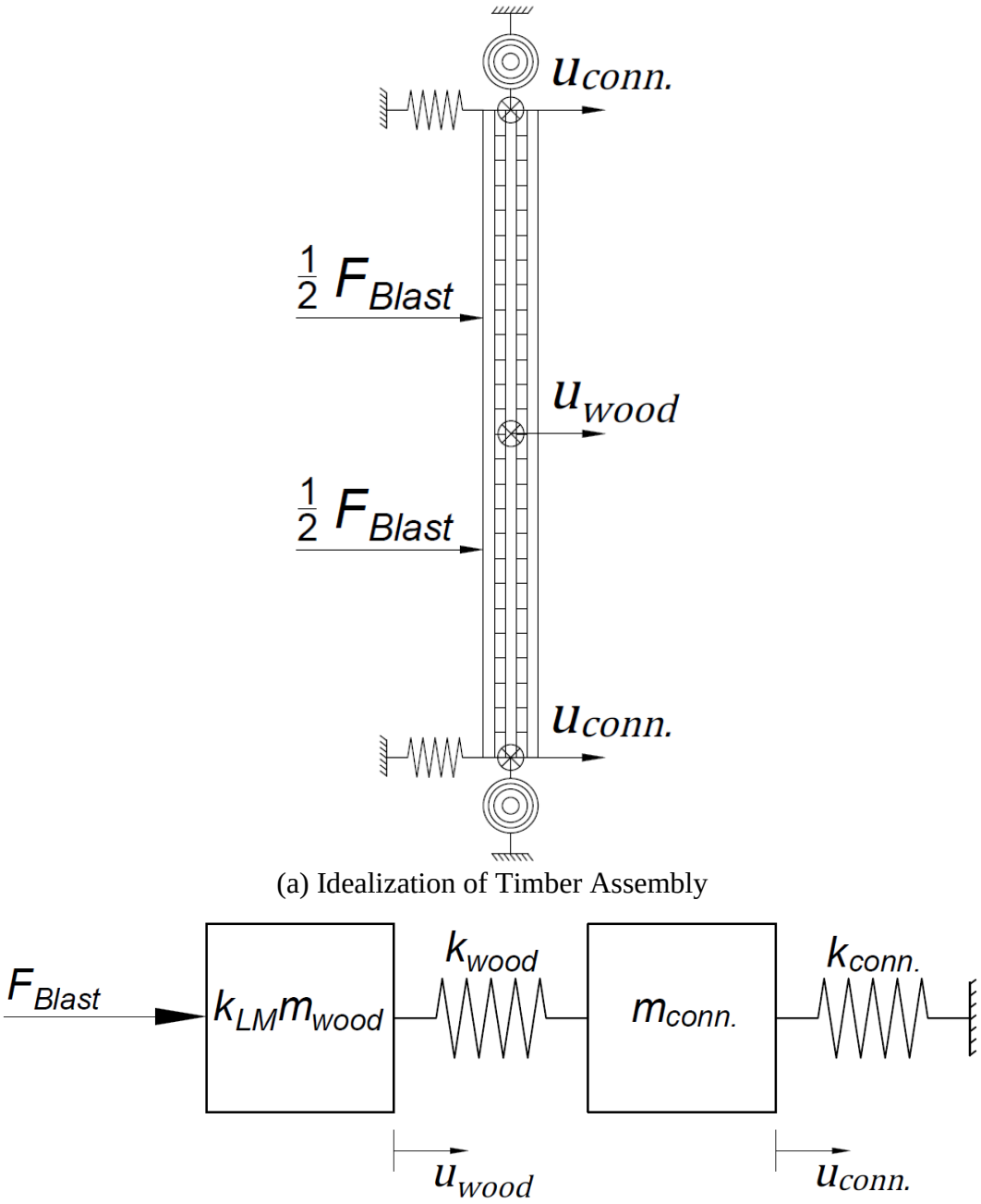
kinetic energy, potential energy, and work done by the force to that of the equivalent SDOF system. This yields the following relationships:

$$K_{Mass} = \frac{\int_0^L \overline{m}(x)\phi^2(x)dx}{\int_0^L \overline{m}(x)dx} \quad \text{Equation 5.1}$$

$$K_{Load} = \frac{\int_0^L f(x,t)\phi(x)dx}{\int_0^L f(x,t)dx} \quad \text{Equation 5.2}$$

Where $\overline{m}(x)$ is the distributed mass, $\phi(x)$ is the shape function based on the first mode deflected shape, $f(x,t)$ is the distributed load per unit length as a function of time, and L is the clear span of the wood member. The resistance transformation factor, K_R, used to transform the actual resistance of the component into an equivalent resistance, can be taken as equal to K_{Load}, due to the fact that resistance is the internal force resisting the externally applied force, and trying to bring the element back to its initial position (Unified Facilities Criteria Program, 2008). The format of the equivalent system is made simpler by using a single transformation factor, defined as the ratio of the mass and load factors, which yields, the load-mass transformation factor, K_{LM}. This factor is thereon applied to the mass of the wood member in order to convert its distributed properties into lumped properties at the respective degree-of-freedom. For the purpose of blast analysis, damping is typically omitted as it has little effect on the peak displacement of the analyzed component (Biggs, 1964; Jansson, 1992).

The end springs account for the translational and rotational stiffness of the connections. Since the end translational connections are acting in parallel, they can be lumped together into a single equivalent translational spring. The connection resistance curve is defined by multiplying the load-displacement curve of the joint in question by the total quantity of connections present in the assembly. The equivalent mass of the wood member and connections are represented as $K_{LM}m_{wood}$ and $m_{conn.}$, respectively, while their respective stiffness is represented by k_{wood} and $k_{conn.}$ In the full-scale tests, the force enacted onto the system (F_{Blast}) consists of a pressure collected by a load-transfer-device (LTD) and applied to the specimens via two equal concentrated point loads. The timber assembly can therefore be modelled as two springs in series, each represented with a SDOF, as shown in Figure 5.1b.



(a) Idealization of Timber Assembly

(b) Equivalent TDOF System

Figure 5.1: Two-Degree-of-Freedom Idealization of a Timber Assembly

For the undamped TDOF system shown in Figure 5.1b, the free-body diagrams of both components yield the following two equations of motions:

$$m_{conn.}\ddot{u}_{conn.} + R_{conn.} - R_{wood} = 0 \qquad \text{Equation 5.3}$$

$$k_{LM} m_{wood}\ddot{u}_{wood} + R_{wood} = F_{Blast} \qquad \text{Equation 5.4}$$

where R_{wood} and $R_{conn.}$ are the resistances of the wood element and connections, respectively. By rewriting Equation 5.3 and Equation 5.4 in matrix format, one obtains the following system of uncoupled linear equations:

$$\begin{bmatrix} m_{conn.} & 0 \\ 0 & k_{LM}m_{wood} \end{bmatrix} \begin{Bmatrix} \ddot{u}_{conn.} \\ \ddot{u}_{wood} \end{Bmatrix} + \begin{Bmatrix} R_{conn.} - R_{wood} \\ R_{wood} \end{Bmatrix} = \begin{Bmatrix} 0 \\ F_{Blast} \end{Bmatrix} \quad \text{Equation 5.5}$$

The stiffness terms in Equation 5.3, Equation 5.4, and Equation 5.5 have been replaced with the respective resistance terms. Using the resistance terms makes the numerical solution more stable given the nonlinear response expected through yielding in the connections as well as the post-peak response of the wood members. For example, numerical instabilities may be encountered in cases where the stiffness term approaches zero or becomes negative. Equation 5.5 is solved using numerical integration methods. The Newmark-beta numerical integration method, using the constant average acceleration method (Newmark, 1959), is particularly useful due to its unconditional stability and ease of implementation.

The mass of the wood component is assumed to be that of the wood member (i.e. CLT or glulam) as well as the weight of the LTD with two load transfer beams. While the mass of the connections is typically negligible when compared to the mass of the LTD and wood member, a non-zero mass must be entered in the TDOF model, in order to attain convergence in the solution. Pressure-time histories can be obtained from experimental testing or be idealized as a triangular or exponential pressure-time history, which is then converted into a forcing function by multiplying the pressure enacted onto the LTD by the effective loaded area of the LTD.

The load-mass factors were determined by calculating the ratio between values obtained from solving Equation 5.1 and Equation 5.2. For the full-scale specimens, load-mass factors for the elastic regime of 0.85 and 0.87 were utilized for CLT panels with end connections and all other full-scale specimens, respectively. The difference in the load-mass factor is attributed to the shortening of the end-connected CLT panels. The distances between the supports and load application points were no longer equal to that of the distance between load application points, which in turn will cause a change in the load-mass factor (i.e. 0.85). For all full-scale specimens, a load-mass factor of 1.00 was utilized when the behaviour of the panels and beams were no longer elastic (i.e. plastic).

5.3 Resistance Curves

An important input in the model includes the resistance curves of the wood member and connections. These can be obtained via experimental testing or derived from published information if available. Research done on glulam beams subjected to blast loads has shown that the dynamic behaviour can be modelled using a linear-elastic resistance curve since little-to-no post-peak strength was observed in the members (Lacroix and Doudak, 2018b). For CLT, the cross-laminations allow for some post-peak resistance, where failure of the outer tension laminates causes a drop in load to an intermediate region based on the remaining transverse and longitudinal layers (Poulin, et al., 2017).

The resistances of the wood members with and without boundary connections were determined based on the dynamic equilibrium of the system using an equivalent single-degree-of-freedom approach. The resistance term is determined based on the measured experimental reactions and applied force as a function of time, as demonstrated in Equation 5.6. The idealized location of the equivalent inertial force on the panel can be determined using Equation 5.7 when the beam is in the elastic range, and Equation 5.8 when in the plastic range. The full derivations of these equations can be found in Appendix D.

$$R(t) = \left(\frac{2}{a}\right)\left(V(t)x_{eq} + \left(a - x_{eq}\right)\frac{F(t)}{2}\right) \qquad \text{Equation 5.6}$$

$$x_{eq-elastic} = \frac{0.0125\bar{m}(4a^2 - 5L^2)^2 + m_c(12La^2 - 16a^3)}{\bar{m}(a^3 - 2a^2L + L^3) + m_c(12La - 16a^2)} \qquad \text{Equation 5.7}$$

$$x_{eq-plastic} = \frac{\frac{\bar{m}(6L^2 - 8a^2)}{48} + m_c a}{0.5\bar{m}(L - a) + m_c} \qquad \text{Equation 5.8}$$

where $R(t)$ is the resistance of the wood element; $V(t)$ is the measured dynamic reaction; $F(t)$ is the applied force; L is the clear span; x_{eq} is the distance from the support to the point of application of the equivalent inertial force; $\bar{m}$ is the distributed mass of the CLT panel; m_c is half the mass of the LTD, representing the portion of the LTD mass lumped at each of the two load application points; and a is the distance between the supports and the load-application points (a = 745 mm for glulam and simply supported CLT specimens and a = 669 mm for end connected CLT specimens).

The applied force, $F(t)$, was determined using the reflected pressure data obtained during the tests and multiplying each value by the effective loaded area of the LTD (3.55 m^2).

The initial stiffness of the wood member for two concentrated point loads (K) can be modified to consider the rotational stiffness of the connections at the wood member ends. This is done through the derivation of an analytical solution of a Euler-Bernoulli beam with semi-rigid springs at its ends. The solution considers a non-dimensional constant (B) defined as the ratio of the rotational stiffness ($K_r l$) to that of the member bending stiffness, EI, as shown in Equation 5.9 and Equation 5.10.

$$K = \frac{1296EI}{L^3}\left(\frac{B+2}{5B+46}\right) \qquad \text{Equation 5.9}$$

$$B = \frac{K_r l}{EI} \qquad \text{Equation 5.10}$$

By setting $B = 0$, the solution given in Equation 5.9 corresponds to the case of simply supported beam, and by determining $\lim_{B\to\infty} K$, the solution corresponds to a beam with fully fixed ends. The input values of the rotational stiffness can also be obtained via experimental testing of the joints in question. It should be noted that in the case of timber joints, the effects of rotational stiffness are generally low and tend not to affect the response significantly. The derivations of Equation 5.9 and Equation 5.10 can be found in Appendix E, in addition to the derivation and solution for a uniformly distributed beam with semi-rigid springs at its ends.

5.4 Inelastic Blast Analysis Software – *BlasTDOF*

In order to conduct TDOF analysis for a wide range of structural components, a blast analysis software, *BlasTDOF*, was developed by the author and coded using the .NET/C# Framework in the *Microsoft Visual Studio* integrated development environment (Microsoft Corporation, 2019). *BlasTDOF* is capable of analyzing two-degree-of-freedom systems subjected to blast loads, and permits the user to input custom resistance curves, masses, as well as pressure-time histories. *BlasTDOF* is comprised of three modules; an input module, a dynamic analysis module, and a results module.

5.4.1 Input Modules

5.4.1.1 Structural Member

Figure 5.2 shows a user input interface where the member resistance curve along with the load-mass factor for each resistance data point is entered. Idealized resistance curves or experimental data from testing can be used as input. Required input variables include member mass, loaded area, and elastic limit of the member. The latter is required in order for the program to differentiate between the elastic and inelastic behaviour of the member, as well as to allow the program to calculate the unloading stiffness based on the initial stiffness of the load-displacement curve, as obtained from the yield displacement. Optional inputs include the load-transfer device mass (i.e. 284 kg), if utilized, and damping.

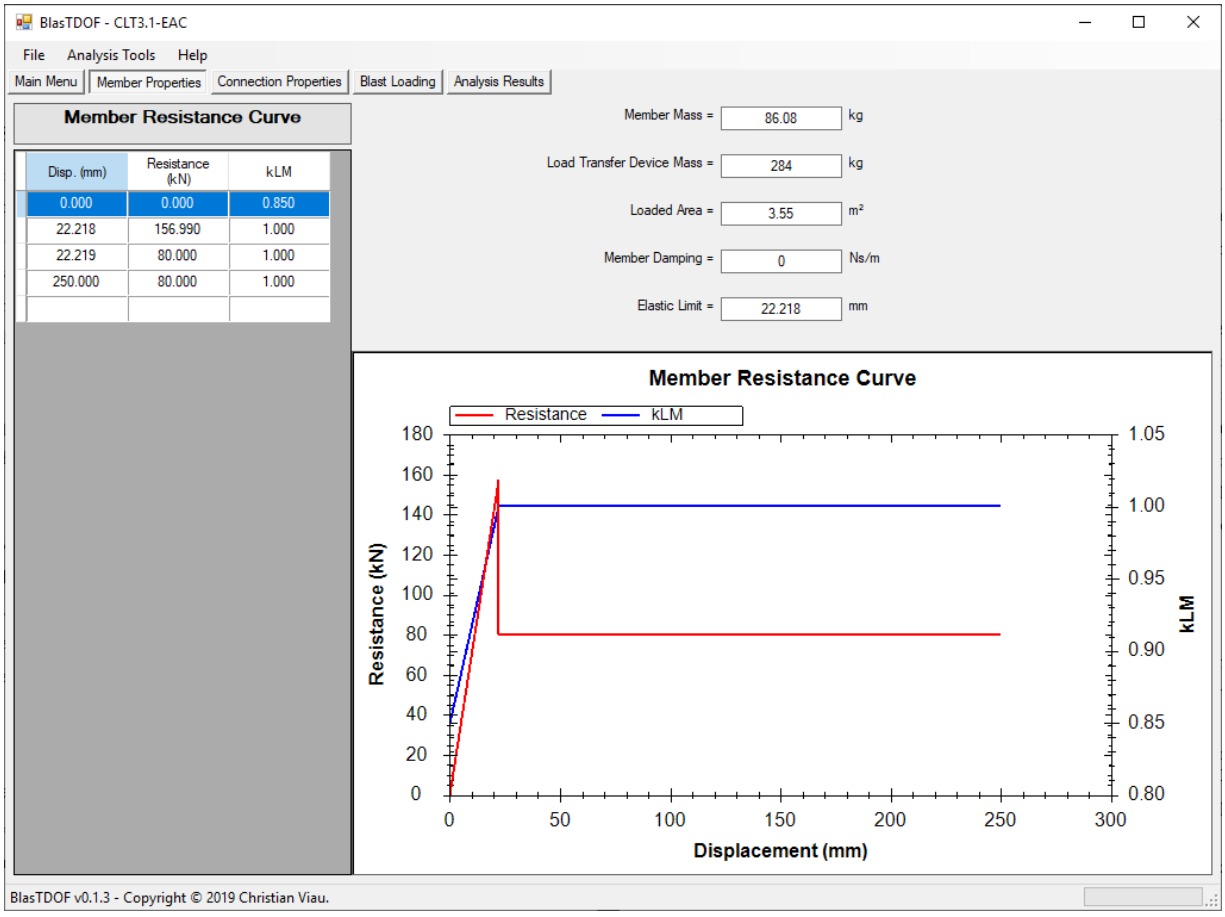


Figure 5.2: Member Properties Tab

5.4.1.2 Connections

The inputs for connections are similar to that of the structural member. The resistance curve is entered by the user, however, since connections consist of lumped systems with concentrated

masses, no load-mass factors are necessary. The user must enter the quantity and the total mass of the connections within the system which may generate inertial forces. It is also required to specify whether both ends of the structural member contain such connections or if the member in question is a cantilever (i.e. only one end connection). If the mass is unknown or is very small, the user has the option of ignoring the connection mass. In doing so, the program will assign a default connection mass of 1 kg, in order to converge to a solution.

For the purpose of analyzing the energy-absorbing connections (EACs) used in the current study, the user has the option of enabling the densification parameter. If this is done, the user will be prompted to enter the displacement at which densification occurs, as well as the densification stiffness. This is required due to the fact that if loading persists past densification, the use of the typical unloading stiffness will likely yield erroneous results. A screenshot of the *Connection Properties* tab is shown in Figure 5.3.

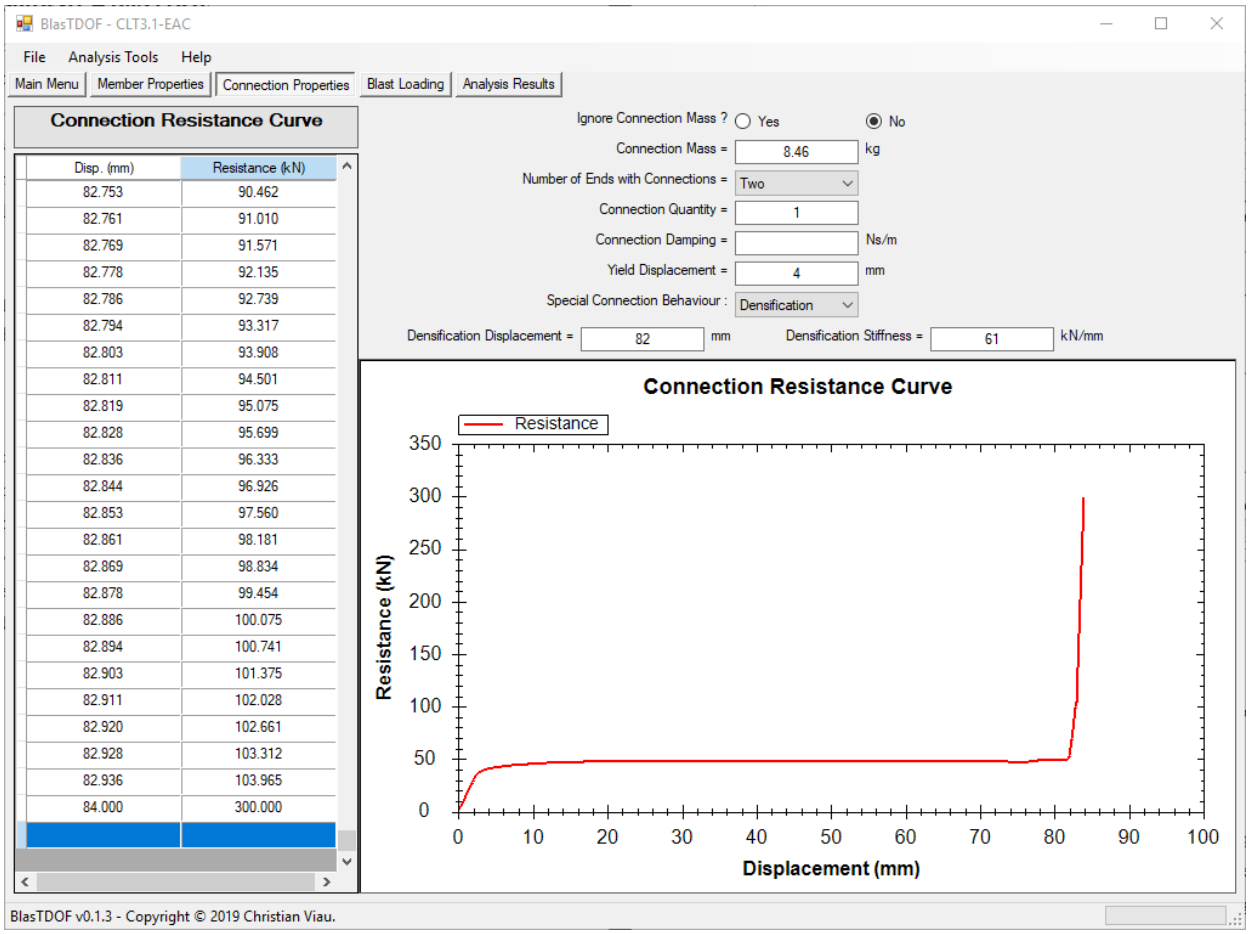
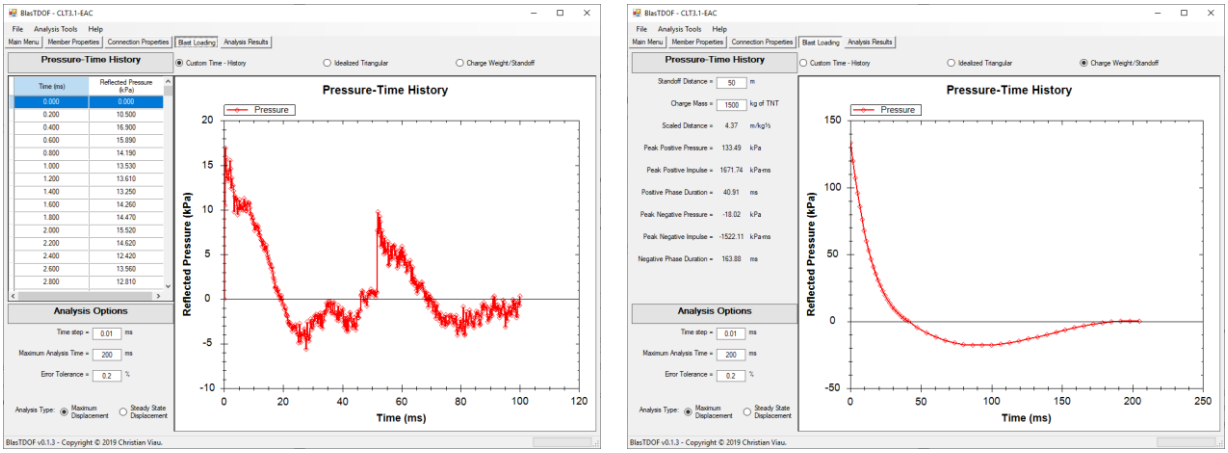


Figure 5.3: Connection Properties Tab

5.4.1.3 Blast Load

BlasTDOF allows the user to input the applied blast load using three different formats. The first format consists of entering experimental pressure-time data points, such as those generated in the current study. The second format consists of idealizing a typical pressure-time history into a triangular curve, where the user must specify the peak reflected pressure, positive phase duration, and, if required, the peak negative reflected pressure and negative phase duration. The third format consists of calculating the expected pressure-time history based on entered charge mass and stand-off distance. The program will then calculate the scaled distance, *Z*, in order to determine various blast parameters such as positive and negative pressures, impulses, and time durations based on UFC 3-340-02 (Unified Facilities Criteria Program, 2008). Using these values, the program will then compute a pressure-time history based on the modified Friedlander equations (Friedlander, 1946), which satisfies the blast parameters obtained from UFC 3-340-02. For the validation of BlasTDOF, experimentally obtained pressure-time histories were used for all analyses. Examples of pressure-time histories based on experimental data points and charge mass with standoff distance are shown in Figure 5.4.



(a) Experimentally Obtained (b) Charge Mass and Standoff Distance

Figure 5.4: Blast Loading Tab

Other important input found in the *Blast Loading* tab include the analysis time step duration, maximum analysis time permitted, permitted error tolerance, and type of analysis (i.e. analysis until maximum displacement or specified time). These will be explained in the next section.

5.4.2 Dynamic Analysis Module

Prior to commencing the analysis loop, the program initializes the mass and damping matrices, as well as displacement, velocity, force and resistance vectors. In order to start the iteration process, an initial acceleration vector will be calculated by multiplying the inverse of the initial mass matrix with the initial force vector (Equation 5.11).

$$\{A\}_0 = [M]_0{}^{-1}\{F\}_0 \qquad \text{Equation 5.11}$$

The program runs through an analysis loop for each time step of the dynamic analysis. The time step duration is set by the user in the Blast Loading tab. As a default, a 0.01 ms time step is used. Within the analysis loop for each time step, *BlasTDOF* may perform several hundreds of iterations in order to converge to a numerical solution. These iterations are performed through an iterative sub-loop, found within the main analysis loop. At the beginning of the analysis loop for each time step, and prior to entering into the iterative sub-loop, the program will initially assign the acceleration vector at the next time step as being equal to that of the previously obtained time step (Equation 5.12), as an approximation.

$$\{A\}_{n+1} = \{A\}_n \qquad \text{Equation 5.12}$$

The next step involves calculating the velocity and displacement vectors at the $(n+1)^{th}$ time step based on the assumed new acceleration vector (Equation 5.12) using Equation 5.13 and Equation 5.14, respectively.

$$\{V\}_{n+1} = \{V\}_n + \frac{\{A\}_{n+1} + \{A\}_n}{2}\Delta t \qquad \text{Equation 5.13}$$

$$\{D\}_{n+1} = \{D\}_n + \frac{\{V\}_{n+1} + \{V\}_n}{2}\Delta t \qquad \text{Equation 5.14}$$

Using the new displacement vector at the $(n+1)^{th}$ time step (Equation 5.14), *BlasTDOF* determines the resistance of the member and connections by scanning through the resistance curve inputs and determining the resistance values which correlate to the displacements obtained in the displacement vector at the $(n+1)^{th}$ time step. If the program determines that any of the displacements exceed that of the maximum displacements entered by the user, the program will

assume that the component in question has failed, and will terminate the analysis. If the resistance values correlate with existing points on the resistance curves, the program will save these resistances into the resistance vector, $\{R\}_{n+1}$, and update the mass matrix with the new load-mass factor for the structural member. The acceleration vector at the $(n+1)^{th}$ time step will then be calculated anew; this time using Equation 5.15.

$$\{A\}_{n+1} = \left([M]_{n+1} + \frac{[C]_{n+1}}{2}\Delta t\right)^{-1}\left(\{F\}_{n+1} - [C]_{n+1}\left(\{V\}_n + \frac{\{A\}_n}{2}\Delta t\right) - \{R\}_{n+1}\right) \qquad \text{Equation 5.15}$$

Before storing all calculated values and beginning the calculations for the next time step, the program verifies if the resistance vector correlating to the obtained displacements at the $(n+1)^{th}$ time step converges towards the previously stored resistance vector determined during the previous iteration. *BlasTDOF* performs this operation by calculating the ratio of change between the previous and current resistance vectors and verifies the calculated error against a specified error tolerance, as described in Equation 5.16.

$$\left|\frac{\{R\}_{i+1} - \{R\}_i}{\{R\}_{i+1}}\right| \leq TOL \qquad \text{Equation 5.16}$$

where *TOL* is the error tolerance that must be met in order for the program to exit the iterative sub-loop, and *i* is the i^{th} iteration of the calculations being performed for the current time step. As a default setting, *TOL* is set to 0.002, correlating to an error rate of 0.2 %. If this condition is not met, the acceleration vector obtained in Equation 5.15 will be stored as the new approximation of the acceleration at the $(n+1)^{th}$ time step (Equation 5.12). The resistance vector correlating to the displacements obtained in Equation 5.14 will also be stored as the resistance vector of the $(i+1)^{th}$ iteration, such that it may be compared to the newly calculated resistance vector when Equation 5.16 is used again in the next iterative sub-loop. The iterative sub-loop will restart once again by calculating the velocity, displacement, and acceleration vectors using Equation 5.13, Equation 5.14, and Equation 5.15, respectively. This sub-loop will be performed until the resistance vector converges and the error becomes lower or equal to the value of *TOL*, given in Equation 5.16.

Once this check is met, *BlasTDOF* exits the iterative loop, stores the values of the accelerations, velocities, displacements, and resistances for the $(n+1)^{th}$ time step, and begins the analysis for the next time step. This numerical procedure is repeated until one of two analytical conditions is

met. The first condition consists of the analysis reaching the limit assigned by the user, related to a maximum displacement or time. The second condition occurs when the displacement value stored for either the connection or member exceeds that of the displacement corresponding to failure in that component. A flowchart of the program's algorithm is presented in Figure 5.5.

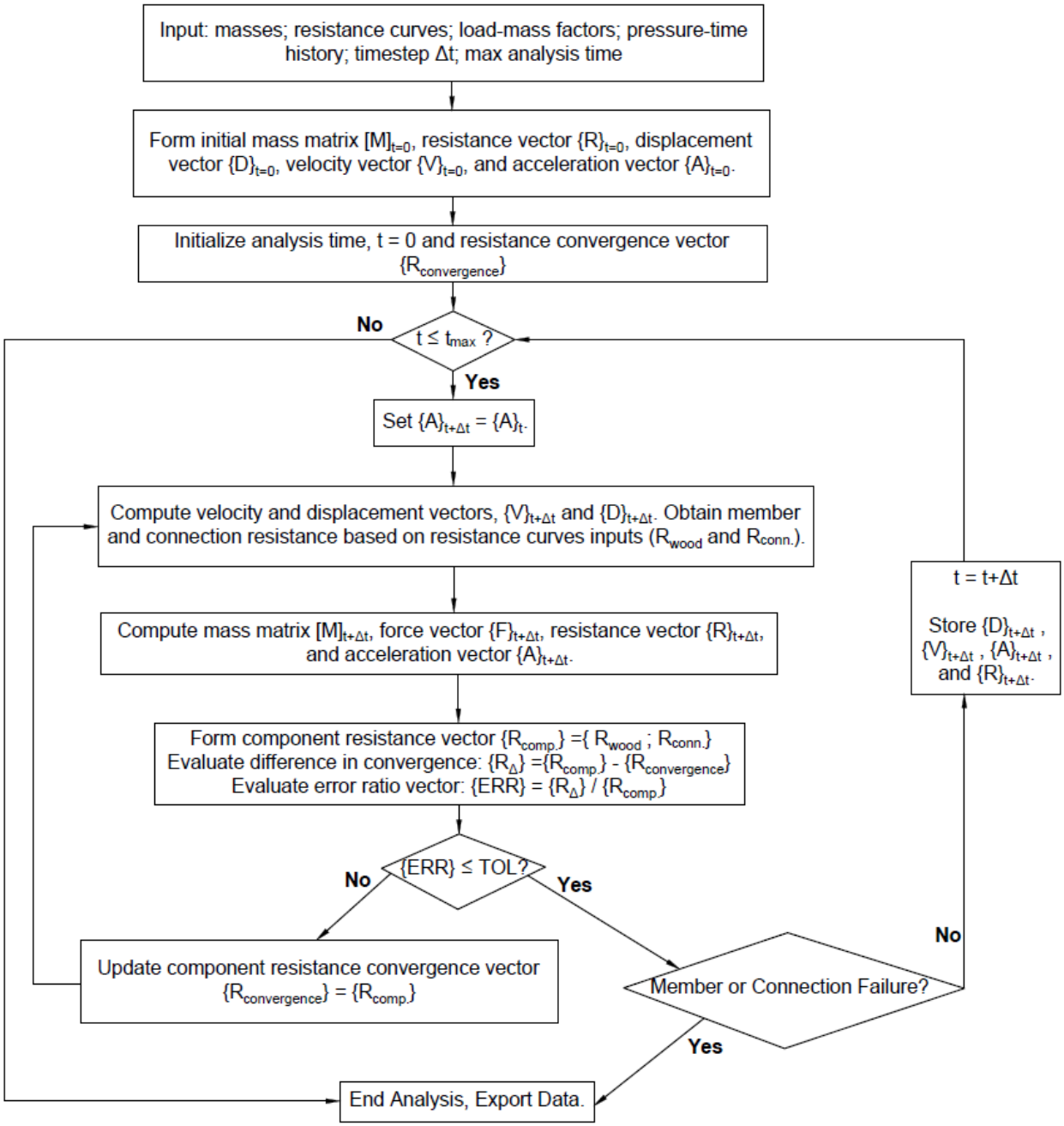


Figure 5.5: Summary of *BlasTDOF* Dynamic Analysis Algorithm

5.4.3 Output Module

Once the program completes the analysis, the results are presented in the Analysis Results tab. Figure 5.6 presents output graphs of the resistance curve of the member and connections, together with graphs indicating the extent of loading level (Figure 5.6a and Figure 5.6b, respectively). This allows for the quantification of damage in each component. Also provided is the system resistance curve (Figure 5.6c), which relates the total mid-span displacement to the member resistance. This resistance curve can be used to describe the TDOF assembly as a SDOF system, since it combines the behaviours of both components into one composite resistance curve. Finally, graphs presenting the displacement-time histories of the system, member, and connections are also provided (Figure 5.6d). The program allows the user to copy all results to the clipboard and paste them into other programs (e.g. *Microsoft Excel*) as needed. The *BlasTDOF* analysis file, which includes all inputs and results, can be saved as a *.tdof* file.

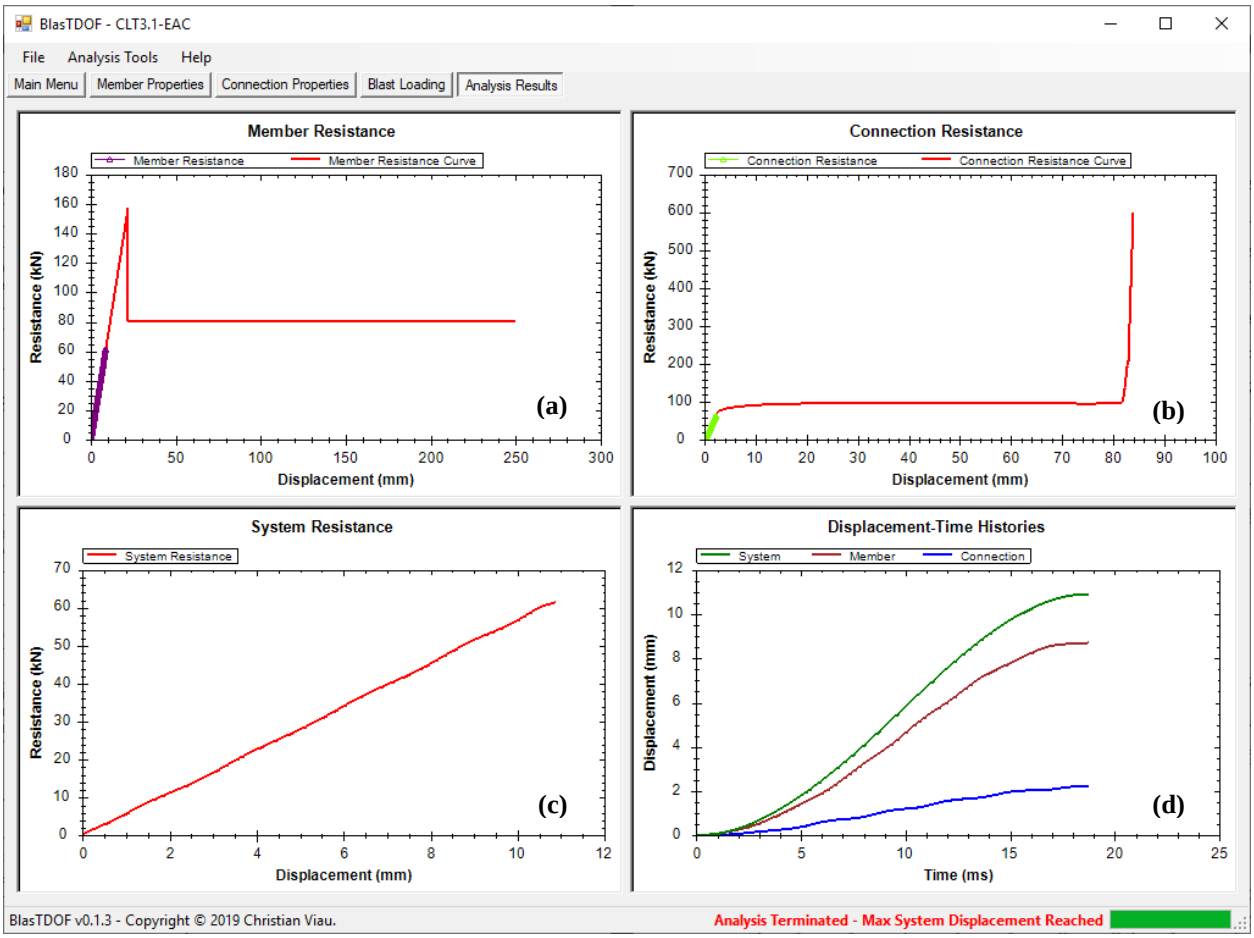


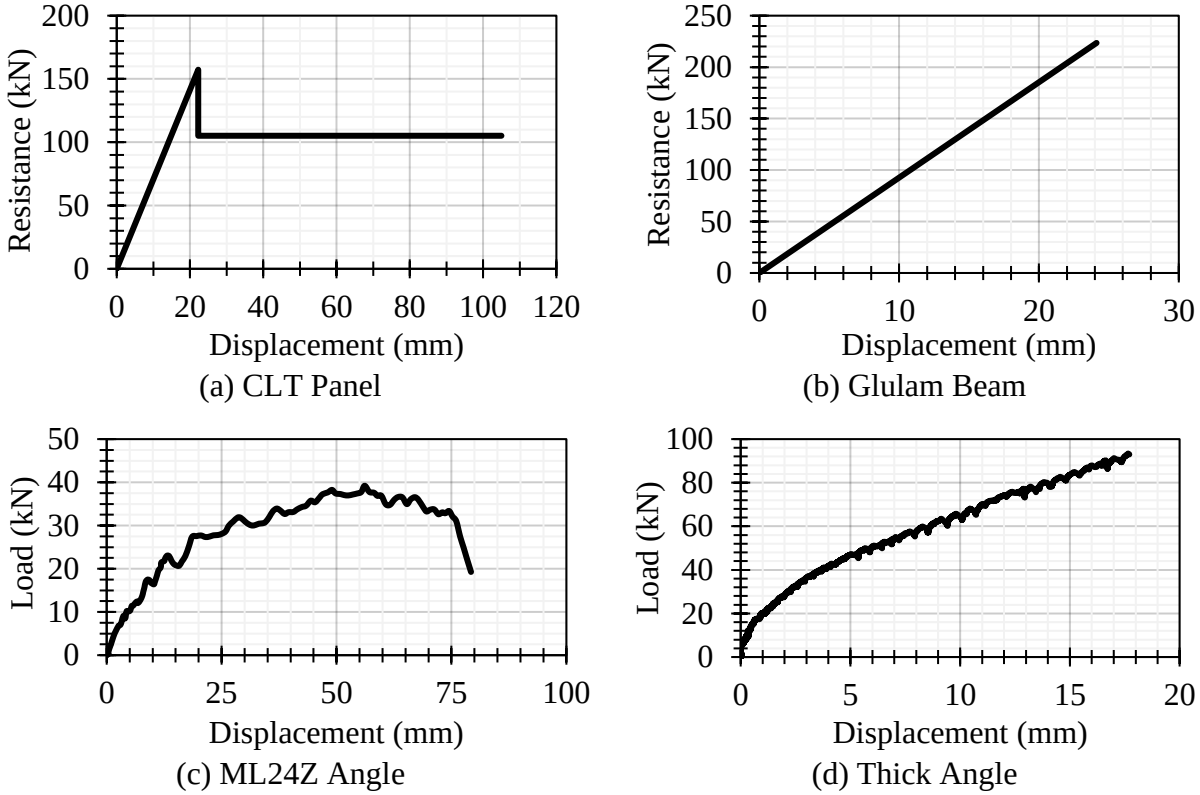
Figure 5.6: Analysis Results Tab

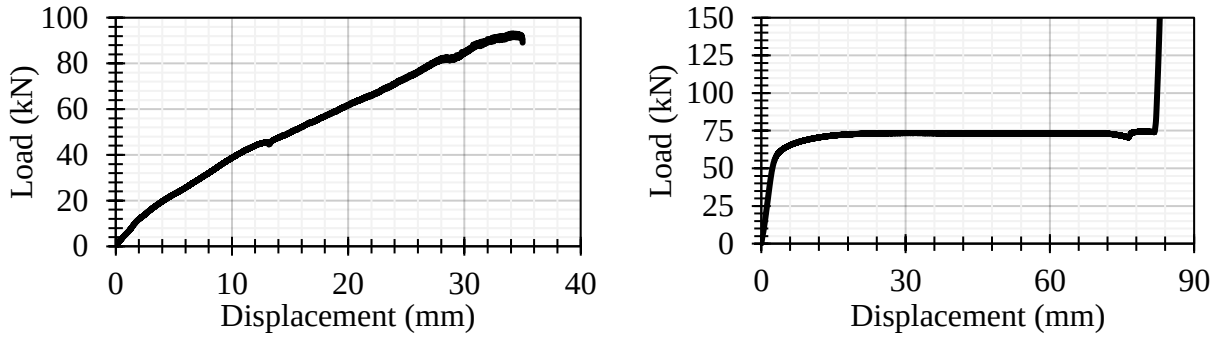
5.5 Analytical Modelling Results

In order to validate *BlasTDOF*, all full-scale test specimens with connections were modelled and the predictions were compared with the experimental full-scale results. Connection resistance curves, representative of the average behaviour for each type of connection were obtained from static and dynamic connection-level testing and used as inputs in the model.

For full-scale assemblies with connections, the connection-level resistance curves with appropriate dynamic increase factors (DIFs) on the connection capacities were used as input. Additionally, full-scale assemblies tested with axial restraints were modelled using resistance curves obtained from connection-level testing where axial restraints were used.

In order to reflect the behaviour of each wood member, idealized resistance curves were generated based on the experimentally measured load-displacement relationships of each member. Examples of representative modelling inputs for CLT panels, glulam beams, and connections are shown in Figure 5.7.





(e) 1x1 Bolted Joint (No Splitting) (f) Energy-Absorbing Connection

Figure 5.7: Representative Resistance Curves for Timber Members and Connections

For the case where splitting failure governed, the bolted joint resistance curve was cut off at a load correlating with the observed splitting load.

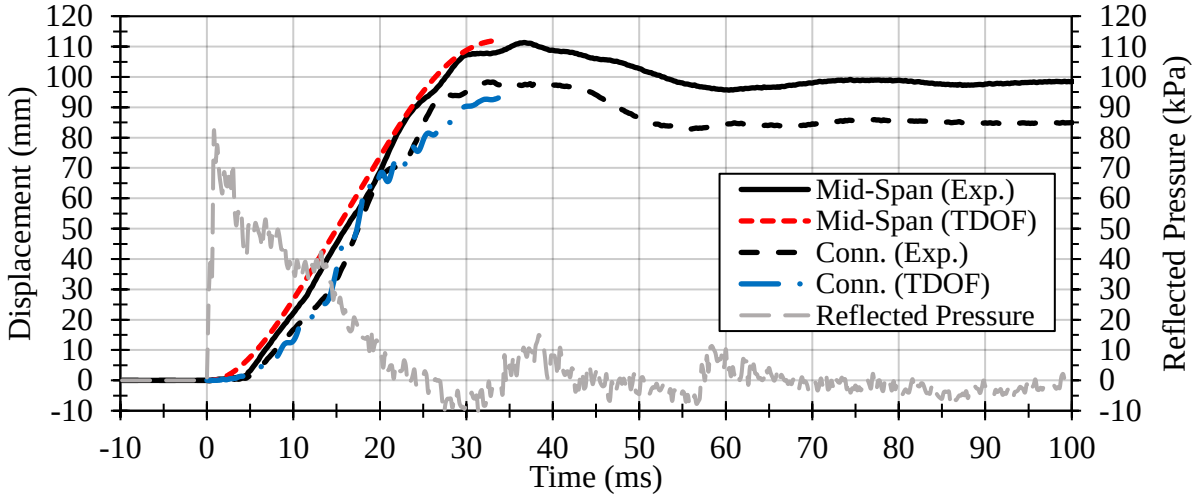
When modelling the full-scale assemblies, mid-span displacements of the glulam beam and CLT panels were used in order to evaluate the accuracy of the TDOF model. For glulam beams, the mid-span displacements corresponded to the displacement at peak resistance (representing beam failure in flexure), whereas for CLT panels, the mid-span displacement corresponded to the maximum displacement of the panels. Quantification of the accuracy of the model for each connection type can be found in Table 5.1, while Table 5.2 presents a summary of the mid-span displacements (i.e. maximum displacement and displacement at peak resistance) and the time-to-displacements for the analytical model and experimental test data. From the results it can be seen that the analytical model seems to accurately predict the correct failure mode (i.e. connection or member failure), as well as the mid-span displacement and time to attain such displacement with average ratios of 1.02 (CoV of 0.06) and 0.98 (CoV of 0.12), respectively. Examples of displacement-time histories obtained from the experimental results and the TDOF blast analysis are shown in Figure 5.8 for various types of tested assemblies.

Table 5.1: Summary of TDOF Prediction Accuracies for Each Full-Scale Assembly Type

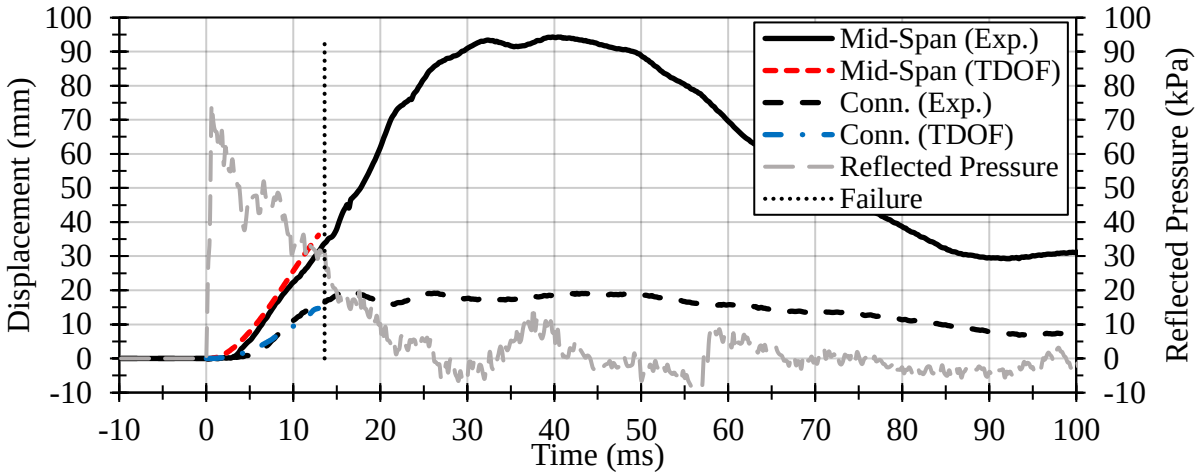
	Number of Tests	**D_{TDOF} / $D_{EXP.}$**		**T_{TDOF} / $T_{EXP.}$**	
		Average	**CoV**	**Average**	**CoV**
All Tests	42	1.02	0.06	0.98	0.12
CLT Bearing Connections	8	1.00	0.02	1.03	0.12
CLT EACs	10	1.00	0.06	0.98	0.17
Glulam Bolted Connections	11	1.06	0.08	0.92	0.07
Glulam EACs	13	1.00	0.05	0.99	0.08

Table 5.2: Summary of All TDOF Modelling Predictions for the Validation of *BlasTDOF*

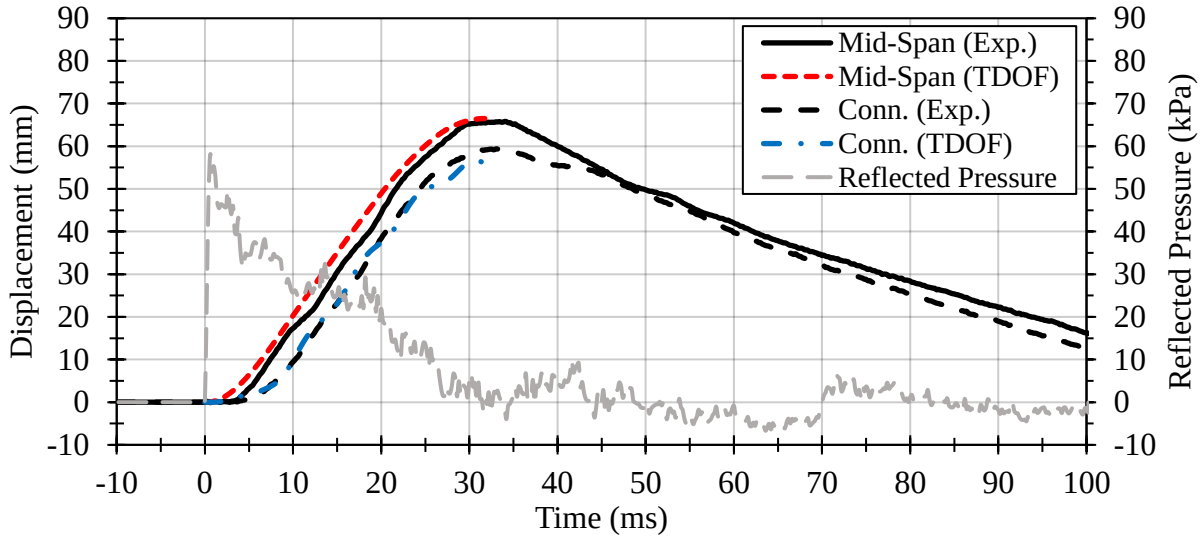
Test Name	Experimental		TDOF Modelling	
	Displacement (mm)	Time (ms)	Displacement (mm)	Time (ms)
CLT4	22.9	10.6	22.3	9.6
CLT5	96.4	32.2	98.0	35.3
CLT6	170.7	63.2	174.3	77.1
CLT7	111.3	36.8	112.1	34.0
CLT8	140.1	37.8	155.9	45.1
CLT9	116.3	44.6	118.4	42.5
CLT10	85.7	34.6	83.1	42.3
CLT11	102.8	36.6	99.7	33.7
CLT12	140.1	37.8	155.9	45.1
CLT13	214.3	56.0	201.4	51.2
CLT14-1	11.1	25.4	10.9	18.8
CLT14-2	27.7	24.4	27.0	22.0
CLT14-3	77.0	30.2	81.5	32.1
CLT14-4	244.6	79.2	262.5	93.7
CLT15-1	9.0	25.6	8.2	18.7
CLT15-2	38.5	28.6	38.0	26.2
CLT15-3	95.8	38.8	93.1	37.6
CLT15-4	172.0	52.8	175.4	61.4
G4	43.4	18.6	44.1	16.0
G5	38.6	15.4	37.1	13.4
G6	36.9	14.6	38.9	13.7
G7	24.1	10.2	29.7	10.9
G8	12.6	7.2	12.0	6.3
G9	5.4	4.8	6.6	4.6
G10	33.8	13.6	36.2	12.9
G11	34.1	13.2	35.8	12.5
G12	41.4	17.8	41.2	14.5
G13	29.9	14.0	32.5	12.8
G14	30.5	13.0	31.7	12.2
G15-1	10.6	18.0	10.6	15.6
G15-2	27.9	12.6	26.1	10.6
G16-1	50.3	24.8	51.4	23.6
G16-2	68.9	27.0	70.2	26.4
G16-3	61.5	26.4	59.9	26.2
G16-4	82.4	29.4	76.9	29.0
G16-5	86.8	30.0	85.6	30.1
G16-6	99.2	31.4	100.6	32.6
G16-7	96.2	20.8	107.8	23.5
G17	105.9	23.0	107.9	25.1
G18	107.8	24.0	107.7	25.9
G19-1	65.8	34.0	66.5	31.8
G19-2	113.3	25.4	109.7	25.7



(a) Test CLT7



(b) Test G10



(c) Test G19-1

Figure 5.8: Displacement Prediction Results for Validation of TDOF Model

From Table 5.1, it can be observed that the model was least accurate in the case of bolted connections, where there was a tendency to overpredict the mid-span displacement on average by 6 %. One possible explanation for these overpredictions is that some rotational stiffness, which may be found in such connections, was not considered when generating the glulam resistance curves. While an analytical modelling method allowing for the implementation of an end rotational spring was developed (i.e. Equation 5.9 and Equation 5.10), such errors were deemed inconsequential to the overall behaviour of the assembly and may fall within typical uncertainties found in such assemblies. The range of values of B (Equation 5.10) to take these rotational restraints into account would be approximately 0.2 – 1.0. These are not significant rotational restraints when compared to the B values of simply supported ($B = 0$) and fully fixed ($B \geq 400$) ends. For this reason, no further investigation of the potential of rotational stiffness was deemed necessary for the current study. In general, it can be concluded that the proposed procedure and the *BlasTDOF* as a modelling tool can accurately predict the behaviour of various timber assemblies, with reasonable accuracy (Figure 5.9).

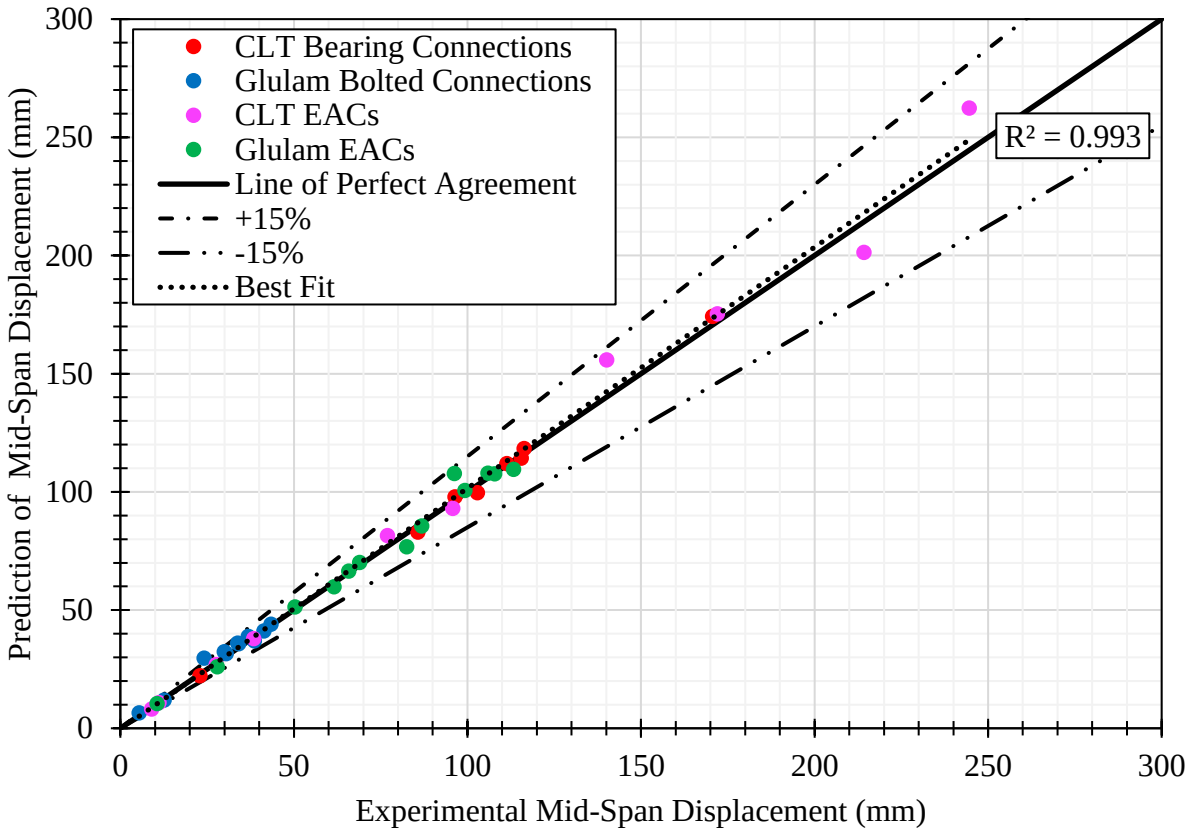
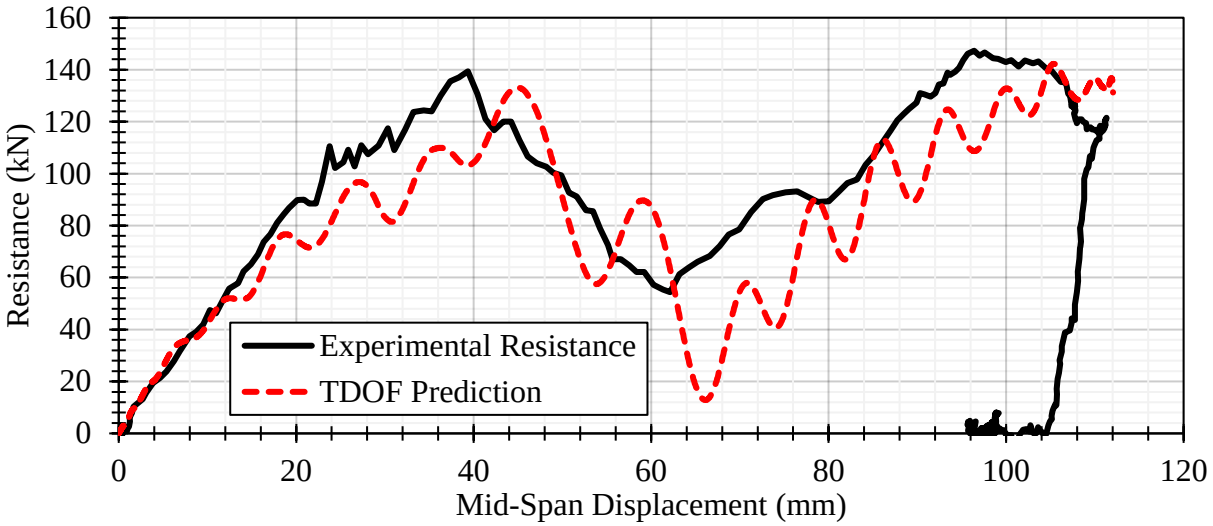
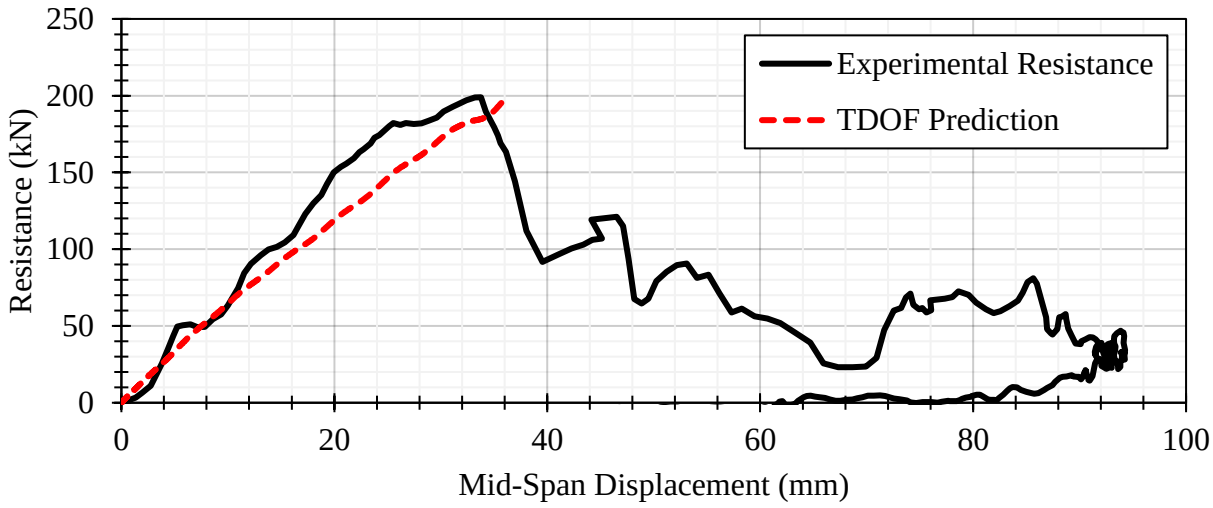


Figure 5.9: Experimental Displacements and Predictions for the Validation of *BlasTDOF*

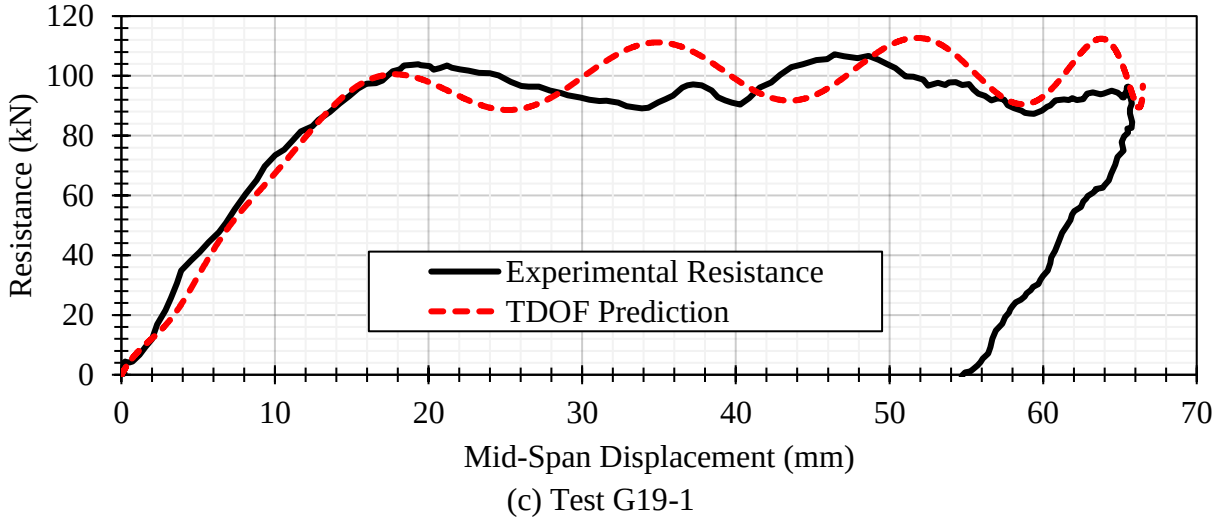
The modelling results also show that *BlasTDOF* is capable of predicting the variation in the system resistance as a function of its mid-span displacement with reasonable accuracy, as shown in Figure 5.10. Figure 5.10b presents the results of a glulam assembly with bolted connection, where it can be seen that the model tends to underpredict the stiffness of the system, which again may be attributed to the rotational restraint. Figure 5.10a and Figure 5.10c show the presence of oscillations in the TDOF modelling results. During these tests, yielding of the connections and loss of load occurred (in the case of Test CLT7) caused the wood member to undergo a state of free vibration as it remained at a constant load or was unloaded. While these oscillations are present in the TDOF model, they tend to be exaggerated when compared to the experimental results, for example, during Test G19-1 (Figure 5.10c). These exaggerations in oscillations are due to the absence of damping in the analytical predictions, which will tend to cause such exaggerations in free vibration. However, these will have minimal impact on the modelling results and their respective accuracy.



(a) Test CLT7



(b) Test G10



(c) Test G19-1

Figure 5.10: System Resistance Prediction Results for Validation of TDOF Model

Chapter 6 - Discussion

6.1 Behaviour of CLT Assemblies with Bearing Connections

6.1.1 Connections Under Dynamic Loading

Observed failure modes in the connection-level tests under dynamic loading were consistent with those during static loading. From video review, rigid body translation of the middle panel was observed throughout the tests, with slight rotation at the supports occurring, in some cases, near maximum displacement. Brasher tearing of the wood fibres at the panel ends was observed during dynamic testing (Figure 6.1a) when compared to static testing for the same connections. No tension failure of the ML24Z angles was observed in any of the tests; however, significant permanent deformations in the angles were noted, as shown in Figure 6.1b. This hierarchy of failure (i.e. failure in the screw fasteners prior to tension failure in angle bracket) is intentional by the manufacturer, provided that the required number and size of screws are used. The predominant failure mode for specimens with the thick angle was shear failure in the screws. This failure type also involves moderate amount of wood crushing. No observable damage was found in the thick angle in any of the tests. Figure 6.1c shows an example of the ultimate failure of a thick angle connection.



(a) Crushing in Panels Ends (ML24Z)



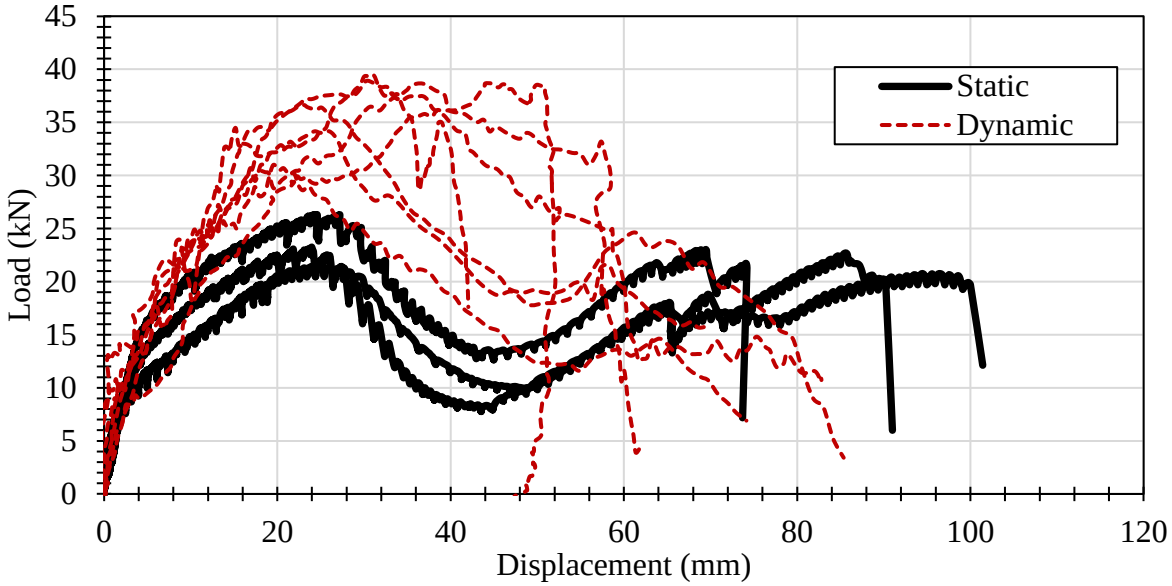
(b) Deformed ML24Z Angle



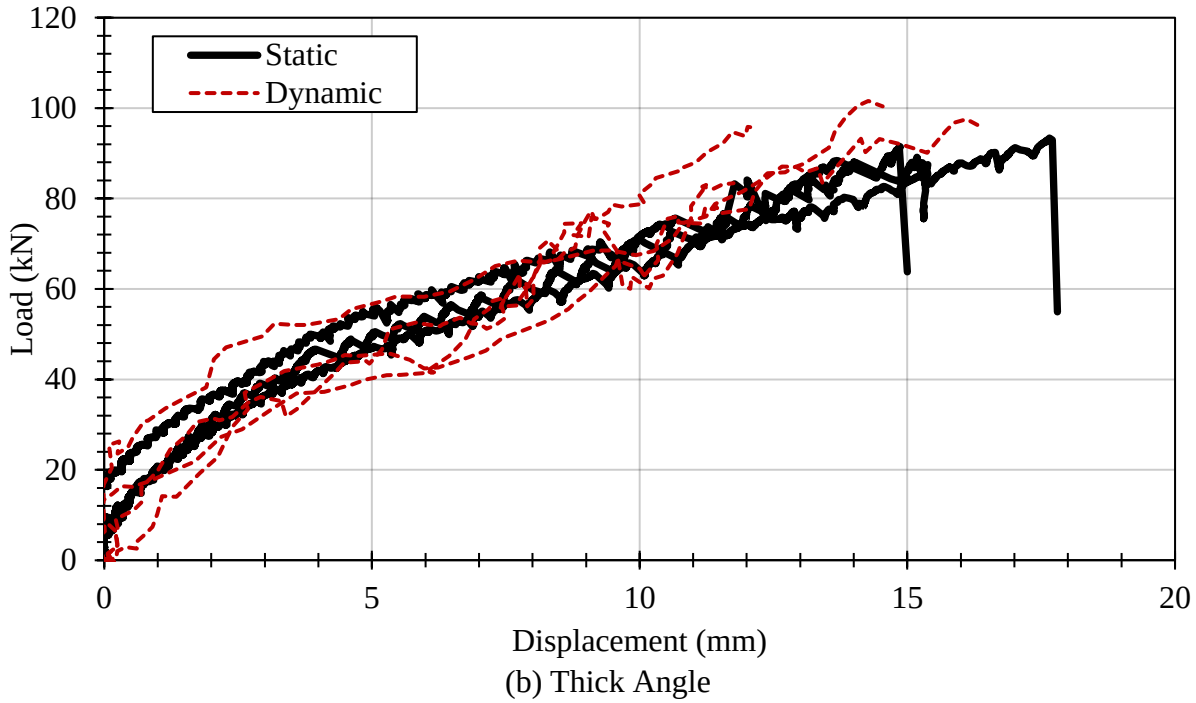
(c) Screw Failure in Support Block (Thick Angle)

Figure 6.1: Representative Dynamic Behaviour of Connections

The use of the load cells during static and dynamic testing permitted direct comparison between the respective load-displacement curves, in order to quantify the high strain-rate effects in the connections. By overlaying the static load-displacement curves with those obtained from dynamic testing, a significant apparent increase in peak load was observed for the connections with the ML24Z angles (Figure 6.2a), while no increase in peak load for the thick angle connections was observed (Figure 6.2b). The load values for specimens with multiple ML24Z angles were divided by the respective number of angles used, while for the thick angles the load was divided by the respective multiple of six screws (e.g. for 9 screws, divide load values by 1.5). For both connections, no significant increase in the connection stiffness was found when comparing the static and dynamic resistance curves.



(a) ML24Z



(b) Thick Angle

Figure 6.2: Experimental Static and Dynamic Load-Displacement Curves

To verify whether any increases in capacity or stiffness are statistically significant, four separate independent-sample t-tests were conducted on the static and dynamic specimens for each connection type (i.e. eight groups, four independent-sample t-tests). Levene's test for equality of variances was performed (Levene, 1960) and equal variances were found between samples for each t-test. The confidence level was chosen to be 95 %. The null hypothesis, which states that no difference exists between the means of the groups, was rejected if the absolute value of t_{stat} was greater than the absolute value of t_{crit}. The t-tests results are presented in Table 6.1. The stiffnesses used in the statistical analyses correlated to the secant line passing through 40 % and 80 % of each specimen's peak load, in order to ignore potential initial artificial increases in stiffness caused by the test setups.

Table 6.1: Results for T-Test Analyses for CLT Bearing Connections

Connection	**Static vs. Dynamic**	**Result of t-test (α = 0.025)**		**Accept or Reject Null Hypothesis**
		t_{stat}	t_{crit}	
ML24Z	Peak Load	-6.349	2.306	Reject
	Stiffness	-1.251	2.306	Accept
Thick Angle	Peak Load	-0.668	2.571	Accept
	Stiffness	-1.614	2.571	Accept

For the peak loads, the results show that the static and dynamic groups of the ML24Z angles can be considered as two separate groups with two different means (i.e. the observed DIF on the peak load is statistically significant), whereas the thick angle showed no difference in means between the static and dynamic loading. This result confirms the visual observation made in Figure 6.2. The analysis yields an average DIF of 1.55 for the ML24Z connections, whereas no statistically significant DIF on the peak load could be reported for the manufactured thick angle. The increase in peak load in the ML24Z connections can be attributed to the failure mode being dominated by wood crushing. The lack of increase in strength in the tests involving the thick angle is likely due to the failure occurring in steel rupturing. These results are consistent with previous studies that have associated a DIF with wood failure (e.g. Jacques, et al., 2014; Lacroix and Doudak, 2015; Poulin, et al., 2017) and little-to-no strain-rate effects on the ultimate strength of steel (CSA, 2012). The t-tests conducted on the stiffness of the joints reported herein found no statistical significance between the values obtained during static and dynamic loading. This finding is also consistent with other studies which reported no increase in the stiffness of wood elements (Jacques, et al., 2014; Viau and Doudak, 2016b; Poulin, et al., 2017).

6.1.2 Effect of Axial Restraint on the Connection Response

To study the effect of axial restraint on the ML24Z connections, two 1500 kg rated tie-down straps were used on specimens C9, C10, and C11 to restrict the outward forces on the blocking. This was done only on connections containing the ML24Z angle, since no separation between the test specimens and support blocks was observed in connections containing the manufactured thick angles. Axial restraint was found to have significant effects on the ML24Z connection's load-displacement curve, particularly in the post-peak region. Figure 6.3 highlights these effects, where the restraints seem to cause average increases of 1.29, 1.62, and 1.37 of the peak load, displacement at peak load, and displacement corresponding to 50 % of the peak load, respectively, compared to the unrestrained specimens. While these findings cannot be generalized, they provide insight to future studies on timber assemblies using heavily deformable connections. Depending on the type of connection and structural element used, omitting the effect of axial restraint may lead to erroneous conclusions regarding the connection behaviour. Evidently, more research is required in this area before generalized conclusions can be made about the effect of axial restraint.

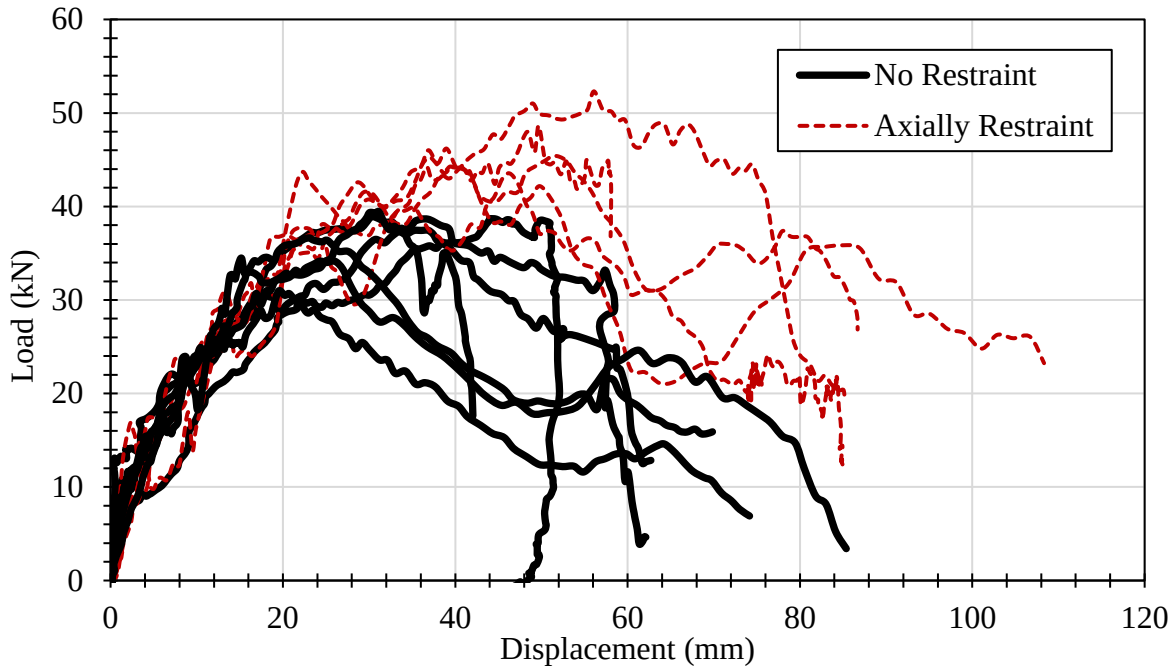


Figure 6.3: Effect of Axial Restraint on Dynamic Load-Displacement Curve for ML24Z Angles

6.1.3 CLT Assemblies Under Dynamic Loading

An average peak resistance of 169.1 kN (CoV = 0.04) was obtained from the results of the three full-scale tests on CLT specimens with simply supported boundary conditions. Comparing this value with the full-scale static test results from Poulin, et al. (2017), for specimens of identical spans and grade, a dynamic increase factor (DIF) of 1.31 was obtained. This value is consistent with the value of 1.28 reported by Poulin, et al. (2017). The failure of the simply supported panels initiated typically on the tension face at a knot or finger joint, however, failure progression was not heavily influenced by the position of the finger joints along the width of the panels. Significant post-peak behaviour in both full-scale specimen groups (i.e. simply supported and end connected) was observed, due to the contributions of the cross-layers, which act as reinforcements to the longitudinal layers. Significant post-peak behaviour is defined as sustained resistance of at least 50 % of the peak resistance of the member, as suggested by Lacroix and Doudak (2019). Similar to the connection-level test results, the failure in CLT assemblies with ML24Z angles was dominated by wood crushing caused by deformation of the brackets, accompanied by some yielding in the screws (Figure 6.4). CLT assemblies equipped with the thick angle connections were limited in connection damage to yielding of the screws.



(a) Bending in ML24Z Angle



(b) Wood Crushing in Panel Ends due to ML24Z Angle



(c) Deformation in Screw

Figure 6.4: Typical ML24Z Connection Damage in CLT Assemblies

6.1.4 Energy Dissipation in CLT Bearing Connections

The tested configurations were varied in order to investigate the effect of end connections' energy dissipative properties on the behaviour of the overall assembly. The ML24Z connections were designed to yield prior to the CLT panel obtaining its ultimate flexural capacity. In the case of critically under-designed connection (Figure 6.5a), this represented an undesirable sequence of failure, whereby the system as a whole failed prematurely, and the load-bearing CLT panels did not achieve their flexural capacity. This is the main reason why design standards include provisions that aim to increase the demand on the connections in order to avoid such failure mechanism. On the other extreme, specimens with overdesigned thick angle connections (Figure 6.5b), were

detailed such that little-to-no damage occurred in the connections. As such, the failure of the assembly consisted of the CLT panel reaching its ultimate flexural capacity with little damage in the connection joints. While this failure sequence is desirable, and consistent with the failure sequence outlined in the Canadian Blast Standard (CSA, 2012), the energy dissipation of the assembly is limited due to the brittle nature of the wood material. To obtain a balanced approach where the connections do not fail prematurely, while still maintaining some level of energy dissipation, connections falling between these two extremes were investigated. This involves implementing connections, which would yield and dissipate inelastic energy, yet allow the CLT panels achieve their respective flexural capacities. An example of a specimen with such a connection is shown in Figure 6.5c. Considering the damage presented in Figure 6.5, it can be observed that the specimens with connections designed to yield but not fail performed better when compared to the other two cases for similar pressure-impulse combination. This design approach achieved full flexural failure in the CLT panels without premature failure occurring in the boundary connections. Observed damage in the CLT panel was also less than the case with over-designed connections, due to dissipation of some energy in the connections.

This shift in failure sequence, whereby some amount of controlled damage is allowed to occur in the connections, provides the CLT assembly with an energy-dissipating fuse. This is evident when calculating the work done (i.e. area under the system resistance curves) and normalizing the value with the panel's respective peak resistance (see Table 6.2) by dividing the total area under the system resistance curve by the peak resistance. Also present in Table 6.2 are the failure type and sequence associated with each connection, such as wood failure (W_F), connection yielding (C_Y), and connection failure (C_F).



(a) Critically Underdesigned (Thick Angle with 3 Screws)



(b) Overdesigned (4 ML24Z)



(c) Underdesigned (2 ML24Z)

Figure 6.5: Effect of Connection Design of Specimens Subjected to Similar Blast Loads

Table 6.2: Effect of Connections and Failure Sequence on Work Done by CLT Assemblies

Connection Yield Load	**Boundary Condition**	**Assembly Failure Sequence**	**Normalized Work Done (Joules/N)**	**Difference (%)**
	Simply Supported	W_F	12.33	-
Highest	4 ML24Z (no axial)	W_F	14.20	15.1
	Thick Angle with 9 Screws	W_F	19.34	56.8
↓	Thick Angle with 6 Screws	$C_Y \rightarrow W_F$	21.85	77.1
	2 ML24Z (axial)	$C_Y \rightarrow W_F$	20.69	67.8
	2 ML24Z (no axial)	C_Y	61.46	398.3
Lowest	Thick Angle with 3 Screws	C_F	9.84	-20.2

The entries in Table 6.2 are presented in descending order of the connection yield capacity. It can be observed that as the connection yield capacity decreases, the work done by the system increases. Thus, allowing for some amount of yielding in the connections prior to the failure of the CLT panel will tend to benefit the overall performance of the assembly. As expected, assemblies with severely underdesigned connections will fail prematurely and thus dissipate less energy than the baseline case of simply supported end conditions.

6.2 Glulam Assemblies with Bolted Connections

6.2.1 General Behaviours and Failure Modes

An average peak resistance of 219.0 kN was obtained from the results of the three full-scale tests on glulam specimens with simply supported boundary conditions, correlating to an average modulus of rupture (MOR) of 50.1 MPa (CoV = 0.04). Comparing this value to the full-scale static test results from Lacroix and Doudak (2018b), for specimens of identical spans, width, and grade, a dynamic increase factor (DIF) of 1.10 is obtained. This value is consistent with the value of 1.14 reported by Lacroix and Doudak (2018b). Flexural failure of the glulam beams was characterized by splintering tension failure, as shown in Figure 6.6. Initiation of failure occurred at defects, such as knots (Figure 6.6a) or finger joints (Figure 6.6b). The beams used throughout this study consisted of multiple laminates across the width, thereby allowing for more staggered finger joints on the tension side. This allowed the beams to experience significantly more crack propagation and splintering (Figure 6.6c). The glulam beams did not have any significant post-peak capacity following the failure of the tension-side laminate.



(a) Failure Initiation at Knot (Specimen G2)



(b) Failure Initiation at Finger Joint (Specimen G5)



(c) Damage Propagation Through Beam Depth (Specimen G13)

Figure 6.6: Representative Dynamic Failure Modes of Glulam Beams

Similar to the connection-level test results, the failure in the glulam assemblies with bolted connections was dominated by bolt bending (yielding) and wood crushing caused by deformation of the bolts (see Figure 6.7). This was most prevalent in specimens where splitting did not occur. As shown in Figure 6.7a, the deformed bolt shape resembles that of the (g) bolt yielding mode as given in the European Yield Model (EYM), where three plastic hinges are formed (CSA, 2019). This represents the most ductile failure mode in three-member bolted connections. In all specimens in the dynamic testing, the glulam beams failed prior to attaining an ultimate shear failure of the bolts.



(a) Bolt Bending and Yielding

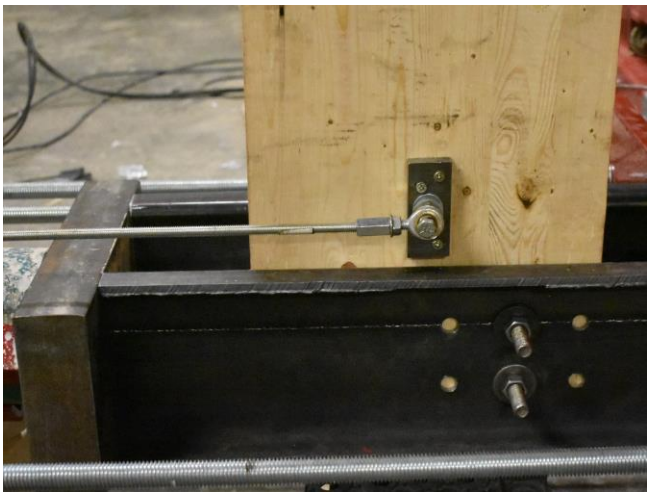


(b) Wood Crushing

Figure 6.7: Representative Bolted Connection Yielding and Wood Crushing in Glulam Beams

6.2.2 Perpendicular-to-Grain Splitting

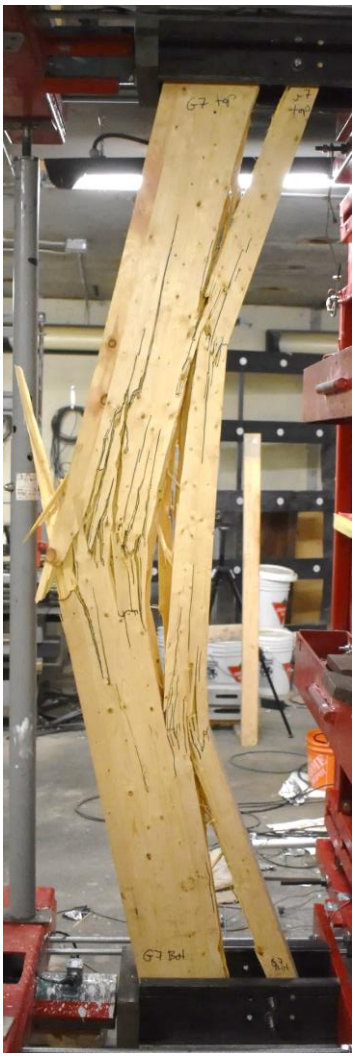
The connections in specimens G7 – G9 were designed specifically to fail in brittle perpendicular-to-grain splitting, characterized by a lengthwise crack passing through the centreline of the bolt holes and propagating throughout the beam, as shown in Figure 6.8. This was done by increasing the unloaded edge distance beyond the code minimum of 19.1 mm. The splitting capacity equation given in CSA O86 (CSA, 2019) was used to estimate the connection capacity. The Canadian blast standard (CSA, 2012) requires that designers detail the connections such that brittle failure modes (e.g. splitting) do not govern. The question that the current investigation attempts to answer is whether self-tapping screws are capable of eliminating such brittle failure modes by reinforcing the wood splitting perpendicular-to-grain.



(a) Connection Prior to Testing (e_p = 203.2 mm)



(b) Splitting Failure



(c) Overview of Failed Specimen

Figure 6.8: Representative Splitting Failure in Glulam Beams

As shown in Figure 6.9, these specimens resulted in various amounts of bolt yielding and wood crushing dependent on the selected unloaded edge distance. As expected, it was observed that the specimens that failed in splitting at a higher load level (i.e. smaller unloaded edge distance) exhibited more inelastic energy dissipation. Specimen G7, shown in Figure 6.9a, was detailed such that the failure sequence would consist of splitting failure, prior to any yielding in the bolts or wood crushing, and prior to the glulam beam failing in flexure. Specimens G8 and G9, shown in Figure 6.9b and Figure 6.9c respectively, were detailed such that the failure sequence shifted to that of bolt yielding and wood crushing, followed by connection failure in splitting. While the beams did not reach their flexural capacity in all three specimens, the shift in failure sequence allowed for progressively more inelastic energy prior to ultimate failure of the assembly.





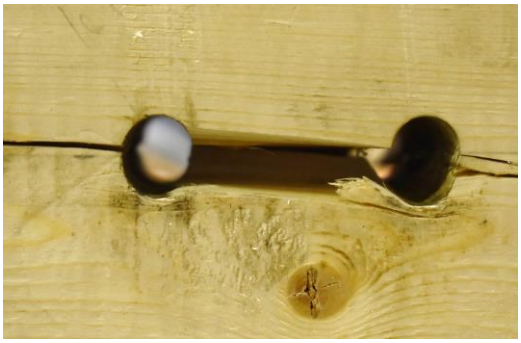
(a) Specimen G7 – No Yielding nor Wood Crushing (e_p = 203.2 mm)





(b) Specimen G8 – Minor Bolt Yielding and Wood Crushing (e_p = 133.5 mm)





(c) Specimen G9 – Moderate Bolt Yielding and Wood Crushing (e_p = 76.2 mm)

Figure 6.9: Bolt Yielding and Wood Crushing in Specimens Failing in Splitting

6.2.3 Use of Self-Tapping Screws to Prevent Splitting Failure

Self-tapping screws (STSs) have been successfully used to reinforce wood members against potential brittle failure modes, including at notches (e.g. Dietsch and Brandner, 2015), connections (e.g. Lam, et al., 2008; Wang, et al., 2015), and in timber-concrete composite systems (e.g. Gerber and Tannert, 2015). To investigate their applicability in reinforcing bolted connections under high strain-rates, bolt configurations that failed in splitting (Section 6.2.2) were tested with STS reinforcement. The results showed that STSs are capable of changing the failure mode to that of ductile bolt yielding and wood crushing. Some superficial splitting occurred in two of the three reinforced specimens, as shown in Figure 6.10a and Figure 6.10b, respectively, with crack widths measuring 3 mm or less. The splitting occurred at large displacement levels (i.e. at a mid-span deflection of approximately 34 mm) and did not affect the overall capacity of the joint. Specimen G12 (Figure 6.10c) showed no signs of splitting. Three rows of three STSs were installed in this specimen, in order to have even stress distribution along the screws and in the bolted joint. The geometry of this connection likely aided in preventing any development of cracks.



(a) Specimen G10 (b) Specimen G11 (c) Specimen G12

Figure 6.10: Glulam Specimens with STS Reinforcement

The use of STSs provided more ductility in the reinforced specimens when compared to those that were unreinforced by preventing perpendicular-to-grain splitting. This was evident when measuring the amount of crushing in the wood at the bolt holes after testing and comparing the unreinforced and reinforced specimens, as shown in Table 6.3. The wood crushing was evaluated by measuring the increase in bolt hole diameter following each test (see Figure 6.7b). The table also shows the amount of wood crushing in specimens detailed such that splitting is not expected to occur (i.e. unloaded edge distances of 19.1 mm and 38.1 mm). It can be observed that the use of STS reinforcement allowed the reinforced specimens to reach a state of bolt yielding and wood crushing similar to the specimens designed against splitting.

Table 6.3: Comparison of Wood Crushing for Unreinforced and Reinforced Specimens

Unloaded Edge Distance, e_p (mm)	**Permanent Wood Crushing (mm)**	
	Unreinforced	**Reinforced**
19.1	8.2	-
38.1	7.7	-
76.2	1.2	7.4
133.5	0.5	6.1
203.2	0.0	8.7

6.2.4 Energy Dissipation in Glulam Bolted Connections

The yield capacity of the bolted connections was varied in order to investigate the effect of energy dissipation in the connections on the performance of the glulam assembly. Two extreme cases were investigated: that of a critically under-designed connection, where premature splitting failure occurred, and that of an over-designed connection, for which little-to-no permanent damage was expected. As predicted, specimens with connections detailed such that splitting failure occurs were found to fail prematurely, resulting in limited amounts of yielding in the connections. This shift in failure sequence is apparent when plotting the load-displacement curve of a typical 2x1 bolted joint (Figure 6.11). Also shown in Figure 6.11 are various capacity limits, which demarcate the loads at which certain failure modes are expected to take place. Based on the experimentally obtained embedment strength and bolt yielding stress, the connection yield line correlates approximately to the elastic limit of the connection. Two lines of splitting capacities are also shown in order to demonstrate the change in failure sequence, whereby splitting failure is expected to occur prior to any yielding in the connection (see Figure 6.9a) and after yielding has occurred (see Figure 6.9c). Finally, a line representing the expected beam failure load is also shown.

By extending this logic and shifting the splitting failure line as high up on the curve as possible, specimens with 2x1 bolted connections detailed against splitting failure (e.g. e_p = 19.1 mm) or reinforced against splitting underwent a different failure sequence. By increasing the splitting capacity above that of the beam failure, the amount of energy dissipation (i.e. area under the load-displacement curve) was significantly higher. As such, the failure sequence for these specimens consisted of connection yielding, followed by beam failure in flexure (Figure 6.11).

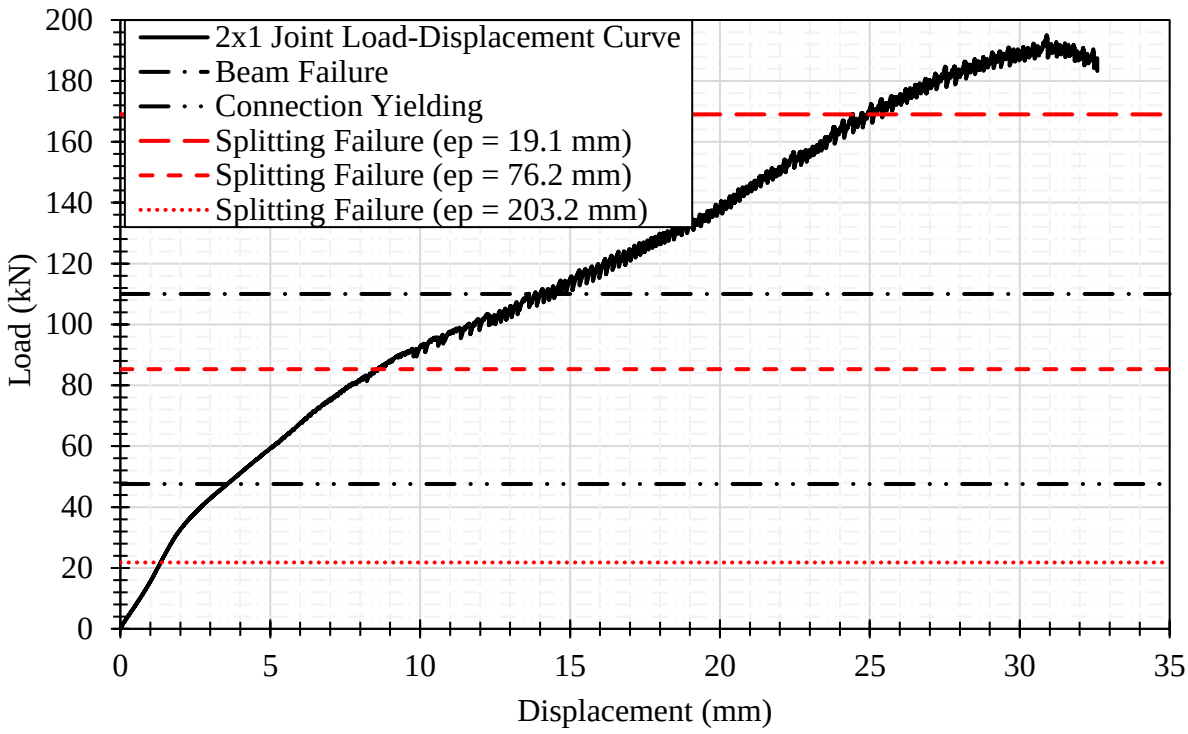
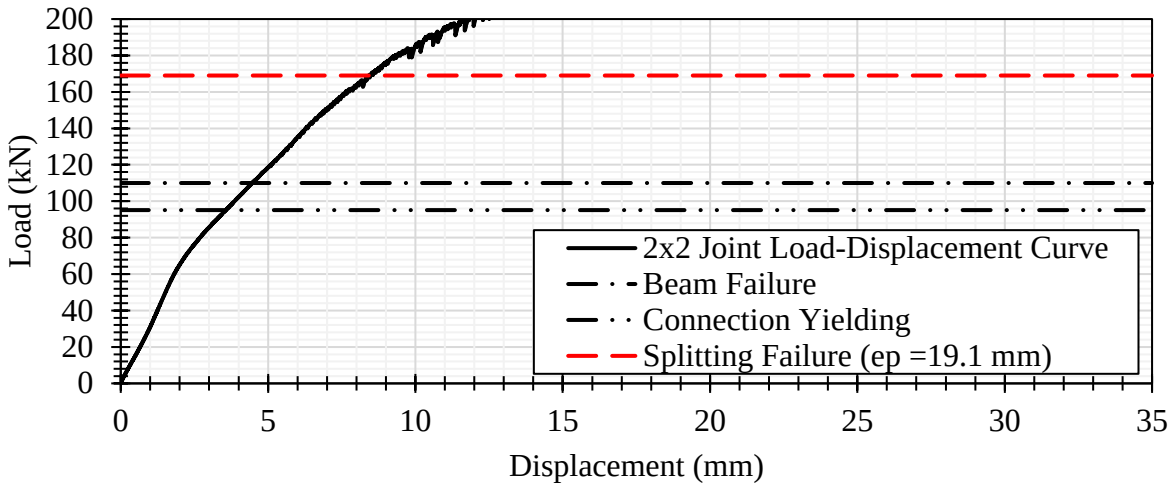
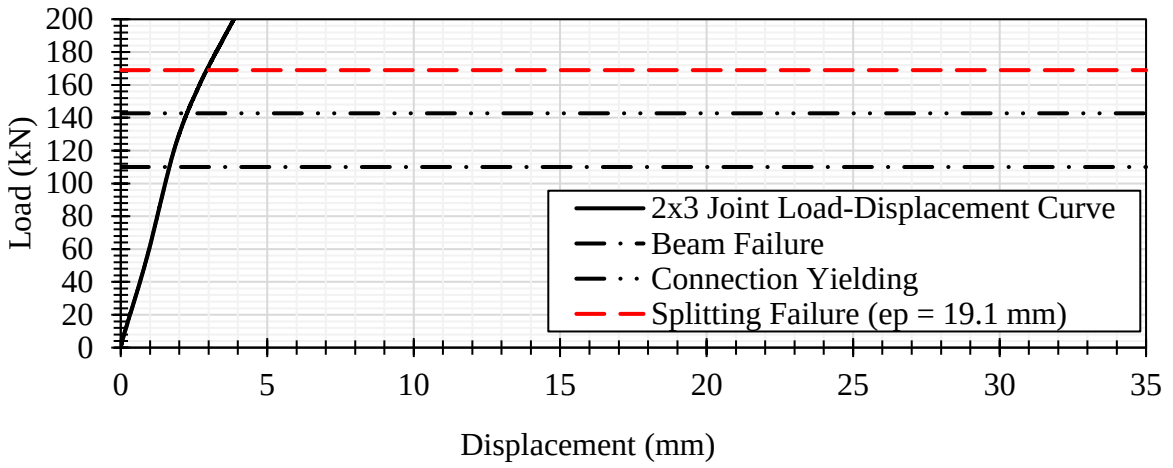


Figure 6.11: Possible Failure Modes and Failure Sequences for 2x1 Bolted Joints

The implication of overdesigning the connections was investigated for bolted assemblies. For these specimens, the unloaded edge distance was maintained at the code minimum (19.1 mm) and the number of bolts were doubled (2x2 joint) and tripled (2x3 joint). The former represented the case where the expected load corresponding to flexural failure of the beam was similar to that of the connection yield load. For this configuration, the splitting capacity was higher than both the beam failure and connection yield capacity (Figure 6.12a). The latter represented the case where connection design would meet and exceed the design provisions of the blast standard CSA (2012). In this case, beam failure is expected to govern the design (Figure 6.12b), and no damage would be expected in the connections.



(a) 2x2 Bolted Joints



(b) 2x3 Bolted Joints

Figure 6.12: Possible Failure Modes and Failure Sequences for Overdesigned Bolted Joints

In order to quantify the amount of energy dissipation in the assemblies considered, the normalized work done by each assembly was calculated and compared. As shown in Table 6.4, when compared to the idealized simply supported boundary conditions, all connections detailed against splitting failure provided some amount of energy dissipation, however, this was most pronounced when the bolted connections were detailed to undergo significant bolt yielding and wood crushing (i.e. 2x1 bolt group). Notably, connections designed to yield had 65 % more energy-dissipating capability compared with idealized pinned connections. When splitting occurred, the total work was reduced in a way that is inversely proportional to the unloaded edge distance. This finding further emphasizes the importance of preventing splitting failure from occurring prior to flexural failure of the glulam beam.

Table 6.4: Effect of Connections and Failure Sequence on Work Done by Glulam Assemblies

Boundary Condition	Assembly Failure Sequence	Normalized Work Done (Joules/N)	Difference (%)
Simply Supported	W_F	13.21	Baseline
2x3	W_F	15.41	16.6
2x2	$C_Y \rightarrow W_F$	16.76	26.8
2x1 (No Splitting)	$C_Y \rightarrow W_F$	21.81	65.0
2x1 (e_p = 76.2 mm)	$C_Y \rightarrow C_S$	11.12	- 15.9
2x1 (e_p = 133.5 mm)	$C_Y \rightarrow C_S$	7.13	- 46.0
2x1 (e_p = 203.2 mm)	C_S	2.16	- 83.6

6.3 Behaviour of Timber Assemblies with Energy-Absorbing Connections

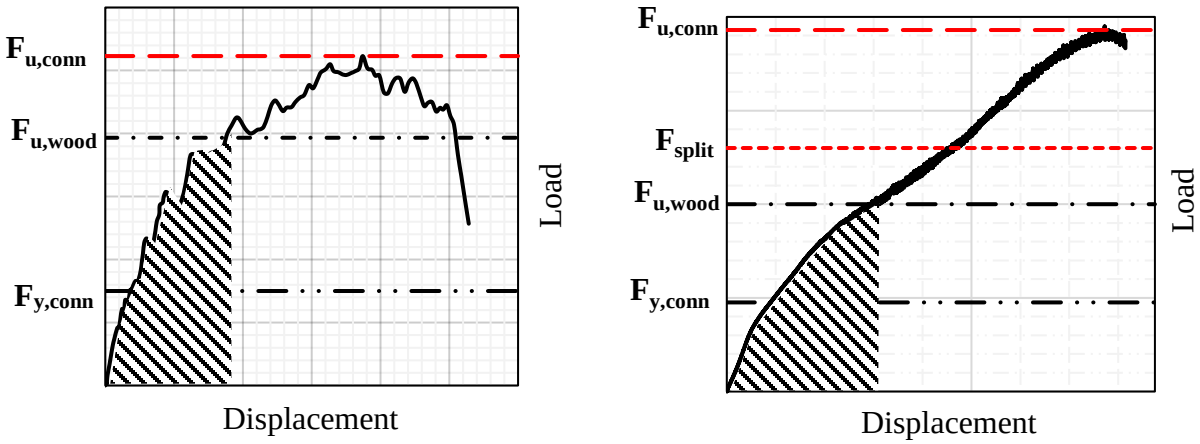
6.3.1 Proposed Capacity-Based Blast Design Philosophy

The results from the full-scale testing on CLT and glulam assemblies with typical connections have shown that additional energy dissipation within the system can be gained when the connections are detailed properly. For the CLT bearing connections, this corresponded to wood crushing in the panel ends and yielding of the ML24Z angles. Similarly, yielding of the bolts and wood crushing within the bolted glulam connections provided the most energy dissipation, prior to any damage in the load-bearing glulam beam.

The aim of the blast design of any timber assembly is to prevent progressive collapse of the structure and preserve its structural integrity as much as physically and economically viable. One way to enhance the strength and ductility of timber assemblies would be to retrofit the load-bearing element in order to increase its strength and ductility (e.g. fibre-reinforced polymers). Another approach would be to introduce alternative well defined and controlled failure mechanisms within the failure sequence. The use of connections consisting of mild steel capable of undergoing inelastic deformations has been explored in earthquake engineering for timber assemblies but not when such assemblies are subjected to blast loading. The main difference between the two loading scenarios is that a mechanism that allows for energy dissipation of cyclic loading is used in earthquake design, whereas only a one-time energy dissipation is generally adequate for blast design. In order to establish a clear failure sequence, three capacity parameters, namely the connection yield load ($F_{y,conn}$), connection failure load ($F_{u,conn}$), and the timber member failure load ($F_{u,wood}$) are defined. It is generally agreed that a failure sequence where connection failure occurs is undesirable. Based on the aforementioned results on full-scale CLT and glulam specimens with

connections, allowing for inelastic deformations in the connections has shown to increase the amount of blast energy that an assembly can absorb prior to failure of the load-bearing element, when compared to overdesigned connections. Therefore, the desired failure sequence can be generalized as that of connection yielding followed by failure of the load-bearing element, while ultimate failure of the connections must be avoided.

As shown in Figure 6.13 for typical CLT and glulam assemblies, the connections can be detailed such that energy dissipation occurs in the connection prior to failure of the wood. This energy is shown as the hatched area under the curves (Figure 6.13).



(a) 2-ML24Z Angles (b) 2x1 Bolted Joint

Figure 6.13: Failure Sequence Parameters and Energy Dissipation in Timber Connections

For both assemblies, the total available energy in the assembly can be defined as the sum of the mostly inelastic energy dissipated in the connections and the elastic energy stored in the wood member. As illustrated in Figure 6.13, it is difficult to benefit from the potential of typical connections to dissipate energy since only a small portion of the load-displacement curve is utilized. The remaining areas under the curves represent a wasted potential in further energy dissipation. One possible method to optimize the use of these connections would be to shift the wood failure line upwards (i.e. overdesign the wood member), or shift the entire connection load-displacement curve downwards (i.e. use smaller/weaker connections). However, this always presents the risk of undesirable and premature connection failure, due to the variability in the wood member capacity.

In order to maximize the use of the potential inelastic energy in the connections, the displacement at which the connection load is equal or higher than the load correlating with failure of the wood member ($F_{u,wood}$) must be delayed. Additionally, the post-yield slope of the load-displacement curve would limit the total amount of ductility and energy dissipated as it causes the load to rise until the value correlates to $F_{u,wood}$. Elastoplastic load-displacement curves provide an efficient method of achieving this design goal by ensuring the yield plateau load, $F_{y,conn}$, remains lower than $F_{u,wood}$, thereby maximizing the areas under the connection load-displacement curve. The relative magnitudes of both of these parameters must take into account the inherent variability in the wood member and connection, and minimize the overlap between these two parameters. As such, a proper ratio between these parameters must be maintained. Equation 6.1 and Equation 6.2 outline the proposed capacity-based blast design requirements for connections, to be met in order to ensure structural integrity of the assembly and optimal energy dissipation. Furthermore, the wood member is required to fail prior to the connection, as stipulated in Equation 6.3 and Equation 6.4.

$$F_{u,wood} \geq F_{y,conn} \qquad \text{Equation 6.1}$$

$$\frac{F_{u,wood}}{F_{y,conn}} \geq \alpha_y \qquad \text{Equation 6.2}$$

$$F_{u,conn} \geq F_{u,wood} \qquad \text{Equation 6.3}$$

$$\frac{F_{u,conn}}{F_{u,wood}} \geq \alpha_u \qquad \text{Equation 6.4}$$

where α_y and α_u are the overstrength factors for connection yielding and failure, respectively.

A generalized load-displacement curve representing the aforementioned concepts is shown in Figure 6.14, along with the failure sequence parameters. It can be seen that the energy dissipation (the hatched area in Figure 6.14) for these connections is significantly greater than those obtained from typical connections used in CLT and glulam assemblies.

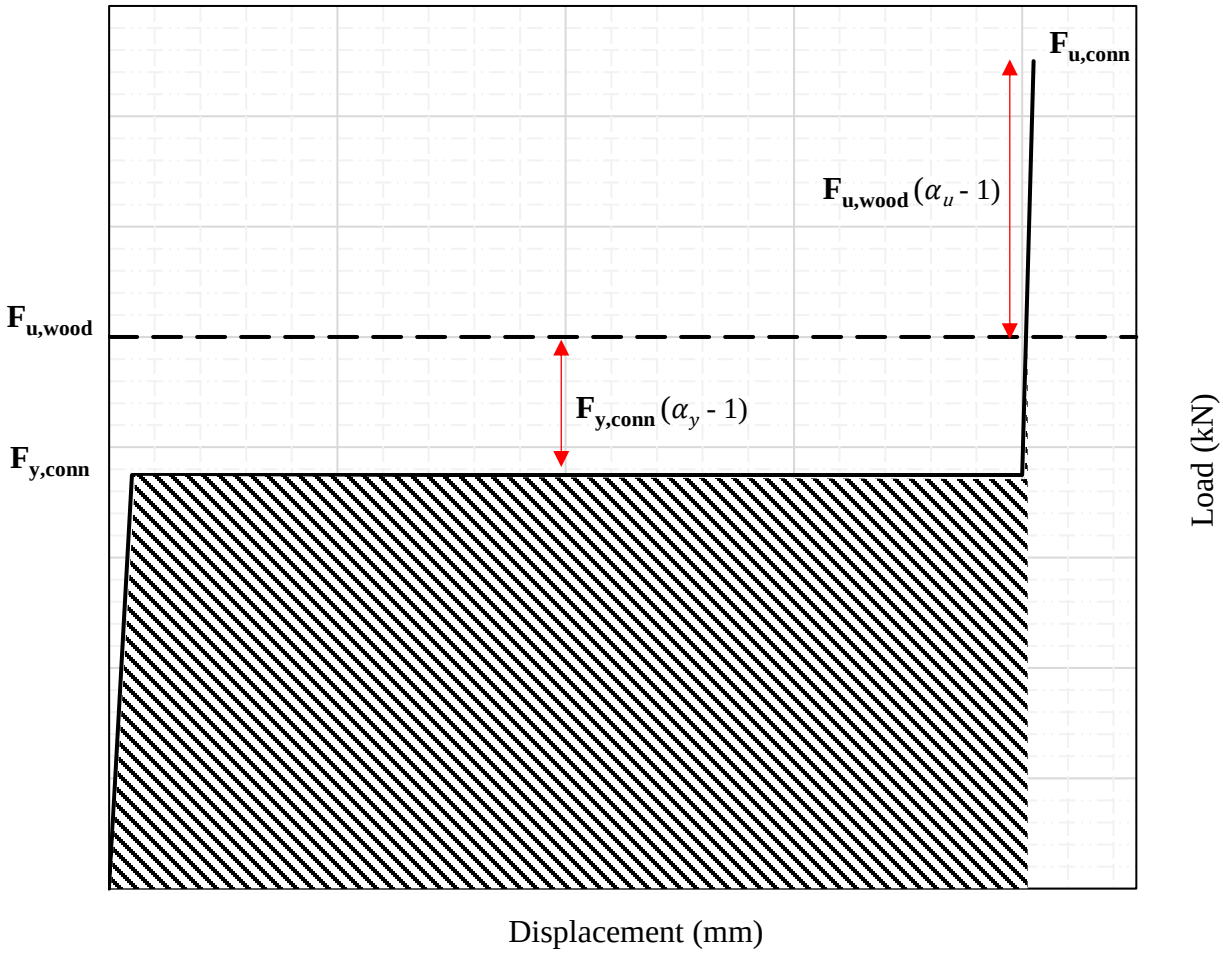


Figure 6.14: Failure Sequence Parameters and Energy Dissipation in Optimized Connections

The energy-absorbing connection (EAC) described in Chapters 3 and 4, presents the opportunity to obtain the desired elastoplastic behaviour, and the proposed requirements outlined Equation 6.1 to Equation 6.4. As shown in Table 6.5, where the same methodology was used to calculate the normalized work done as that for Table 6.2, an EAC with yield load ($F_{y,conn}$) that is close to the member failure load will provide the highest amount of energy dissipation. As the overstrength factors for connection yielding, α_y (Equation 6.2), increases, the energy dissipation provided by the EAC will decrease. However, even for the highest value of α_y, the EACs would provide a significant addition in energy dissipation. If the EAC is designed such that little-to-no yielding occurs in the EAC (i.e. α_y of unity), the increase will be limited in magnitude, and will depend simply on the elastic portion of the EAC's load-displacement curve. This conveys the fact that the design philosophy of underdesigning the connections' yield capacity with reasonable safety margins will yield better overall system performance.

Table 6.5: Effect of Overstrength Factor on Work Done by Energy-Absorbing Assemblies

α_y	**Normalized Work Done (Joules/N)**	**Increase (%)**
1.0	16.04	21.4
1.4	63.40	396.3
1.8	55.20	347.6
2.0	47.59	260.2

6.3.2 Comparisons with Typical CLT and Glulam Connections

Various metrics were utilized to evaluate the performance of the EACs relative to the typical timber connections (e.g. angles, bolts). These include the work done by the assembly, qualitative system performance (i.e. extent of damage), and the maximum ductility ratio. The latter is defined as the ratio of the maximum displacement over the yield displacement, as given in Equation 6.5.

$$\mu_{max} = \frac{\Delta_{max}}{\Delta_{yield}} \qquad \text{Equation 6.5}$$

While the ductility ratio does not directly assess the amount of energy absorbed by the connections, it serves as an indicator of the amount of inelastic energy available within the connections. For example, a connection with a ductility ratio of 1 can only dissipate elastic energies prior to failure. By normalizing representative load-displacement curves of each connection tested throughout this study as a function of the yield load and yield displacement, the maximum ductility ratios of each connection can be directly compared. As shown in Figure 6.15, the typical connections allow for maximum ductility ratios of 9 to 13, whereas the EAC is capable of undergoing deformations up to a maximum ductility ratio of 23. Whereas the load in the EACs stays constant through the response up to failure of the wood member, the loads in the typical connections at which failure of the timber member occurs are at least twice that of the yield load, correlating to a progressive increase in loading up until beam failure.

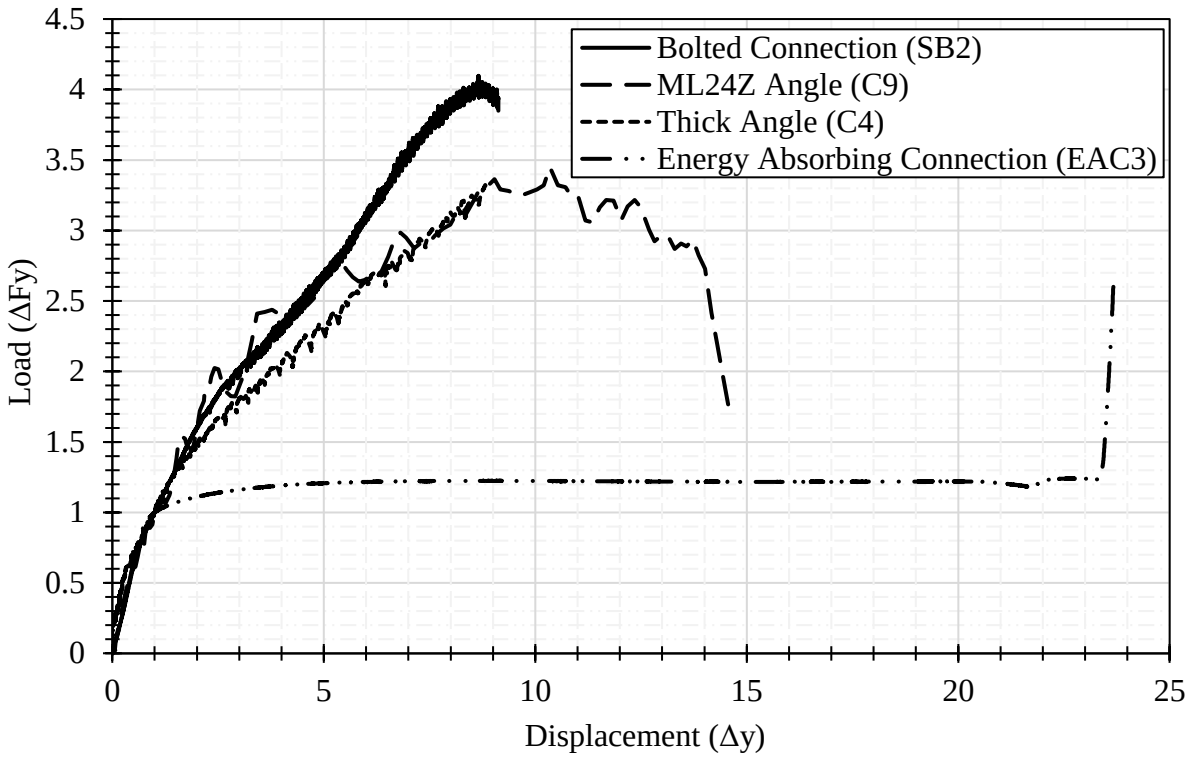


Figure 6.15: Normalized Load-Displacement Curves of Various Connections Relative to Yield

The areas under the curves in Figure 6.15 indicate that the energy dissipation in the typical connections are within similar magnitudes, whereas the EAC presents the potential for significantly higher energy dissipation. Quantification of these energies can be made by comparing the work done by each connection, as shown in Table 6.2 for CLT bearing connections, Table 6.4 for bolted glulam connections, and Table 6.5 for EACs. Shown in Figure 6.16 are CLT and glulam assemblies with varying connections types subjected to similar pressure-impulse combination. The level of damage in the wood member can be observed to reduce as the connections are better able to absorb energy. For both glulam and CLT assemblies, the lack of damage within the wood members display the benefit of utilizing optimized connections following the proposed capacity-based blast design guidelines and elastoplastic load-displacement curves.



(a) 2x3 Bolted Connection



(b) 2x1 Bolted Connection



(c) EAC for Glulam



(d) Thick Angle (9 Screws)



(e) Two ML24Z Angles

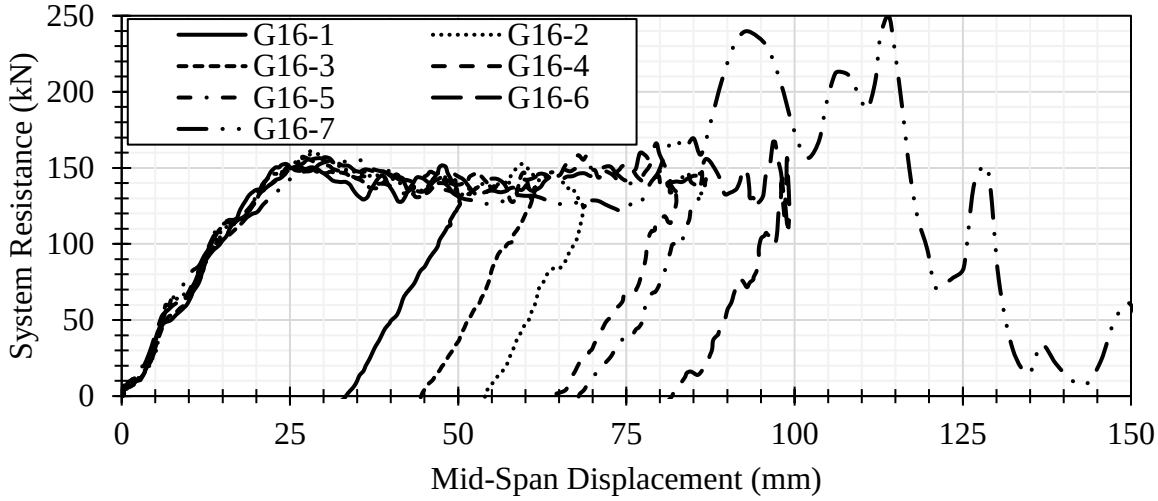


(f) EAC for CLT

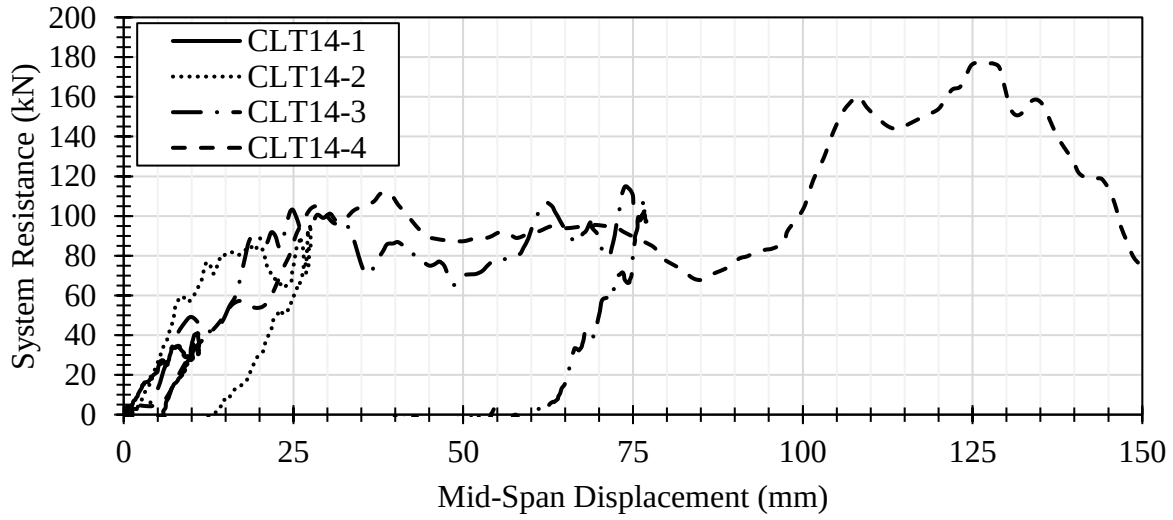
Figure 6.16: Effect of Connections on Damage Reduction in Wood Members

6.3.3 Assemblies Subjected to Multiple Blast Loads and Replaceability of EACs

In order to investigate the effect of multiple blast loads enacted onto a timber assembly, some full-scale specimens were subjected to multiple pressure-impulse combinations. This included a glulam member subjected to seven different pressure-impulse combinations, and two CLT panels each subjected to four pressure-impulse combinations. Results from these tests show that as long as the elastic limit of the wood member is not reached, the wood member would remain elastic, for various levels of loading. As shown in Figure 6.17a for the glulam specimen and Figure 6.17b for one of the two CLT specimens, no degradation in the initial system stiffness was observed.



(a) System Resistance Curves of Specimen G16



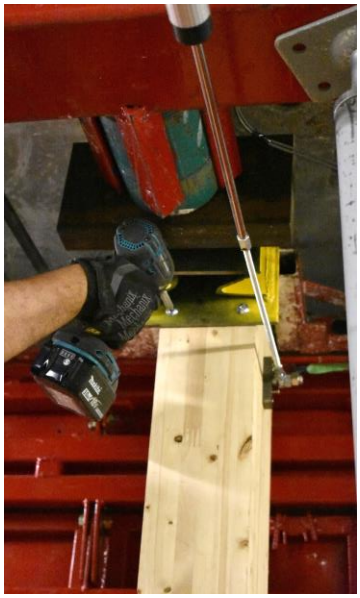
(b) System Resistance Curves of Specimen CLT14

Figure 6.17: Effect of Multiple Shots on Glulam and CLT Specimens

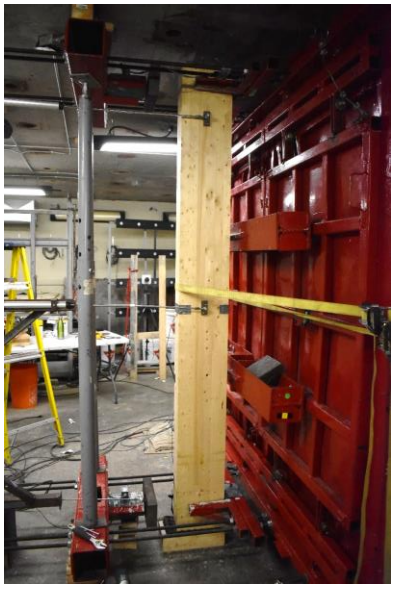
The EACs were designed such that they would be easily replaceable following a blast event, thus resulting in less occupation time lost for the building owners. As an example, following each test shown in Figure 6.17a, the glulam beam was secured to the shock tube frame using strapping and adjustable steel posts. This simulated the shoring and securing of an actual member in a building during repairs following a blast event. Once secured, the EACs were detached from the specimen using a hand-operated drill, and new undamaged EACs were installed. This process is demonstrated in Figure 6.18.



(a) Shoring and Strapping of Beam



(b) Removal of Damaged EAC



(c) Specimen Prior to Installation of EACs



(d) Specimen with New EACs

Figure 6.18: Process of EAC Replacement Following a Blast Test

6.4 Analytical Modelling

6.4.1 TDOF Versus SDOF

The goal in developing a two-degree-of-freedom (TDOF) analytical model was to create a framework in which the effects of realistic connections could be considered when predicting the response of timber assemblies subjected to blast loads. In order to conceive a model that is representative and accurate, one must be able to capture the complex interactions between different components and the dynamic effects of the load being applied. The end goal is to be able to change any parameter of a timber assembly and still be able to accurately predict the assembly performance.

The TDOF modelling predictions presented in Chapter 5 summarize the accuracy entailed when utilizing such modelling methods to represent full-scale timber assemblies with various connections. This includes accurate predictions of failure sequence, member displacement, connection displacements, and system resistance. To further justify the use of such an analytical approach, equivalent single-degree-of-freedom (SDOF) modelling was conducted using *RCBlast*, a blast analysis software capable of performing equivalent single-degree-of-freedom analysis (Jacques, 2014). The SDOF approach is similar to that of the procedure outlined in Chapter 5 for TDOF, in regards to how the timber member is lumped into an equivalent mass. SDOF is limited to displacement occurring at the mid-span of the member and represent a singular failure mode. Comparisons between the experimentally obtained mid-span displacements and predictions from SDOF analysis are presented in Figure 6.19. The use of SDOF led to an average mid-span displacement prediction ratio of 0.85, versus the 1.02 ratio obtained when utilizing TDOF modelling. Additional to the reduction in average prediction accuracy, significant variability could be observed in the predictions with a coefficient of variation of 0.83 and 0.06, for the results obtained through the SDOF and TDOF analyses, respectively. The results are also illustrated in Figure 6.19, where large spread within the dataset can be observed. One noticeable cluster of data points is found in the lower left corner of Figure 6.19, where a plateau seems to form at an analytical prediction displacement of roughly 25 mm. The plateau represents the average elastic limit of the glulam specimens. This is due to the fact that SDOF is only based on the displacements of the wood members, and thus, no contribution from the connections is captured. The rest of the data points consists of CLT specimens. The analytical predictions for these tend to correlate better

with the experimental results due to the fact that CLT panels have significant post-peak capacities when compared to the glulam beams. For example, a glulam assembly with energy-absorbing connections (EACs) will typically have a maximum displacement of approximately 100 mm, where 25 % is of the displacement is caused by the bending of the glulam beam, whereas a CLT assembly with EACs will typically have a maximum displacement of approximately 250 mm, where roughly 70 % is caused by the bending of the CLT panel. This will cause the prediction error to be significantly higher for glulam assemblies versus CLT assemblies.

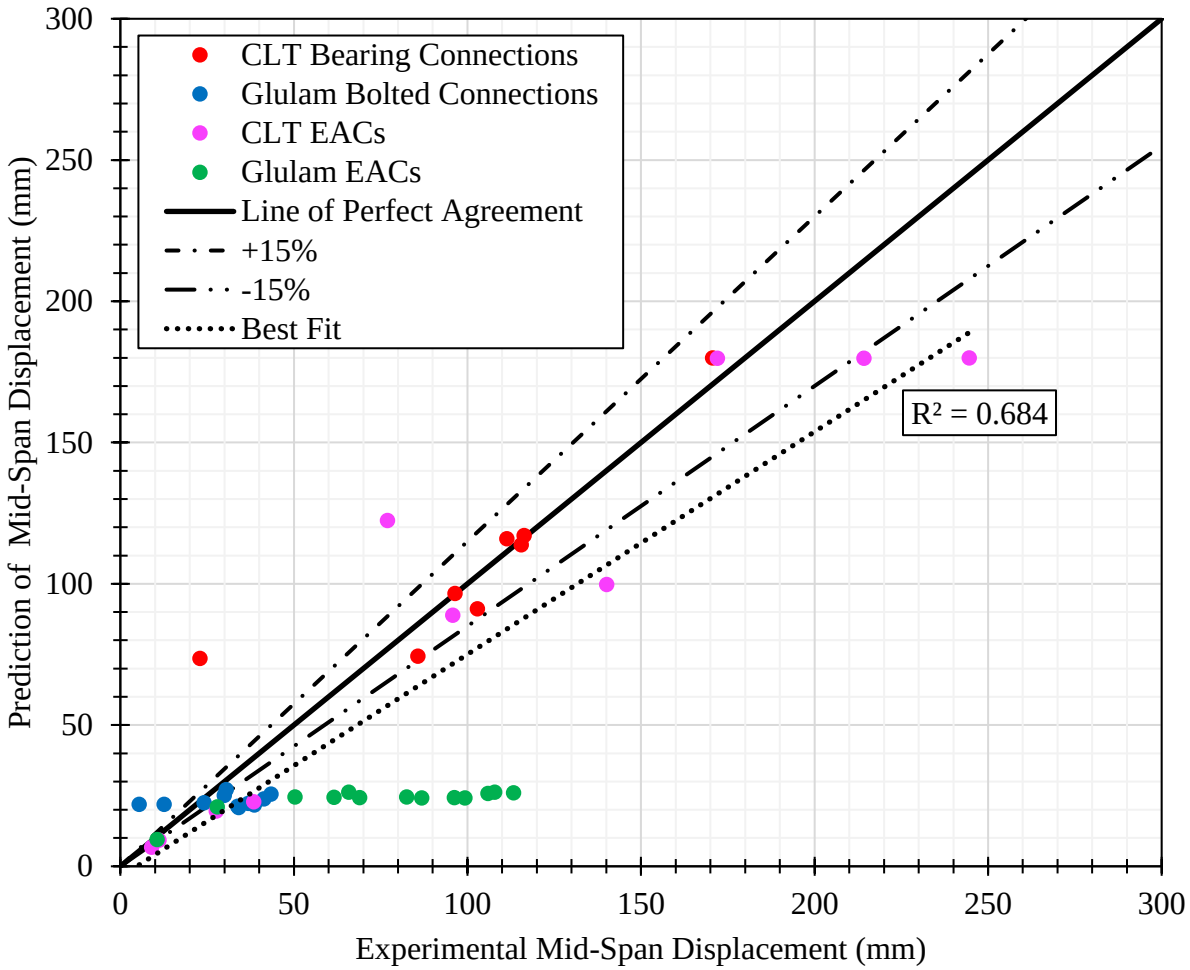


Figure 6.19: Experimental Displacements Versus SDOF Predictions

Quantification of the accuracy of the model for each failure sequence can be found in Table 6.6, where the accuracy of SDOF modelling is shown to decrease significantly when inelastic damage in the connections takes place and where connection failure occurs. This is expected, however, as SDOF cannot take any connection behaviour into account when analyzing an assembly. In cases

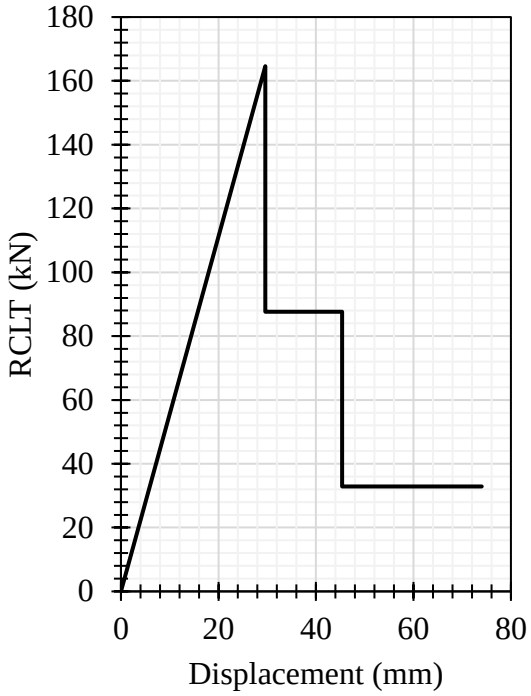
where the assemblies were detailed with overdesigned connections, SDOF tended to predict the mid-span displacement of the assemblies with acceptable accuracy and variability. This is expected, as these connections will tend to resemble the case with idealized pin-ended boundary conditions.

Table 6.6: Summary of SDOF Prediction Accuracies for Various Failure Sequences

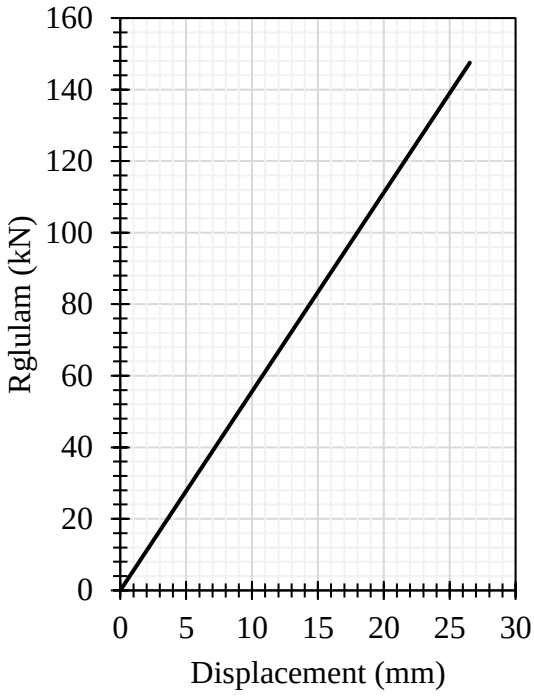
Assembly Failure Sequence	Number of Tests	$D_{SDOF} / D_{EXP.}$	
		Average	CoV
No Failure (Elastic)	3	0.82	0.07
W_F	7	0.93	0.11
$C_Y \rightarrow W_F$	27	0.59	0.20
$C_Y \rightarrow C_F$ and C_F	5	2.19	0.56

6.4.2 Sensitivity Analyses for SDOF and TDOF Modelling

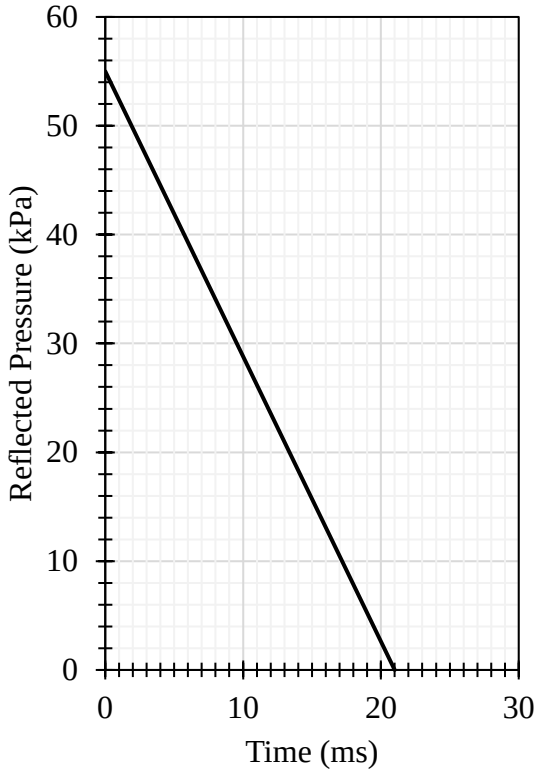
The results outlined in the previous section show that the use of SDOF modelling generally cannot be utilized when dealing with flexible end connections. However, the findings also show that SDOF modelling may be adequate in certain modelling situations. This raises the question about the suitability of using advanced modelling methodologies, such as TDOF modelling, versus simplified SDOF models without introducing any major errors into the calculations. To address this question, sensitivity analyses were conducted in order to establish cases where the use of TDOF modelling would not be required, and where SDOF modelling may be justified. Two parameters, namely the ratio of the connection stiffness and maximum resistance to those of the wood member, were evaluated. For all analyses, a bilinear resistance curve, with a ductility limit of 2.0, was used to represent the behaviour of the connections. The reference resistance curves of the CLT and glulam members are shown in Figure 6.20a and Figure 6.20b, respectively. These are based on the proposed models from studies on CLT panels (Poulin, et al., 2017) and glulam members (Lacroix and Doudak, 2018b) subjected to blast loads. Forcing functions described by idealized triangular pressure-time histories were used and are presented in Figure 6.20c and Figure 6.20d for the CLT and glulam cases, respectively. The forcing functions represent a reflected pressure and impulse combination which will allow the CLT and glulam member to reach their respective ultimate failure displacement. The sensitivity analyses are summarized in Table 6.7.



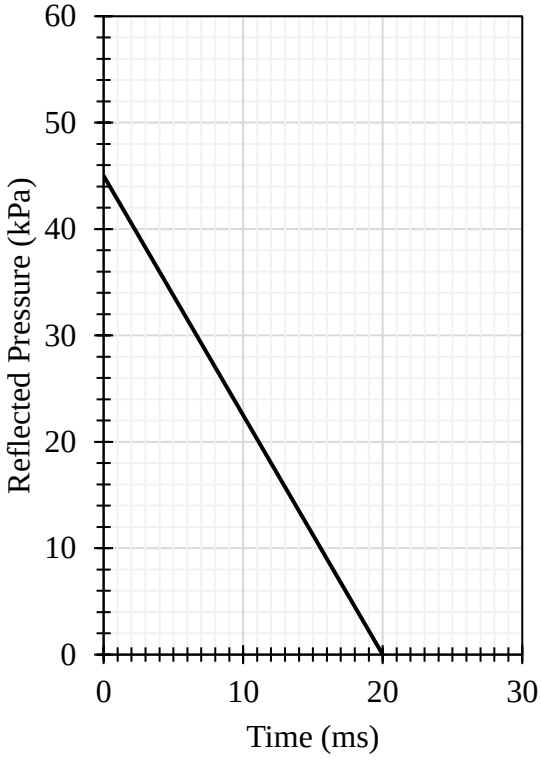
(a) CLT Resistance Curve



(b) Glulam Resistance Curve



(c) Pressure-Time History for CLT Groups



(d) Pressure-Time History for Glulam Groups

Figure 6.20: Inputs for Sensitivity Analyses

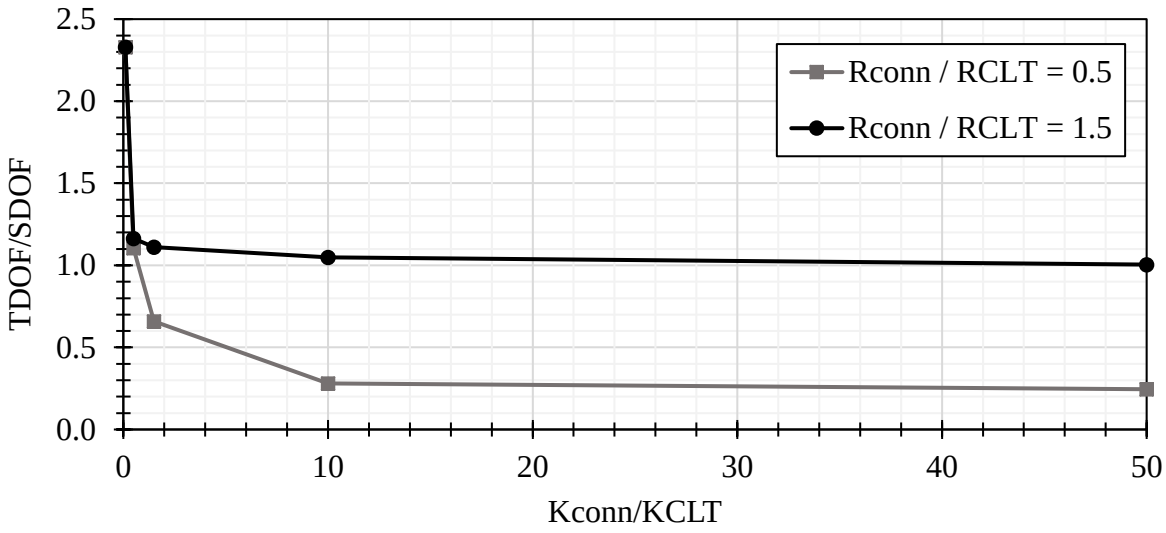
Table 6.7: Sensitivity Analyses

Groups	Variable	Variable Ratios	Constants
CLT-K	K_{conn} / K_{CLT}	0.1, 0.5, 1.5, 10, 50	Case 1: $R_{conn} / R_{CLT} = 0.5$ Case 2: $R_{conn} / R_{CLT} = 1.5$
CLT-R	R_{conn} / R_{CLT}	0.5, 0.8, 1, 1.05, 1.125, 1.25	Case 1: $K_{conn} / K_{CLT} = 0.5$ Case 2: $K_{conn} / K_{CLT} = 1.5$ Case 3: $K_{conn} / K_{CLT} = 10$
LAM-K	K_{conn} / K_{glulam}	0.1, 0.5, 1.5, 10, 50	Case 1: $R_{conn} / R_{glulam} = 0.5$ Case 2: $R_{conn} / R_{glulam} = 1.5$
LAM-R	R_{conn} / R_{glulam}	0.5, 0.8, 1, 1.05, 1.125, 1.25	Case 1: $K_{conn} / K_{glulam} = 0.5$ Case 2: $K_{conn} / K_{glulam} = 1.5$ Case 3: $K_{conn} / K_{glulam} = 10$

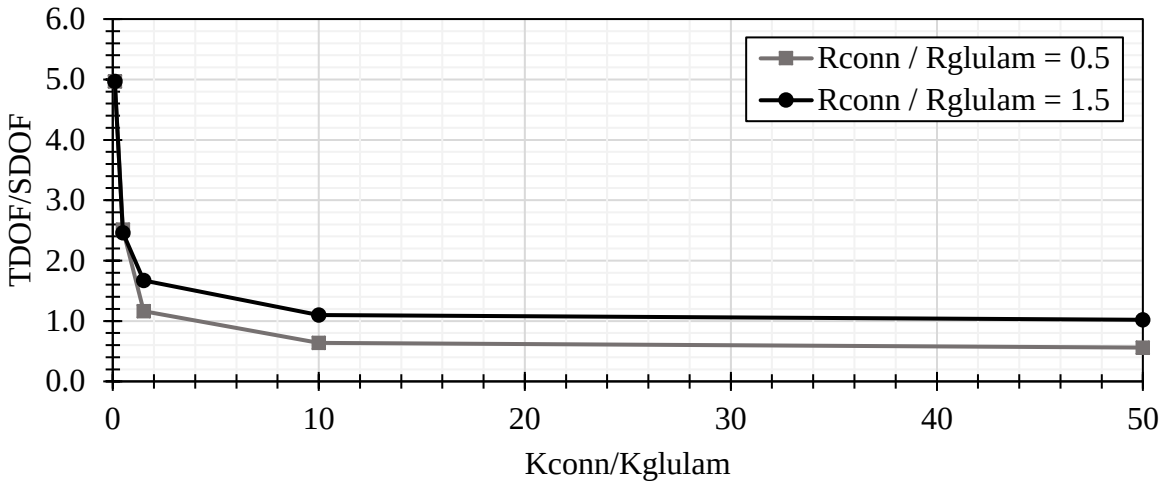
Groups CLT-K and LAM-K consisted of varying the stiffness ratios for two cases of maximum connection resistance, one being smaller and one larger than the maximum resistance of the wood member. This is meant to represent two different design philosophies, where the connection is overdesigned to reach the ultimate capacity of the structural member, or where the connection is intentionally under-designed in order to dissipate energy in the ductile connections rather than the brittle wood member. Figure 6.21a and Figure 6.21b show that for the case where the connection is stronger than the wood member, SDOF analysis can accurately predict the response only if the stiffness of the connection is at least ten times that of the wood member. Using SDOF analysis to analyze a case containing connections with lower stiffness is expected to lead to significant error in results, and in those cases, the use of TDOF may be required. For the case of overdesigned wood members, the results clearly show that using SDOF analysis can no longer adequately predict the correct displacement or failure mode, regardless of the stiffness ratio.

Groups CLT-R and LAM-R consisted of varying the maximum resistance ratio for three values of connection stiffness. As shown in Figure 6.21c and Figure 6.21d, a plateau seems to form when the ratio of connection to wood member resistance becomes greater than one. This can be explained by the fact that beyond a ratio of one, the behaviour of the wood member will tend to govern the overall displacement, and additional connection resistance will no longer play a role. It is also

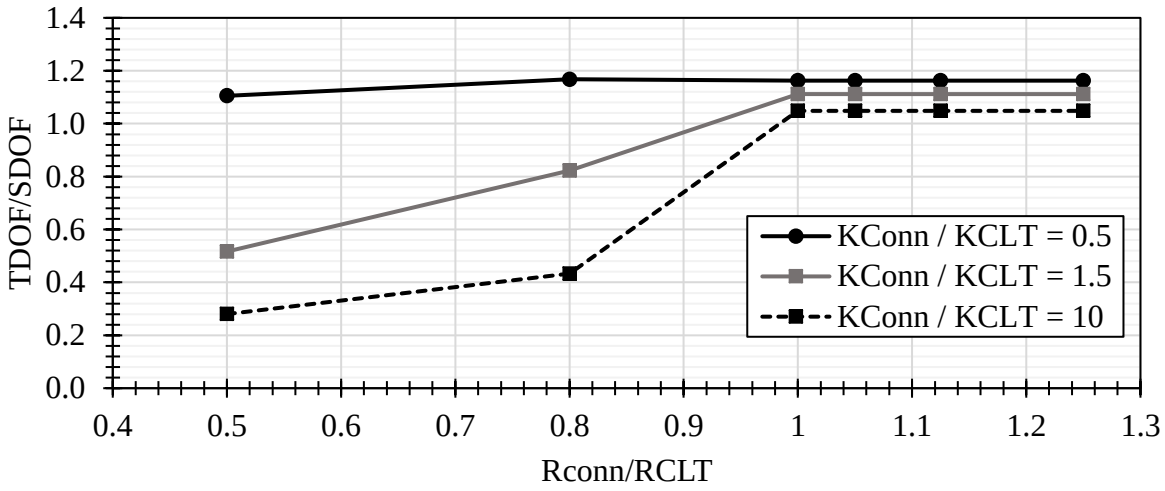
observed that the more flexible the connections are, the higher the TDOF/SDOF ratio is for the plateau values. Once the resistance of the connection becomes less than that of the wood member, the SDOF predictions will diverge from the actual displacement and failure mode. It is interesting to note that when CLT is used, the use of SDOF analysis seems adequate for all stiffness ratios as long as the connection capacity is greater than the panel capacity. A better fit is obtained when the stiffness of the connection is relatively higher than the panel stiffness, however, in general all cases produce a reasonable agreement between the two analysis methods. The results for glulam are significantly different, where only the case with very high relative connection stiffness ratio (i.e. ≥ 10) yields adequate use of the SDOF modelling methodology. As expected, the scenario where the connection stiffness is ten times that of the wood member and with a resistance that is half that of the CLT panel yields the least accurate prediction when using SDOF modelling. This is attributed to the fact that the connection will fail at a significantly lower displacement than that of a more flexible connection, and the wood member will play a significantly lesser role in the response of the system as a whole.



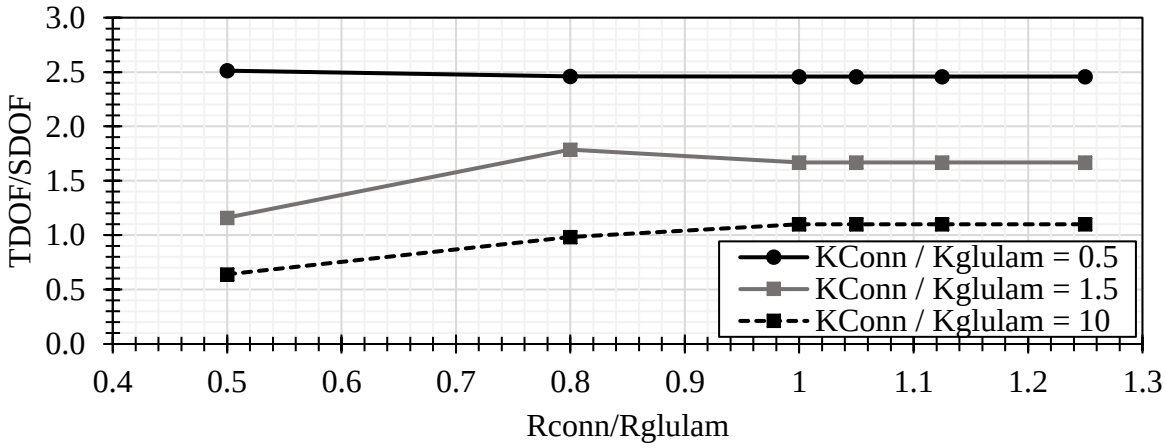
(a) CLT-K



(b) LAM-K



(c) CLT-R



(d) LAM-R

Figure 6.21: Results of Sensitivity Analyses for Predictions of Maximum Mid-Span Deflection

6.4.3 SDOF Analysis using Composite Resistance Curves

The use of SDOF analysis for the purpose of modelling assemblies with flexible connections may lead to erroneous results, since the contribution of the connections to the overall response of the assembly is omitted. TDOF has shown to overcome this limitation by adding a secondary degree-of-freedom to represent the connection behaviour. That being said, SDOF analysis can likely produce reasonable results if one is capable of implementing the effects of the connections into the overall behaviour of the assembly. This section investigates a third modelling approach which merges the characteristics of both the SDOF analysis and TDOF analysis methods. As the structural member and connections are in essence acting as two springs in series (see Chapter 5), one may combine them into an equivalent system. This is accomplished through the use of a composite resistance curve. While this process is easily accomplished when the behaviour of the member and connections are relatively simple (e.g. linear-elastic, elastic-perfectly-plastic, etc.), one may run into issues when sudden load drops or softening behaviours are present in the load-displacement relationships of either component, such as that for CLT panels and unrestrained ML24Z angles, respectively.

Upon completion of an analysis, the aforementioned two-degree-of-freedom blast analysis software *BlasTDOF* outputs the system resistance curve, equivalent to the composite resistance curve one would need to perform SDOF analysis, taking into account the effects of the connections. This method of generating the composite resistance curve allows for any type of member and connection load-displacement relationships to be considered. An example of a generated composite resistance curve is shown in Figure 6.22 for a CLT panel with EACs, where the composite resistance curve can be observed to include characteristics of both the CLT panel and connections, such as the CLT load plateaus and EAC densification.

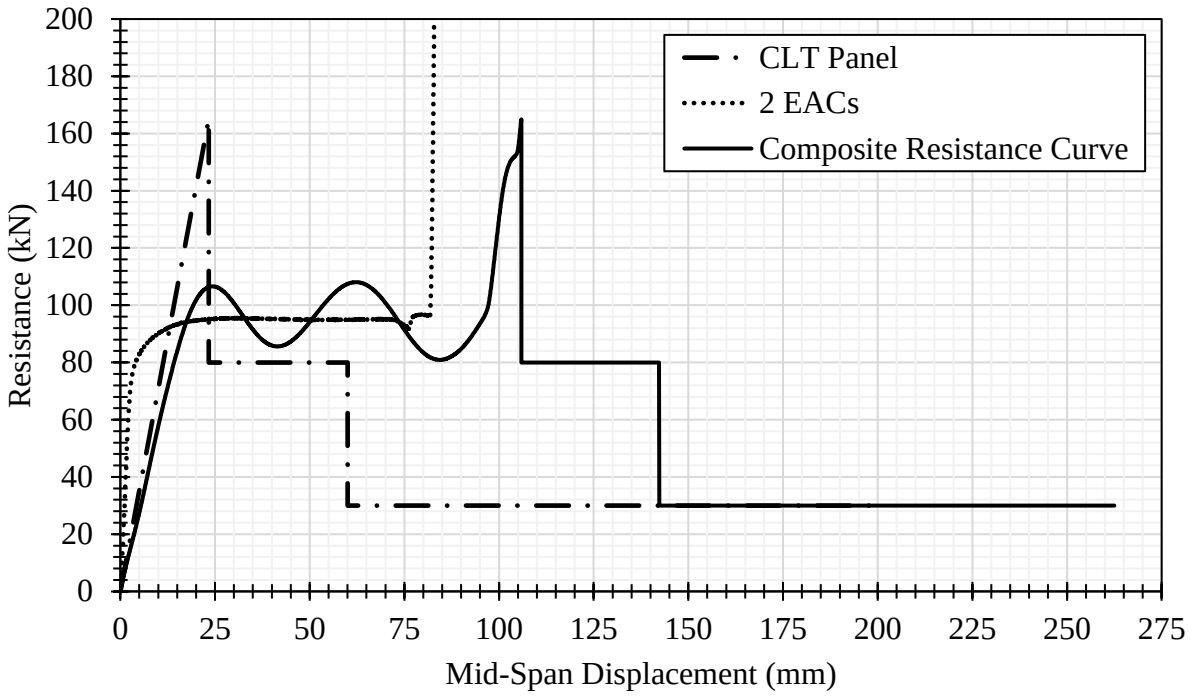


Figure 6.22: Generation of the Composite Resistance Curve for CLT14-3 using *BlasTDOF*

To verify the applicability of using composite resistance curves to predict the displacement of structural assemblies with connections, the previously described SDOF analyses were reanalyzed using composite resistance curves instead of the resistance curves obtained from the wood members alone. From the results, it was determined that the SDOF model with composite resistance curves seems to accurately predict the mid-span displacement and time to attain such displacement with average ratios of 1.02 (CoV of 0.07) and 0.97 (CoV of 0.12), respectively, which are nearly identical to those obtained when performing TDOF analyses using *BlasTDOF*. In general, it can be concluded that the use of SDOF analysis using properly generated composite resistance curves to represent the assembly can accurately predict the behaviour of various timber assemblies, with accuracies similar to those found if performing TDOF analysis (Figure 6.23). As observed in Figure 6.23, while the data point spread is slightly larger than those obtained from TDOF analysis (Figure 5.9), the overall accuracy is similar, and spread is limited to within $\pm$15 % error. However, accurate generation of a composite resistance curve requires that the analyst has a good understanding of the governing failure sequence and failure mode of the assembly. Additionally, analytical tools and solutions may be required, such as those provided by *BlasTDOF*, which generates a composite resistance curve indirectly by first performing a TDOF analysis.

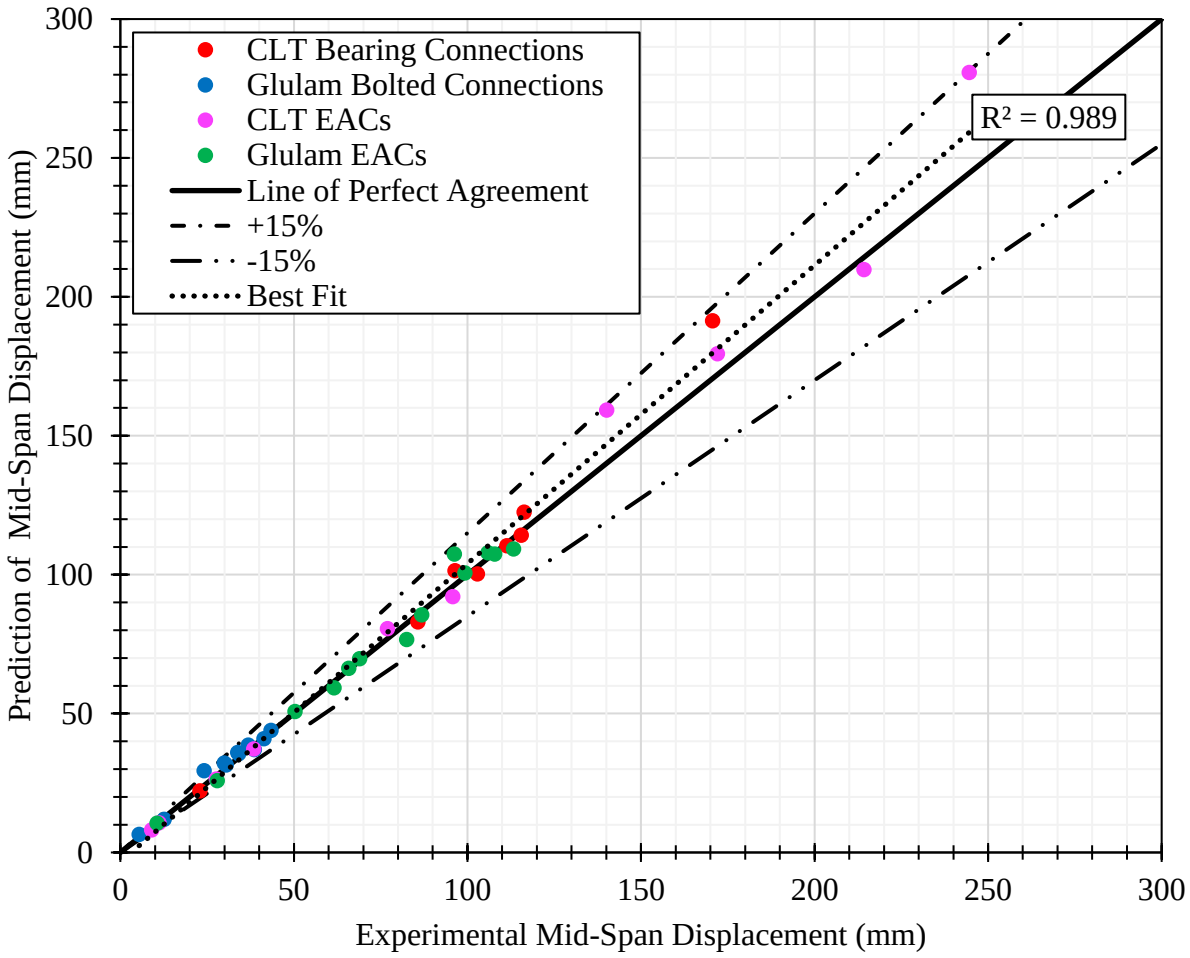


Figure 6.23: Experimental Displacements Versus SDOF Predictions using Composite Resistance Curves

Chapter 7 - Blast Design Considerations

7.1 Overview

The current Canadian blast design provisions (CSA, 2012) for bolted connections in timber assemblies can be summarized as limiting the connection failure mode to that of ductile failure, and overdesigning the connection relative to the capacity of the load-bearing member. This is typically done by designing the connections for forces corresponding to 1.2 times the capacity of the load-bearing timber member and ensuring that none of the brittle failure modes govern the connection design.

The average dynamic bending moment capacity of the timber element can be determined experimentally, or by using published design values from manufacturers and relevant design provisions (e.g. CEN, 2004b; CSA, 2012; AWC, 2015; CSA, 2019). The specified static bending moment capacity can, for example, be calculated following the CSA O86 (2019) code provisions, as shown in Equation 7.1:

$$M_r = \phi_b f_b (K_D K_H K_{Sb} K_D) S K_X \times \min(K_{Zbg}, K_L) \qquad \text{Equation 7.1}$$

where ϕ_b is the resistance factor for bending and f_b is the specified strength in bending. $K_D K_H K_{Sb} K_T$ are the load duration, load sharing, serviceability, and treatment factors, respectively. S is the section modulus of the glulam beam, K_X is the curvature factor, K_{Zbg} is the size factor in bending for glulam, and K_L is the lateral stability factor. These parameters are summarized in Table 7.1 for the glulam beams used in the current study.

Table 7.1: Summary of Design Parameters for Glulam Beams

Notation	Parameter Value	Comment
ϕ_b	1.0	Rare event
f_b	30.7 MPa	Nordic Structures (2015)
K_D	1.25	Foschi, et al. (1989)
$K_H K_{Sb} K_T$	1.0	Single beam element, dry and untreated
S	$1.63*10^6$ mm^3	137 mm x 267 mm rectangular section
K_X	1.0	Straight beam
K_{Zbg}	1.24	Clause 7.5.6.5.1 of CSA O86 (2019)
K_L	1.0	Clause 7.5.6.4 of CSA O86 (2019)

Although the CSA S850 design standard specifies that a load duration factor of 1.0 applies when used concurrently with a DIF, this approach is meant to be conservative for the design of the load-bearing member itself. However, this is non-conservative when the intent is to overdesign the connections. The load duration factors found in the current CSA O86 are based on work by Foschi, et al. (1989) which investigated the effect of long-term and transient loads on wood members. By normalizing the load duration factors based on the standard load duration, the short-term load duration factor is taken as 1.25.

Using the parameters defined in Table 7.1 to evaluate Equation 7.1, a specified static bending moment capacity of 62.5 kN-m is obtained. The average dynamic bending moment capacity is determined by modifying the specified static bending moment capacity using a SIF and a DIF, as shown in Equation 7.2 (CSA, 2012).

$$M_{r-D} = M_r \times SIF \times DIF \qquad \text{Equation 7.2}$$

A SIF of 1.2 is applicable to glulam and engineered wood products according to the Canadian blast design standard (CSA, 2012). While a DIF of 1.4 is provided in the design standard, a value of 1.1 is deemed more appropriate for glulam, based on the findings of the current study and those found in the literature (Lacroix and Doudak, 2018b). This yields an average dynamic bending moment capacity of 82.5 kN-m, which coincides with an end reaction at peak load of 110.5 kN. It can be seen that this value is nearly identical to that obtained experimentally in the current study (i.e. 110 kN).

7.2 Design of Bolted Connections Based on CSA S850 Code Provisions

Brittle failure modes, such as brittle bolt fracturing and wood perpendicular-to-grain splitting, must be avoided when detailing timber connections for blast. Based on the findings from the current study, preventing splitting failure can be accomplished by minimizing the unloaded edge distance or reinforcing the bolted connections with STS. When designing timber assemblies with connections susceptible to splitting, CSA O86 (2019) provides an expression for the splitting capacity of bolted timber connections, as shown in Equation 2.1.

Similar to the design requirements for beams, the blast design standard requires that the specified splitting capacity be modified using SIF and DIF for wood splitting to obtain the dynamic average splitting capacity (Equation 7.3).

$$QS_{rT-D} = QS_{rT} \times SIF_{splitting} \times DIF_{splitting} \quad \text{Equation 7.3}$$

Provisions in the CSA S850 for wood connections stipulate that a SIF and DIF of unity must be used, unless other values can be justified by testing, for example (CSA, 2012). A strength increase factor for splitting of 1.2 was selected based on experimental test data found in the literature (Quenneville and Mohammad, 2001). A recent study investigating the behaviour of bolts subjected to blast loading found no significant increase in the dynamic capacity for slender bolts loaded perpendicular-to-grain (McGrath, 2020), and thus a DIF of unity is chosen.

Figure 7.1 compares the experimentally obtained capacities of the specimens that failed in splitting, with those calculated using Equation 2.1 and Equation 7.3. The results show that while the prediction of the average dynamic splitting capacity is obtained with reasonable accuracy (± 25 %), this variability can, in some cases, lead to non-conservative designs. This is in part due to the fact that the value of 1.2 used to protect load-bearing member failure is not based on rigorous investigation into the variability of different timber products.

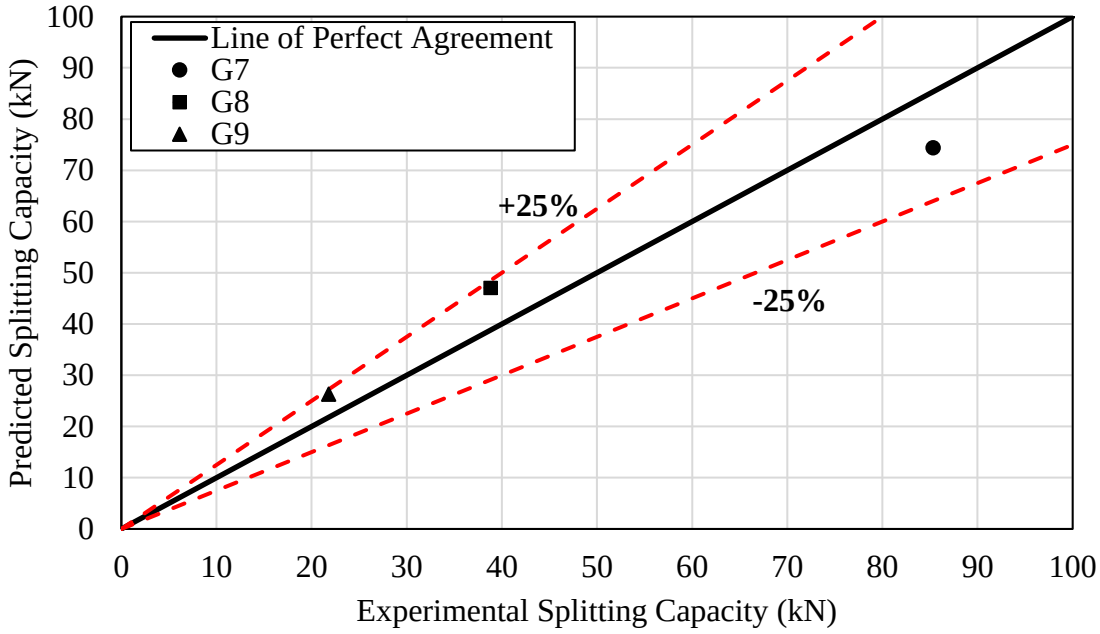


Figure 7.1: Predictions of Splitting Capacities

In the current study, the CSA O86 specified minimum edge distance, e_p, of 1.5 times the fastener diameter (i.e. 19.1 mm) was used, yielding a splitting capacity of 169 kN per connection. Comparing this value to the reaction-at-peak corresponding to beam failure (110 kN), it is expected

that the beam would reach its flexural capacity prior to any splitting. The minimum edge distance in this case provides approximately 50% of an overcapacity in the splitting failure and as such ensures that no such failure can occur even with the variability observed in Figure 7.1.

The average embedment strength and average bolt yield stress obtained from static component-level testing were used to determine the connection yield load using the European Yield Model (EYM) (CSA, 2019), resulting in a value of 24 kN for a single steel-wood-steel bolted connection. Consequently, for a 2x3 bolt group, a value of 144 kN is obtained. This represents the case where the bearing failure load is overdesigned by factors of approximately 1.3 times the beam capacity. Specimen G14 was constructed with such a connection and failed, as expected, in beam flexure (Figure 7.2a). Post-test examination of the bolted connections revealed no signs of permanent damage in the connections (Figure 7.2b).



(a) Overview of Specimen G14



(b) Lack of Damage in Bottom Connection After Testing

Figure 7.2: Behaviour of Glulam Assembly Designed According to CSA S850 (2012)

It can therefore be concluded that following CSA O86 and CSA S850 design provisions is expected to lead to a behaviour where the connections are protected and the beam attains its full flexural

capacity, albeit in a brittle manner. In the next section, an alternative design approach is proposed aiming at optimizing the energy dissipation in the connections, while maintaining the overall intent of the design standard concerning the ultimate failure being in the load-bearing member.

7.3 Proposed Approach for the Design of Optimized Bolted Connections

The previous section demonstrated that although following the current blast design standard may lead to satisfactory performance, the lack of ductility in the timber member limits the ability of the assembly to dissipate energy inelastically because the connections are not allowed to yield. The yielding in the connections can be relied upon to dissipate energy, while maintaining a high ultimate capacity in the connections, such that the ultimate failure still occurs in the load-bearing timber member. It is important to maintain limitation on the brittle failure modes, such as splitting failure in the connection.

It is proposed that an overstrength factor be imposed on the splitting failure alone. The magnitude of such factor is subject to further research, however, it appears that using a factor of 1.2, as proposed by the Canadian blast design standard may not be adequate, based on the limited results from the current study. A more conservative approach may be required to limit brittle failure mode in the connection and a factor of 1.5 is conservatively proposed based on the preliminary data analyses. The requirements can be expressed as proposed in Equation 7.4:

$$QS_{rT-D} \geq 1.5 \times Rxn_{peak} \qquad \text{Equation 7.4}$$

where Rxn_{peak} represents the ultimate capacity of the wood member element in terms of reaction.

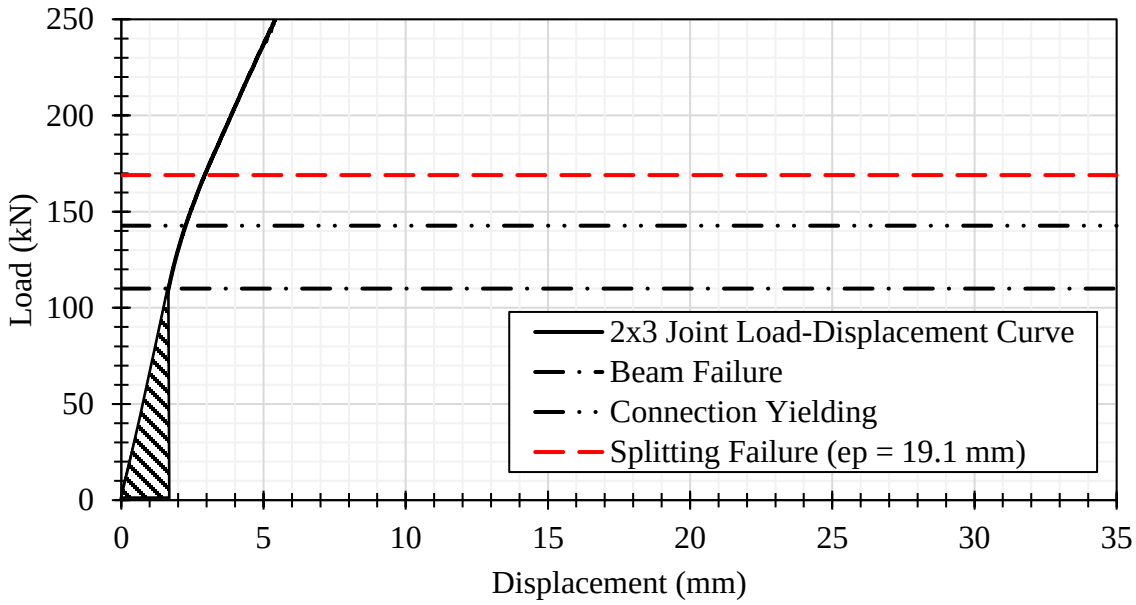
While limiting the splitting failure is desired, preventing yielding in the connection hinders the assembly's ability to dissipate energy. Allowing yielding in the connections can be ensured by considering the inequality in Equation 7.5:

$$N_r \leq \gamma \times Rxn_{peak} \qquad \text{Equation 7.5}$$

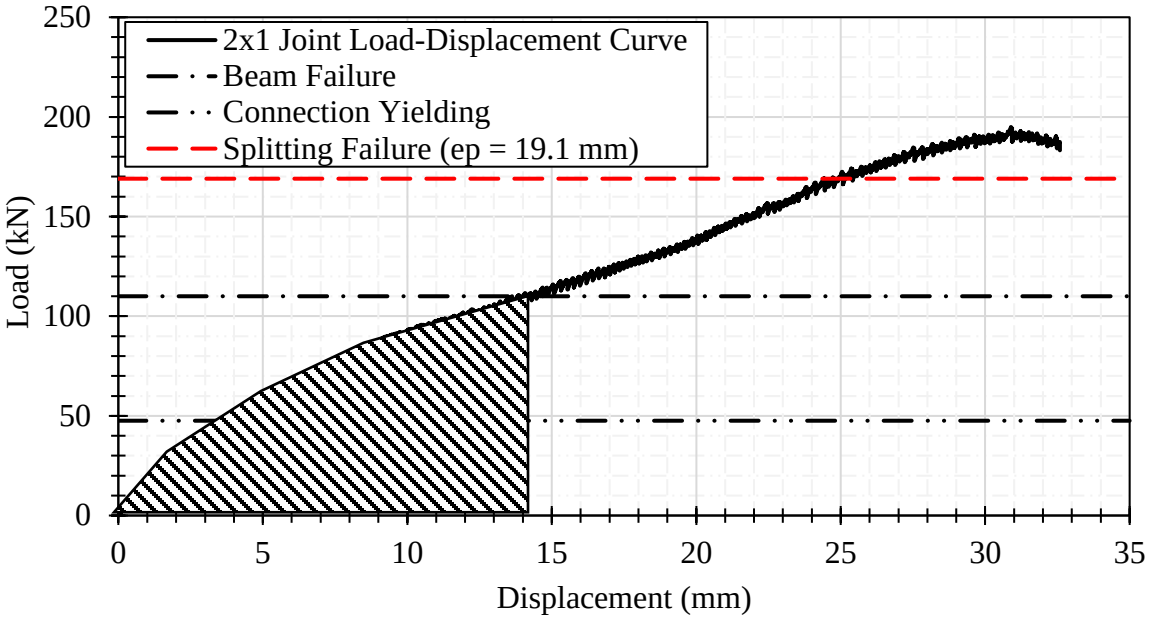
where N_r is the connection yield capacity, and γ is the yield factor. When γ is less than unity, energy dissipation can occur in the connection. Values greater than unity would be associated with little-to-no yielding in the connection.

A slight increase in the energy-absorbing capability of the assembly is observed in the overdesigned connection, with 2x3 bolt group (see Figure 7.3a), where the value of γ is equal to

1.3. The horizontal lines in Figure 7.3 represent different possible events in the failure sequence. Additional energy dissipation can be achieved by reducing the number of bolts. As shown in Figure 7.3b, the amount of energy dissipation occurring within the assembly for the 2x1 bolt group is significantly greater than that observed in 2x3 bolt group. The figure shows that the bolts undergo approximately 14 mm of deformation prior to flexural failure of the glulam beam, which is approximately seven times greater than the deformation occurring in the 2x3 connections. The 2x1 bolt group configuration corresponds to a γ-factor of 0.44, and represents an optimized condition for this specific assembly. In this example, the splitting capacity is approximately 1.5 times the beam ultimate capacity and as such Equation 7.4 is satisfied. By overdesigning the splitting and bolt fracture capacities, the ultimate failure of the assembly remains that of flexural failure in the timber beam element.



(a) 2x3 Bolted Connection



(b) 2x1 Bolted Connection

Figure 7.3: Load-Displacement Curves of Tested Bolted Connections

The discussion herein proposes an important philosophical shift from the current blast design provisions, where the connections are overdesigned to protect against brittle failure only, and some inelastic energy dissipation is allowed through connection yielding. It is paramount to emphasize that the current proposed design approach maintains the important requirement that the ultimate failure still needs to occur in the load-bearing element. As demonstrated in this study, such an approach will enhance the energy dissipative capabilities of timber structures, where little-to-no energy dissipation occurs in the material itself. It should be noted in this context that proper understanding of the failure sequence, as well as the behaviour and variability of the load-bearing element and the connections, is imperative.

Chapter 8 - Conclusions and Recommendations

8.1 General

The current study deals with the behaviour of heavy-timber assemblies with boundary connections subjected to simulated blast loads. The main objective was to establish the effect of typical and innovative connections on the response of timber assemblies, with focus on the assembly failure sequence and energy dissipation capabilities. This chapter summarizes the main findings and conclusions of the current study and proposes possible future research work.

8.2 Conclusions

From the current research study, the following conclusions can be drawn:

- A significant increase in dynamic peak load by a factor of 1.55 was observed for flexible angle type bearing connection (ML24Z), where the dominating failure mode was in wood crushing and yielding of the steel angle bracket. Connections designed with a thick angle bracket failed in the screw fasteners and no increase in the peak load was observed. For both connection types, no increase was observed on the stiffness. Full-scale dynamic testing of simply supported CLT and glulam specimens at an average strain-rate of 0.3 s^{-1} yielded average dynamic increase factors (DIF) of 1.31 and 1.10, respectively, on the peak resistance when compared to the static full-scale test data reported in the literature.

- Full-scale glulam specimens with bolted connections having a slenderness ratio of 10.8, designed to yield via wood crushing and bolt bending, performed better than overdesigned bolted connections, in which little-to-no permanent damage occurred. Bolted connections which failed in splitting led to premature failure of the glulam assembly. Proper detailing of the bolt group geometry, particularly the unloaded edge distance, was found to be necessary in order to achieve the proper failure sequence. Reinforcement with self-tapping screws allowed the bolted joints to fail in a combination of bolt yielding and wood crushing, and provided more ductility when compared to the unreinforced specimens.

- Energy-absorbing connections (EACs) significantly increased the energy-absorbing capabilities of glulam and CLT assemblies. The basis of these connections was to allow for connection yielding while delaying failure of the glulam beam or CLT panel. This was

achieved via elastoplastic connection behaviour, which effectively limited the load on the wood member.

- Limitations in the current Canadian blast provisions (CSA, 2012) were highlighted and discussed. The optimization of the assemblies to dissipate energy was achieved by detailing the connections such that the maximum amount of inelastic energy dissipation occurs in the connection prior to failure of the load-bearing wood member.

- A two-degree-of-freedom (TDOF) blast analysis software was developed and validated using full-scale and connection-level experimental results. It was found to adequately capture the system response with reasonable accuracy. Sensitivity analyses regarding the applicability of using single-degree-of-freedom (SDOF) analysis were presented and discussed.

8.3 Recommendations for Future Research Work

Based on the work done in the current study, the following areas and topics have been identified for future research work:

- Since typical heavy-timber members are load-bearing, the effect of axial load is expected play a significant role in how various timber assemblies behave when subjected to a blast load. This was observed for certain connection types when the effect of axial restraint was investigated in the current study. It is therefore recommended that future studies perform similar full-scale tests on assemblies with boundary connections with and without the effect of axial loading. Similar approach has been done before on glulam members with simply supported boundary conditions (Lacroix and Doudak, 2018a) but not those with boundary connections.

- The timber members used as part of the current study consisted of 137 mm by 267 mm glulam beams and 445 mm by 175 mm CLT panels. Additional dynamic testing of members with different span-to-depth ratio, layups, and cross-section sizes would aid in further validating or improving the DIF values, failure mode observations, failure sequences, and modelling techniques presented in the current study. This may entail the testing of realistic model assemblies (i.e. complete assemblies) in order to achieve real-life conditions.

- In the current study, splitting failure mode was investigated in a cursory manner. The failure was induced in the assembly and methods to restore the full joint capacity was suggested by means of reinforcement using self-tapping screws. However, still lacking in the current knowledge is establishing a DIF specifically for wood splitting capacity, investigating whether differences between static and dynamic failure modes exist, and validating the splitting capacity equation found in the Canadian wood design standard (or other models). More work on reinforcing techniques, specifically suitable for blast design, could also be explored and new methodologies proposed.

- It is recommended that a study be undertaken to further investigate the effect of typical bolted connections on the behaviour of timber assemblies. The groups of connections in the current study were limited to a few fasteners and as such rotational restraint in the bolted connections was found to be negligible. A study of the full-scale behaviour of glulam beams with bolted connections with larger groups of bolts could investigate the contribution and significance of rotational restraints on the assembly behaviour. Another aspect that could be investigated is the generation of complete load-displacement relationships for bolted connections with various failure modes to establish important design parameters such as stiffness and ductility.

- The energy-absorbing connections investigated in the current study showed promising results and allowed the optimization of the inelastic energy dissipation in assemblies subjected to blast loads. Investigation of other types of energy-absorbing connections is recommended. This may include other steel profiles, such as hollow structural sections (HSS), or connections utilizing other energy dissipative mechanisms, such as springs, slip-friction joints, dampers, etc. Potential key parameters to investigate and optimize include the ability of the connections to dissipate a significant amount of energy prior to the failure of the wood member, limiting the overall deformation in the connections, and develop connections that can be easily replaceable in real construction after a loading event.

- A two-degree-of-freedom (TDOF) software was developed and validated using the experimental test data. While such analysis technique was found to be sufficiently sophisticated to outperform SDOF modelling for certain assembly types, further

development and comparisons to test results as well as finite-element-analysis (FEA) software packages could provide additional validation of the accuracy of such analysis.

References

Abladey, L., and Braimah, A. (2014). "Near-Field Explosion Effects on the Behaviour of Reinforced Concrete Columns: A Numerical Investigation." *International Journal of Protective Structures*, 5(4), 475-499.

ANSI/APA (2012). "ANSI/APA PRG 320: Standard for Performance-Rated Cross Laminated Timber." APA – The Engineered Wood Association, Tacoma, WA.

Ansys. (2019). "Ansys Autodyn." (Version 18). Canonsburg, PA, USA.

ASCE (2011). "Blast Protection of Buildings." *ASCE/SEI 59-11*, American Society of Civil Engineers, Reston, VA.

ASTM (2011). "Standard Specification for Testing and Establishing Allowable Loads of Joist Hangers." *ASTM D7147-11*, ASTM International, West Conshohocken, PA.

ASTM (2015). "Standard Test Methods for Single-Bolt Connections in Wood and Wood-Based Products." *ASTM D5652-15*, ASTM International, West Conshohocken, PA.

ASTM (2017a). "Standard Test Method for Determining Bending Yield Moment of Nails." *ASTM F1575-17*, ASTM International, West Conshohocken, PA.

ASTM (2017b). "Standard Test Methods for Density and Specific Gravity (Relative Density) of Wood and Wood-Based Materials." *ASTM D2395-17*, ASTM International, West Conshohocken, PA.

ASTM (2018). "Standard Test Method for Evaluating Dowel-Bearing Strength of Wood and Wood-Based Products." *ASTM D5764-97AR18*, ASTM International, West Conshohocken, PA.

AWC (2015). "National Design Specification for Wood Construction." American Wood Council, Leesburg, VA.

Barrett, J. D., and Lau, W. (1994). "Canadian lumber properties." Canadian Wood Council, Ottawa, ON.

Biggs, J. M. (1964). *Introduction to Structural Dynamics*, McGraw-Hill, New York, NY.

Blaß, H. J., and Schädle, P. (2011). "Ductility aspects of reinforced and non-reinforced timber joints." *Engineering Structures*, 33(11), 3018-3026.

Bogosian, D., and Avanessian, H. D. (2004). "Blunt trauma from blast-induced building debris." DTIC Document.

Bornstein, H., and Ackland, K. (2013). "Evaluation of energy absorbing materials under blast loading." *Materials Characterisation VI*, 77, 125-136.

Braimah, A. (2013). *Blast Load Effects on Structures*, Ottawa, ON.

Breyer, D., Cobeen, K., Fridley, K., and Pollock, D. (2015). *Design of Wood Structures-ASD/LRFD*, McGraw-Hill USA.

Brühl, F., Kuhlmann, U., and Jorissen, A. (2011). "Consideration of plasticity within the design of timber structures due to connection ductility." *Engineering Structures*, 33(11), 3007-3017.

CEN (2004a). "Eurocode 8: Design of structures for earthquake resistance – Part 1: General rules, seismic actions and rules for buildings." *EN 1998-1:2004*, Comité Européen de Normalisation, Brussels.

CEN (2004b). "Eurocode 5: Design of timber structures." *ENV 1995-1-1*, Comité Européen de Normalisation, Brussels.

Closen, M. (2014). "White Paper: Full Thread SWG ASSY Screws as Reinforcement." MyTiCon Timber Connectors, Surrey, BC.

Clough, R. W., and Penzien, J. (1991). *Dynamics of structures*, McGraw-Hill, New York.

Côté, D., and Doudak, G. (2019). "Experimental investigation of cross-laminated timber panels with realistic boundary conditions subjected to simulated blast loads." *Engineering Structures*, 187, 444-456.

Crawford, J. E. (2013). "State of the art for enhancing the blast resistance of reinforced concrete columns with fiber-reinforced plastic." *Canadian Journal of Civil Engineering*, 40(11), 1023-1033.

Crawford, J. E., Morrill, K. B., Sunshine, D. A., and Magallanes, J. M. (2012). "Date and Modeling for the Performance of Pristine and Blast Damaged Connections." *Structures Congress 2012*, ASCE, Chicago, Illinois.

CSA (2012). "Design and assessment of buildings subjected to blast loads." *CSA S850*, CSA Group, Mississauga, ON.

CSA (2013). "General Requirements for Rolled or Welded Structural Quality Steel/Structural Quality Steel." *CAN/CSA G40.20-13/G40.21-13*, Canadian Standards Association, Toronto, Ontario, Canada.

CSA (2019). "Engineering design in wood." *CSA O86*, CSA Group, Mississauga, ON.

Daneff, G. (1997). "Response of Bolted Connections to Pseudodynamic (Cyclic) Loading." MSc Thesis, University of New Brunswick, New Brunswick.

Dassault Systèmes Simulia Corp. (2014). "Abaqus Unified FEA." (Version 6.14-2). Providence, RI, USA.

Davis, T. L. (1972). *The Chemistry of Powder and Explosives*, Angriff Press.

Department of the Air Force (2006). "Force Protection Battlelab Vehicle Bomb Mitigation Guide." *Air Force Handbook 10-2401*,Lackland AFB, TX.

Dietsch, P., and Brandner, R. (2015). "Self-tapping screws and threaded rods as reinforcement for structural timber elements – A state-of-the-art report." *Construction and Building Materials*, 97, 78-89.

Dusenberry, D. O. (2010). *Handbook for Blast-Resistant Design of Buildings*, John Wiley & Sons Inc., Hoboken, NJ.

Ehlbeck, J., Görlacher, R., and Werner, H. (1989). "Determination of perpendicular-to-grain tensile stresses in joints with dowel-type fasteners: a draft proposal for design rules." *Paper 22-7-2*CIB-W18A Meeting.

El-Dakhakhni, W. W., Changiz Rezaei, S. H., Mekky, W. F., and Razaqpur, A. G. (2009). "Response sensitivity of blast-loaded reinforced concrete structures to the number of degrees of freedom." *Canadian Journal of Civil Engineering*, 36(8), 1305-1320.

El-Hashimy, T., Campidelli, M., Tait, M., and El-Dakhakhni, W. (2017). "Modeling of Reinforced Masonry Walls with Boundary Elements Under Blast Loading." *13th Canadian Masonry Symposium*, Canada Masonry Design Centre, Halifax, NS.

ETA (2016). "HECO-TOPIX screws for use in timber constructions." *ETA-11/0284*, European Technical Assessment, Germany.

Foschi, R. O. (1973). "Stress analysis and design of glulam rivet connections for perpendicular-to-grain loading of wood." *Information Report VP-X-117*, Department of the Environment, Canadian Forestry Service.

Foschi, R. O., Folz, B., and Yao, F. (1989). "Realibility-Based Design of Wood Structures." *Structural Research Series, Report No. 34*, University of British Columbia, Vancouver, BC.

FPInnovations (2011). "CLT handbook : cross-laminated timber." S. Gagnon, and C. Pirvu, eds., FPInnovations, Quebec, QC, 594.

Friedlander, F. G. (1946). "The diffraction of sound pulses I. Diffraction by a semi-infinite plane." *Proceedings of the Royal Society of London. Series A. Mathematical and Physical Sciences*, 186(1006), 322-344.

Gagnet, E. M., Hoemann, J. M., and Davidson, J. S. (2017). "Blast resistance of membrane retrofit unreinforced masonry walls with flexible connections." *International Journal of Protective Structures*, 8(4), 539-559.

Gerber, A., and Tannert, T. (2015). "Timber-Concrete Composites Using Flat-Plate Engineered Wood Products." *Structures Congress 2015*, 2314-2325.

Gilbertson, C. G., and Bulleit, W. M. (2013). "Load Duration Effects in Wood at High Strain Rates." *Journal of Materials in Civil Engineering*, 25(11), 1647-1654.

Girhammar, U. A., and Andersson, H. (1988). "Effect of Loading Rate on Nailed Timber Joint Capacity." *Journal of Structural Engineering*, 114(11), 2439-2456.

Guner, S. (2016). "Simplified Modeling of Frame Elements Subjected to Blast Loads." *ACI Structural Journal*, 113(2), 363-372.

Hadianfard, M. A., and Shekari, M. (2018). "An Equivalent Single-Degree-of-Freedom System to Estimate Nonlinear Response of Semi-fixed Flexural Members Under Impact Load." *Iranian Journal of Science and Technology, Transactions of Civil Engineering*.

Heine, C. P. (2001). "Simulated Response of Degrading Hysteretic Joints With Slack Behavior." PhD Dissertation, Virginia Polytechnic Institute and State University, Blacksburg, Virginia.

Jacques, E. (2014). "RCBlast." (Version 0.5.1). Ottawa, ON. Retrieved from http://www.rcblast.ca

Jacques, E., Lloyd, A., Braimah, A., Saatcioglu, M., Doudak, G., and Abdelalim, O. (2014). "Influence of high strain-rates on the dynamic flexural material properties of spruce–pine–fir wood studs." *Canadian Journal of Civil Engineering*, 41(1), 56-64.

Jacques, E., Lloyd, A., and Saatcioglu, M. (2012). "Predicting reinforced concrete response to blast loads." *Canadian Journal of Civil Engineering*, 40(5), 427-444.

Jacques, E., and Saatcioglu, M. (2018). "Computer Software for the Design of Blast Resistant Window Retention Anchors." *CSCE 2018 Annual Conference*, Canadian Society for Civil Engineering, Fredericton, NB.

Jama, H. H., Bambach, M. R., Nurick, G. N., Grzebieta, R. H., and Zhao, X. L. (2009). "Numerical modelling of square tubular steel beams subjected to transverse blast loads." *Thin-Walled Structures*, 47(12), 1523-1534.

Jansson, B. (1992). "Impact loading of timber beams." MSc Thesis, University of British Columbia, Vancouver, BC.

Johansen, K. (1949). "Theory of timber connections." *Int Assoc Bridge Struct Eng*, 9, 249-262.

Jorissen, A. (1998). "Double shear timber connections with dowel type fasteners." PhD Dissertation, Delft University Press Delft, The Netherlands.

Jorissen, A., and Fragiacomo, M. (2011). "General notes on ductility in timber structures." *Engineering Structures*, 33(11), 2987-2997.

Karns, J. E., Houghton, D. L., Hall, B. E., Kim, J., and Lee, K. (2007). "Analytical verification of blast testing of steel frame moment connection assemblies." *Research Frontiers at Structures Congress*, ASCE, 1-19.

Kimbell, R. G., and Fies, J. (1953). "Two Typical Wood Frame Houses Exposed to Energy Released by Nuclear Fission." National Lumber Manufacturers Association, Washington, D.C., 16.

Krauthammer, T. (2008). *Modern Protective Structures*, Taylor & Francis Group, Boca Raton, FL.

Lacroix, D. (2017). "Investigating the Behaviour of Glulam Beams and Columns Subjected to Simulated Blast Loading." PhD Dissertation, University of Ottawa, Ottawa, ON.

Lacroix, D., and Doudak, G. (2019). "Towards Enhancing the Post-Peak Performance of Glued-Laminated Timber Beams Using Multi-Directional Fibre Reinforced Polymers." *Manuscript submitted for publication.*

Lacroix, D. N., and Doudak, G. (2015). "Investigation of Dynamic Increase Factors in Light-Frame Wood Stud Walls Subjected to Out-of-Plane Blast Loading." *Journal of Structural Engineering*, 141(6), 04014159.

Lacroix, D. N., and Doudak, G. (2018a). "Effects of High Strain Rates on the Response of Glulam Beams and Columns." *Journal of Structural Engineering*, 144(5), 04018029.

Lacroix, D. N., and Doudak, G. (2018b). "Determining the Dynamic Increase Factor for Glued-Laminated Timber Beams." *Journal of Structural Engineering*, 144(9), 04018160.

Lacroix, D. N., and Doudak, G. (2018c). "Experimental and Analytical Investigation of FRP Retrofitted Glued-Laminated Beams Subjected to Simulated Blast Loading." *Journal of Structural Engineering*, 144(7), 04018089.

Lacroix, D. N., Doudak, G., and El-Domiaty, K. (2014). "Retrofit Options for Light-Frame Wood Stud Walls Subjected to Blast Loading." *Journal of Structural Engineering*, 140(4), 04013104.

Lam, F., Schulte-Wrede, M., Yao, C. C., and Gu, J. J. (2008). "Moment resistance of bolted timber connections with perpendicular to grain reinforcements." *10th World Conference on Timber Engineering*, Curran Associates, Inc., Miyazaki, Japan.

Lavarnway, D., and Pollino, M. (2015). "Mitigation of Air-Blast Pressure Impulses on Building Envelopes through Blast Resistant Ductile Connectors." *Journal of Engineering and Architecture*, 3(2), 9-24.

Levene, H. (1960). "Robust Tests for Equality of Variances." *Contributions to Probability and Statistics: Essays in Honor of Harold Hotelling*, I. Olkin, S. Ghurye, W. Hoeffding, W. Madow, and H. Mann, eds., Stanford University Press, 278-292.

Liska, J. A. (1950). "Effect of rapid loading on the compressive and flexural strength of wood." U.S. Dept. of Agriculture, Forest Service, Forest Products Laboratory, Madison, WI. Report 1767.

Logan, D. (2011). *A First Course in the Finite Element Method, SI Version*, Cengage Learning.

Lowak, M. J. (2015). "Static and Dynamic Testing of Cross-Laminated Timber Panels." Baker Engineering and Risk Consultants, Inc., San Antonio, TX. Project No. 01-05261-001-15.

Lowak, M. J. (2016). "Additional Static and Dynamic Testing of Cross-Laminated Timber Panels.", Baker Engineering and Risk Consultants, Inc., San Antonio, TX. Project No. 01-05261-002-15.

LSTC. (2015). "LS-DYNA." (Version R8.0). Livermore, CA, USA: Livermore Software Technology Corporation.

Marchand, K. A. (2002). "BAIT, BASS & RODS Testing Results." Applied Research Associates, Prepared for the USAF Force Protection Battlelab.

McGrath, A. (2020). "Investigating the Response of Bolted Wood Connections Subjected to Blast Loads." MASc Thesis, University of Ottawa, Ottawa, ON.

Microsoft Corporation. (2019). "Microsoft Visual Studio." (Version 16.3.3). Redmond, Washington: Microsoft Corporation.

Mischler, A., Prion, H., and Lam, F. (2000). "Load-carrying behaviour of steel-to-timber dowel connections." *World Conference of Timber Engineering 2000*, J. D. Barrett, ed., University of British Columbia, British Columbia, Canada.

Morrill, K. B., Crawford, J. E., Magallanes, J. M., and Choi, H. J. (2007). "Development of Simplified Tools to Predict Blast Response of Steel Beam-Column Connections." *Research Frontiers at Structures Congress*, ASCE, Long Beach, California.

Mpidi Bita, H., Currie, N., and Tannert, T. (2018). "Disproportionate collapse analysis of mid-rise cross-laminated timber buildings." *Structure and Infrastructure Engineering*, 1-14.

Nadeau, J. S., Bennett, R., and Fuller, E. R. (1982). "An explanation for the rate-of-loading and the duration-of-load effects in wood in terms of fracture mechanics." *Journal of Materials Science*, 17(10), 2831-2840.

Nassr, A. A., Razaqpur, A. G., Tait, M. J., Campidelli, M., and Foo, S. (2012). "Single and multi degree of freedom analysis of steel beams under blast loading." *Nuclear Engineering and Design*, 242, 63-77.

Neumann, M., Herter, J., Droste, B. O., and Hartwig, S. (2011). "Compressive behaviour of axially loaded spruce wood under large deformations at different strain rates." *European Journal of Wood and Wood Products*, 69(3), 345-357.

Newmark, N. M. (1959). "A Method of Computation for Structural Dynamics." *Journal of the Engineering Mechanics Division*, 85(EM 3), 67-94.

Nolet, V., Casagrande, D., and Doudak, G. (2019). "Multipanel CLT shearwalls: an analytical methodology to predict the elastic-plastic behaviour." *Engineering Structures*, 179, 640-654.

Nordic Structures (2015). "Nordic Engineered Wood Non-Residential Design Construction Guide." Nordic Structures. Document N-C122.

Office of the Deputy Prime Minister (2004). "The Building Regulations 2000 —Approved Document A: Structure. A3 — Disproportionate Collapse." Her Majesty's Stationery Office, Norwich, UK.

Oswald, C. (2018). "Blast Testing of Energy Absorbing Connectors for Blast Resistant Design." *Structures Under Shock and Impact XV*, S. Syngellakis, and G. Schleyer, eds., WIT Press, Southampton, UK, 57-67.

Oswald, C. J. (2005). "Component Explosive Damage Assessment Workbook (CEDAW) Methodology Manual V1.0.", Prepared for the Protective Design Center, US Army Corps of Engineers, San Antonio, TX. BakerRisk Project No. 02-0752-001.

Park, J. Y., and Krauthammer, T. (2009). "Inelastic two-degree-of-freedom model for roof frame under airblast loading." *Structural Engineering and Mechanics*, 32(2), 321-335.

Parlin, N. J., Davids, W. G., Nagy, E., and Cummins, T. (2014). "Dynamic response of lightweight wood-based flexible wall panels to blast and impulse loading." *Construction and Building Materials*, 50, 237-245.

Paulay, T., and Priestley, M. J. N. (1992). *Seismic Design of Reinforced Concrete and Masonry Buildings*, John Wiley & Sons, Inc.

Paz, M., and Leigh, W. (2006). *Structural Dynamics: Theory and Computation*, Springer US.

PDC (2008). "Methodology manual for the Single-Degree-of-Freedom Blast Effects Design Spreadsheets (SBEDS)." *Technical Report 06-01 Rev 1*, U.S. Army Corps of Engineers, Protective Design Center (PDC), Omaha, NE.

Pirinen, M. (2014). "Ductility of Wood and Wood Members Connected with Mechanical Fasteners." MSc Thesis, Aalto University.

Poulin, M., Viau, C., Lacroix, D. N., and Doudak, G. (2017). "Experimental and Analytical Investigation of Cross-Laminated Timber Panels Subjected to Out-of-Plane Blast Loads." *Journal of Structural Engineering*, 144(2), 04017197.

Quenneville, J. H., and Mohammad, M. (2001). "Design method for bolted connections loaded perpendicular-to-grain." *Canadian Journal of Civil Engineering*, 28(6), 949-959.

Randall, P. A. (1961). "Damage to conventional and special types of residences exposed to nuclear effects." *ORINS [reports]. U.S. Atomic Energy Commission*, Wt-1194, 1-83.

Reshke, R. G., Mohammad, M., and Quenneville, J. H. P. (2000). "Influence of joint configuration parameters on strength of perpendicular-to-grain bolted timber connections." *6th World Timber Engineering Conference*, J. D. Barrett, ed., Univeristy of British Columbia, Whistler, Canada.

Rosowsky, D. V., and Reinhold, T. A. (1999). "Rate-of-Load and Duration-of-Load Effects for Wood Fasteners." *Journal of Structural Engineering*, 125(7), 719-724.

Ross, R. J. (2010). *Wood handbook - Wood as an engineering material*, Forest Products Laboratory, USDA Forest Service, Madison, WI.

Saatci, S., and Vecchio, F. J. (2009). "Nonlinear Finite Element Modeling of Reinforced Concrete Structures under Impact Loads." *ACI Structural Journal*, 106(5), 717-725.

Sanborn, K. P. (2018). "Exploring Cross-Laminated Timber Use for Temporary Military Structures: Ballistic Considerations." PhD Dissertation, Georgia Institute of Technology, Atlanta, Georgia.

Sawata, K. (2015). "Strength of bolted timber joints subjected to lateral force." *Journal of Wood Science*, 61(3), 221-229.

Spencer, R. (1978). "Rate of Loading Effect in Bending for Douglas-Fir Lumber." *First International Conference on Wood Fracture*, Forintek Canada Corp., Western Forest Products Laboratory, Vancouver, BC, 259-265.

Steinfeld, J. I., and Wormhoudt, J. (1998). "Explosives Detections: A Challenge for Physical Chemistry." *Annual Review of Physical Chemistry*, 49(1), 203-232.

Stoddart, E. P., Byfield, M. P., and Tyas, A. (2014). "Blast Modeling of Steel Frames with Simple Connections." *Journal of Structural Engineering*, 140(1), 04013027.

Syron, W., Lopez-Anido, R. A., and Nagy, E. (2010). "High Strain Rate Effects in Composite Wooden Bolted Connections." *WCTE 2010: World Conference on Timber Engineering*, A. Ceccotti, and J.-W. V. d. Kuilen, eds., WCTE, Trento, Italy.

Syron, W. D. (2010). "Strain Rate-Dependent Behavior of Laminated Strand Lumber." MSc Thesis, University of Maine, Orono, ME.

Unified Facilities Criteria Program (2008). "Structures to resist the effects of accidental explosions (UFC 03-340-02).", United States of America Department of Defense, Washington, D.C.

Unified Facilities Criteria Program (2009). "Design of Buildings to Resist Progressive Collapse (UFC 04-023-03).", United States of America Department of Defense, Washington, D.C.

Unified Facilities Criteria Program (2012). "DoD Minimum Antiterrorism Standards for Buildings (UFC 4-010-01).", United States of America Department of Defense, Washington, D.C.

USACE (2015). "TechNote 23 Cross Laminated Timber (CLT)." United States Army Corps of Engineers, Centers of Standardization, Washington, D.C.

Viau, C., and Doudak, G. (2016a). "Investigating the behaviour of typical and designed wall-to-floor connections in light-frame wood stud wall structures subjected to blast loading." *Canadian Journal of Civil Engineering*, 43(6), 562-572.

Viau, C., and Doudak, G. (2016b). "Investigating the Behavior of Light-Frame Wood Stud Walls Subjected to Severe Blast Loading." *Journal of Structural Engineering*, 142(12), 04016138.

Wang, M., Song, X., Gu, X., Zhang, Y., and Luo, L. (2015). "Rotational Behavior of Bolted Beam-to-Column Connections with Locally Cross-Laminated Glulam." *Journal of Structural Engineering*, 141(4), 04014121.

Wang, Y., Zhai, X., and Wang, W. (2017). "Numerical studies of aluminum foam filled energy absorption connectors under quasi-static compression loading." *Thin-Walled Structures*, 116, 225-233.

Weaver, M. K., Newberry, C. M., Podesto, L., and O'Laughlin, C. (2018). "Blast Testing of Loaded Cross-Laminated Timber Structures." *SEI Structures Congress 2018*, J. G. Soules, ed., American Society of Civil Engineers, Fort Worth, Texas.

Weaver, M. K., O'Laughlin, C., and Newberry, C. M. (2017). "Blast Resistance of Cross-Laminated Timber Construction." *International Symposium on the Interactions of the Effects of Munitions with Structures (17th ISIEMS)*, Federal Office of Bundeswehr Infrastructure, Environmental Protection and Services, Bad Neuenahr, Germany.

Whitney, M. G. (1996). "Blast Damage Mitigation Using Reinforced Concrete Panels and Energy Absorbing Connectors." Wilfred Baker Engineering, Inc., San Antonio, Texas.

WoodWorks (2016). "WoodWorks Case Study WW-020: Candlewood Suites at Redstone Arsenal." Wood Products Council.

Wouts, J., Haugou, G., Oudjene, M., Coutellier, D., and Morvan, H. (2016). "Strain rate effects on the compressive response of wood and energy absorption capabilities – Part A: Experimental investigations." *Composite Structures*, 149, 315-328.

Wu, K.-C., Li, B., and Tsai, K.-C. (2011). "The effects of explosive mass ratio on residual compressive capacity of contact blast damaged composite columns." *Journal of Constructional Steel Research*, 67(4), 602-612.

Xu, J., Wu, C., Li, J., and Cui, J. (2017). "Simplified finite element method analysis of ultra-high-performance fibre-reinforced concrete columns under blast loads." *Advances in Structural Engineering*, 20(1), 139-151.

Appendix A – Test Results of Connection-Level CLT Specimens

This appendix contains the experimental static and dynamic results of all tests conducted on connection-level CLT specimens. Typical data presented in the appendix includes a brief synopsis of each test, as well as relevant test results and photographs taken before and after testing. Prior to testing, the moisture content (MC) of each specimen was measured using a *Tramex Moisture Encounter Plus* pinless moisture meter. The MC varied from 13 % to 15 %.

Connection-level Specimen C1

Specimen C1, comprised of a CLT panel with a single ML24Z angle at each end, was statically tested on October 14th 2017. The specimen failed at the left support by fracturing of a single screw at the angle-support interface. Time-to-ultimate failure was 388.6 sec.

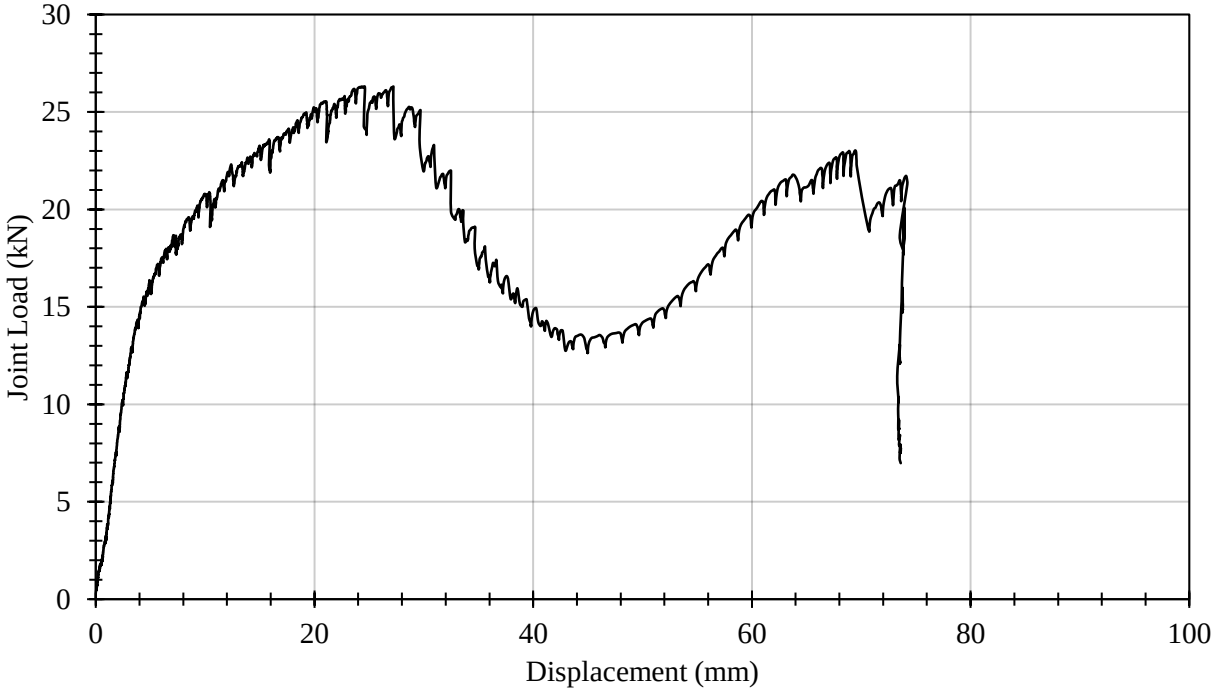


Figure A.1: Load-Displacement Relationship of Specimen C1 Left-Support Joint



(a) Prior to Testing (b) After Testing

Figure A.2: Specimen C1 Before and After Testing



(a) Deformation in ML24Z Angle



(b) Crushing at Panel End

Figure A.3: Damage in Specimen C1 After Testing

Connection-level Specimen C2

Specimen C2, comprised of a CLT panel with a single ML24Z angle at each end, was statically tested on October 15th 2017. The specimen failed at the right support by fracturing of all three screws at the angle-support interface. Time-to-ultimate failure was 421.0 sec.

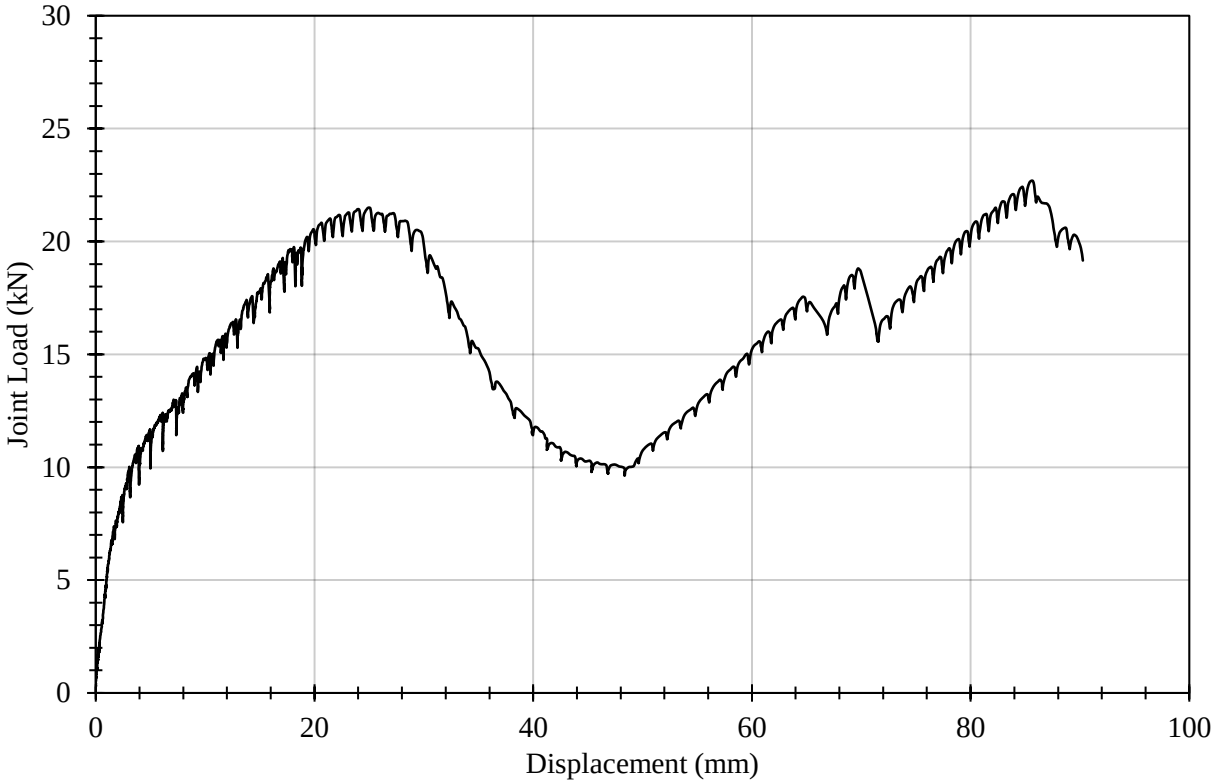


Figure A.4: Load-Displacement Relationship of Specimen C2 Right-Support Joint



(a) Prior to Testing (b) After Testing

Figure A.5: Specimen C2 Before and After Testing



(a) Deformation in ML24Z Angle



(b) Crushing at Panel End and Rupturing of Screws

Figure A.6: Damage in Specimen C2 After Testing

Connection-level Specimen C3

Specimen C3, comprised of a CLT panel with a single ML24Z angle at each end, was statically tested on October 19th 2017. The specimen failed at the right support by wood crushing at the angle-support interface. Time-to-ultimate failure was 525.9 sec.

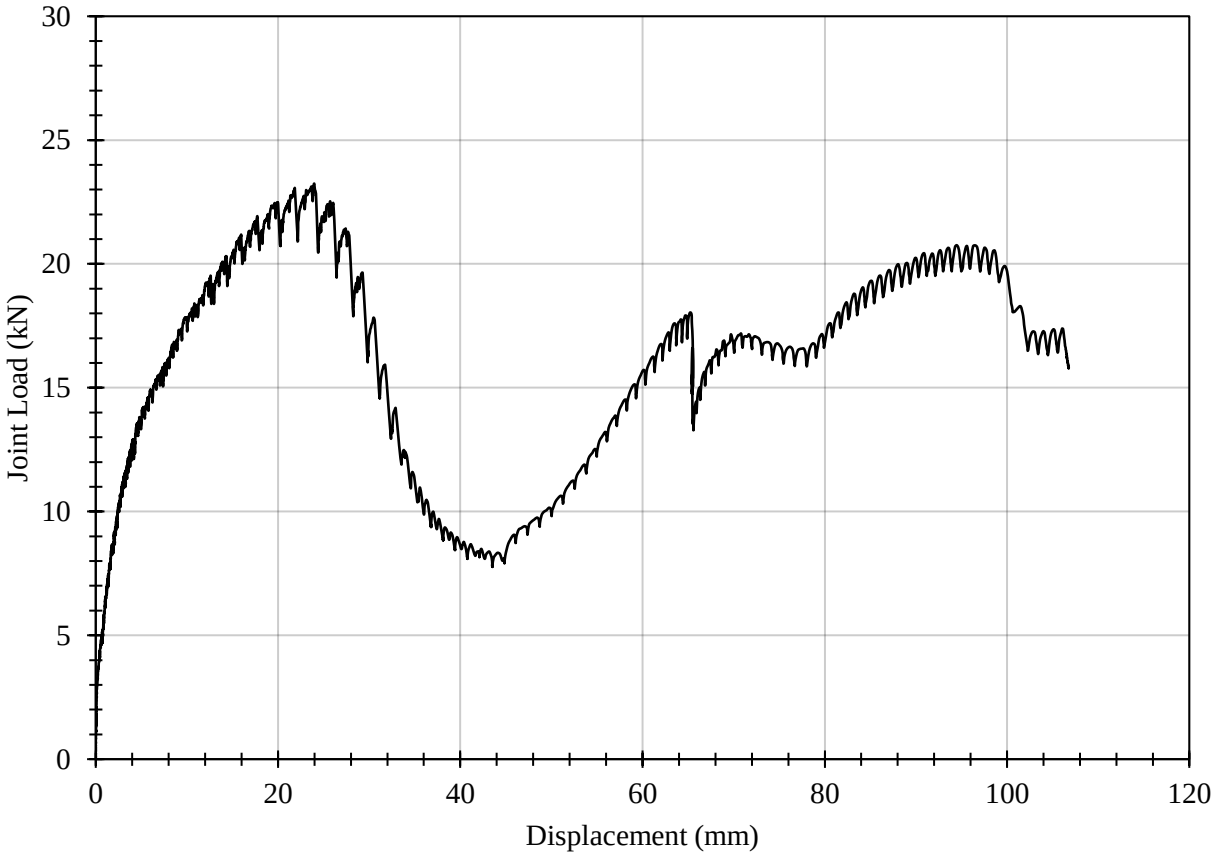
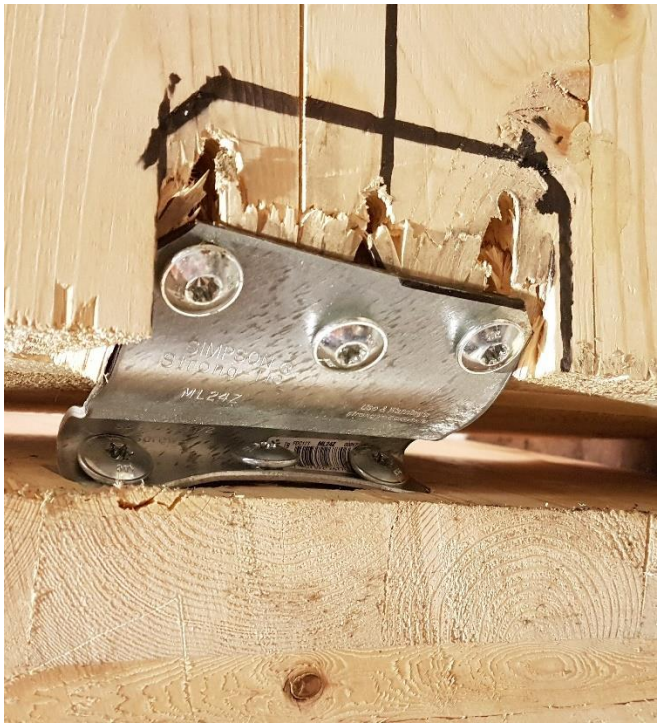


Figure A.7: Load-Displacement Relationship of Specimen C3 Right-Support Joint



(a) Prior to Testing (b) After Testing

Figure A.8: Specimen C3 Before and After Testing



(a) Crushing Failure in Right Support



(b) Crushing at Panel End (Right Side)

Figure A.9: Damage in Specimen C3 After Testing

Connection-level Specimen C4

Specimen C4, comprised of a CLT panel with a thick angle with six screws at each end, was statically tested on October 17th 2017. The specimen failed at the left support by fracturing of all six screws at the angle-support interface. Time-to-ultimate failure was 464.4 sec.

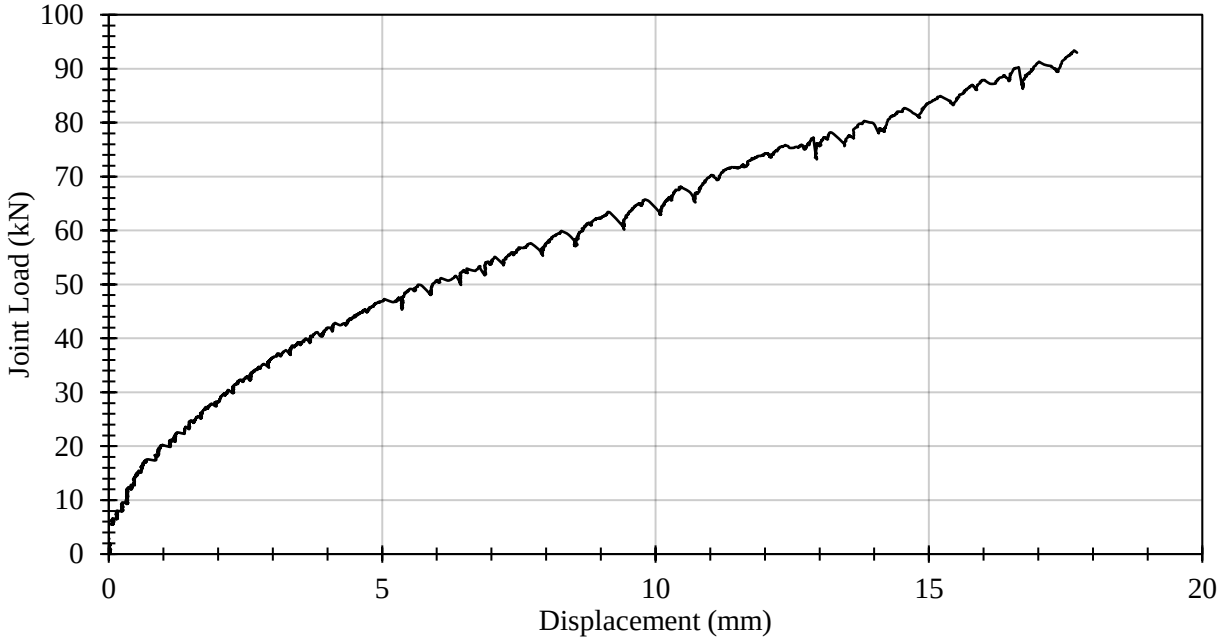


Figure A.10: Load-Displacement Relationship of Specimen C4 Left-Support Joint



(a) Prior to Testing (b) After Testing

Figure A.11: Specimen C4 Before and After Testing



Figure A.12: Screw Failure in Left Support Block of Specimen C4 After Testing

Connection-level Specimen C5

Specimen C5, comprised of a CLT panel with a thick angle with six screws at each end, was statically tested on October 19th 2017. The specimen failed at the right support by fracturing of all six screws at the angle-support interface. Time-to-ultimate failure was 510.8 sec.

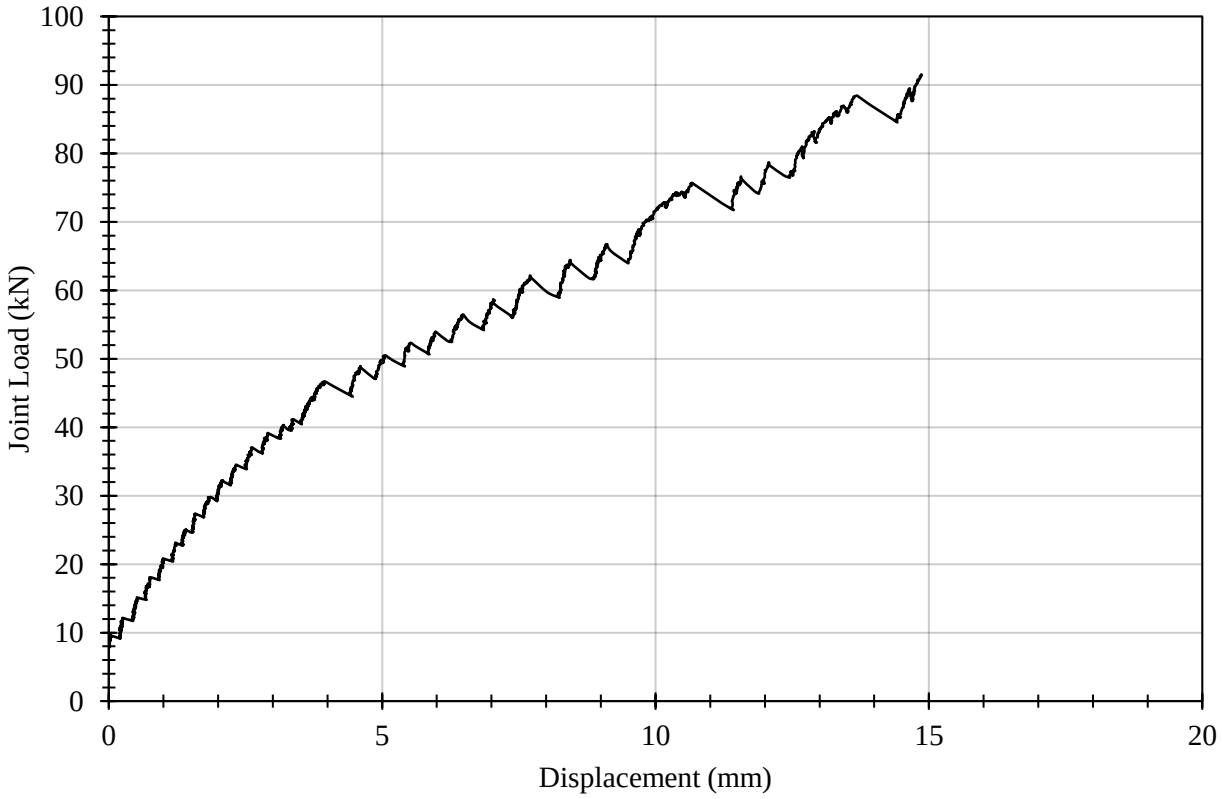


Figure A.13: Load-Displacement Relationship of Specimen C5 Right-Support Joint



(a) Prior to Testing (b) After Testing

Figure A.14: Specimen C5 Before and After Testing



(a) Screw Rupturing (b) Failed Screw Head

Figure A.15: Screw Failure in Specimen C5 After Testing

Connection-level Specimen C6

Specimen C6, comprised of a CLT panel with a thick angle with six screws at each end, was statically tested on October 20th 2017. The specimen failed at the right support by fracturing of all six screws at the angle-support interface. Time-to-ultimate failure was 330.8 sec. All photographs taken during the test on specimen C6 were corrupted and inaccessible.

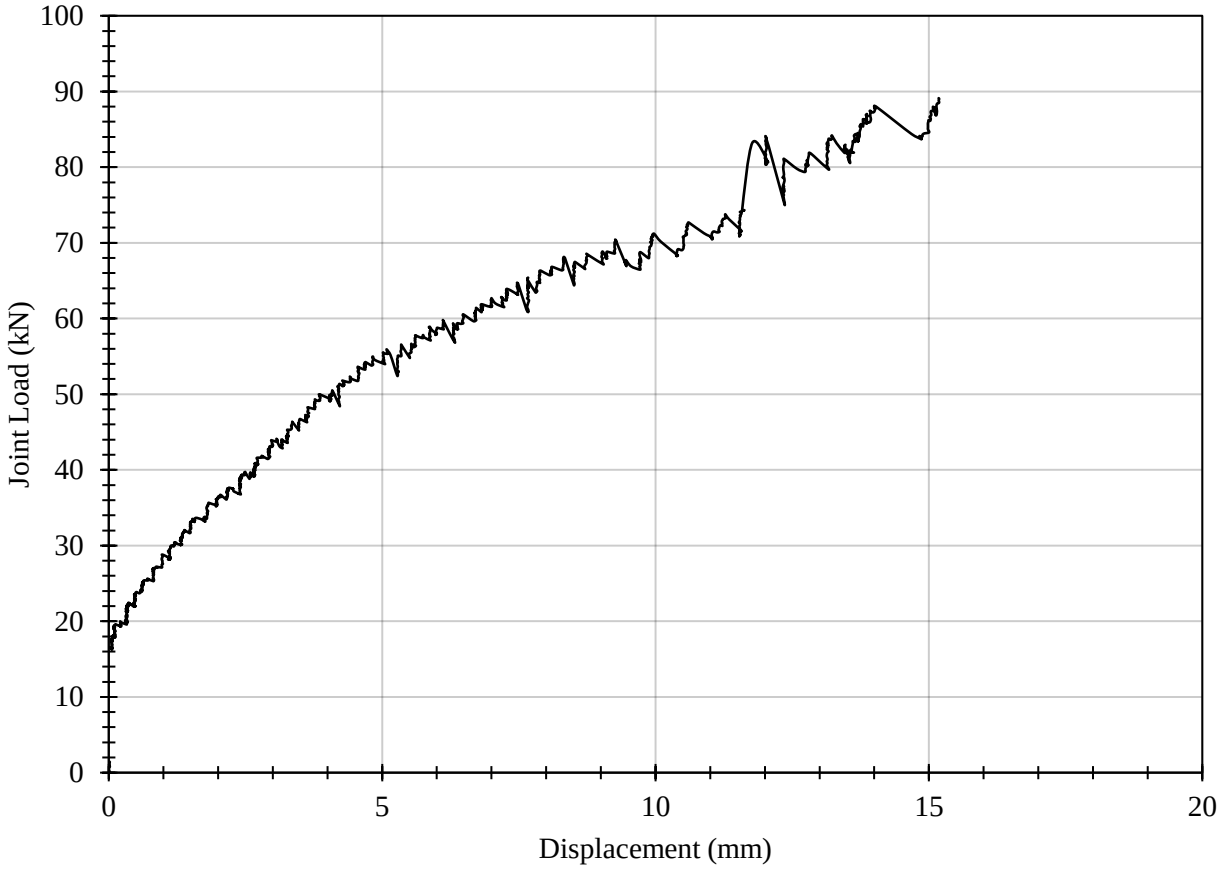
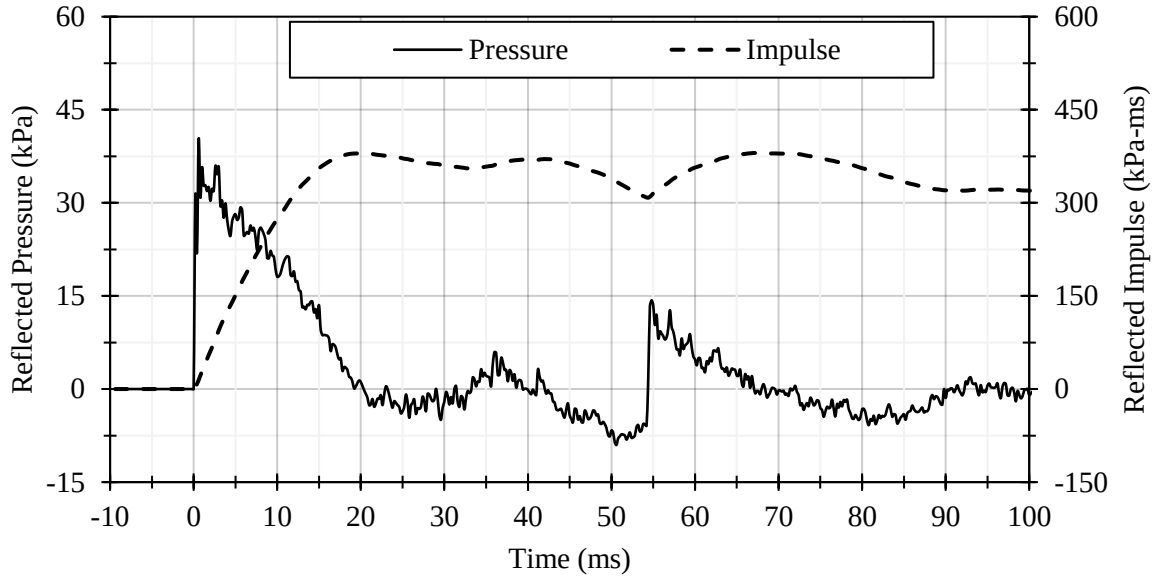


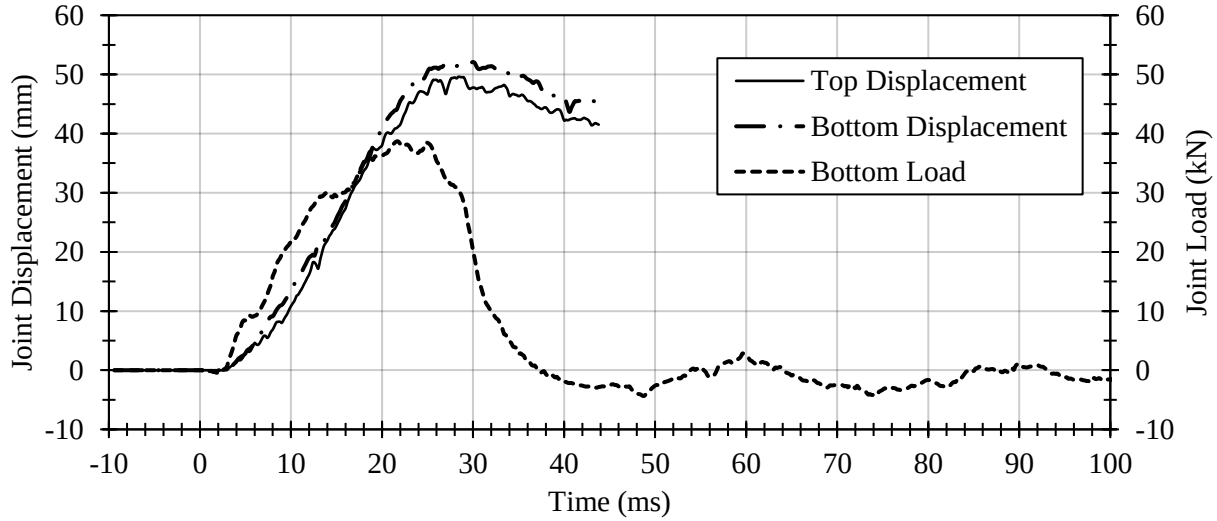
Figure A.16: Load-Displacement Relationship of Specimen C6 Right-Support Joint

Connection-level Specimen C7

Specimen C7, comprised of a CLT panel with a single ML24Z angle at each end, was dynamically tested on November 12th 2018. A driver pressure of 295.8 kPa was used, which resulted in a positive peak reflected pressure and impulse of 40.3 kPa and 380.3 kPa-ms, respectively. Malfunctioning of the top joint load cell resulted in no load data for the top joint. Additionally, displacement measurements were obtained via the high-speed cameras, due to the malfunctioning of a critical LVDT, and as such, displacement readings are only available until 45 ms.



(a) Pressure and Impulse



(b) Joint Loads and Displacements

Figure A.17: Dynamic Test Results for Specimen C7



(a) Specimen Prior to Testing



(b) Specimen After Testing



(c) Bending of Angle and Crushing of Wood

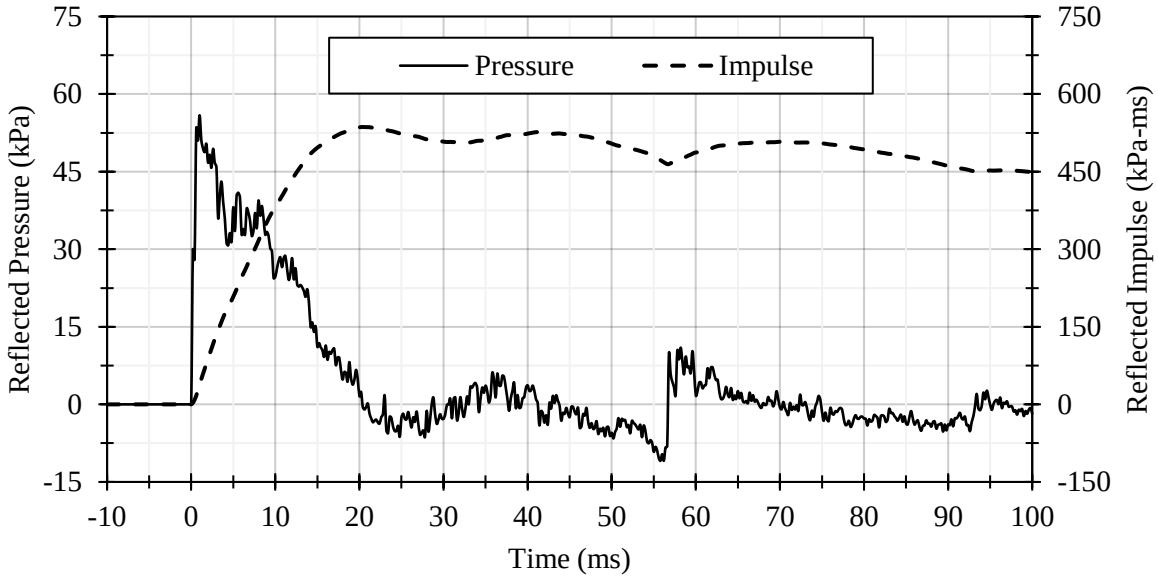


(d) Crushing of Wood in Screw Holes

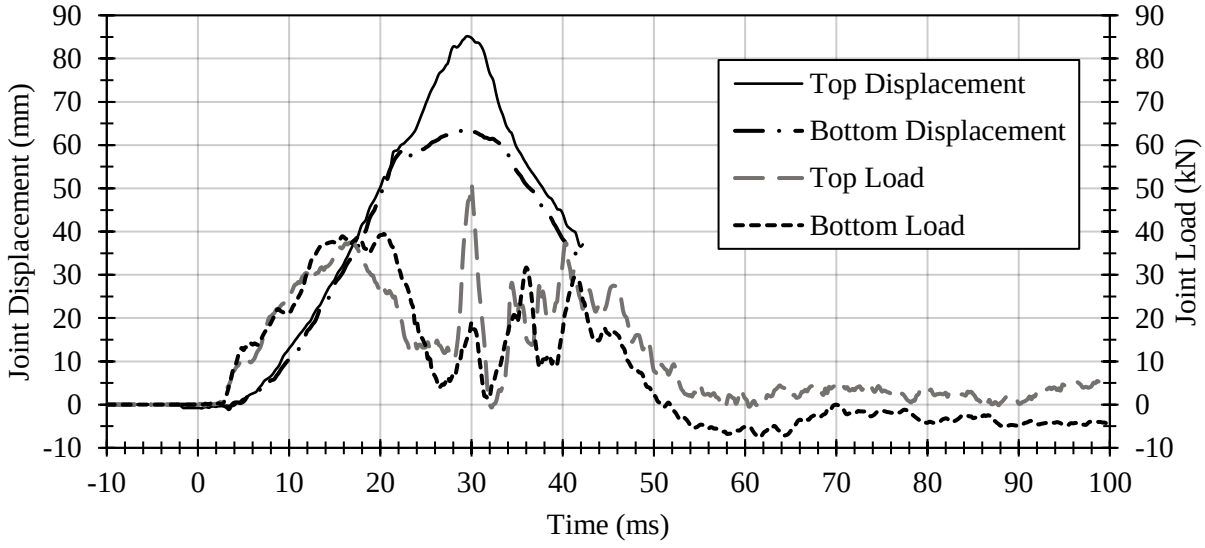
Figure A.18: Documentation of Damage for Specimen C7

Connection-level Specimen C8

Specimen C8, comprised of a CLT panel with a single ML24Z angle at each end, was dynamically tested on November 13th 2018. A driver pressure of 439.9 kPa was used, which resulted in a positive peak reflected pressure and impulse of 55.9 kPa and 536.3 kPa-ms, respectively. Displacement measurements were obtained via the high-speed cameras, due to the malfunctioning of a critical LVDT, and as such, displacement readings are only available until 42 ms.



(a) Pressure and Impulse



(b) Joint Loads and Displacements

Figure A.19: Dynamic Test Results for Specimen C8



(a) Specimen Prior to Testing



(b) Specimen After Testing



(c) Bottom Joint Damage

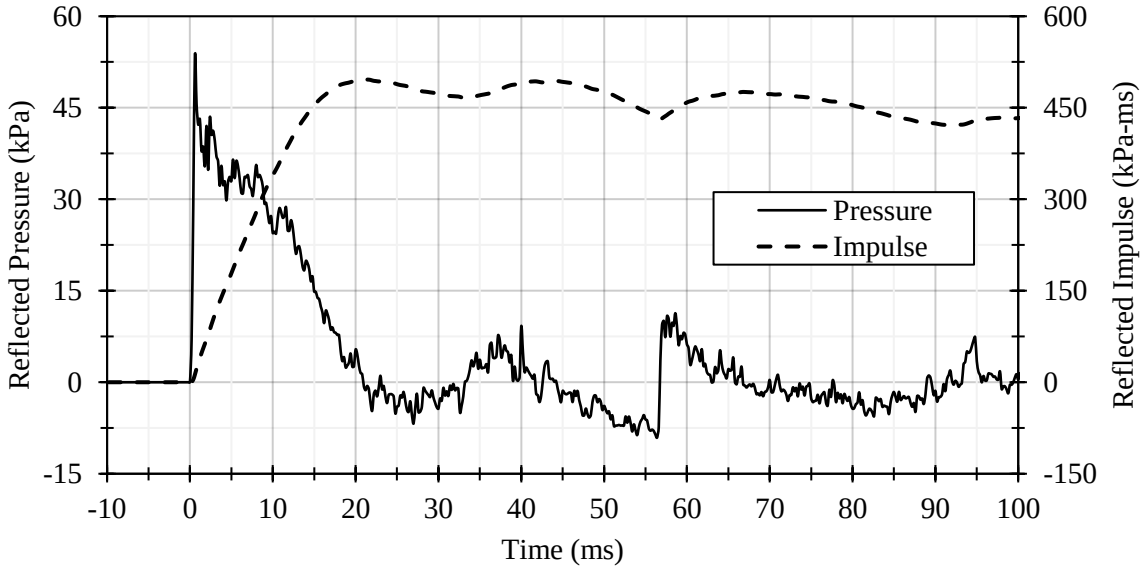


(d) Top Joint Damage

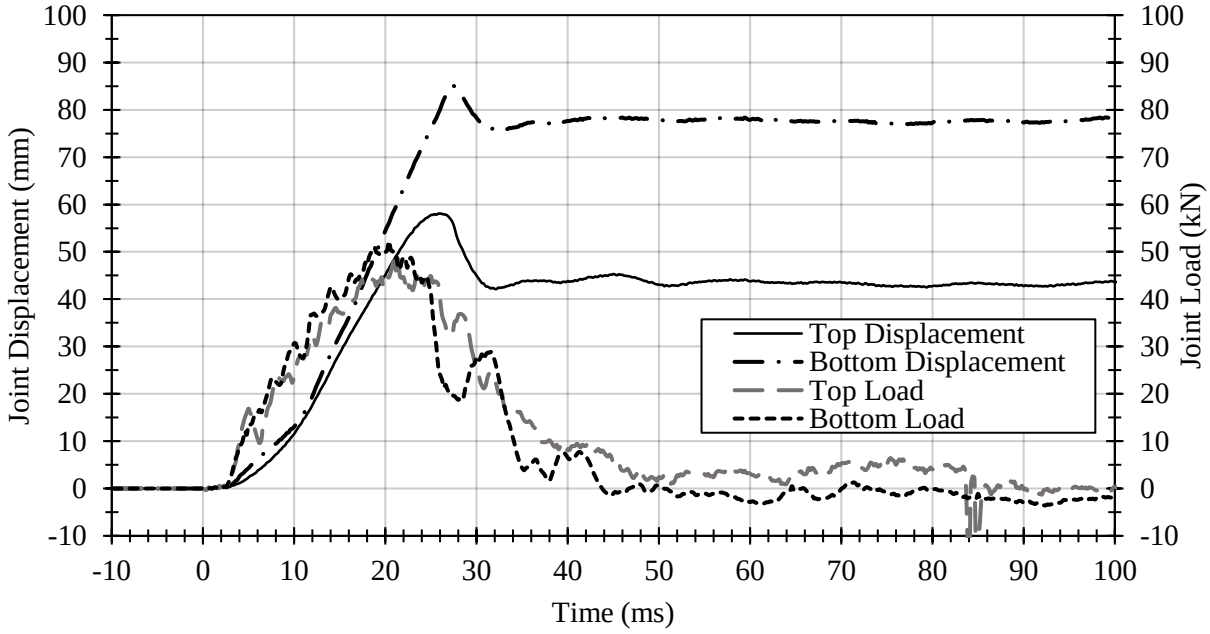
Figure A.20: Documentation of Damage for Specimen C8

Connection-level Specimen C9

Specimen C9, comprised of a CLT panel with a single ML24Z angle at each end, was dynamically tested on November 21st 2018. A driver pressure of 438.5 kPa was used, which resulted in a positive peak reflected pressure and impulse of 53.4 kPa and 496.7 kPa-ms, respectively. Two 1500 kg rated straps were applied onto the specimen in order to apply partial axial restraint.



(a) Pressure and Impulse



(b) Joint Loads and Displacements

Figure A.21: Dynamic Test Results for Specimen C9



(a) Specimen Prior to Testing



(b) Specimen After Testing



(c) Bottom Joint Damage

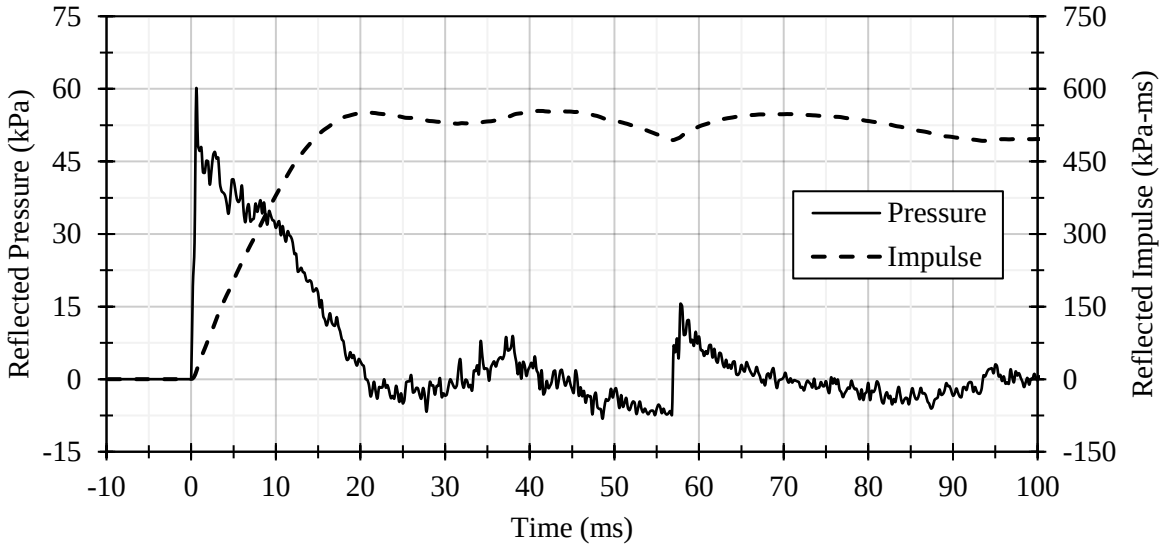


(d) Top Joint Damage

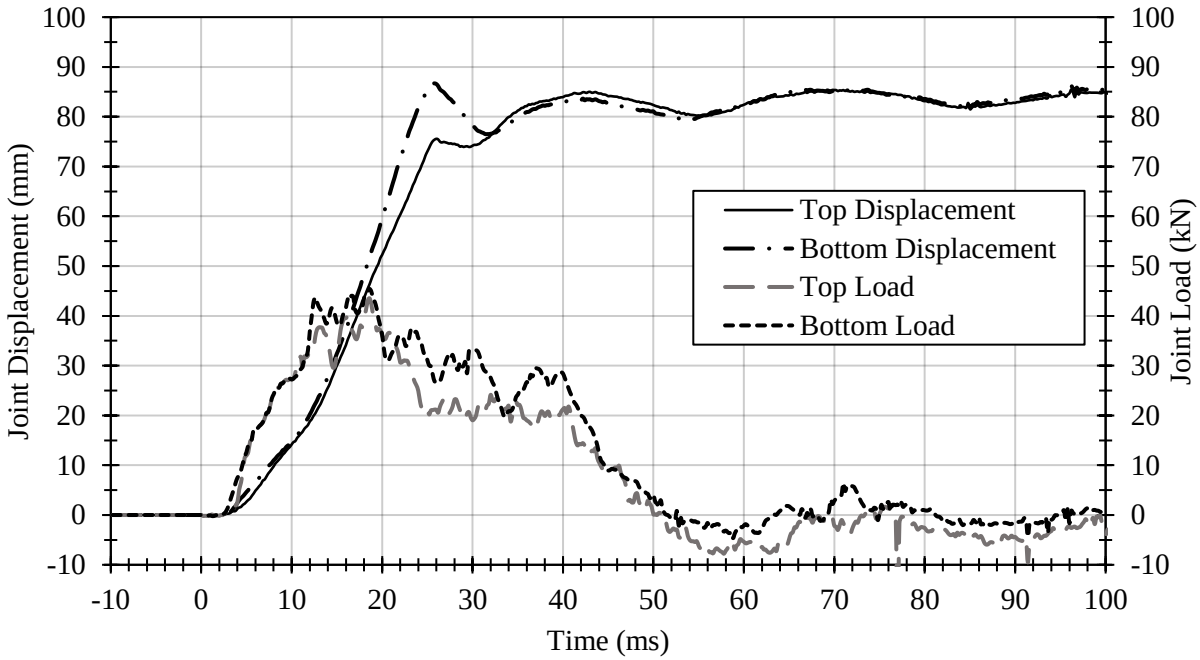
Figure A.22: Documentation of Damage for Specimen C9

Connection-level Specimen C10

Specimen C10, comprised of a CLT panel with a single ML24Z angle at each end, was dynamically tested on November 22nd 2018. A driver pressure of 450.2 kPa was used, which resulted in a positive peak reflected pressure and impulse of 59.7 kPa and 551.7 kPa-ms, respectively. Two 1500 kg rated straps were applied onto the specimen in order to apply partial axial restraint.



(a) Pressure and Impulse



(b) Joint Loads and Displacements

Figure A.23: Dynamic Test Results for Specimen C10



(a) Specimen Prior to Testing



(b) Specimen After Testing



(c) Bottom Joint Damage

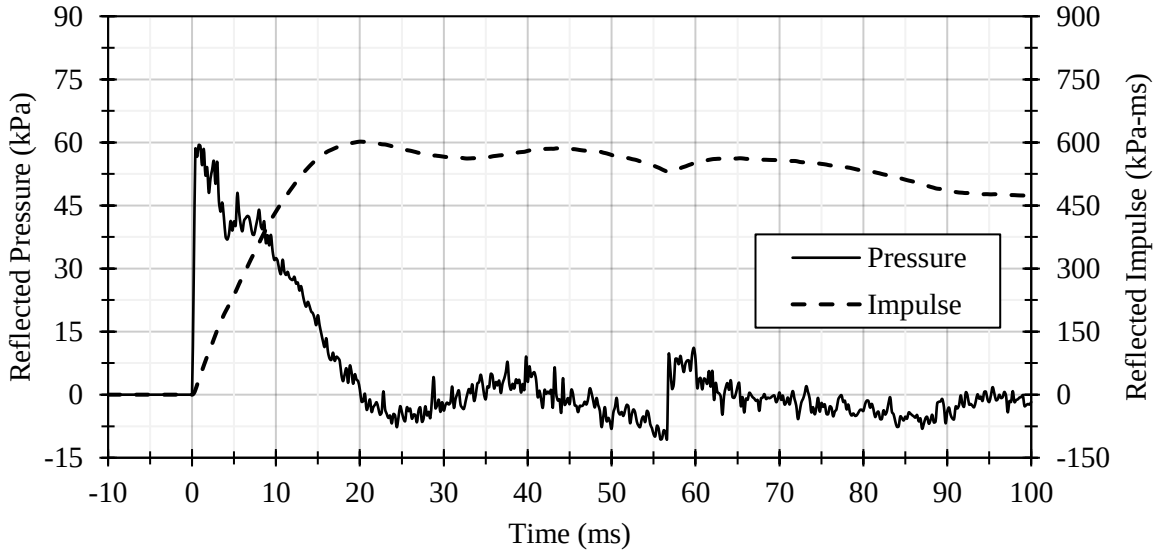


(d) Top Joint Damage

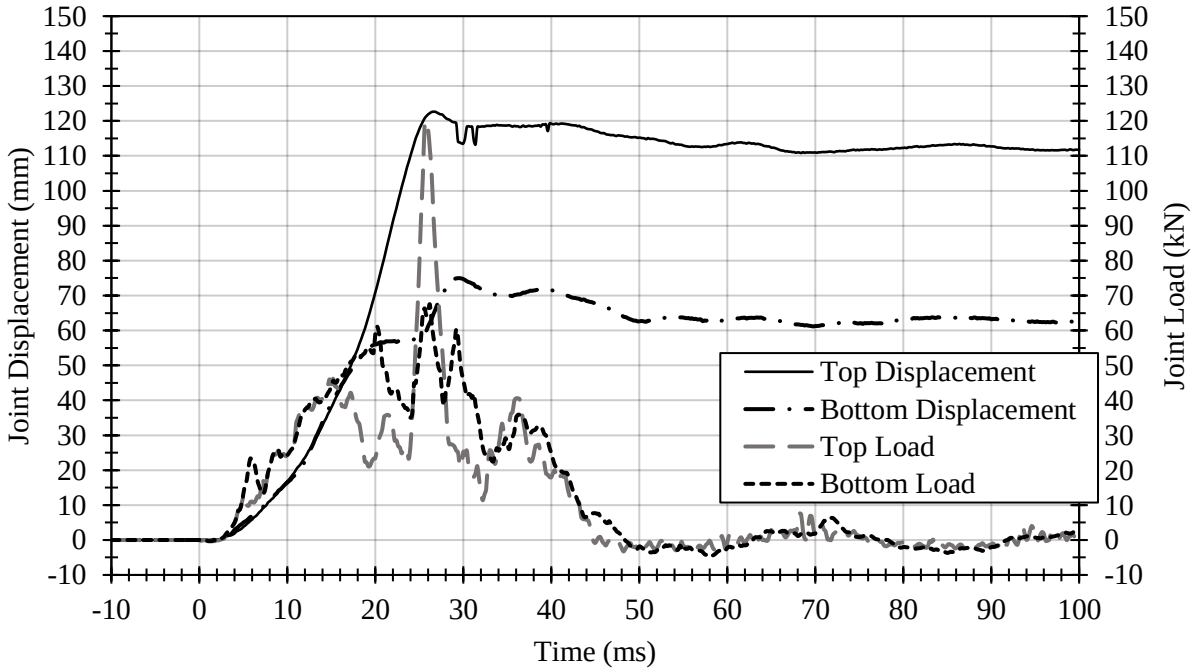
Figure A.24: Documentation of Damage for Specimen C10

Connection-level Specimen C11

Specimen C11, comprised of a CLT panel with a single ML24Z angle at each end, was dynamically tested on November 22nd 2018. A driver pressure of 484.7 kPa was used, which resulted in a positive peak reflected pressure and impulse of 59.4 kPa and 601.9 kPa-ms, respectively. Two 1500 kg rated straps were applied onto the specimen in order to apply partial axial restraint.



(a) Pressure and Impulse



(b) Joint Loads and Displacements

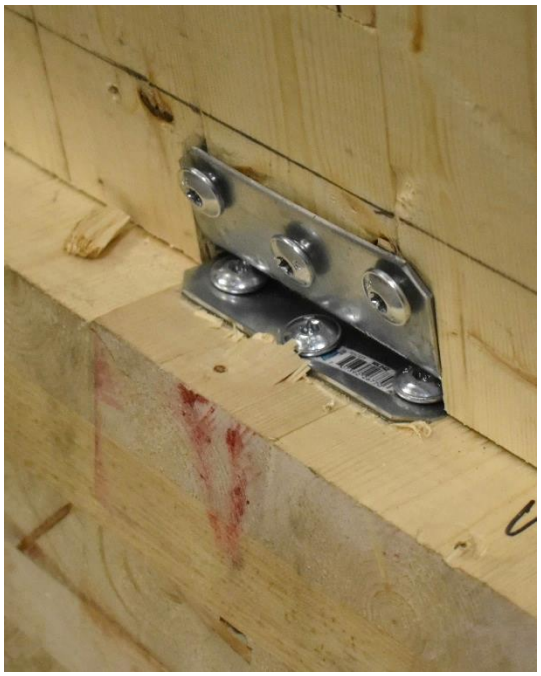
Figure A.25: Dynamic Test Results for Specimen C11



(a) Specimen Prior to Testing



(b) Specimen After Testing



(c) Bottom Joint Damage

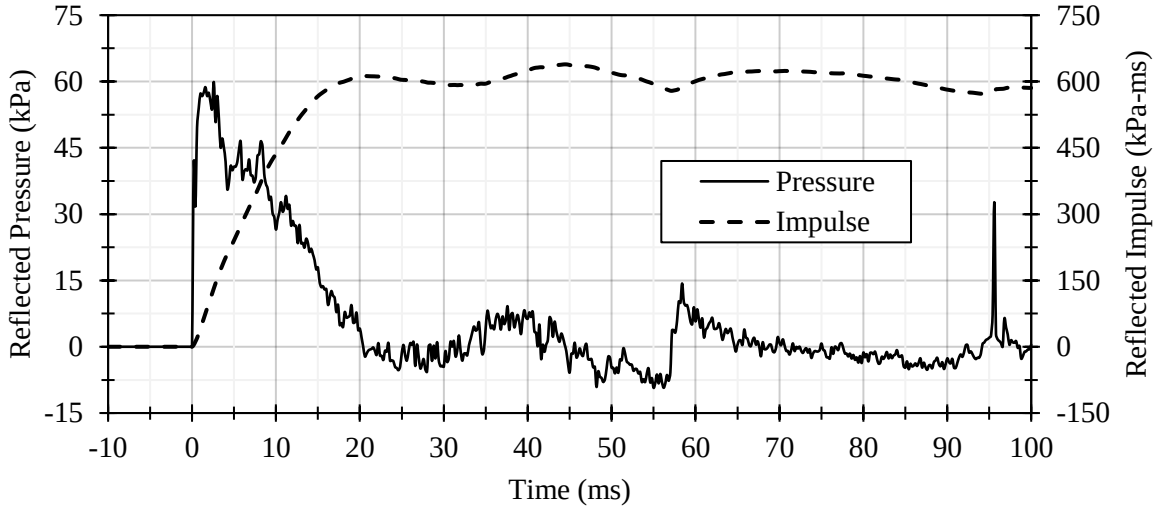


(d) Top Joint Damage

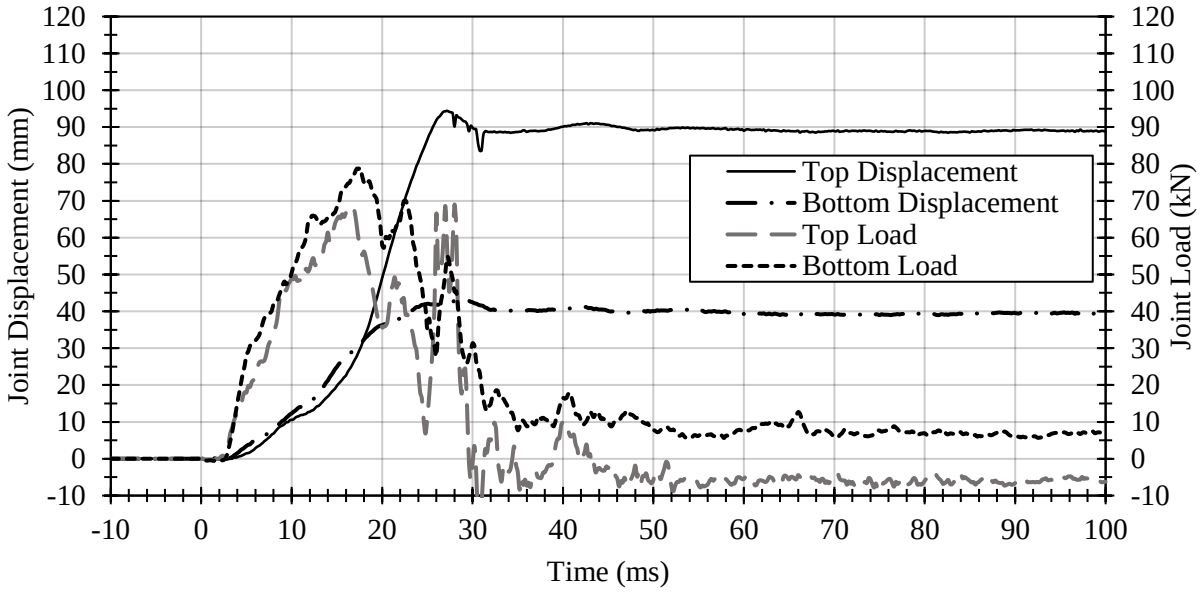
Figure A.26: Documentation of Damage for Specimen C11

Connection-level Specimen C12

Specimen C12, comprised of a CLT panel with two ML24Z angle at each end, was dynamically tested on November 19th 2018. A driver pressure of 515.0 kPa was used, which resulted in a positive peak reflected pressure and impulse of 59.9 kPa and 612.9 kPa-ms, respectively. A single 1500 kg rated strap was applied onto the specimen in order to apply partial axial restraint, however, the location and quantity of strap was insufficient as to provide any noticeable amount of axial restraint.



(a) Pressure and Impulse



(b) Joint Loads and Displacements

Figure A.27: Dynamic Test Results for Specimen C12



(a) Specimen Prior to Testing



(b) Specimen After Testing



(c) Bottom Joint Damage



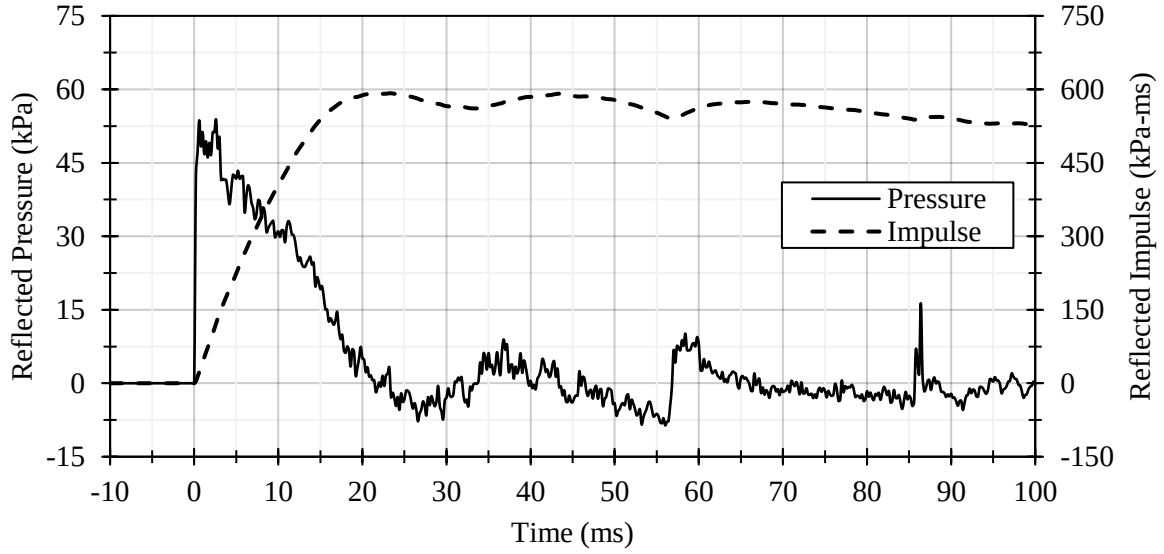


(d) Top Joint Damage

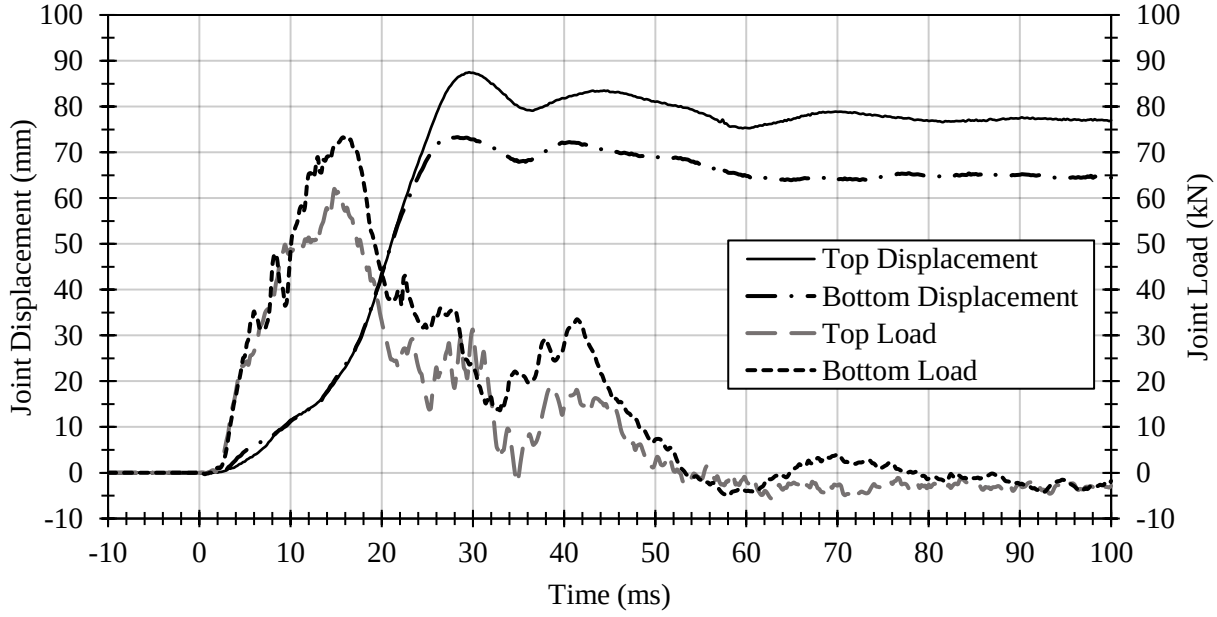
Figure A.28: Documentation of Damage for Specimen C12

Connection-level Specimen C13

Specimen C13, comprised of a CLT panel with two ML24Z angle at each end, was dynamically tested on November 20th 2018. A driver pressure of 512.3 kPa was used, which resulted in a positive peak reflected pressure and impulse of 53.8 kPa and 591.3 kPa-ms, respectively. Lack of axial restraint caused significant opening of the specimen due to the upward force generated by the bending of the angles.



(a) Pressure and Impulse



(b) Joint Loads and Displacements

Figure A.29: Dynamic Test Results for Specimen C13



(a) Specimen Prior to Testing



(b) Specimen After Testing



(c) Bottom Joint Damage

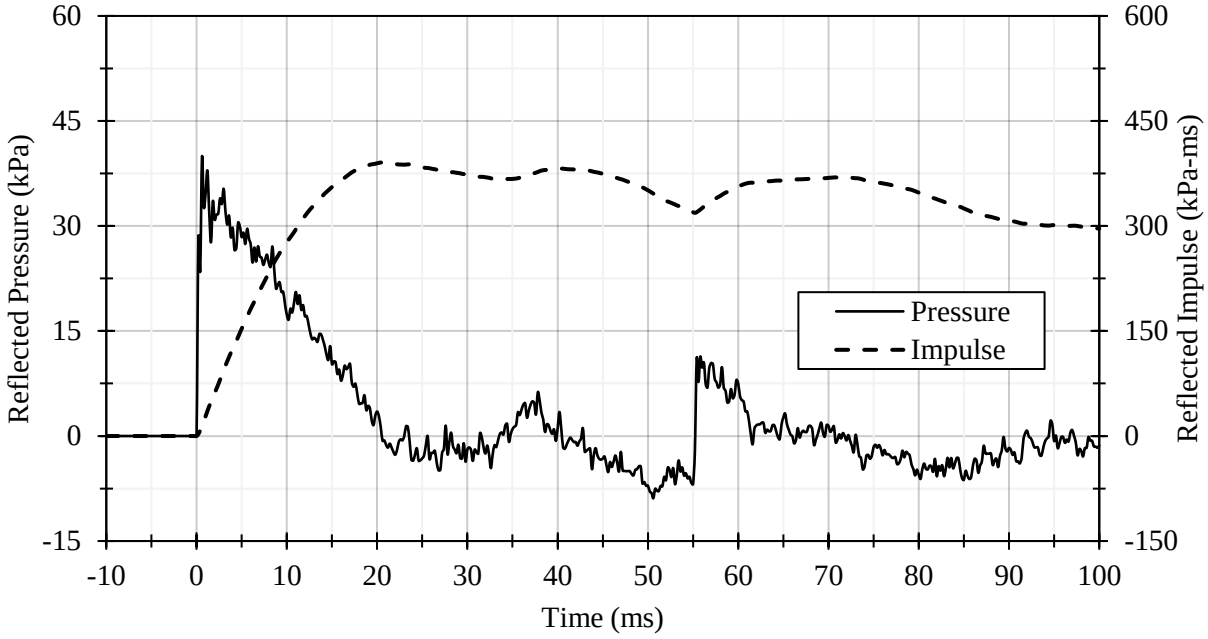


(d) Top Joint Damage

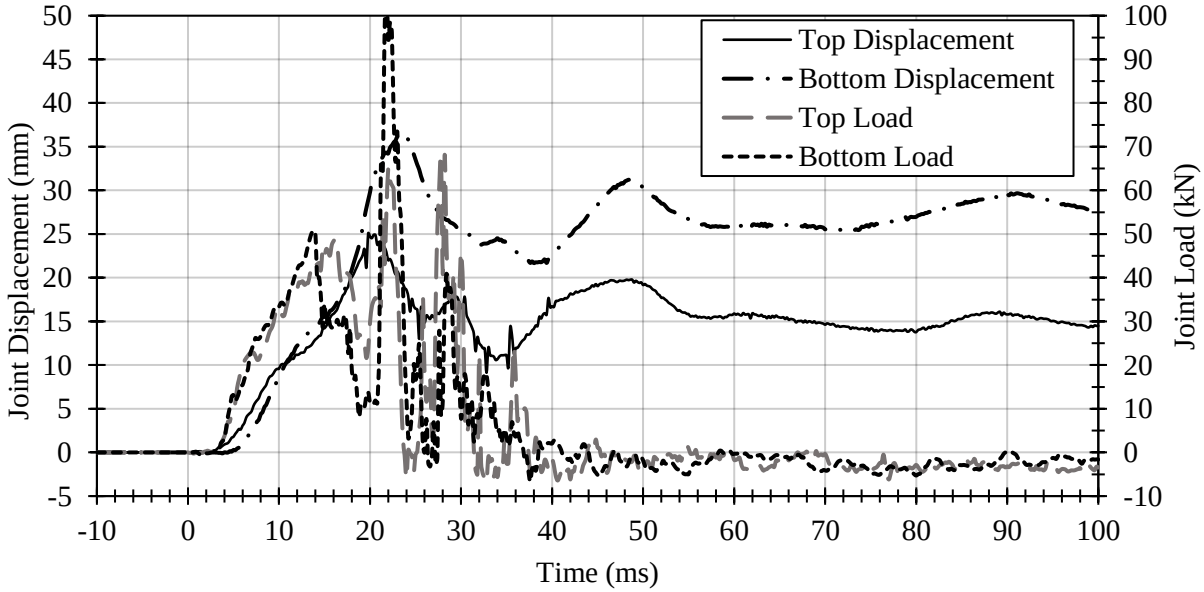
Figure A.30: Documentation of Damage for Specimen C13

Connection-level Specimen C14

Specimen C14, comprised of a CLT panel with a thick angle with three screws at each end, was dynamically tested on November 15th 2018. A driver pressure of 313.0 kPa was used, which resulted in a positive peak reflected pressure and impulse of 39.8 kPa and 390.7 kPa-ms, respectively.



(a) Pressure and Impulse



(b) Joint Loads and Displacements

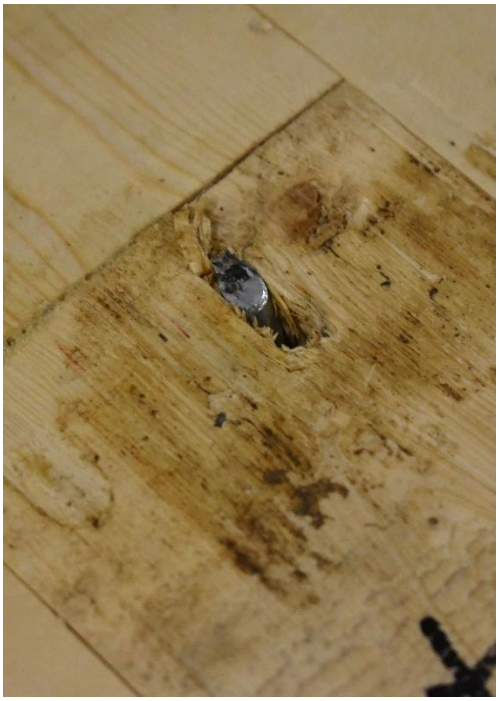
Figure A.31: Dynamic Test Results for Specimen C14



(a) Specimen Prior to Testing



(b) Specimen After Testing



(c) Screw Failure in Bottom Joint

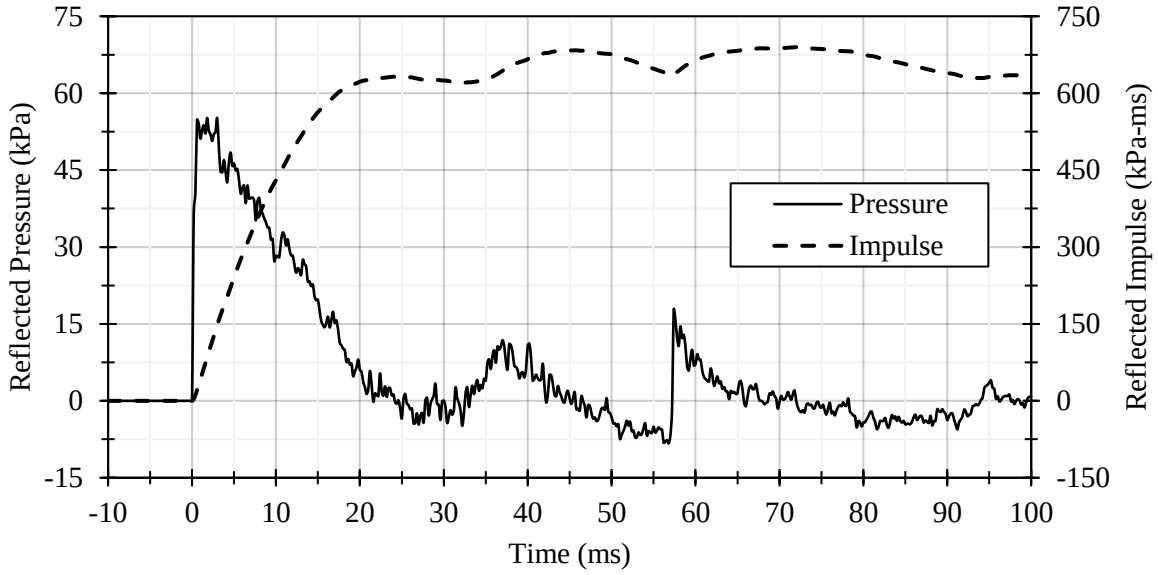


(d) Top Joint Damage

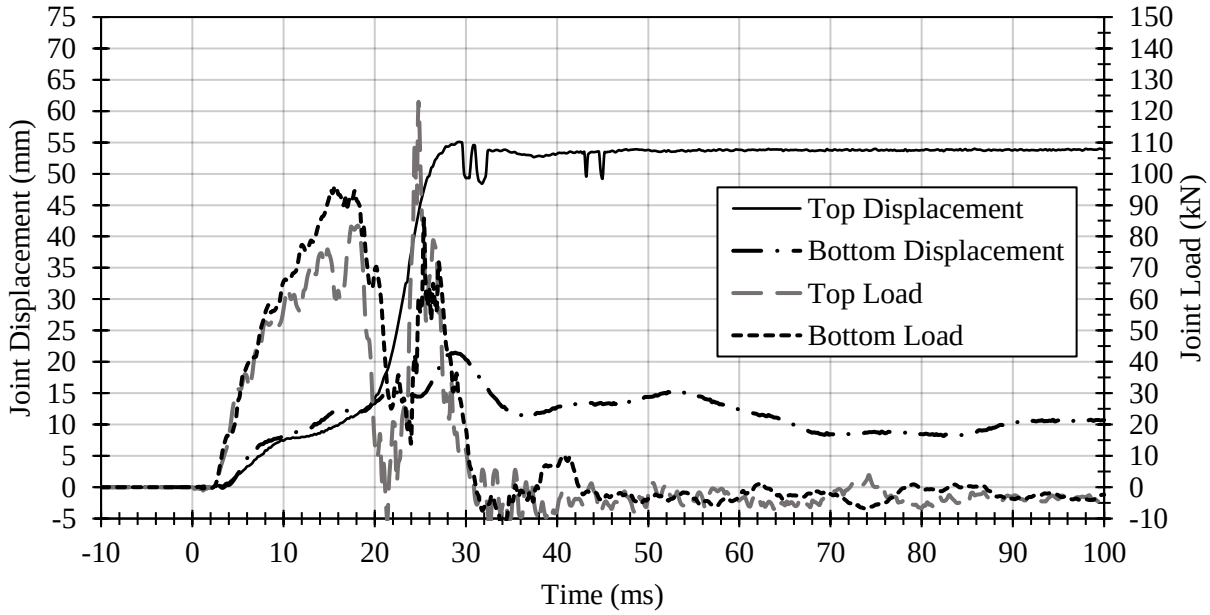
Figure A.32: Documentation of Damage for Specimen C14

Connection-level Specimen C15

Specimen C15, comprised of a CLT panel with a thick angle with six screws at each end, was dynamically tested on November 16th 2018. A driver pressure of 514.3 kPa was used, which resulted in a positive peak reflected pressure and impulse of 55.2 kPa and 632.2 kPa-ms, respectively.



(a) Pressure and Impulse



(b) Joint Loads and Displacements

Figure A.33: Dynamic Test Results for Specimen C15



(a) Specimen Prior to Testing



(b) Specimen After Testing



(c) Screw Failure in Bottom Joint

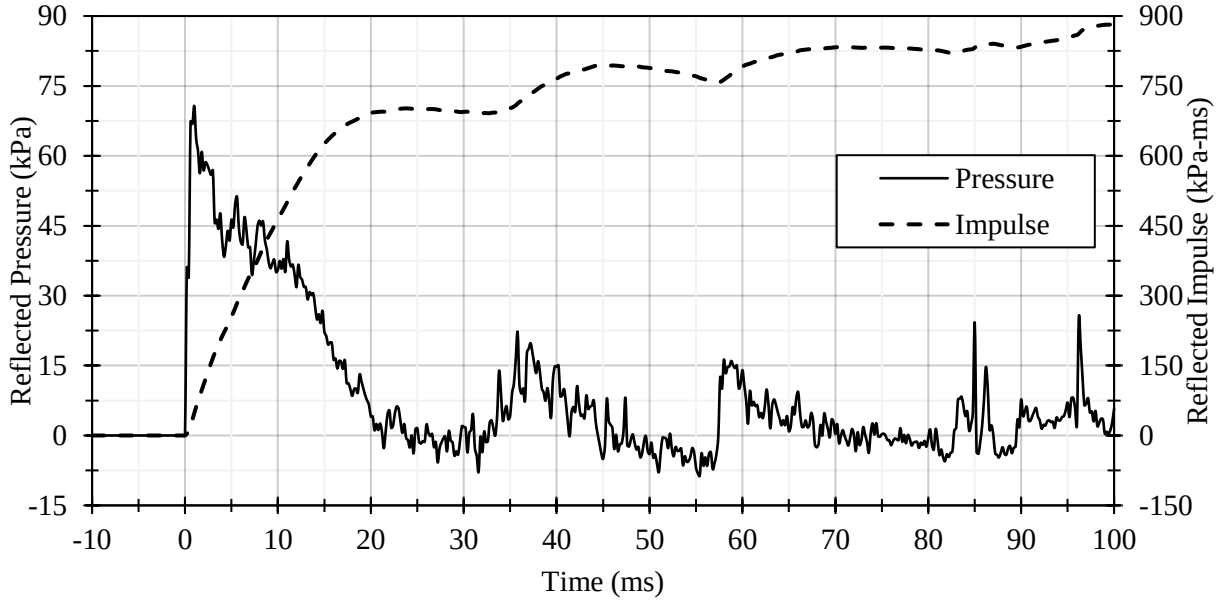


(d) Screw Failure in Top Joint

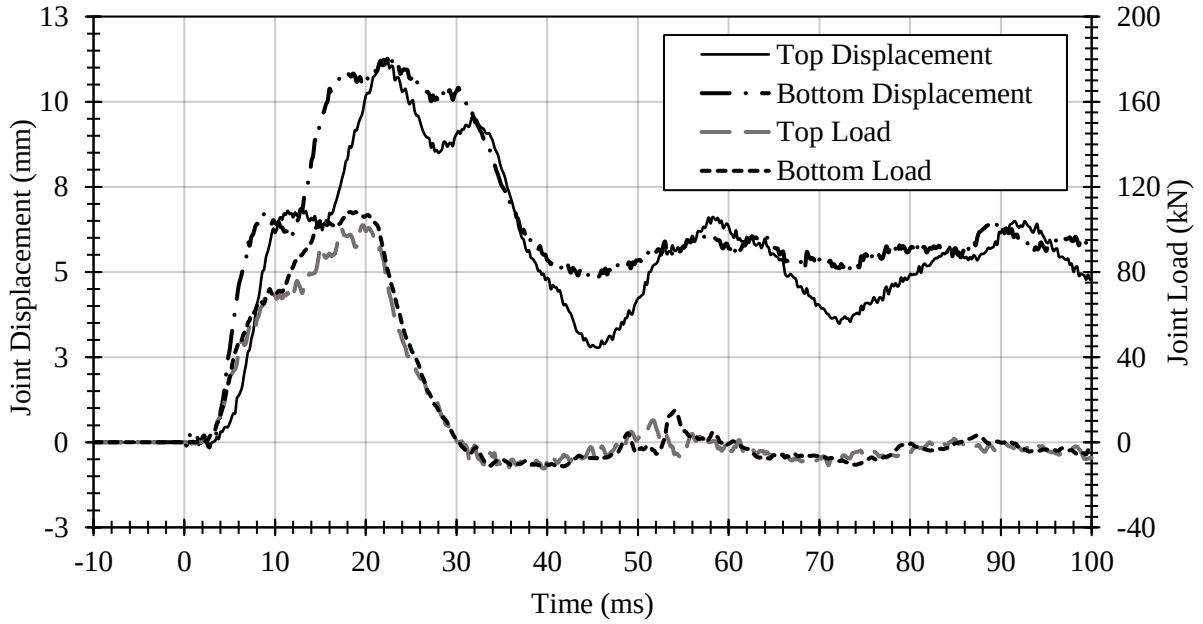
Figure A.34: Documentation of Damage for Specimen C15

Connection-level Specimen C16

Specimen C16, comprised of a CLT panel with a thick angle with nine screws at each end, was dynamically tested on November 16th 2018. A driver pressure of 561.9 kPa was used, which resulted in a positive peak reflected pressure and impulse of 70.7 kPa and 699.0 kPa-ms, respectively.



(a) Pressure and Impulse



(b) Joint Loads and Displacements

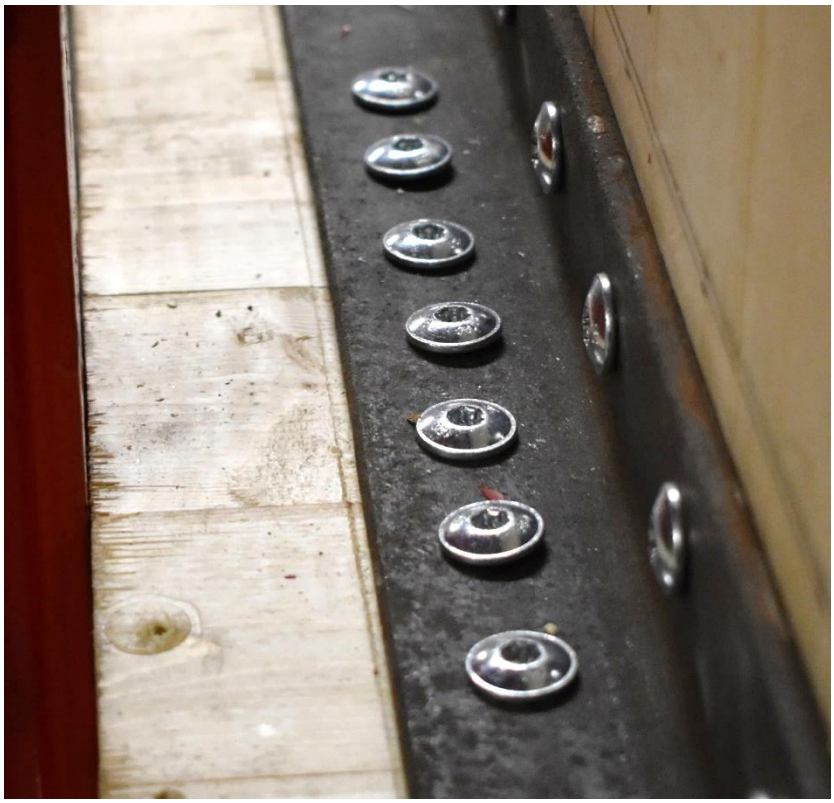
Figure A.35: Dynamic Test Results for Specimen C16



(a) Specimen Prior to Testing



(b) Specimen After Testing



(c) Drag Marks due to Elastic Deformation of Screws and Angles

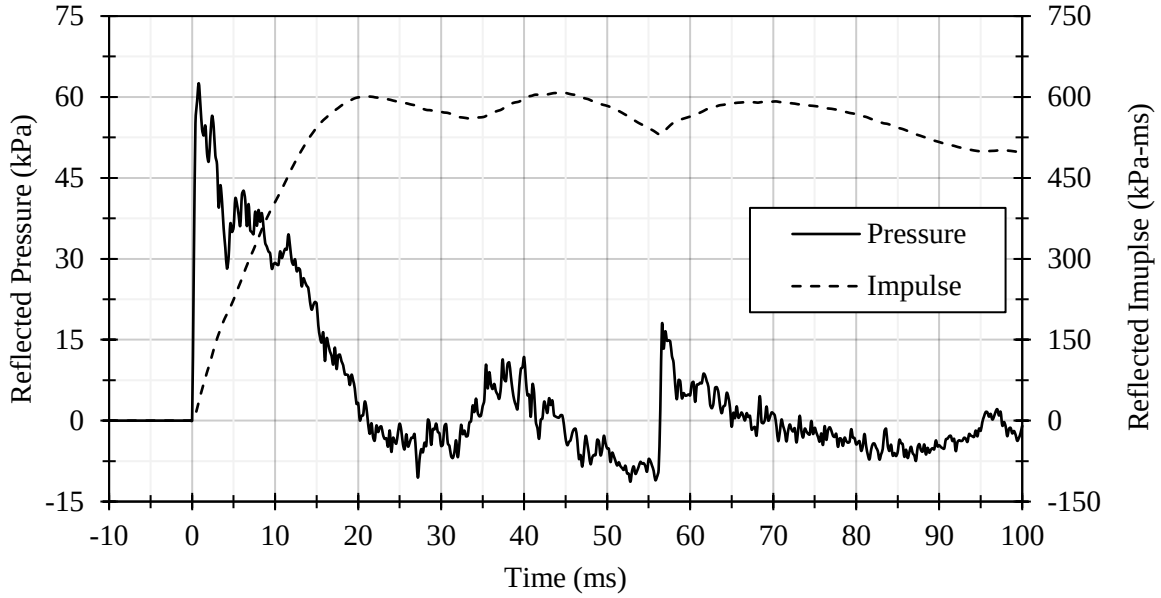
Figure A.36: Documentation of Damage for Specimen C16

Appendix B – Test Results of Full-Scale CLT Specimens

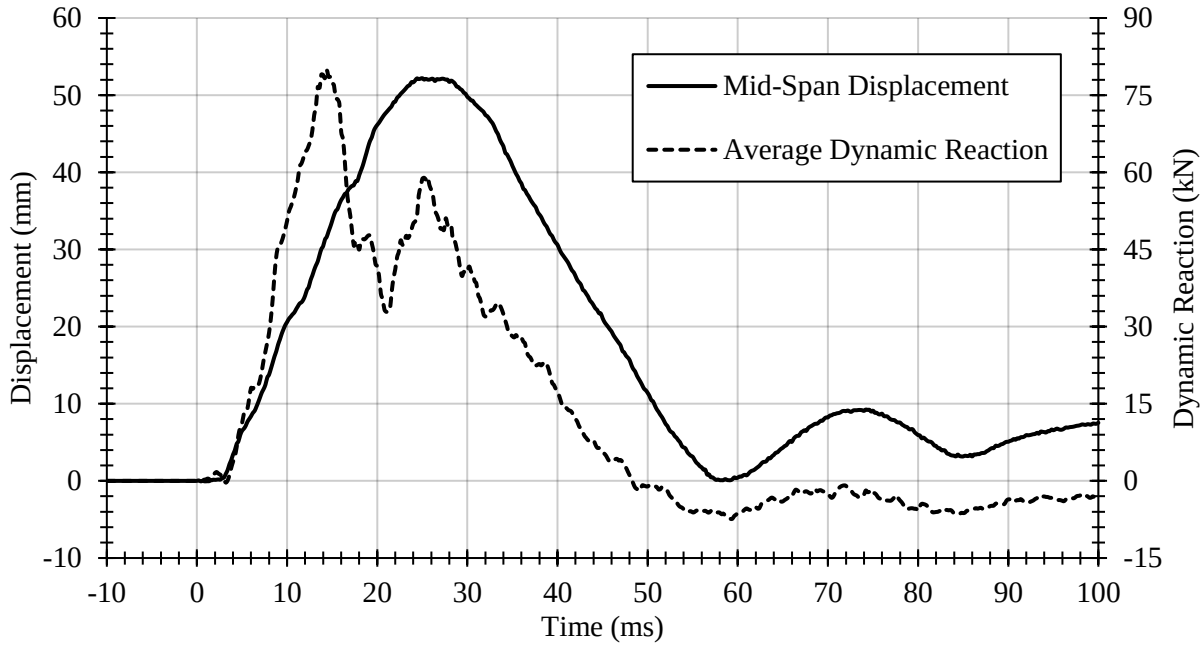
This appendix contains the experimental dynamic results of all tests conducted on full-scale CLT specimens. Typical data presented in the appendix includes a brief synopsis of each test, as well as relevant test results and photographs taken before and after testing. Prior to testing, the moisture content (MC) of each specimen was measured using a *Tramex Moisture Encounter Plus* pinless moisture meter. The MC varied from 10 % to 15 %.

Specimen CLT1

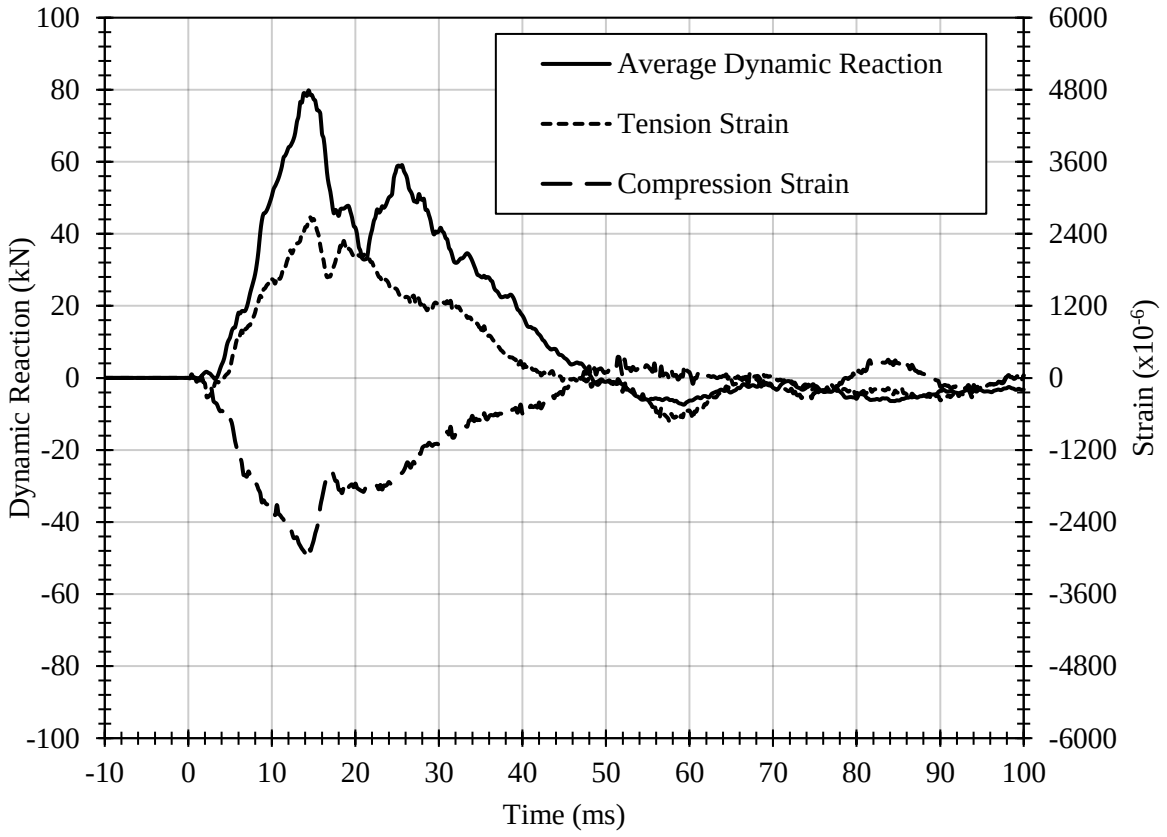
Specimen CLT1, comprised of a simply-supported CLT panel, was dynamically tested on November 28th 2018. A driver pressure of 485.4 kPa was used, which resulted in a positive peak reflected pressure and impulse of 62.5 kPa and 601.1 kPa-ms, respectively.



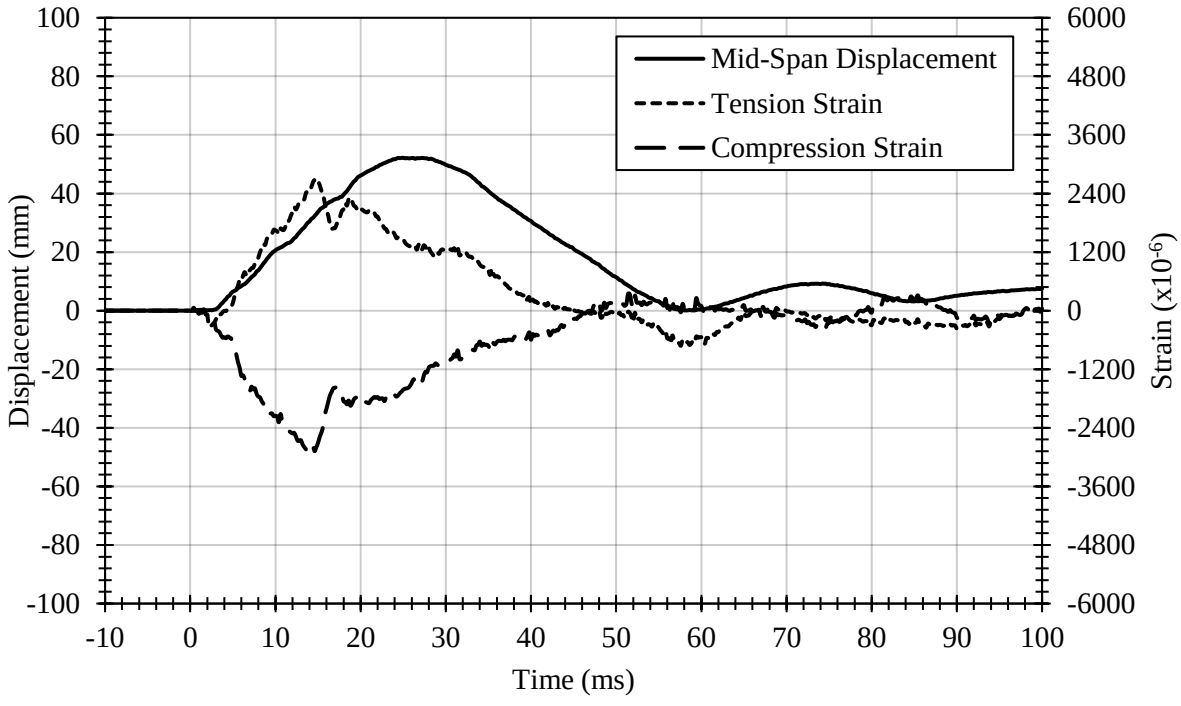
(a) Pressure and Impulse



(b) Reaction and Displacement



(c) Reaction and Strains



(d) Displacement and Strains

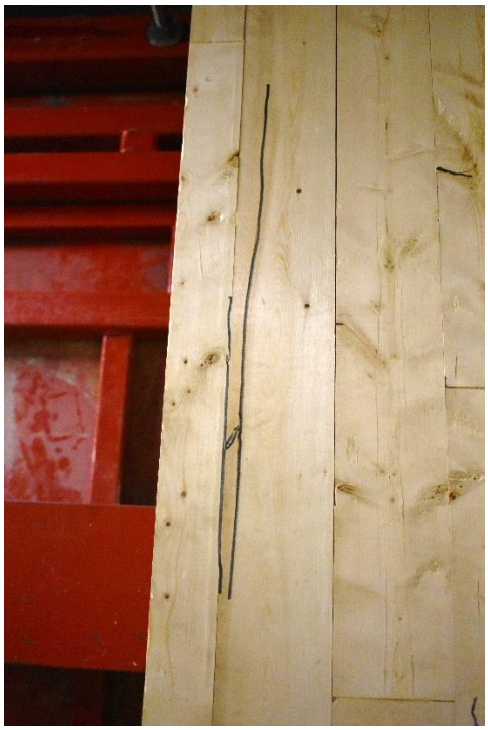
Figure B.1: Dynamic Test Results for Specimen CLT1



(a) Specimen Prior to Testing



(b) Specimen After Testing



(c) Superficial Flexural Failure

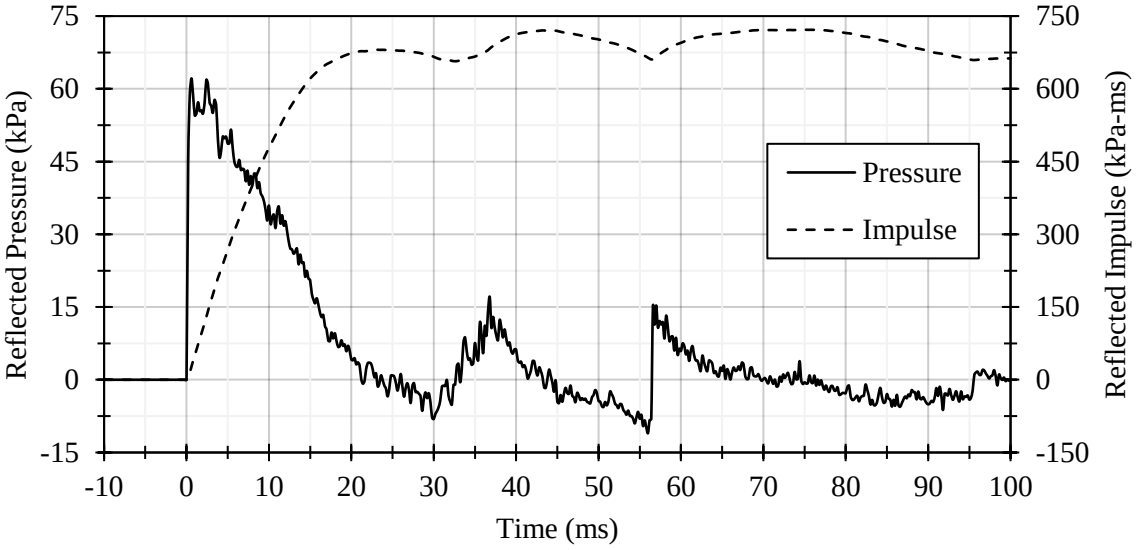


(d) Shear Damage at Top Support

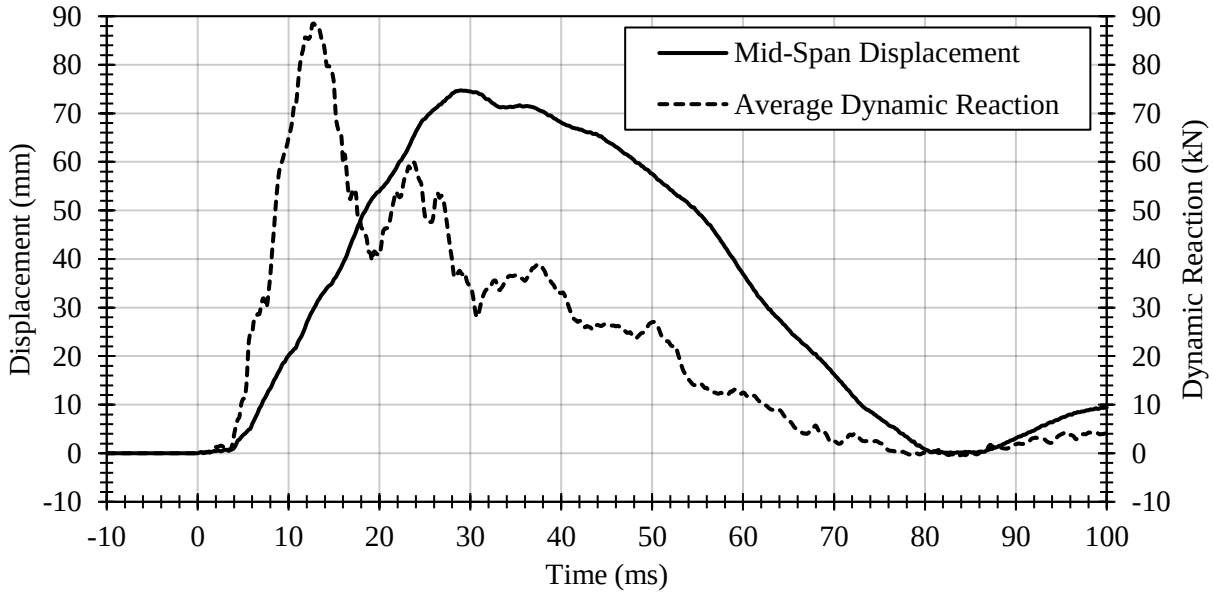
Figure B.2: Documentation of Damage for Specimen CLT1

Specimen CLT2

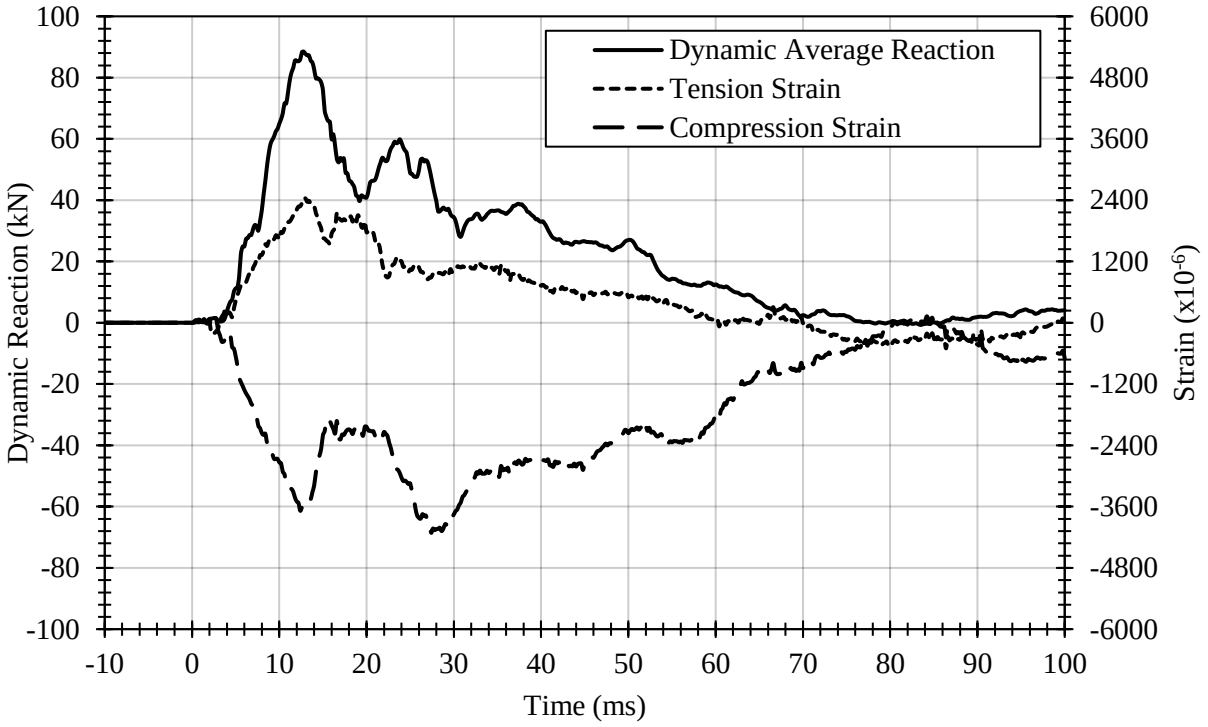
Specimen CLT2, comprised of a simply-supported CLT panel, was dynamically tested on November 29th 2018. A driver pressure of 519.2 kPa was used, which resulted in a positive peak reflected pressure and impulse of 62.2 kPa and 680.4 kPa-ms, respectively.



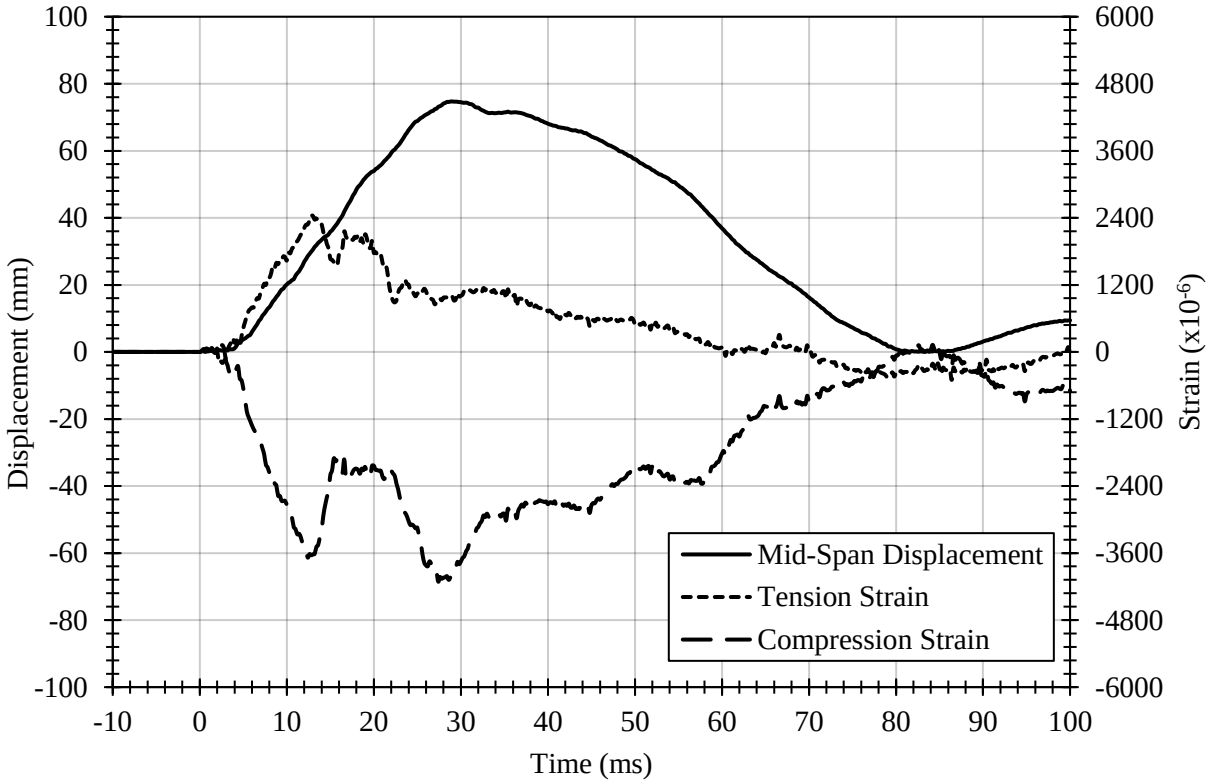
(a) Pressure and Impulse



(b) Reaction and Displacement



(c) Reaction and Strains



(d) Displacement and Strains

Figure B.3: Dynamic Test Results for Specimen CLT2



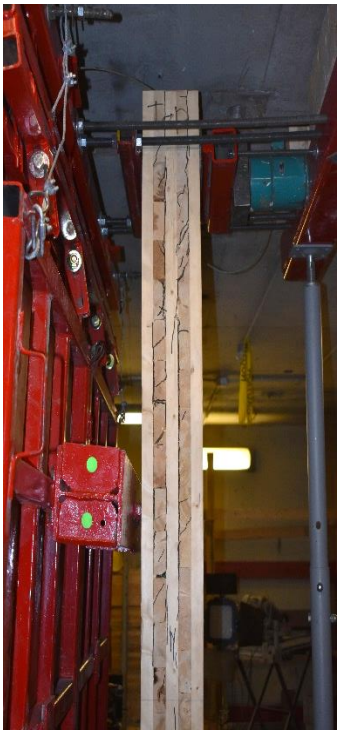
(a) Specimen Prior to Testing



(b) Specimen After Testing



(c) Flexural Damage

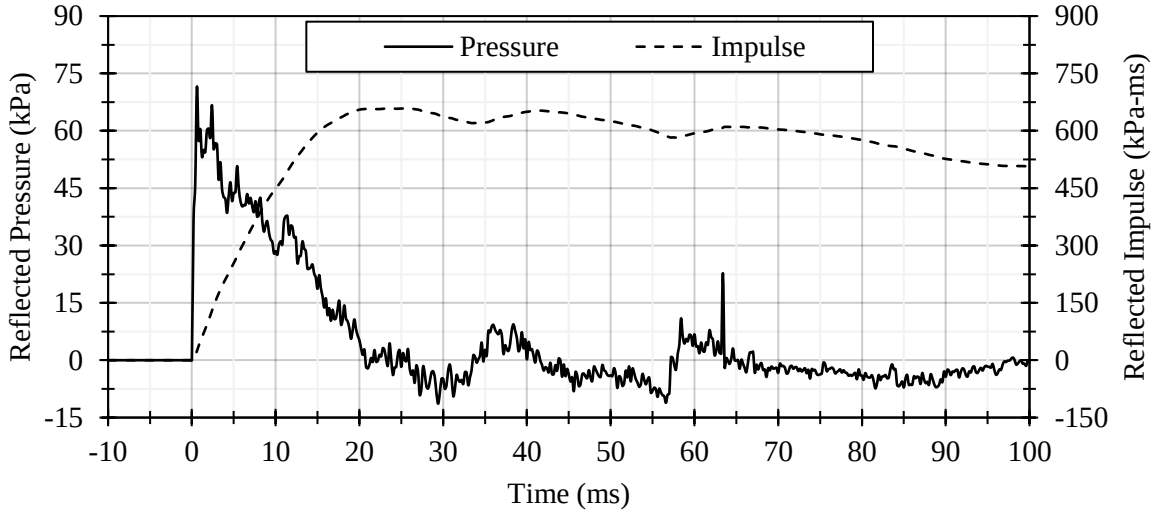


(d) Shear Damage at Top Support

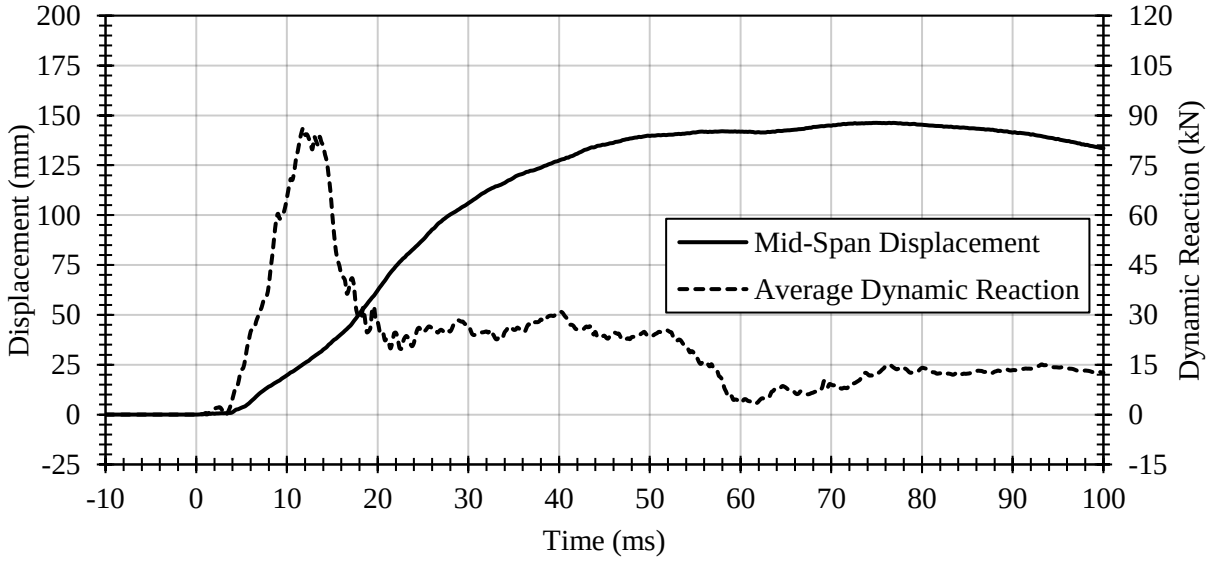
Figure B.4: Documentation of Damage for Specimen CLT2

Specimen CLT3

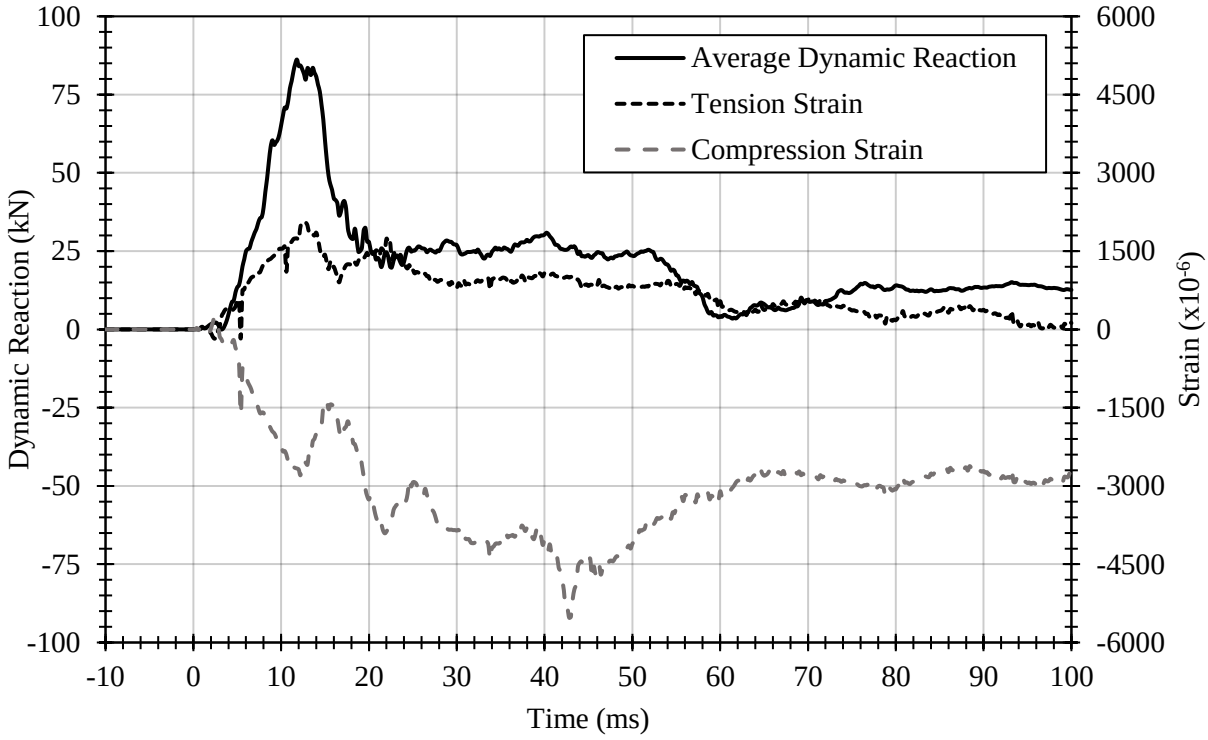
Specimen CLT3, comprised of a simply-supported CLT panel, was dynamically tested on November 30th 2018. A driver pressure of 550.9 kPa was used, which resulted in a positive peak reflected pressure and impulse of 71.4 kPa and 657.4 kPa-ms, respectively.



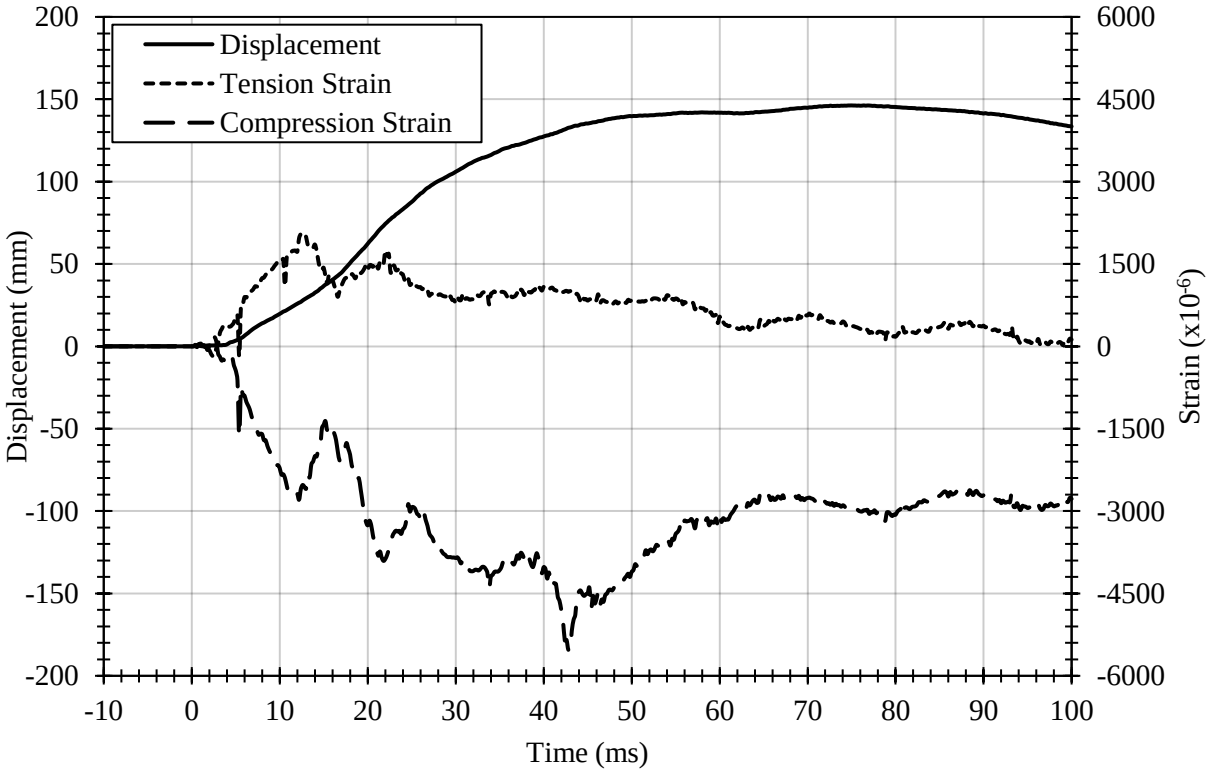
(a) Pressure and Impulse



(b) Reaction and Displacement



(c) Reaction and Strains



(d) Displacement and Strains

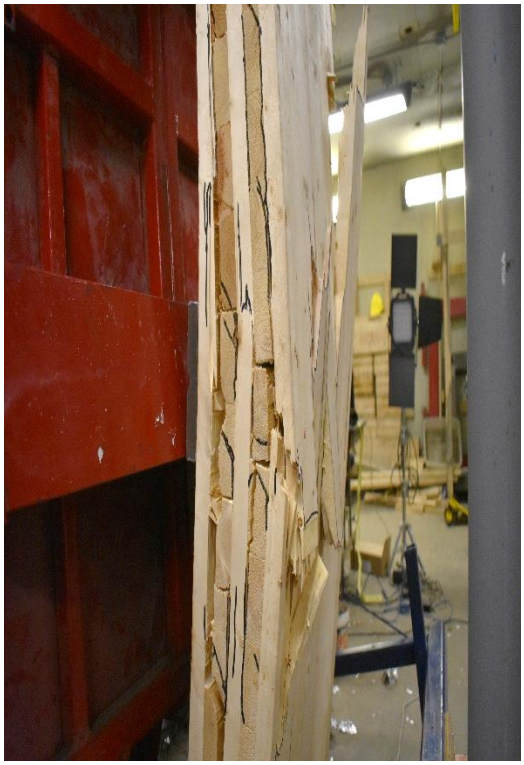
Figure B.5: Dynamic Test Results for Specimen CLT3



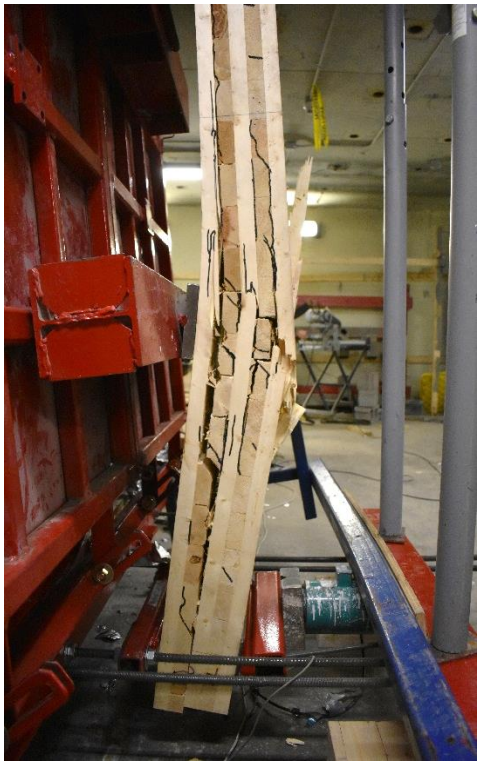
(a) Specimen Prior to Testing



(b) Specimen After Testing



(c) Flexural Failure

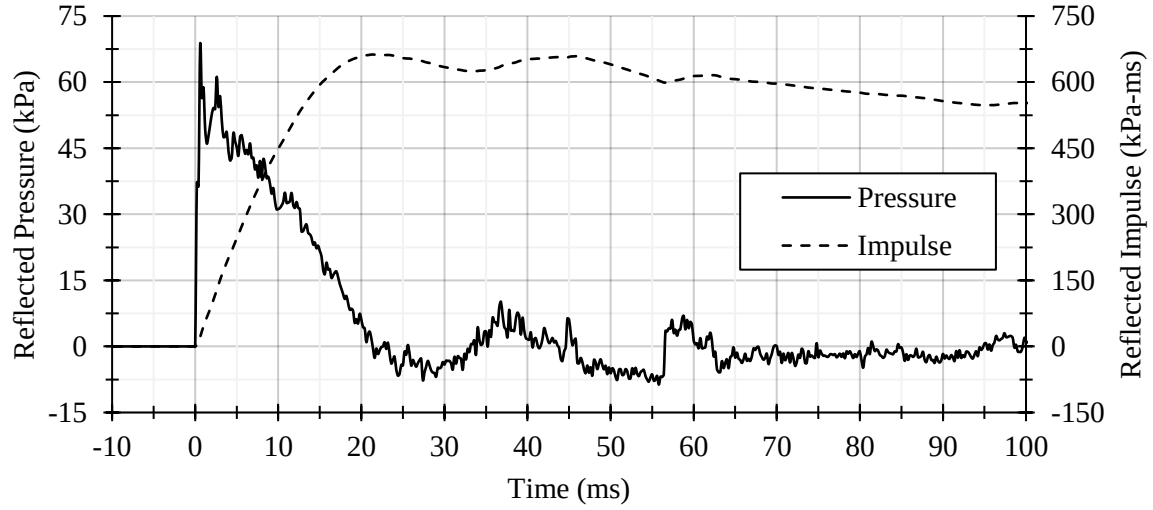


(d) Progression of Complete Failure

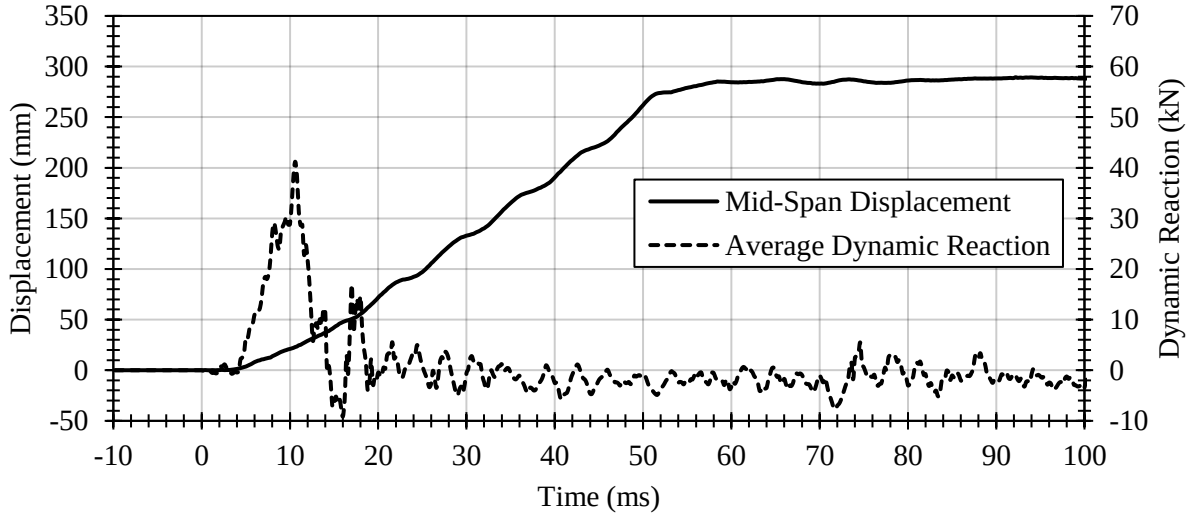
Figure B.6: Documentation of Damage for Specimen CLT3

Specimen CLT4

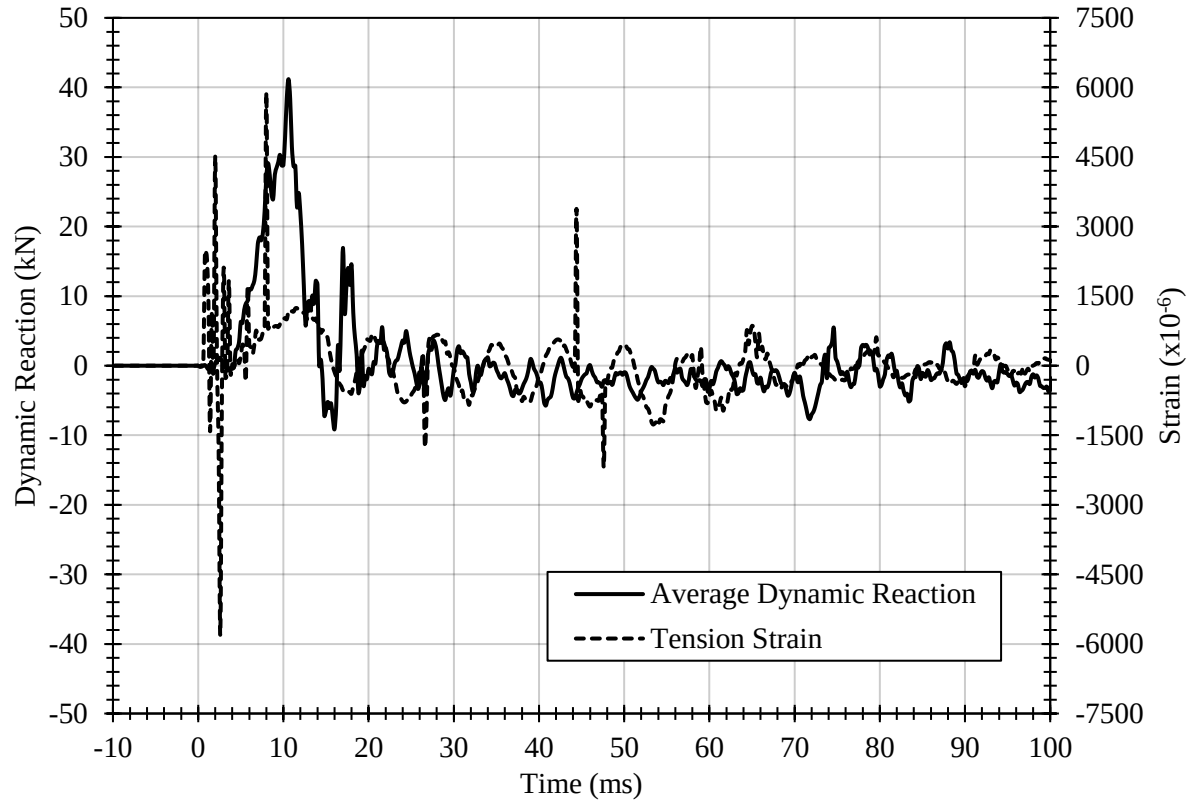
Specimen CLT4, comprised of a CLT panel with a thick angle with three screws at each end, was dynamically tested on December 4th 2018. A driver pressure of 516.4 kPa was used, which resulted in a positive peak reflected pressure and impulse of 68.4 kPa and 662.7 kPa-ms, respectively.



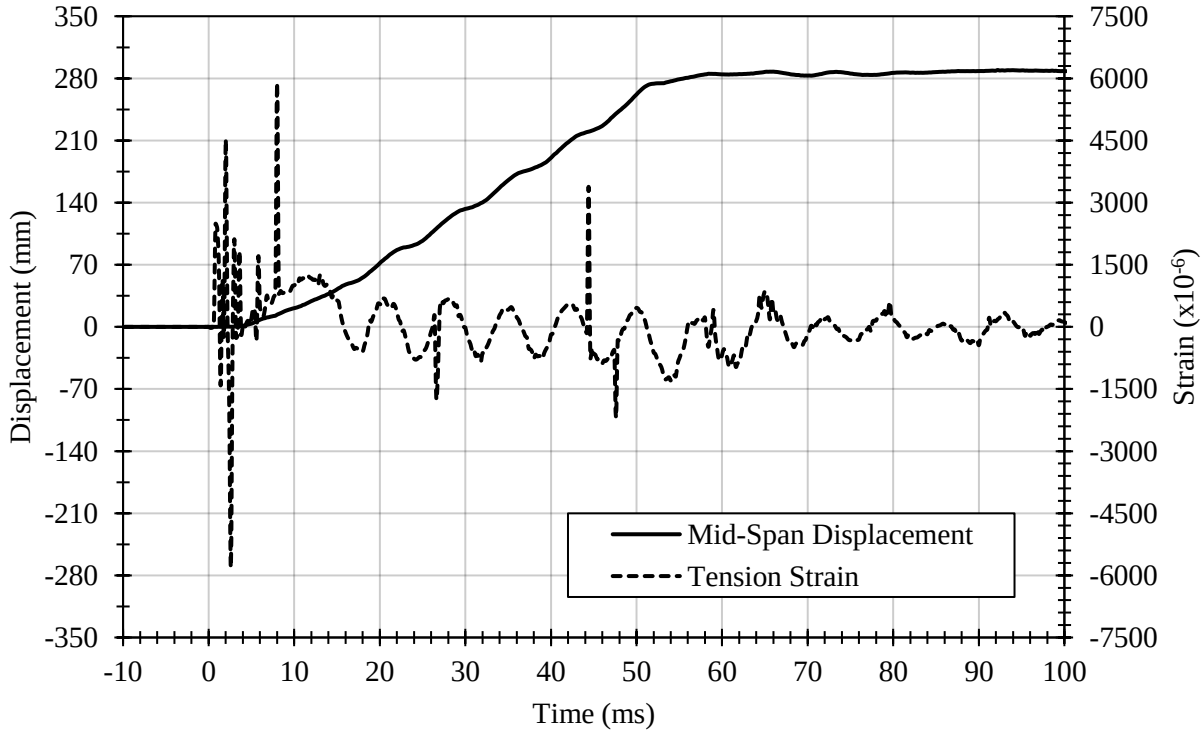
(a) Pressure and Impulse



(b) Reaction and Displacement



(c) Reaction and Strains



(d) Displacement and Strains

Figure B.7: Dynamic Test Results for Specimen CLT4



(a) Specimen Prior to Testing



(b) Specimen After Testing



(c) Screw Failure in Bottom Joint

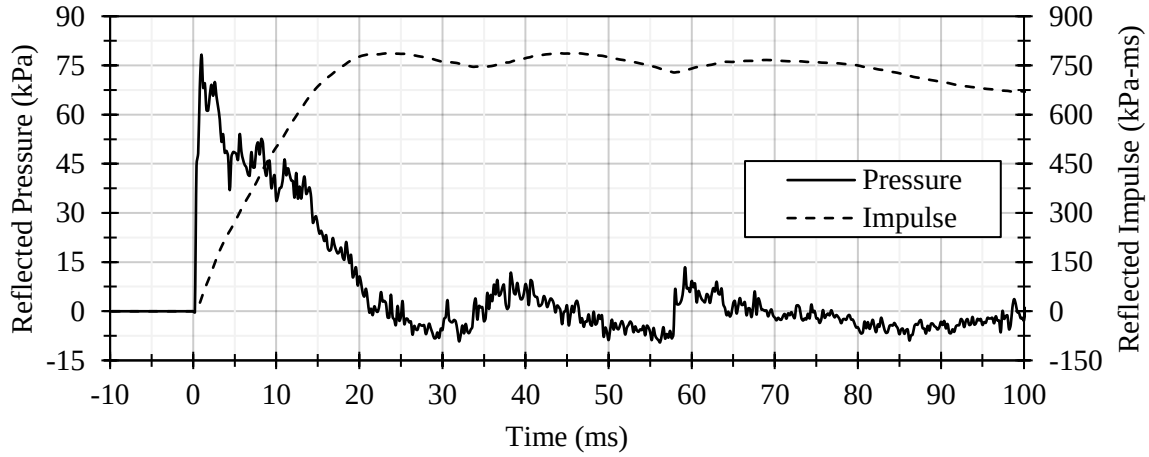


(d) Screw Failure in Top Joint

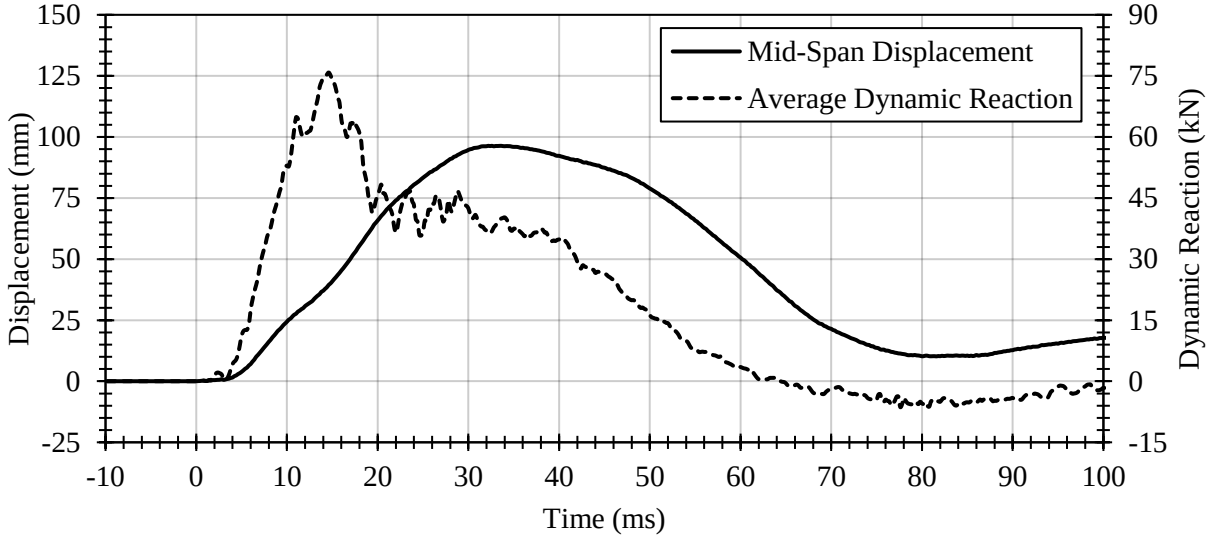
Figure B.8: Documentation of Damage for Specimen CLT4

Specimen CLT5

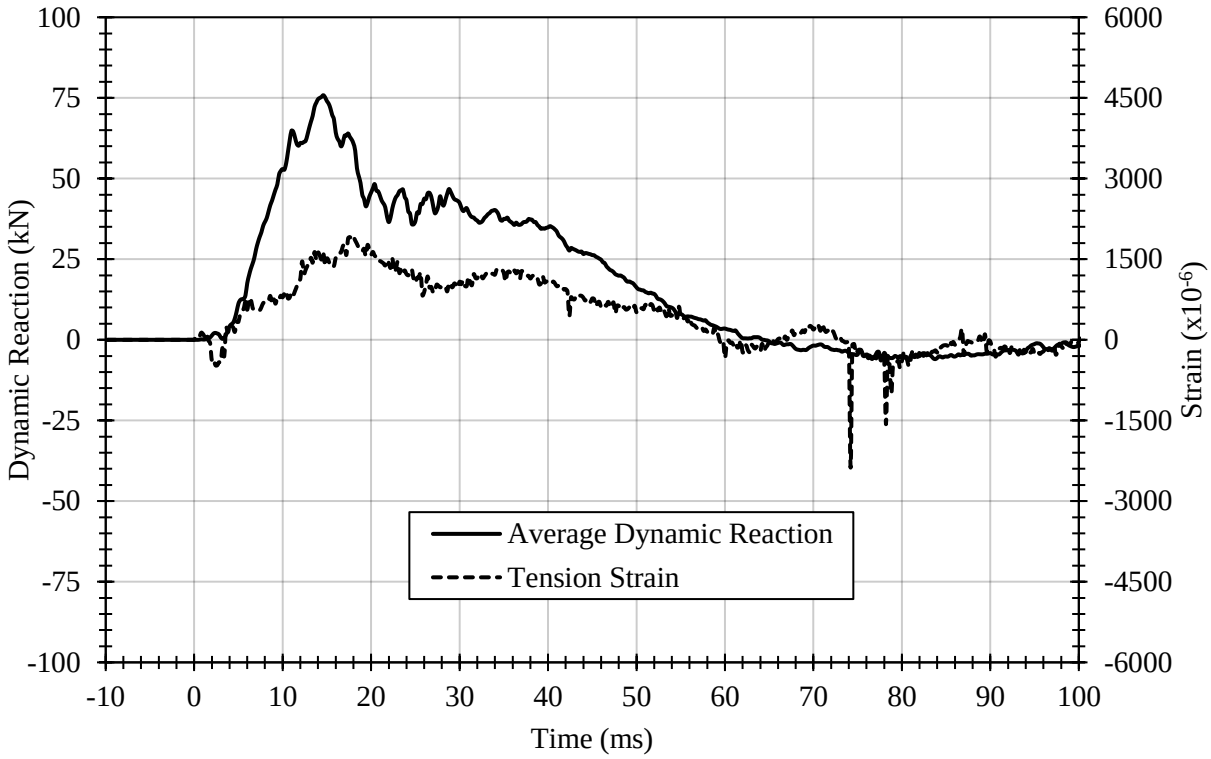
Specimen CLT5, comprised of a CLT panel with a thick angle with six screws at each end, was dynamically tested on December 6th 2018. A driver pressure of 617.8 kPa was used, which resulted in a positive peak reflected pressure and impulse of 78.3 kPa and 787.2 kPa-ms, respectively. An instrumentation error led to the compression-side strain gauge being unreadable



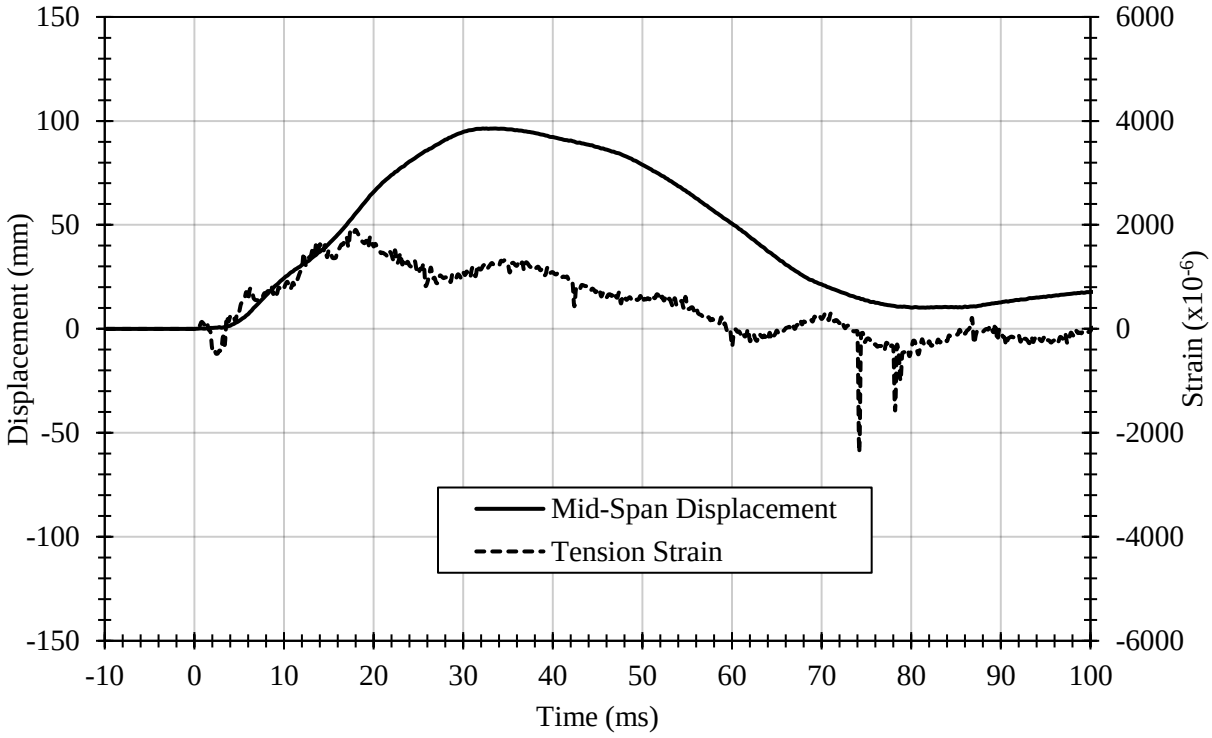
(a) Pressure and Impulse



(b) Reaction and Displacement



(c) Reaction and Strains



(d) Displacement and Strains

Figure B.9: Dynamic Test Results for Specimen CLT5
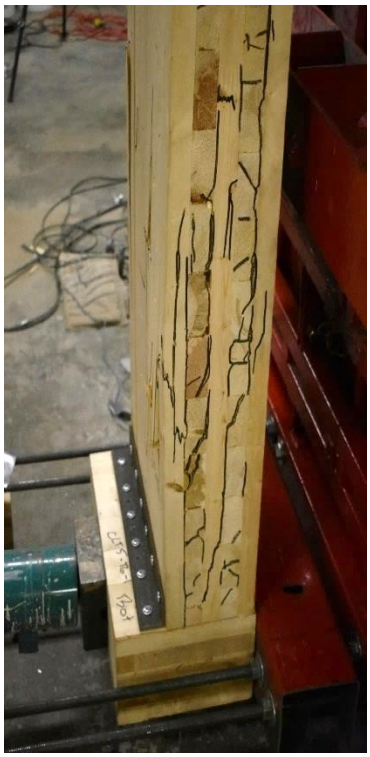


(a) Specimen Prior to Testing



(b) Specimen After Testing



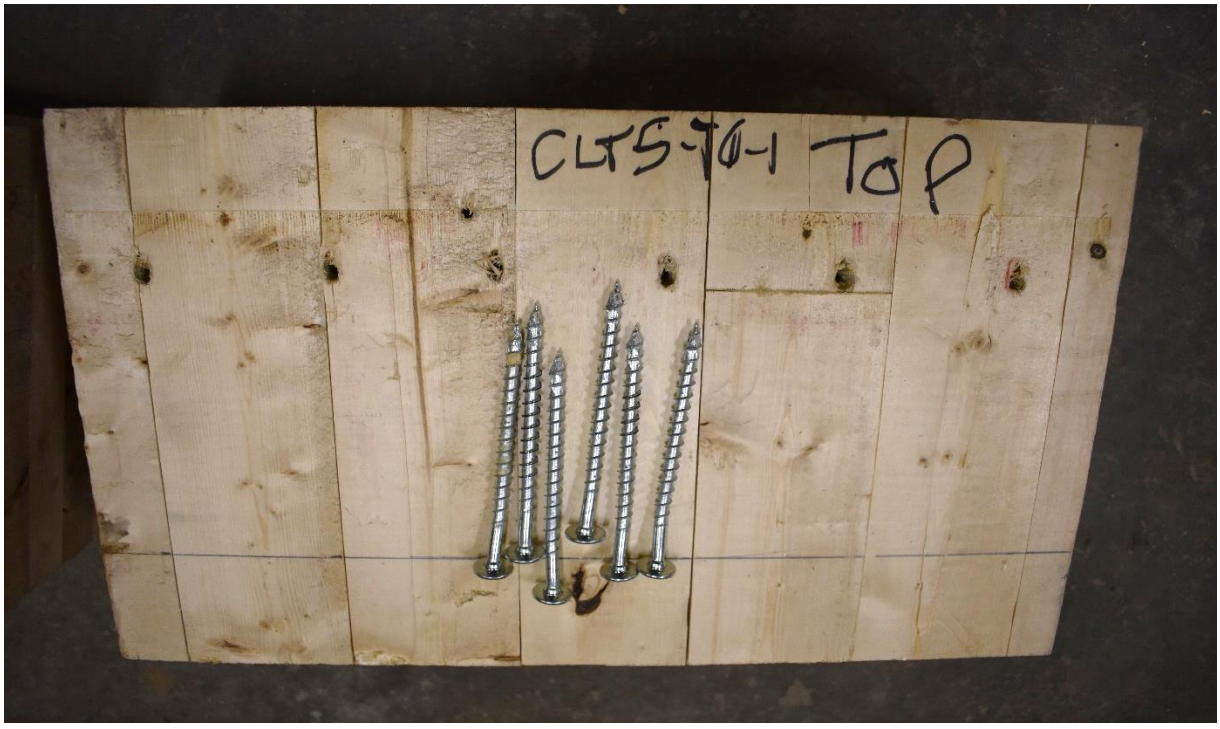
(c) Flexural Failure in Panel



(d) Shear Damage in Lower Half of Panel



(e) Damage in Bottom Joint

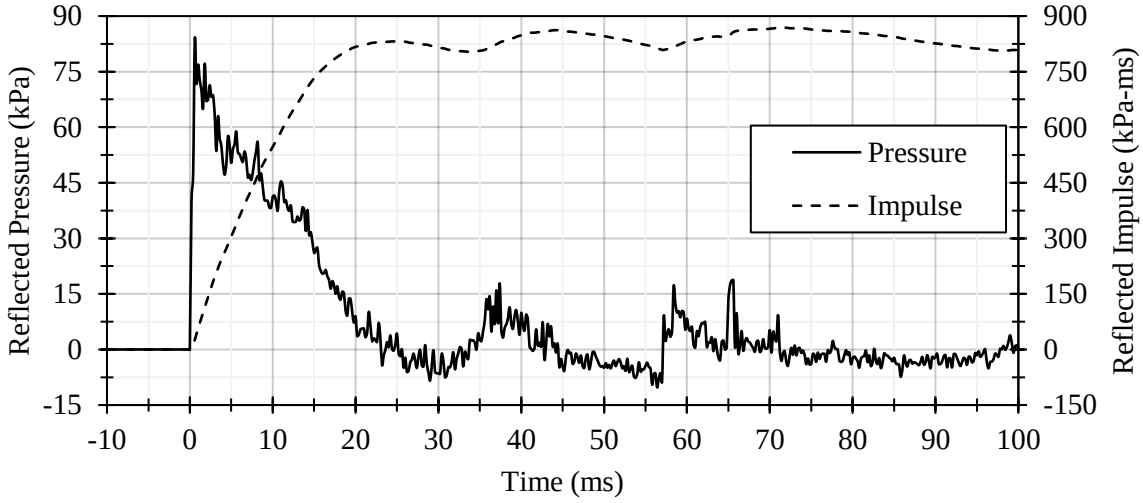


(f) Damage in Top Joint

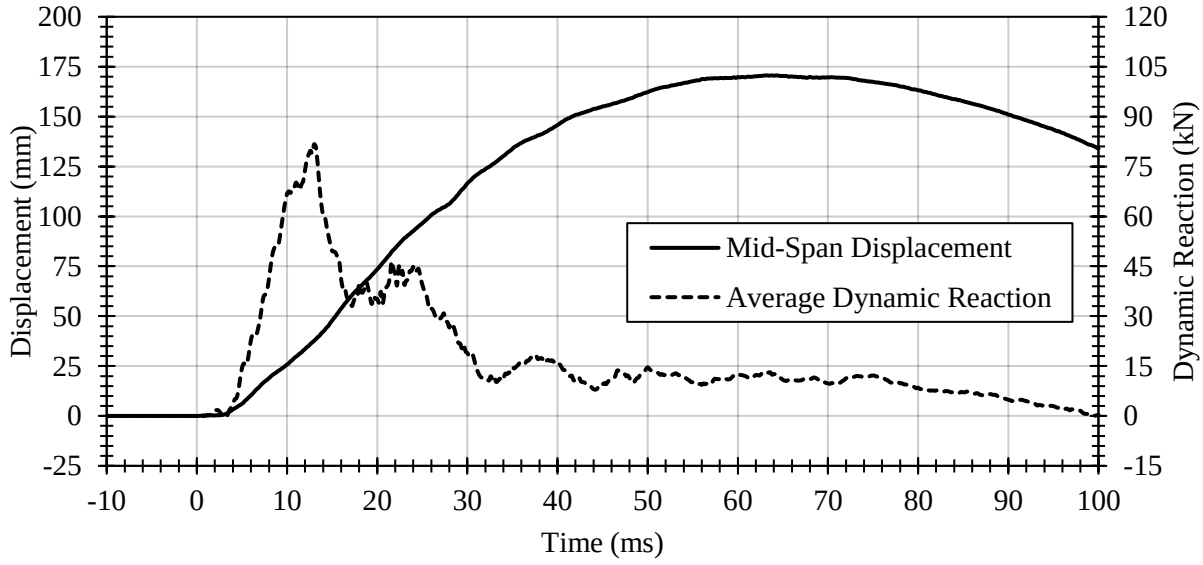
Figure B.10: Documentation of Damage for Specimen CLT5

Specimen CLT6

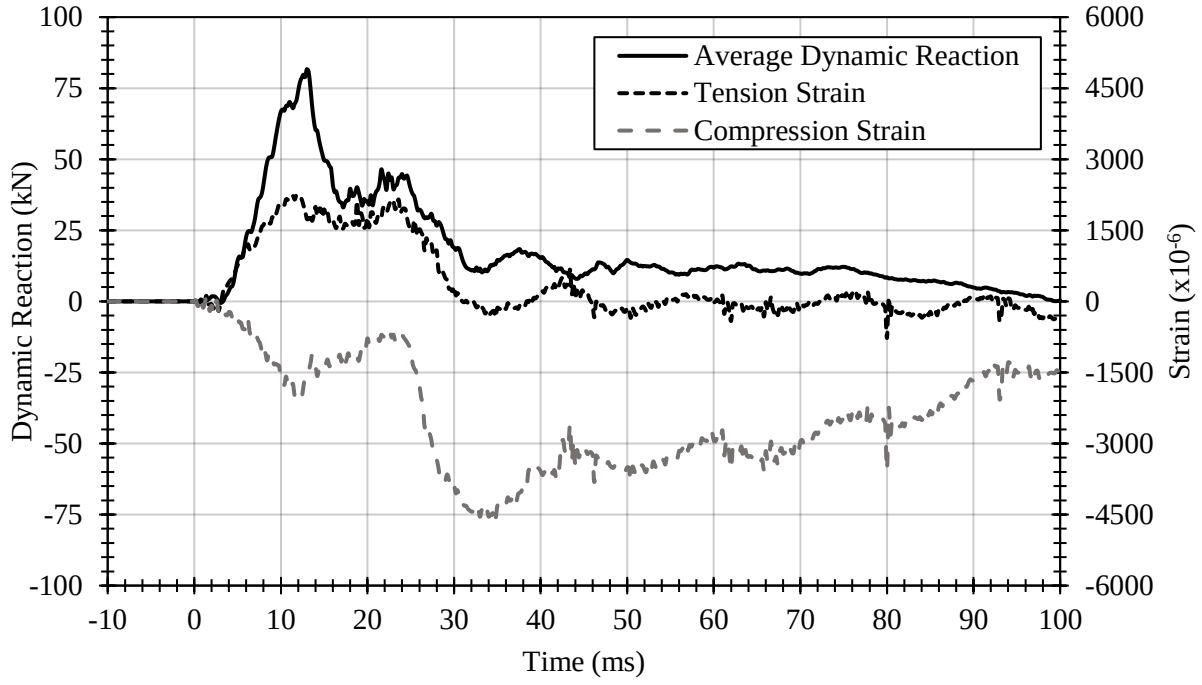
Specimen CLT6, comprised of a CLT panel with a thick angle with nine screws at each end, was dynamically tested on December 7th 2018. A driver pressure of 630.9 kPa was used, which resulted in a positive peak reflected pressure and impulse of 83.6 kPa and 832.5 kPa-ms, respectively.



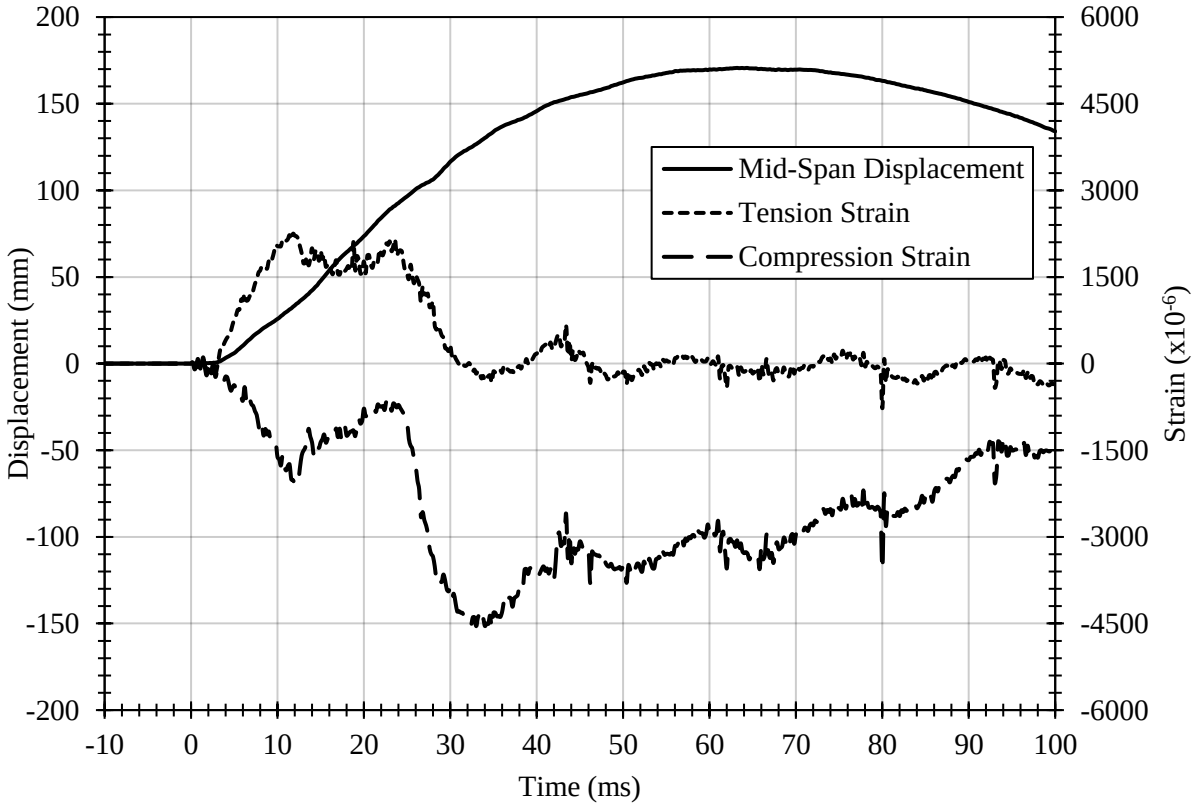
(a) Pressure and Impulse



(b) Reaction and Displacement



(c) Reaction and Strains



(d) Displacement and Strains

Figure B.11: Dynamic Test Results for Specimen CLT6



(a) Specimen Prior to Testing



(b) Specimen After Testing



(c) Flexural Failure in Panel



(d) Failure in Lower Half of Panel

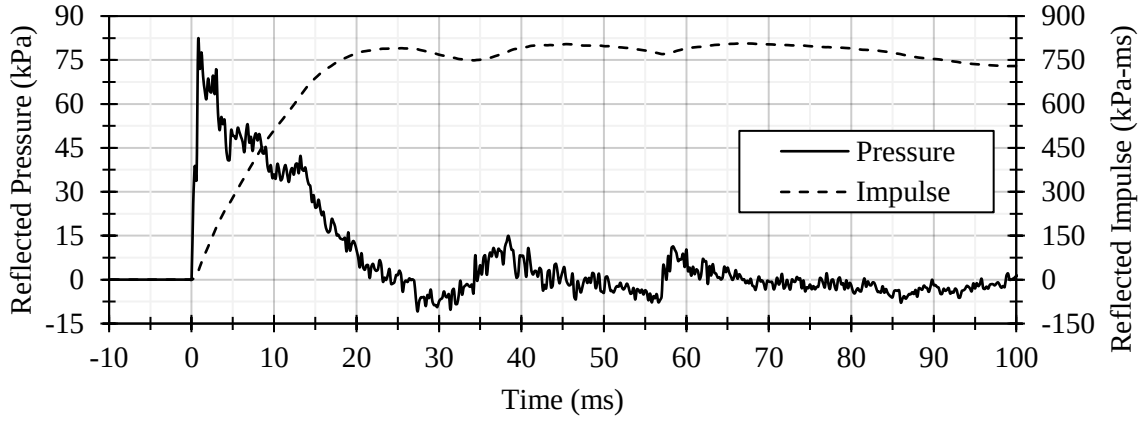


(e) Shear Damage in Specimen

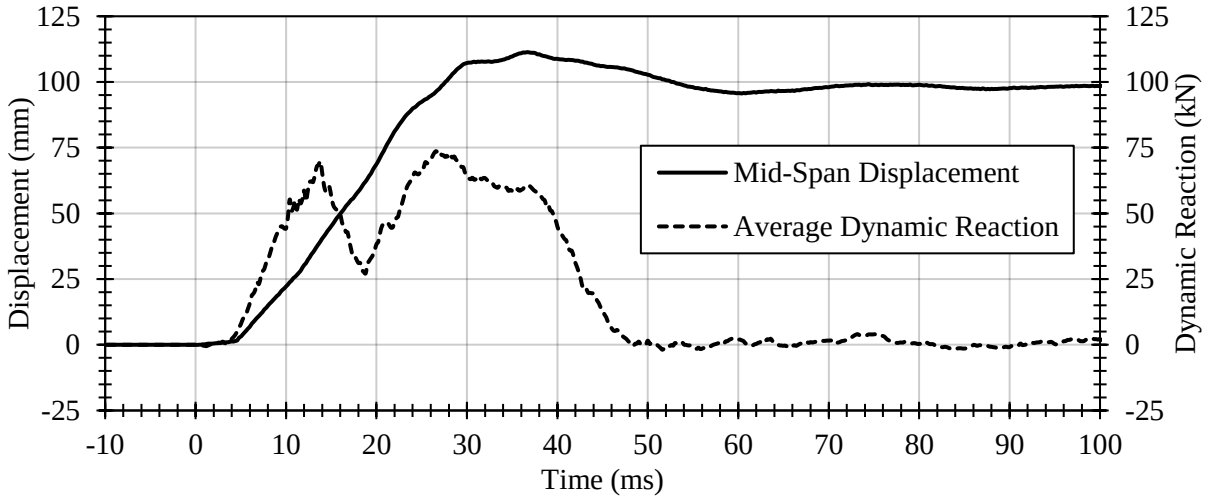
Figure B.12: Documentation of Damage for Specimen CLT6

Specimen CLT7

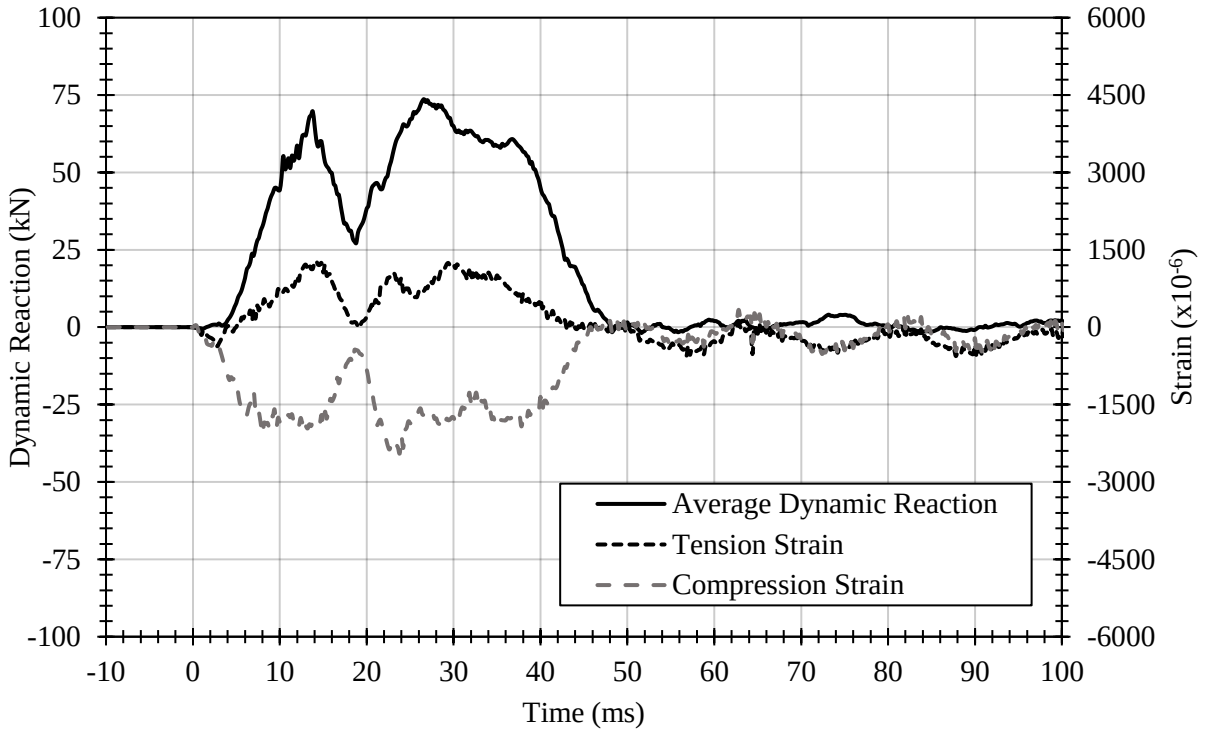
Specimen CLT7, comprised of a CLT panel with two ML24Z angle at each end, was dynamically tested on December 12th 2018. A driver pressure of 630.2 kPa was used, which resulted in a positive peak reflected pressure and impulse of 81.5 kPa and 790.3 kPa-ms, respectively.



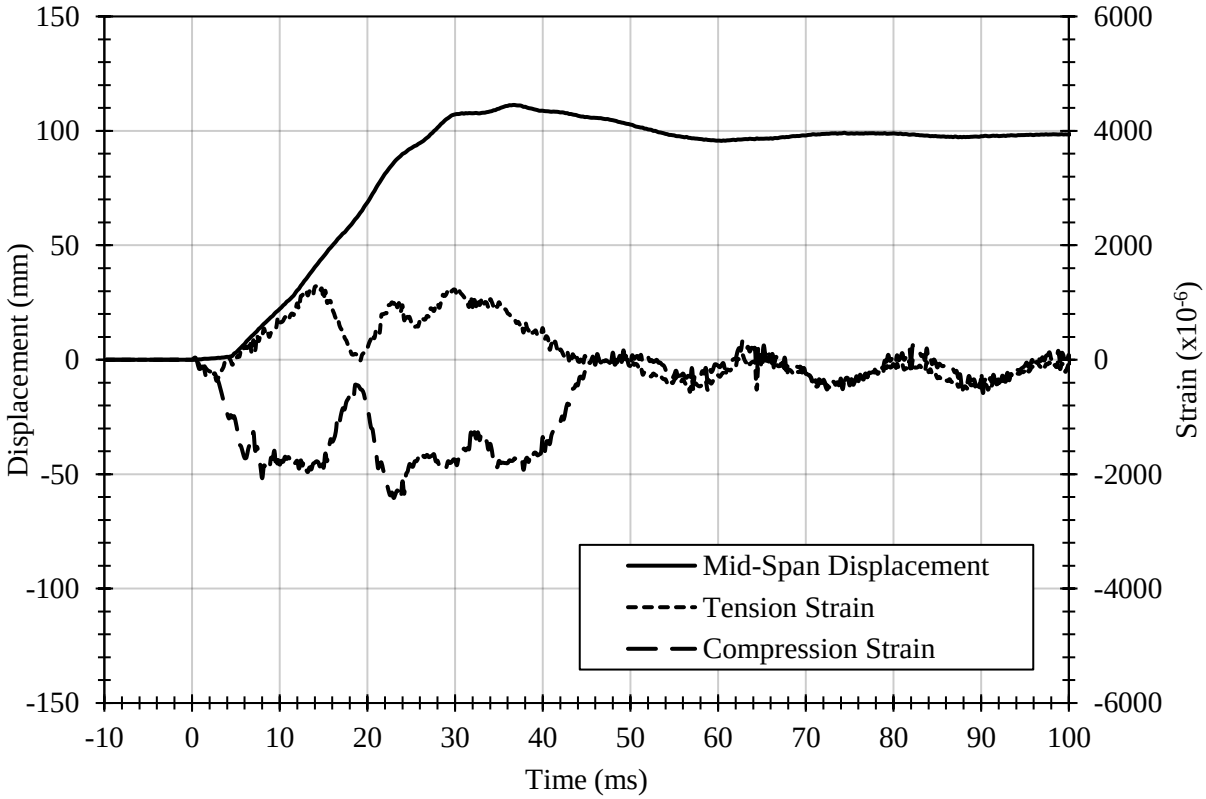
(a) Pressure and Impulse



(b) Reaction and Displacement



(c) Reaction and Strains



(d) Displacement and Strains

Figure B.13: Dynamic Test Results for Specimen CLT7



(a) Specimen Prior to Testing



(b) Specimen After Testing



(c) Damage in Bottom Joint (Still Assembled)



(d) Damage in Top Joint (Still Assembled)



(e) Damage in Bottom Joint

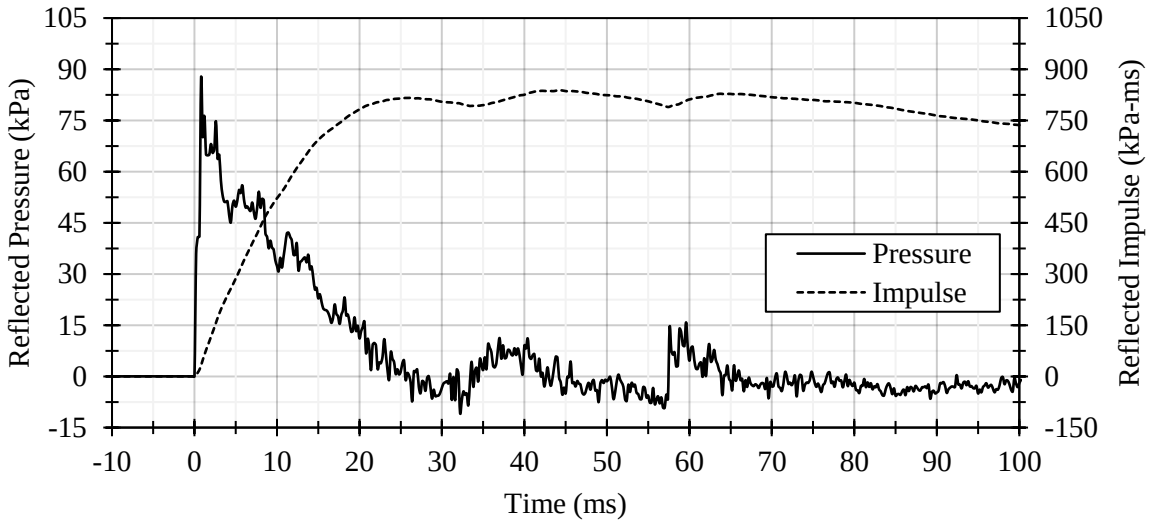


(f) Damage in Top Joint

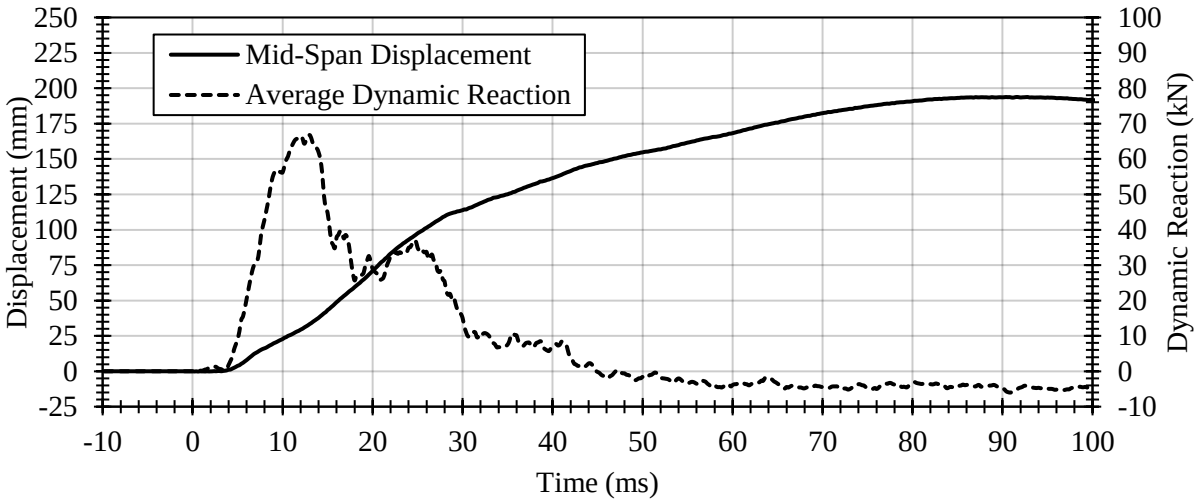
Figure B.14: Documentation of Damage for Specimen CLT7

Specimen CLT8

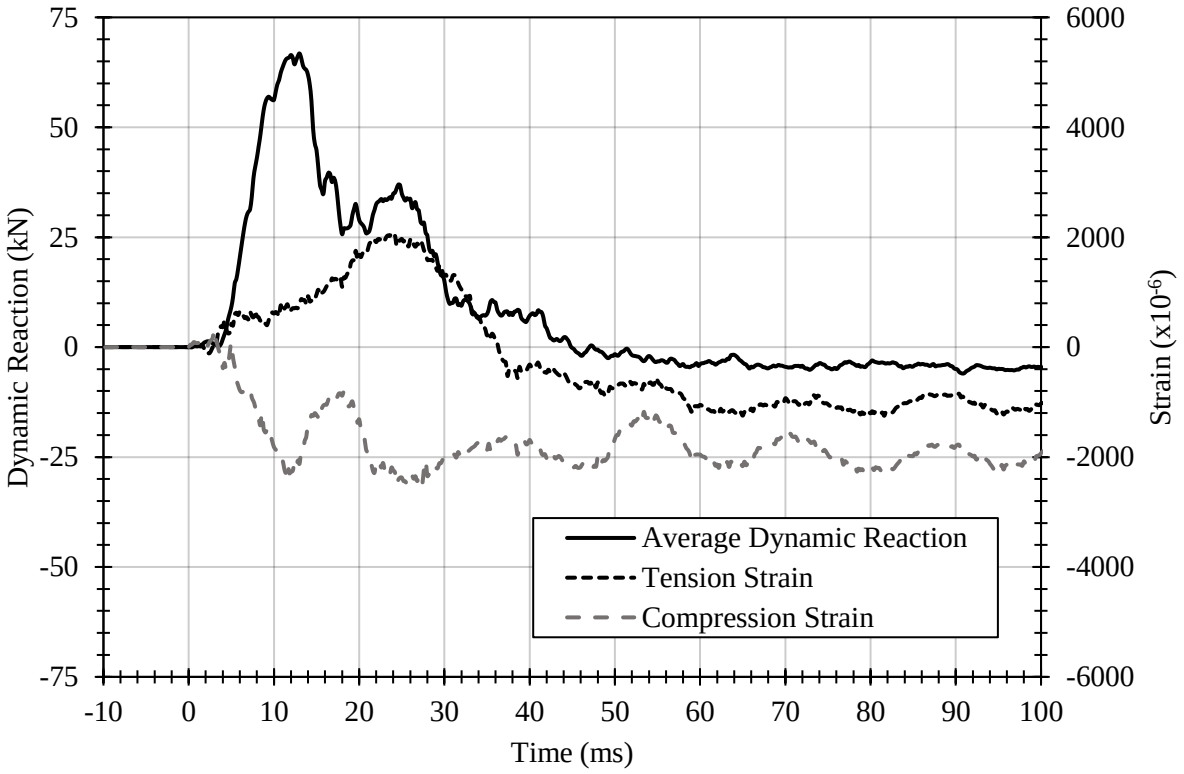
Specimen CLT8, comprised of a CLT panel with three ML24Z angle at each end, was dynamically tested on December 14th 2018. A driver pressure of 626.0 kPa was used, which resulted in a positive peak reflected pressure and impulse of 87.2 kPa and 816.1 kPa-ms, respectively.



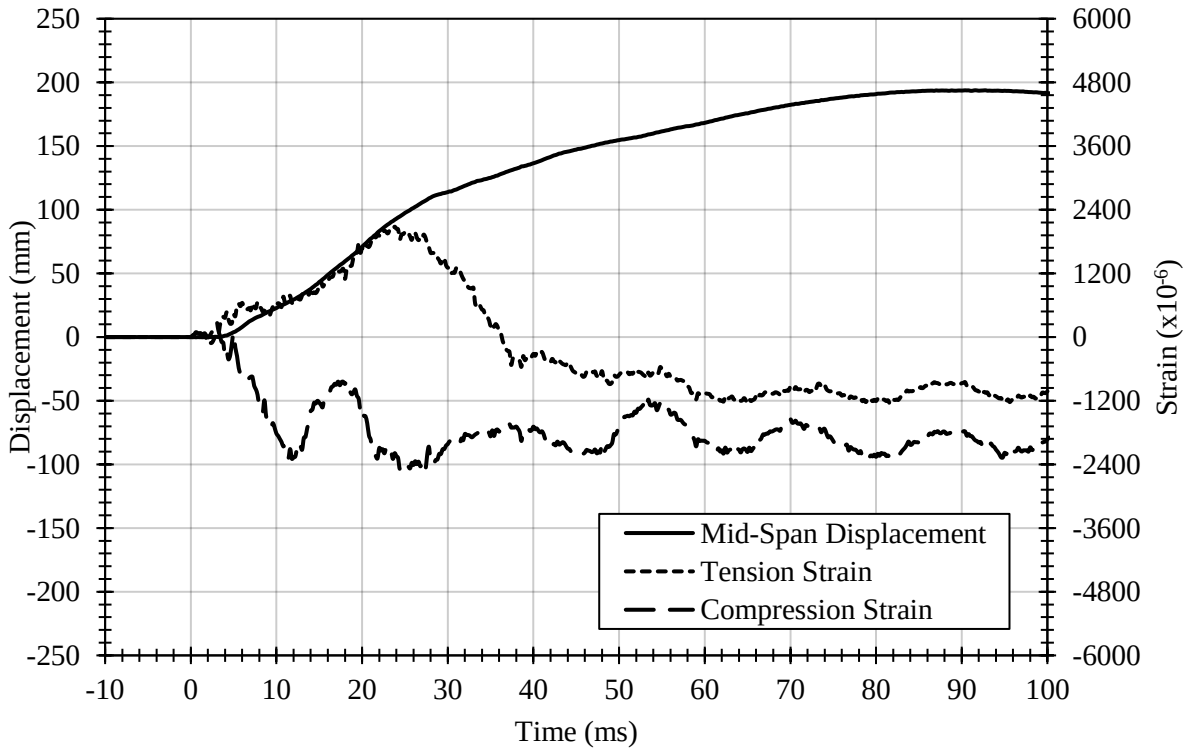
(a) Pressure and Impulse



(b) Reaction and Displacement



(c) Reaction and Strains

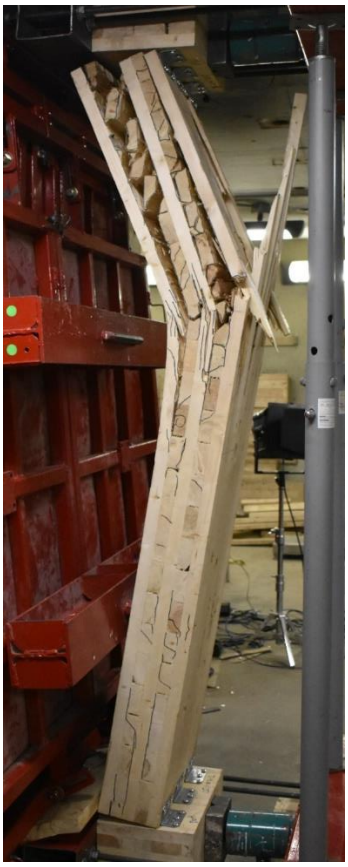


(d) Displacement and Strains

Figure B.15: Dynamic Test Results for Specimen CLT8



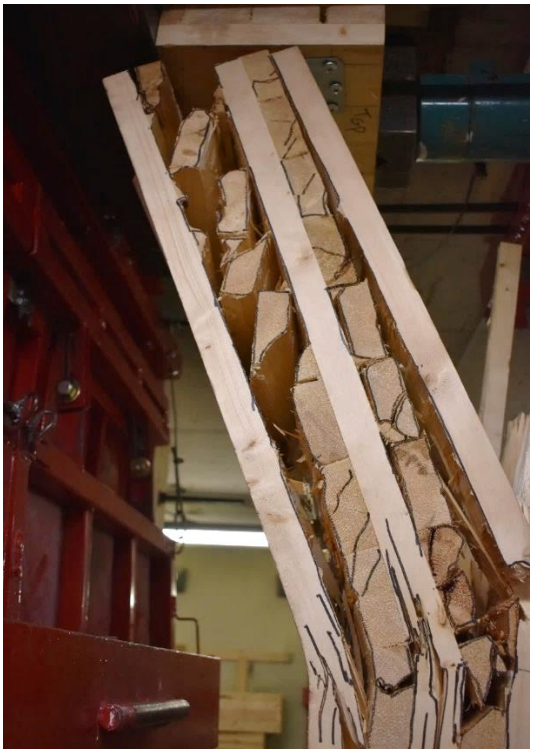
(a) Specimen Prior to Testing



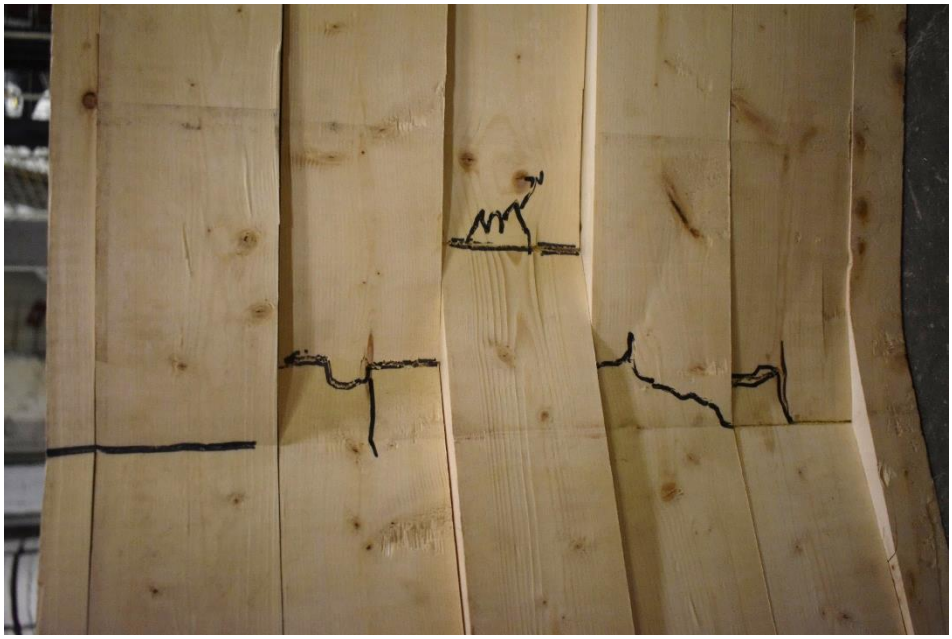
(b) Specimen After Testing



(c) Flexural Failure in Panel



(d) Rolling Shear Damage



(e) Compression-Side Failure

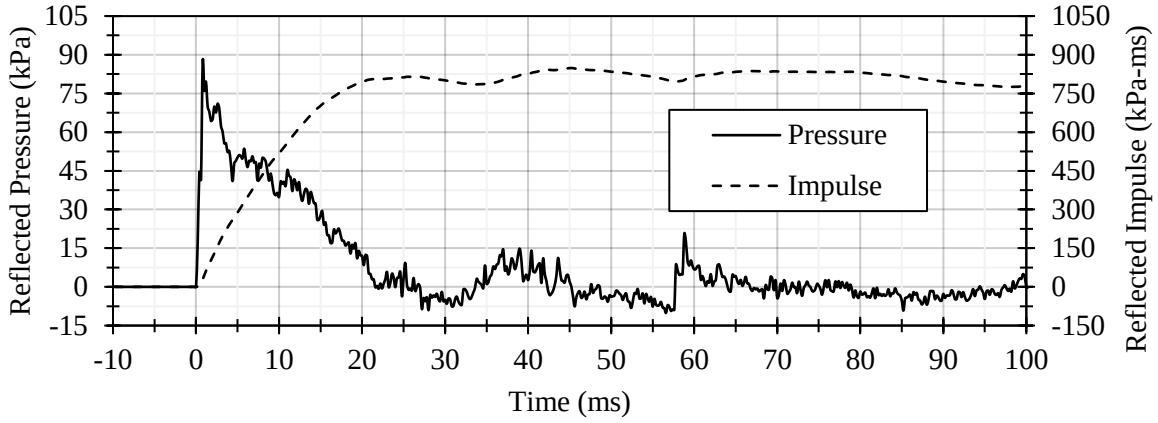


(f) Shear Damage in Top Joint

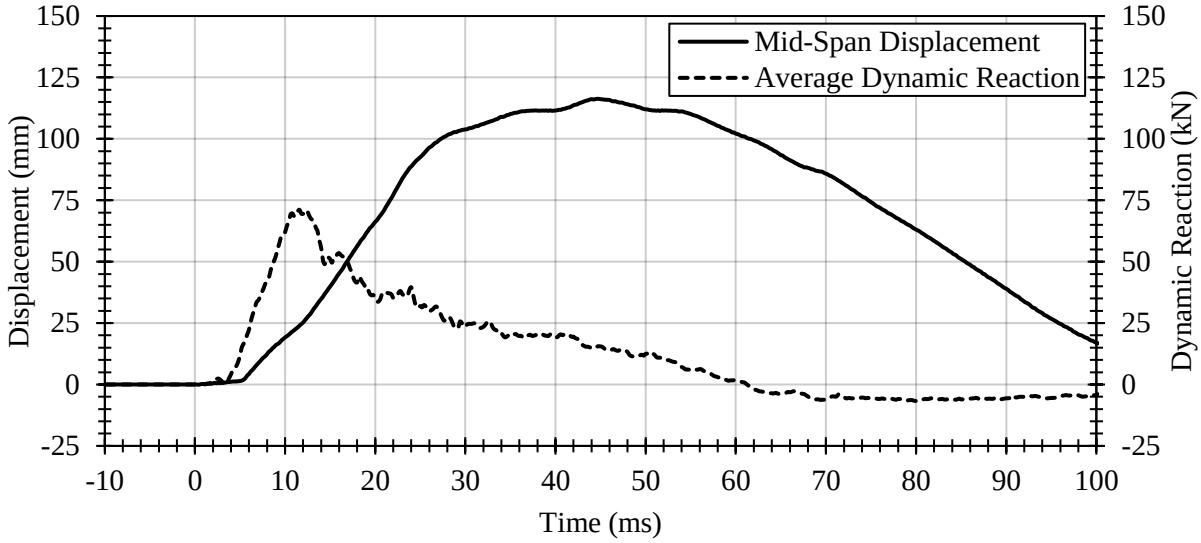
Figure B.16: Documentation of Damage for Specimen CLT8

Specimen CLT9

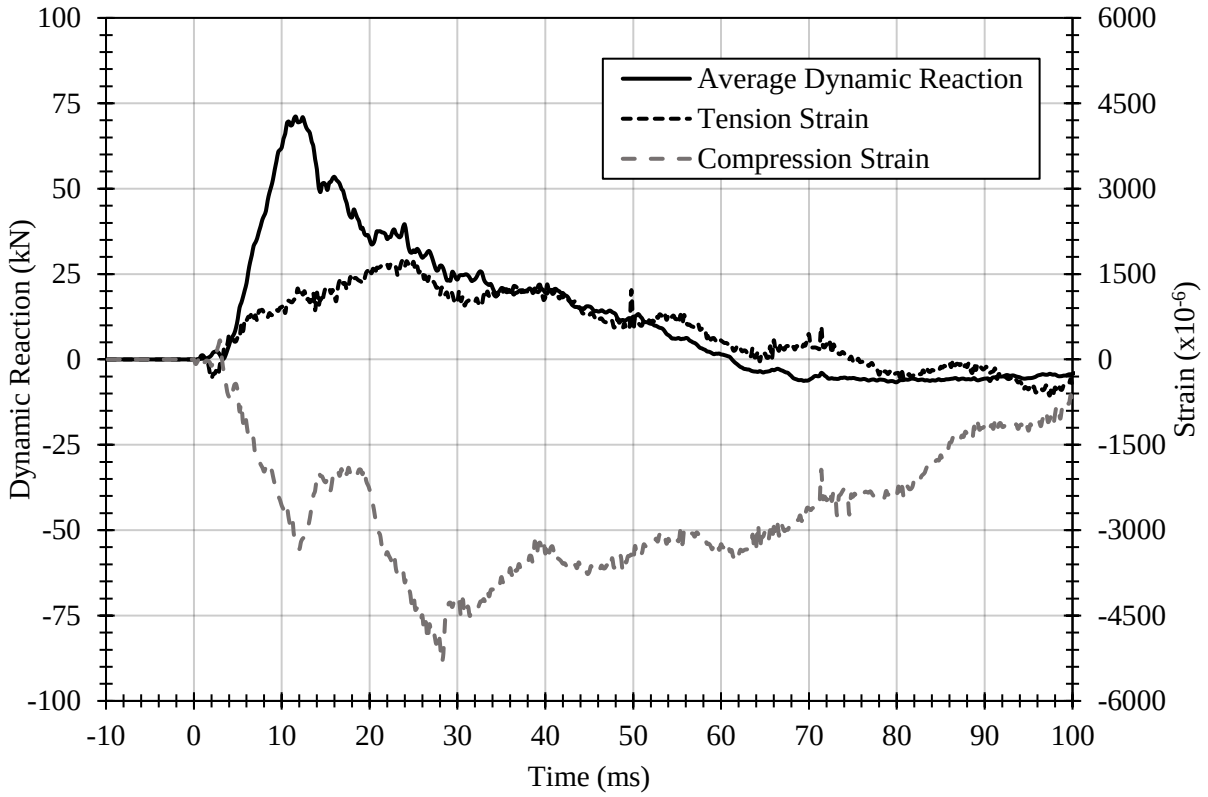
Specimen CLT9, comprised of a CLT panel with four ML24Z angle at each end, was dynamically tested on December 13th 2018. A driver pressure of 629.5 kPa was used, which resulted in a positive peak reflected pressure and impulse of 87.2 kPa and 814.6 kPa-ms, respectively.



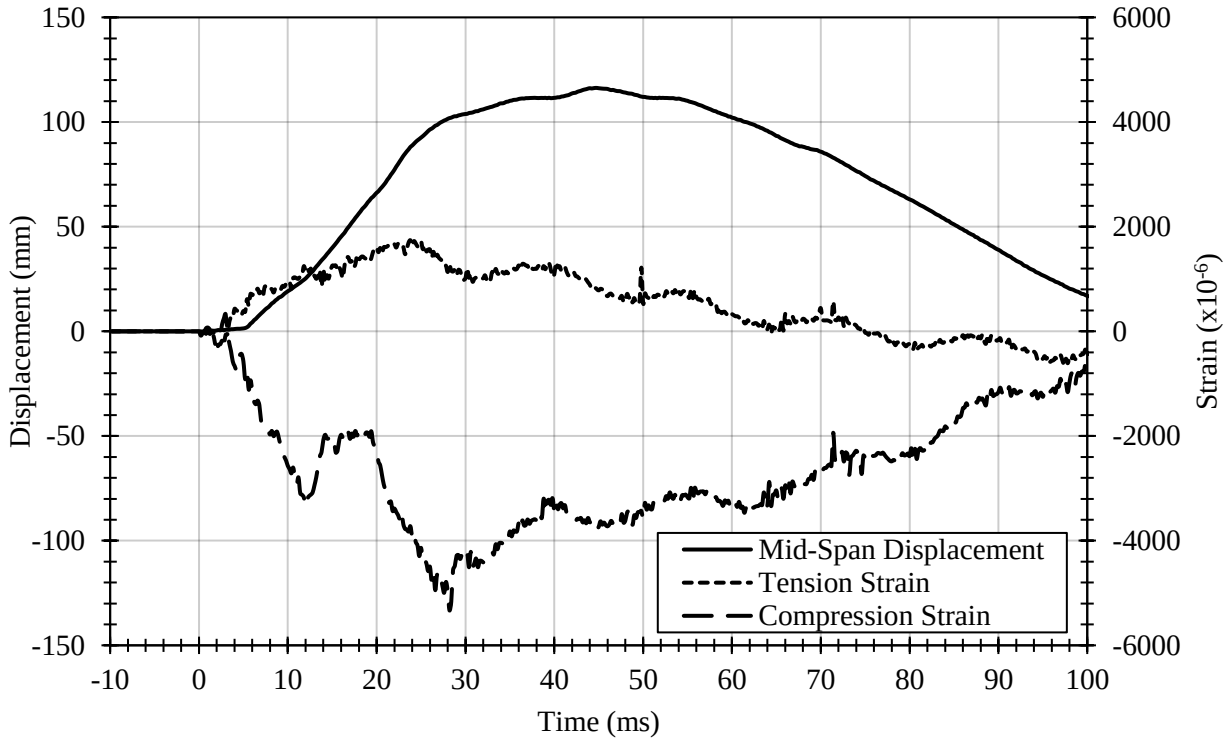
(a) Pressure and Impulse



(b) Reaction and Displacement



(c) Reaction and Strains



(d) Displacement and Strains

Figure B.17: Dynamic Test Results for Specimen CLT9



(a) Specimen Prior to Testing



(b) Specimen After Testing

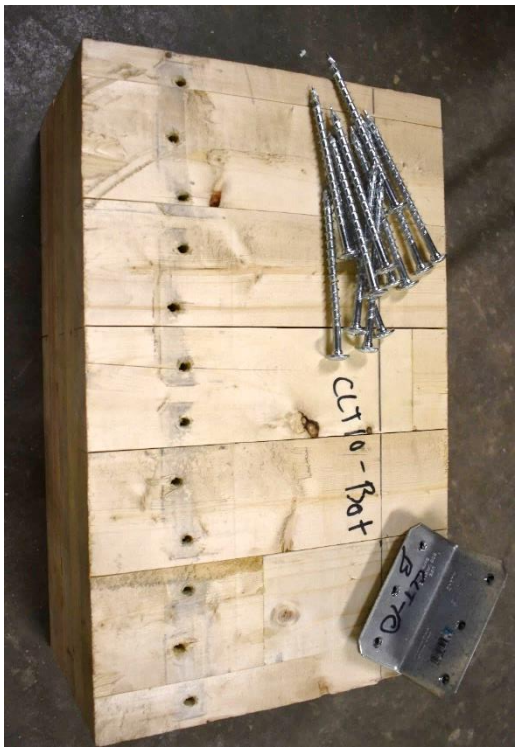


(c) Flexural Failure in Panel



(d) Shear Damage in Top Half of Panel





(e) Minor Damage in Bottom Joint



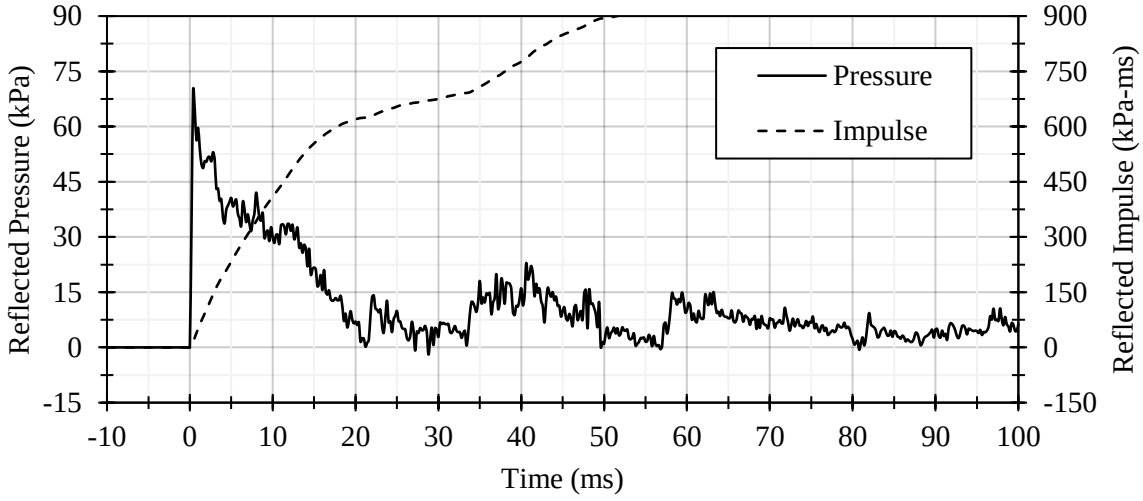


(f) Connection and Shear Damage in Top Joint

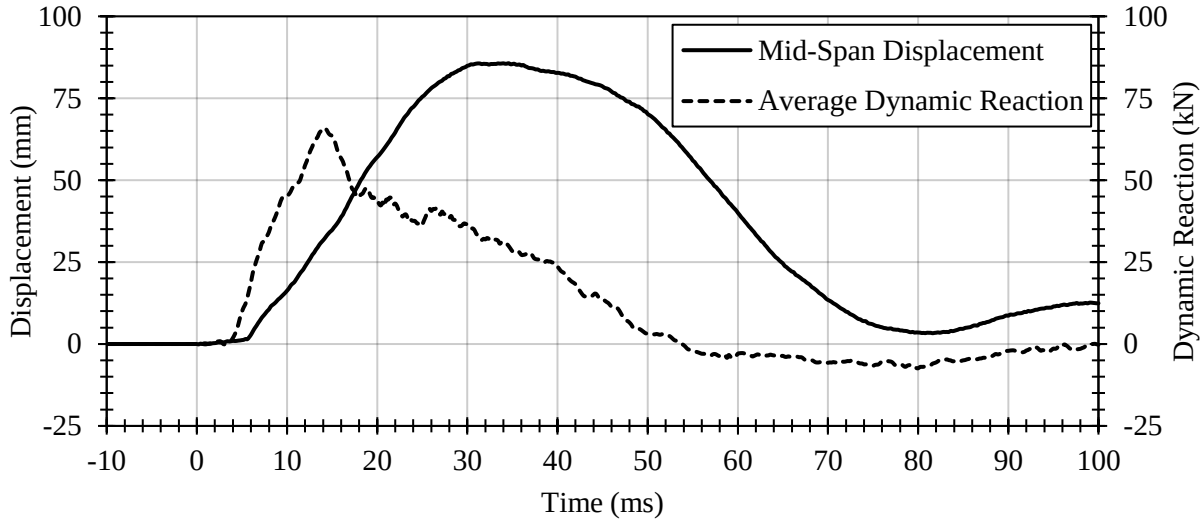
Figure B.18: Documentation of Damage for Specimen CLT9

Specimen CLT10

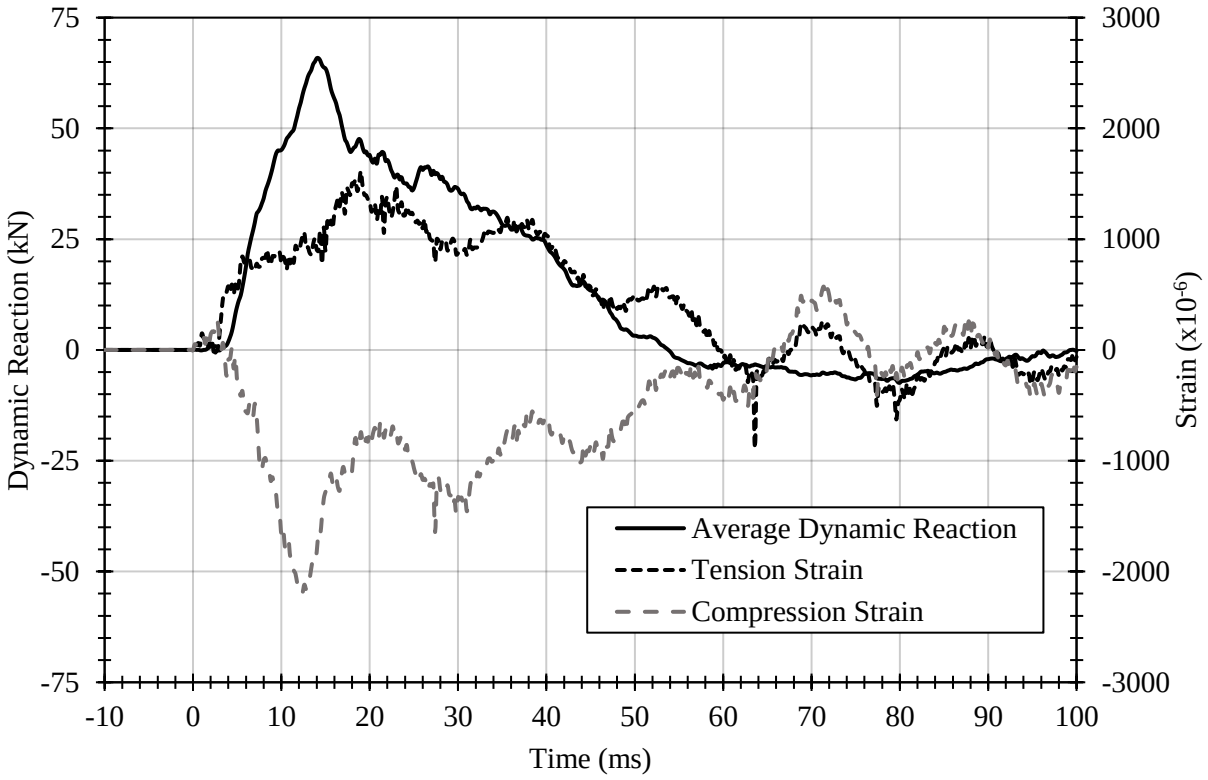
Specimen CLT10, comprised of a CLT panel with two ML24Z angle at each end, was dynamically tested on December 10th 2018. A driver pressure of 617.8 kPa was used, which resulted in a positive peak reflected pressure and impulse of 69.8 kPa and 624.6 kPa-ms, respectively.



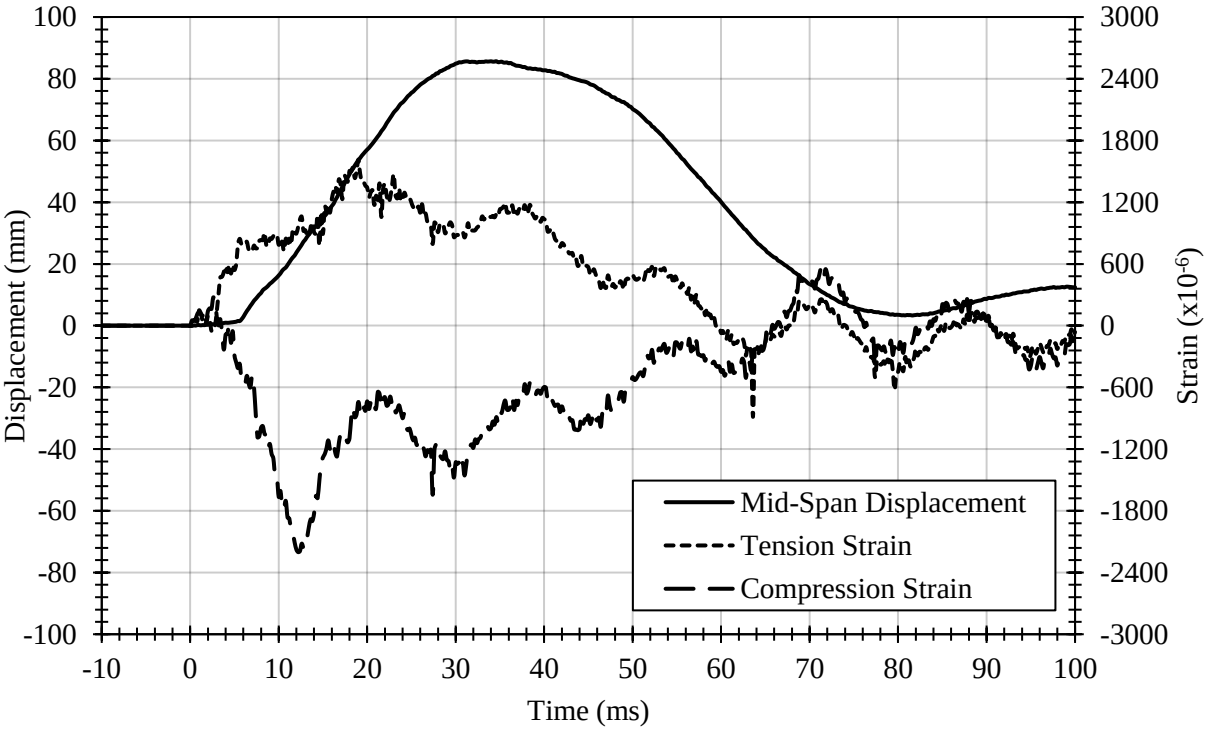
(a) Pressure and Impulse



(b) Reaction and Displacement

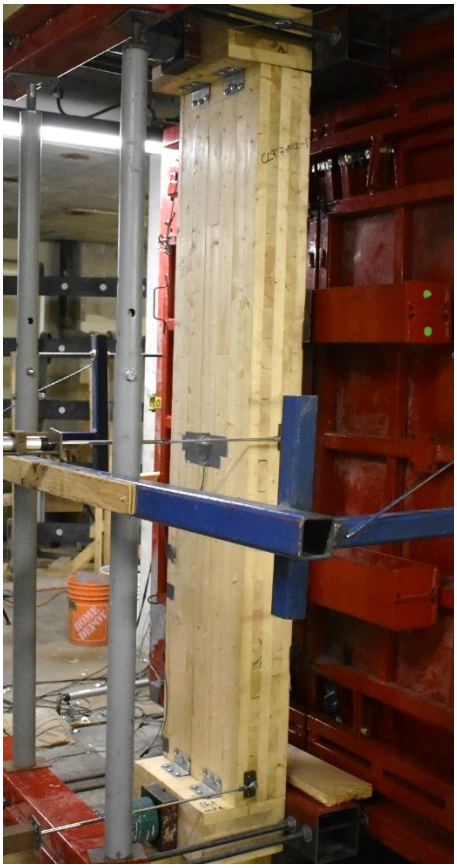


(c) Reaction and Strains



(d) Displacement and Strains

Figure B.19: Dynamic Test Results for Specimen CLT10



(a) Specimen Prior to Testing



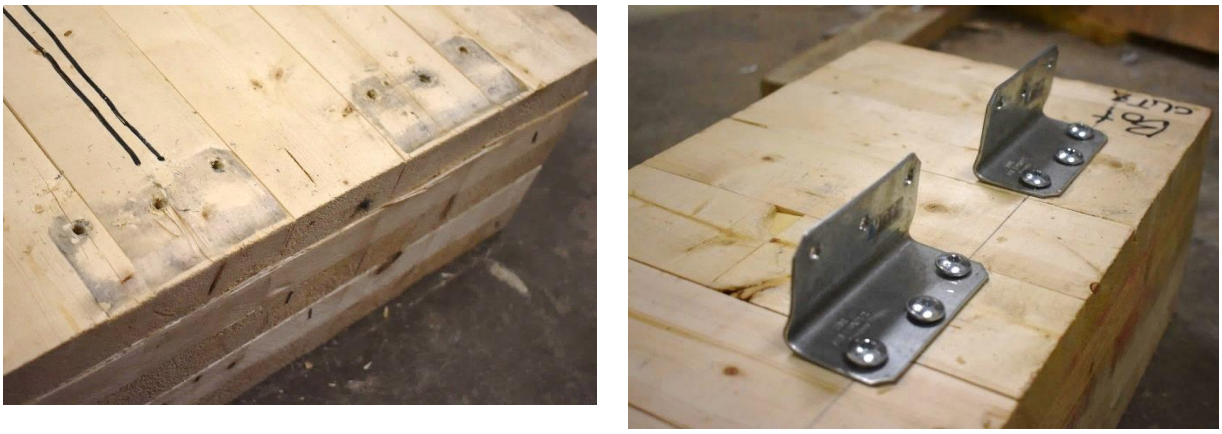
(b) Specimen After Testing



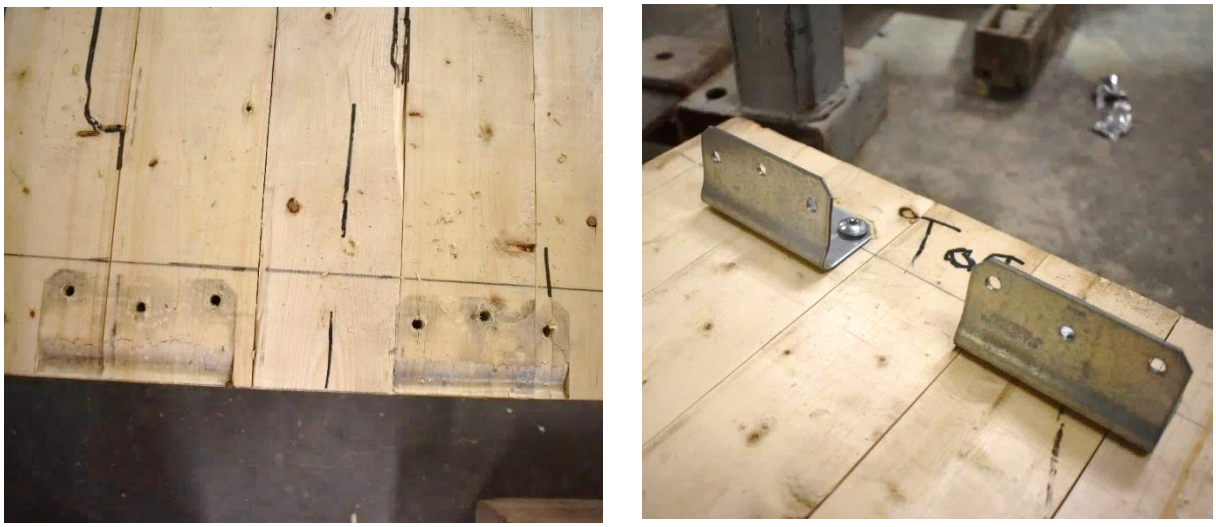
(c) Flexural Damage in Panel



(d) Shear Damage in Top Half of Panel



(e) Damage in Bottom Joint

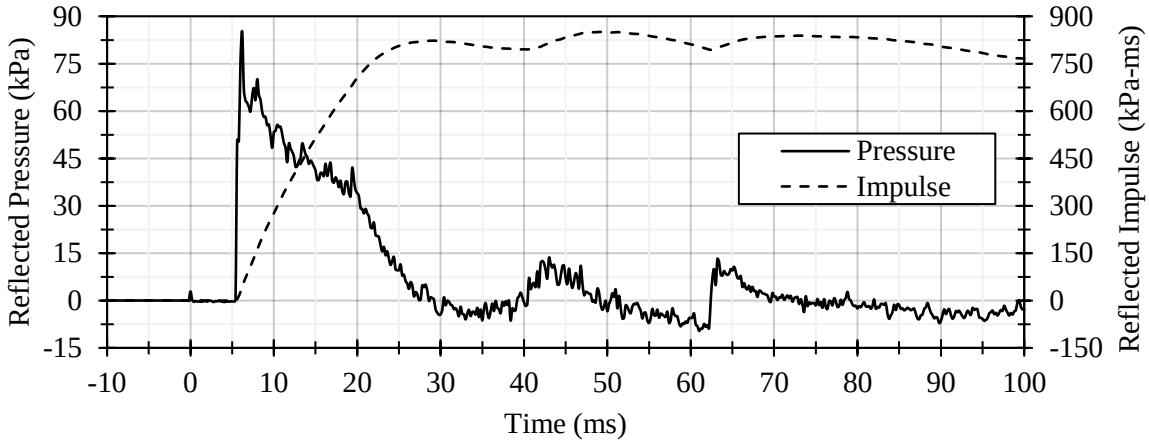


(f) Damage in Top Joint

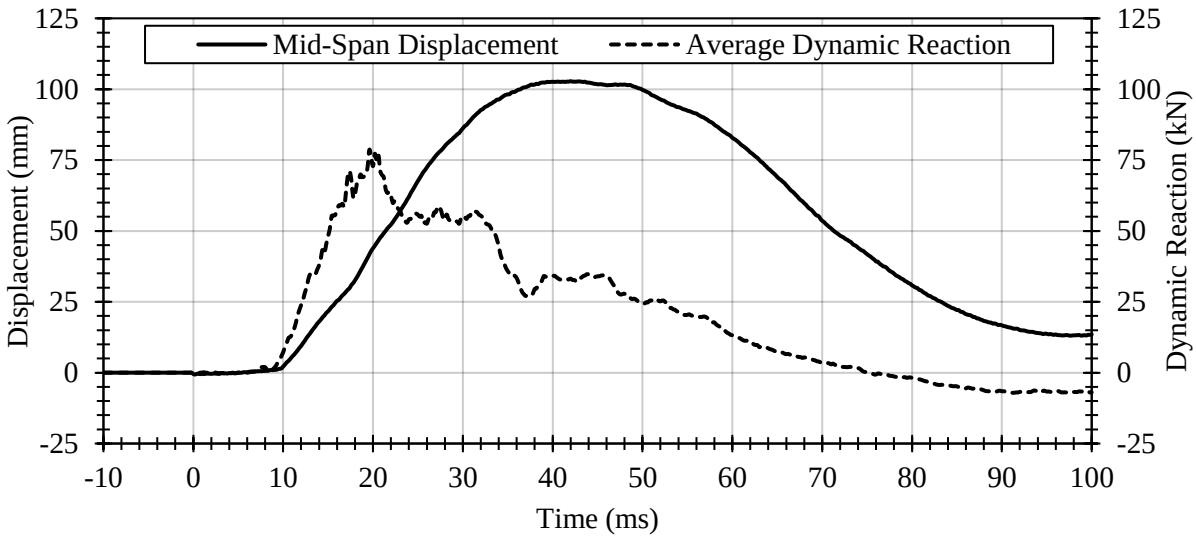
Figure B.20: Documentation of Damage for Specimen CLT10

Specimen CLT11

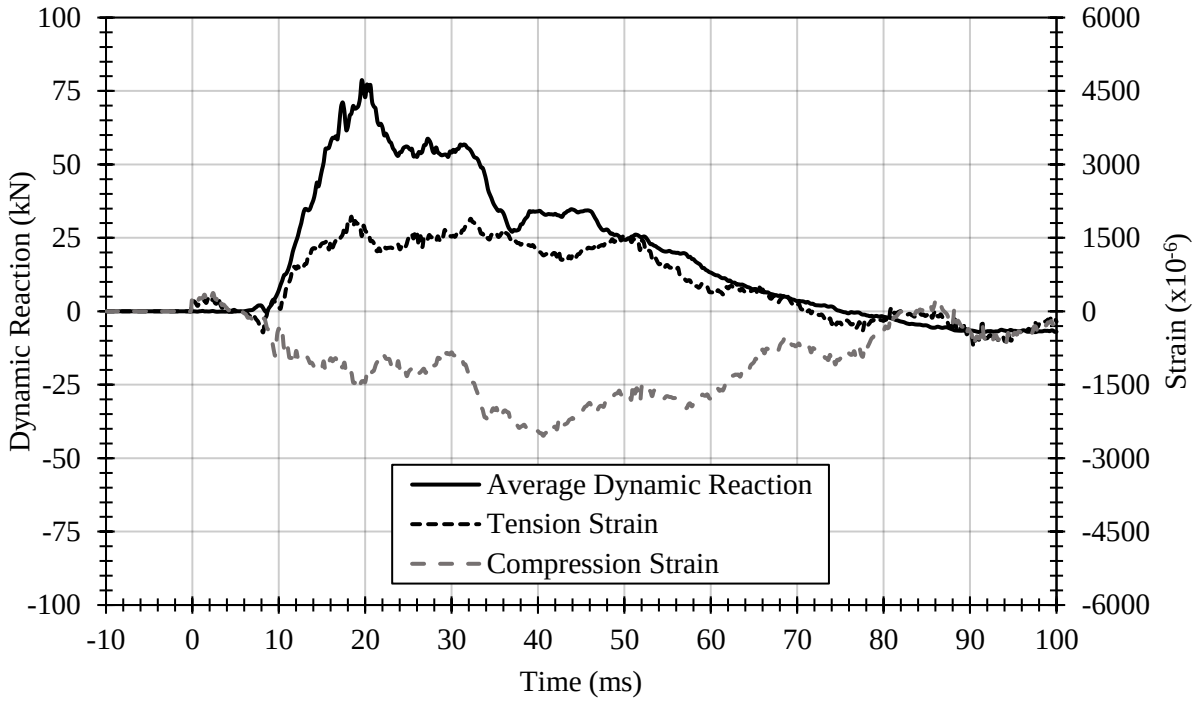
Specimen CLT11, comprised of a CLT panel with three ML24Z angle at each end, was dynamically tested on December 11th 2018. A driver pressure of 631.6 kPa was used, which resulted in a positive peak reflected pressure and impulse of 85.2 kPa and 822.8 kPa-ms, respectively.



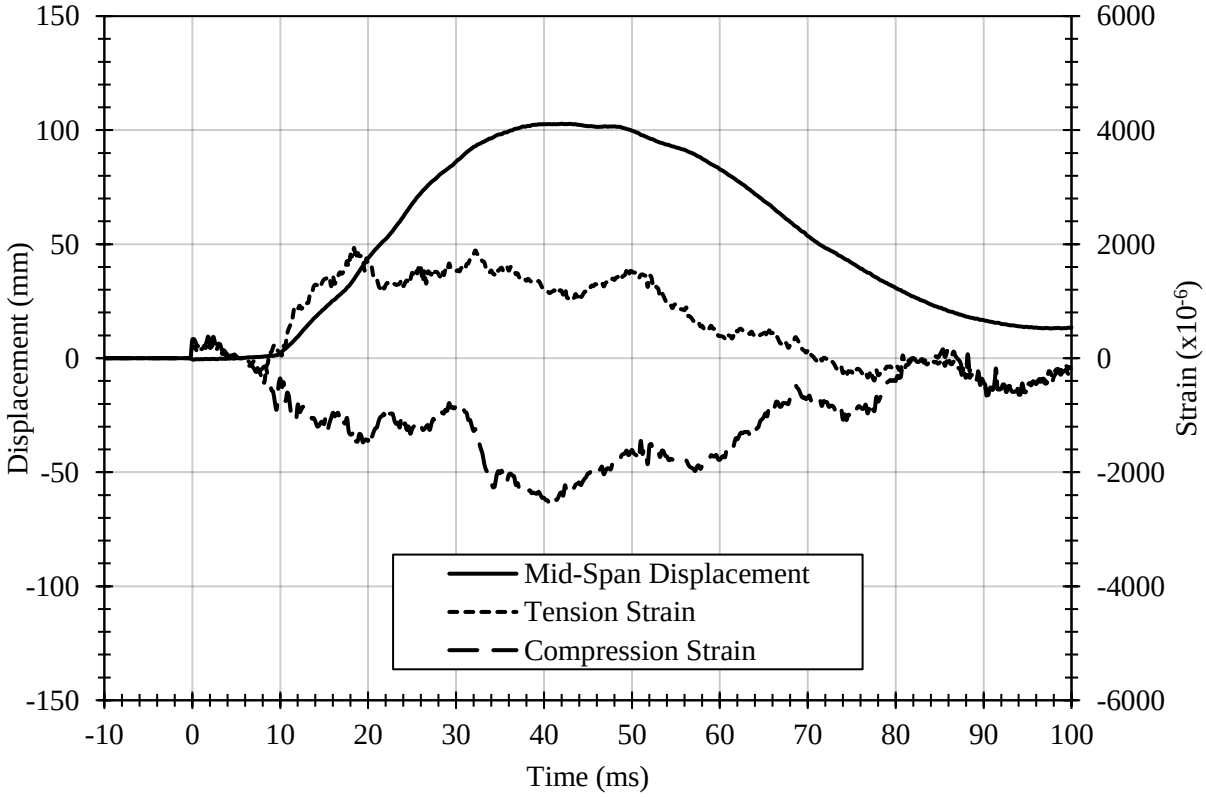
(a) Pressure and Impulse



(b) Reaction and Displacement

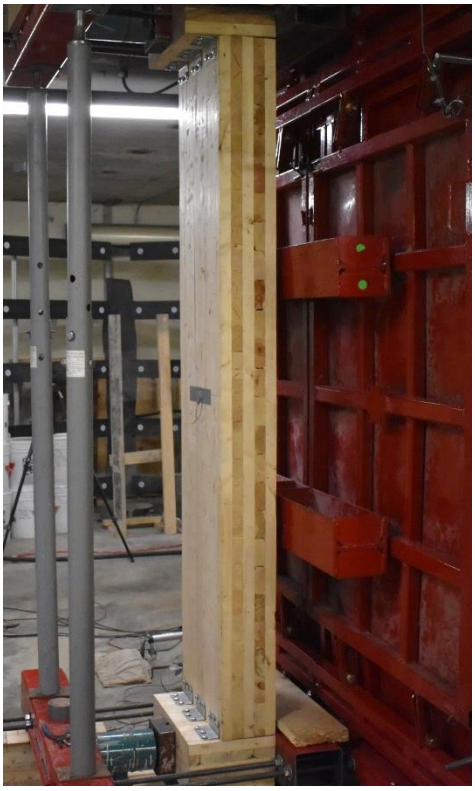


(c) Reaction and Strains

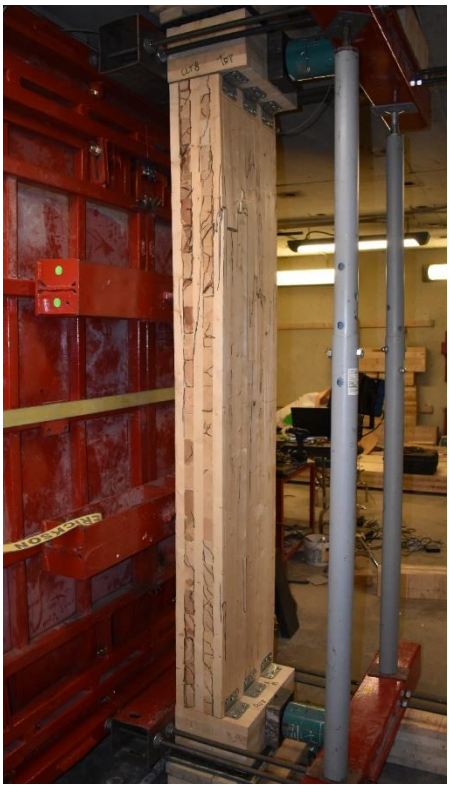


(d) Displacement and Strains

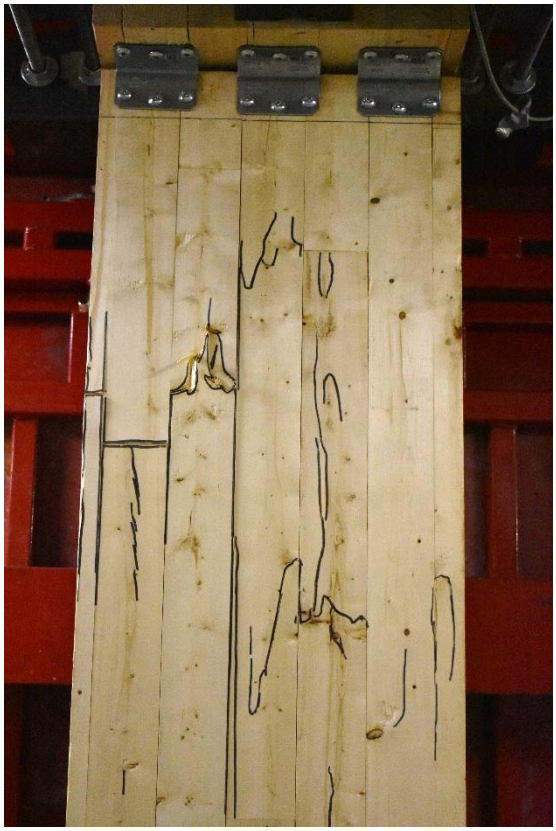
Figure B.21: Dynamic Test Results for Specimen CLT11



(a) Specimen Prior to Testing



(b) Specimen After Testing



(c) Flexural Failure in Panel



(d) Shear Damage in Top Half of Panel





(e) Damage in Bottom Joint



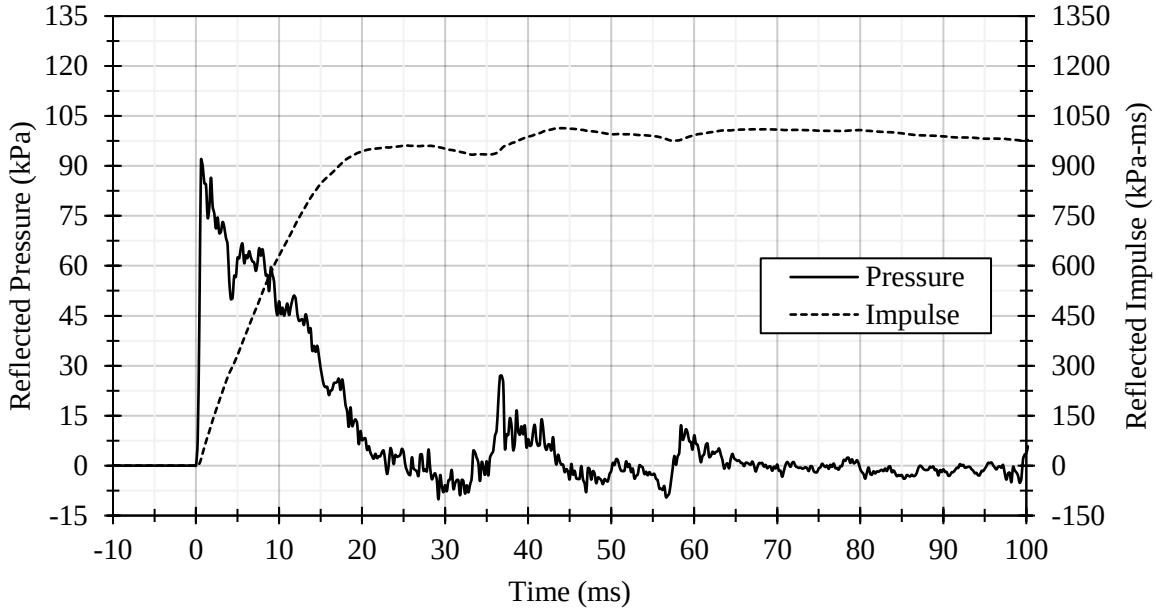


(f) Damage in Top Joint

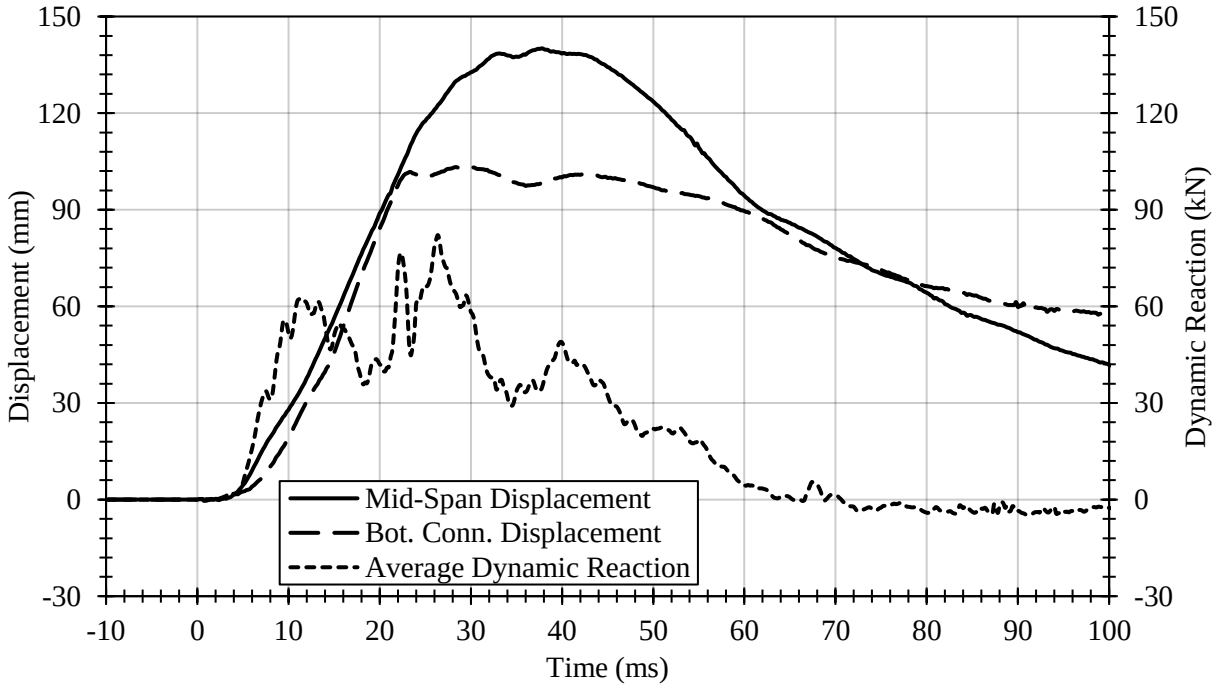
Figure B.22: Documentation of Damage for Specimen CLT11

Specimen CLT12

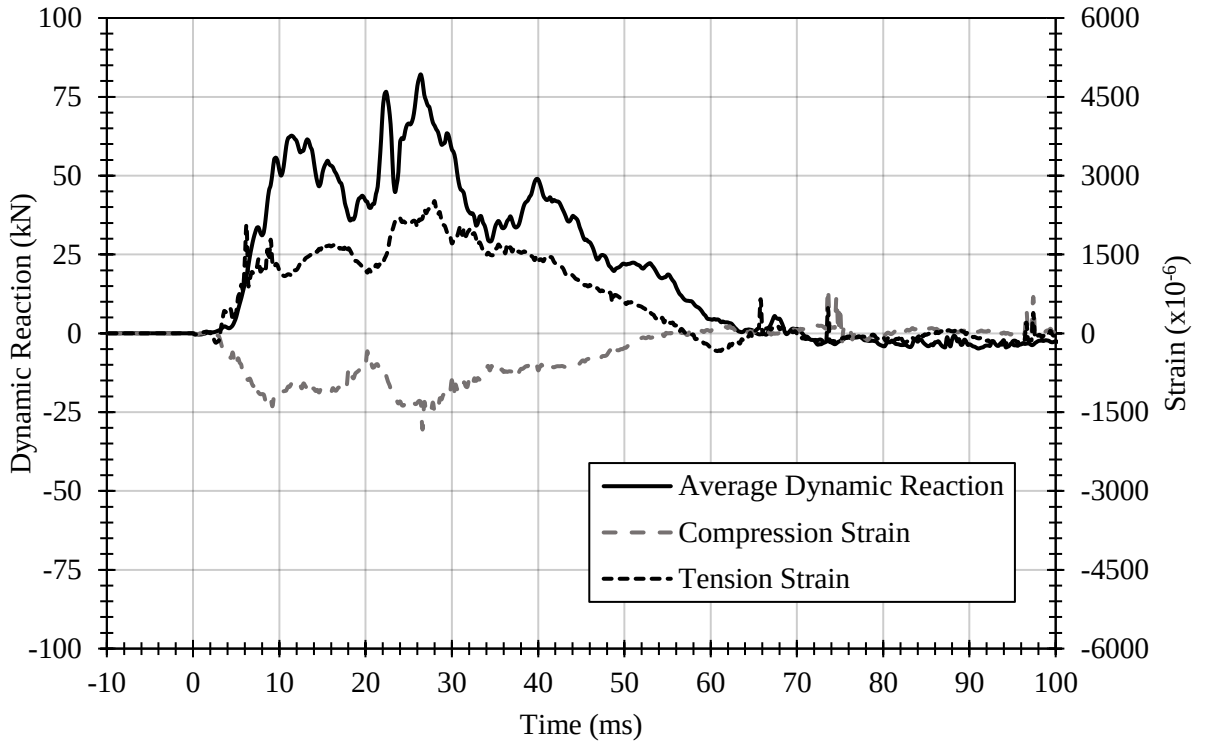
Specimen CLT12, comprised of a CLT panel with a 3.25" deep EAC at each end, was dynamically tested on September 25th 2019. A driver pressure of 750.1 kPa was used, which resulted in a positive peak reflected pressure and impulse of 91.9 kPa and 961.4 kPa-ms, respectively.



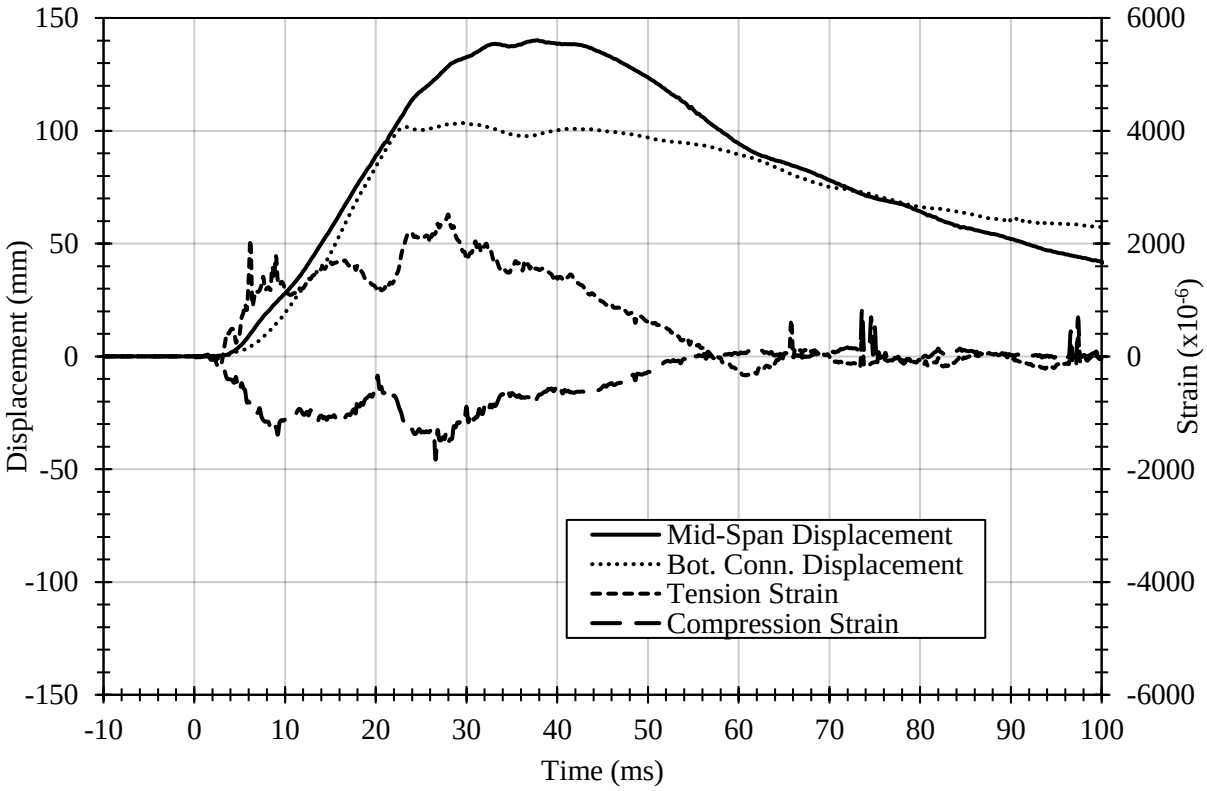
(a) Pressure and Impulse



(b) Reaction and Displacements



(c) Reaction and Strains

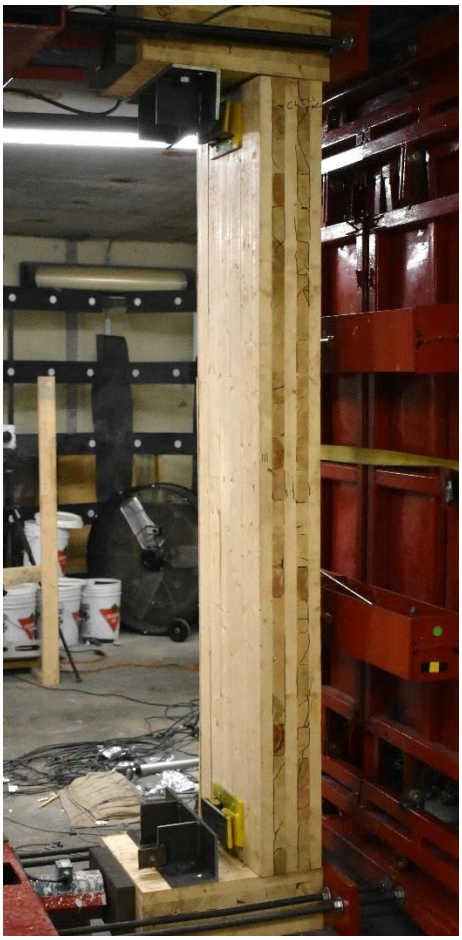


(d) Displacement and Strains

Figure B.23: Dynamic Test Results for Specimen CLT12



(a) Specimen Prior to Testing



(b) Specimen After Testing



(c) Onset of Flexural Failure in Panel



(d) Rolling Shear Damage



(e) Damage in Bottom EAC

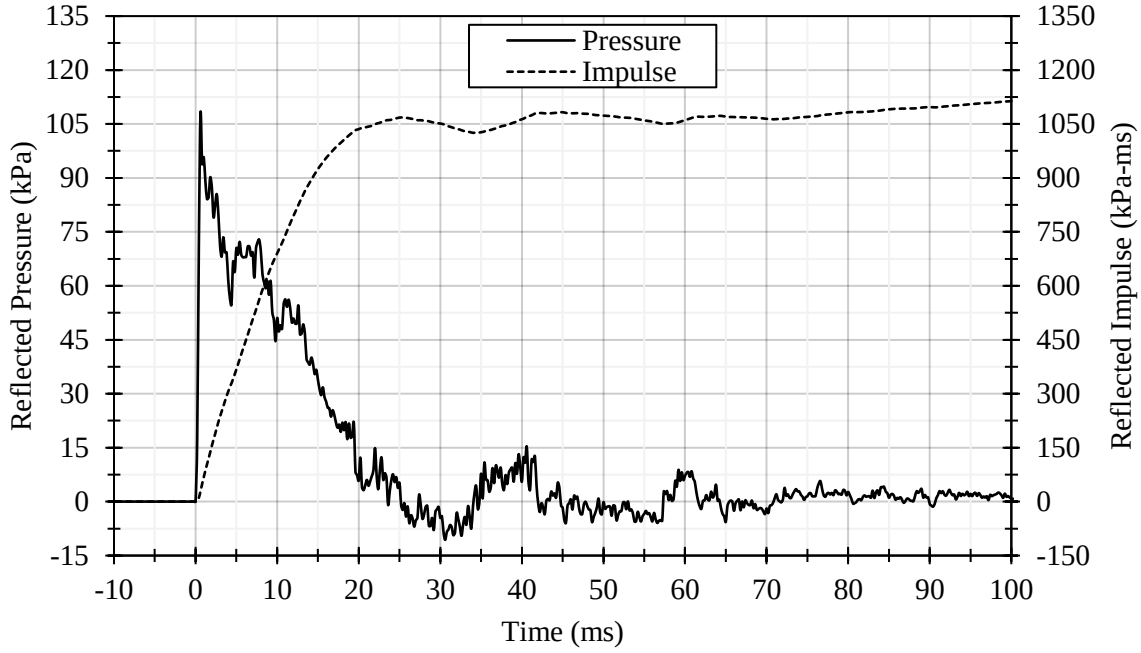


(f) Damage in Top EAC

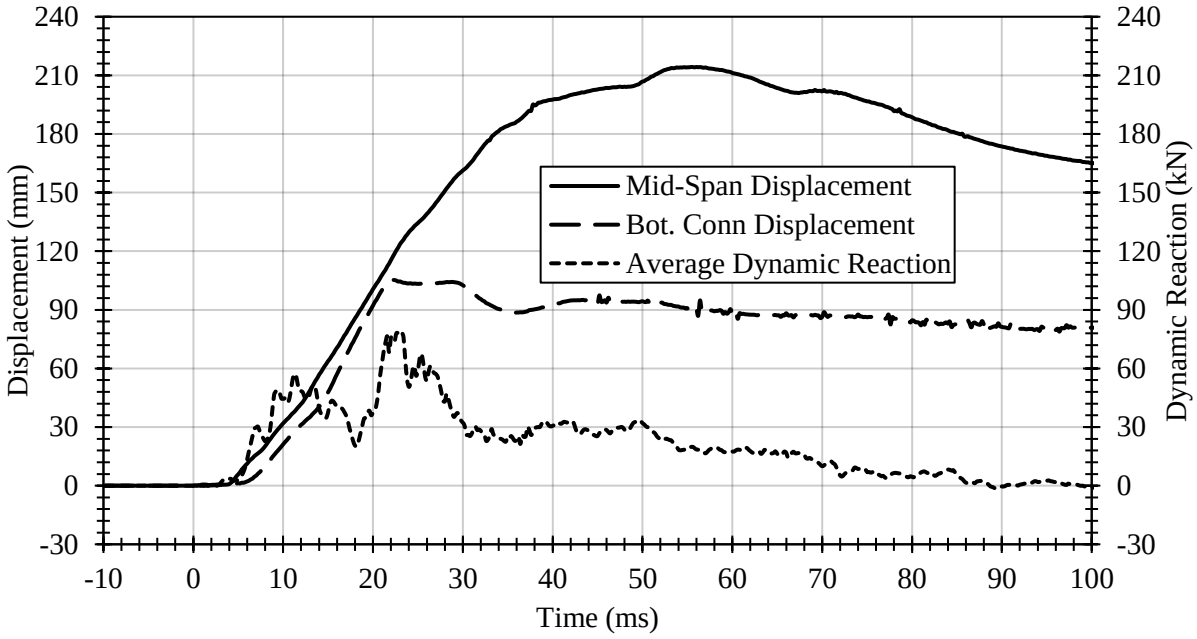
Figure B.24: Documentation of Damage for Specimen CLT12

Specimen CLT13

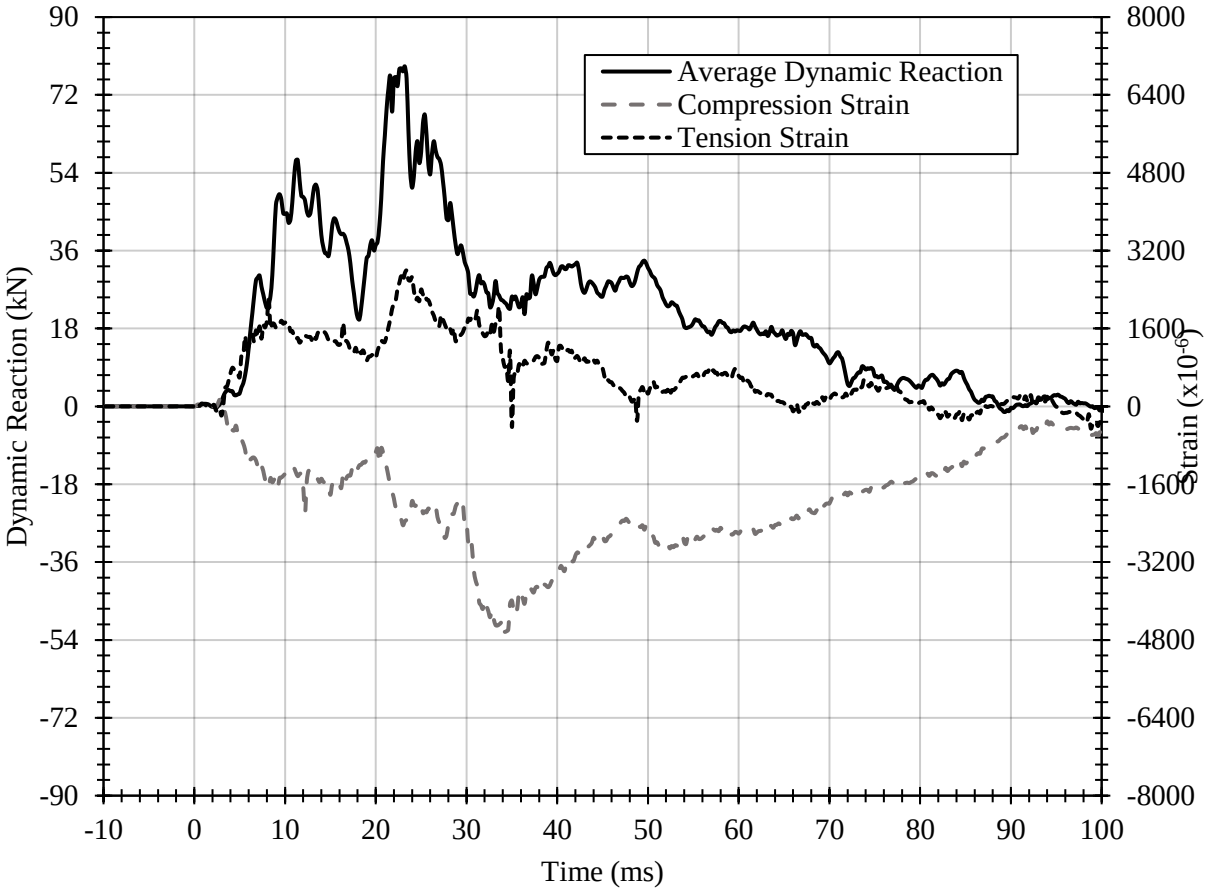
Specimen CLT13, comprised of a CLT panel with a 3.25" deep EAC at each end, was dynamically tested on September 25th 2019. A driver pressure of 846.0 kPa was used, which resulted in a positive peak reflected pressure and impulse of 107.9 kPa and 1068.1 kPa-ms, respectively.



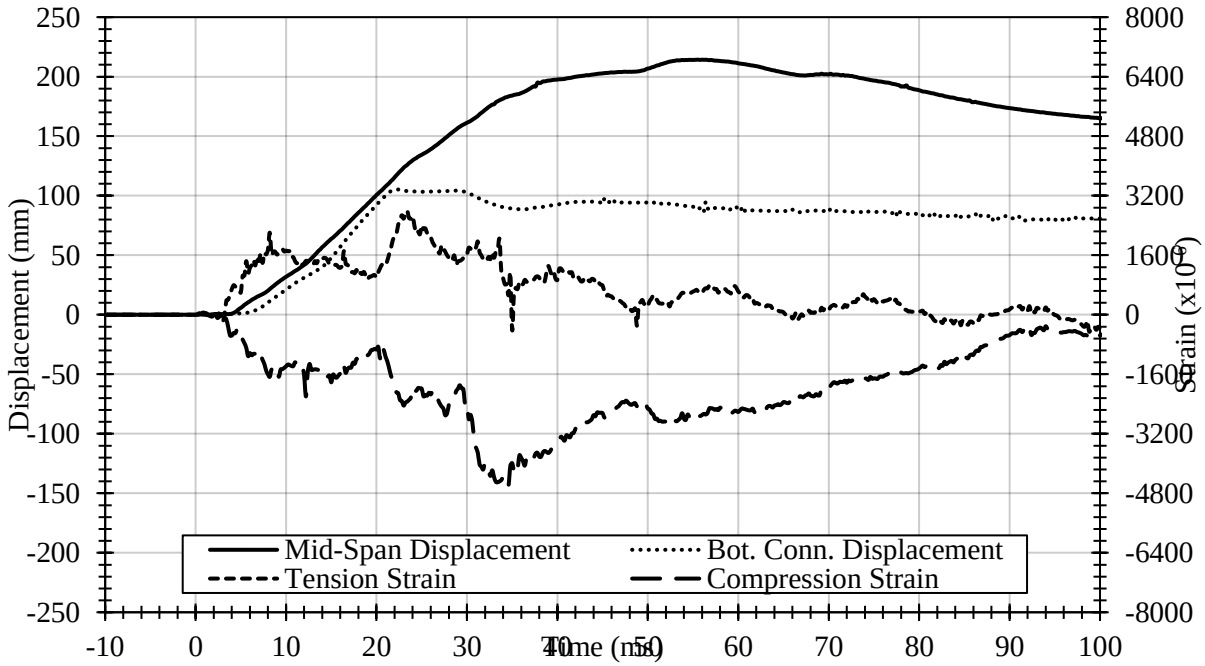
(a) Pressure and Impulse



(b) Reaction and Displacements



(c) Reaction and Strains



(d) Displacement and Strains

Figure B.25: Dynamic Test Results for Specimen CLT13



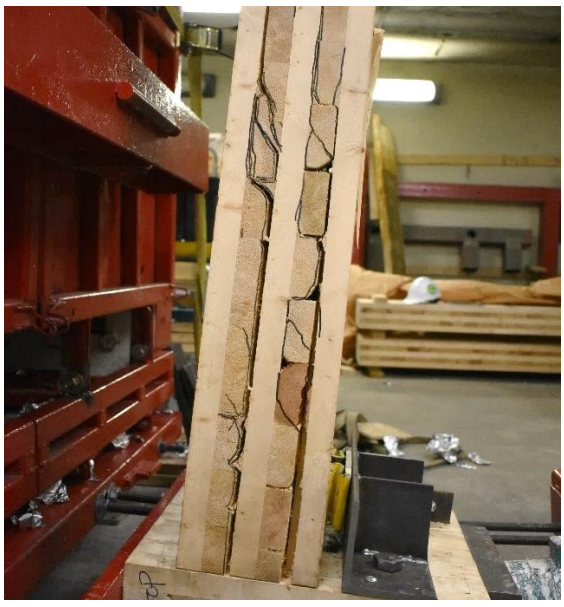
(a) Specimen Prior to Testing



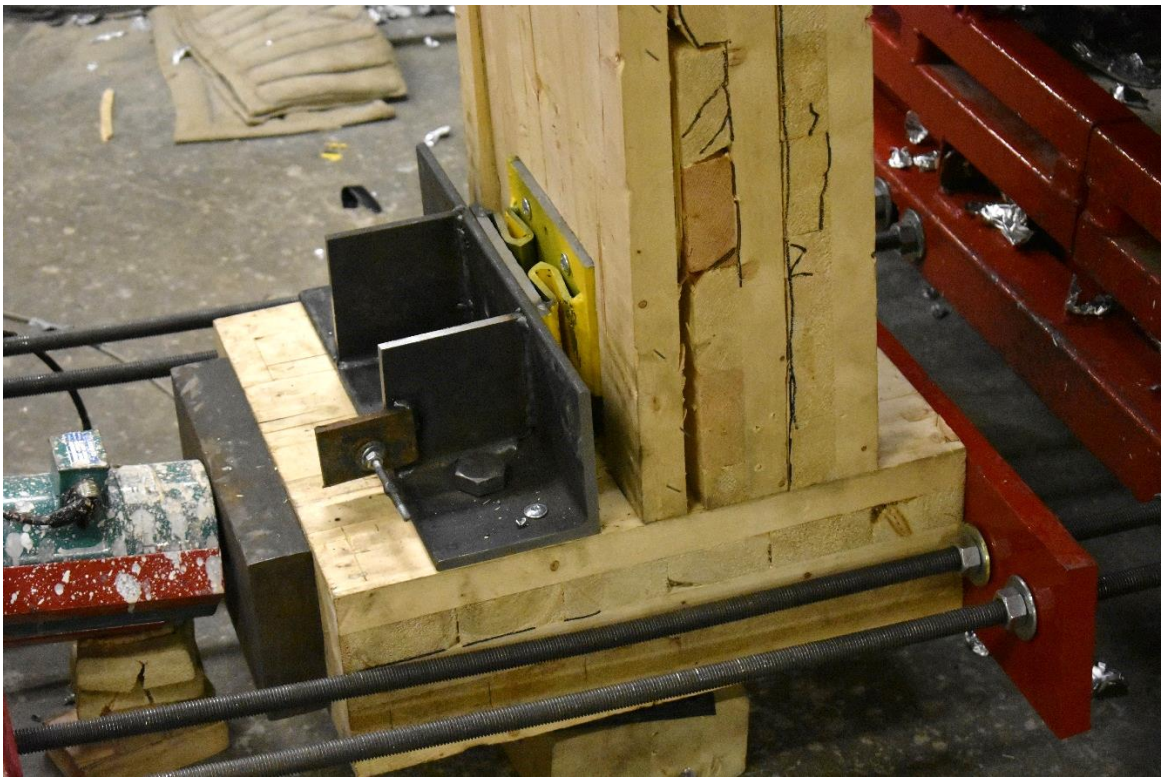
(b) Specimen After Testing



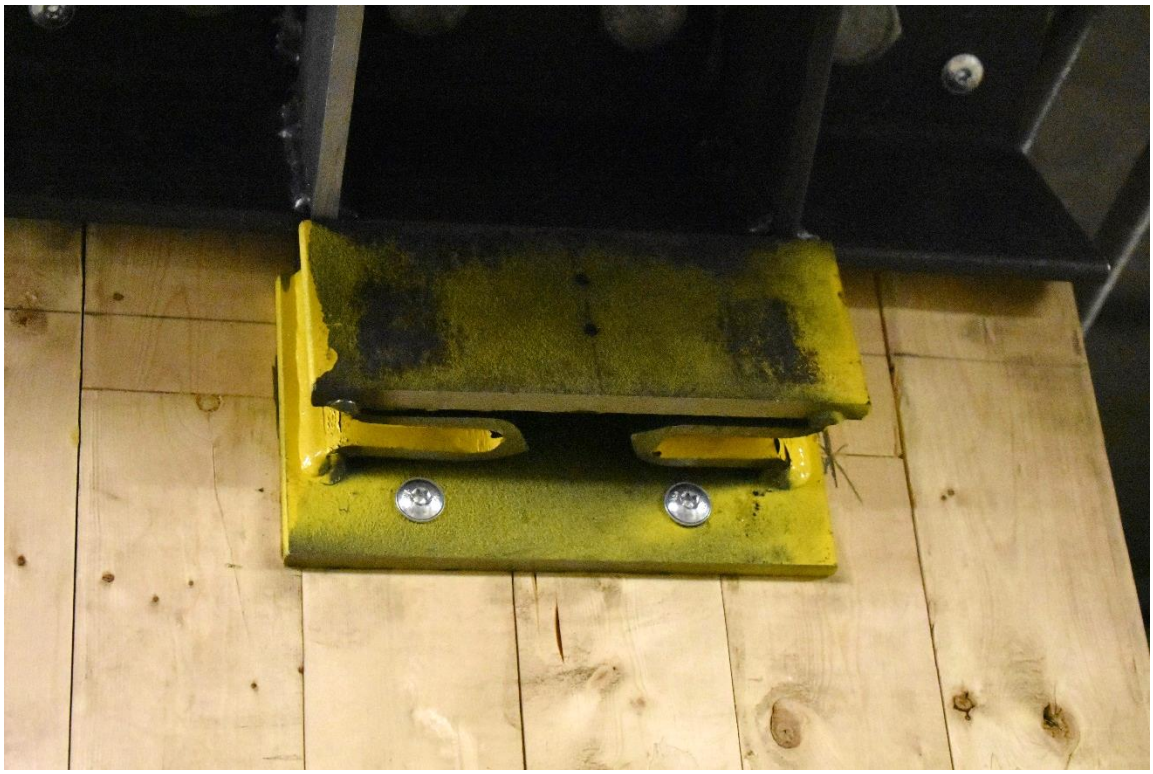
(c) Flexural Failure in Panel



(d) Rolling Shear Damage



(e) Damage in Bottom EAC

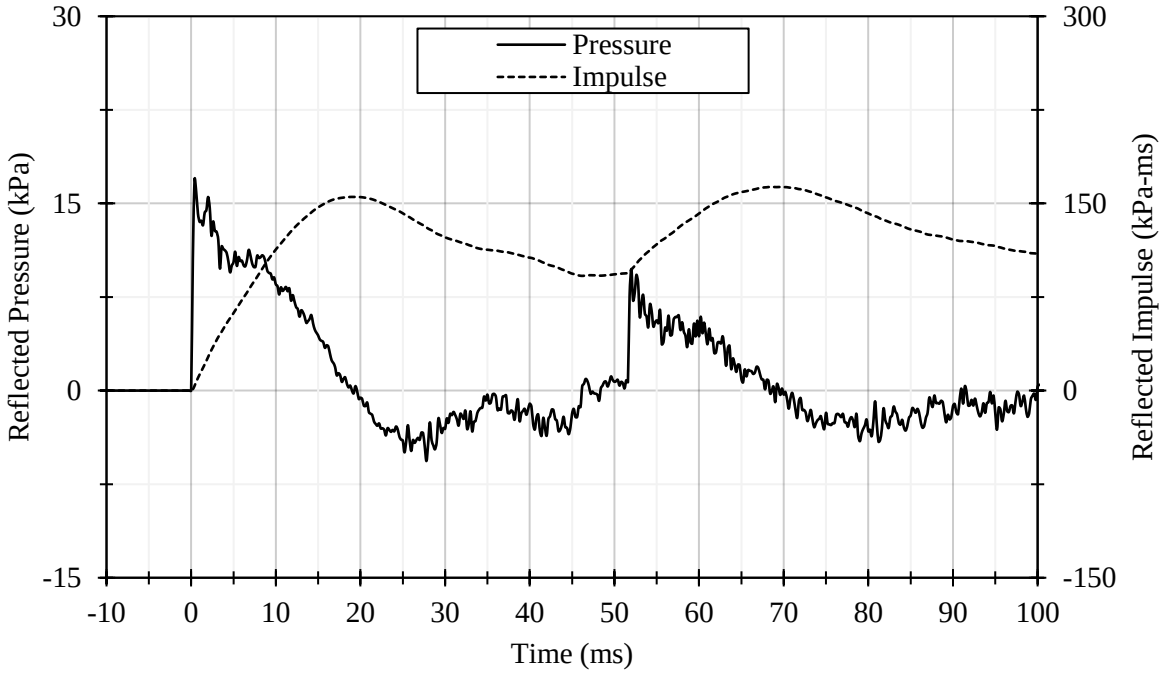


(f) Damage in Top EAC

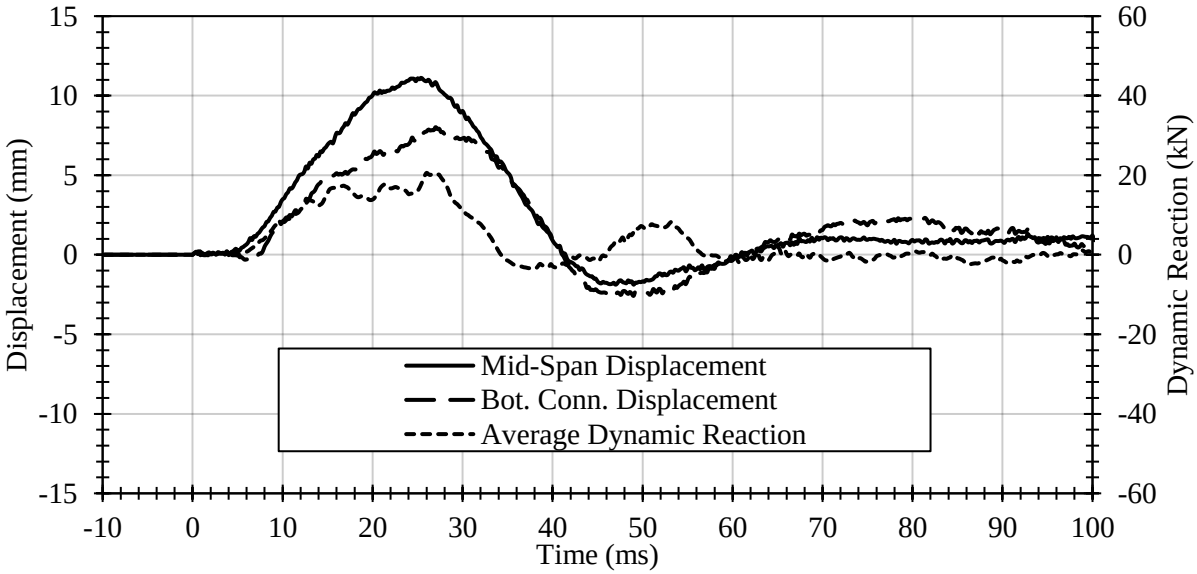
Figure B.26: Documentation of Damage for Specimen CLT13

Specimen CLT14 – Shot #1

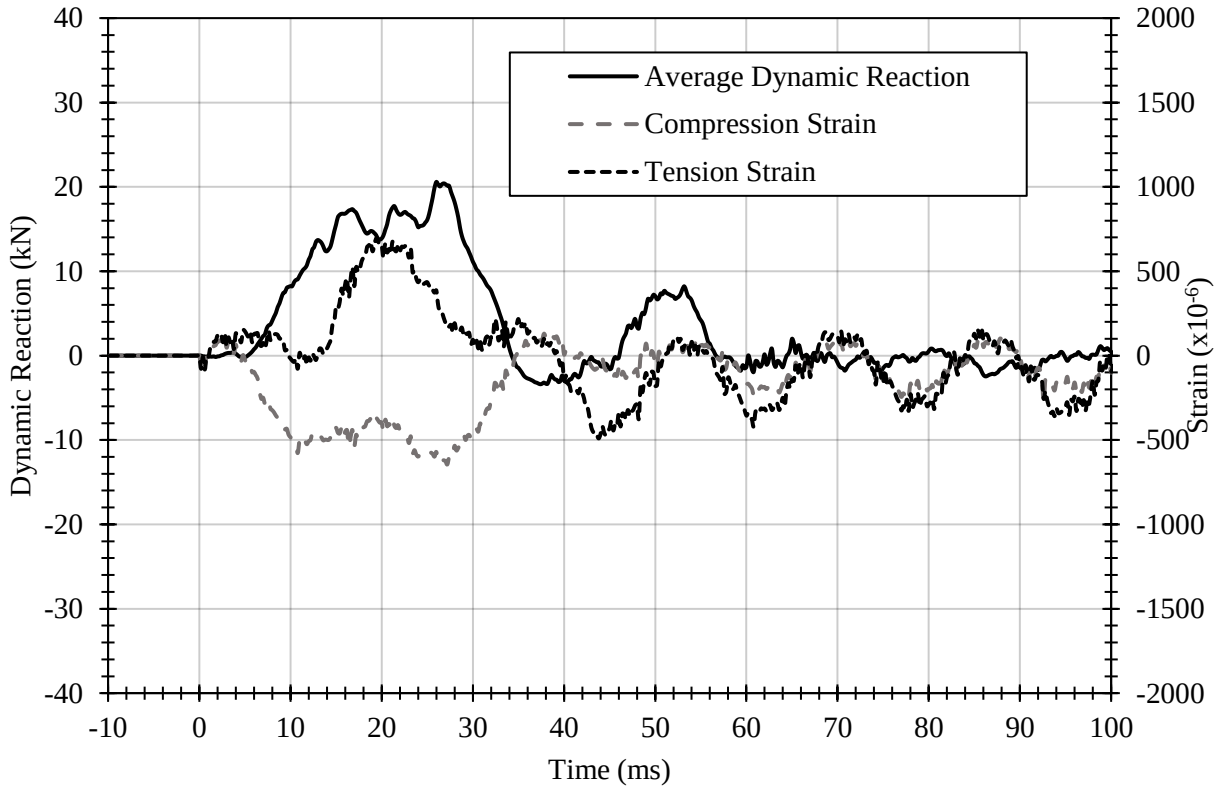
Specimen CLT14, comprised of a CLT panel with a 3.25” deep EAC at each end, was subjected to four different pressure-impulse combinations. For the first shot, it was dynamically tested on September 27th 2019. A driver pressure of 93.8 kPa was used, which resulted in a positive peak reflected pressure and impulse of 16.9 kPa and 155.3 kPa-ms, respectively.



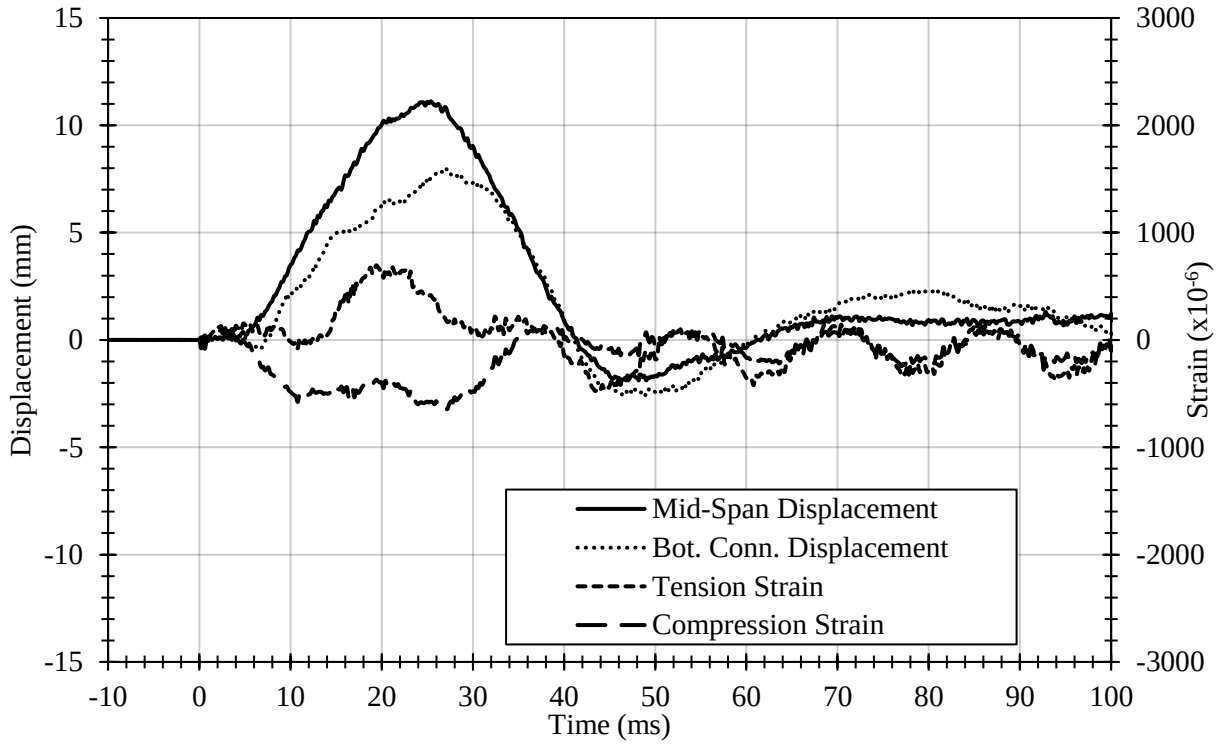
(a) Pressure and Impulse



(b) Reaction and Displacements



(c) Reaction and Strains



(d) Displacement and Strains

Figure B.27: Dynamic Test Results for Test CLT14-1



(a) Specimen Prior to Testing



(b) Specimen After Testing



(c) Lack of Damage in Bottom EAC

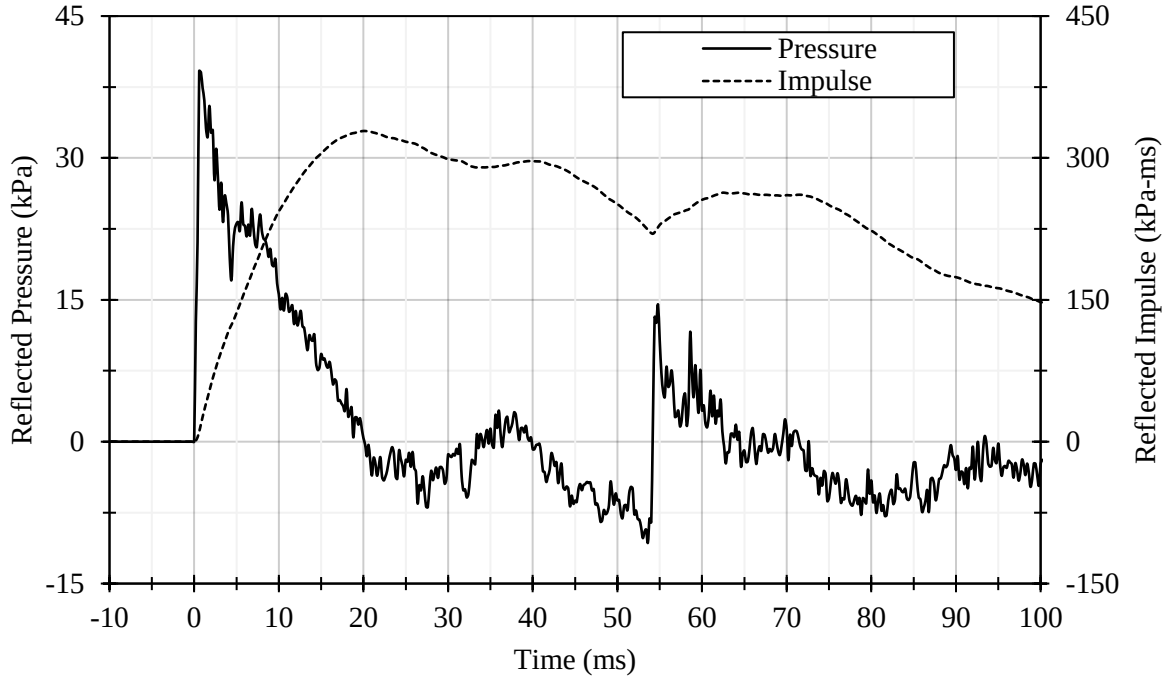


(d) Lack of Damage in Top EAC

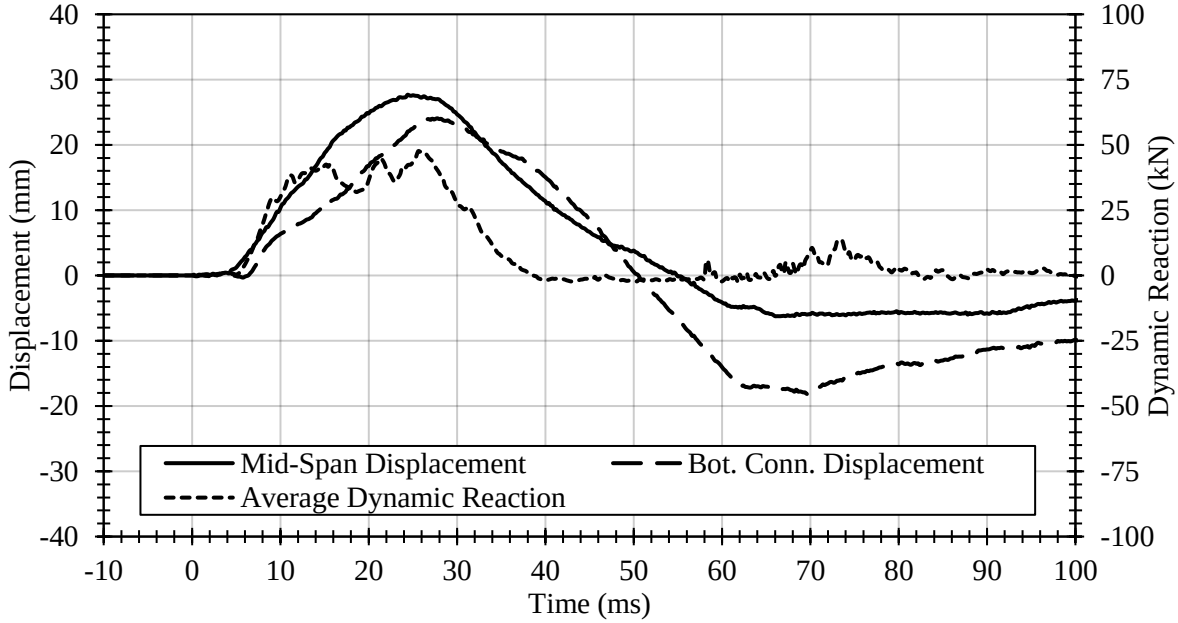
Figure B.28: Documentation of Damage for Test CLT14-1

Specimen CLT14 – Shot #2

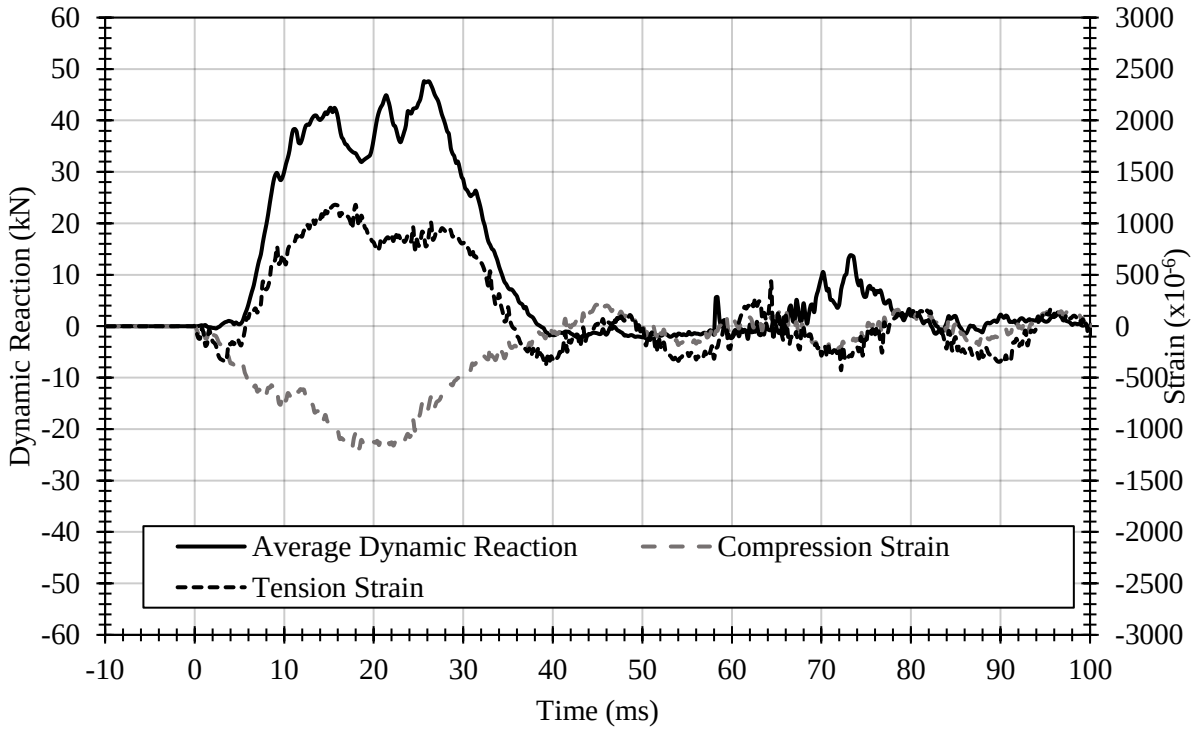
For the second shot, it was dynamically tested on September 27th 2019. A driver pressure of 252.3 kPa was used, which resulted in a positive peak reflected pressure and impulse of 39.2 kPa and 328.5 kPa-ms, respectively.



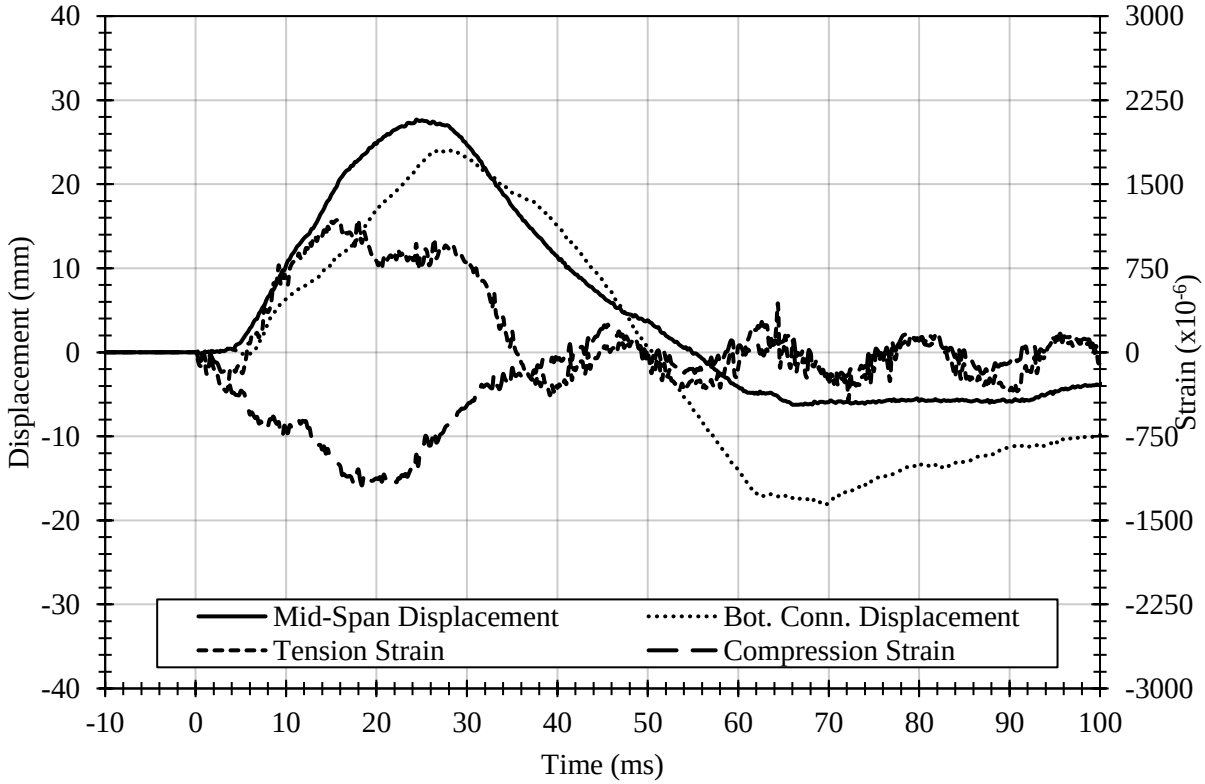
(a) Pressure and Impulse



(b) Reaction and Displacements



(c) Reaction and Strains

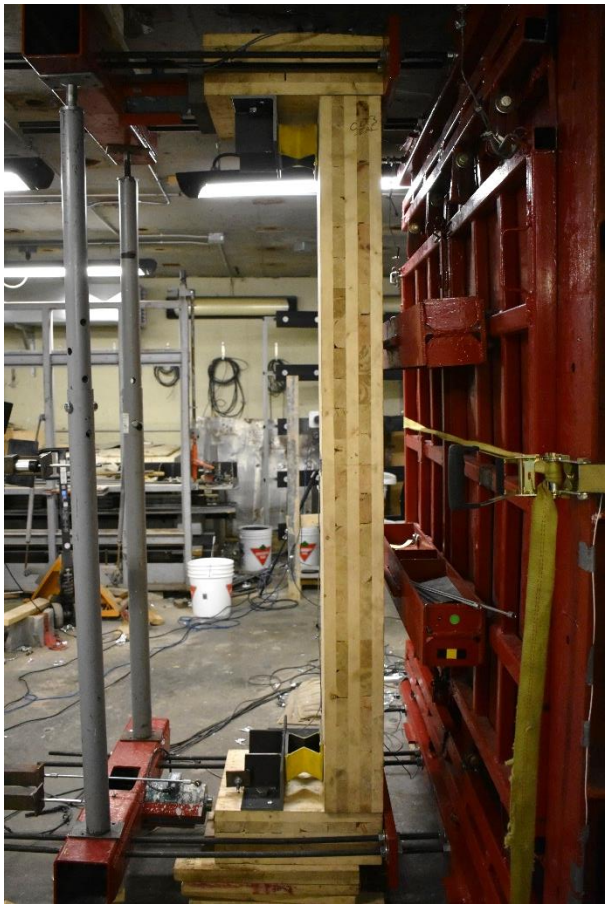


(d) Displacement and Strains

Figure B.29: Dynamic Test Results for Test CLT14-2



(a) Specimen Prior to Testing



(b) Specimen After Testing



(c) Residual Displacement at Bottom Connection

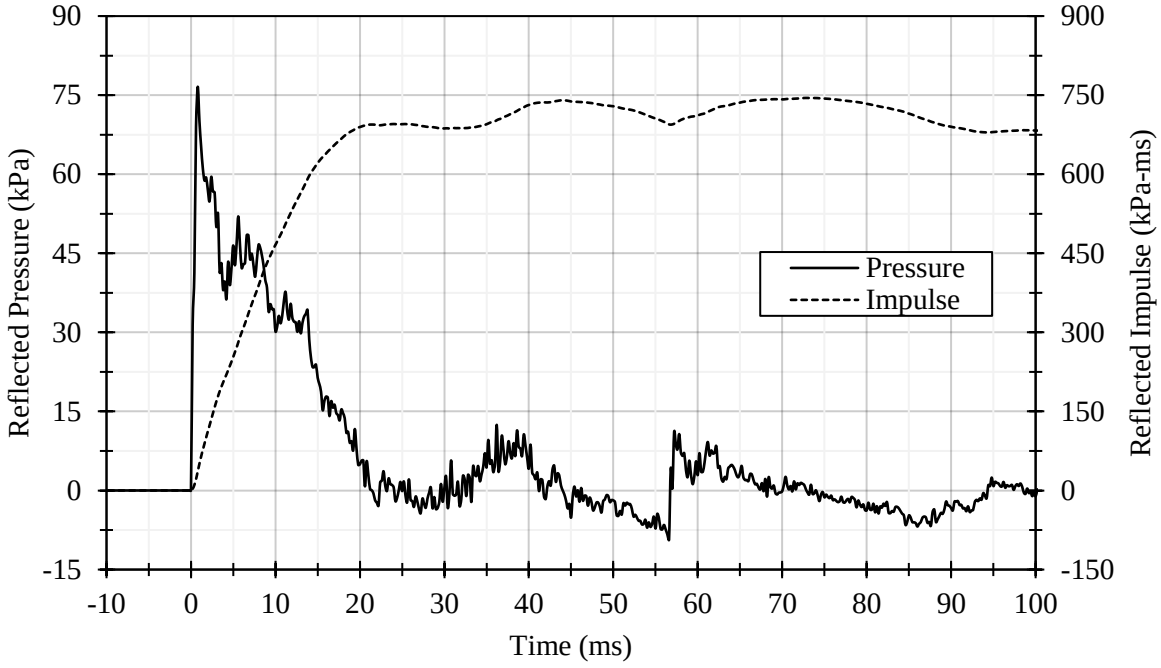


(d) Residual Displacement at Top Connection

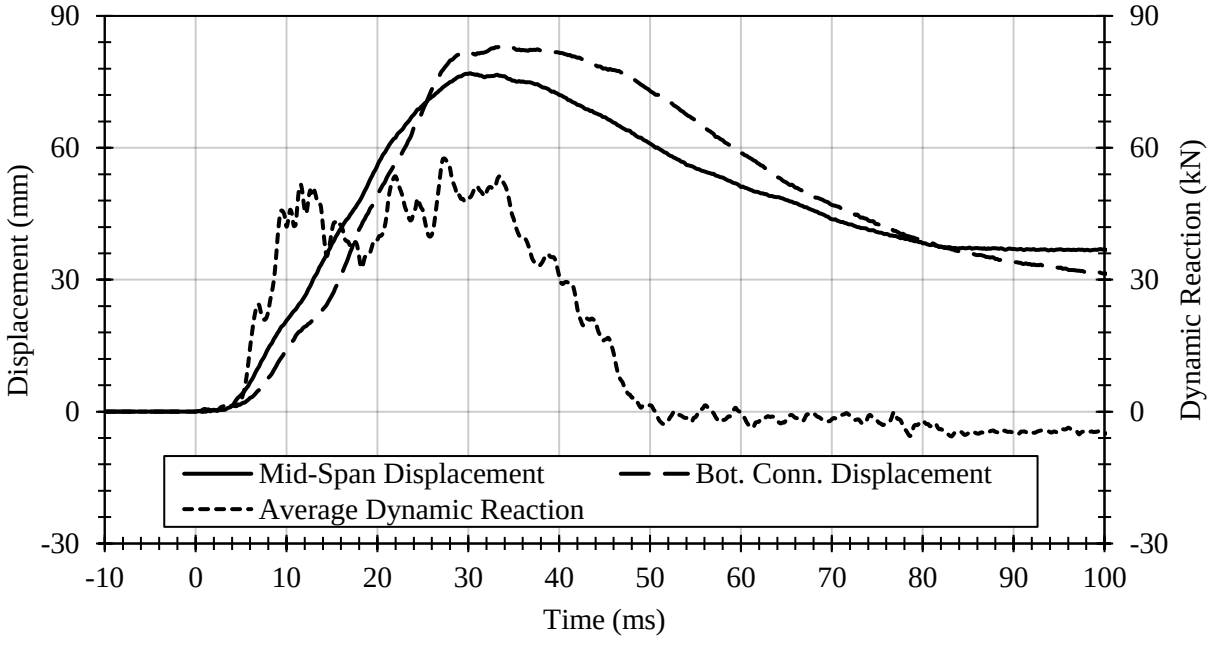
Figure B.30: Documentation of Damage for Test CLT14-2

Specimen CLT14 – Shot #3

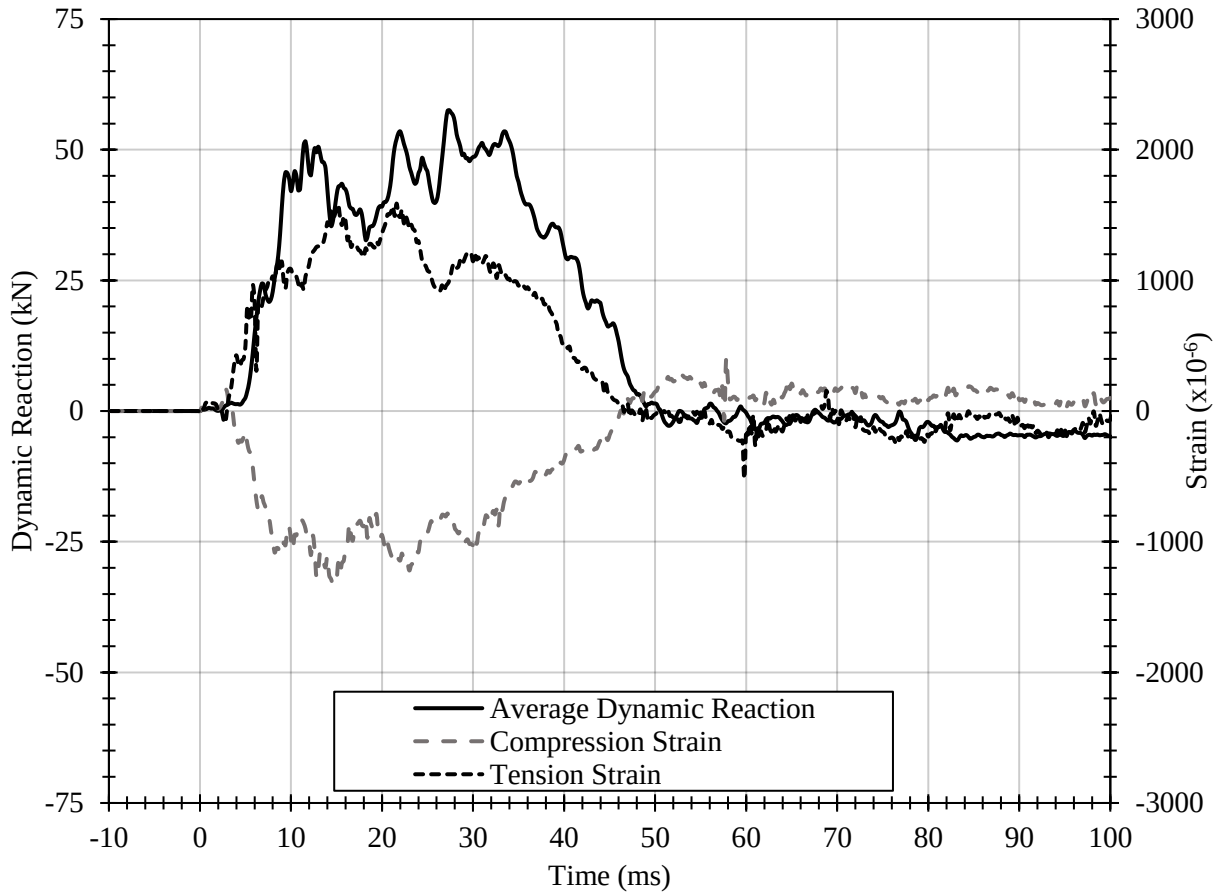
For the third shot, it was dynamically tested on September 27th 2019. A driver pressure of 514.3 kPa was used, which resulted in a positive peak reflected pressure and impulse of 76.6 kPa and 695.2 kPa-ms, respectively.



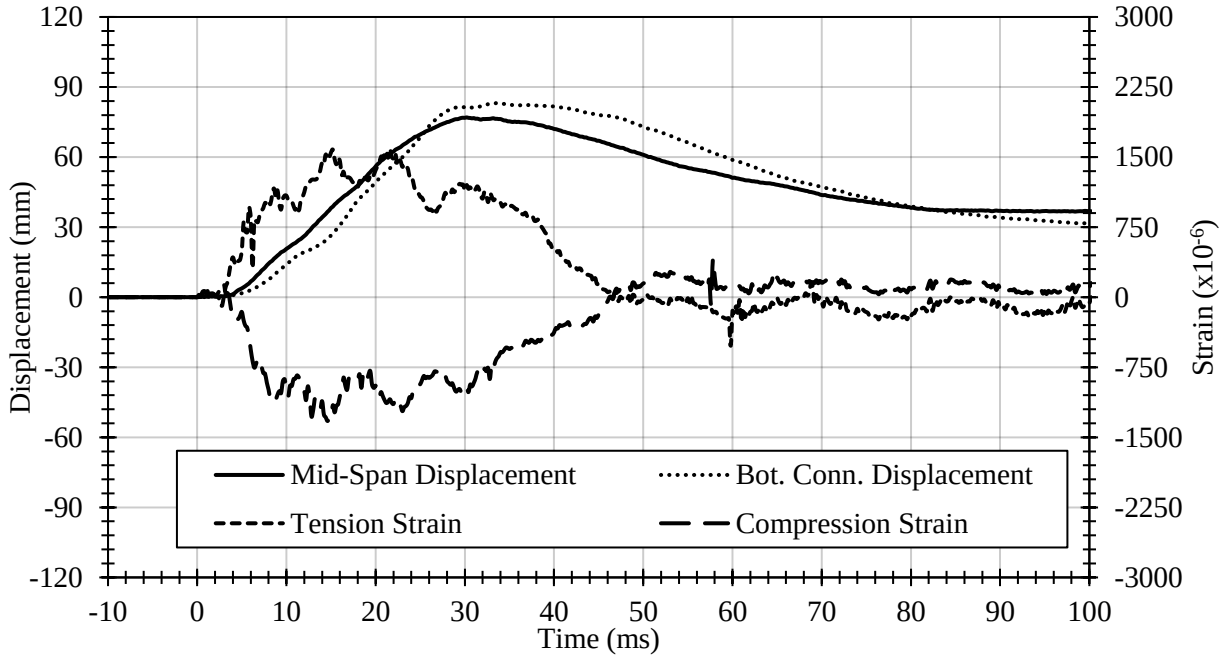
(a) Pressure and Impulse



(b) Reaction and Displacements

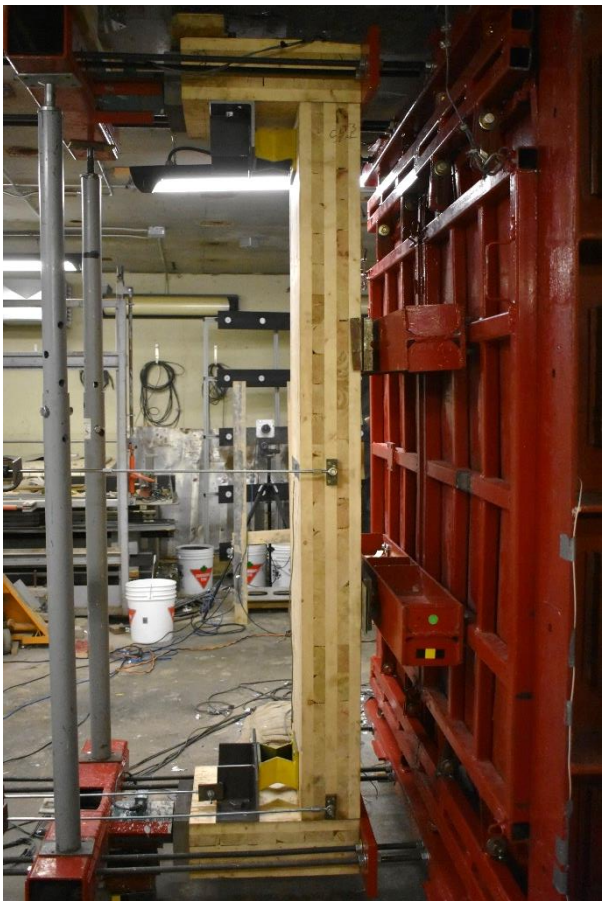


(c) Reaction and Strains

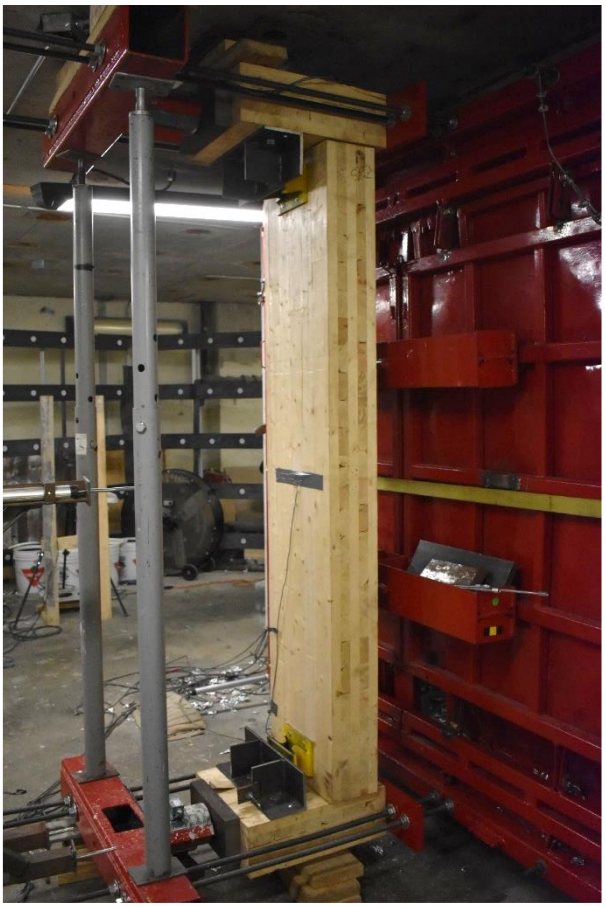


(d) Displacement and Strains

Figure B.31: Dynamic Test Results for Test CLT14-3



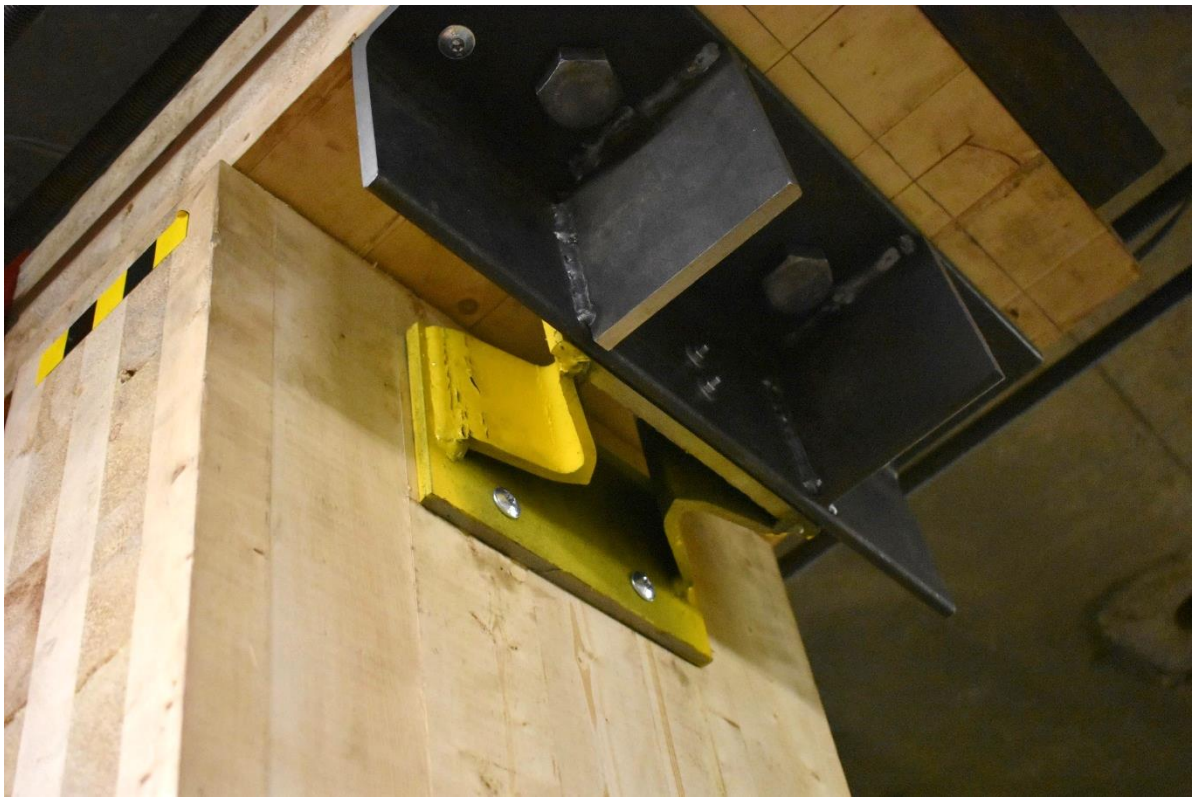
(a) Specimen Prior to Testing



(b) Specimen After Testing



(c) Damage in Bottom EAC

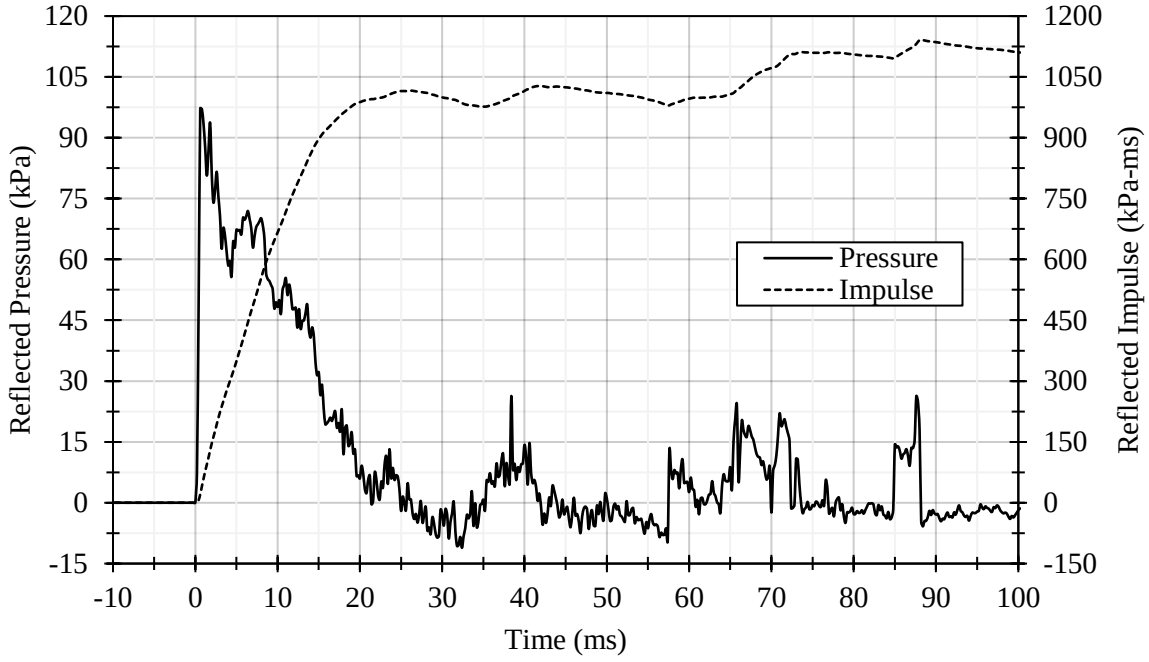


(d) Damage in Top EAC

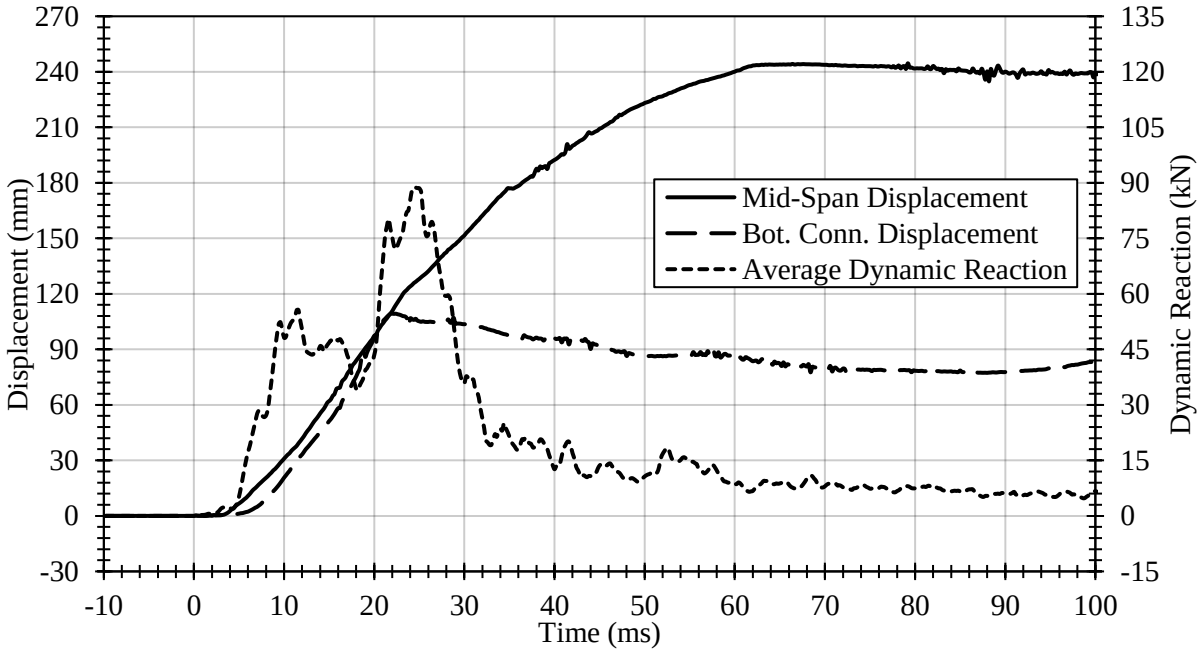
Figure B.32: Documentation of Damage for Test CLT14-3

Specimen CLT14 – Shot #4

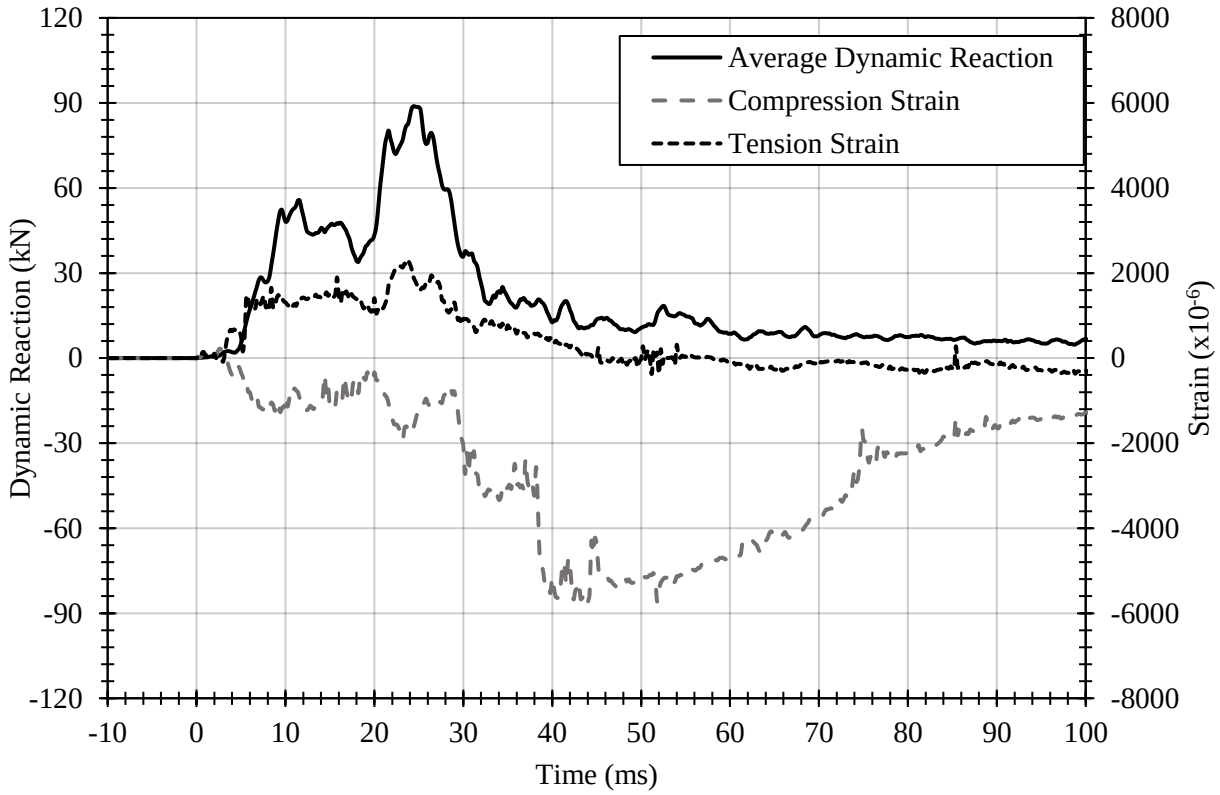
For the fourth shot, it was dynamically tested on September 30th 2019. A driver pressure of 823.9 kPa was used, which resulted in a positive peak reflected pressure and impulse of 97.3 kPa and 1016.0 kPa-ms, respectively.



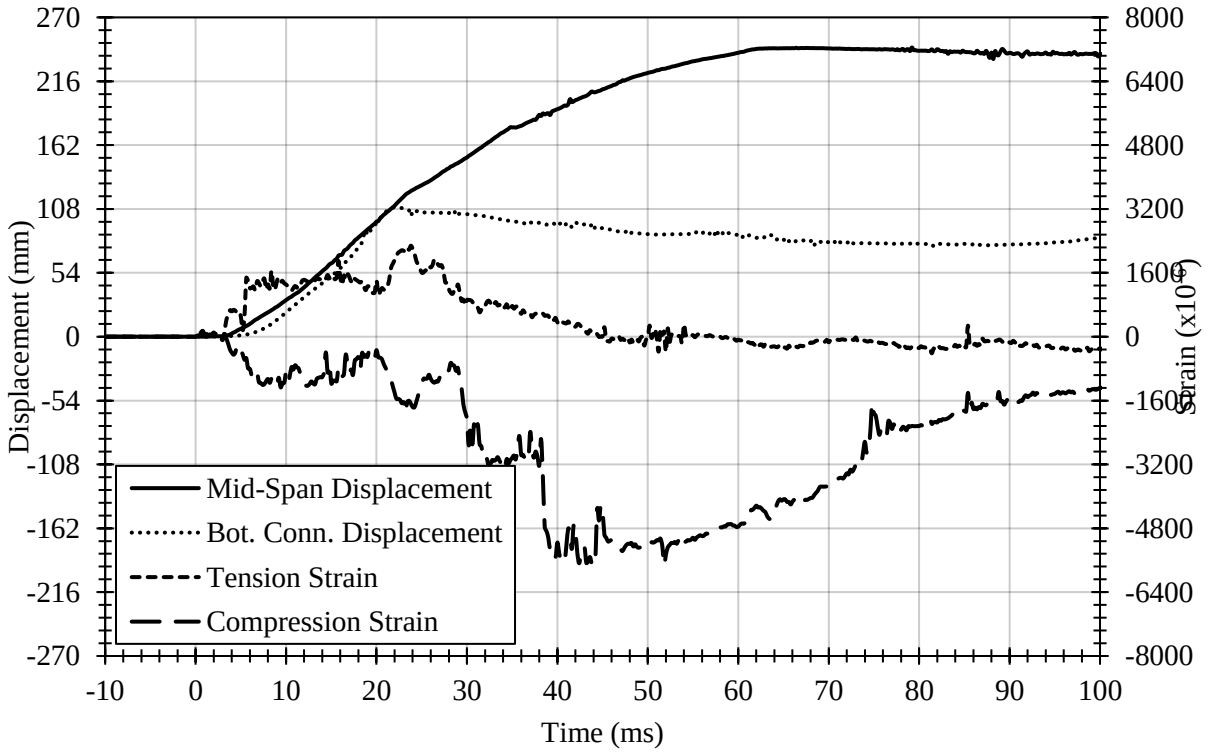
(a) Pressure and Impulse



(b) Reaction and Displacements

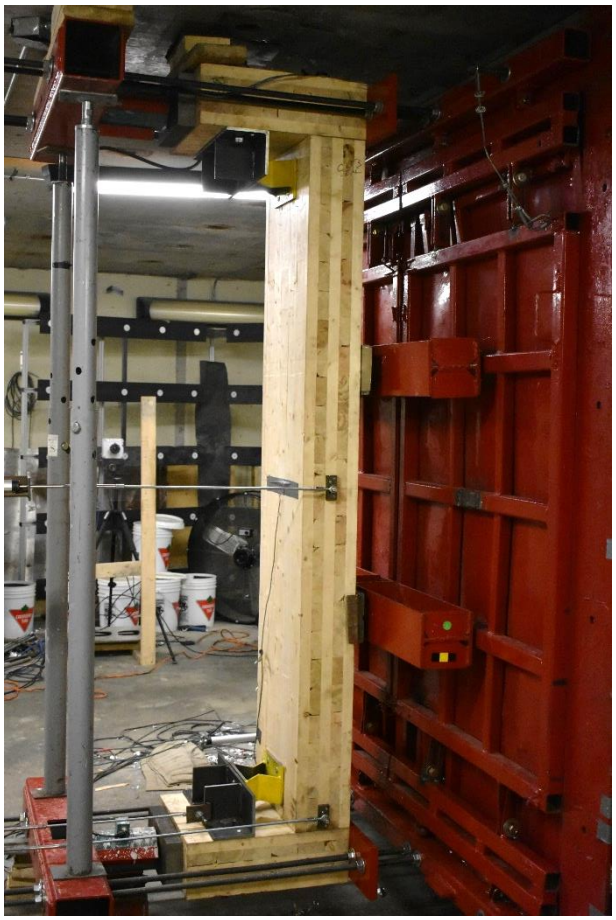


(c) Reaction and Strains

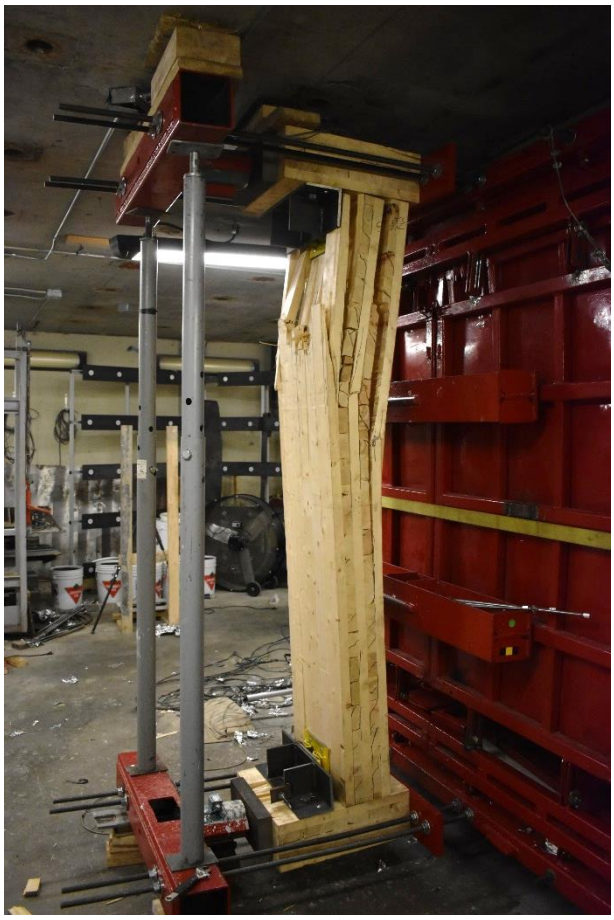


(d) Displacement and Strains

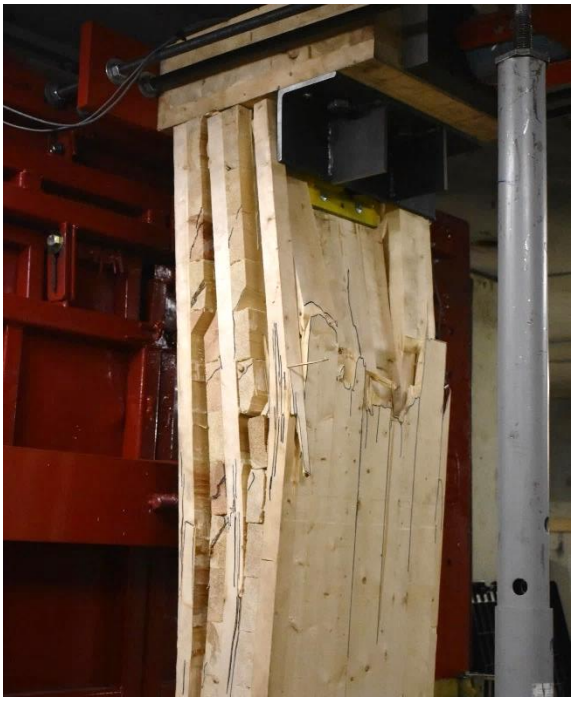
Figure B.33: Dynamic Test Results for Test CLT14-4



(a) Specimen Prior to Testing



(b) Specimen After Testing



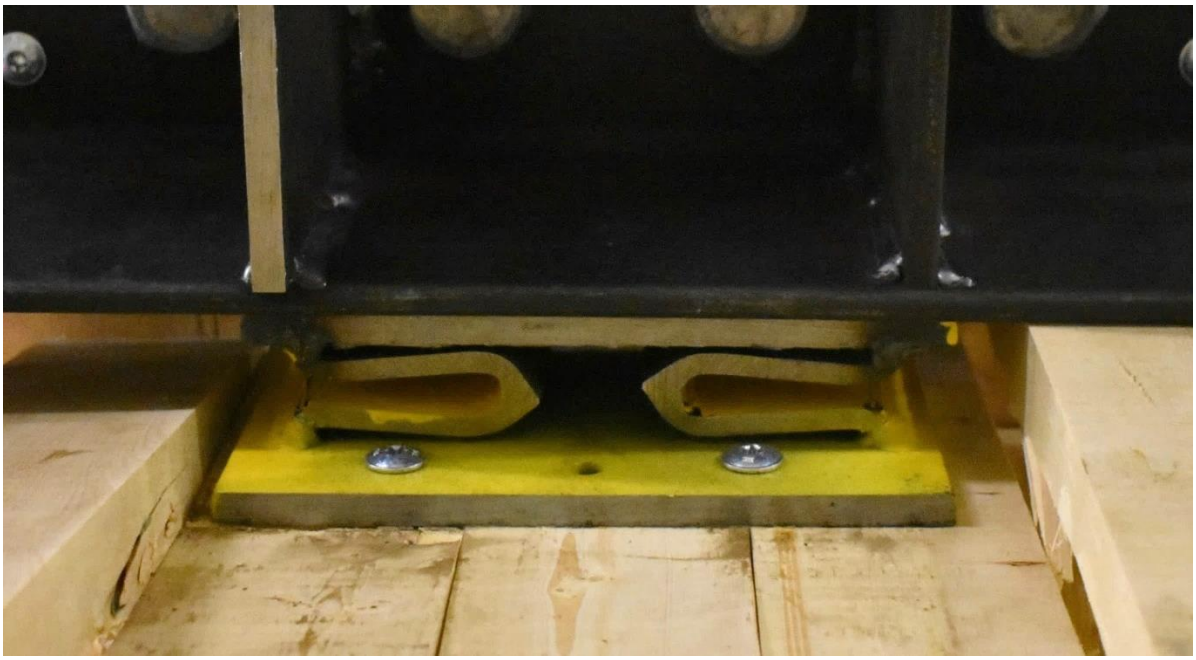
(c) Flexural Failure in Panel



(d) Rolling Shear Damage



(e) Damage in Bottom EAC

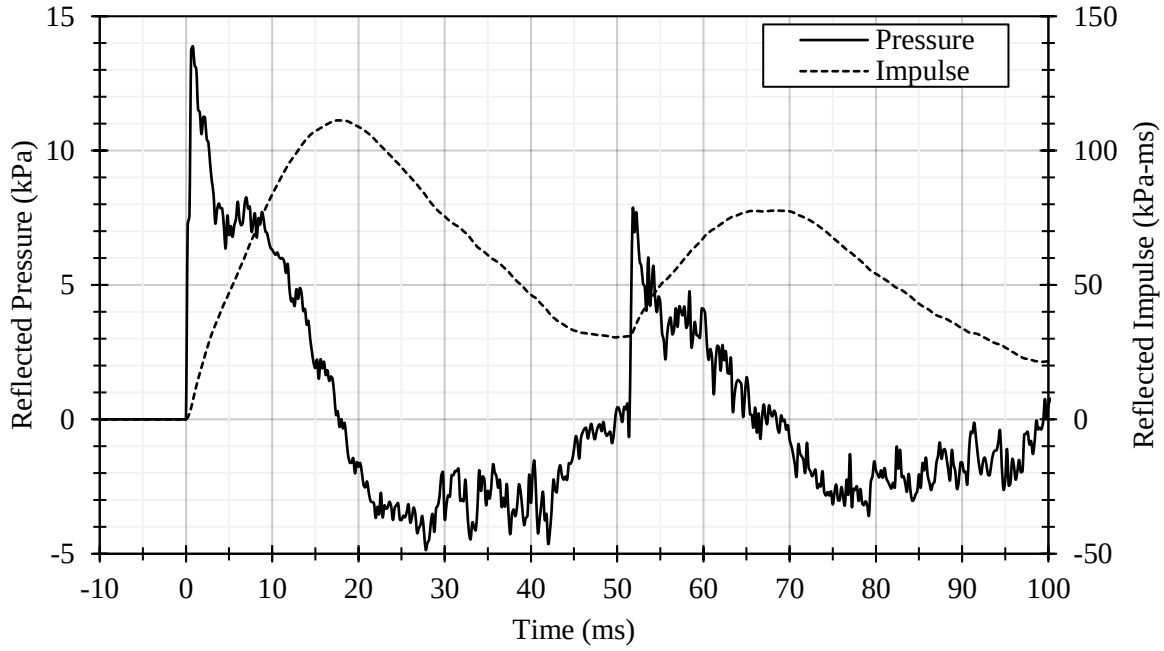


(f) Damage in Top EAC

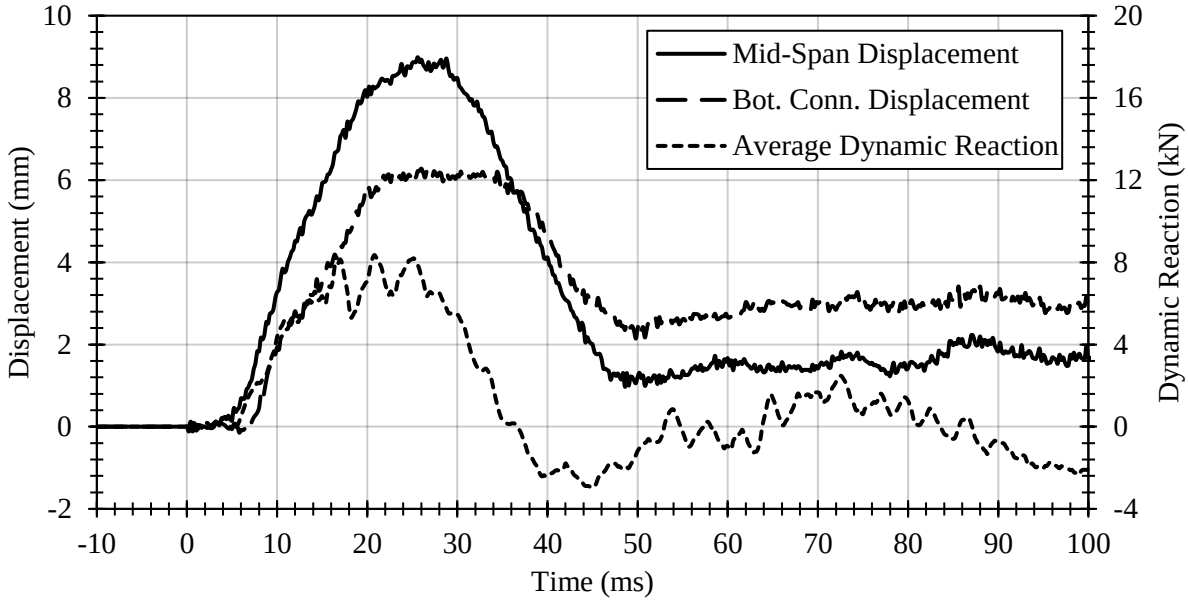
Figure B.34: Documentation of Damage for Test CLT14-4

Specimen CLT15 – Shot #1

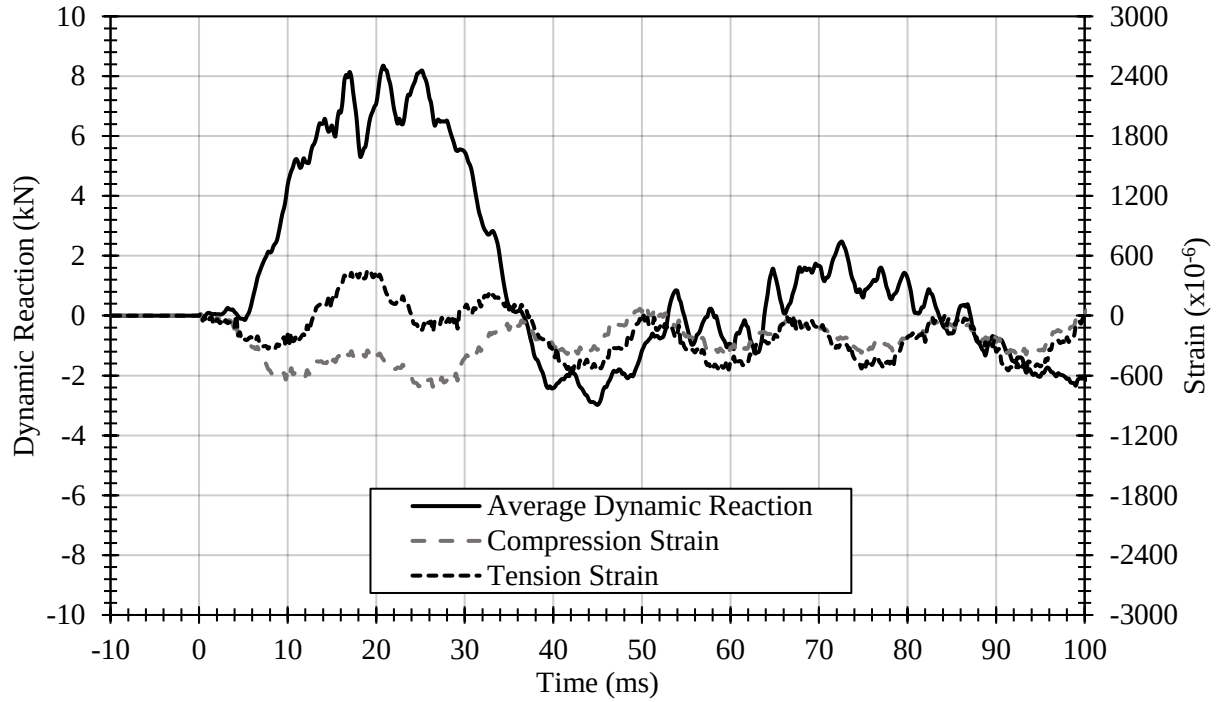
Specimen CLT15, comprised of a CLT panel with a 2.5" deep EAC at each end, was subjected to four different pressure-impulse combinations. For the first shot, it was dynamically tested on October 1st 2019. A driver pressure of 82.0 kPa was used, which resulted in a positive peak reflected pressure and impulse of 13.9 kPa and 111.3 kPa-ms, respectively.



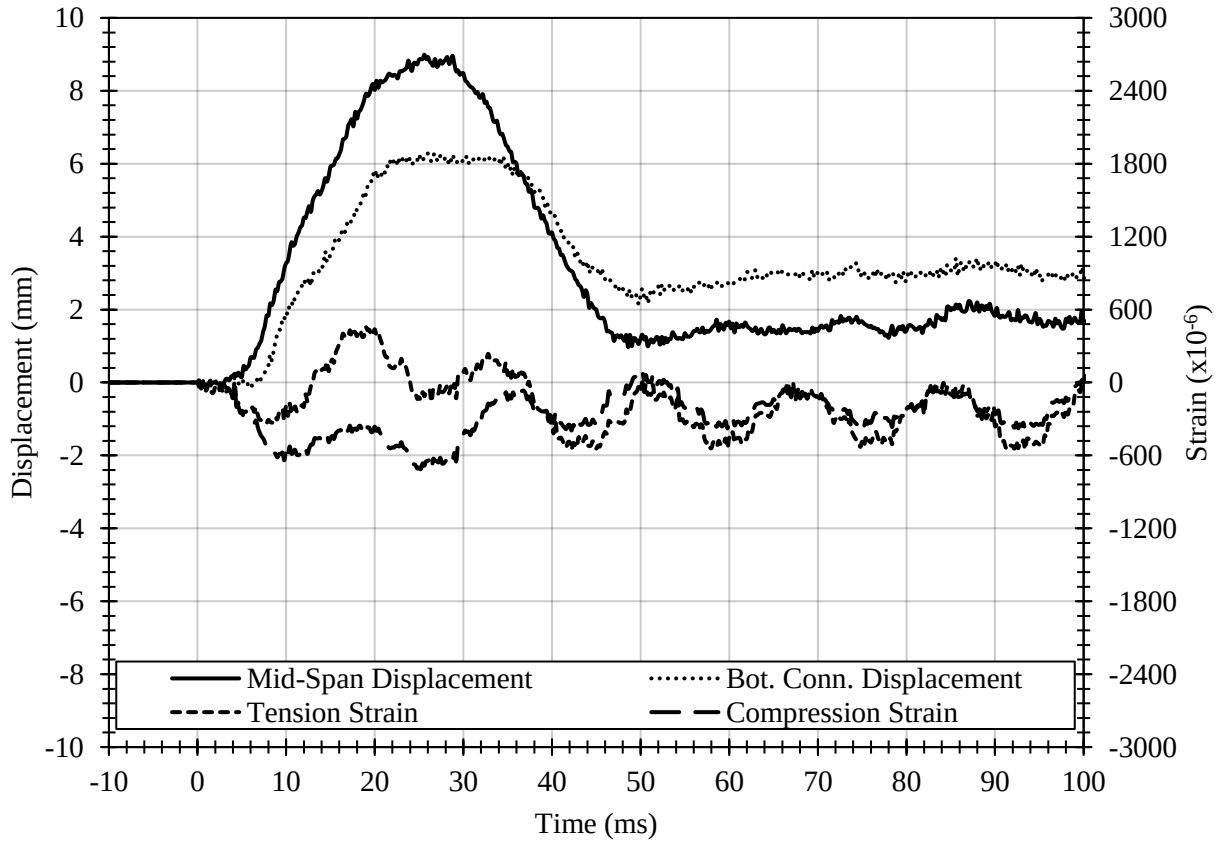
(a) Pressure and Impulse



(b) Reaction and Displacements

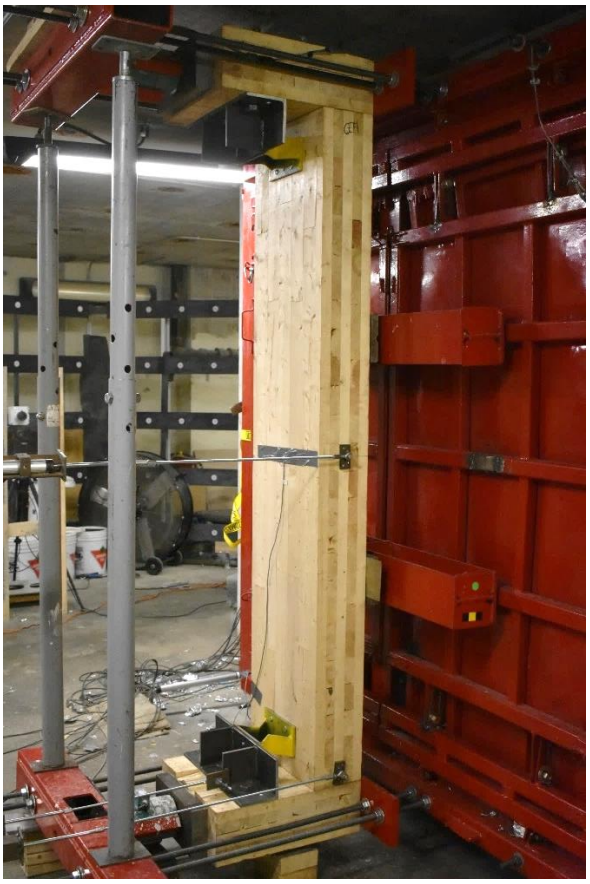


(c) Reaction and Strains

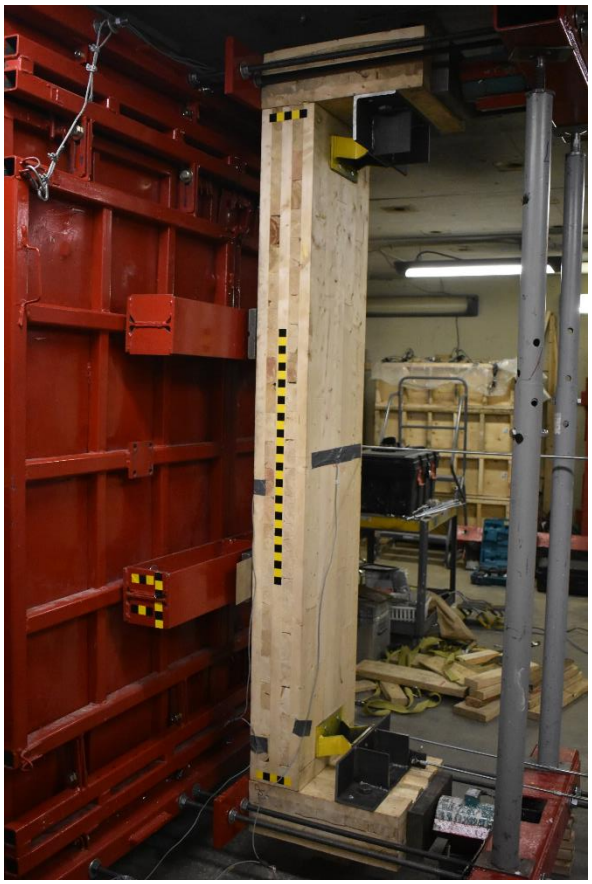


(d) Displacement and Strains

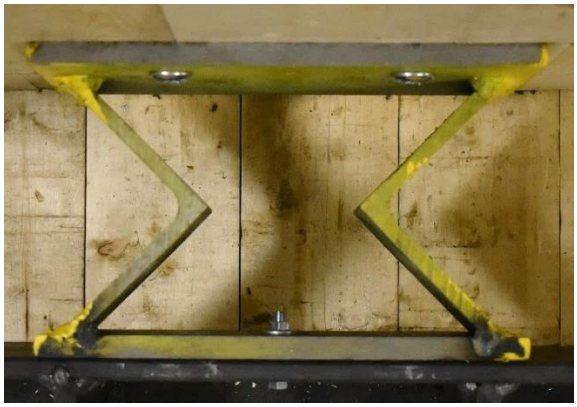
Figure B.35: Dynamic Test Results for Test CLT15-1



(a) Specimen Prior to Testing



(b) Specimen After Testing



(c) Lack of Damage in Bottom EAC

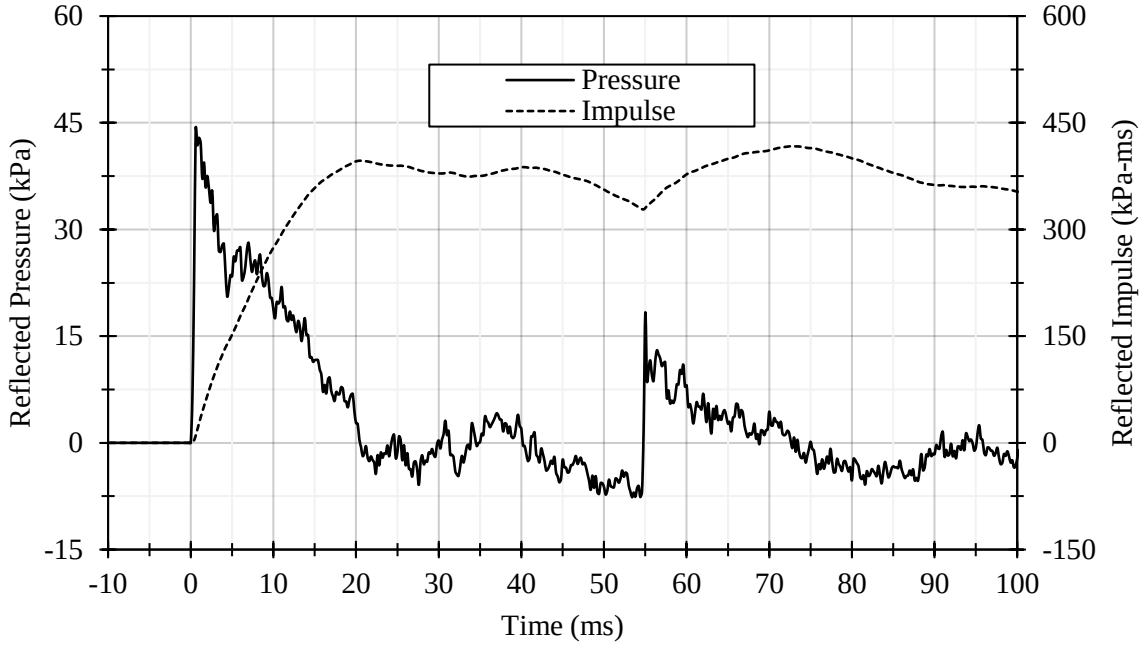


(d) Lack of Damage in Top EAC

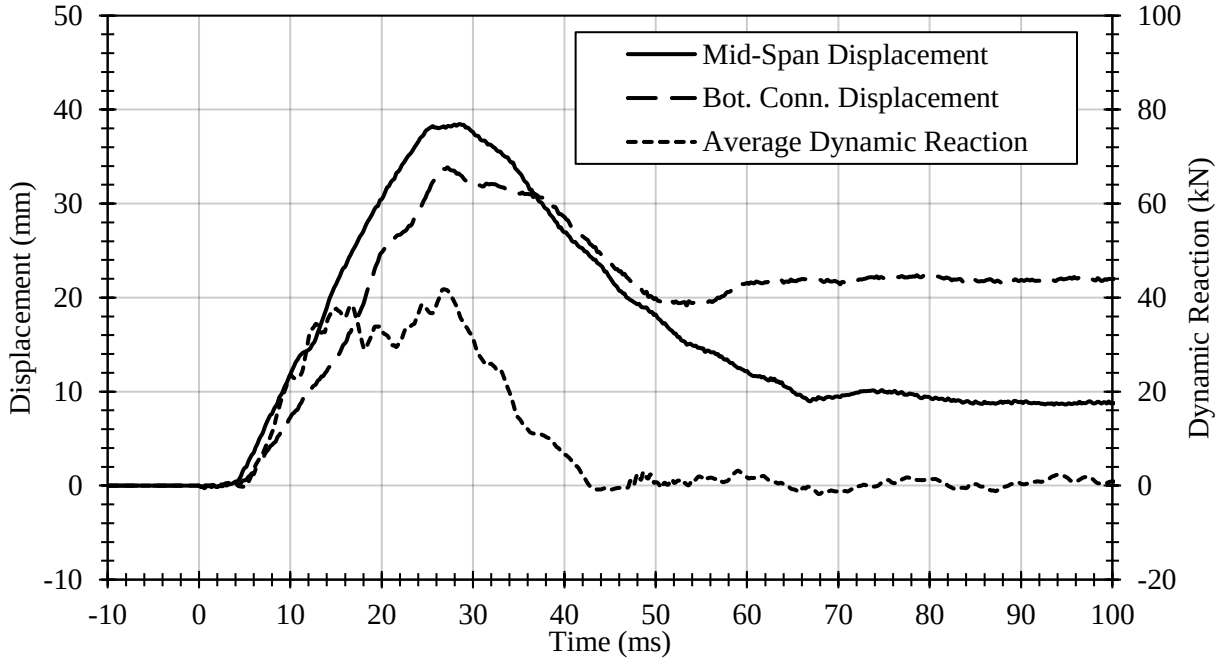
Figure B.36: Documentation of Damage for Test CLT15-1

Specimen CLT15 – Shot #2

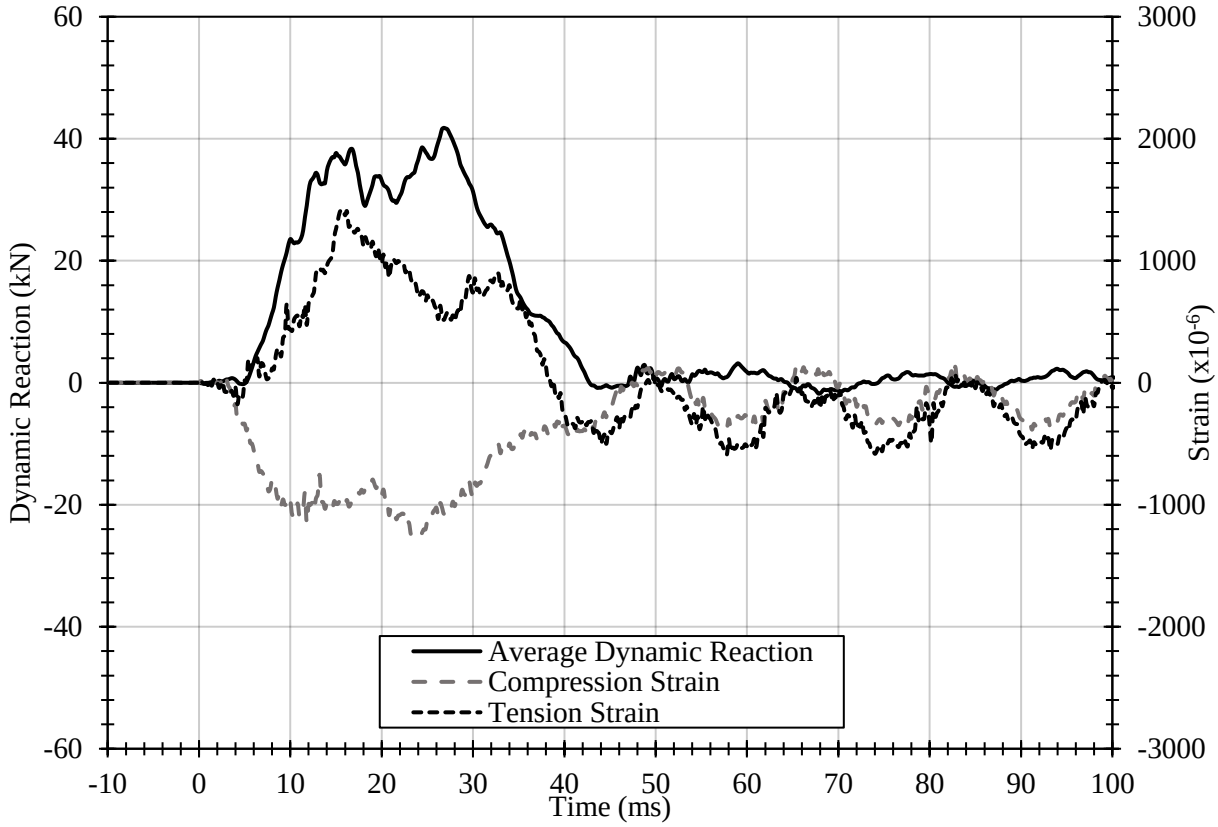
For the second shot, it was dynamically tested on October 1st 2019. A driver pressure of 279.9 kPa was used, which resulted in a positive peak reflected pressure and impulse of 44.2 kPa and 396.6 kPa-ms, respectively.



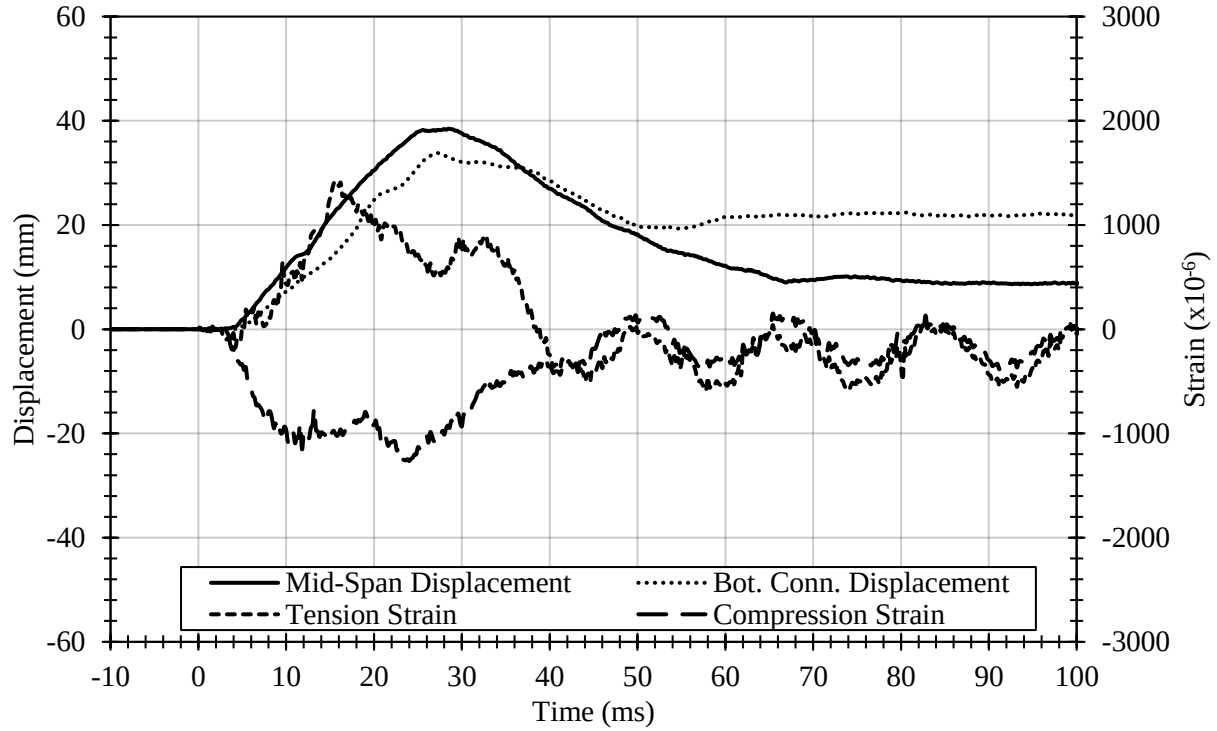
(a) Pressure and Impulse



(b) Reaction and Displacements

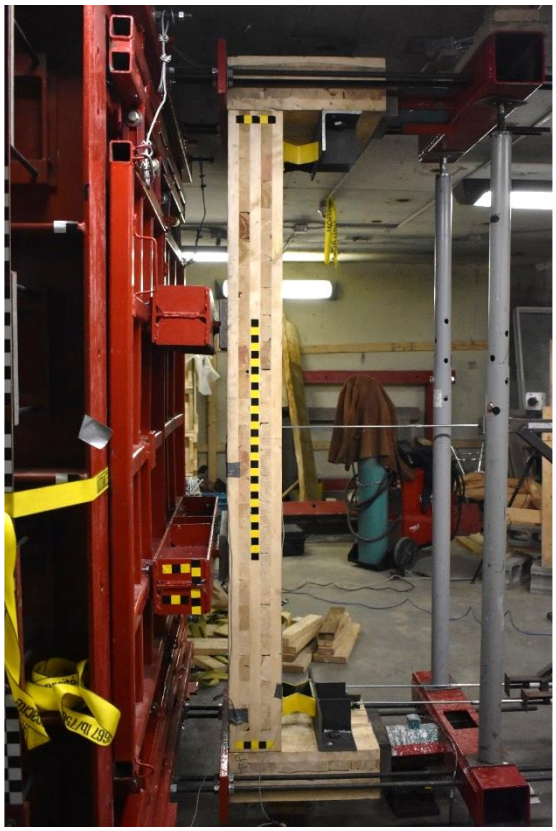


(c) Reaction and Strains

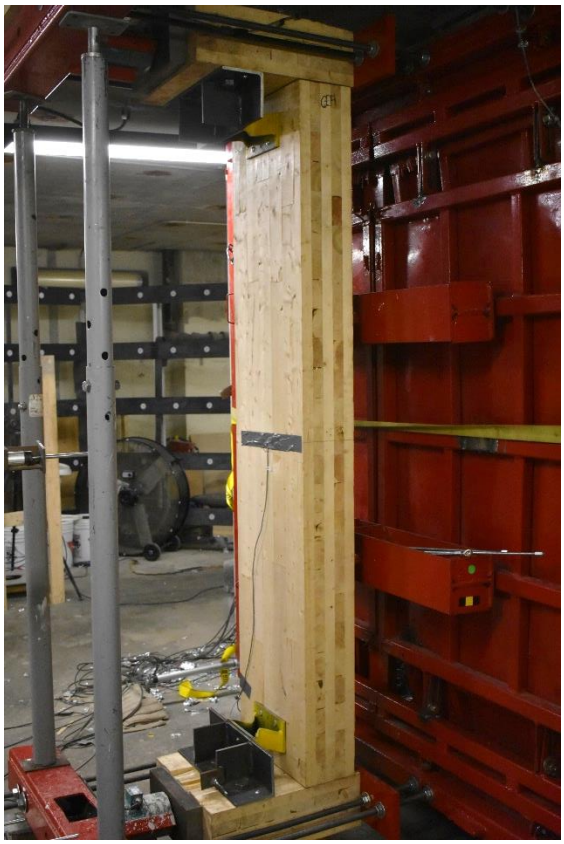


(d) Displacement and Strains

Figure B.37: Dynamic Test Results for Test CLT15-2



(a) Specimen Prior to Testing



(b) Specimen After Testing



(c) Residual Displacement at Bottom Connection

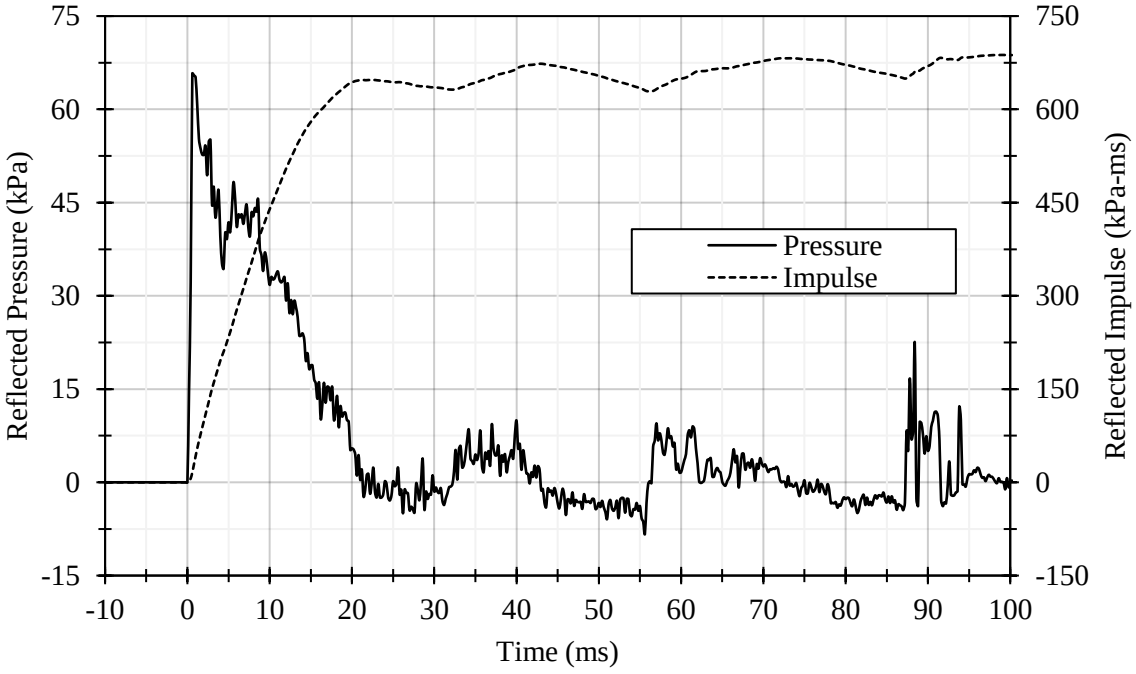


(d) Residual Displacement at Top Connection

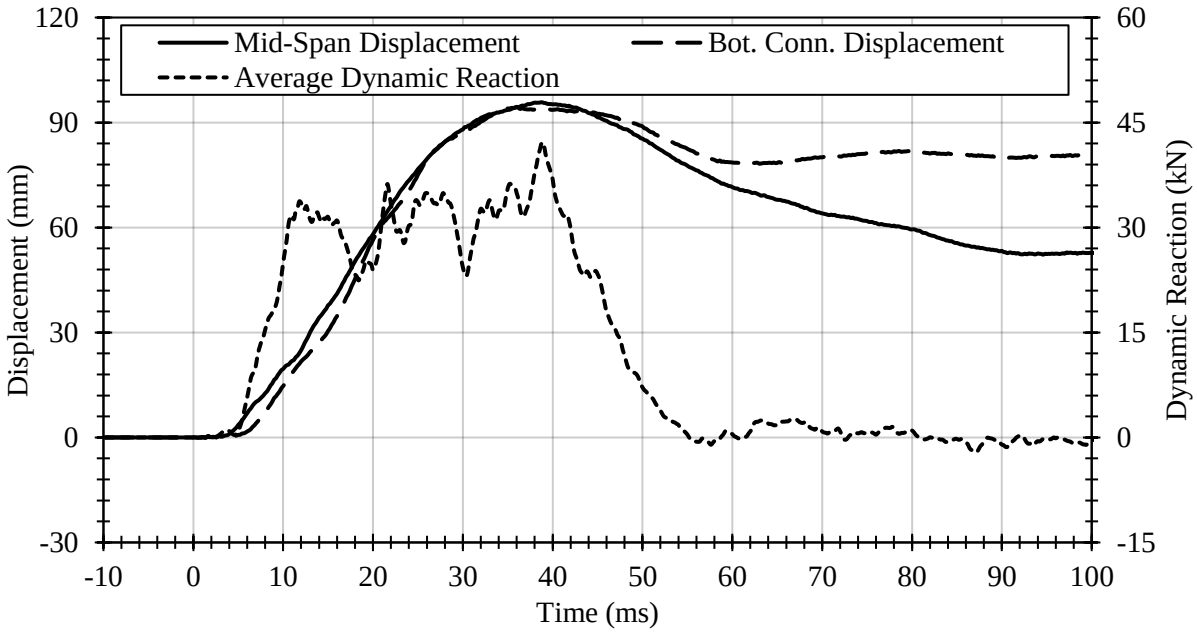
Figure B.38: Documentation of Damage for Test CLT15-2

Specimen CLT15 – Shot #3

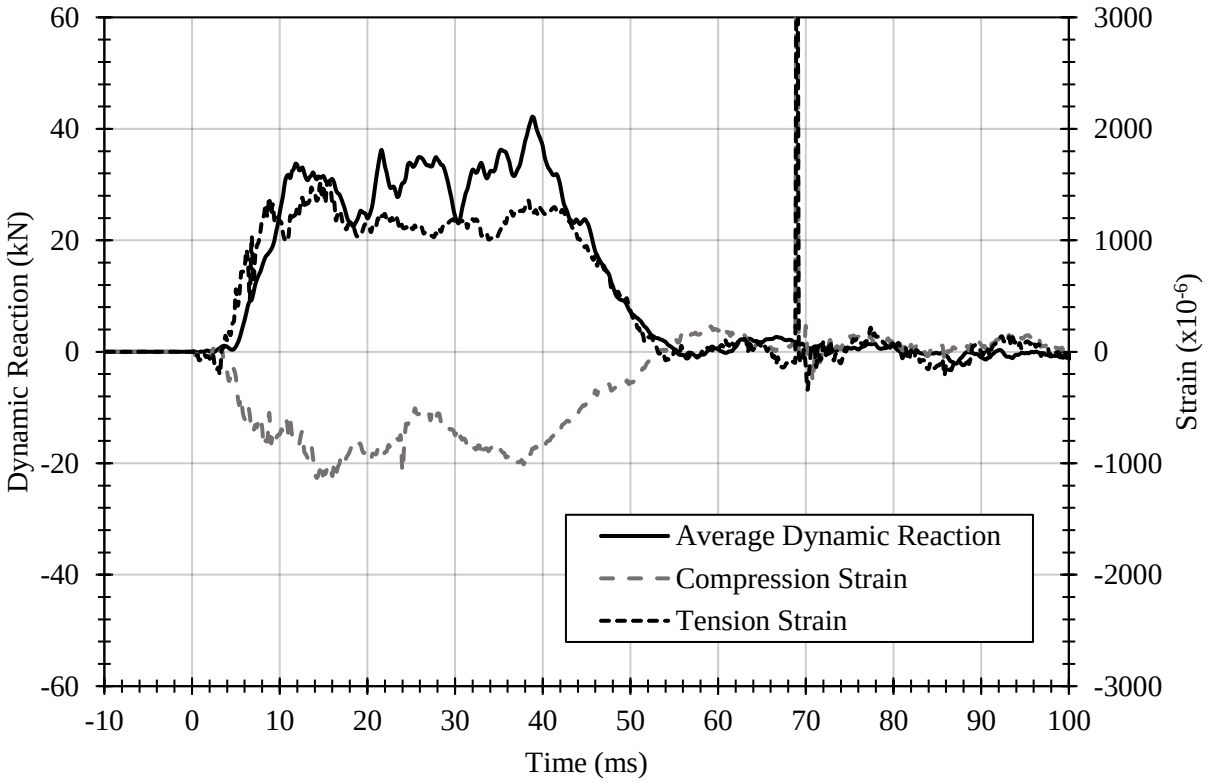
For the third shot, it was dynamically tested on October 1st 2019. A driver pressure of 477.8 kPa was used, which resulted in a positive peak reflected pressure and impulse of 65.8 kPa and 865.8 kPa-ms, respectively.



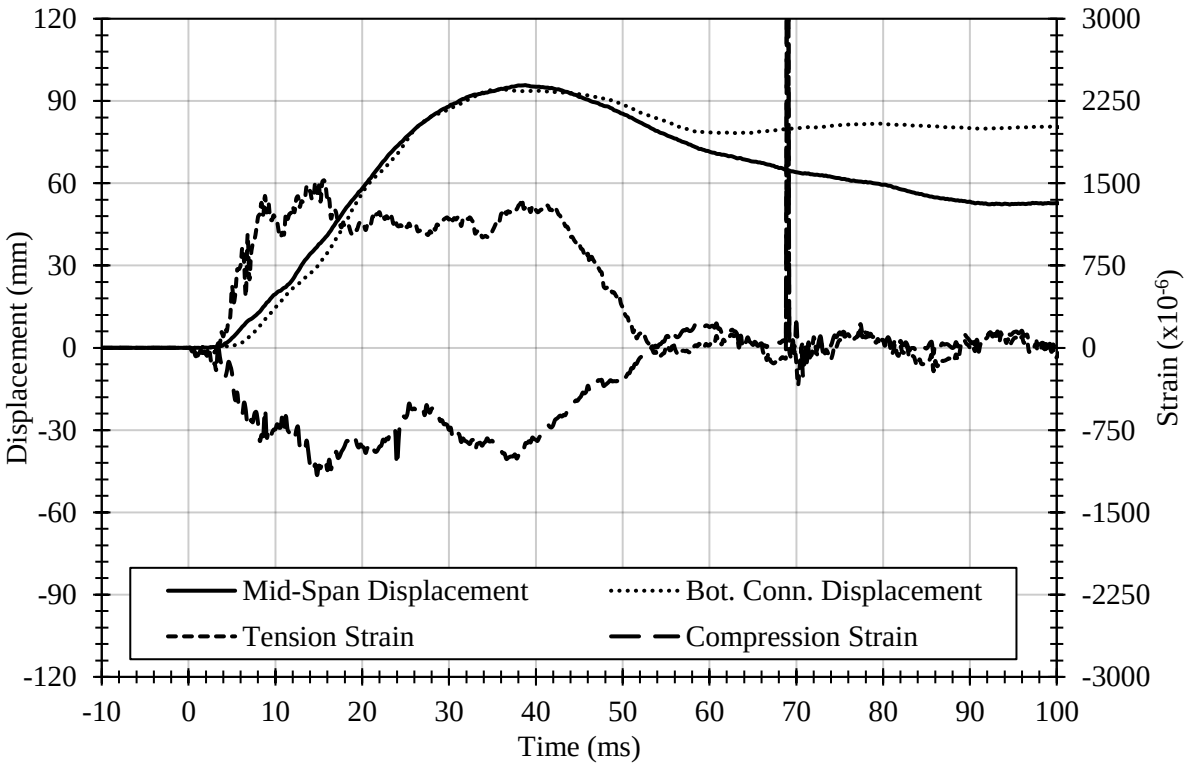
(a) Pressure and Impulse



(b) Reaction and Displacements



(c) Reaction and Strains

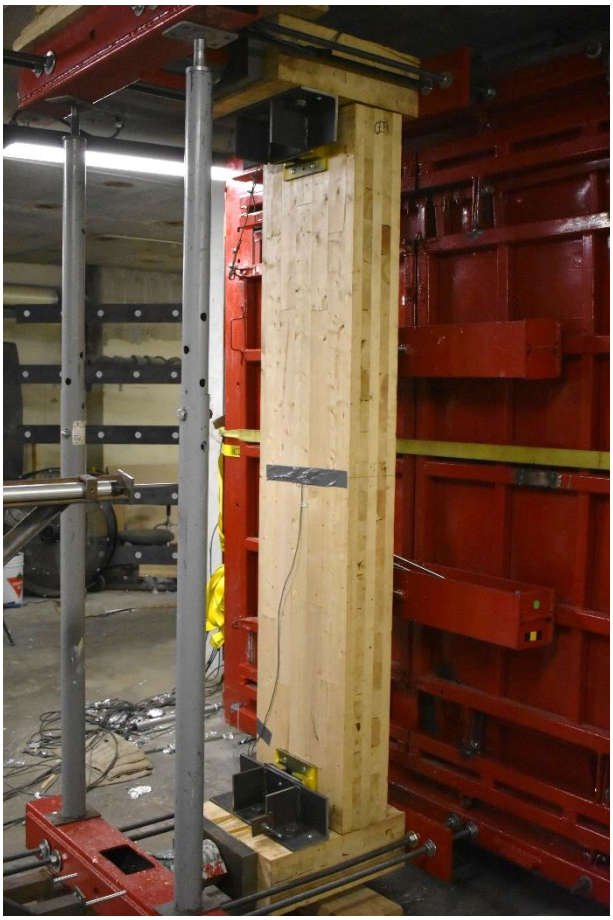


(d) Displacement and Strains

Figure B.39: Dynamic Test Results for Test CLT15-3



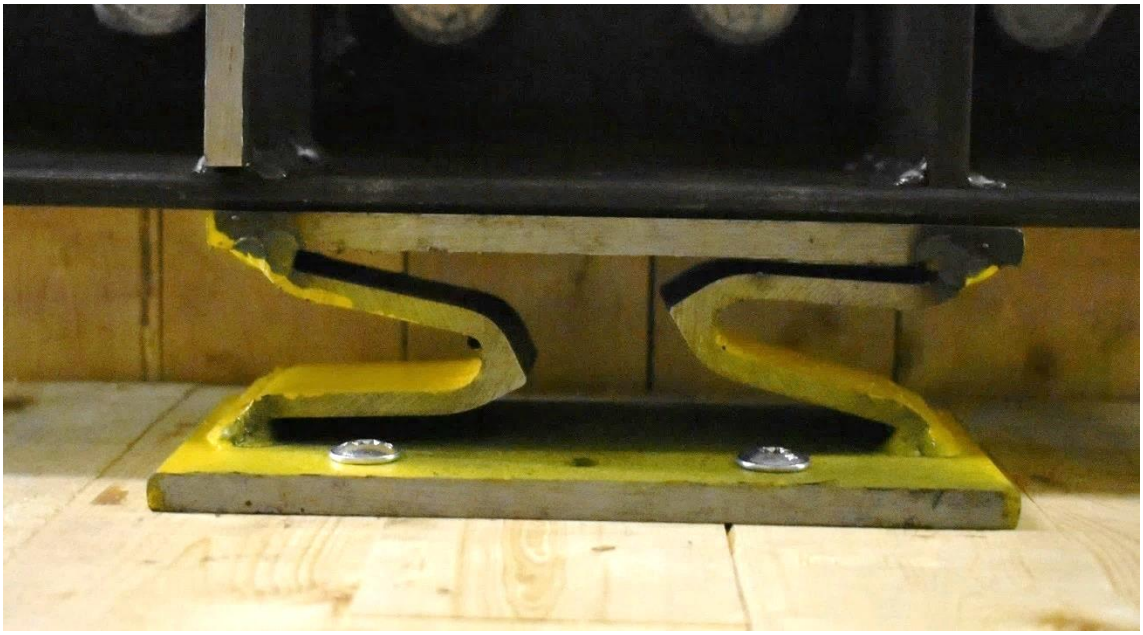
(a) Specimen Prior to Testing



(b) Specimen After Testing



(c) Damage in Bottom EAC

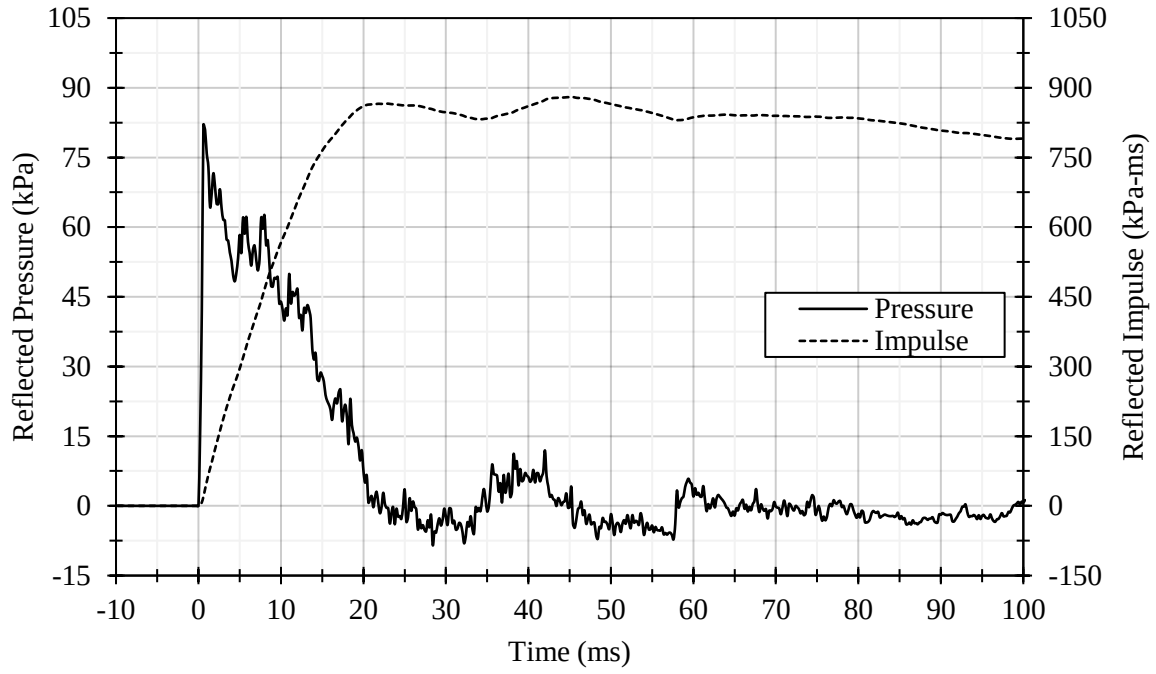


(d) Damage in Top EAC

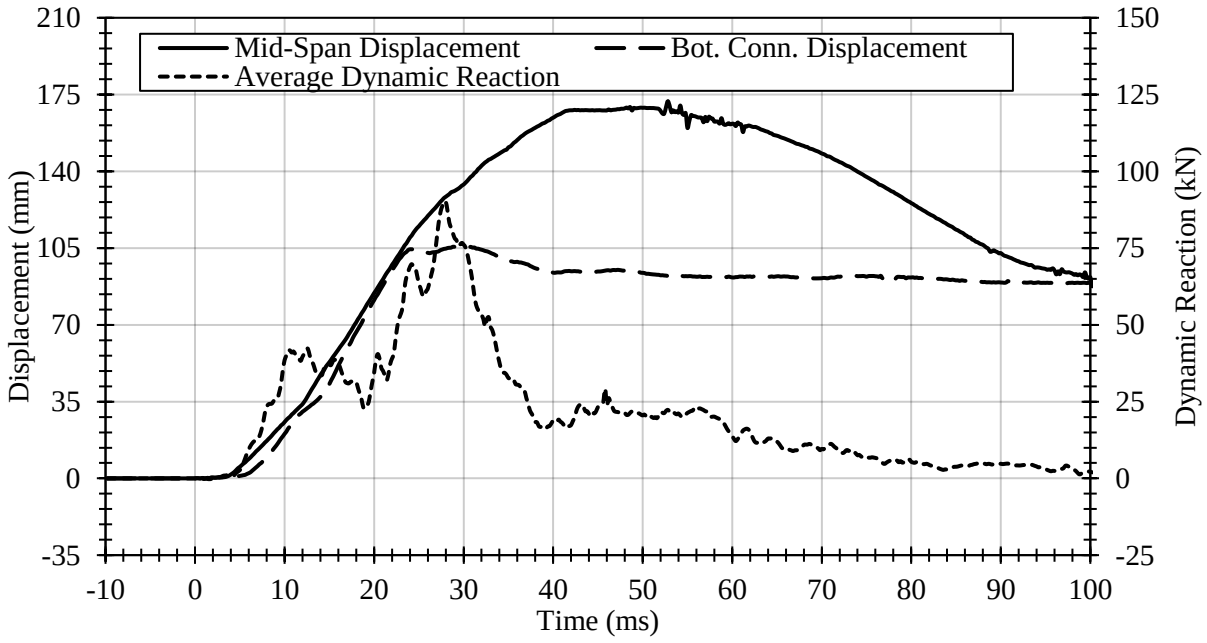
Figure B.40: Documentation of Damage for Test CLT15-3

Specimen CLT15 – Shot #4

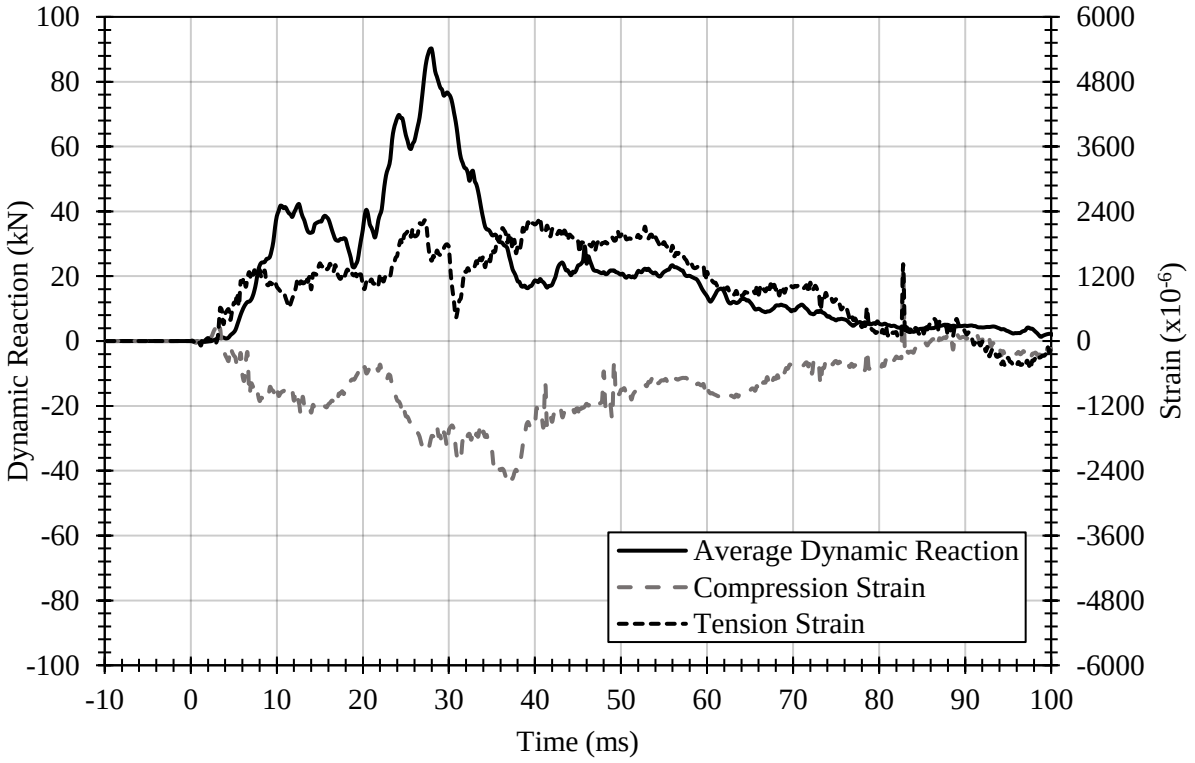
For the fourth shot, it was dynamically tested on October 2nd 2019. A driver pressure of 688.1 kPa was used, which resulted in a positive peak reflected pressure and impulse of 82.0 kPa and 865.8 kPa-ms, respectively.



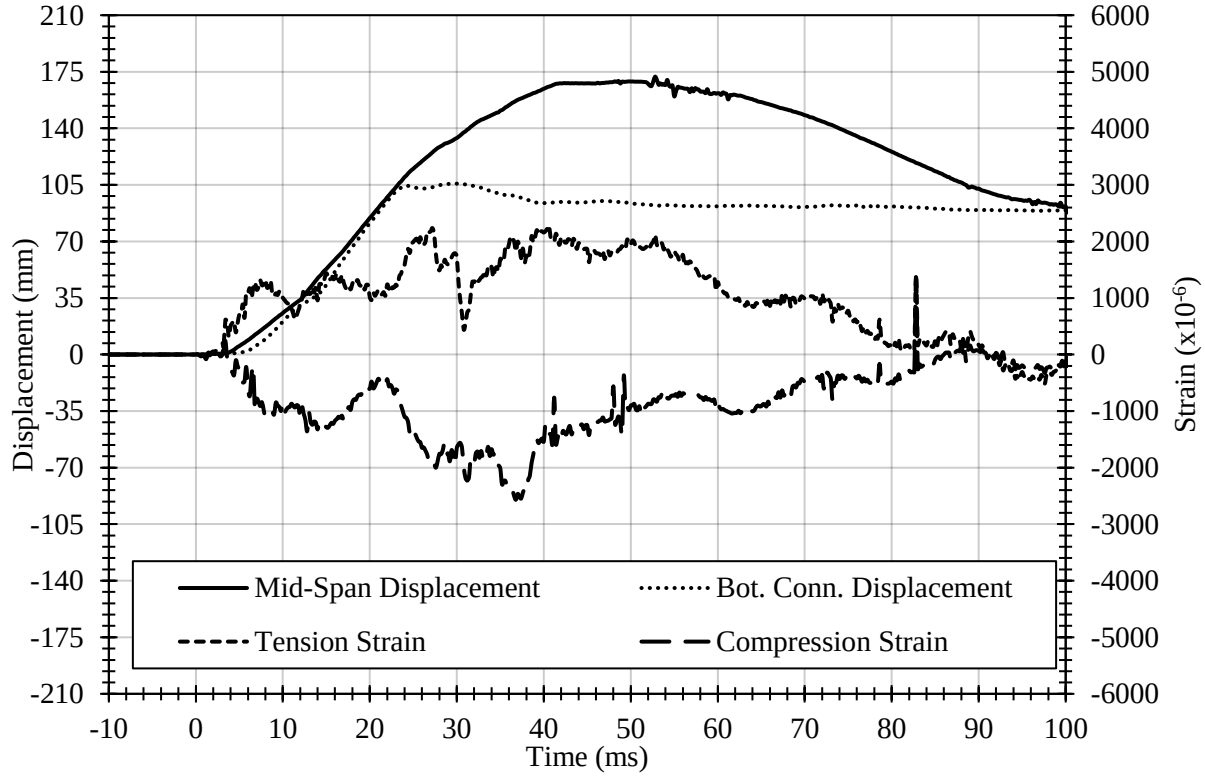
(a) Pressure and Impulse



(b) Reaction and Displacements

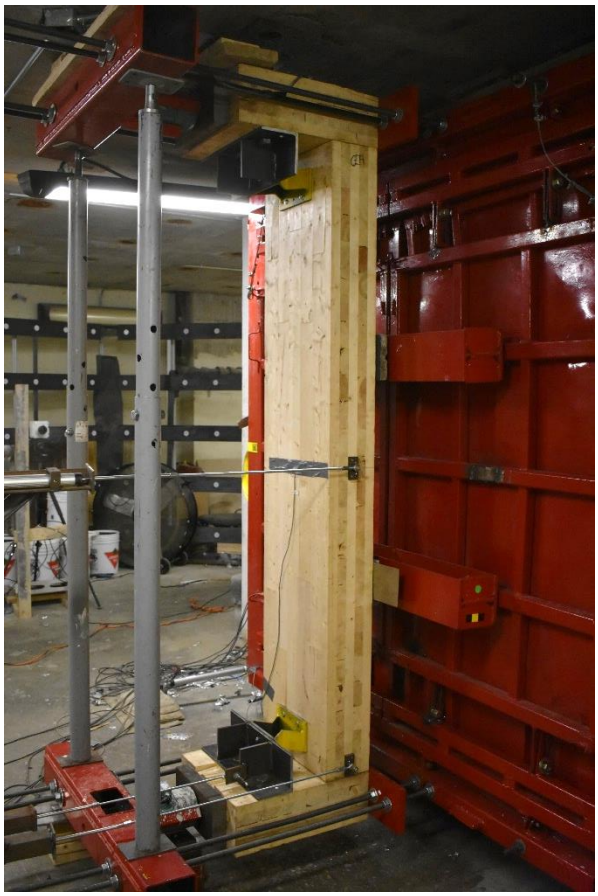


(c) Reaction and Strains

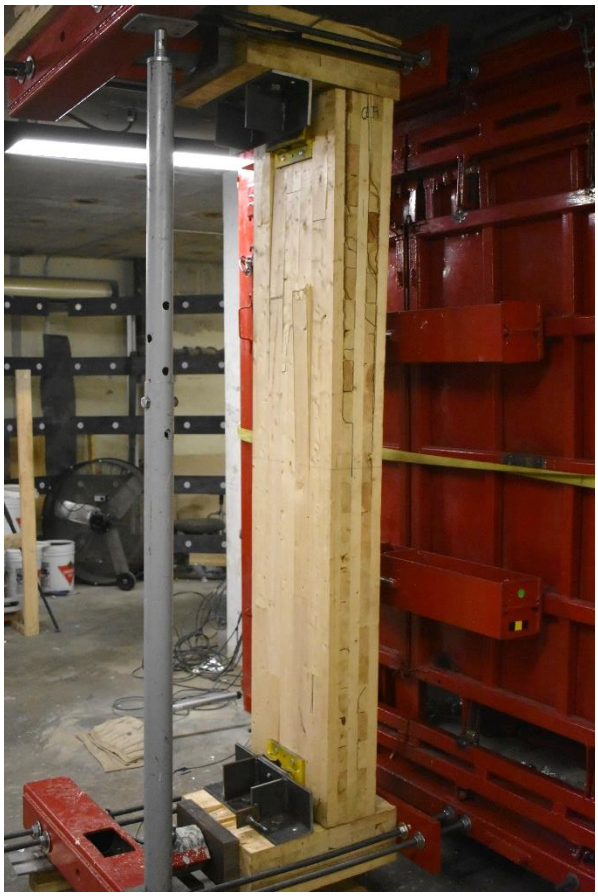


(d) Displacement and Strains

Figure B.41: Dynamic Test Results for Test CLT15-4



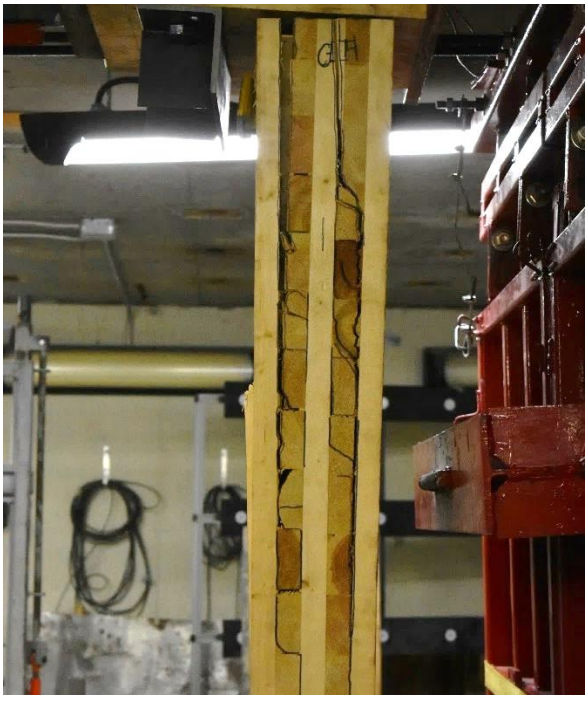
(a) Specimen Prior to Testing



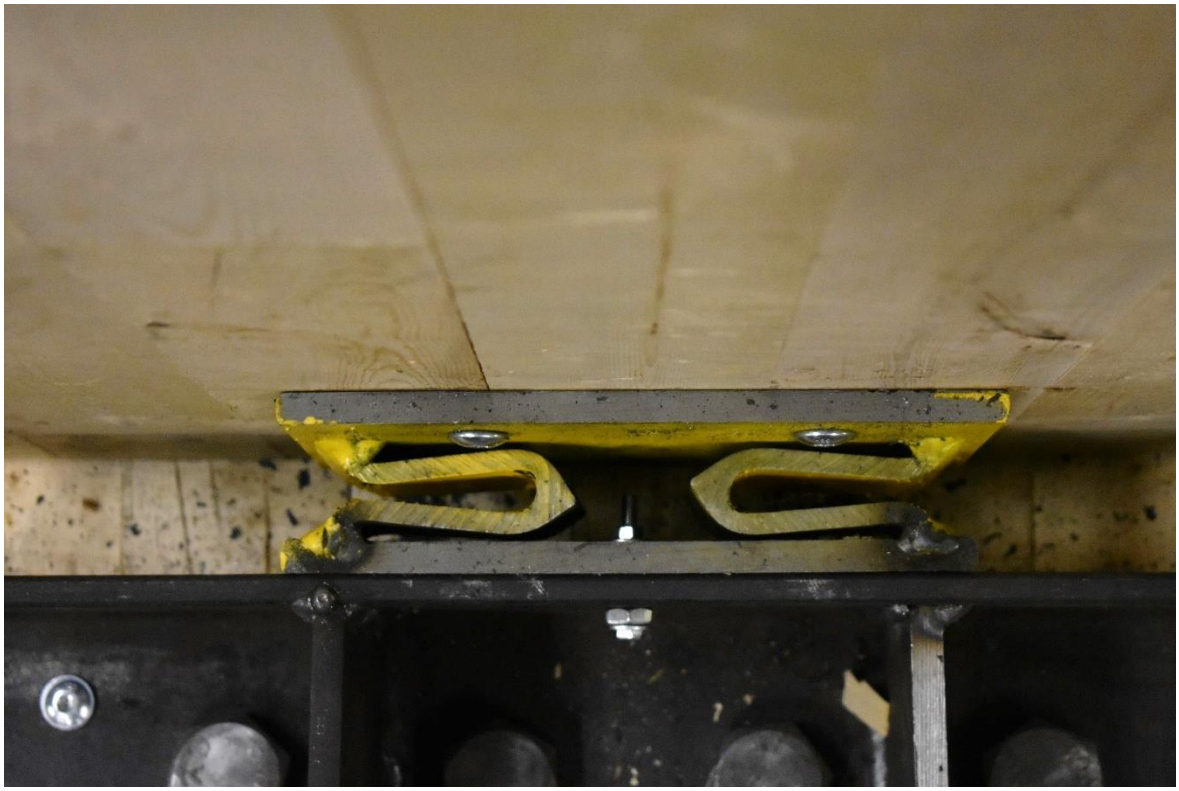
(b) Specimen After Testing



(c) Flexural Failure in Panel



(d) Rolling Shear Damage



(e) Damage in Bottom EAC



(f) Damage in Top EAC

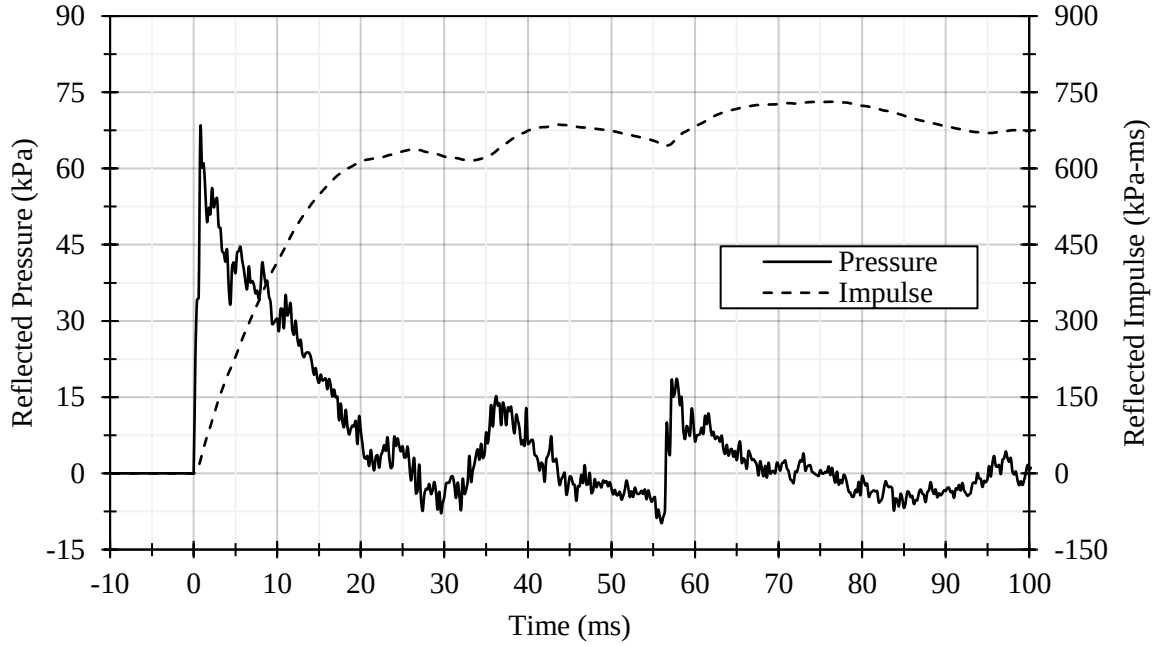
Figure B.42: Documentation of Damage for Test CLT15-4

Appendix C – Test Results of Full-Scale Glulam Specimens

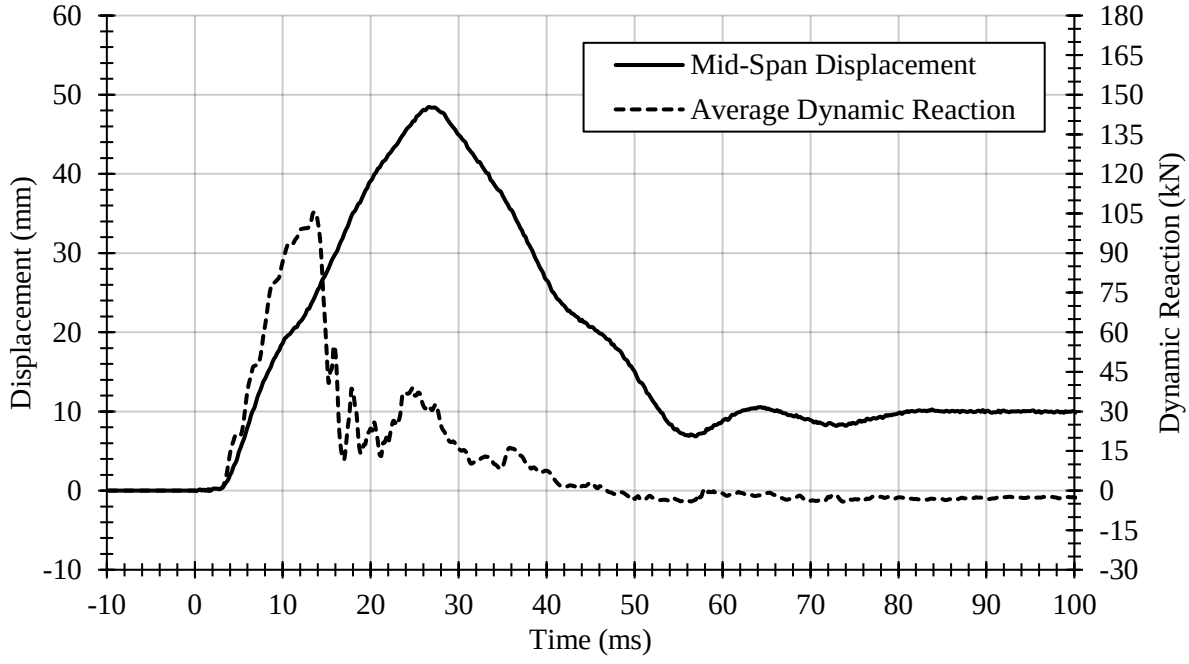
This appendix contains the experimental dynamic results of all tests conducted on full-scale glulam specimens. Typical data presented in the appendix includes a brief synopsis of each test, as well as relevant test results and photographs taken before and after testing. Prior to testing, the moisture content (MC) of each specimen was measured using a *Tramex Moisture Encounter Plus* pinless moisture meter. The MC varied from 10 % to 15 %.

Specimen G1

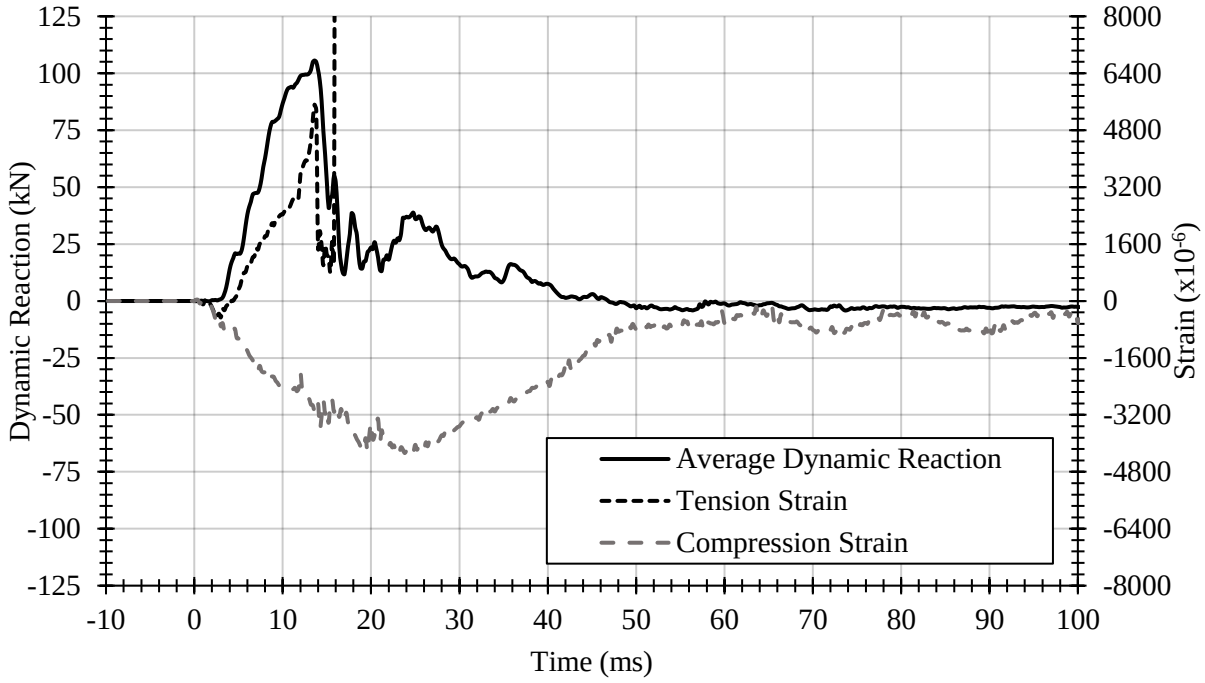
Specimen G1, comprised of a simply-supported glulam beam, was dynamically tested on December 17th 2018. A driver pressure of 461.9 kPa was used, which resulted in a positive peak reflected pressure and impulse of 67.7 kPa and 637.2 kPa-ms, respectively.



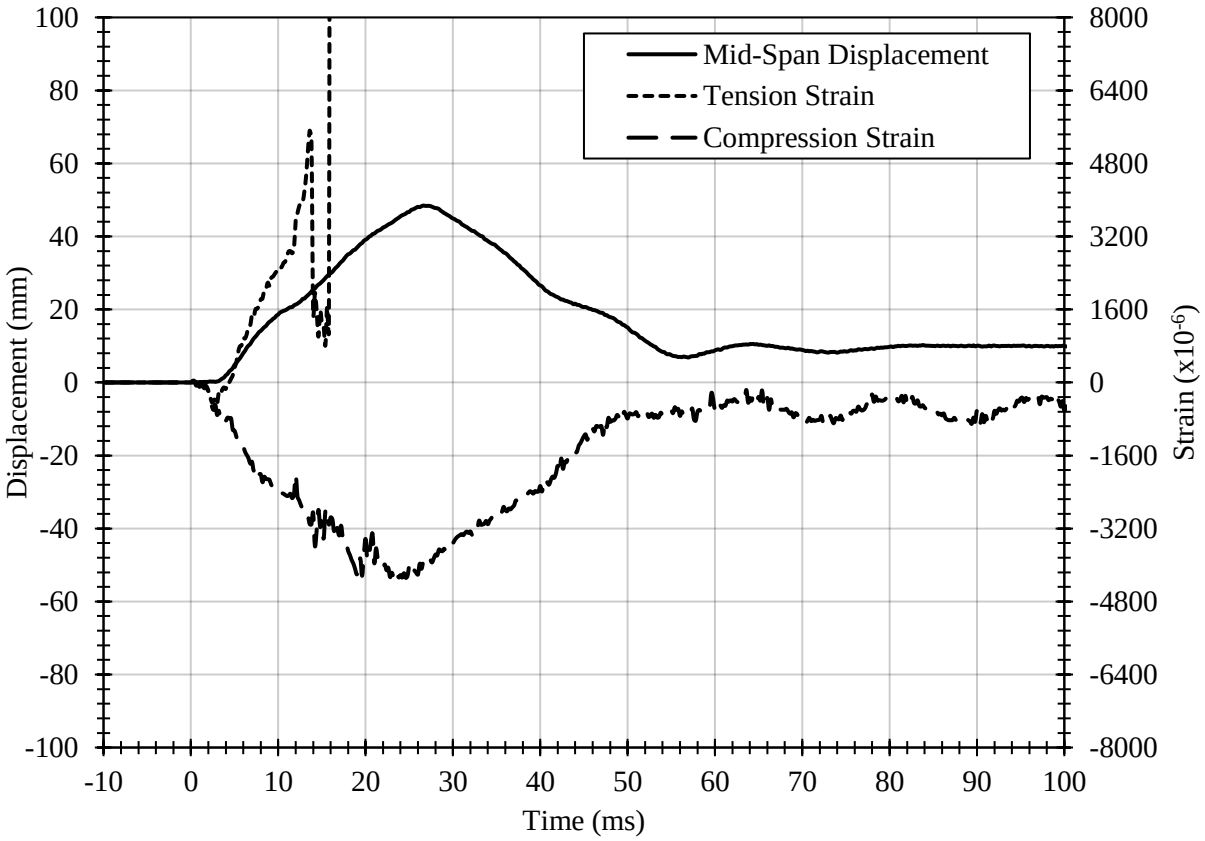
(a) Pressure and Impulse



(b) Reaction and Displacement

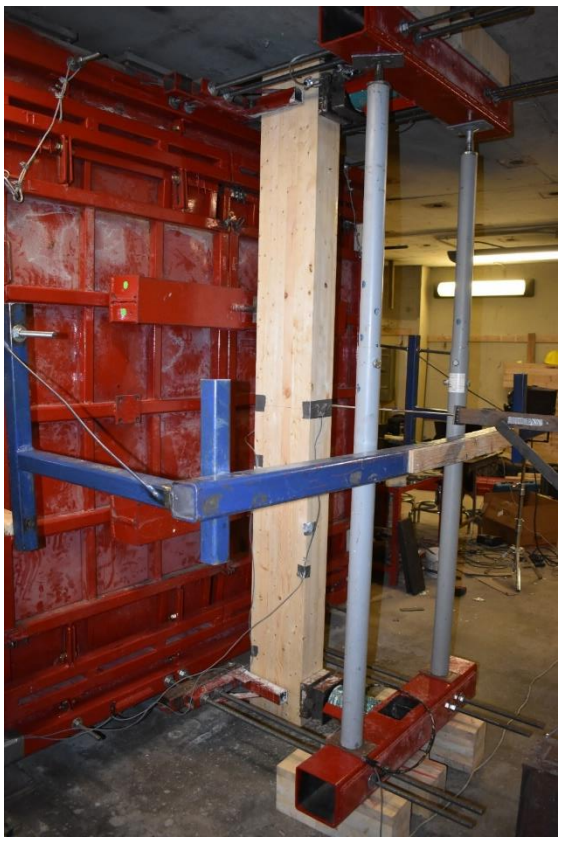


(c) Reaction and Strains

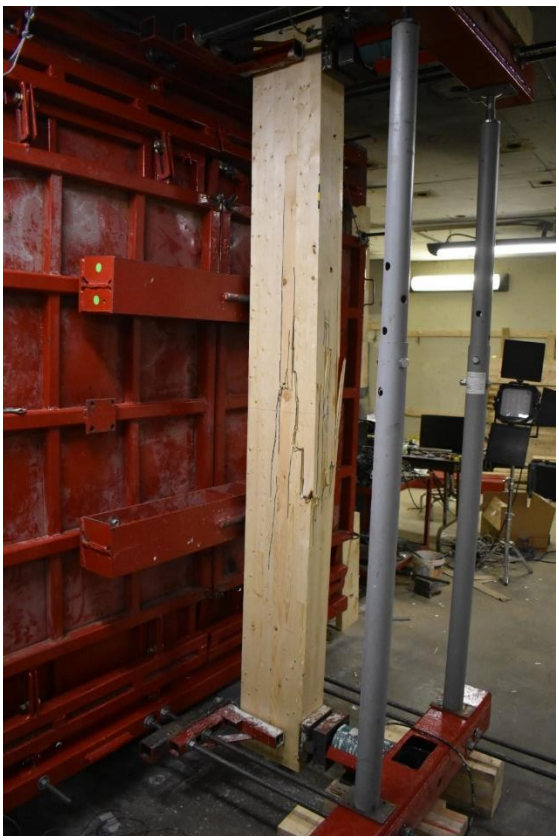


(d) Displacement and Strains

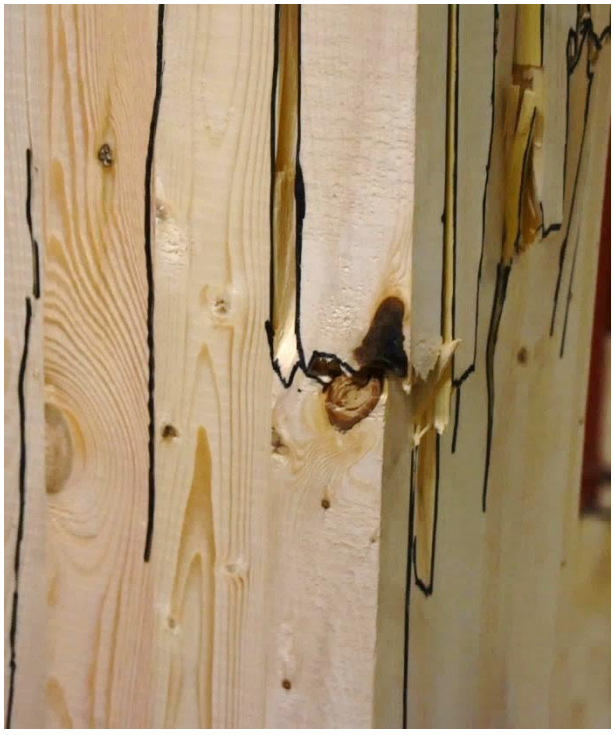
Figure C.1: Dynamic Test Results for Specimen G1



(a) Specimen Prior to Testing



(b) Specimen After Testing



(c) Flexural Failure Initiated at Knot

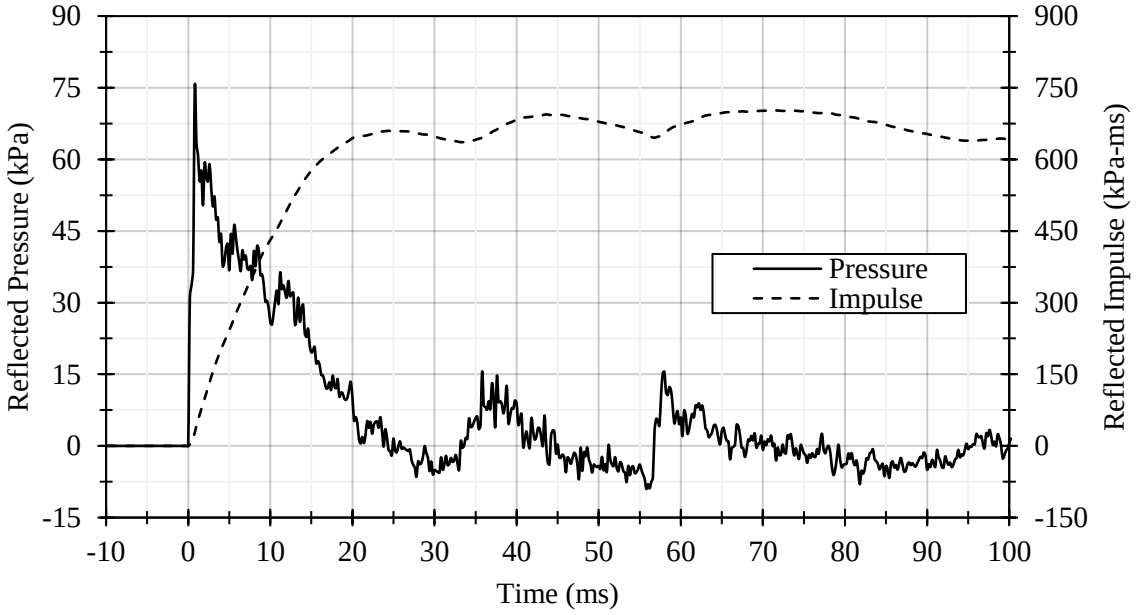


(d) Damage Propagation Through Depth

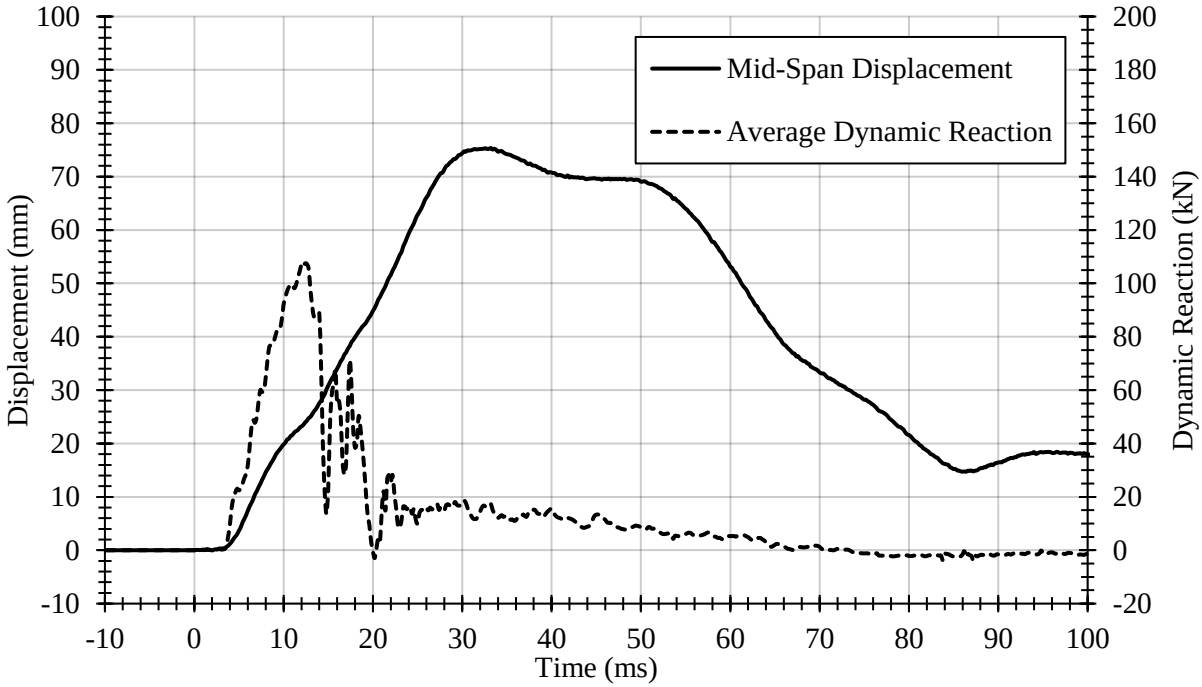
Figure C.2: Documentation of Damage for Specimen G1

Specimen G2

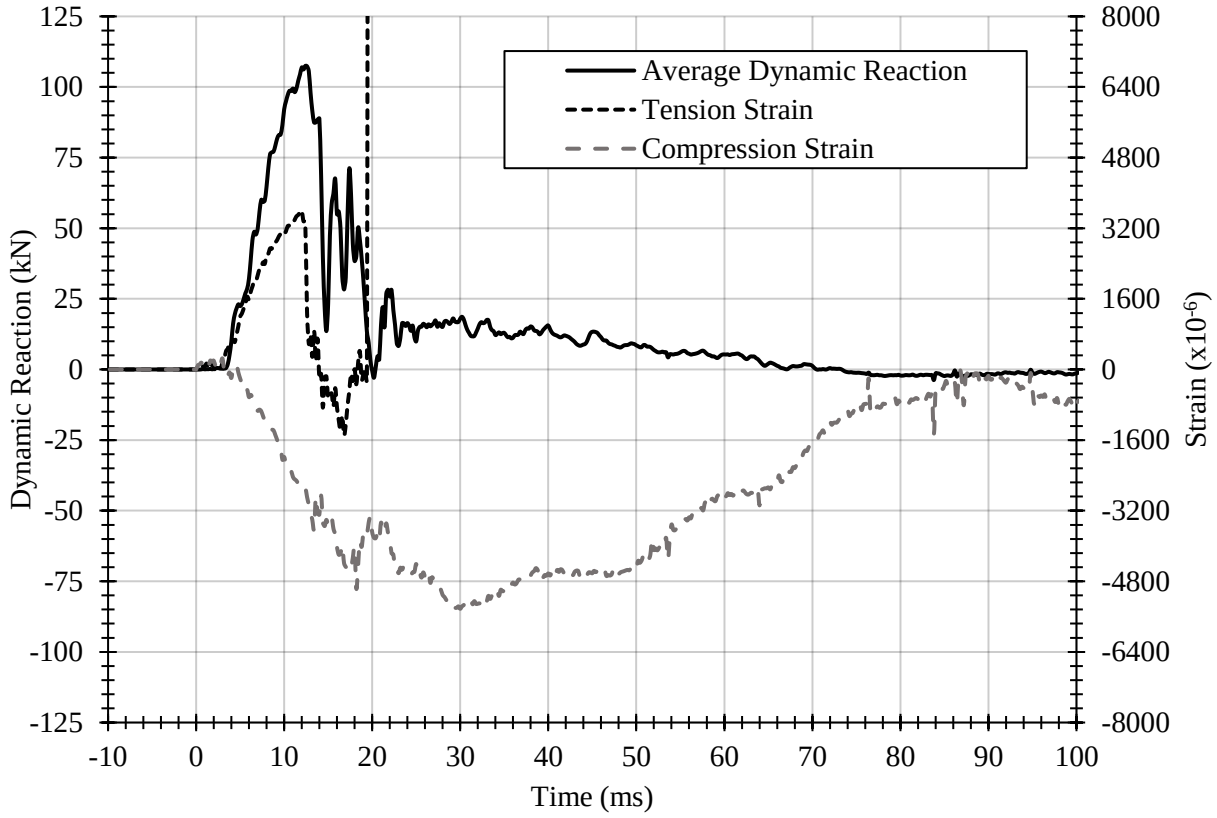
Specimen G2, comprised of a simply-supported Glulam beam, was dynamically tested on December 18th 2018. A driver pressure of 494.4 kPa was used, which resulted in a positive peak reflected pressure and impulse of 75.0 kPa and 659.7 kPa-ms, respectively.



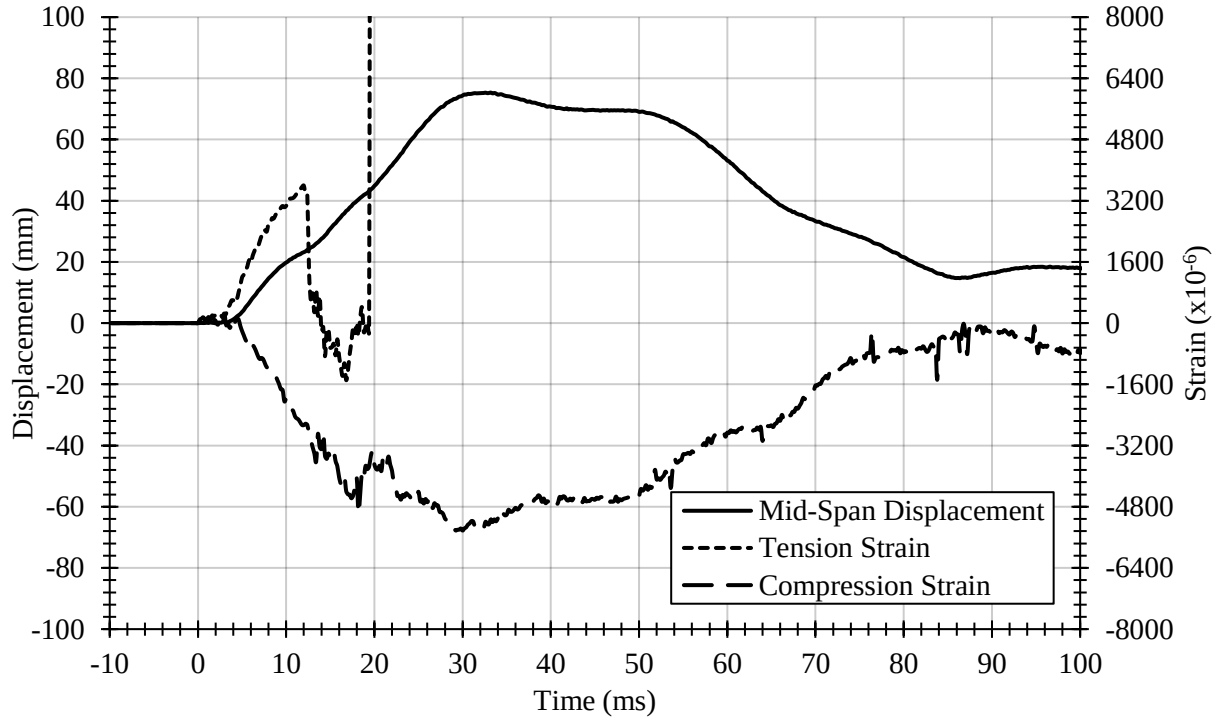
(a) Pressure and Impulse



(b) Reaction and Displacement

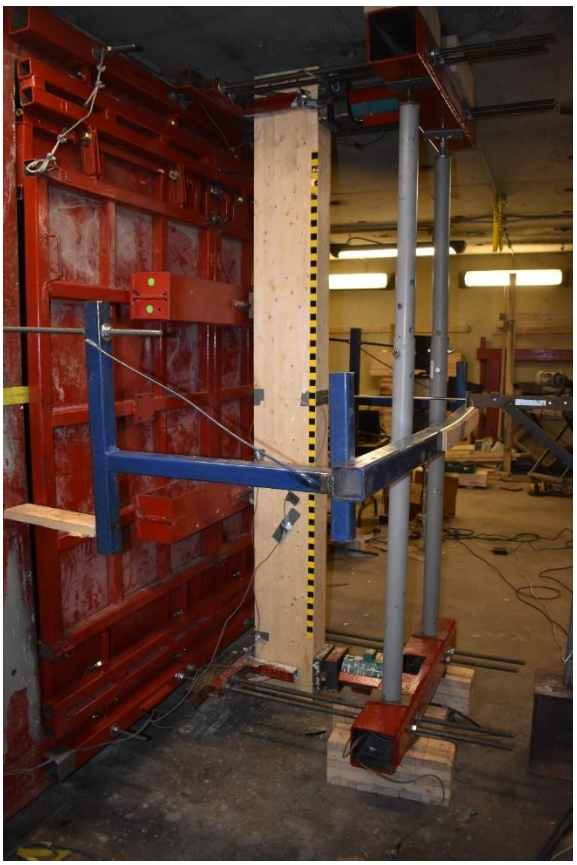


(c) Reaction and Strains



(d) Displacement and Strains

Figure C.3: Dynamic Test Results for Specimen G2



(a) Specimen Prior to Testing



(b) Specimen After Testing



(c) Flexural Damage

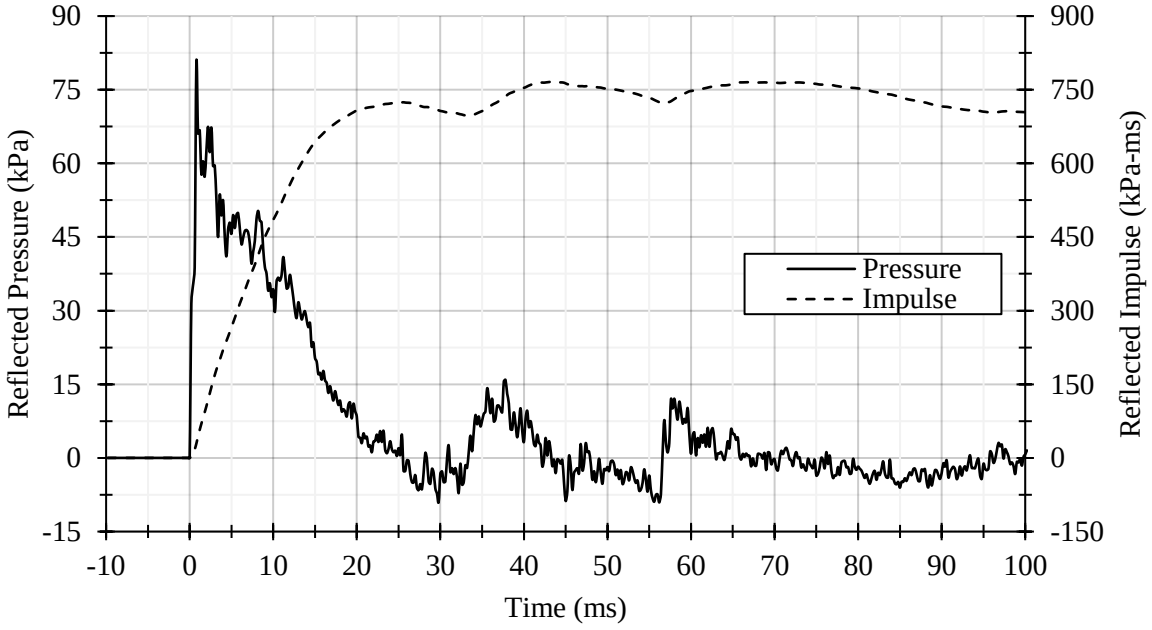


(d) Damage Progression Through Beam

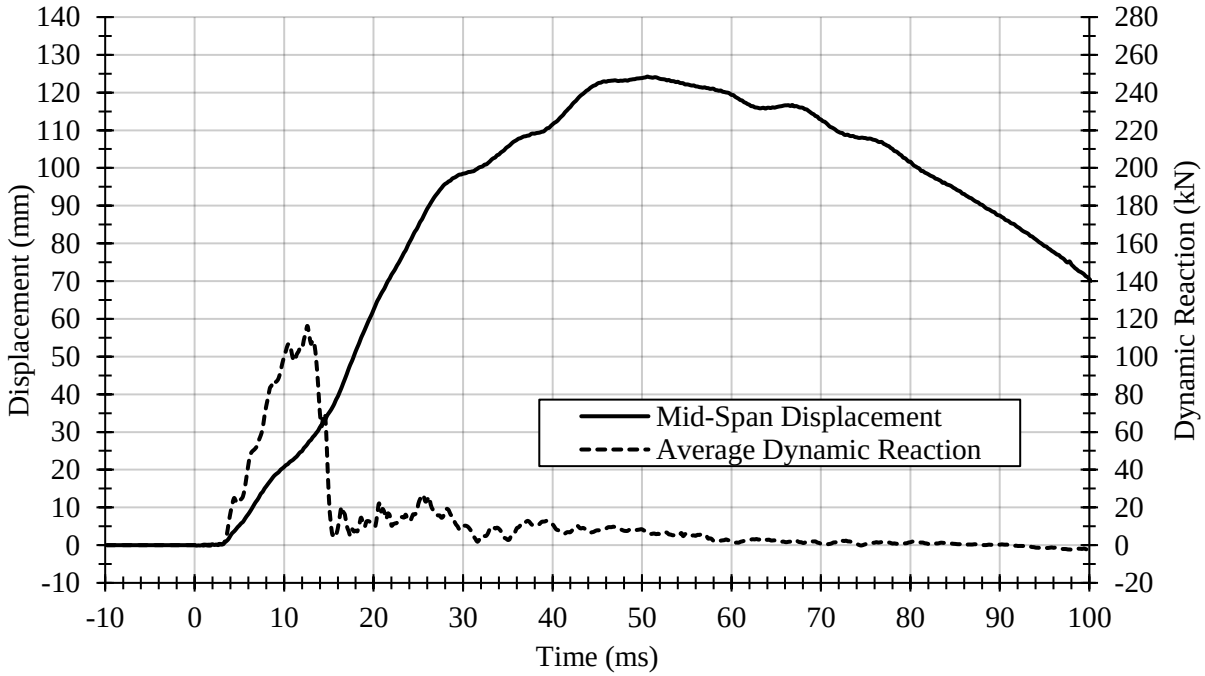
Figure C.4: Documentation of Damage for Specimen G2

Specimen G3

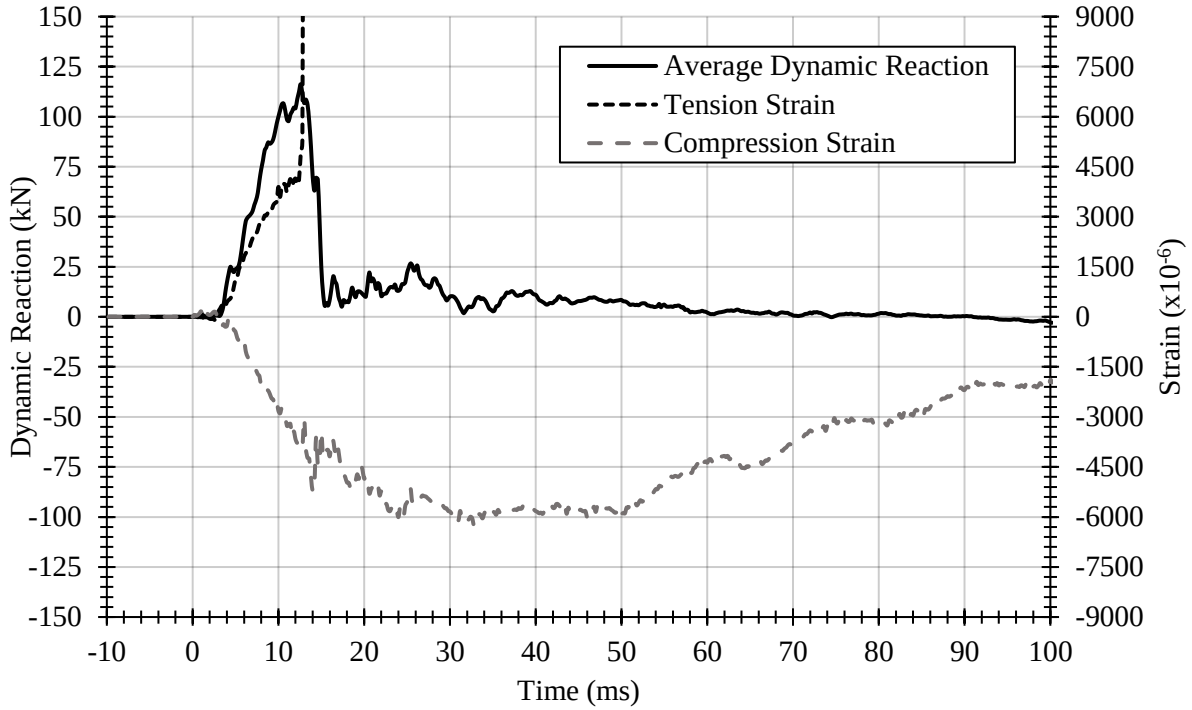
Specimen G3, comprised of a simply-supported Glulam beam, was dynamically tested on December 19th 2018. A driver pressure of 534.3 kPa was used, which resulted in a positive peak reflected pressure and impulse of 80.4 kPa and 724.4 kPa-ms, respectively.



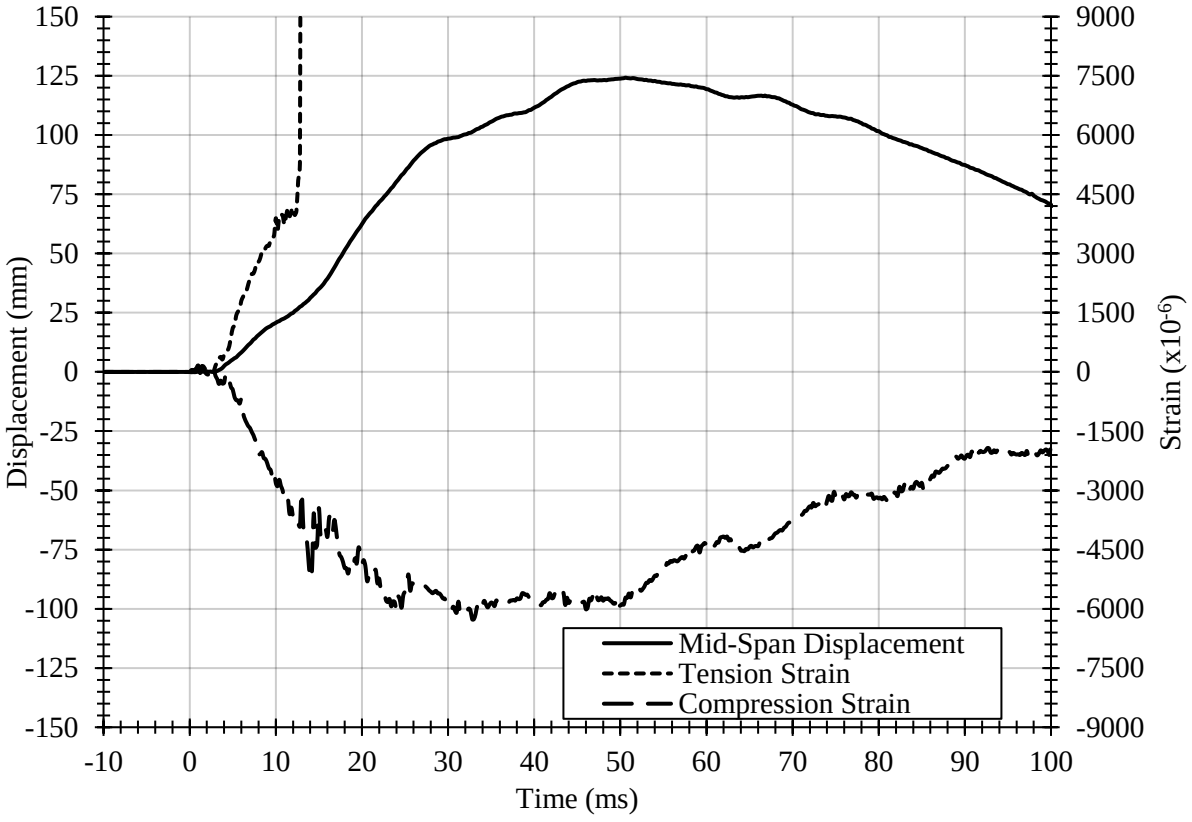
(a) Pressure and Impulse



(b) Reaction and Displacement

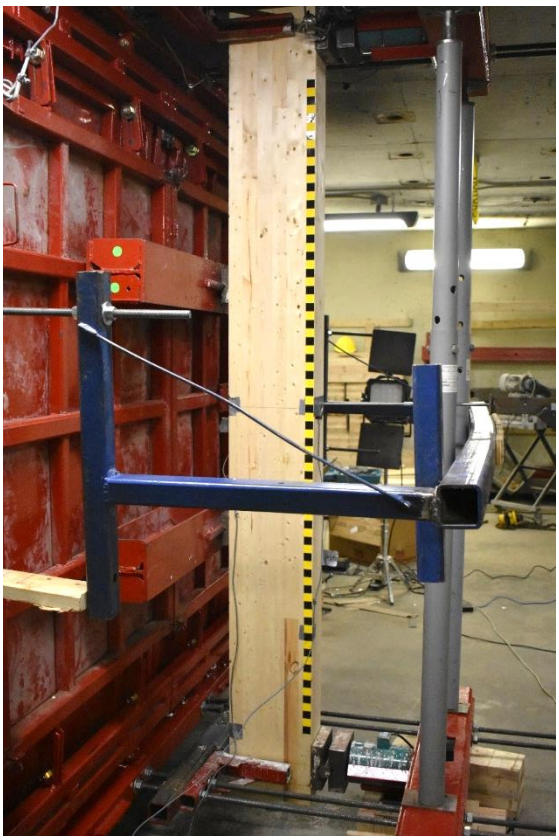


(c) Reaction and Strains

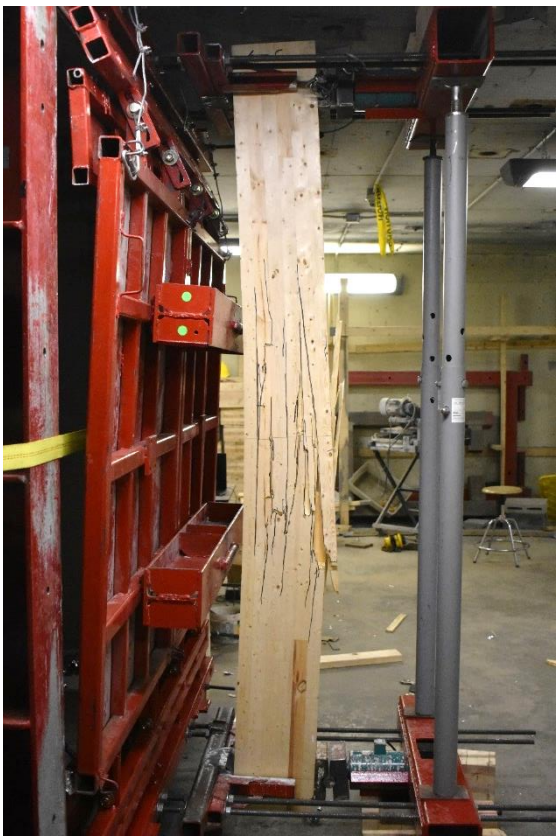


(d) Displacement and Strains

Figure C.5: Dynamic Test Results for Specimen G3



(a) Specimen Prior to Testing



(b) Specimen After Testing



(c) Flexural Failure

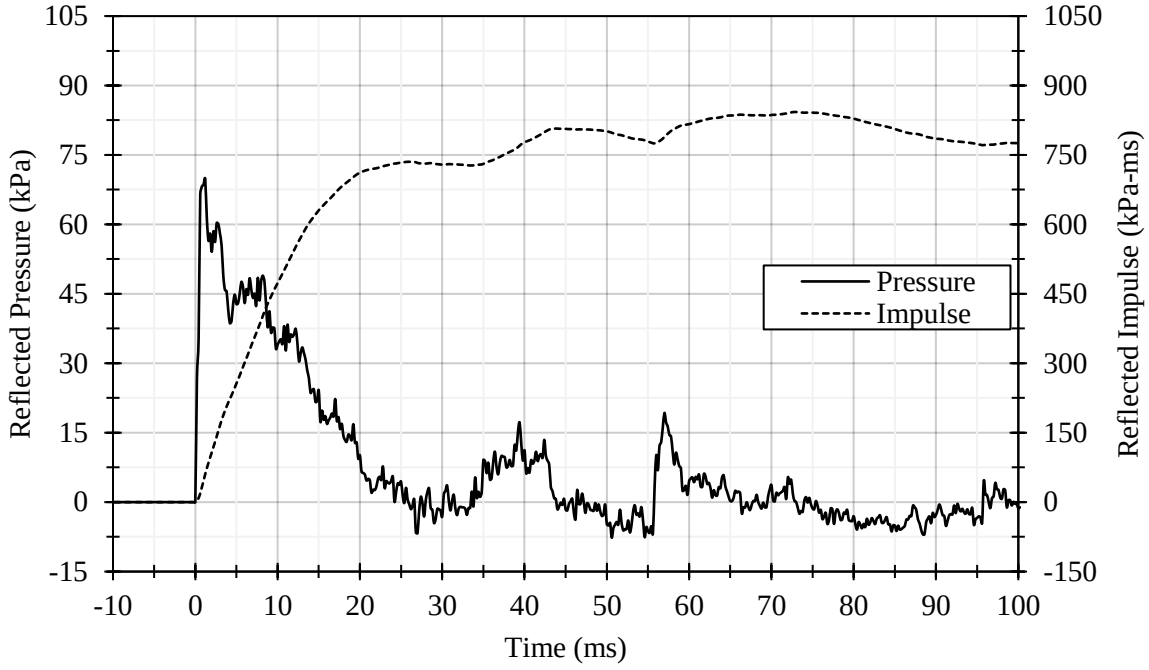


(d) Damage Progression Through Beam

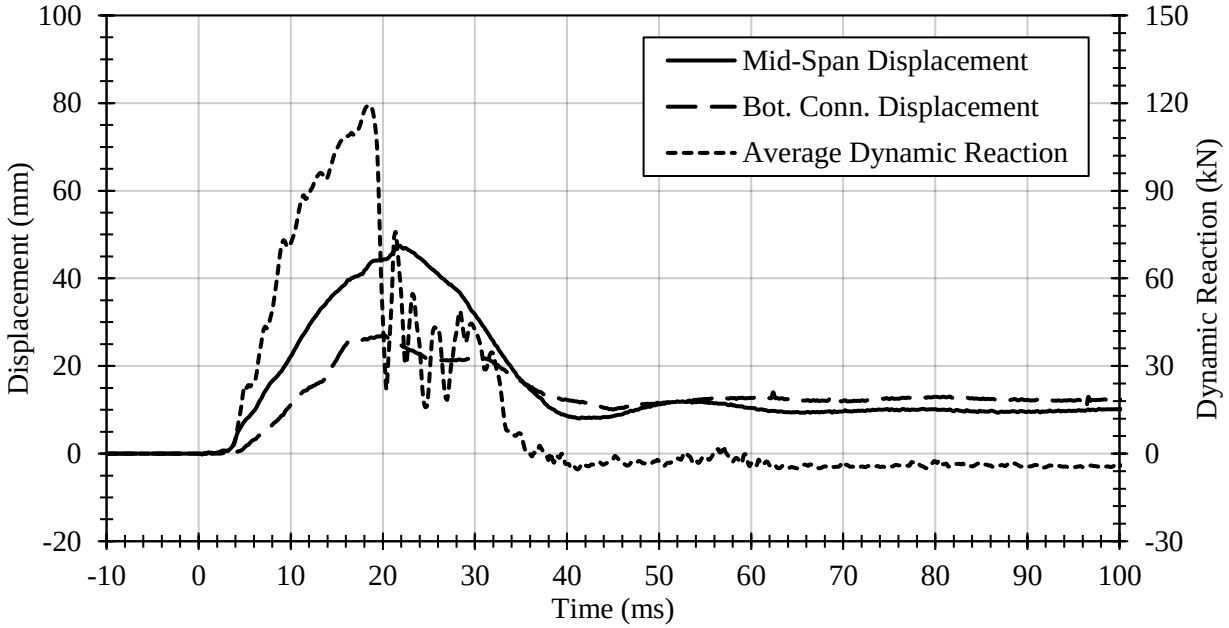
Figure C.6: Documentation of Damage for Specimen G3

Specimen G4

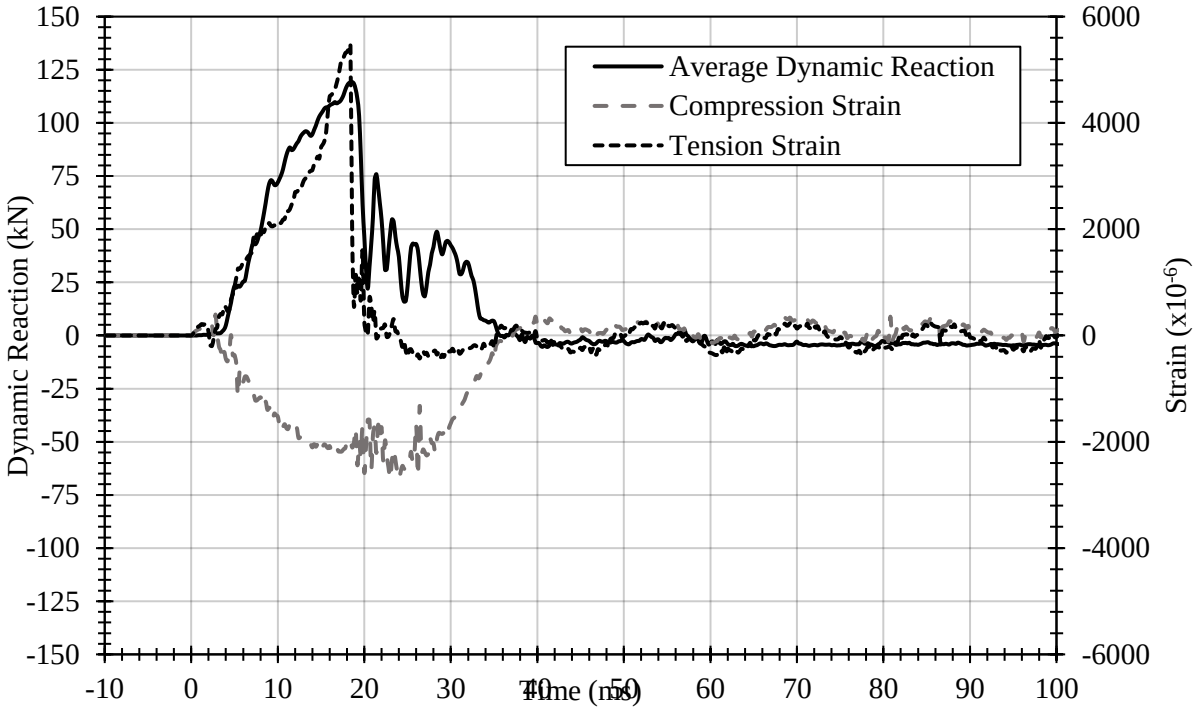
Specimen G4, comprised of a Glulam beam with a 2x1 bolted connection at each end, was dynamically tested on July 16th 2019. A driver pressure of 548.1 kPa was used, which resulted in a positive peak reflected pressure and impulse of 69.9 kPa and 735.2 kPa-ms, respectively.



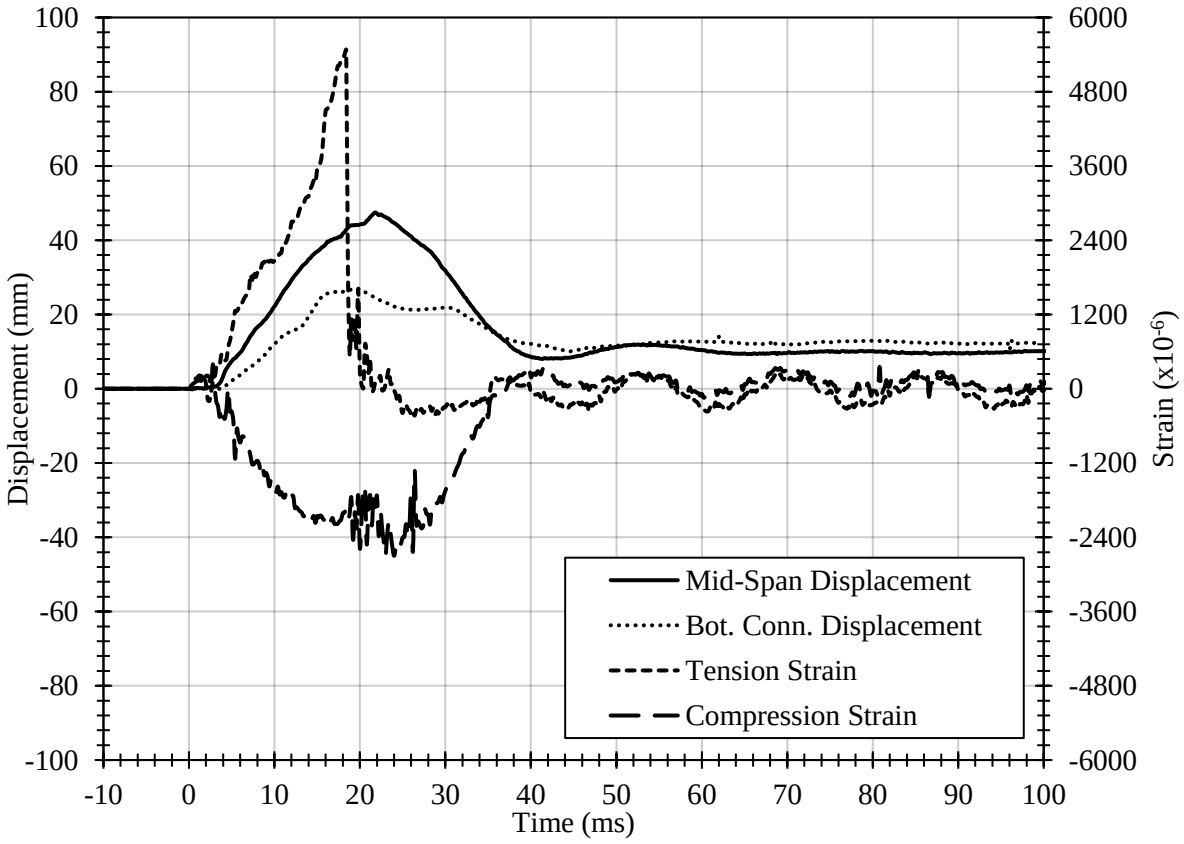
(a) Pressure and Impulse



(b) Reaction and Displacement



(c) Reaction and Strains

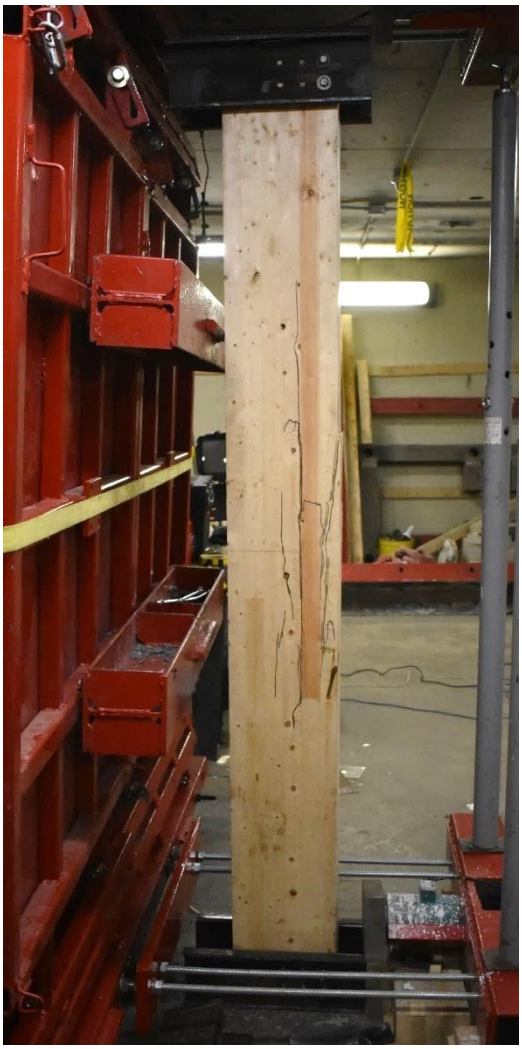


(d) Displacement and Strains

Figure C.7: Dynamic Test Results for Specimen G4



(a) Specimen Prior to Testing



(b) Specimen After Testing



(c) Flexural Failure



(d) Wood Crushing in Bottom Joint



(e) Wood Crushing in Top Joint

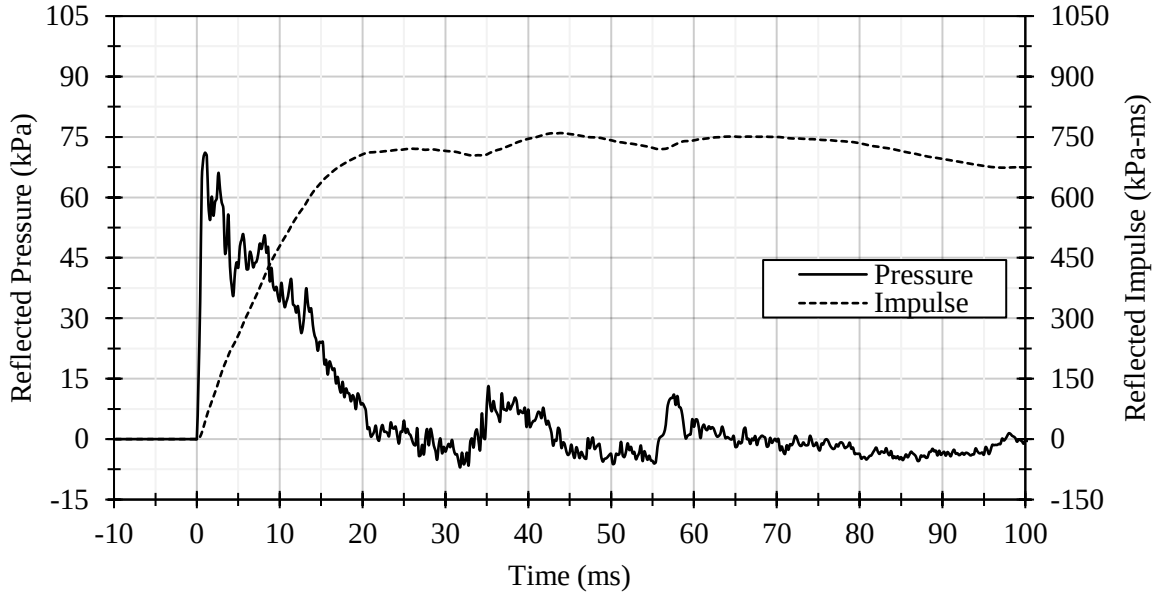


(f) Yielding of Bolts

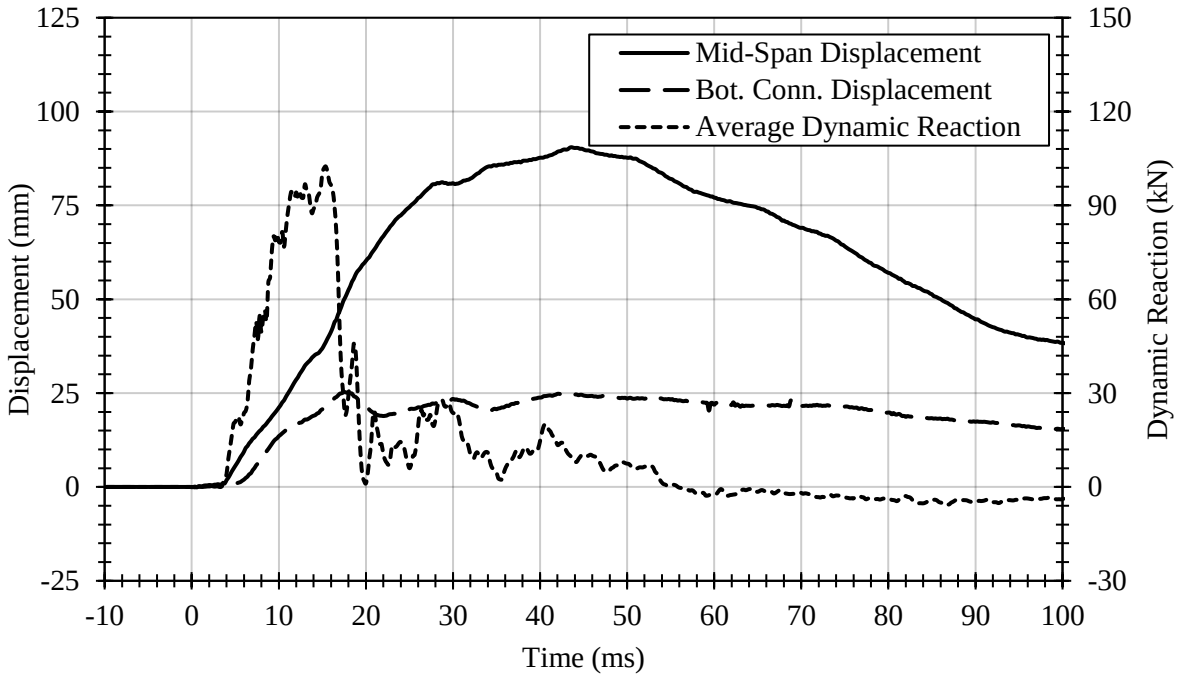
Figure C.8: Documentation of Damage for Specimen G4

Specimen G5

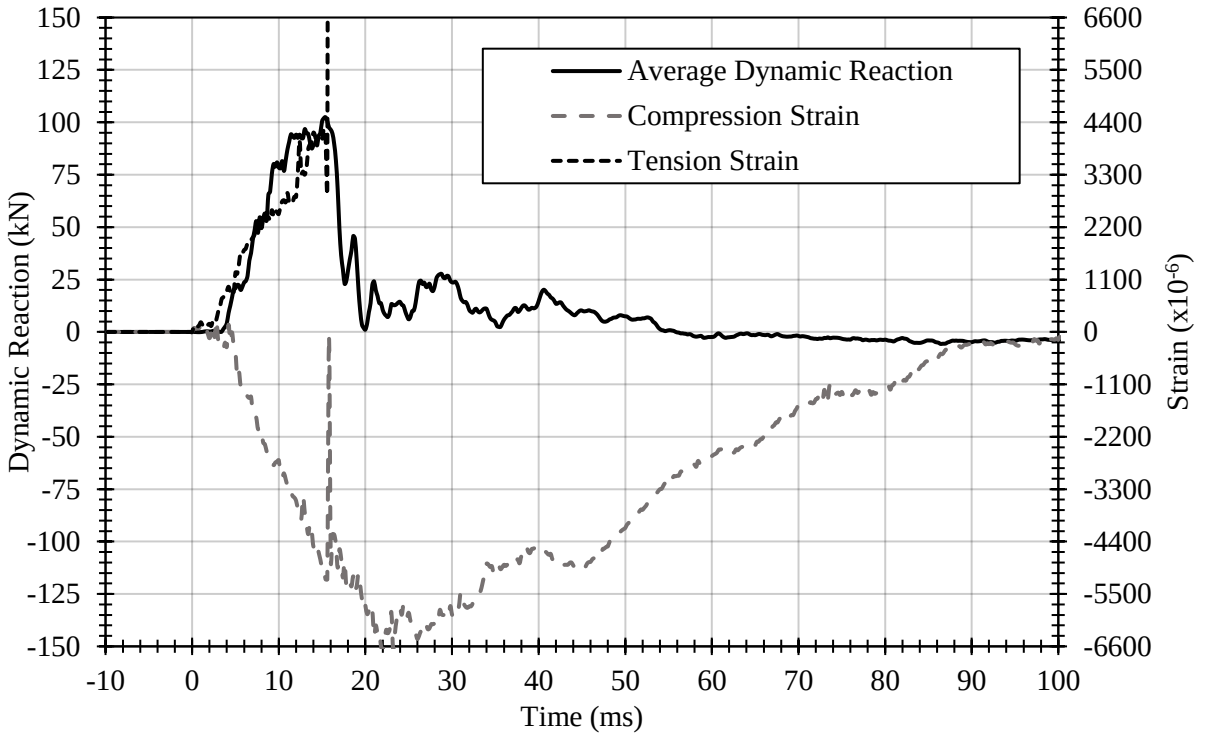
Specimen G5, comprised of a Glulam beam with a 2x1 bolted connection at each end, was dynamically tested on July 18th 2019. A driver pressure of 559.2 kPa was used, which resulted in a positive peak reflected pressure and impulse of 71.1 kPa and 720.8 kPa-ms, respectively.



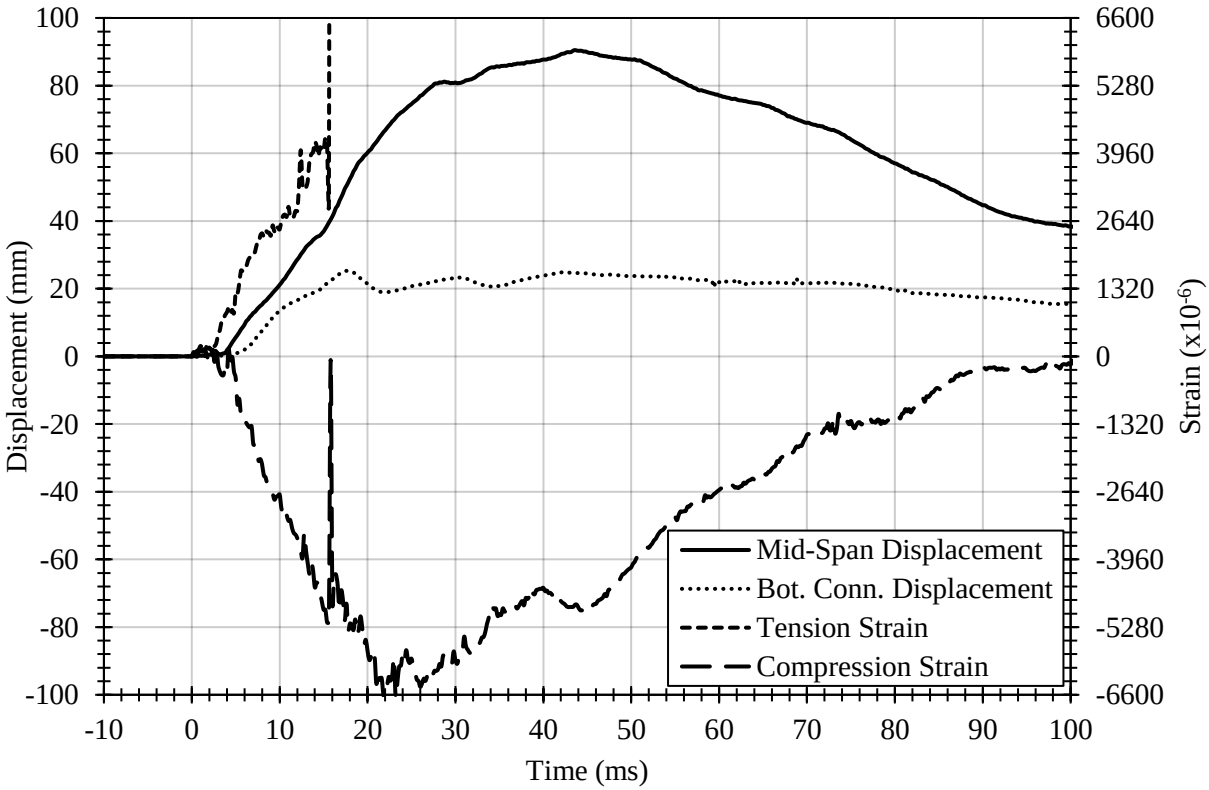
(a) Pressure and Impulse



(b) Reaction and Displacement



(c) Reaction and Strains

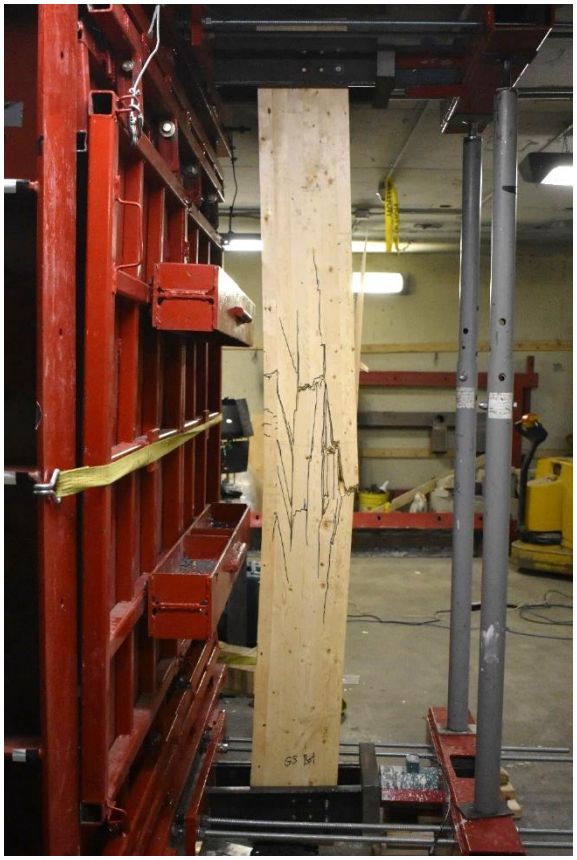


(d) Displacement and Strains

Figure C.9: Dynamic Test Results for Specimen G5



(a) Specimen Prior to Testing



(b) Specimen After Testing



(c) Flexural Failure



(d) Wood Crushing in Bottom Joint



(e) Wood Crushing in Top Joint

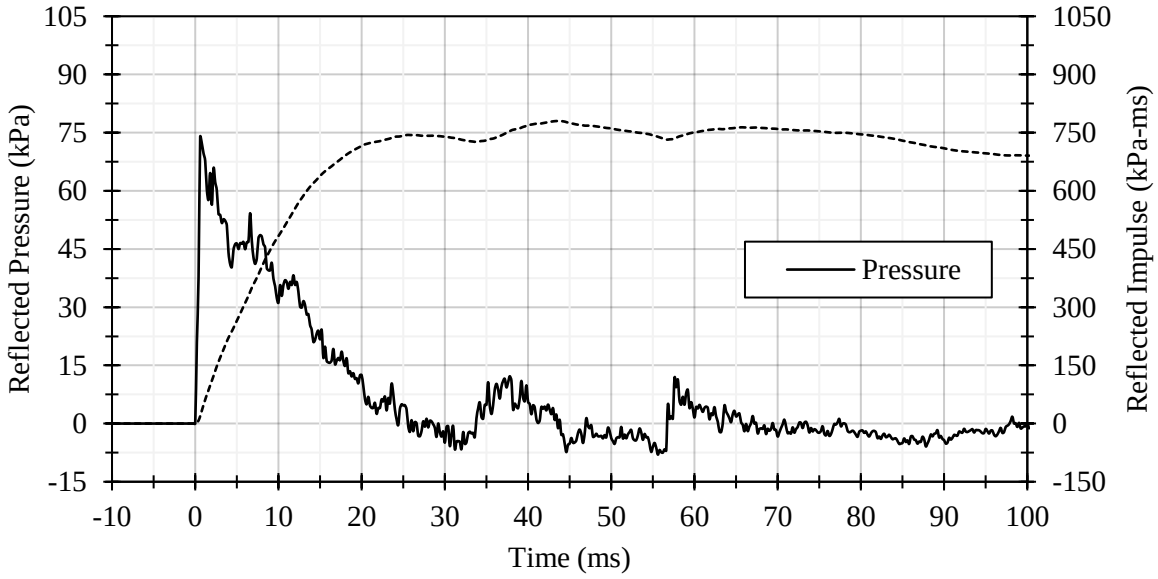


(f) Yielding of Bolts

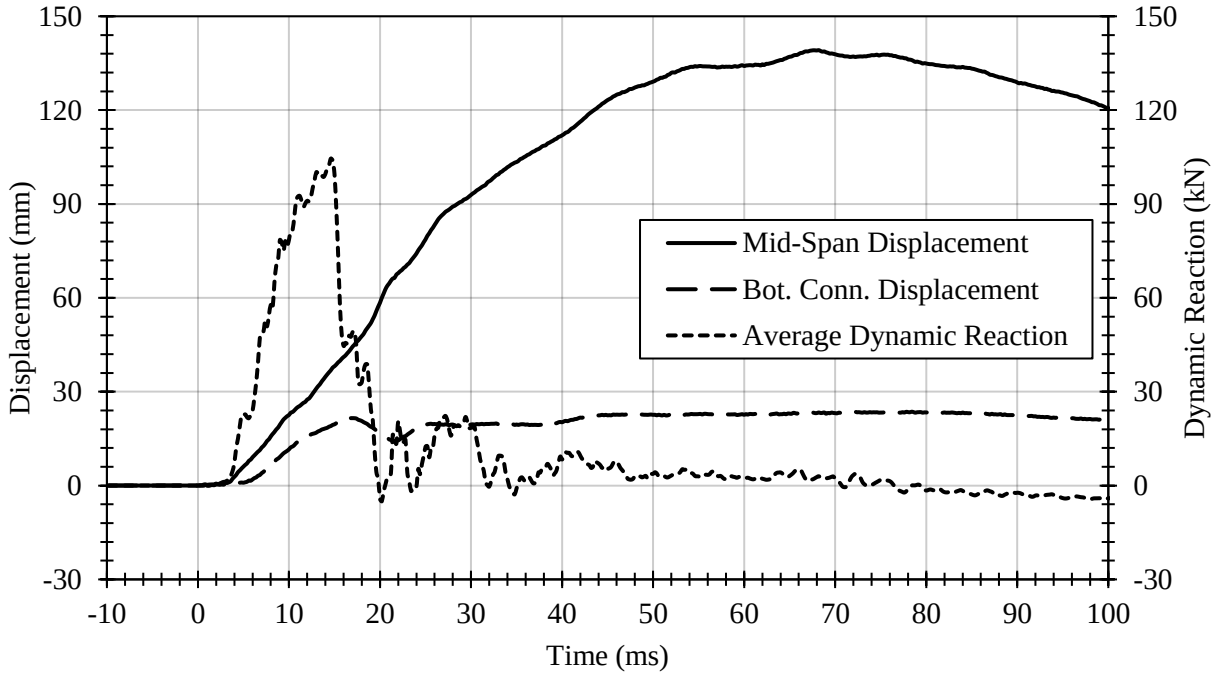
Figure C.10: Documentation of Damage for Specimen G5

Specimen G6

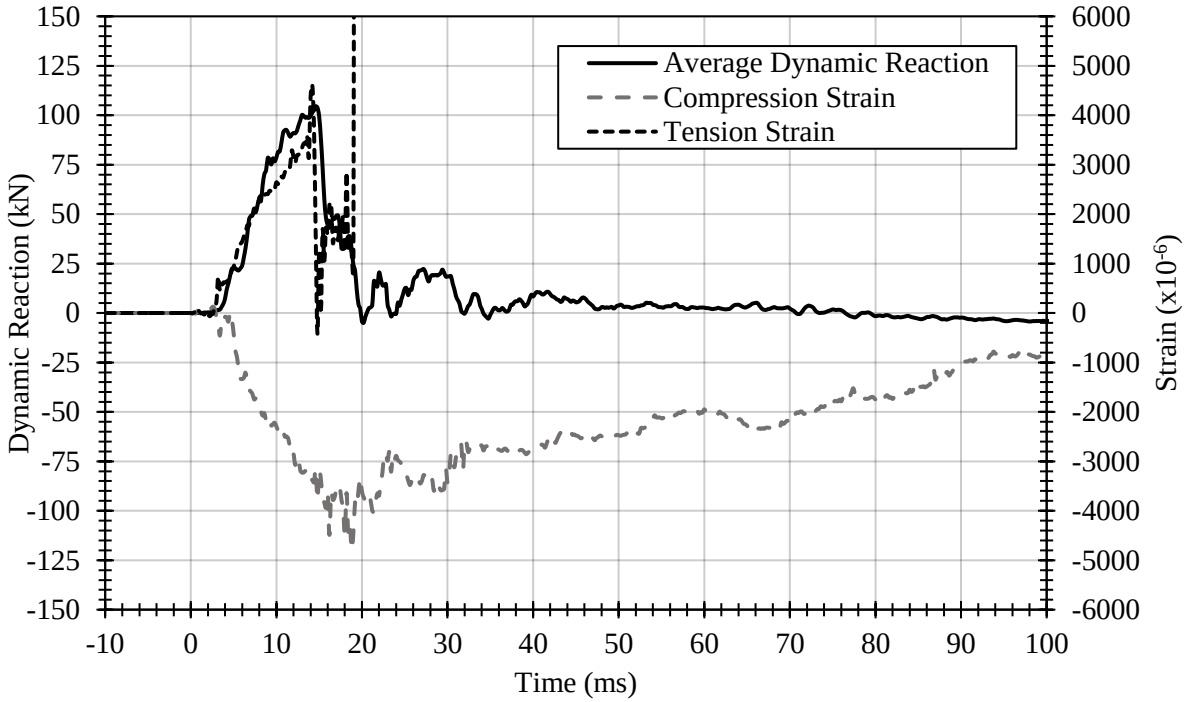
Specimen G6, comprised of a Glulam beam with a thick angle with a 2x1 bolted connection at each end, was dynamically tested on July 25th 2019. A driver pressure of 555.7 kPa was used, which resulted in a positive peak reflected pressure and impulse of 73.9 kPa and 744.1 kPa-ms, respectively.



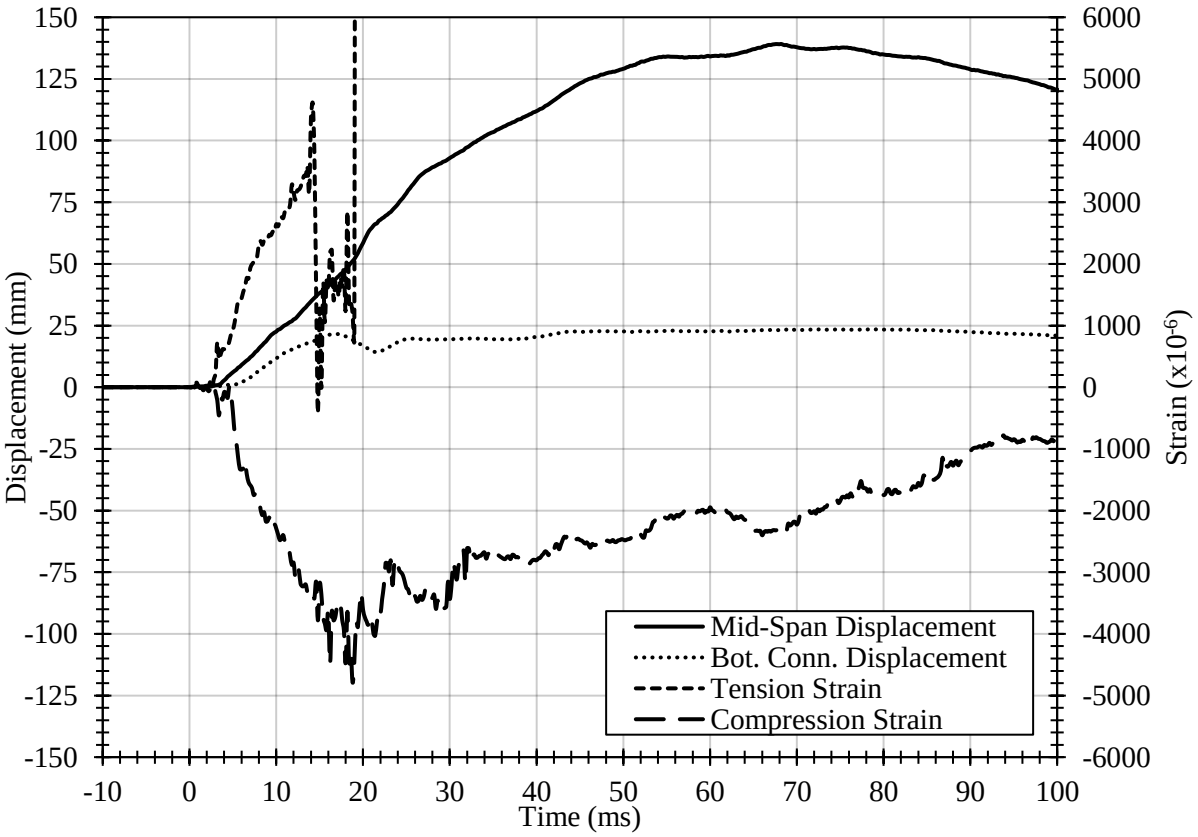
(a) Pressure and Impulse



(b) Reaction and Displacement



(c) Reaction and Strains

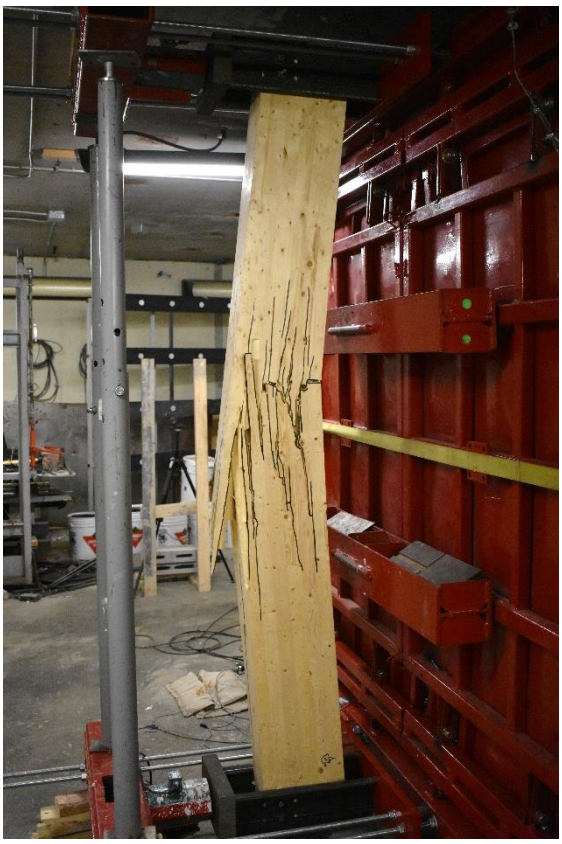


(d) Displacement and Strains

Figure C.11: Dynamic Test Results for Specimen G6



(a) Specimen Prior to Testing



(b) Specimen After Testing



(c) Flexural Failure



(d) Wood Crushing in Bottom Joint



(e) Wood Crushing in Top Joint

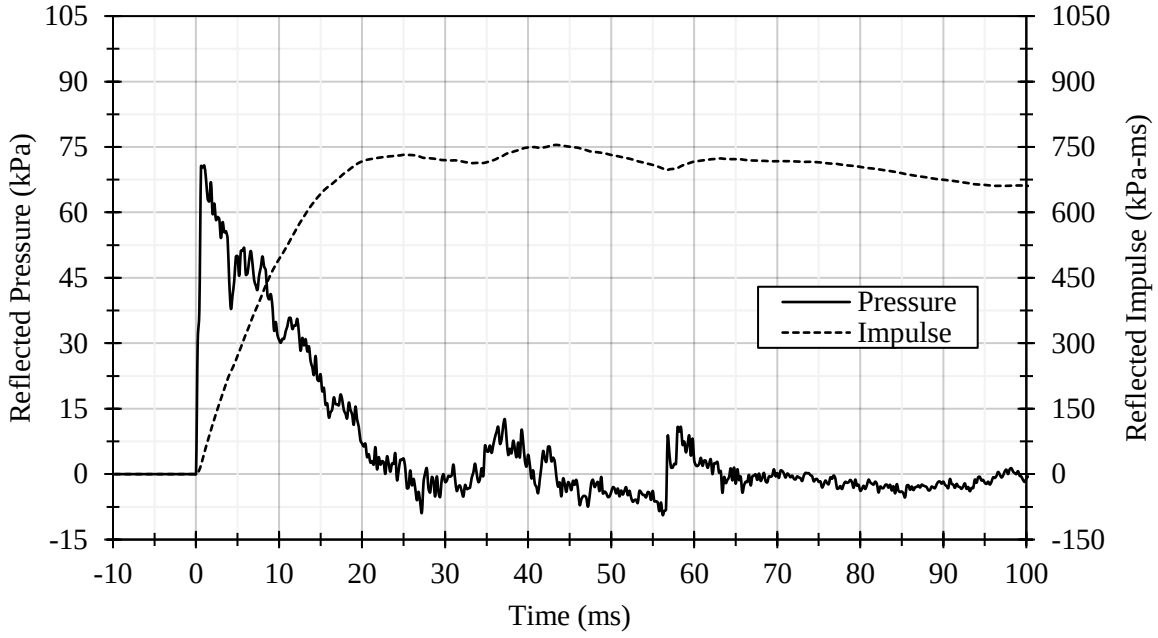


(f) Yielding of Bolts

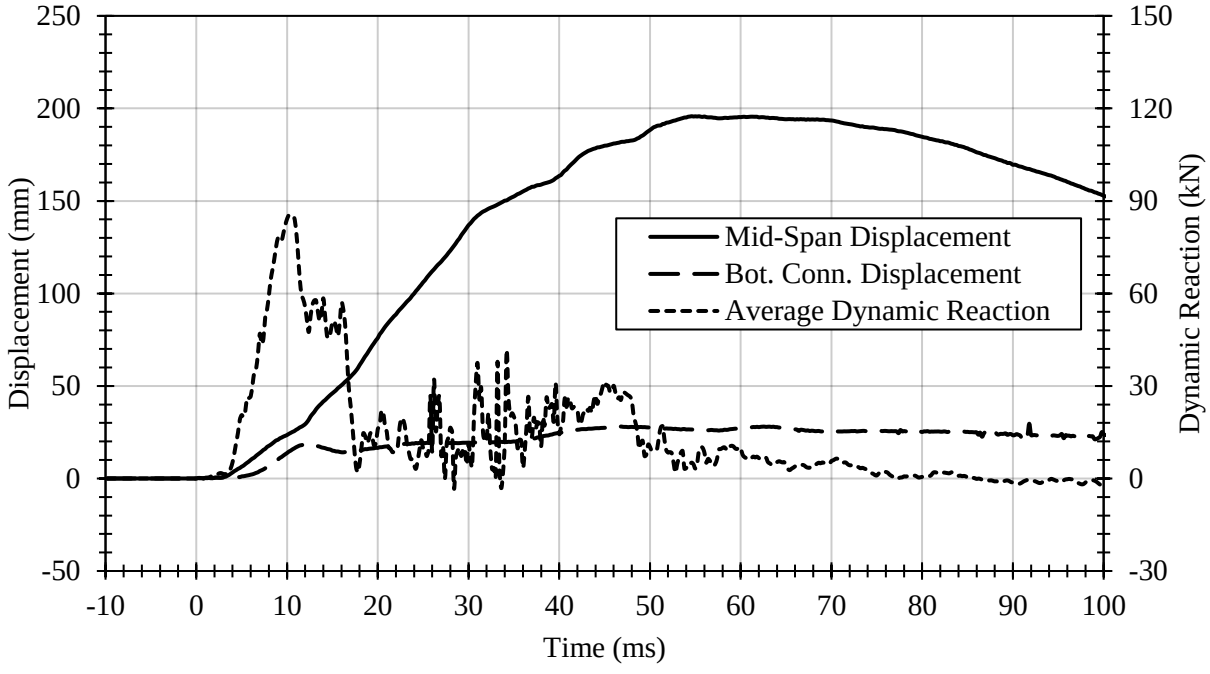
Figure C.12: Documentation of Damage for Specimen G6

Specimen G7

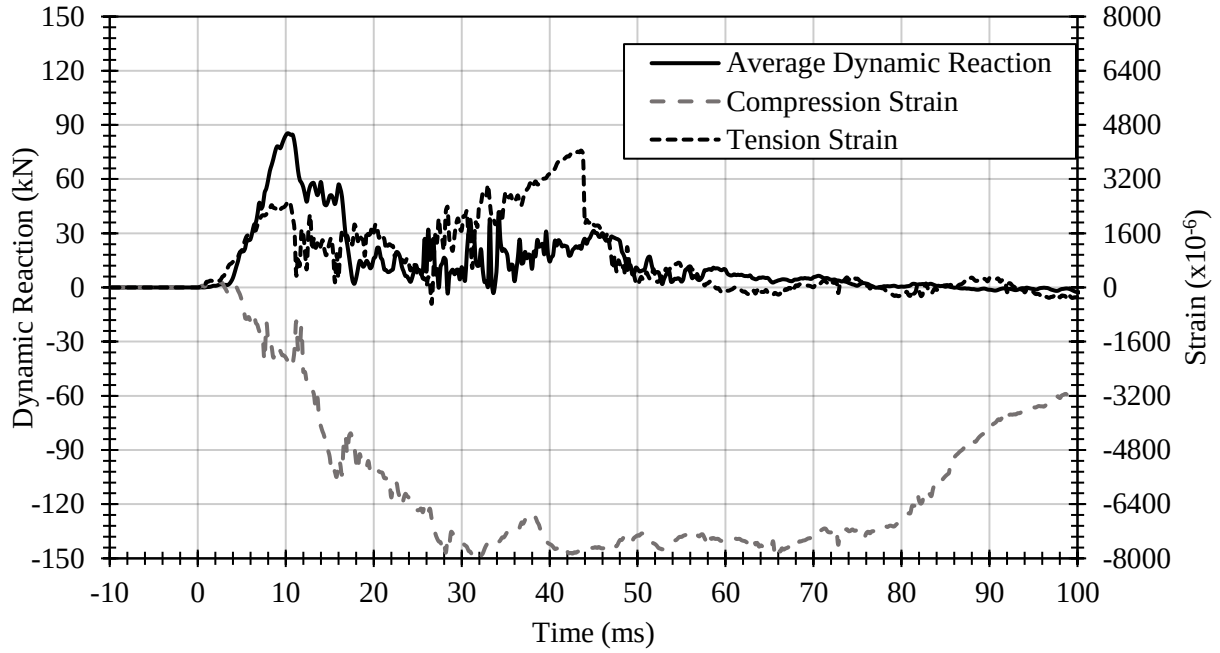
Specimen G7, comprised of a Glulam beam with a 2x1 bolted connection at each end, was dynamically tested on July 26th 2019. A driver pressure of 553.0 kPa was used, which resulted in a positive peak reflected pressure and impulse of 70.7 kPa and 732.6 kPa-ms, respectively.



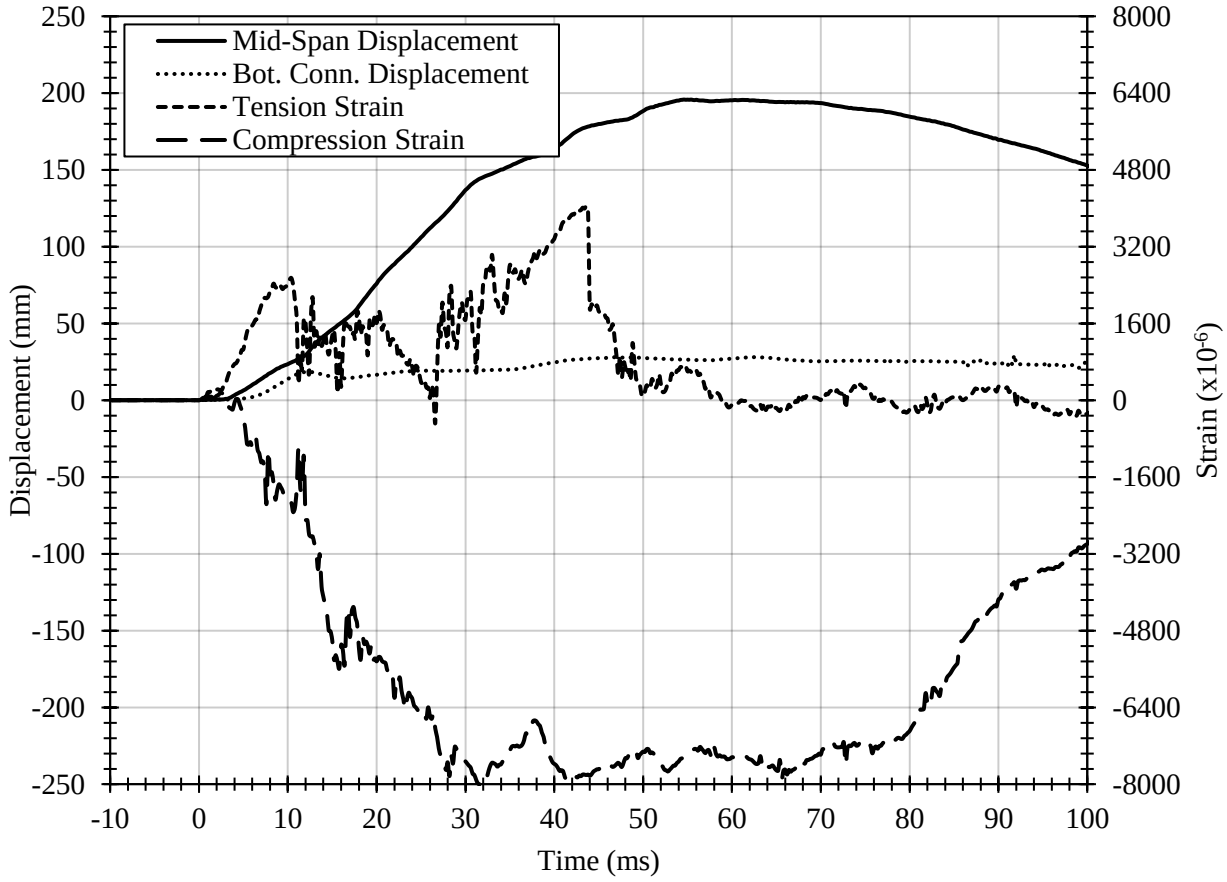
(a) Pressure and Impulse



(b) Reaction and Displacement



(c) Reaction and Strains

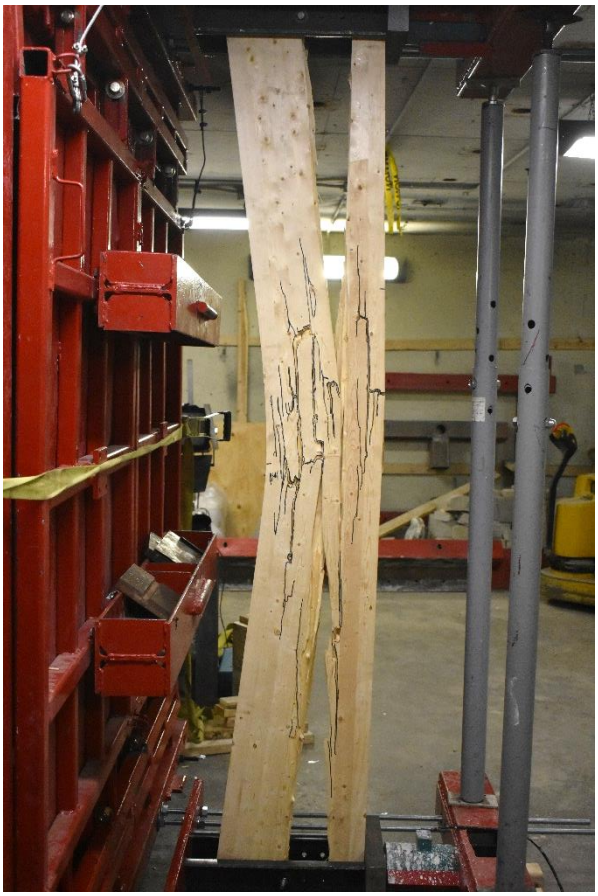


(d) Displacement and Strains

Figure C.13: Dynamic Test Results for Specimen G7



(a) Specimen Prior to Testing



(b) Specimen After Testing



(c) Splitting at Bottom Joint



(d) Damage in Bottom Joint



(e) Damage in Top Joint

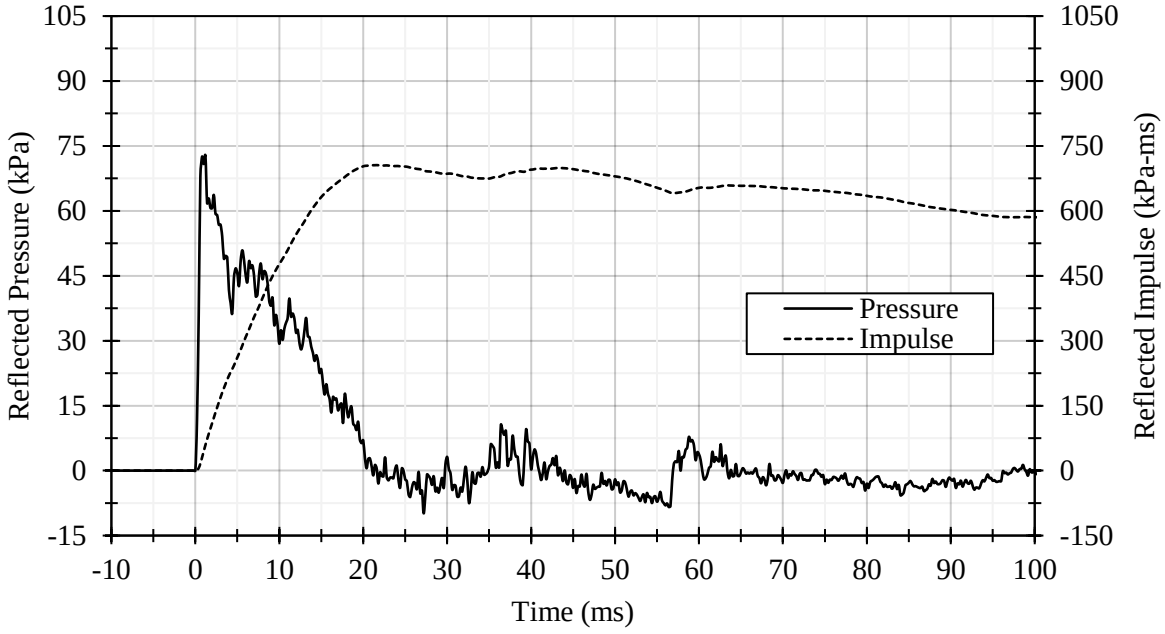


(f) Yielding of Bolts

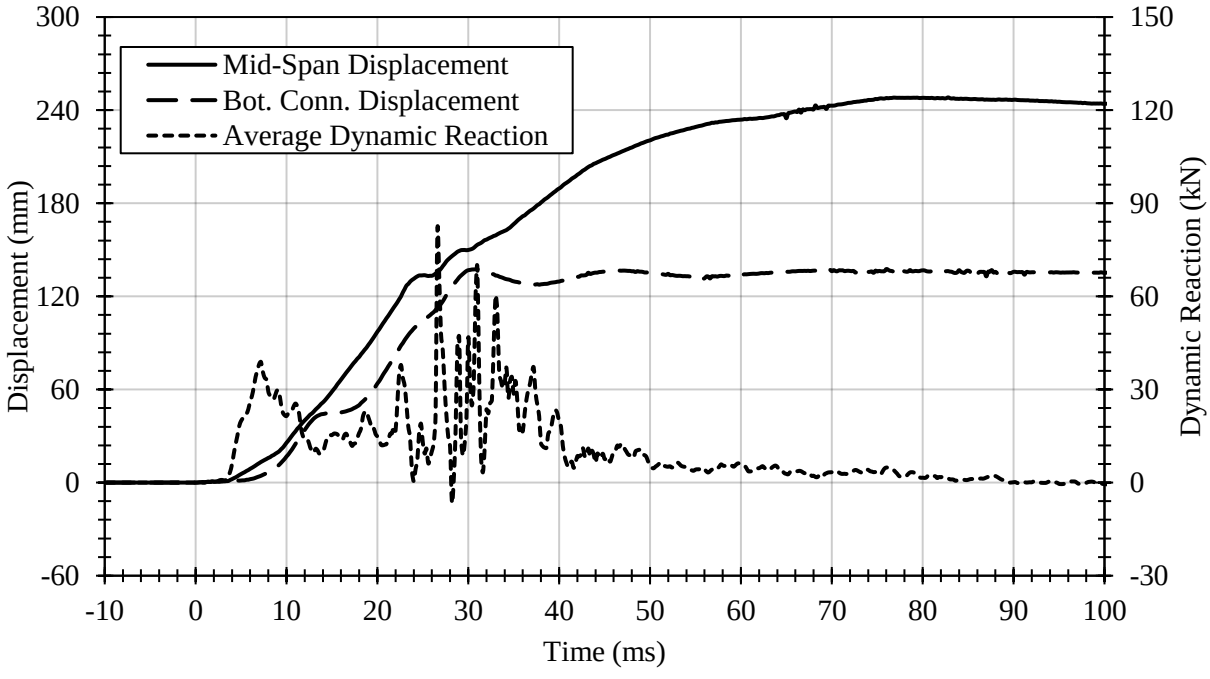
Figure C.14: Documentation of Damage for Specimen G7

Specimen G8

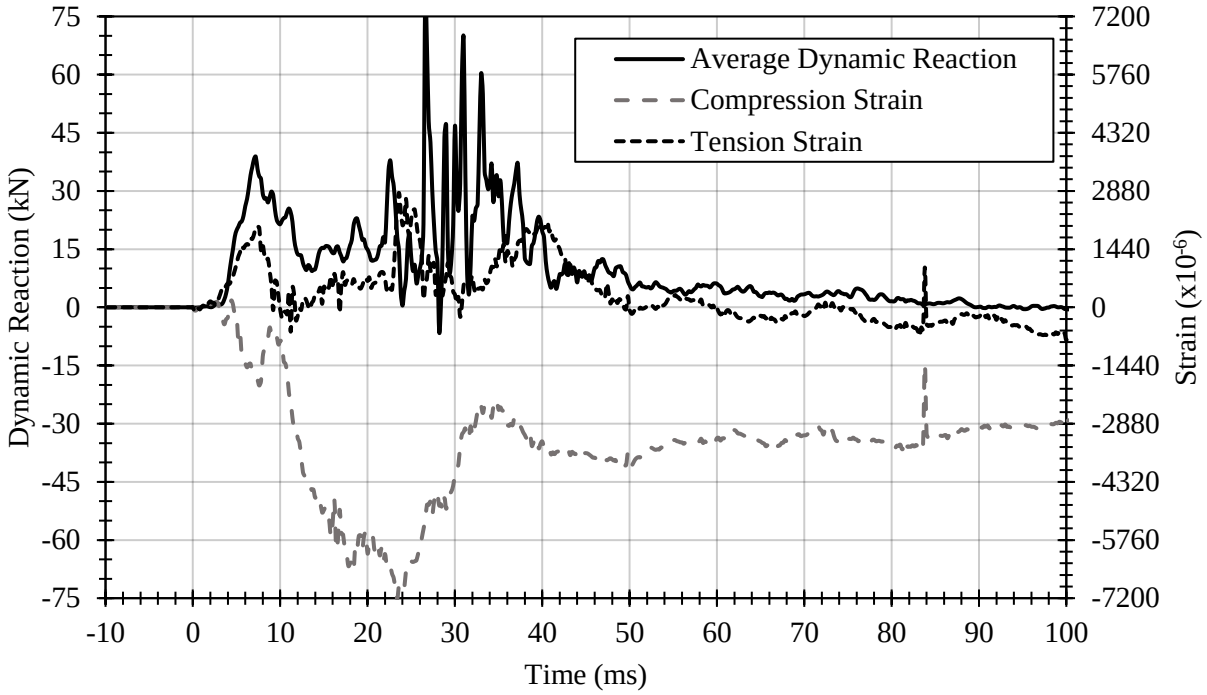
Specimen G8, comprised of a Glulam beam with a 2x1 bolted connection at each end, was dynamically tested on July 22nd 2019. A driver pressure of 557.1 kPa was used, which resulted in a positive peak reflected pressure and impulse of 72.8 kPa and 705.7 kPa-ms, respectively.



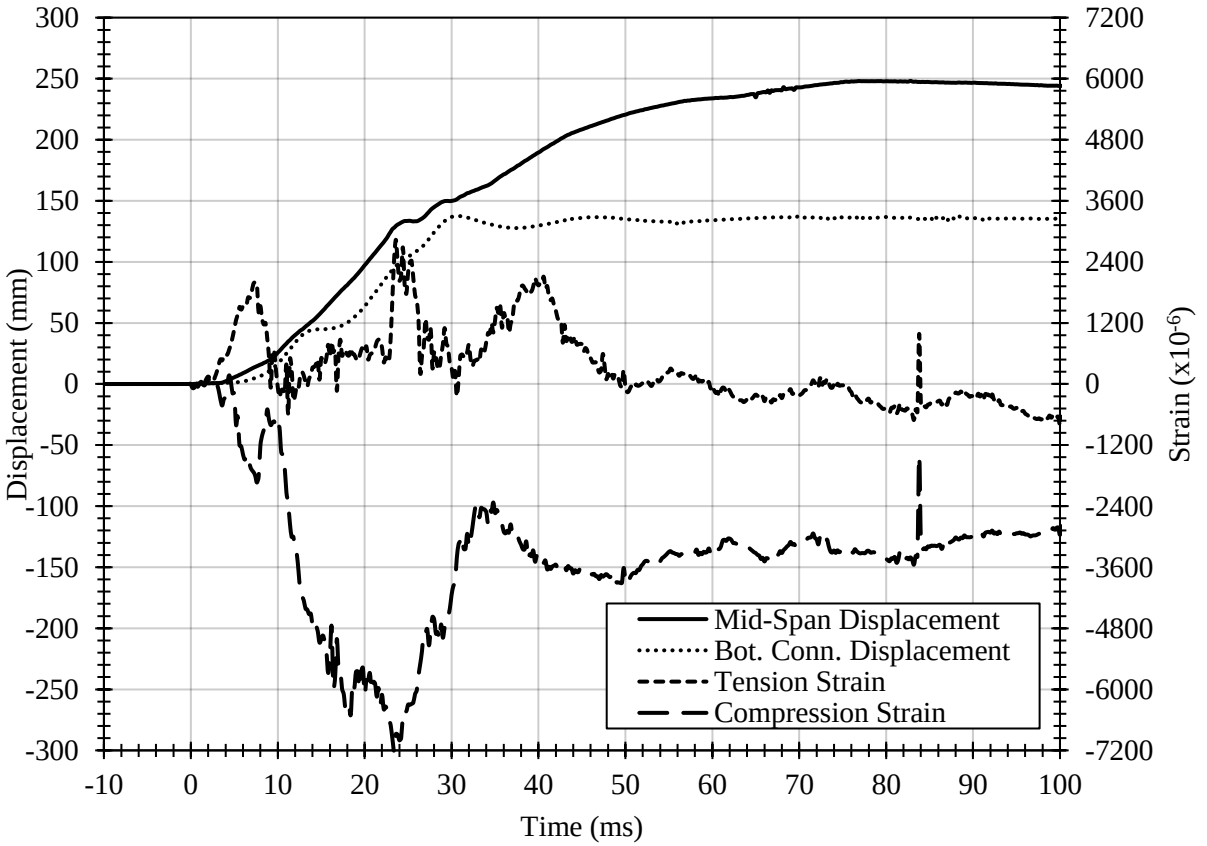
(a) Pressure and Impulse



(b) Reaction and Displacement



(c) Reaction and Strains

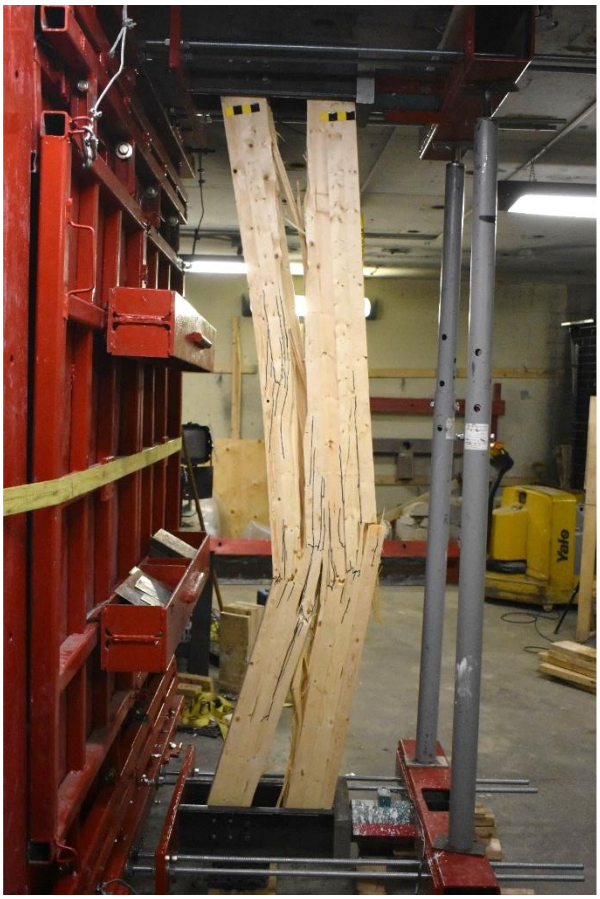


(d) Displacement and Strains

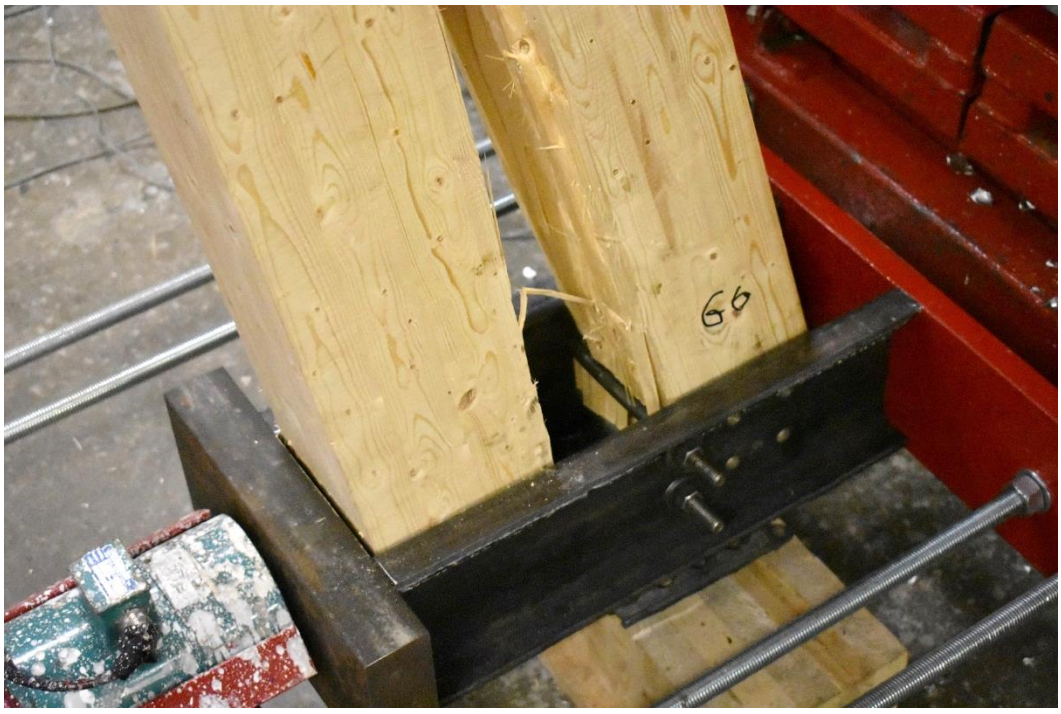
Figure C.15: Dynamic Test Results for Specimen G8



(a) Specimen Prior to Testing



(b) Specimen After Testing



(c) Splitting at Bottom Joint



(d) Damage in Bottom Joint



(e) Damage in Top Joint

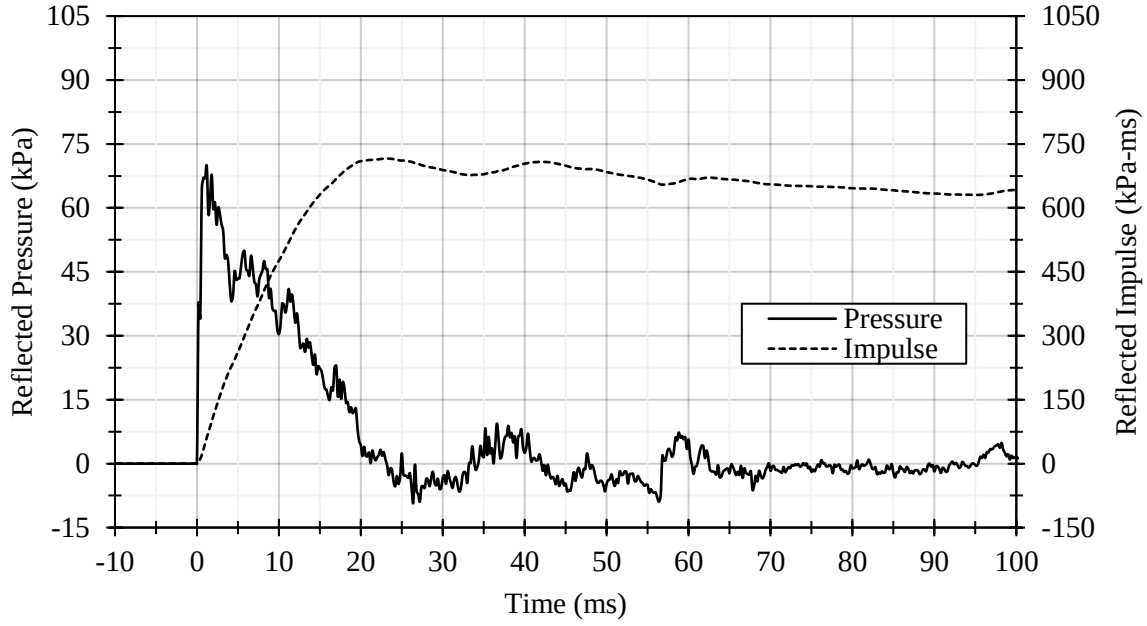


(f) Minimal Yielding of Bolts

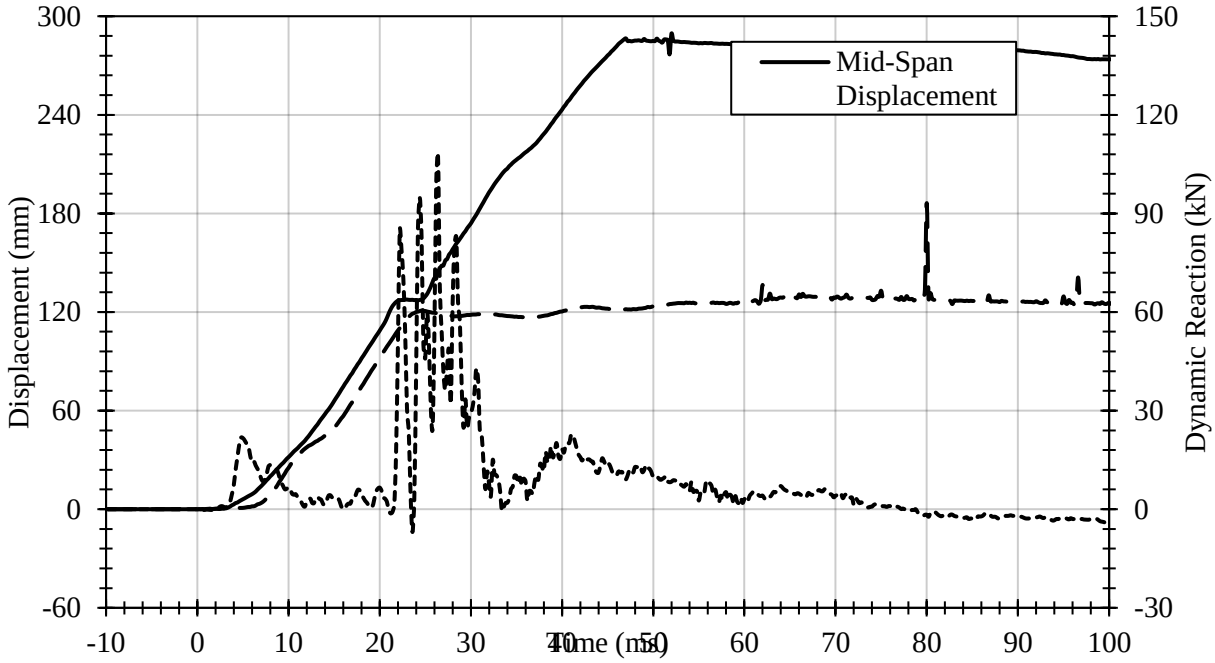
Figure C.16: Documentation of Damage for Specimen G8

Specimen G9

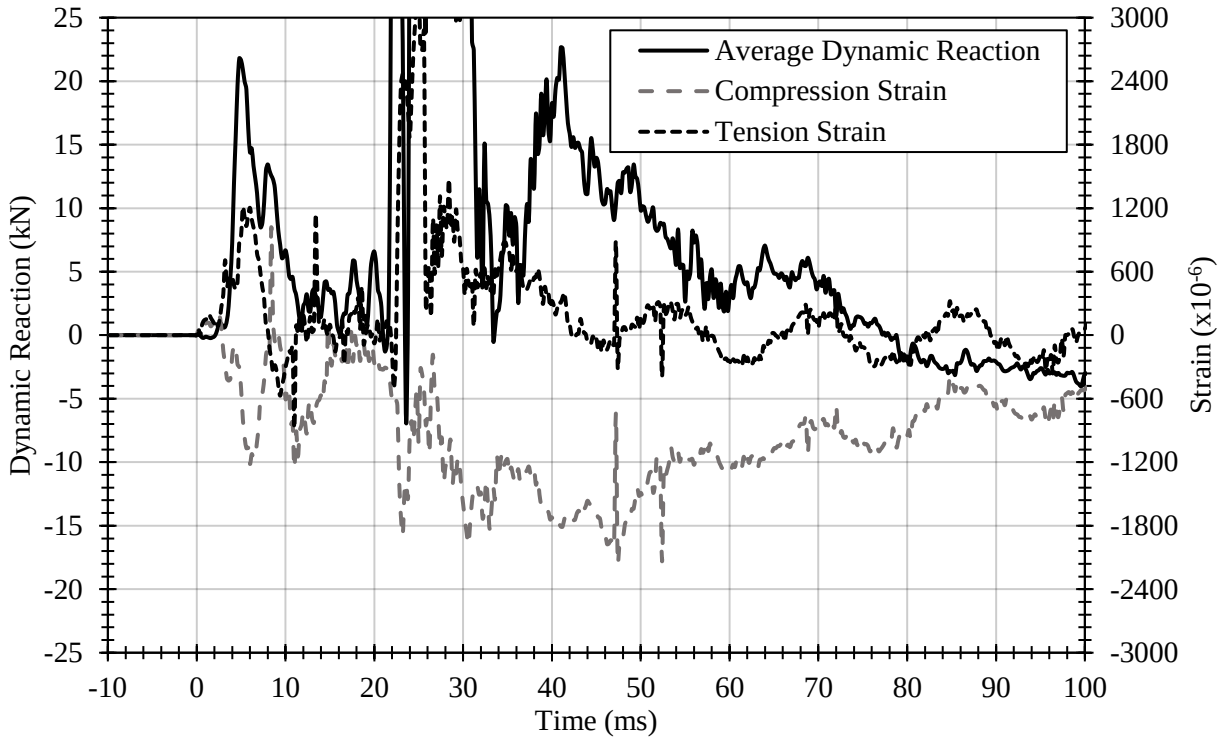
Specimen G9, comprised of a Glulam beam with a 2x1 bolted connection at each end, was dynamically tested on July 23rd 2019. A driver pressure of 549.5 kPa was used, which resulted in a positive peak reflected pressure and impulse of 69.7 kPa and 716.0 kPa-ms, respectively.



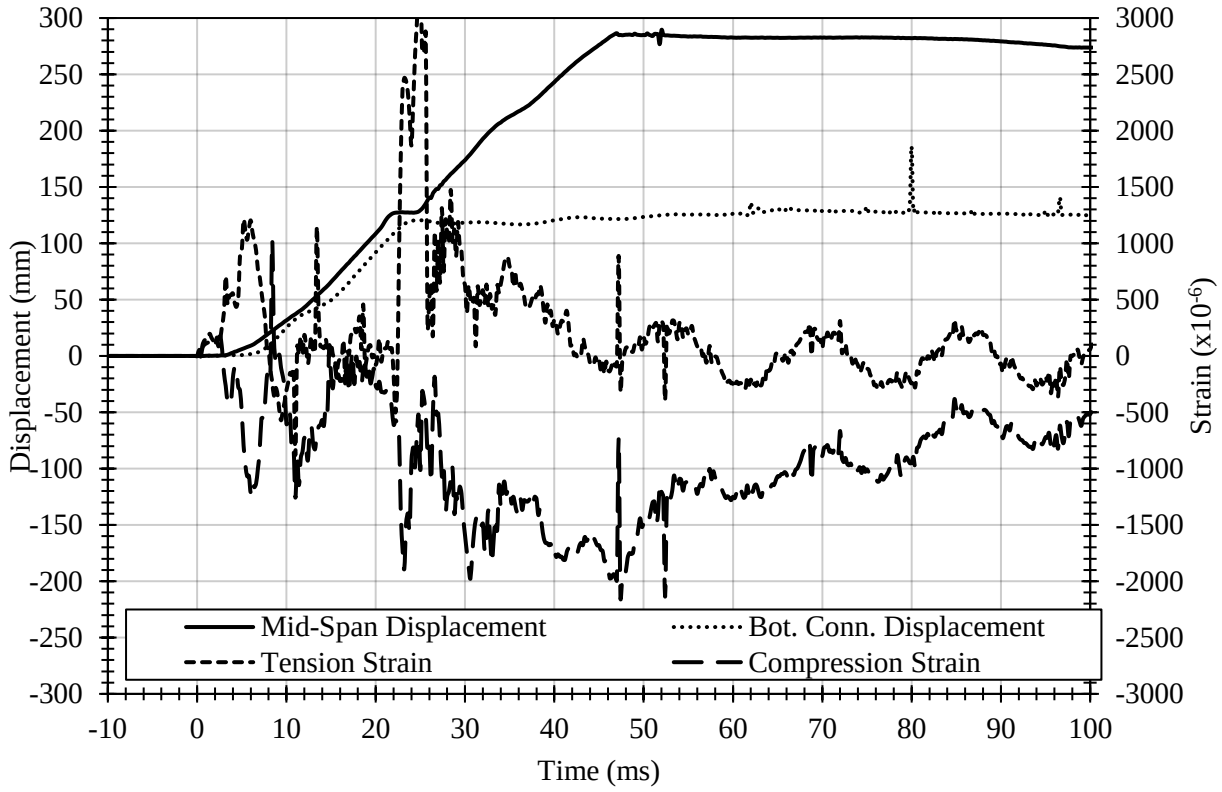
(a) Pressure and Impulse



(b) Reaction and Displacement



(c) Reaction and Strains

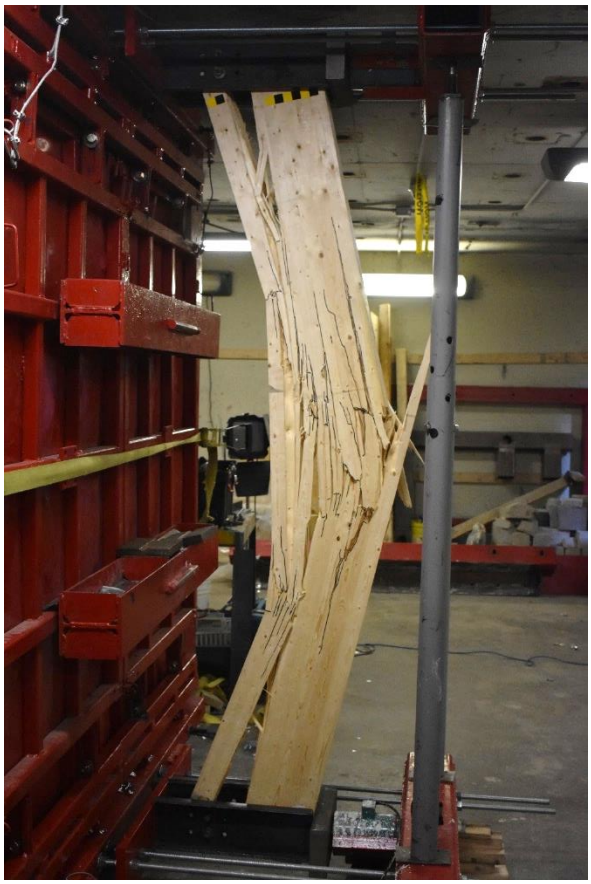


(d) Displacement and Strains

Figure C.17: Dynamic Test Results for Specimen G9



(a) Specimen Prior to Testing



(b) Specimen After Testing



(c) Splitting at Bottom Joint



(d) Damage in Bottom Joint



(e) Damage in Top Joint

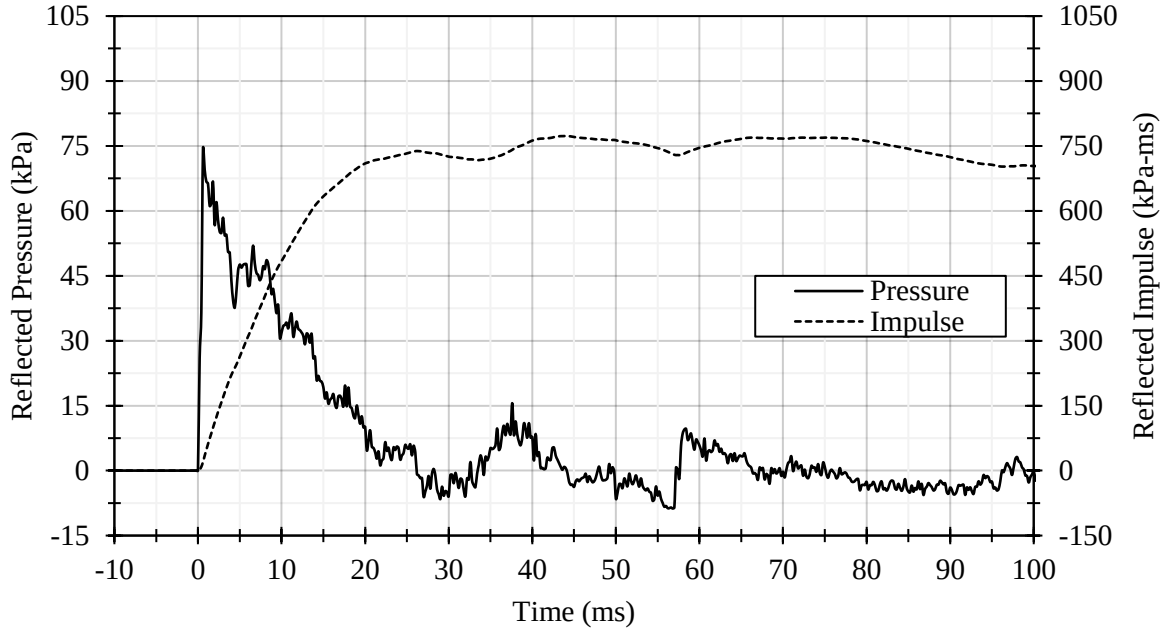


(f) Lack of Yielding in Bolts

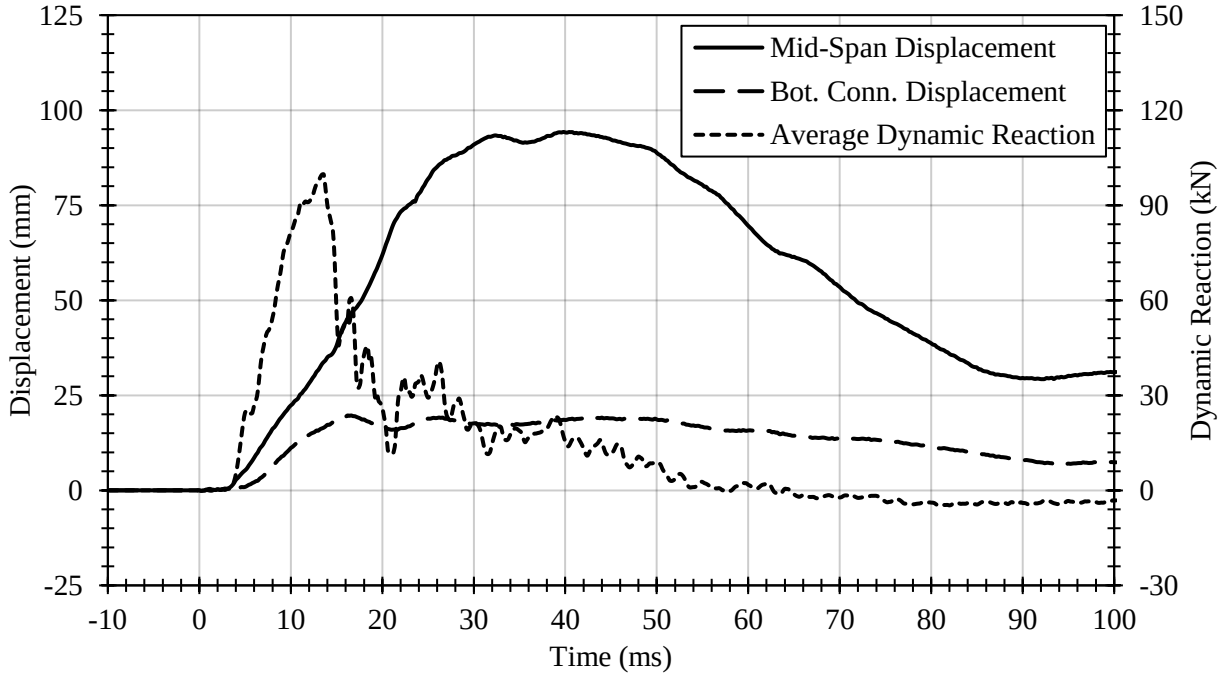
Figure C.18: Documentation of Damage for Specimen G9

Specimen G10

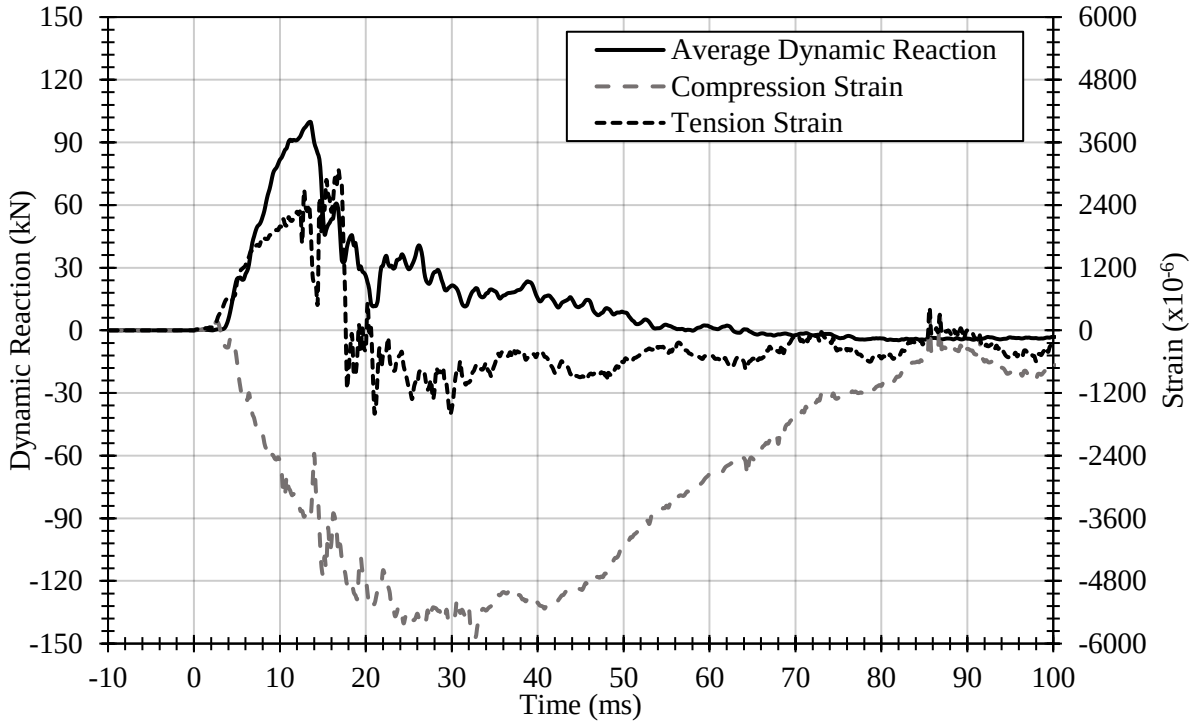
Specimen G10, comprised of a Glulam beam with a reinforced 2x1 bolted connection at each end, was dynamically tested on July 30th 2019. A driver pressure of 552.3 kPa was used, which resulted in a positive peak reflected pressure and impulse of 74.2 kPa and 738.2 kPa-ms, respectively.



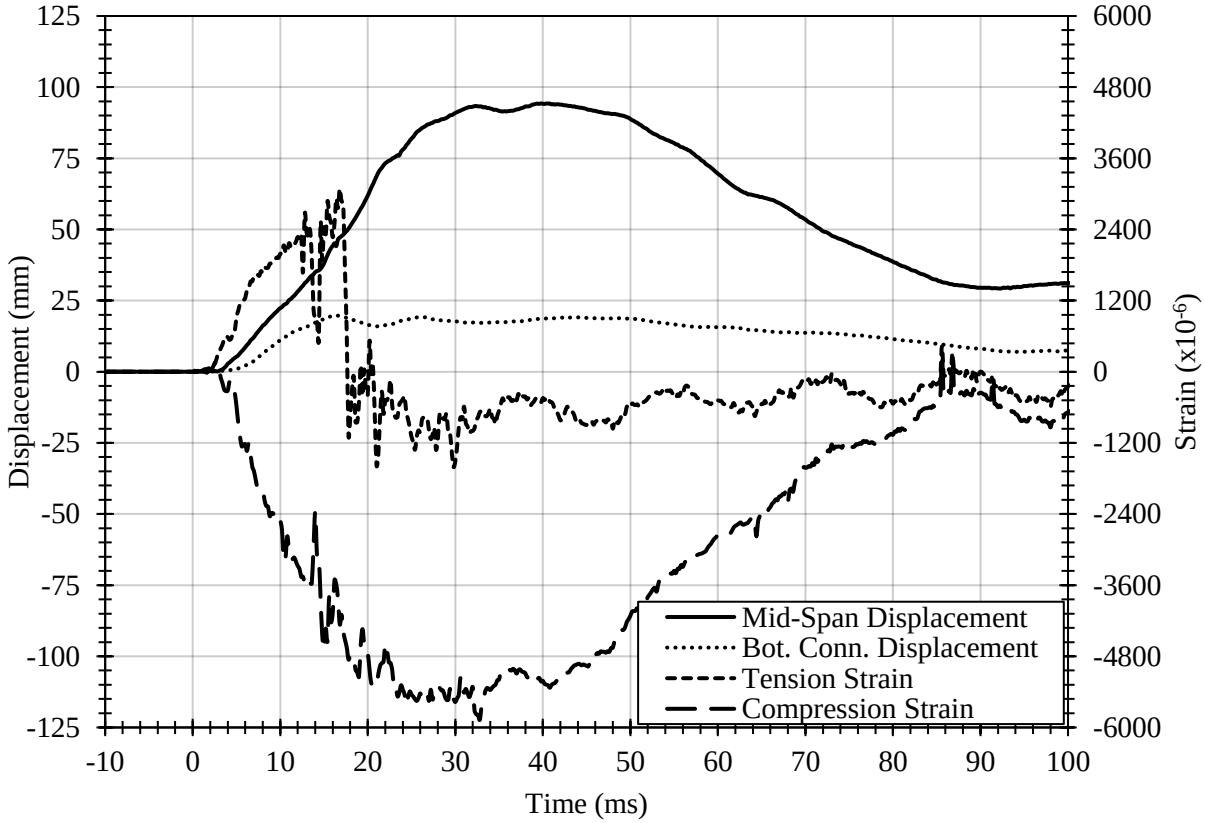
(a) Pressure and Impulse



(b) Reaction and Displacement



(c) Reaction and Strains



(d) Displacement and Strains

Figure C.19: Dynamic Test Results for Specimen G10



(a) Specimen Prior to Testing



(b) Specimen After Testing



(c) Flexural Failure



(d) Wood Crushing in Bottom Joint



(e) Wood Crushing & Splitting in Top Joint

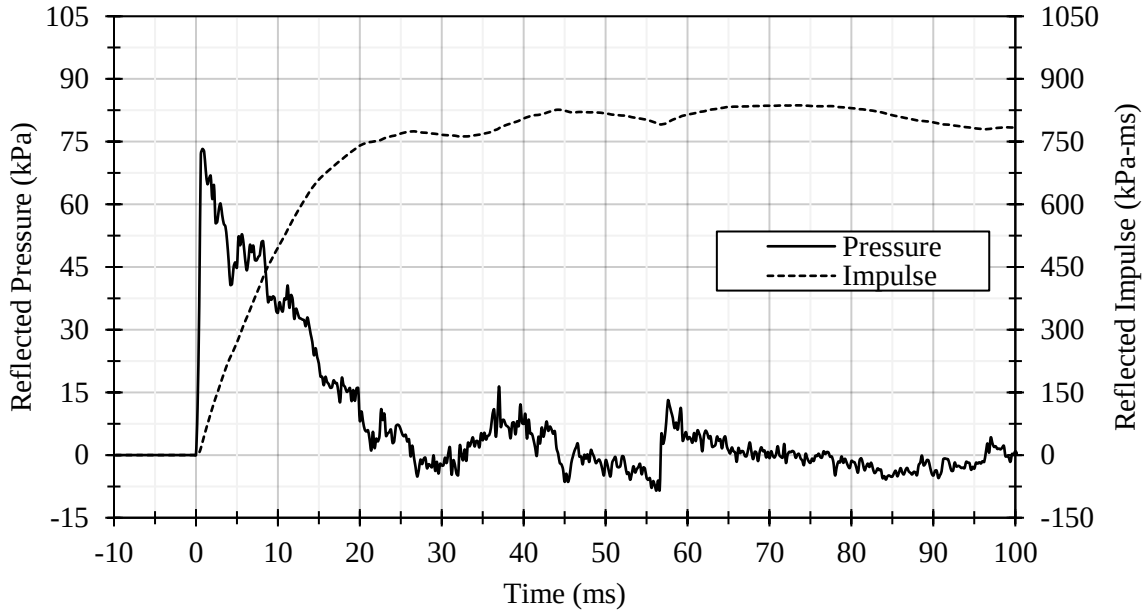


(f) Yielding of Bolts

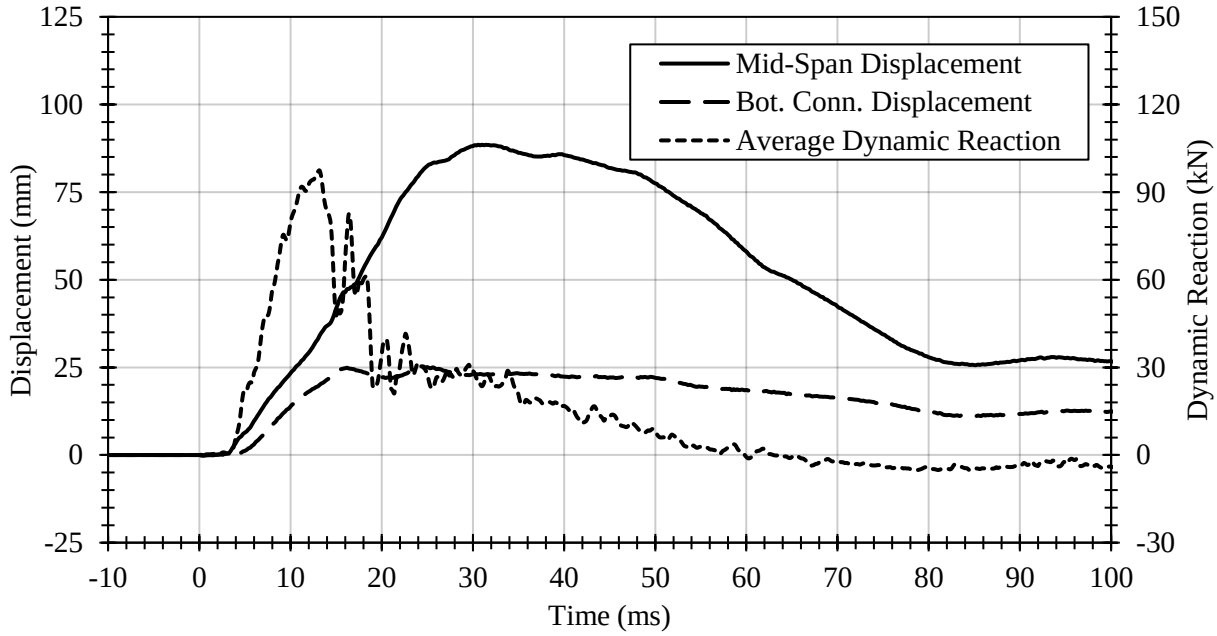
Figure C.20: Documentation of Damage for Specimen G10

Specimen G11

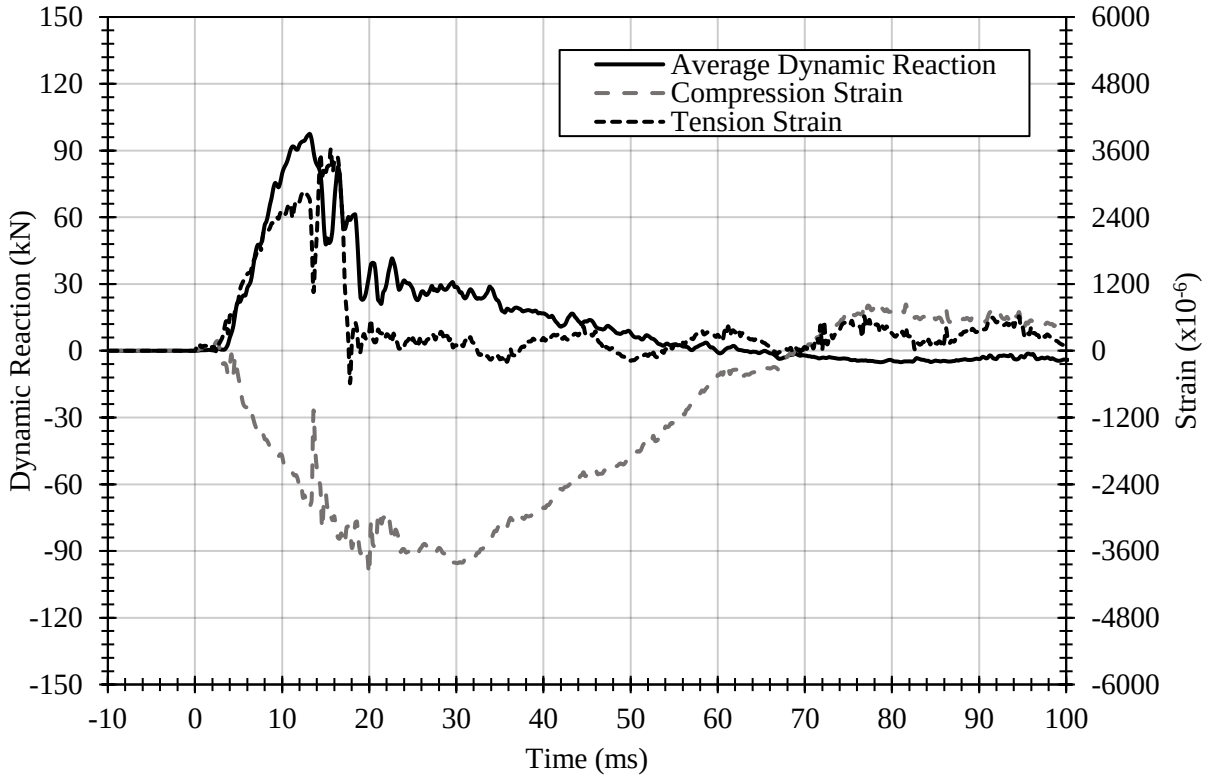
Specimen G11, comprised of a Glulam beam with a reinforced 2x1 bolted connection at each end, was dynamically tested on August 2nd 2019. A driver pressure of 564.7 kPa was used, which resulted in a positive peak reflected pressure and impulse of 73.3 kPa and 774.6 kPa-ms, respectively.



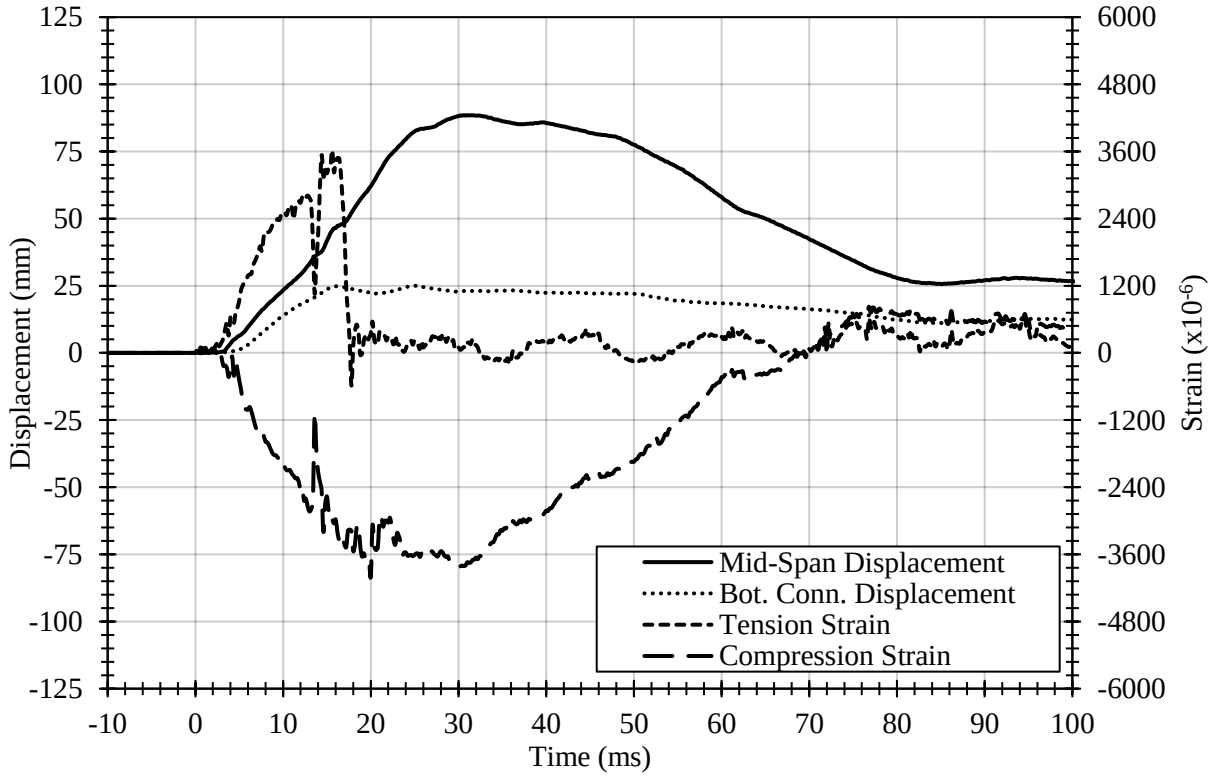
(a) Pressure and Impulse



(b) Reaction and Displacement



(c) Reaction and Strains

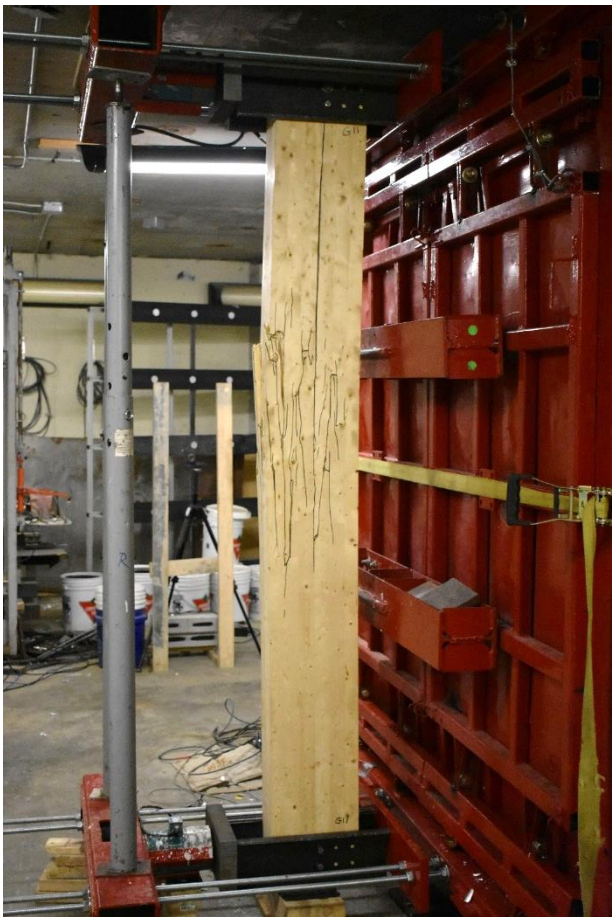


(d) Displacement and Strains
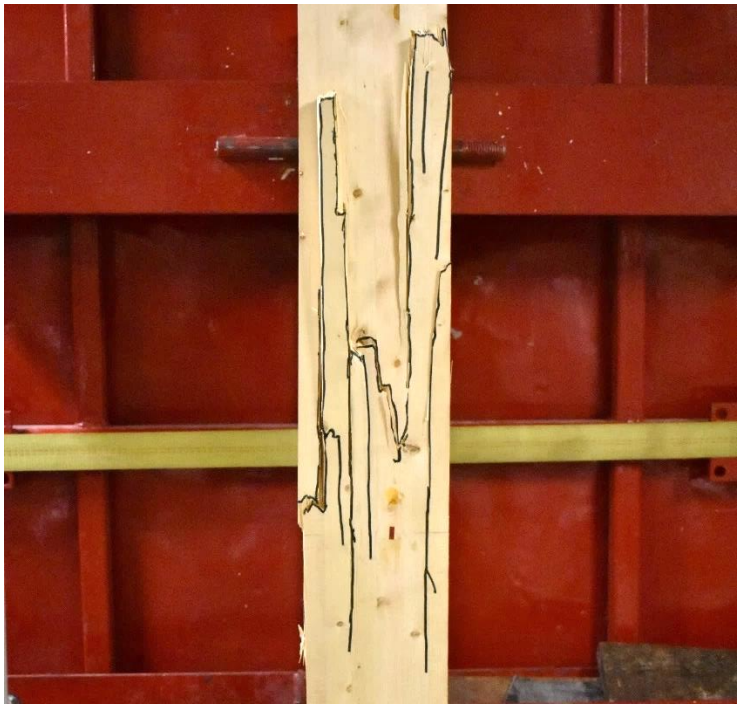
Figure C.21: Dynamic Test Results for Specimen G11



(a) Specimen Prior to Testing



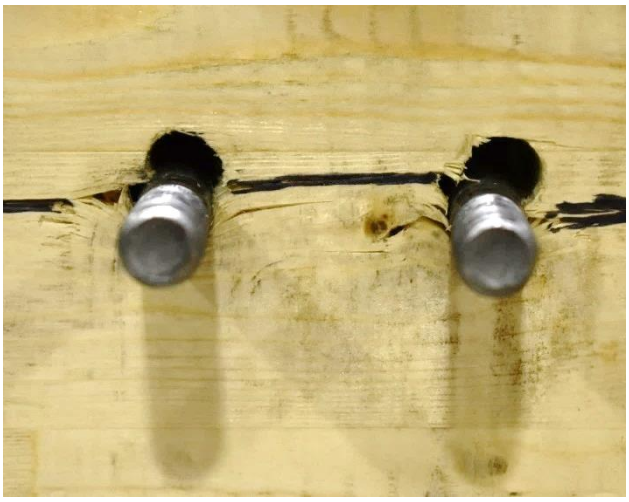
(b) Specimen After Testing



(c) Flexural Failure



(d) Wood Crushing in Bottom Joint



(e) Wood Crushing in Top Joint

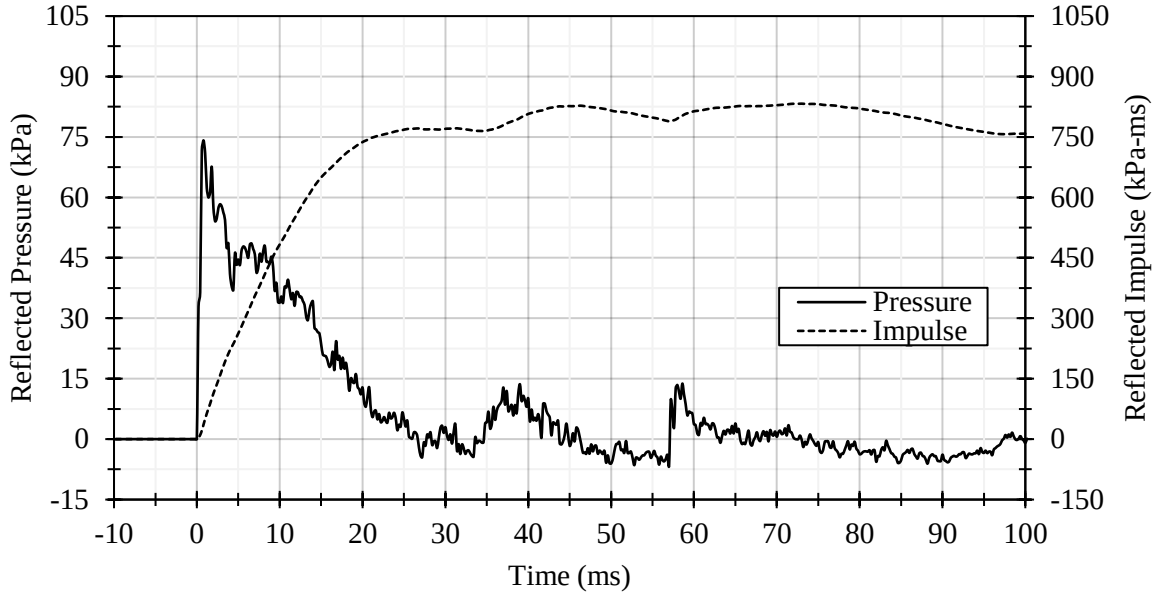


(f) Yielding of Bolts

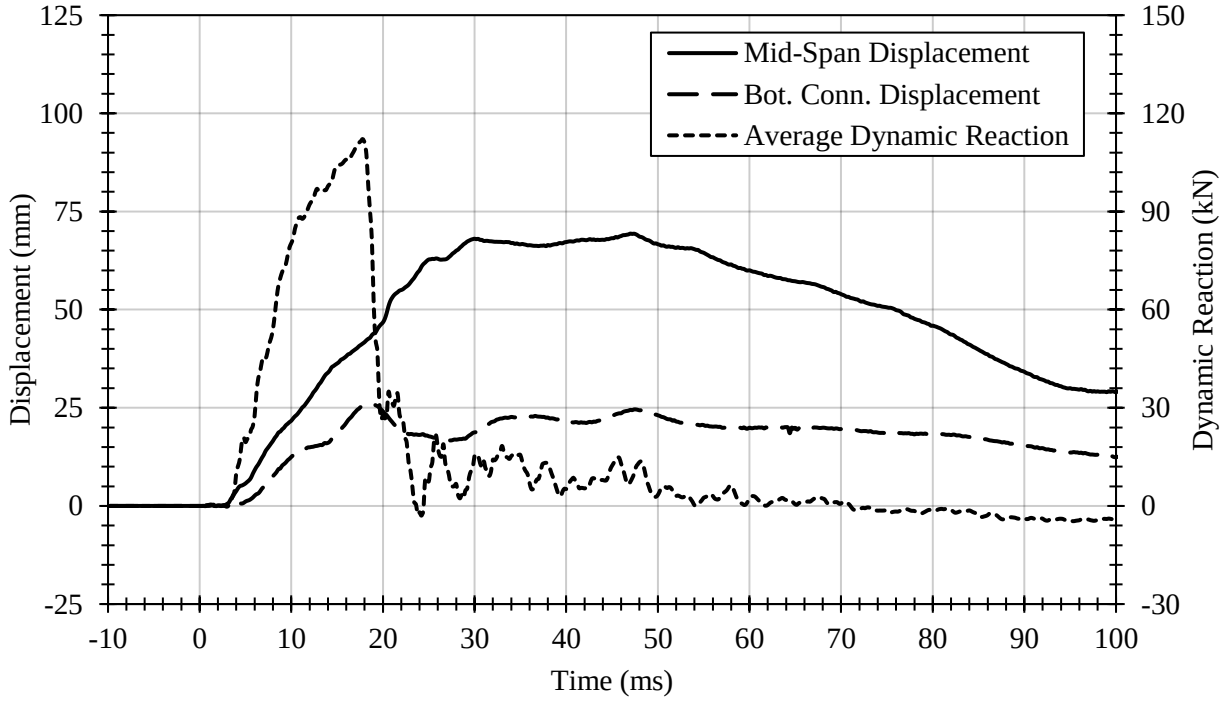
Figure C.22: Documentation of Damage for Specimen G11

Specimen G12

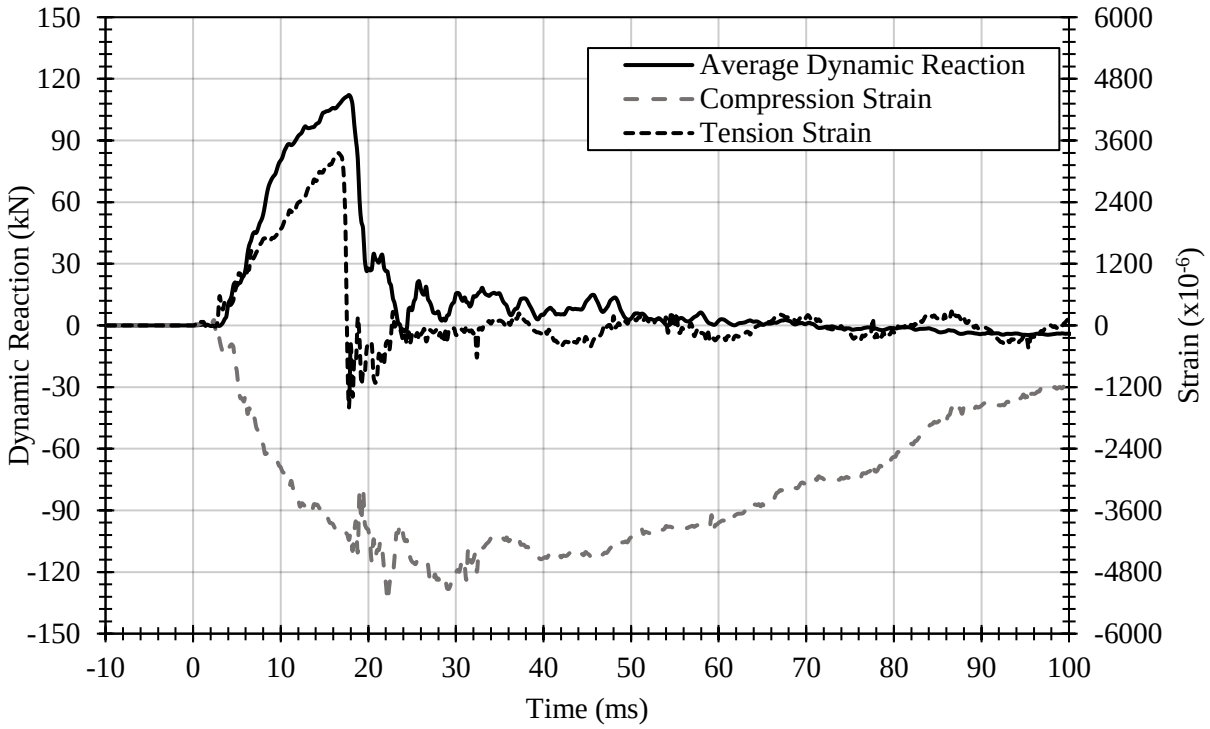
Specimen G12, comprised of a Glulam beam with a reinforced 2x1 bolted connection each end, was dynamically tested on July 30th 2019. A driver pressure of 562.6 kPa was used, which resulted in a positive peak reflected pressure and impulse of 74.2 kPa and 771.1 kPa-ms, respectively.



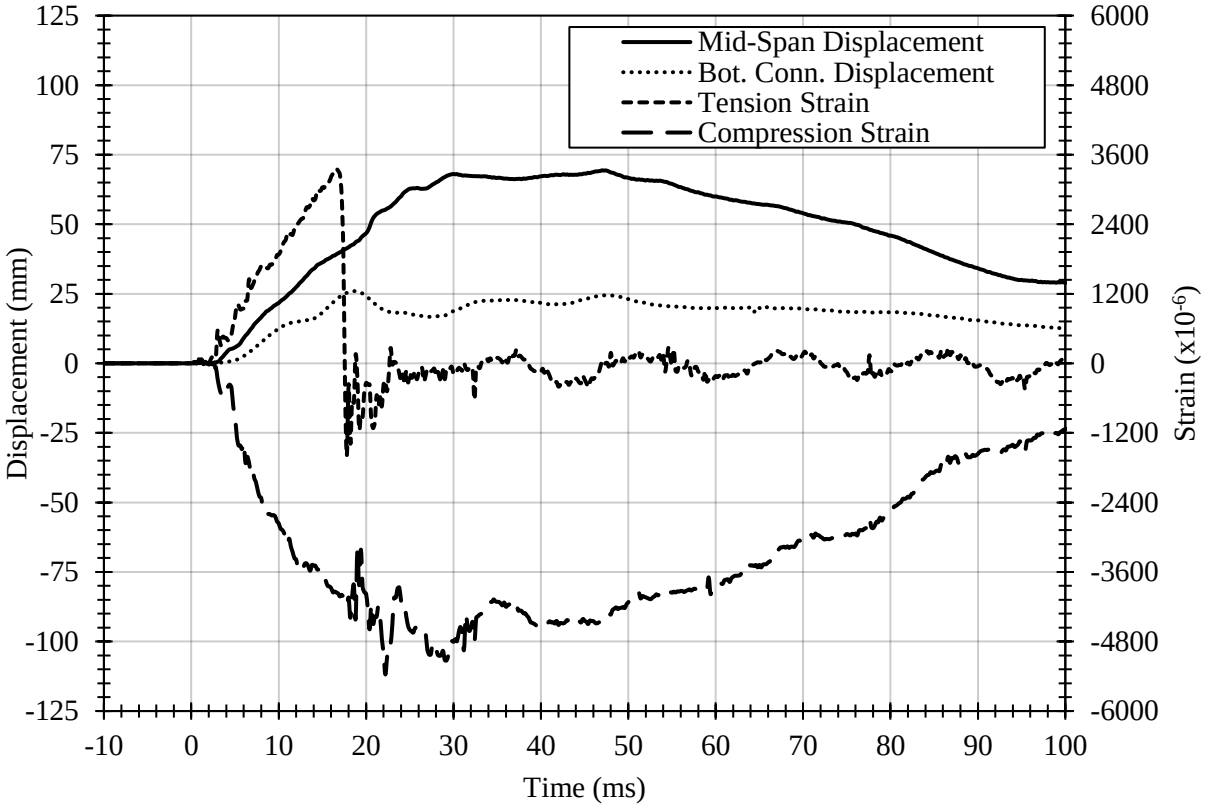
(a) Pressure and Impulse



(b) Reaction and Displacements



(c) Reaction and Strains

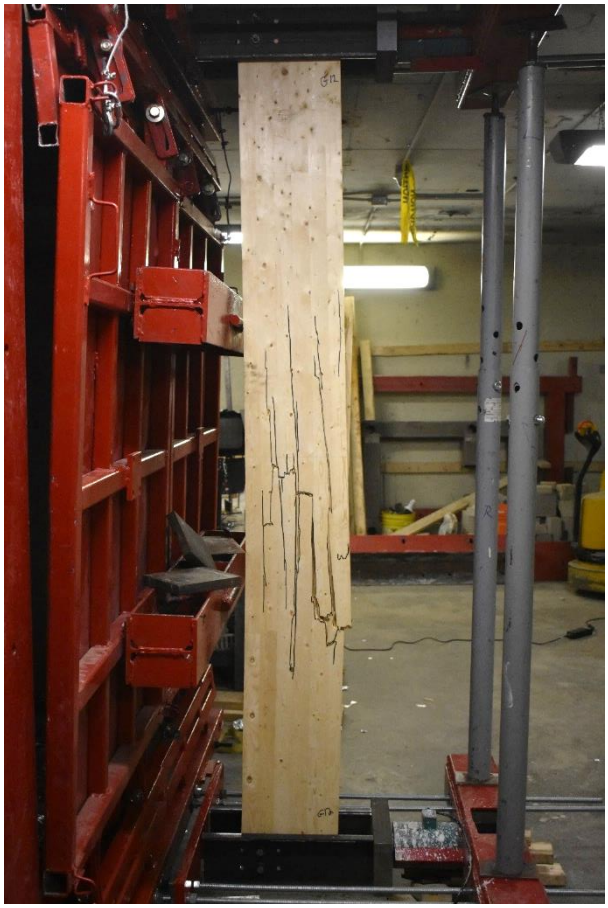


(d) Displacement and Strains

Figure C.23: Dynamic Test Results for Specimen G12



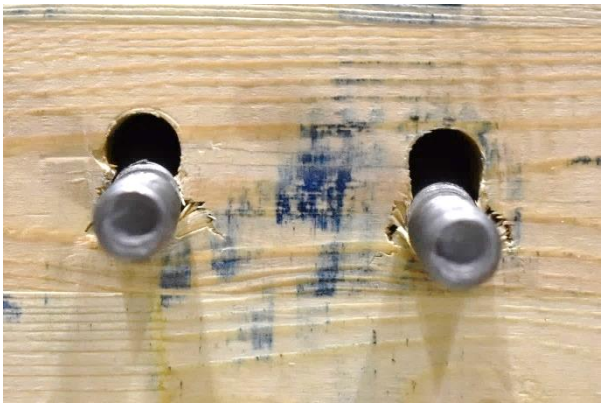
(a) Specimen Prior to Testing



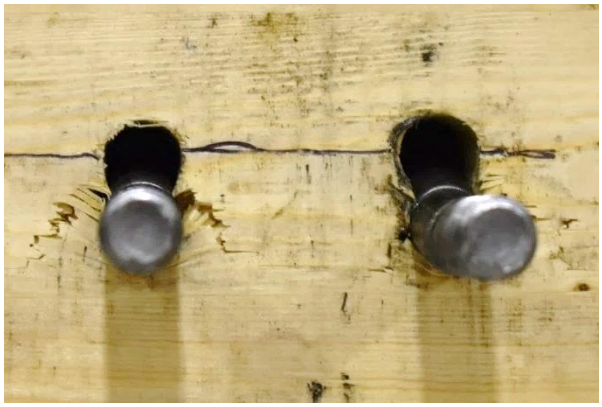
(b) Specimen After Testing



(c) Flexural Failure



(d) Wood Crushing in Bottom Joint



(e) Wood Crushing in Top Joint

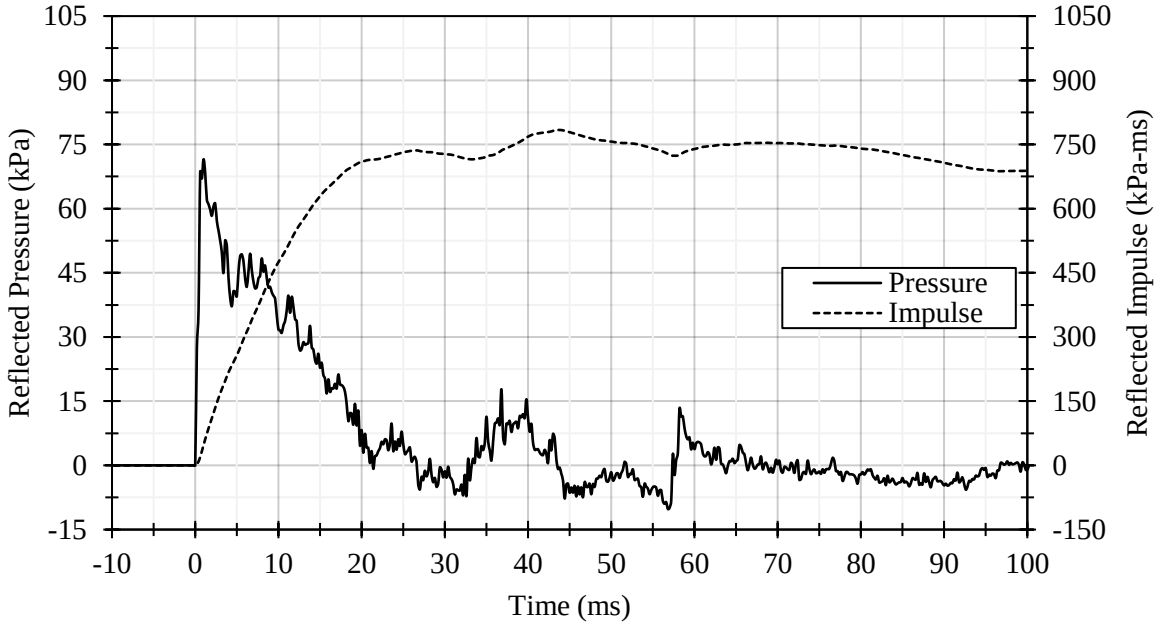


(f) Yielding of Bolts

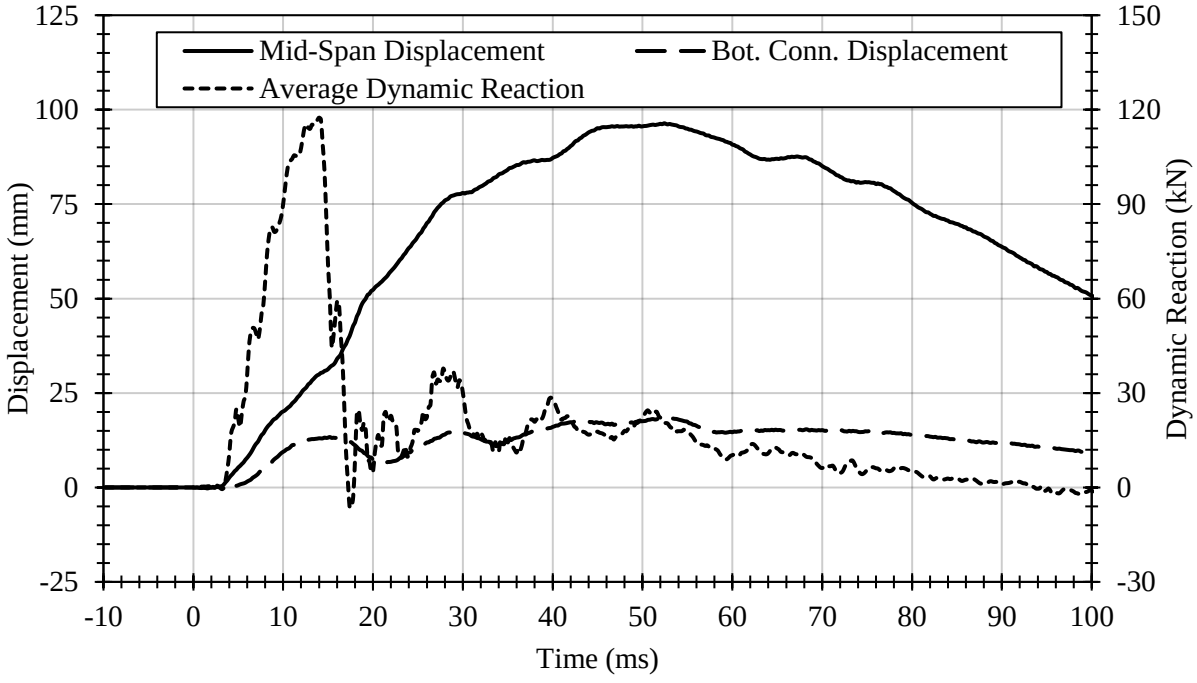
Figure C.24: Documentation of Damage for Specimen G12

Specimen G13

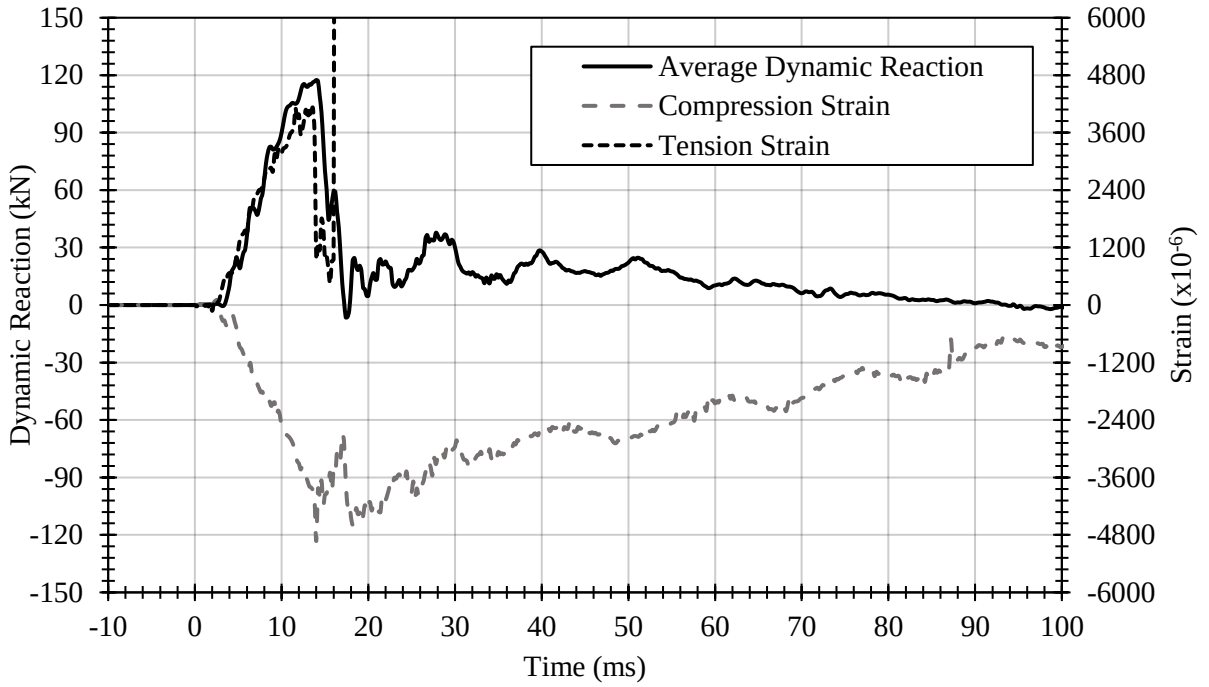
Specimen G13, comprised of a Glulam beam with a 2x2 bolted connection at each end, was dynamically tested on August 6th 2019. A driver pressure of 548.1 kPa was used, which resulted in a positive peak reflected pressure and impulse of 71.5 kPa and 736.0 kPa-ms, respectively.



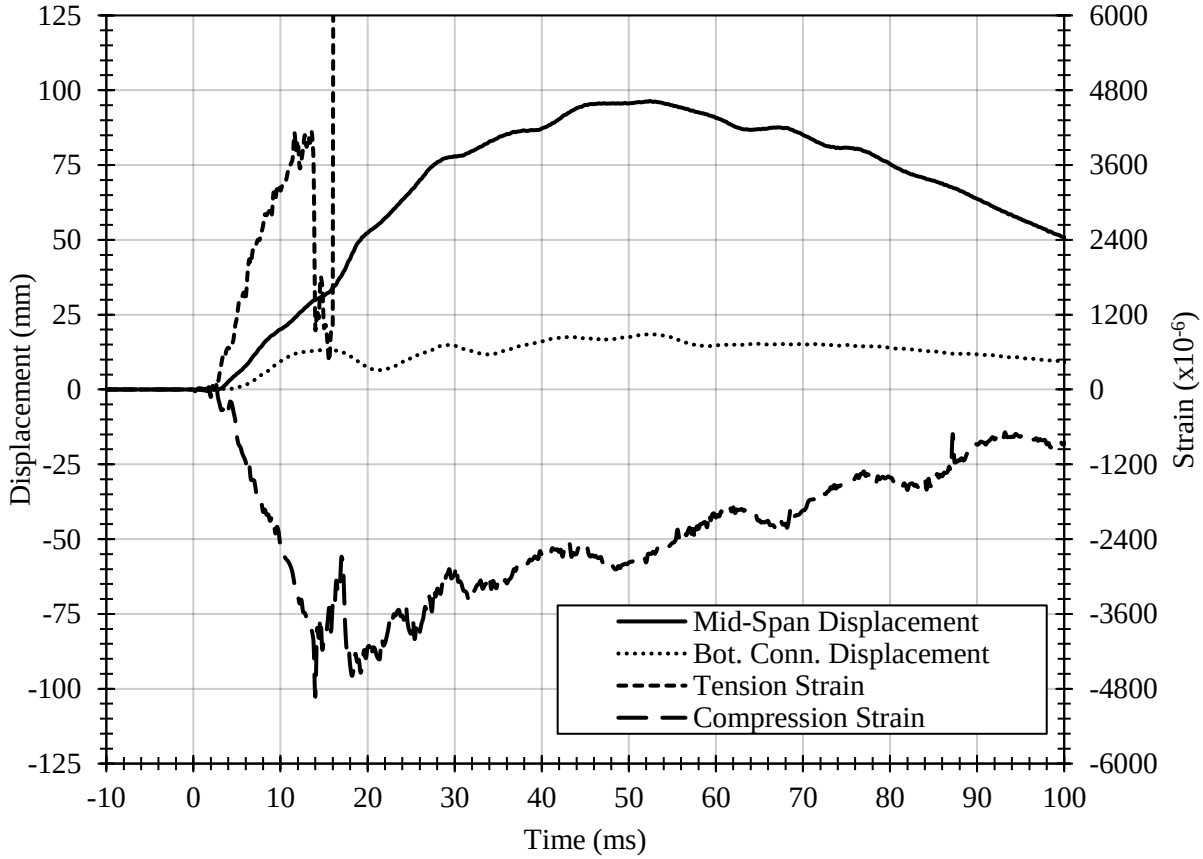
(a) Pressure and Impulse



(b) Reaction and Displacements



(c) Reaction and Strains

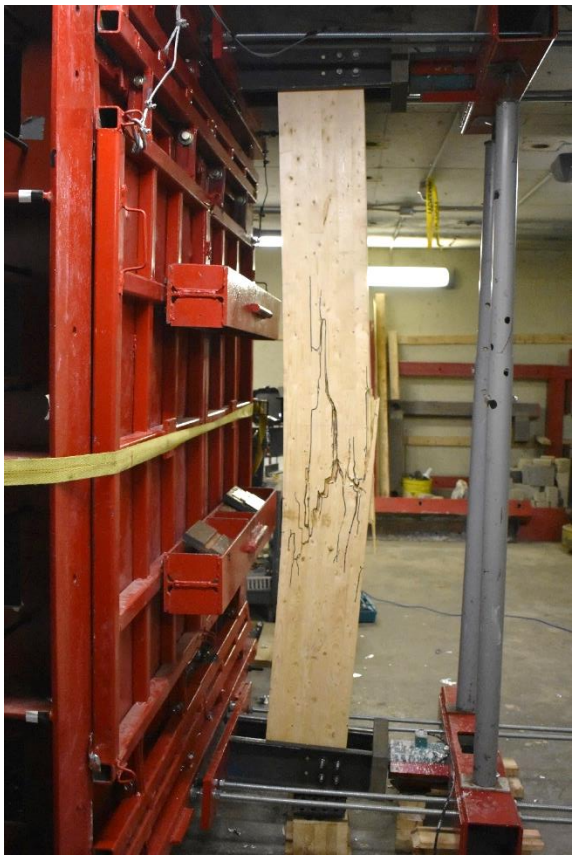


(d) Displacement and Strains

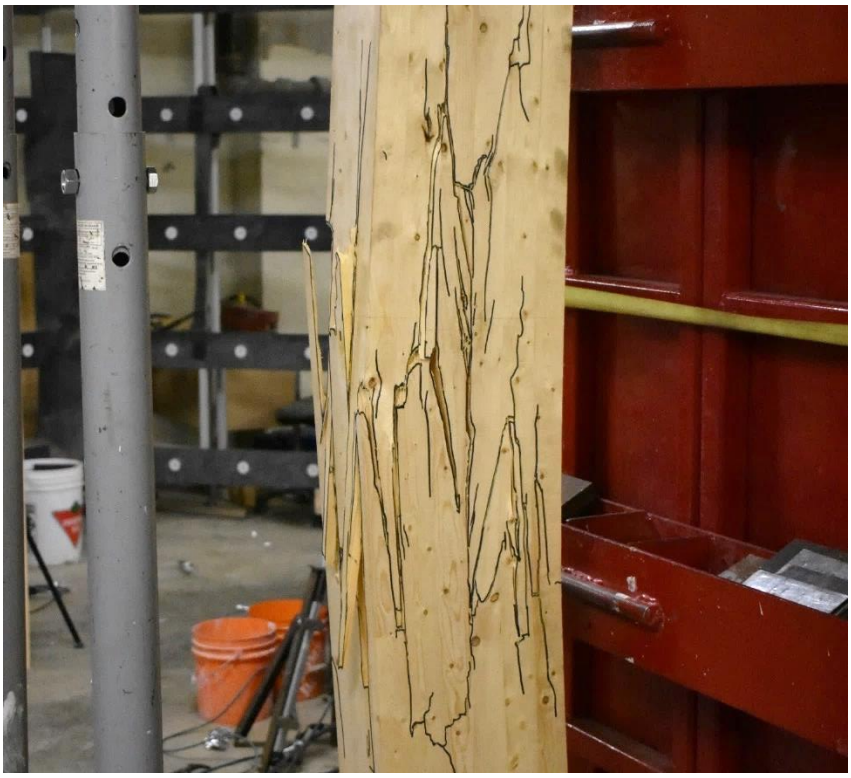
Figure C.25: Dynamic Test Results for Specimen G13



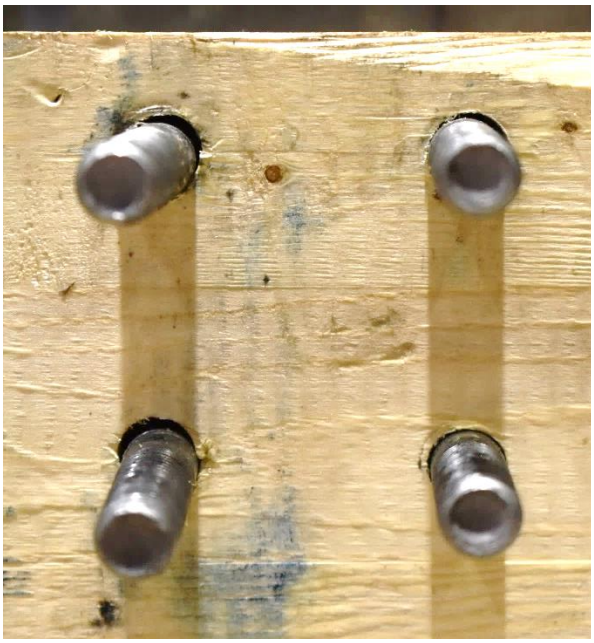
(a) Specimen Prior to Testing



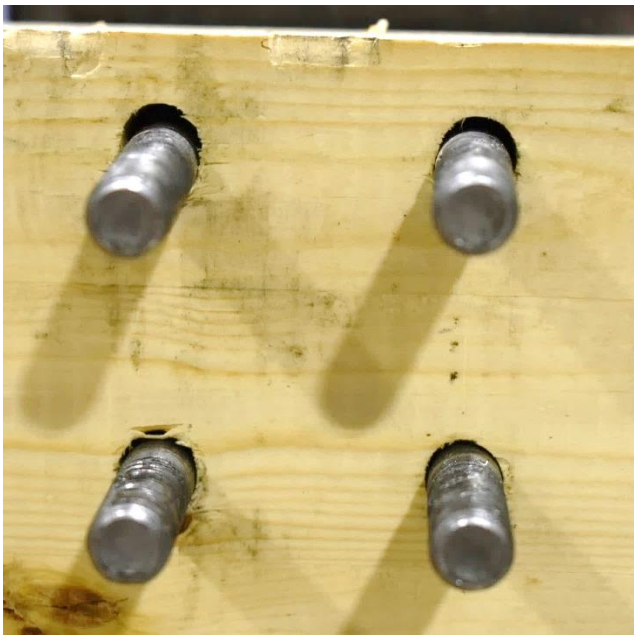
(b) Specimen After Testing



(c) Flexural Failure



(d) Wood Crushing in Bottom Joint



(e) Wood Crushing in Top Joint

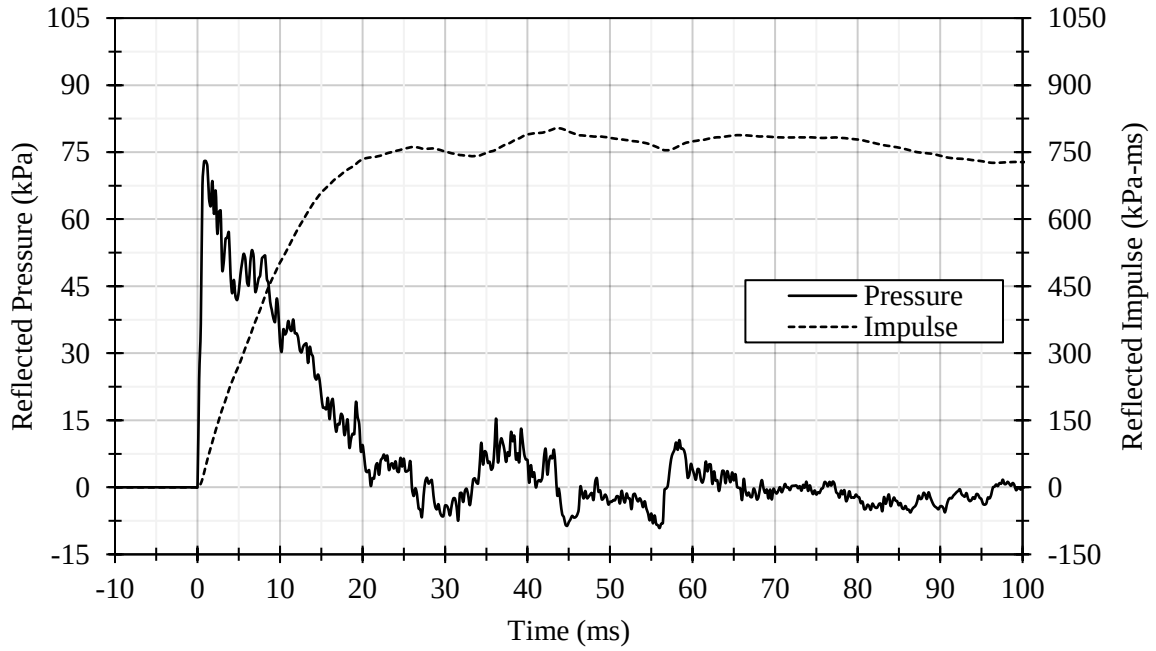


(f) Minimal Yielding of Bolts

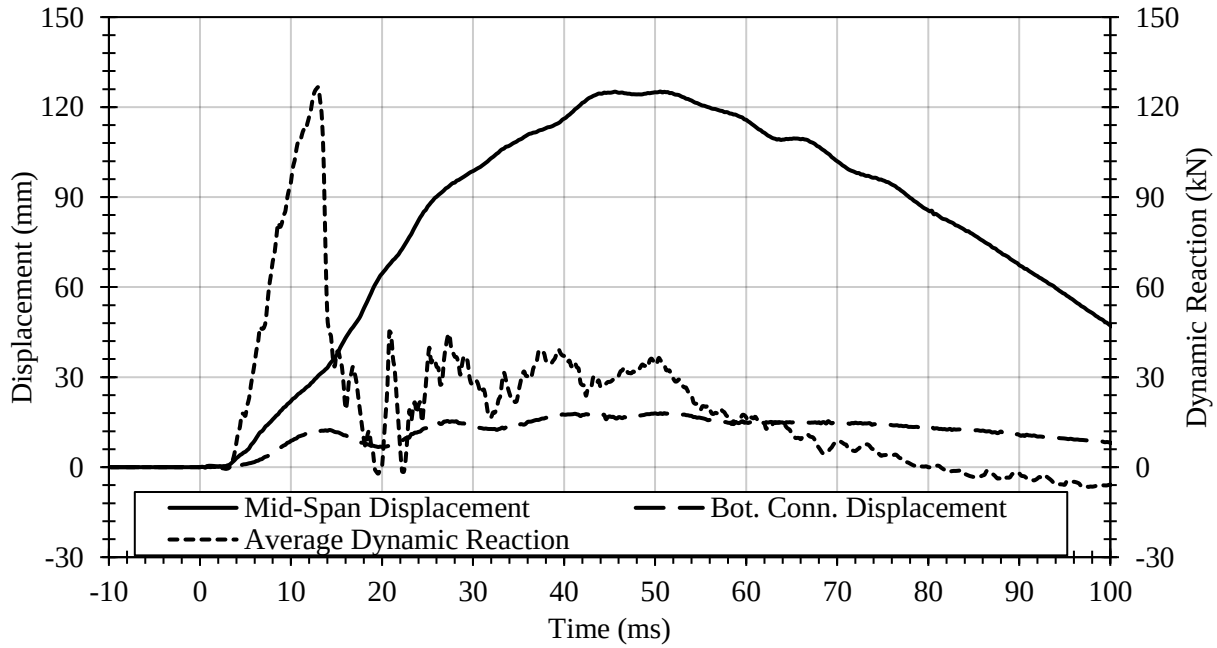
Figure C.26: Documentation of Damage for Specimen G13

Specimen G14

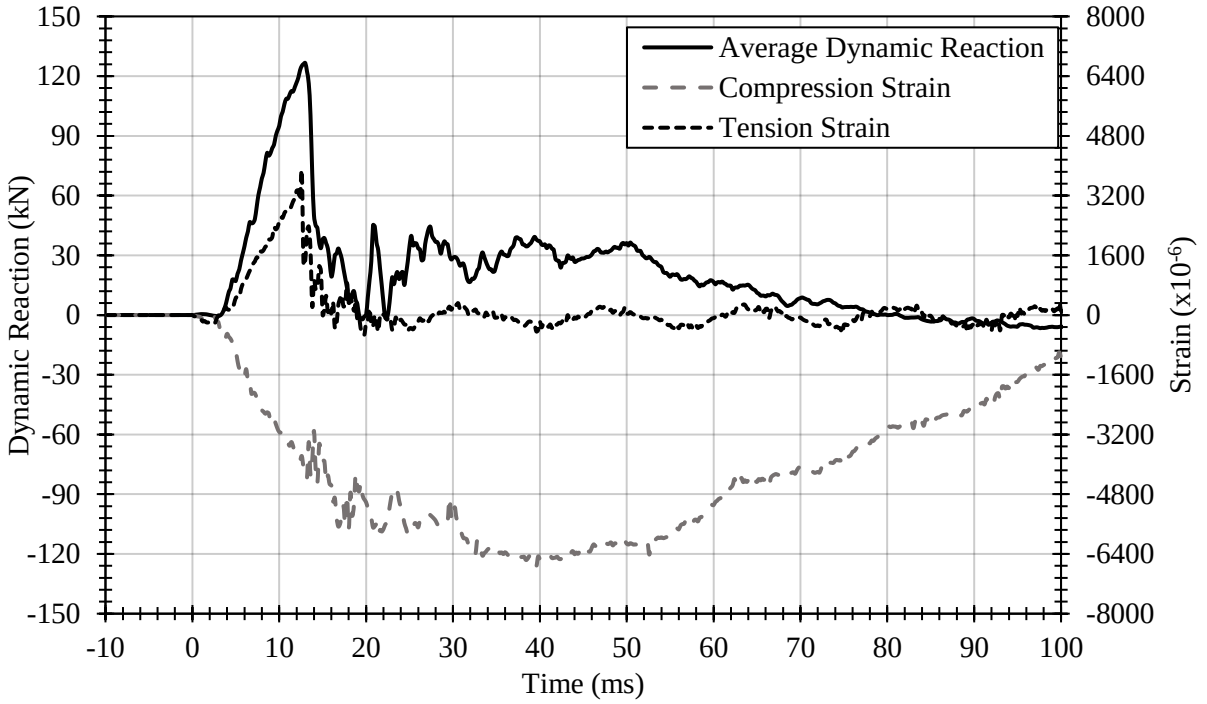
Specimen G14, comprised of a Glulam beam with a 2x3 bolted connection at each end, was dynamically tested on August 1st 2019. A driver pressure of 563.3 kPa was used, which resulted in a positive peak reflected pressure and impulse of 73.0 kPa and 761.4 kPa-ms, respectively.



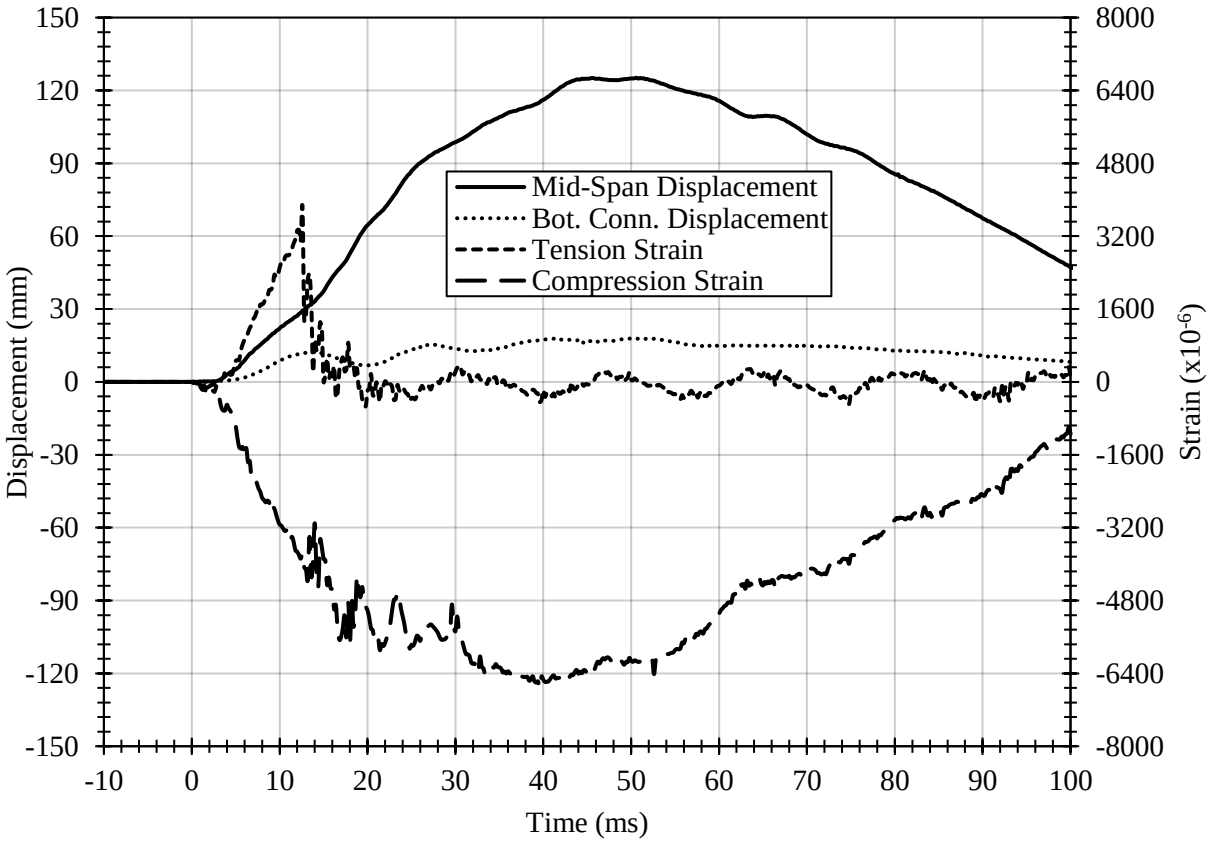
(a) Pressure and Impulse



(b) Reaction and Displacements

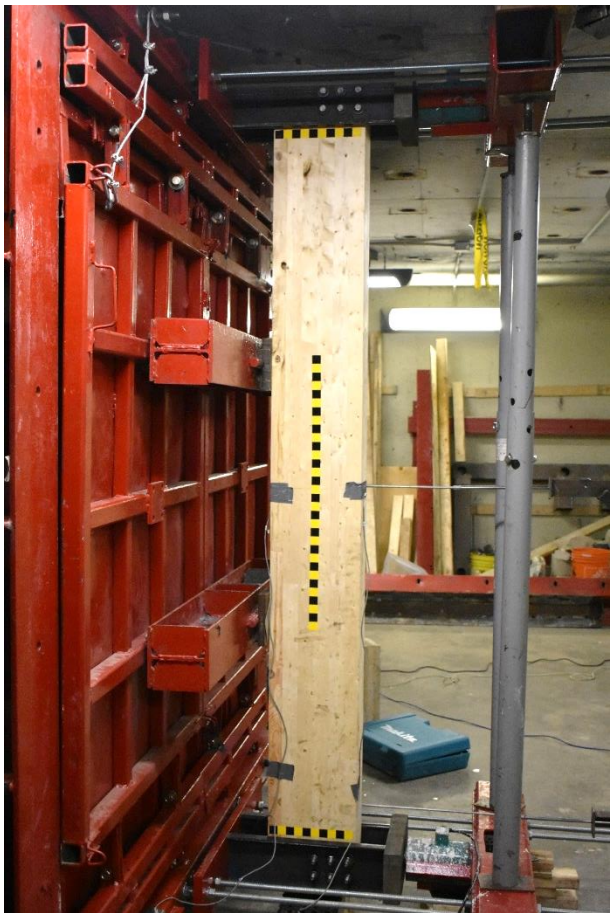


(c) Reaction and Strains

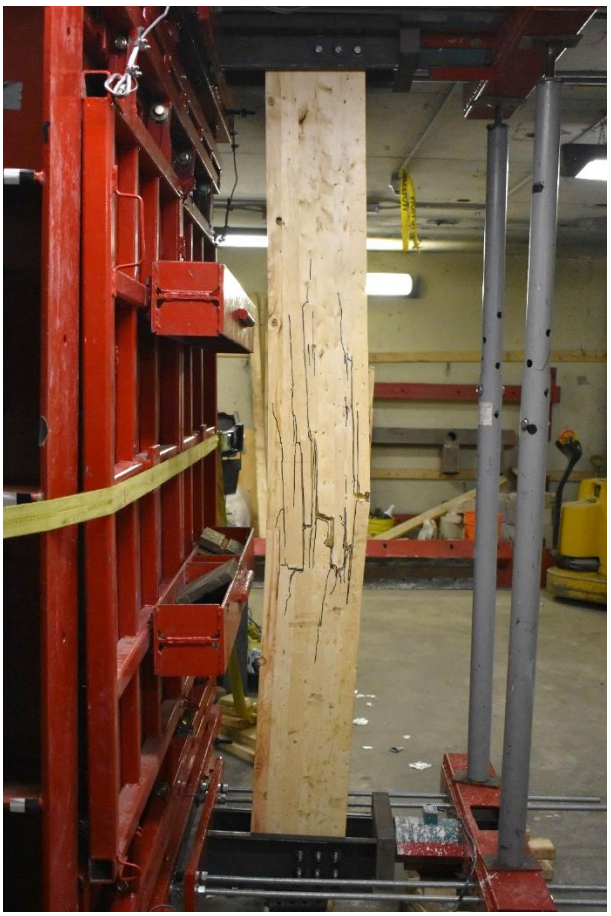


(d) Displacement and Strains

Figure C.27: Dynamic Test Results for Specimen G14



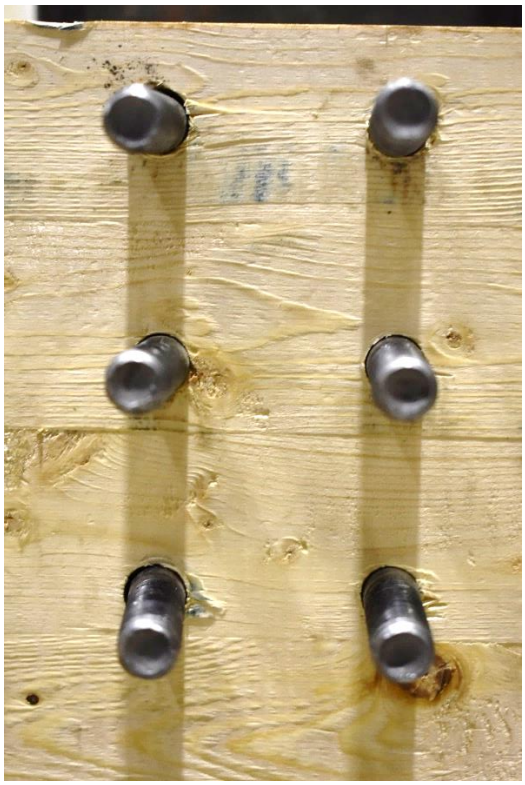
(a) Specimen Prior to Testing



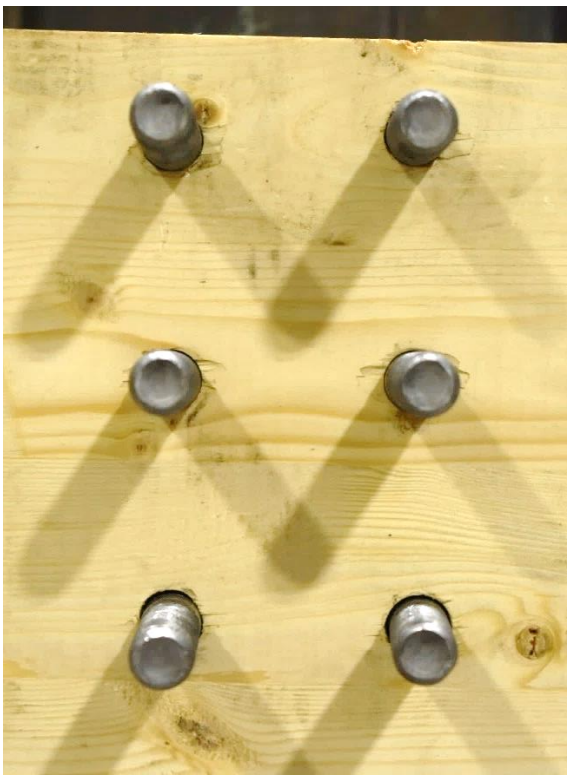
(b) Specimen After Testing



(c) Flexural Failure



(d) Lack of Wood Crushing in Bottom Joint



(e) Lack of Wood Crushing in Top Joint

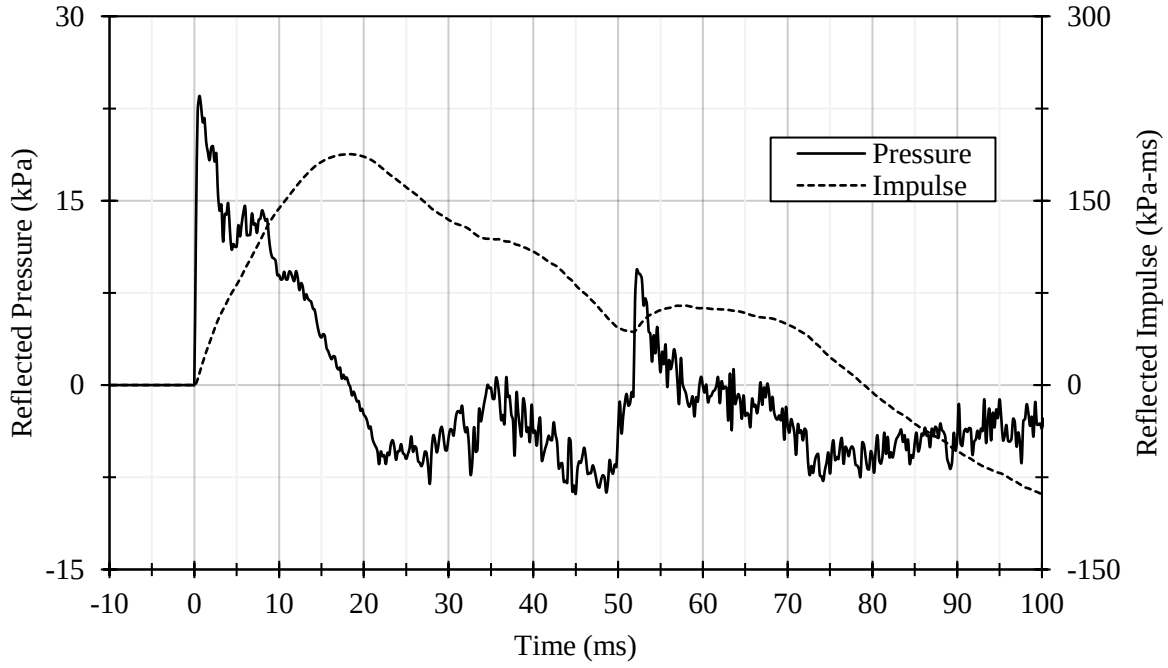


(f) Very Minimal Yielding of Bolts

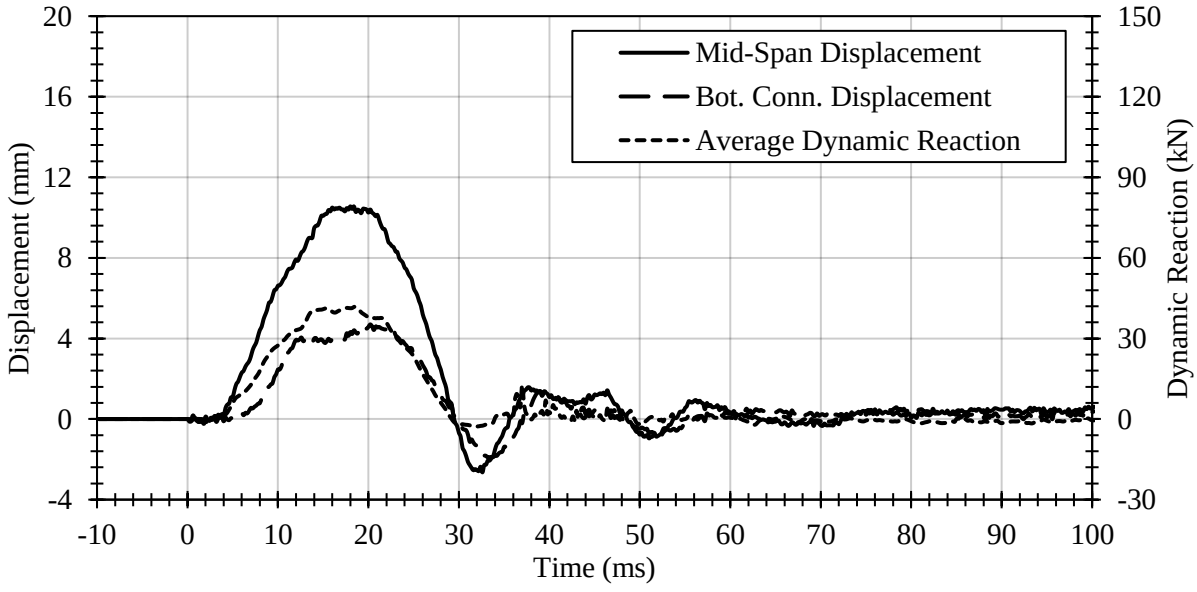
Figure C.28: Documentation of Damage for Specimen G14

Specimen G15 – Shot #1

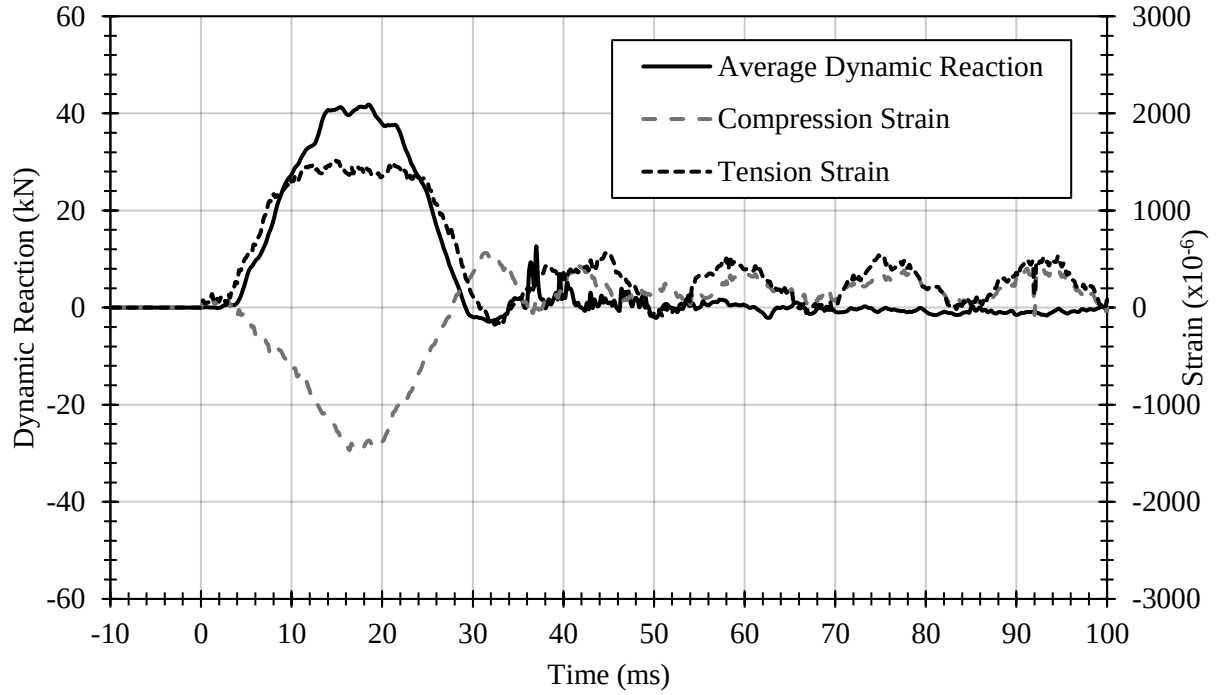
Specimen G15, comprised of a Glulam beam with a 7.5" deep EAC at each end, was subjected to two different pressure-impulse combinations. For the first shot, it was dynamically tested on September 9th 2019. A driver pressure of 143.4 kPa was used, which resulted in a positive peak reflected pressure and impulse of 23.5 kPa and 187.8 kPa-ms, respectively.



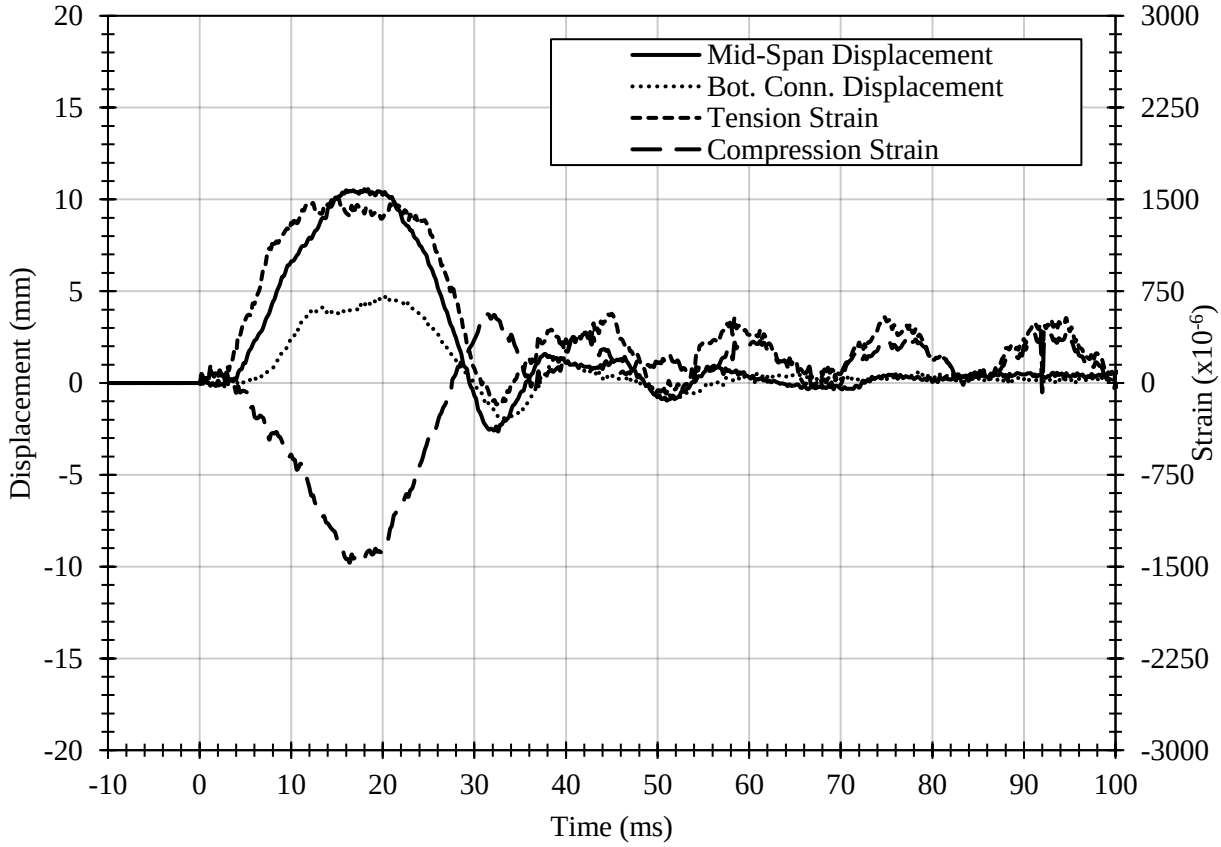
(a) Pressure and Impulse



(b) Reaction and Displacements

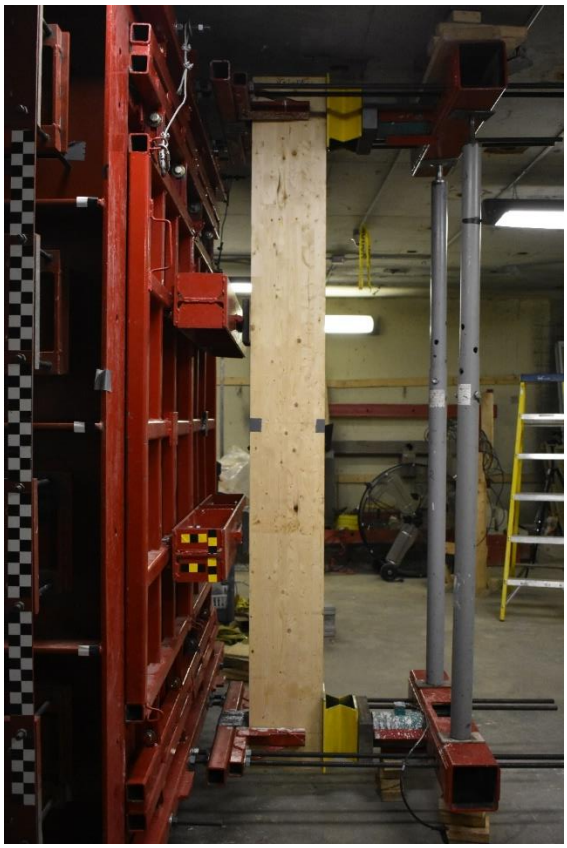


(c) Reaction and Strains

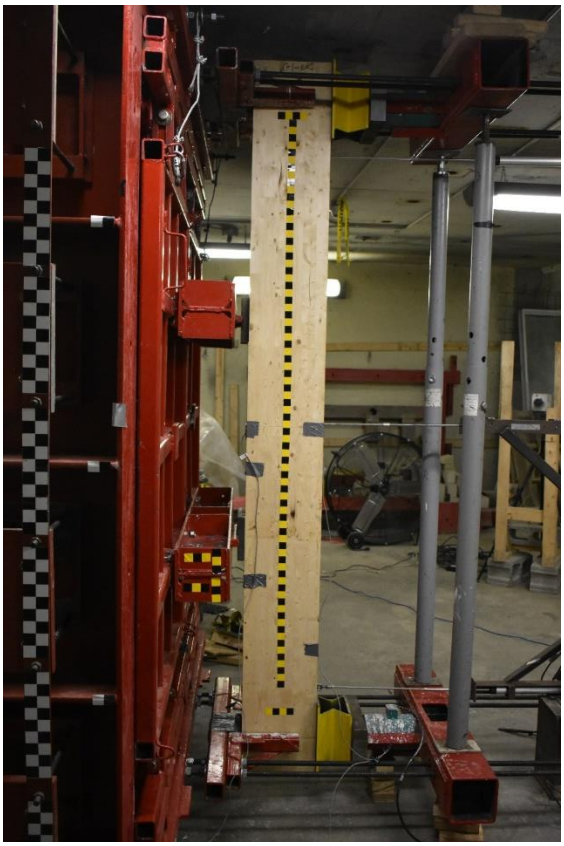


(d) Displacement and Strains

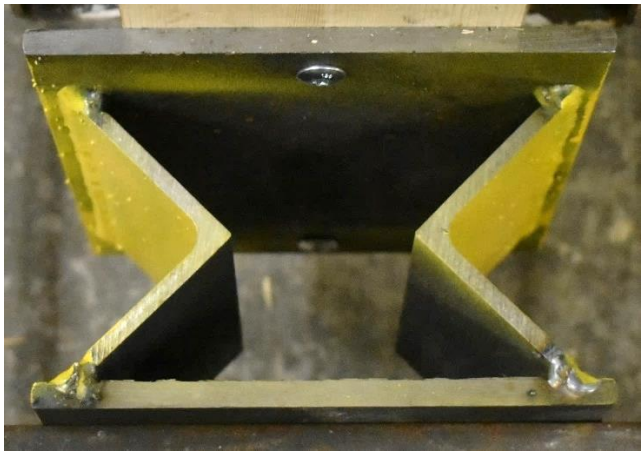
Figure C.29: Dynamic Test Results for Test G15-1



(a) Specimen Prior to Testing



(b) Specimen After Testing



(c) Lack of Damage in Bottom EAC

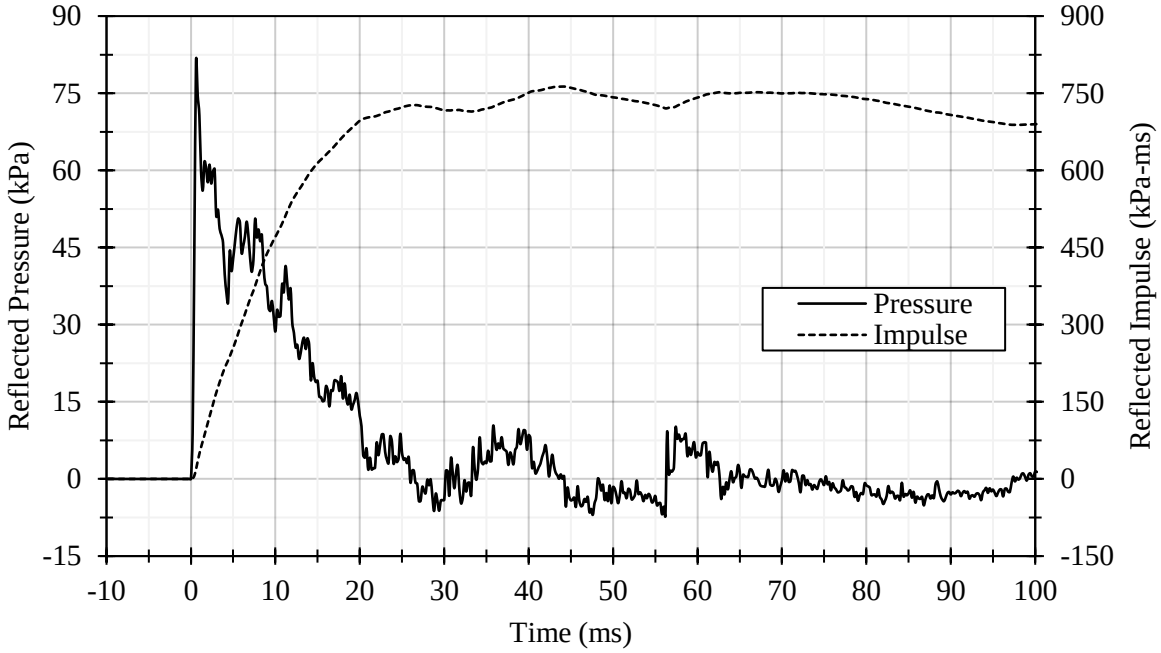


(d) Lack of Damage in Top EAC

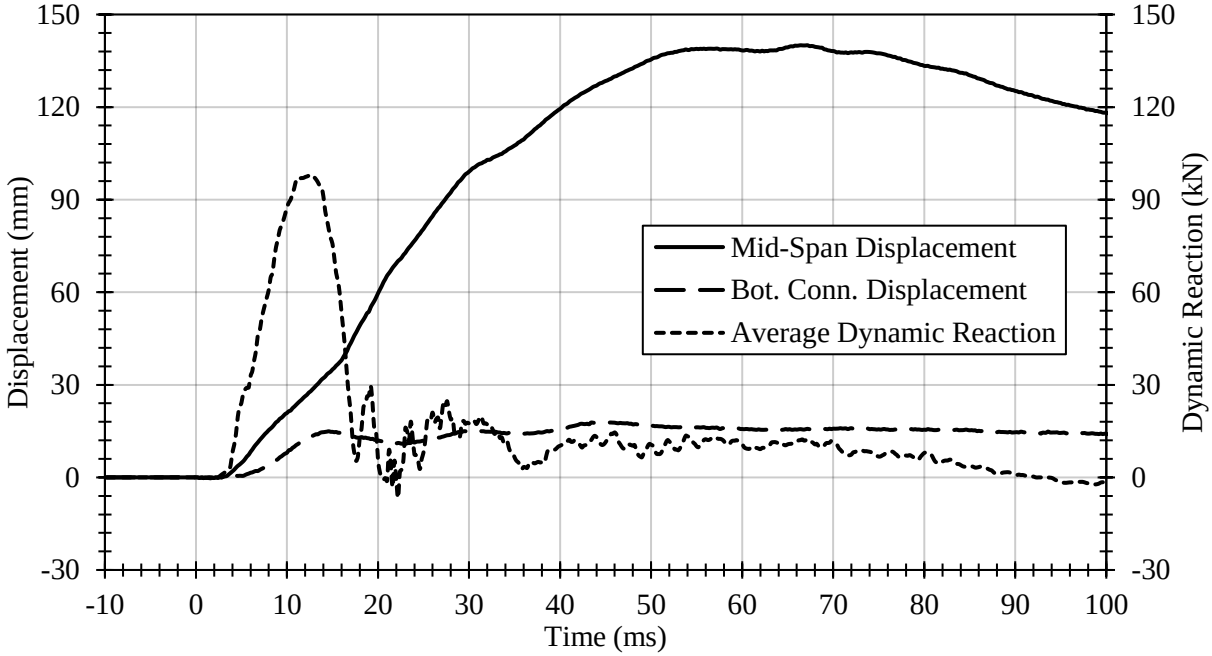
Figure C.30: Documentation of Damage for Test G15-1

Specimen G15 – Shot #2

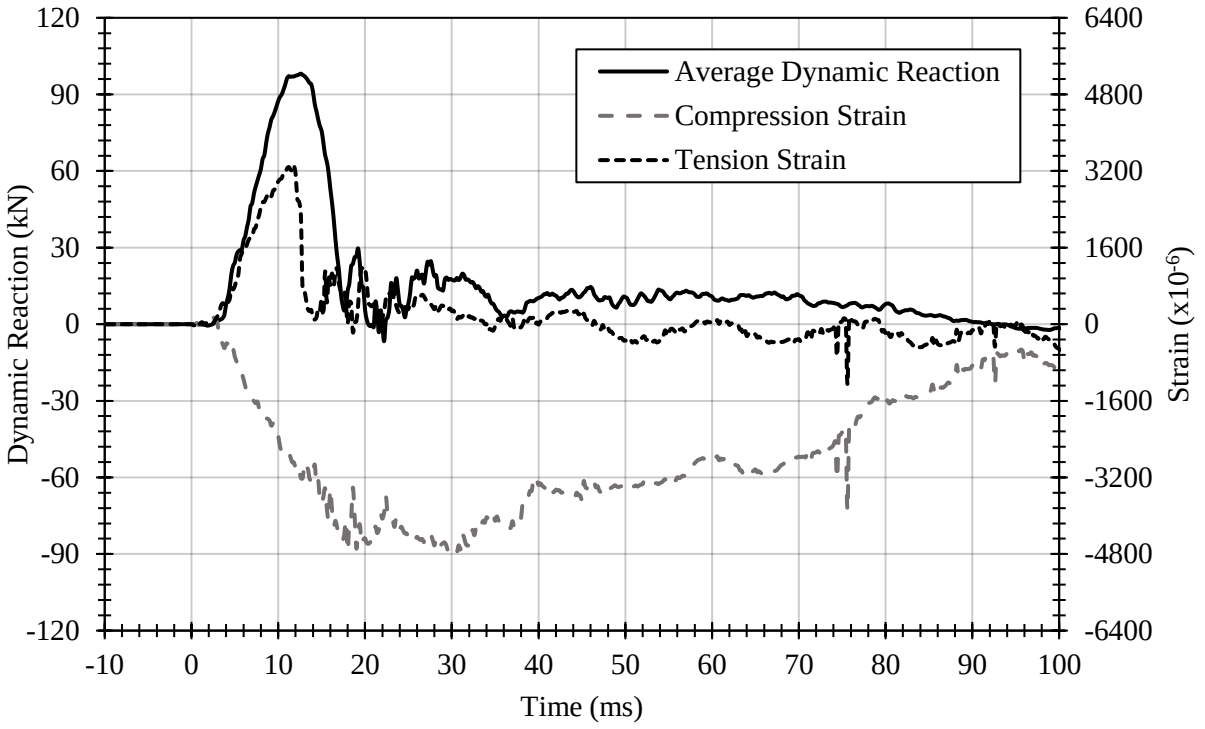
For the second shot, it was dynamically tested on September 9th 2019. A driver pressure of 536.4 kPa was used, which resulted in a positive peak reflected pressure and impulse of 81.1 kPa and 726.9 kPa-ms, respectively.



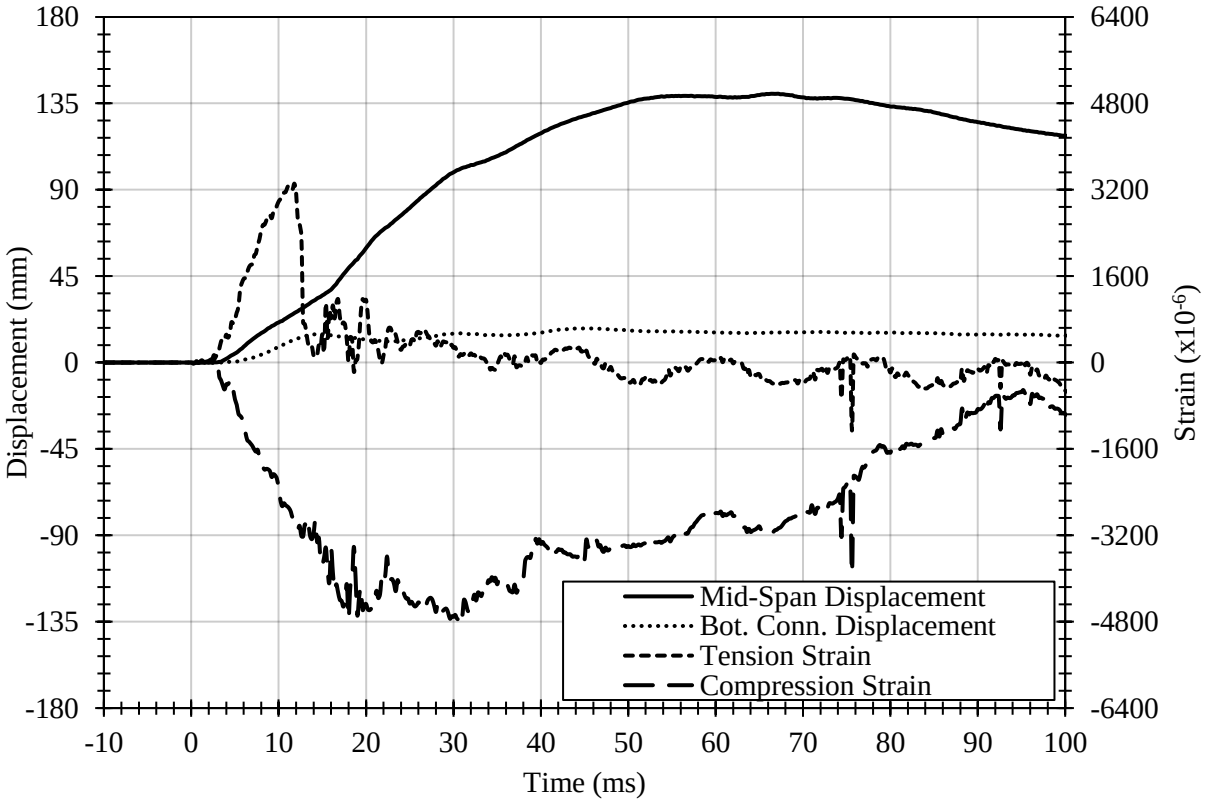
(a) Pressure and Impulse



(b) Reaction and Displacements



(c) Reaction and Strains

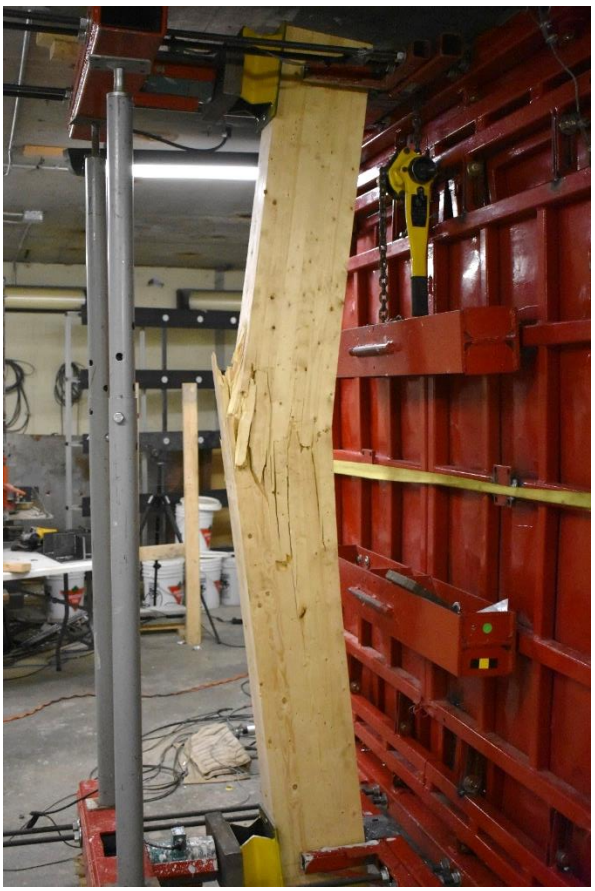


(d) Displacement and Strains

Figure C.31: Dynamic Test Results for Test G15-2



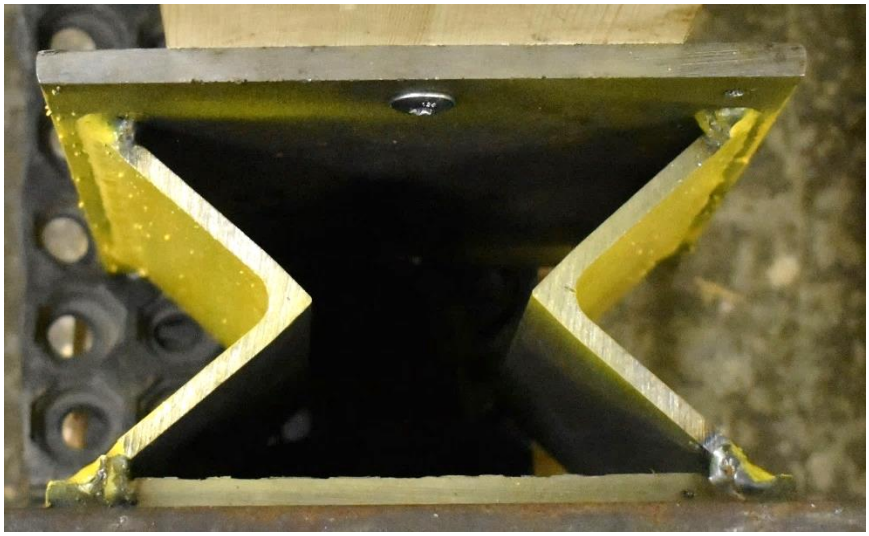
(a) Specimen Prior to Testing



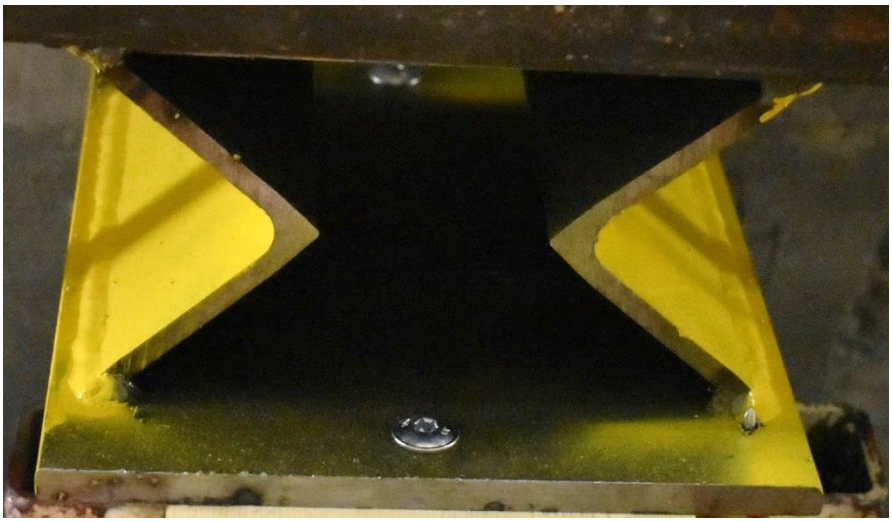
(b) Specimen After Testing



(c) Flexural Failure of Beam



(d) Minimal Damage in Bottom EAC

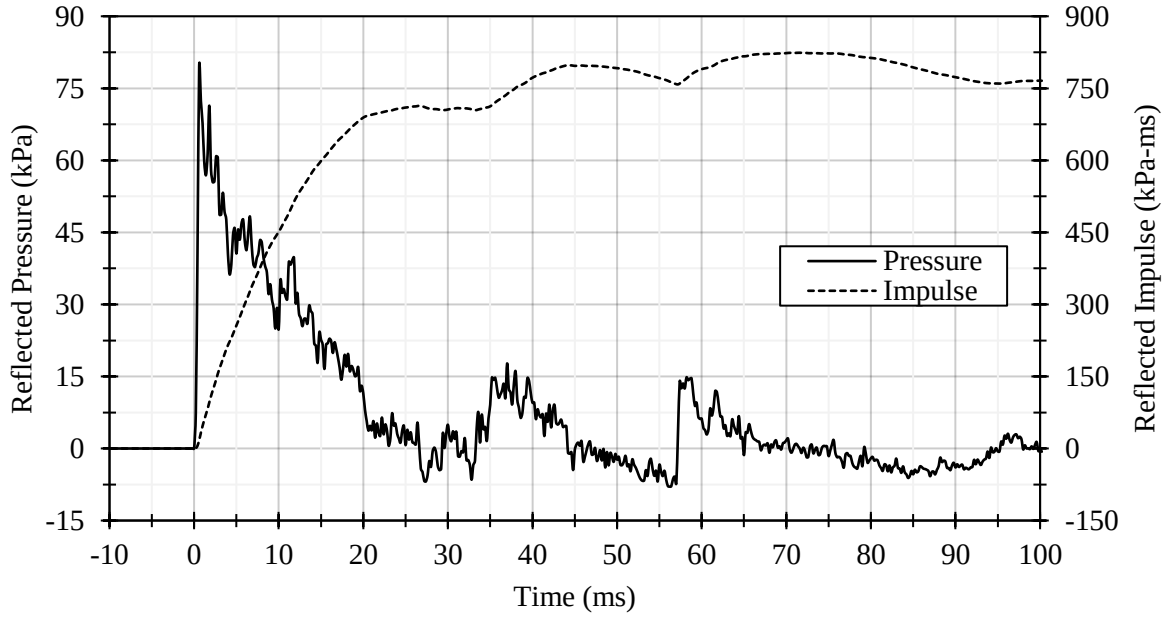


(e) Minimal Damage in Top EAC

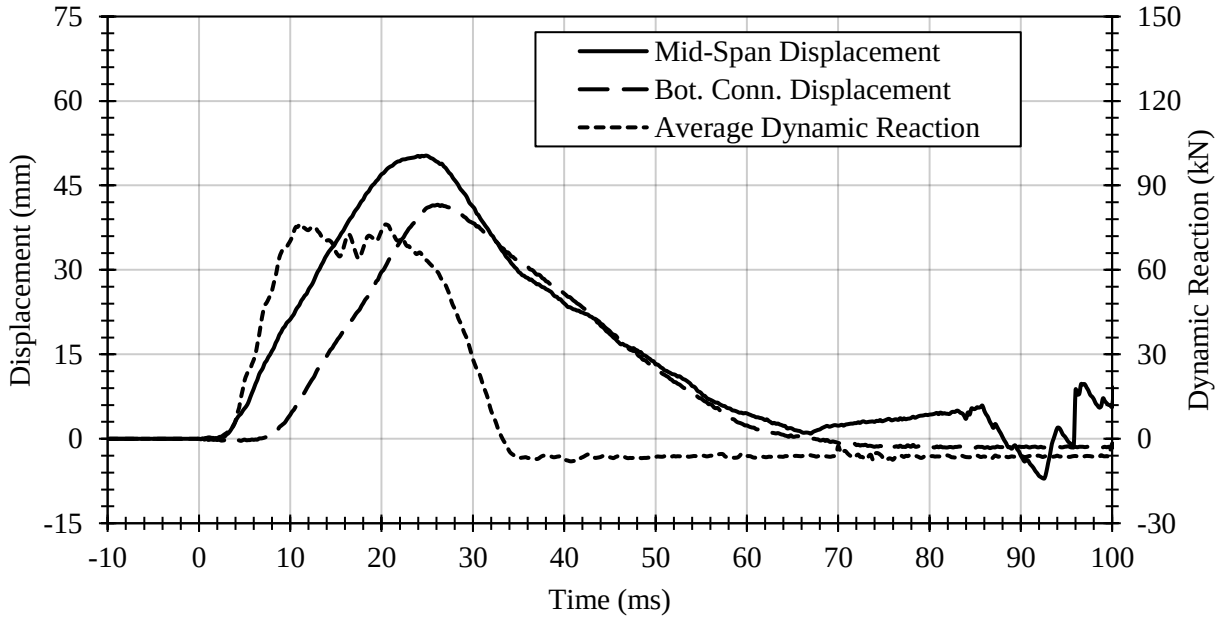
Figure C.32: Documentation of Damage for Test G15-2

Specimen G16 – Shot #1

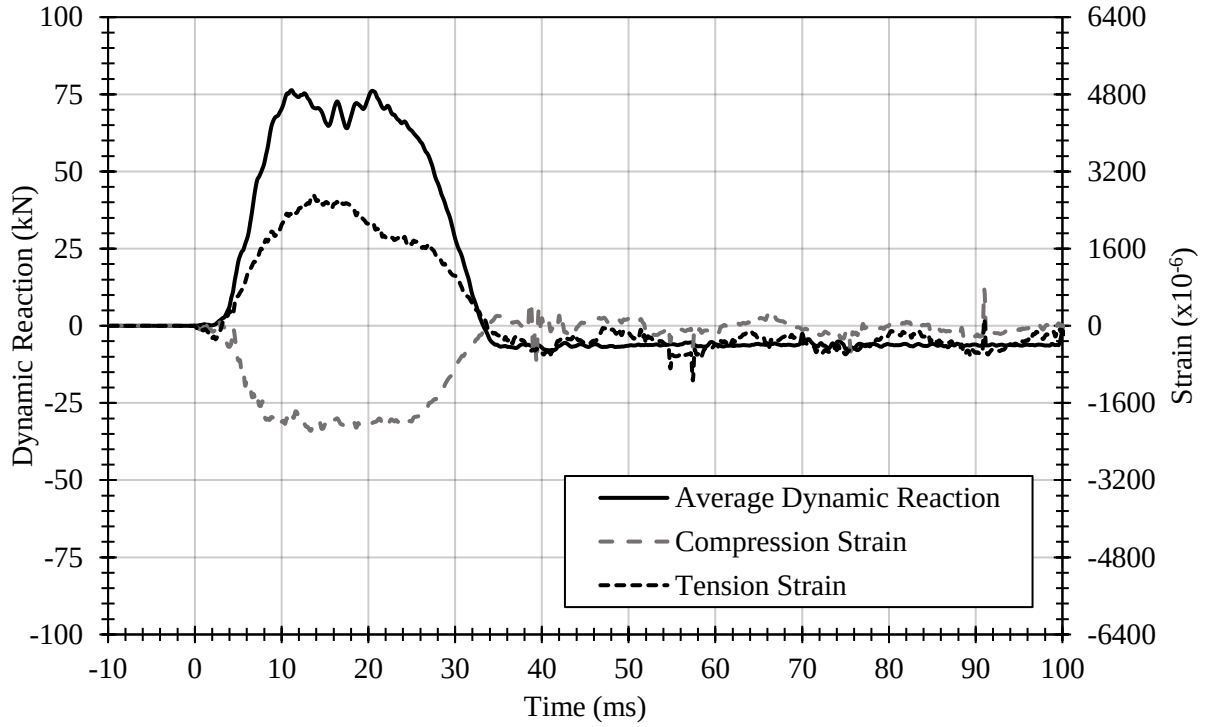
Specimen G16, comprised of a Glulam beam with a 5.0” deep EAC at each end, was subjected to seven different pressure-impulse combinations. For the first shot, it was dynamically tested on September 11th 2019. A driver pressure of 532.3 kPa was used, which resulted in a positive peak reflected pressure and impulse of 79.5 kPa and 713.6 kPa-ms, respectively.



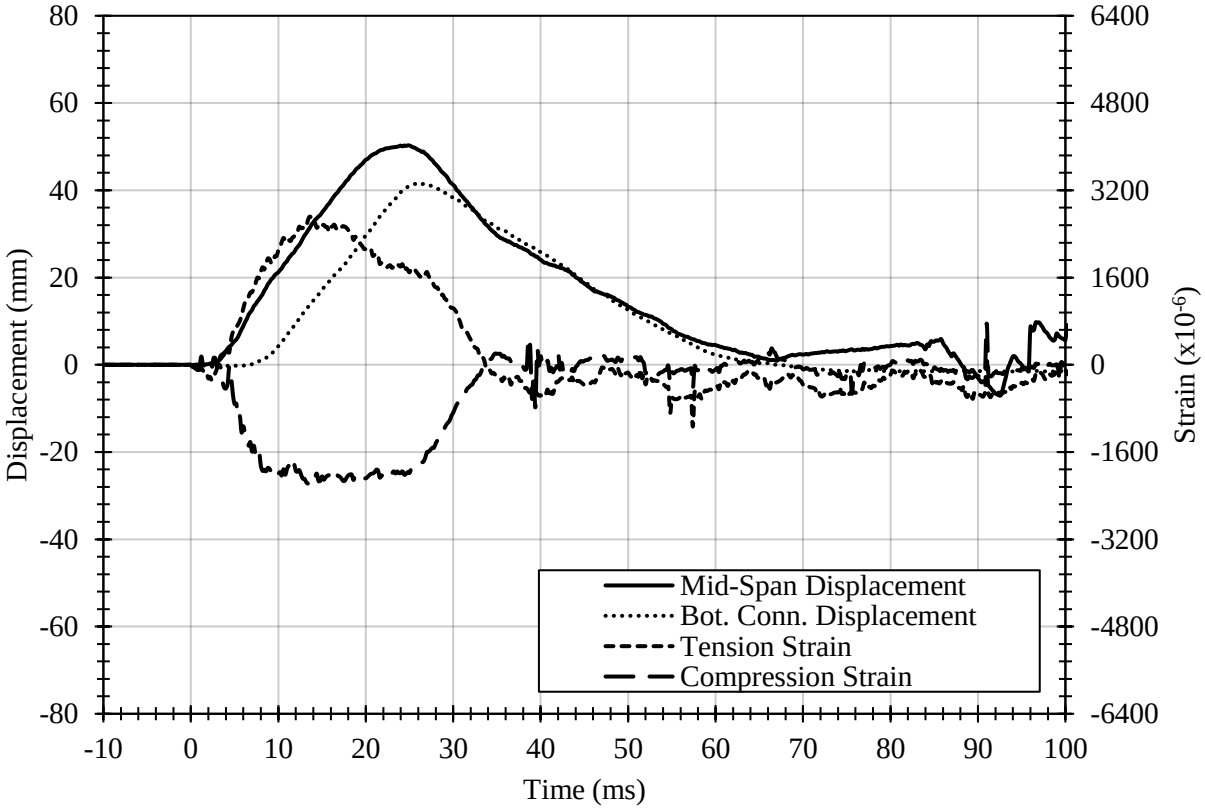
(a) Pressure and Impulse



(b) Reaction and Displacements

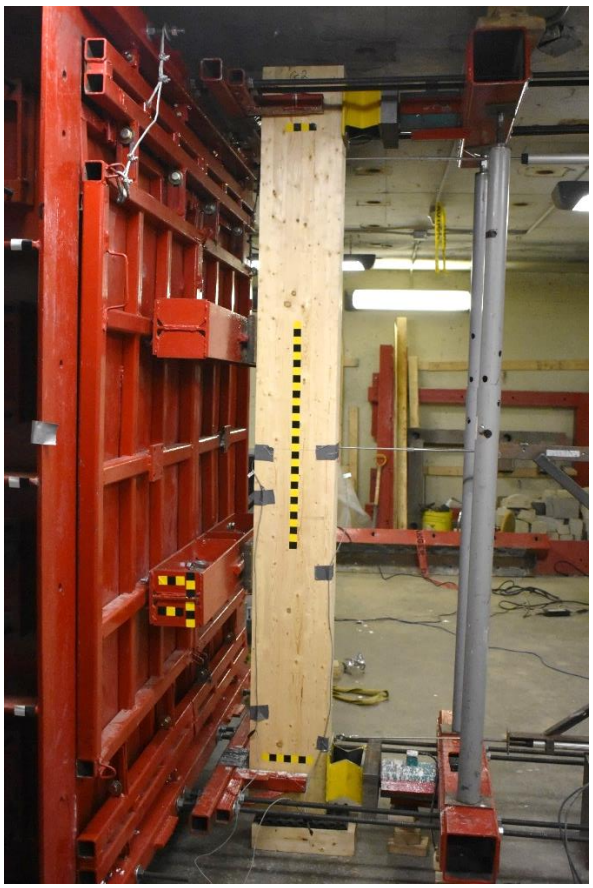


(c) Reaction and Strains

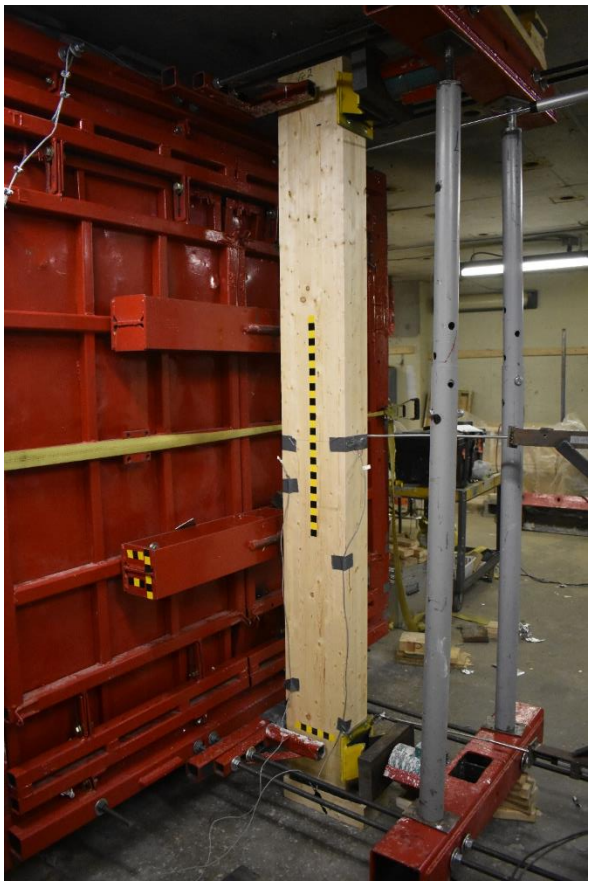


(d) Displacement and Strains

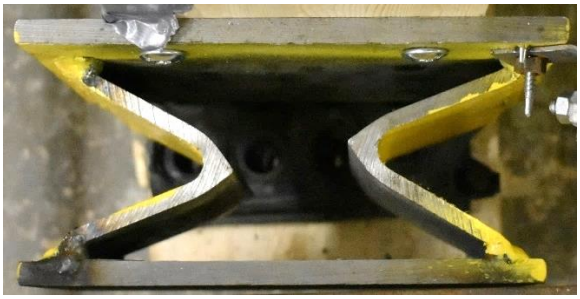
Figure C.33: Dynamic Test Results for Test G16-1



(a) Specimen Prior to Testing



(b) Specimen After Testing



(c) Damage in Bottom EAC

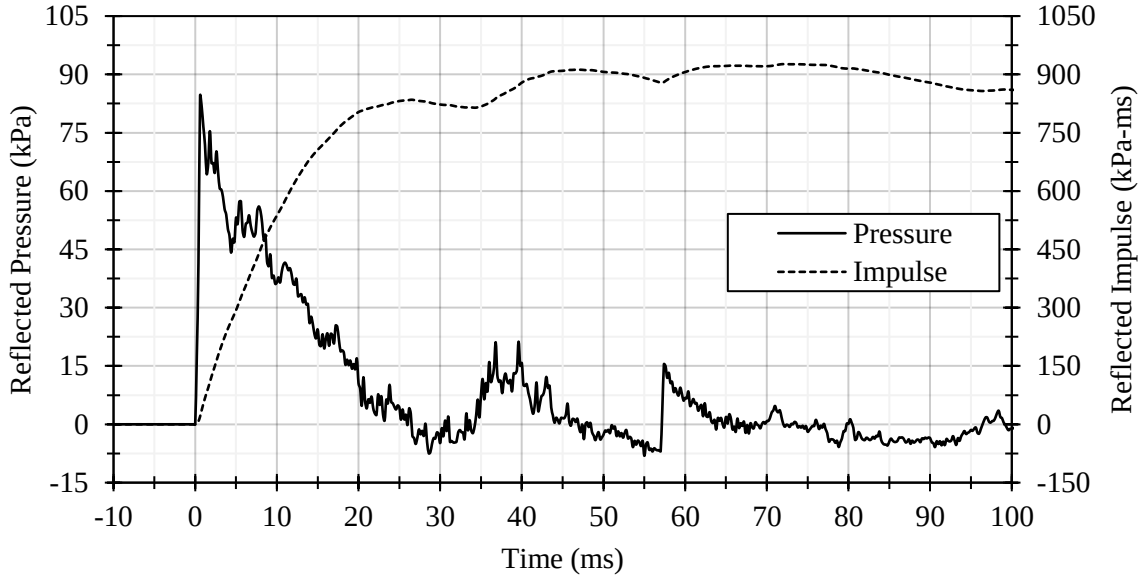


(d) Damage in Top EAC

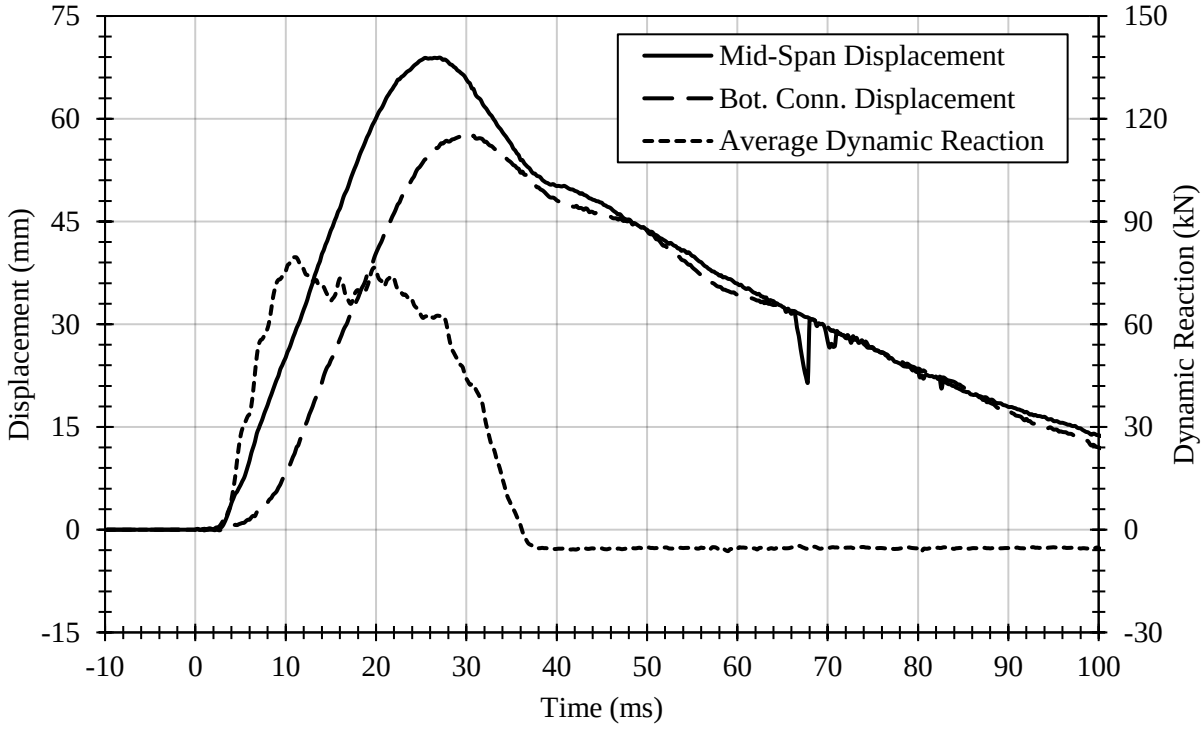
Figure C.34: Documentation of Damage for Test G16-1

Specimen G16 – Shot #2

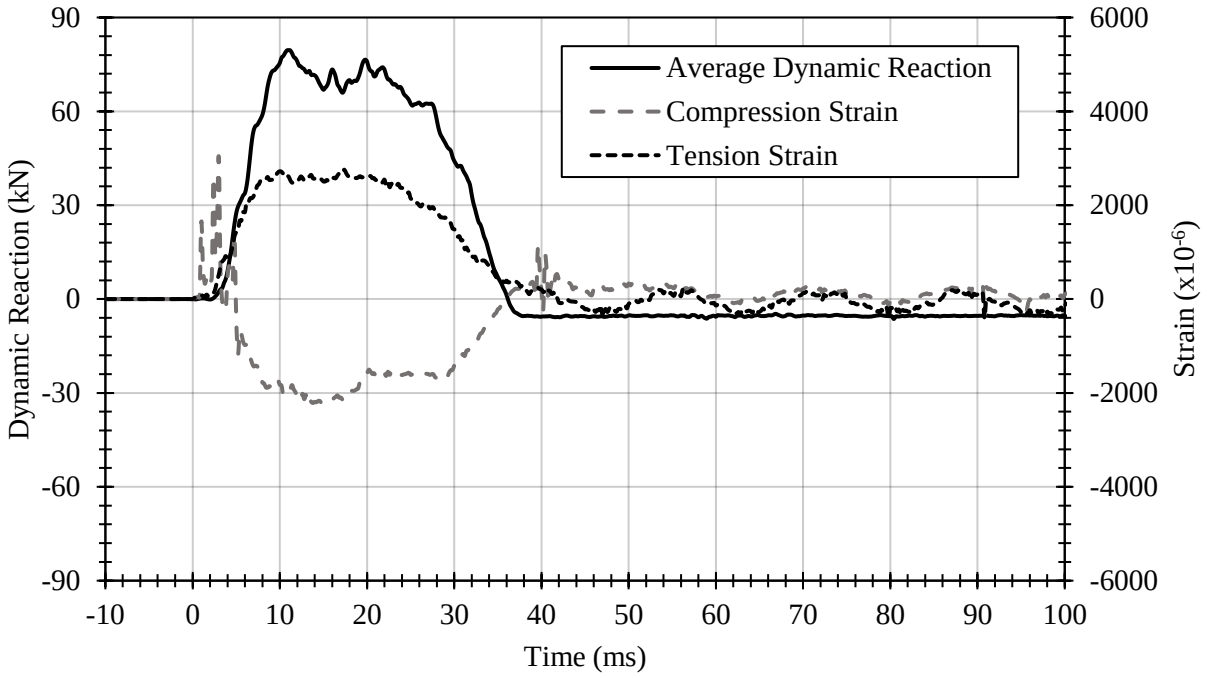
For the second shot, it was dynamically tested on September 11th 2019. A driver pressure of 536.4 kPa was used, which resulted in a positive peak reflected pressure and impulse of 84.5 kPa and 834.7 kPa-ms, respectively.



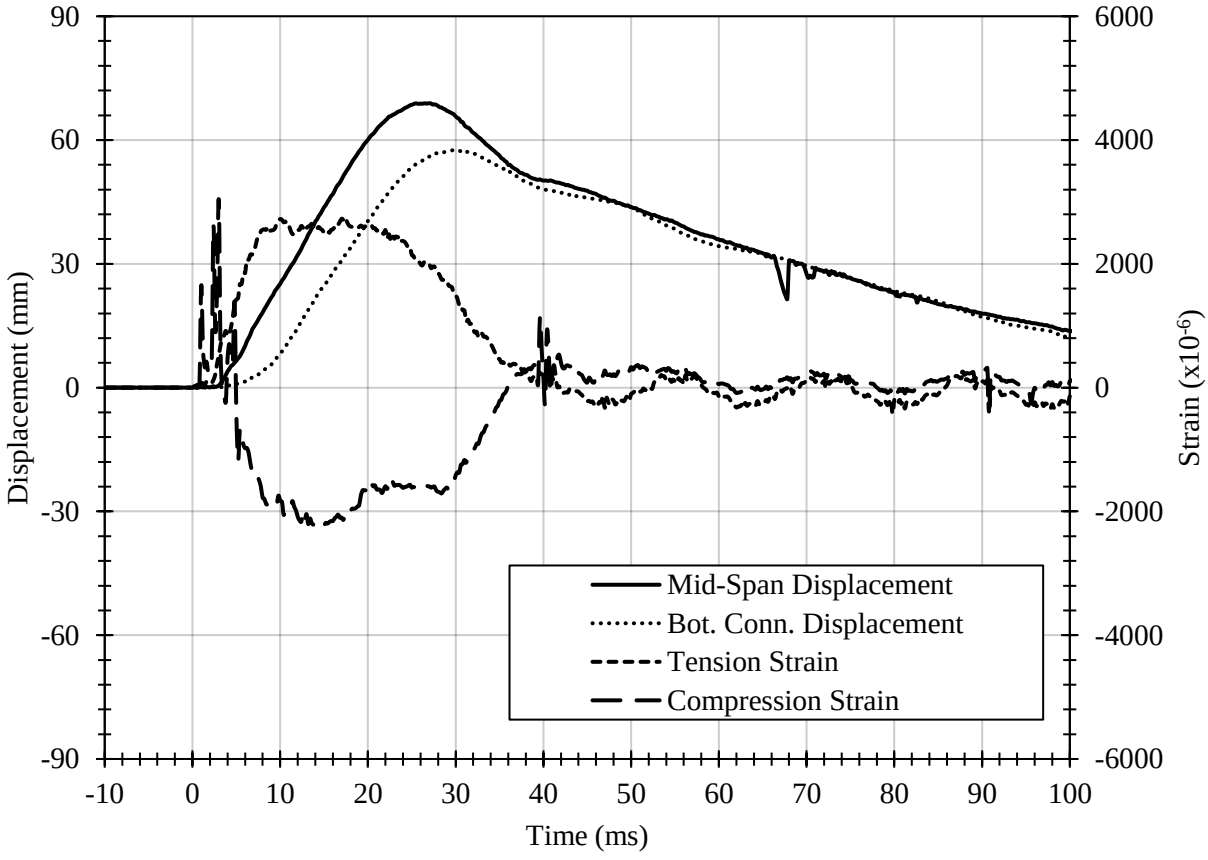
(a) Pressure and Impulse



(b) Reaction and Displacements



(c) Reaction and Strains

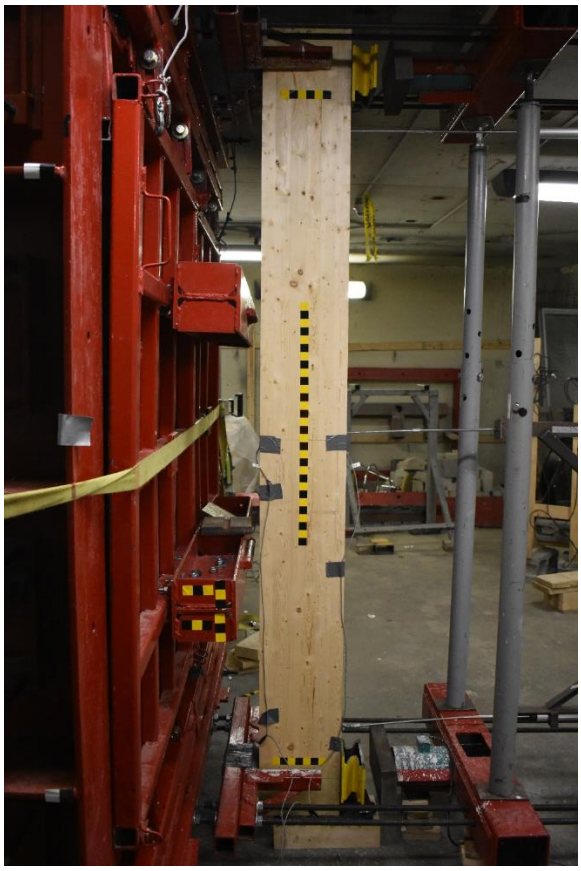


(d) Displacement and Strains

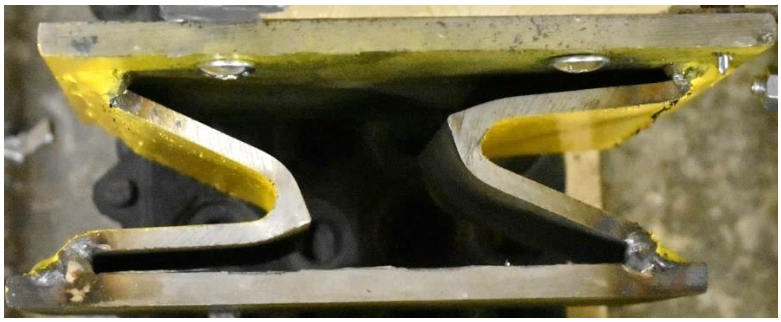
Figure C.35: Dynamic Test Results for Test G16-2



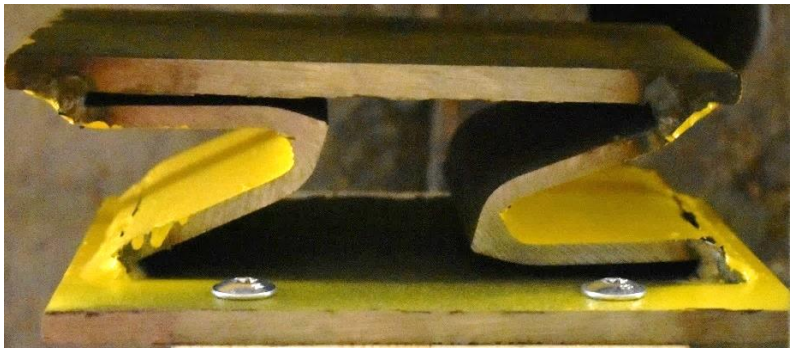
(a) Specimen Prior to Testing



(b) Specimen After Testing



(c) Damage in Bottom EAC

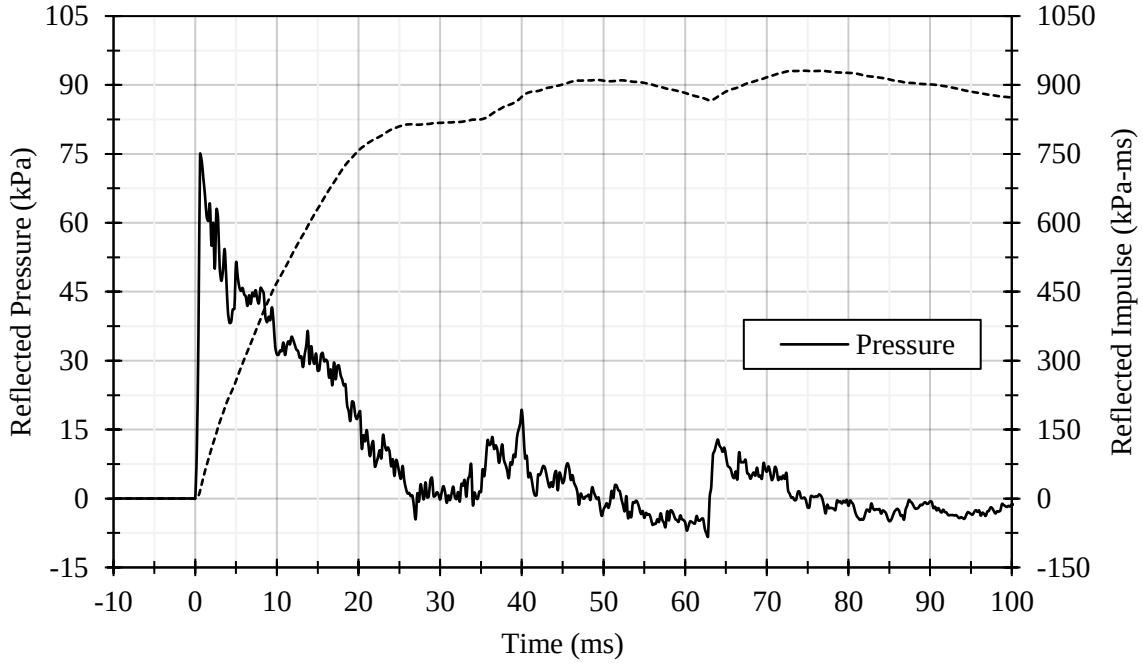


(d) Damage in Top EAC

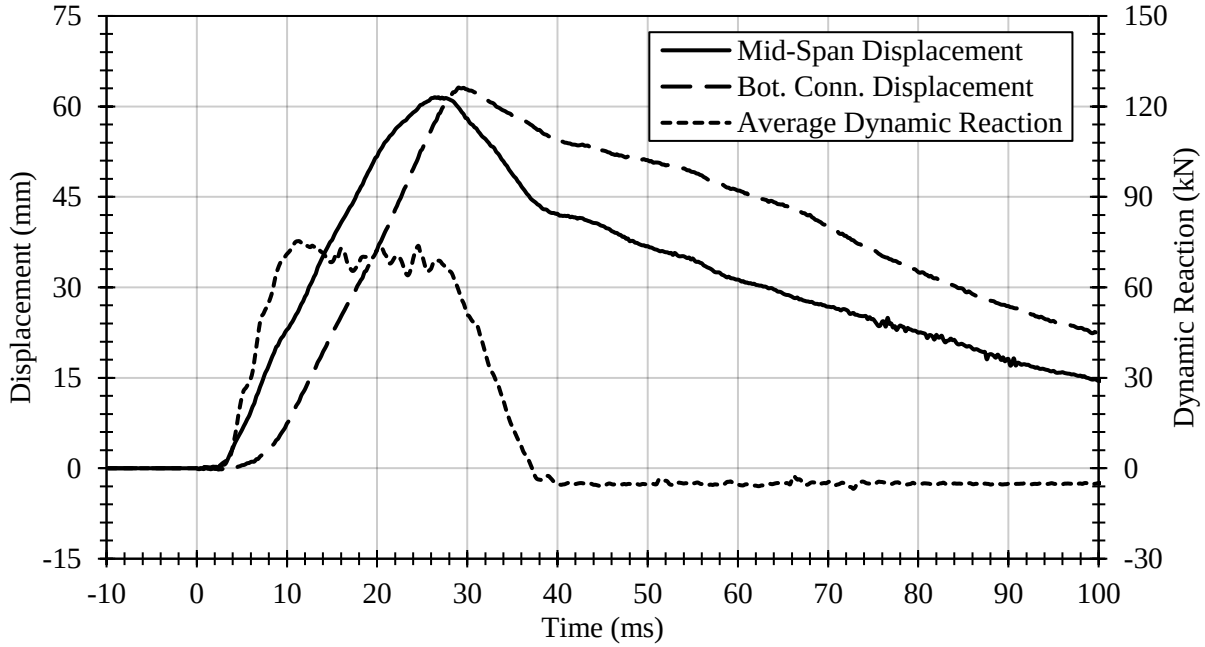
Figure C.36: Documentation of Damage for Test G16-2

Specimen G16 – Shot #3

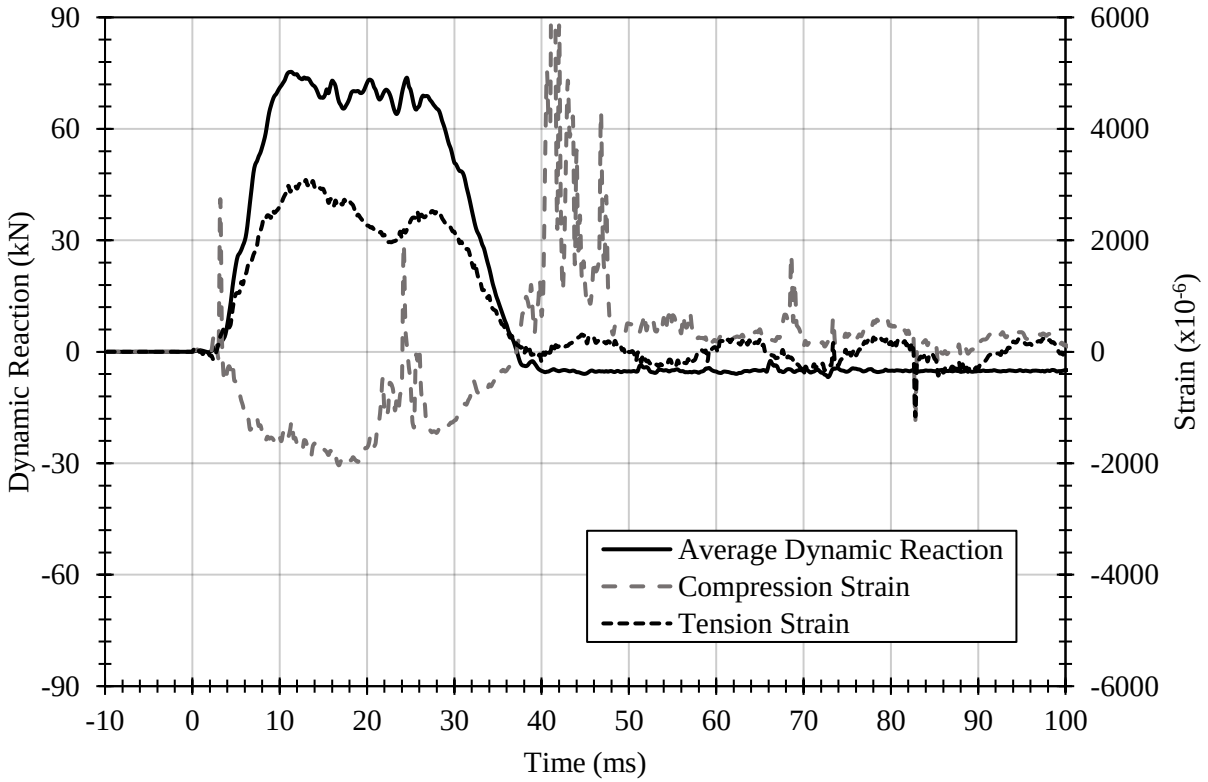
For the third shot, it was dynamically tested on September 12th 2019 with an 11 ft. driver. A driver pressure of 521.9 kPa was used, which resulted in a positive peak reflected pressure and impulse of 75.0 kPa and 814.7 kPa-ms, respectively.



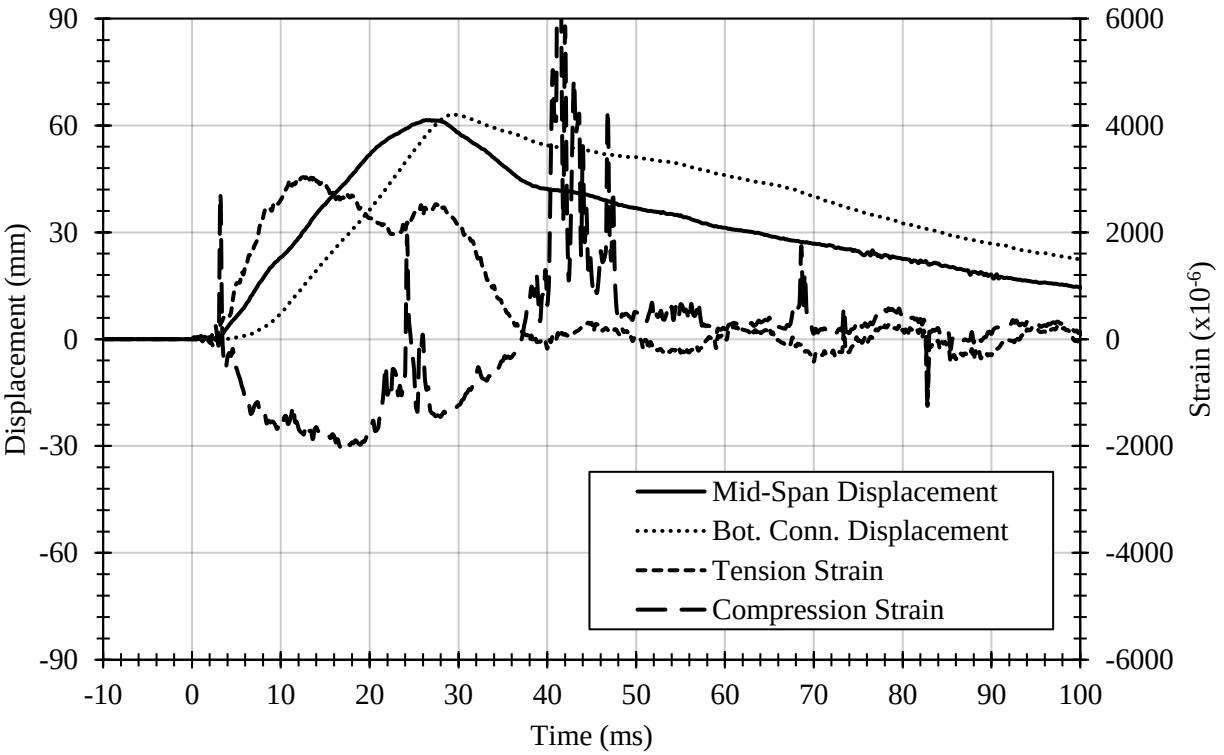
(a) Pressure and Impulse



(b) Reaction and Displacements

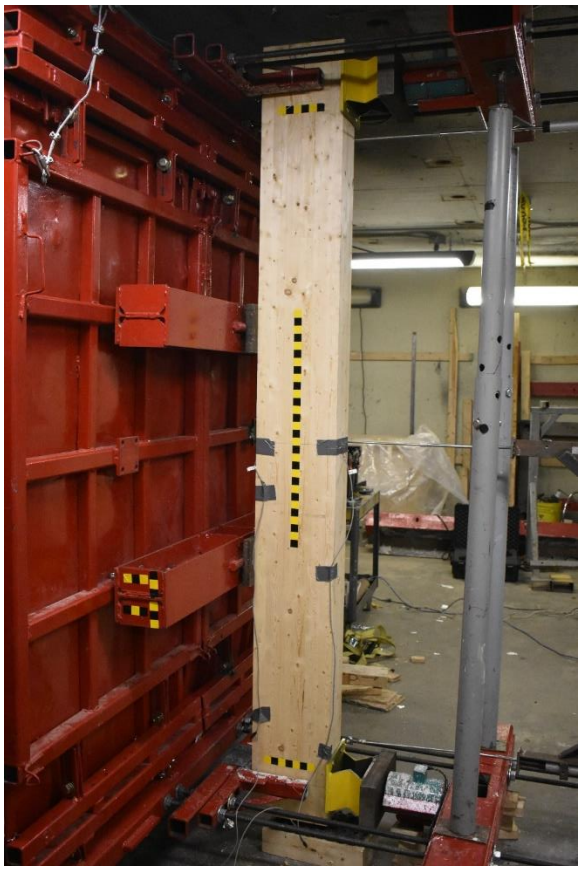


(c) Reaction and Strains

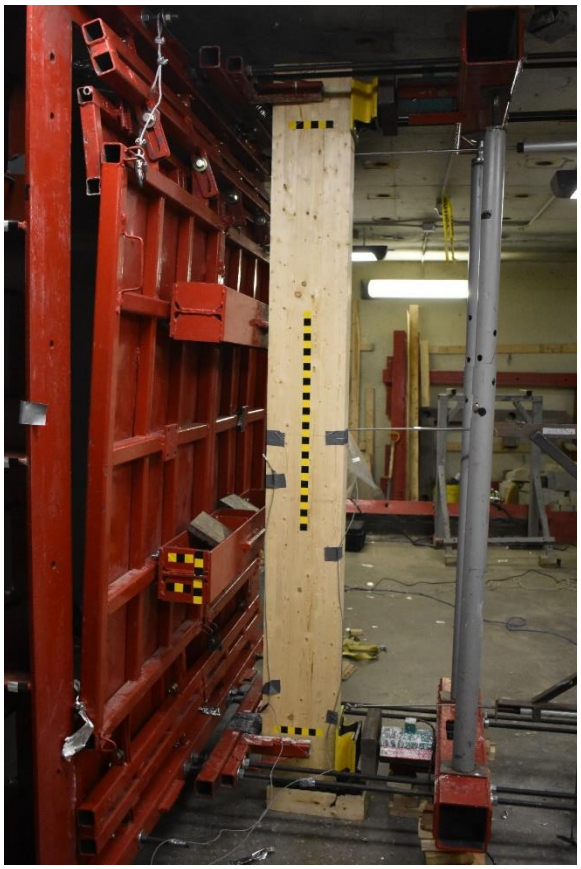


(d) Displacement and Strains

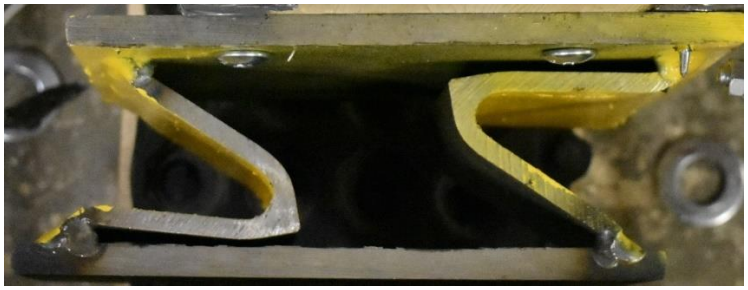
Figure C.37: Dynamic Test Results for Test G16-3



(a) Specimen Prior to Testing



(b) Specimen After Testing



(c) Damage in Bottom EAC

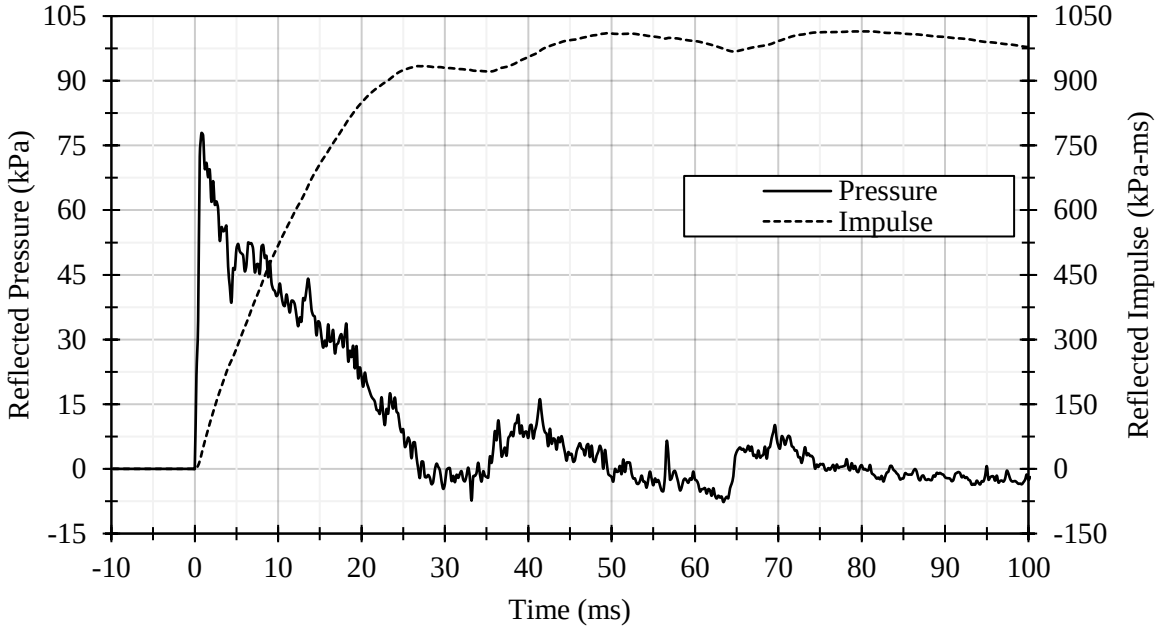


(d) Damage in Top EAC

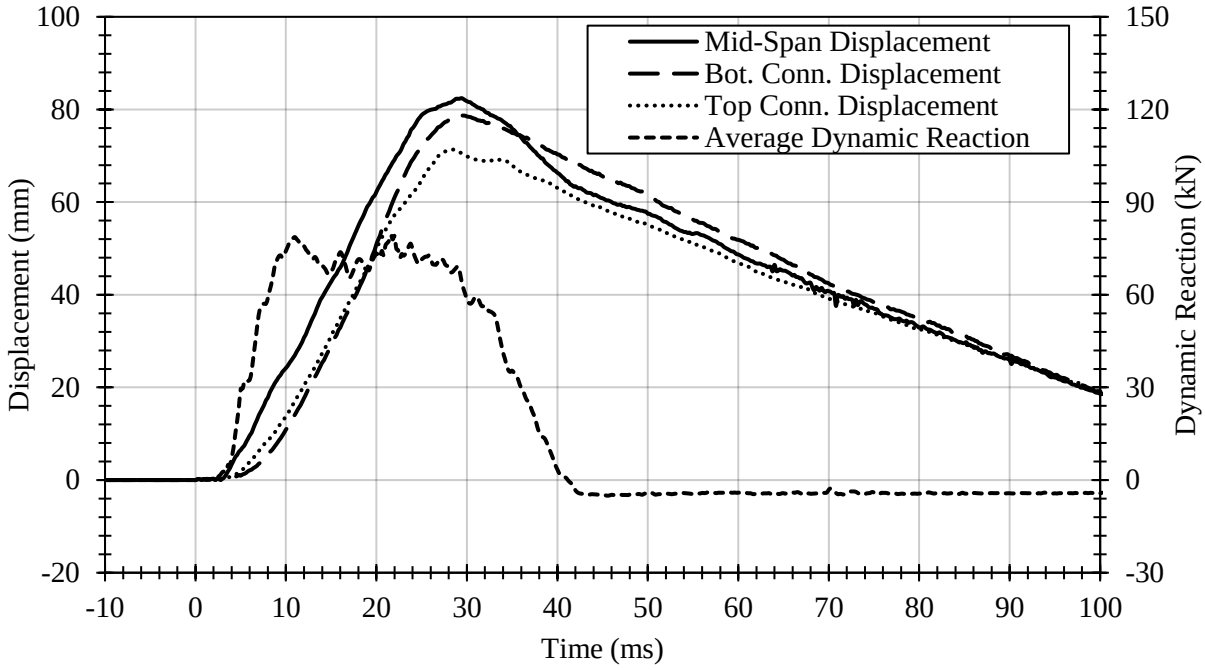
Figure C.38: Documentation of Damage for Test G16-3

Specimen G16 – Shot #4

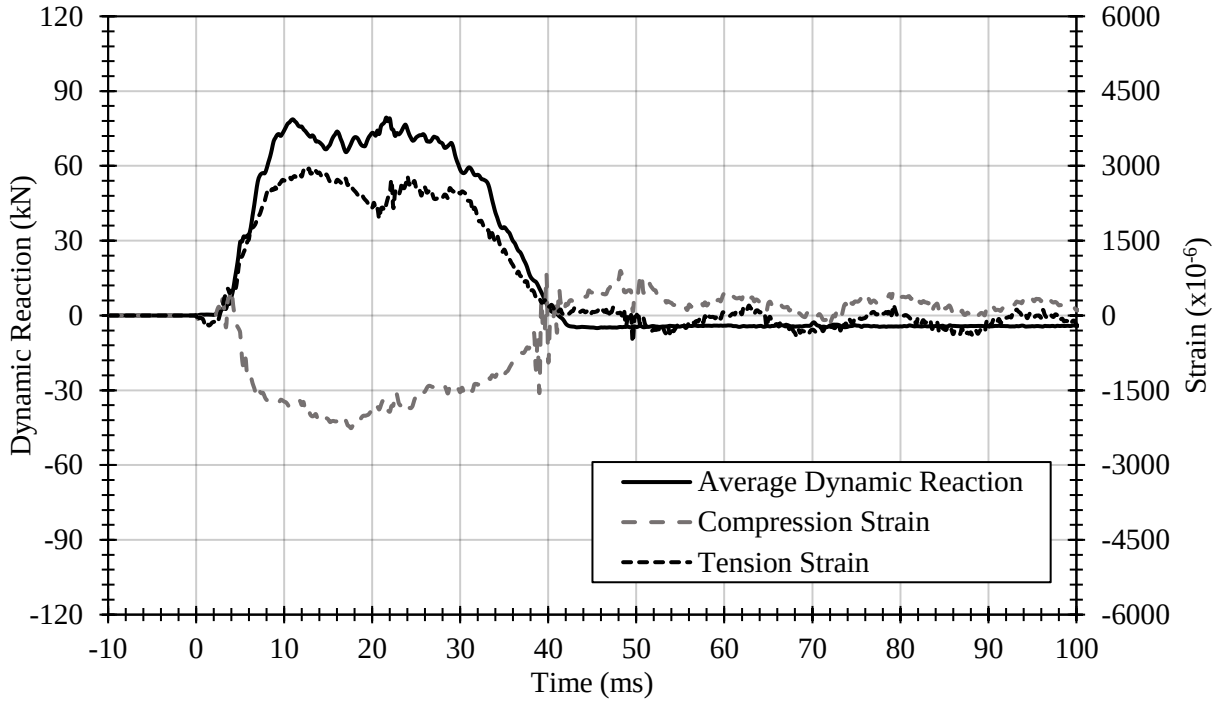
For the fourth shot, it was dynamically tested on September 13th 2019 with an 11 ft. driver. A driver pressure of 621.2 kPa was used, which resulted in a positive peak reflected pressure and impulse of 77.8 kPa and 934.0 kPa-ms, respectively.



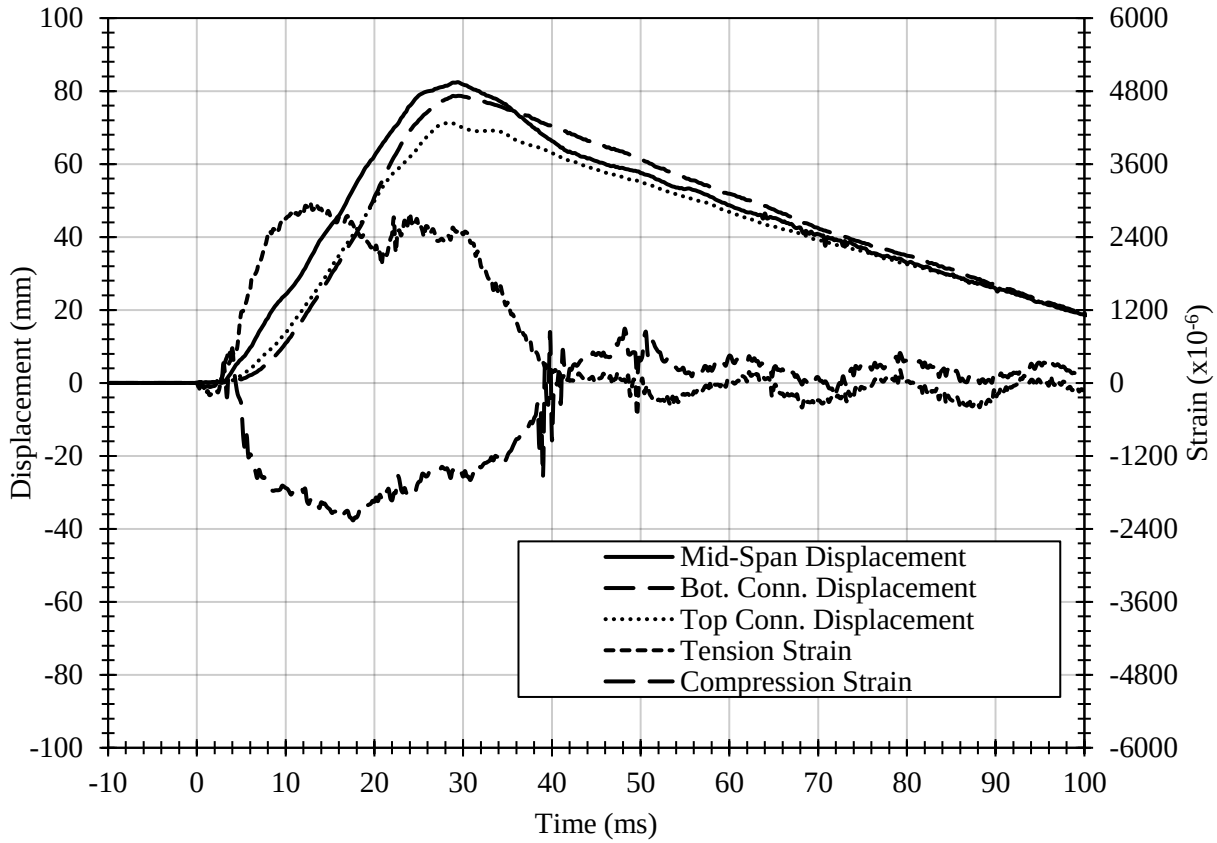
(a) Pressure and Impulse



(b) Reaction and Displacements

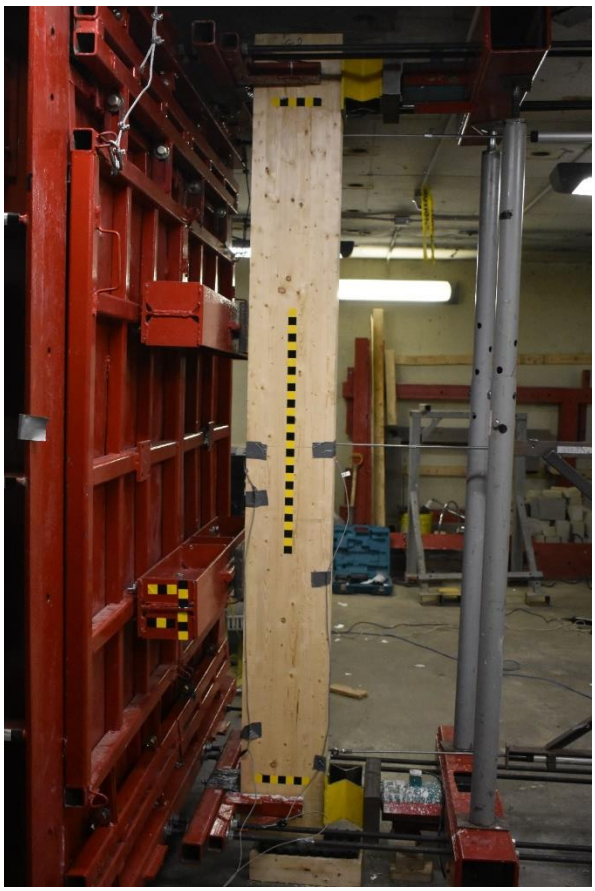


(c) Reaction and Strains



(d) Displacement and Strains

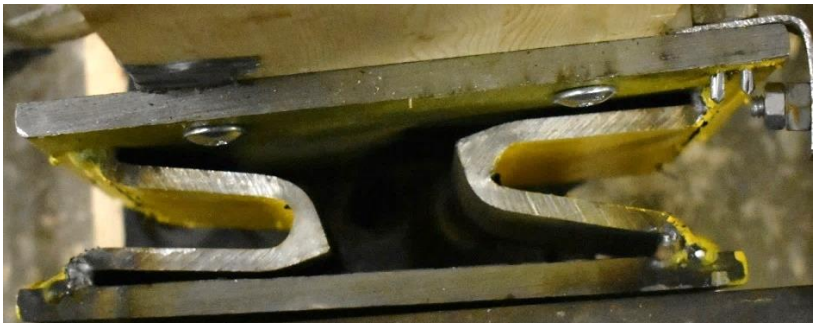
Figure C.39: Dynamic Test Results for Test G16-4



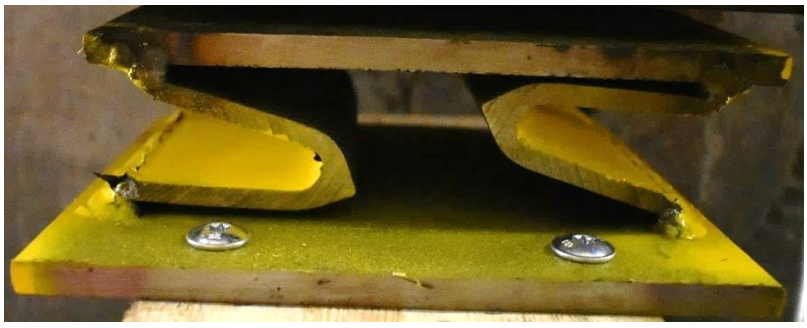
(a) Specimen Prior to Testing



(b) Specimen After Testing



(c) Damage in Bottom EAC

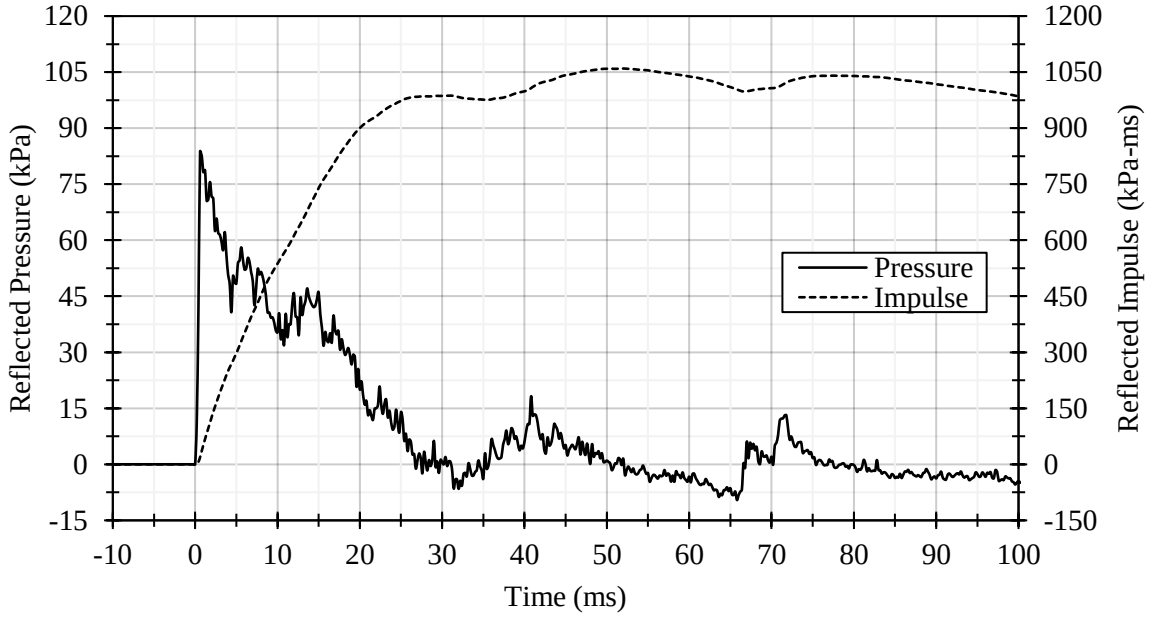


(d) Damage in Top EAC

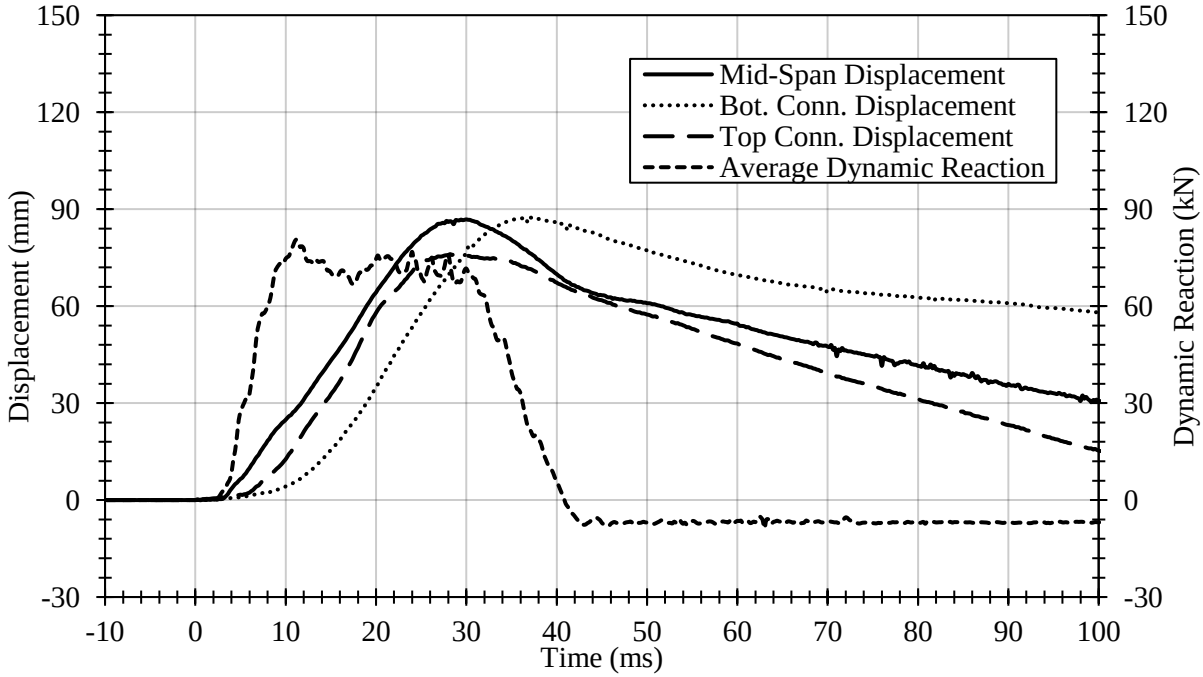
Figure C.40: Documentation of Damage for Test G16-4

Specimen G16 – Shot #5

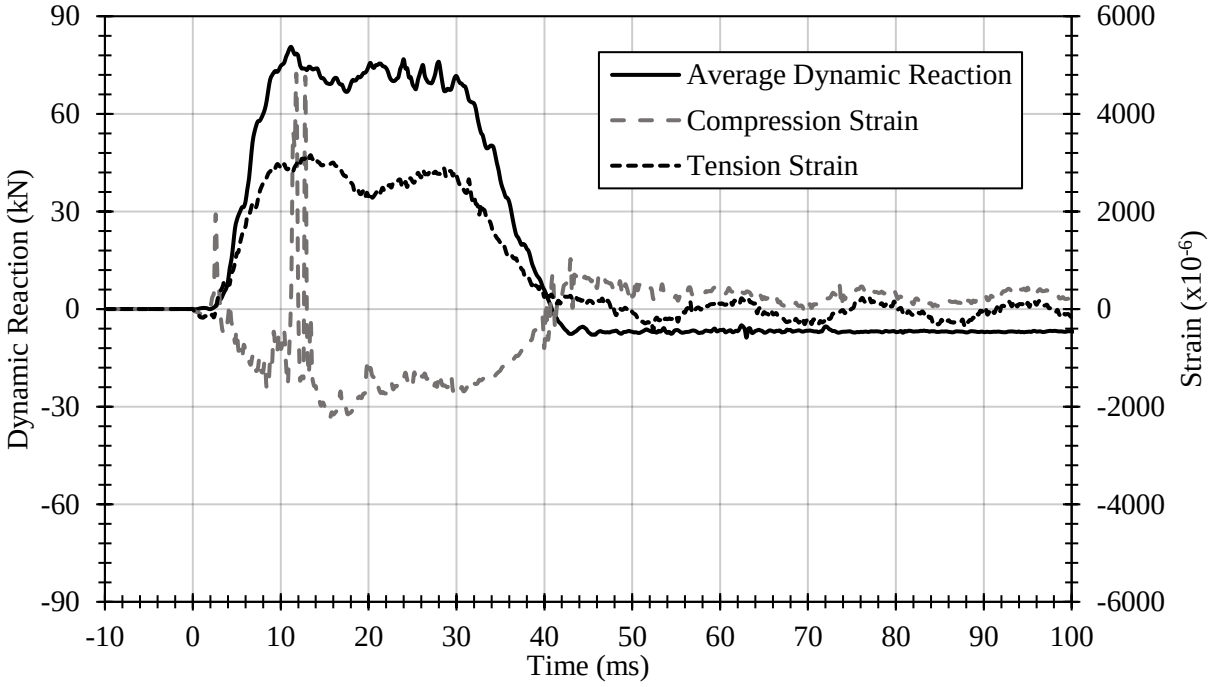
For the fifth shot, it was dynamically tested on September 13th 2019 with an 11 ft. driver. A driver pressure of 682.6 kPa was used, which resulted in a positive peak reflected pressure and impulse of 83.8 kPa and 986.6 kPa-ms, respectively.



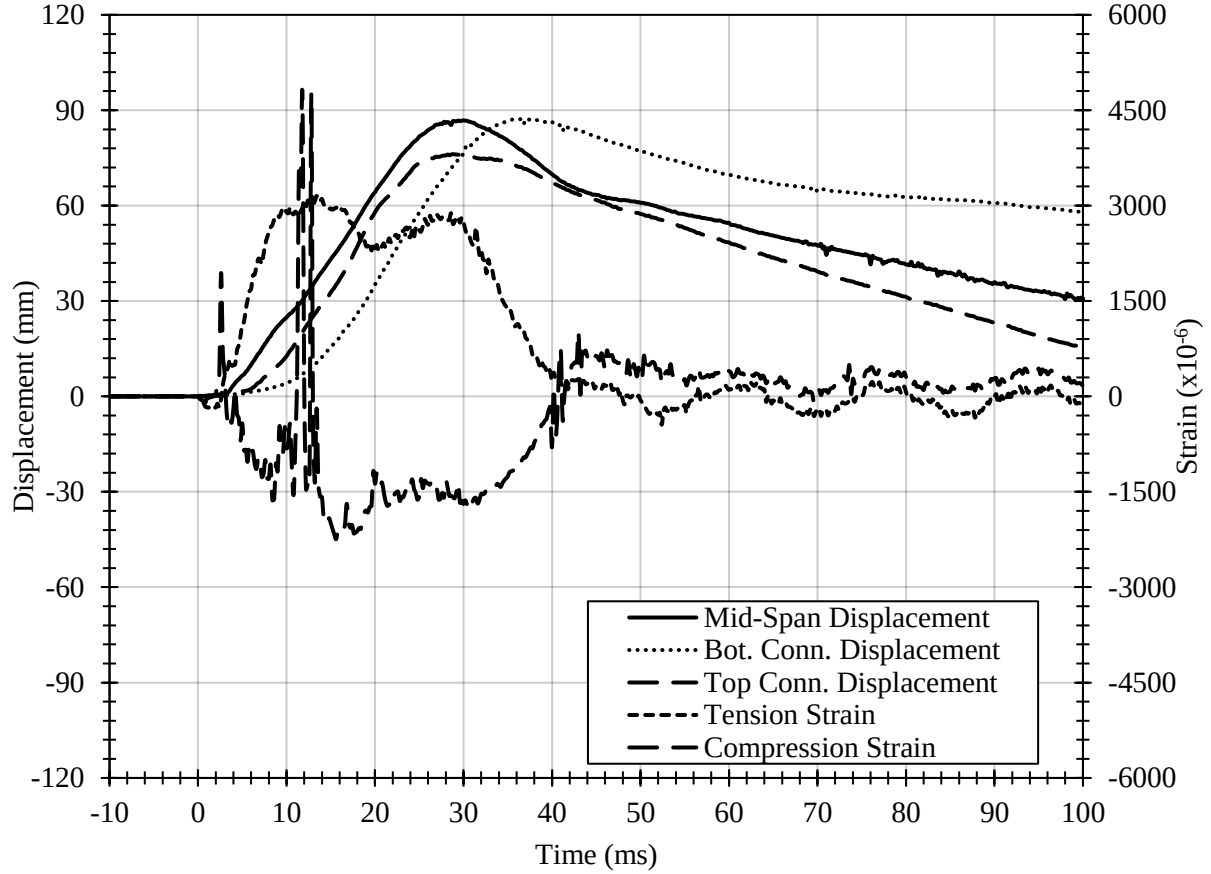
(a) Pressure and Impulse



(b) Reaction and Displacements



(c) Reaction and Strains

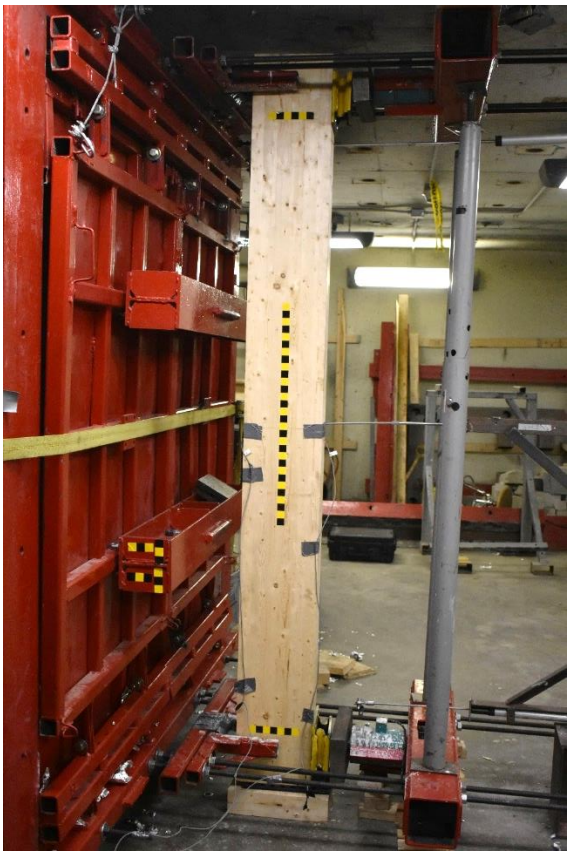


(d) Displacement and Strains

Figure C.41: Dynamic Test Results for Test G16-5



(a) Specimen Prior to Testing



(b) Specimen After Testing



(c) Damage in Bottom EAC

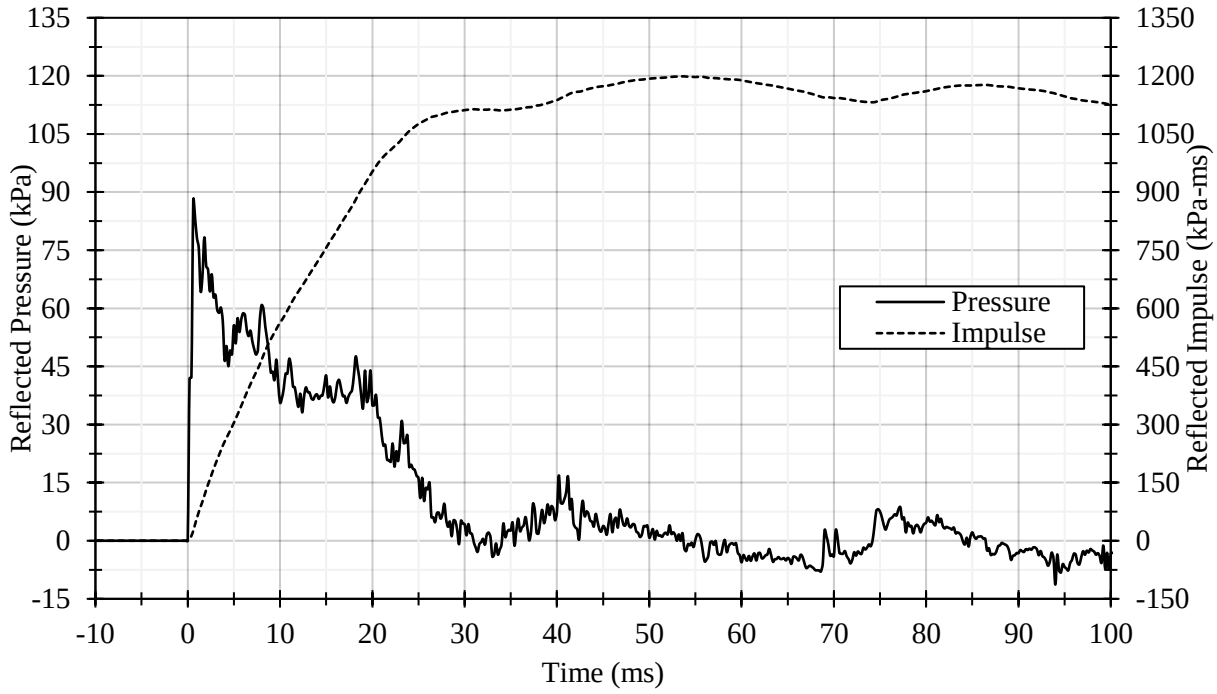


(d) Damage in Top EAC

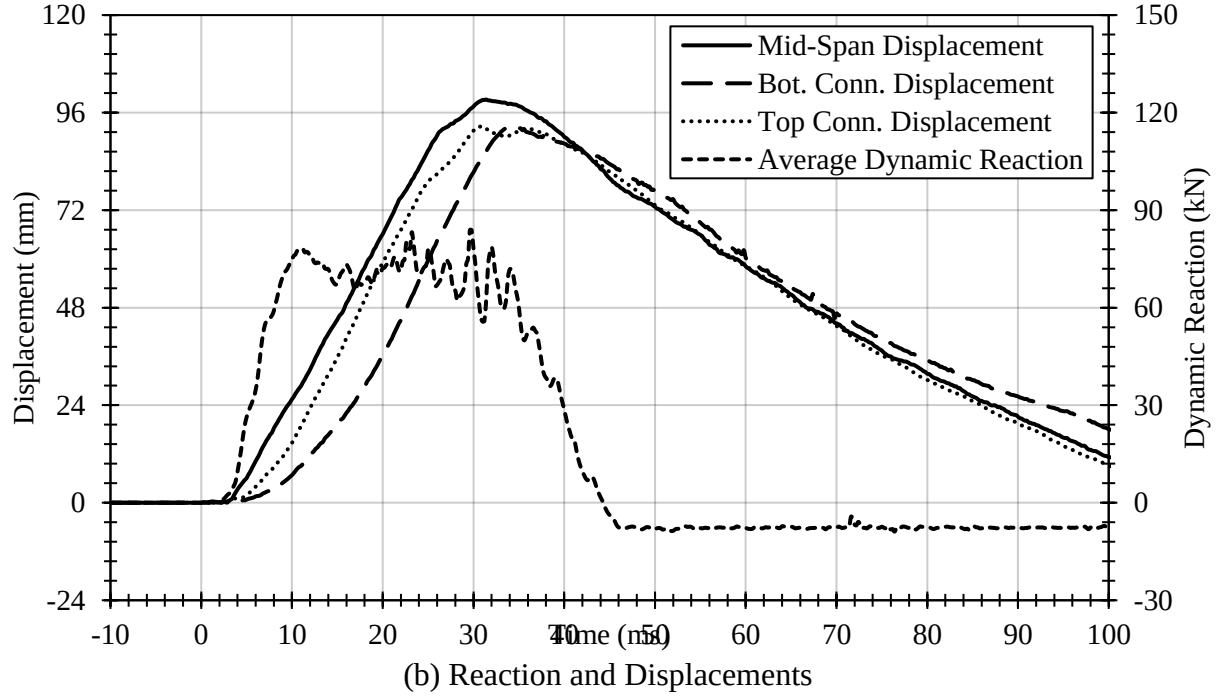
Figure C.42: Documentation of Damage for Test G16-5

Specimen G16 – Shot #6

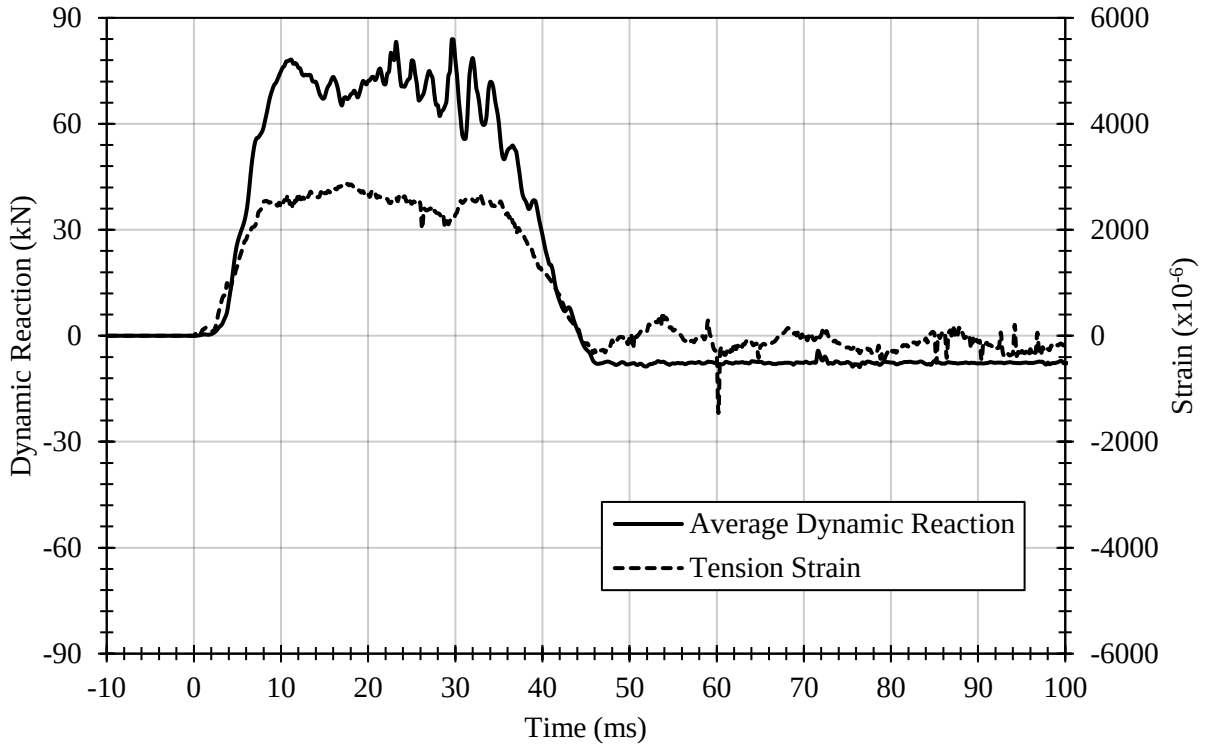
For the sixth shot, it was dynamically tested on September 16th 2019 with a 13 ft. driver. A driver pressure of 647.4 kPa was used, which resulted in a positive peak reflected pressure and impulse of 87.9 kPa and 1113.9 kPa-ms, respectively.



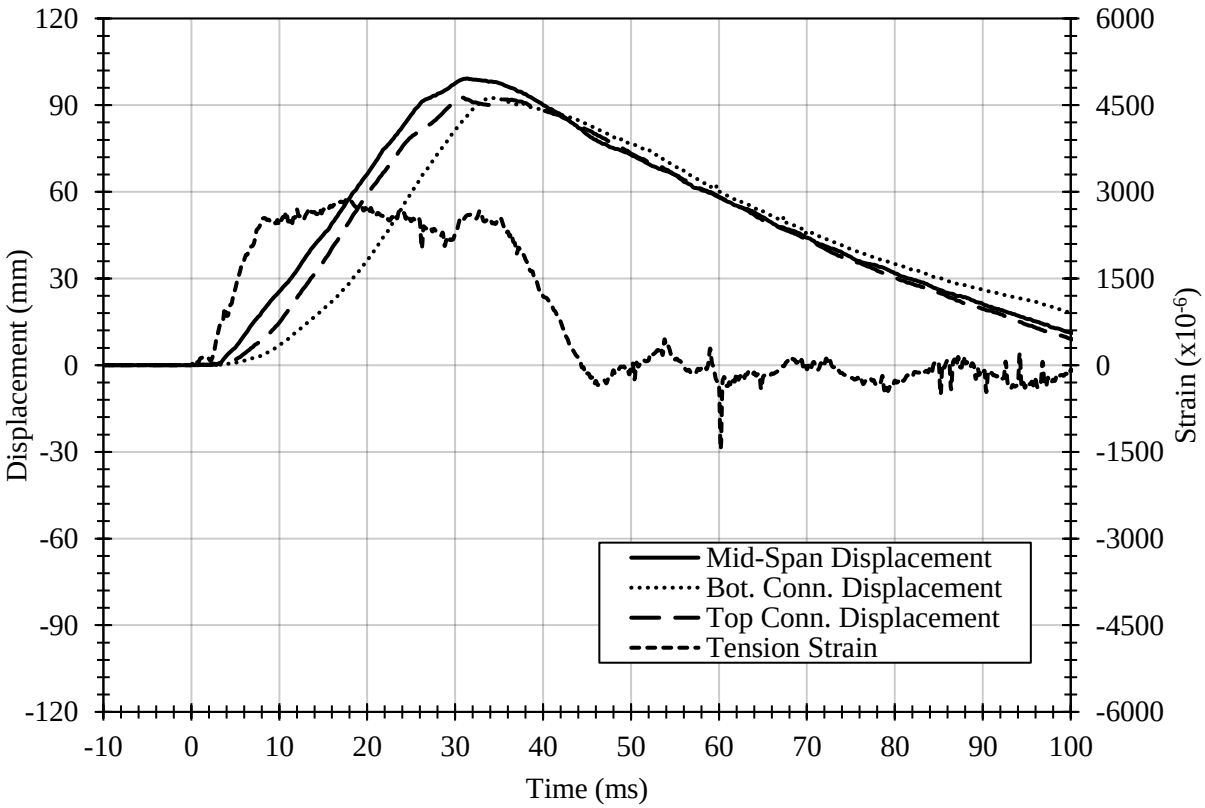
(a) Pressure and Impulse



(b) Reaction and Displacements



(c) Reaction and Strains

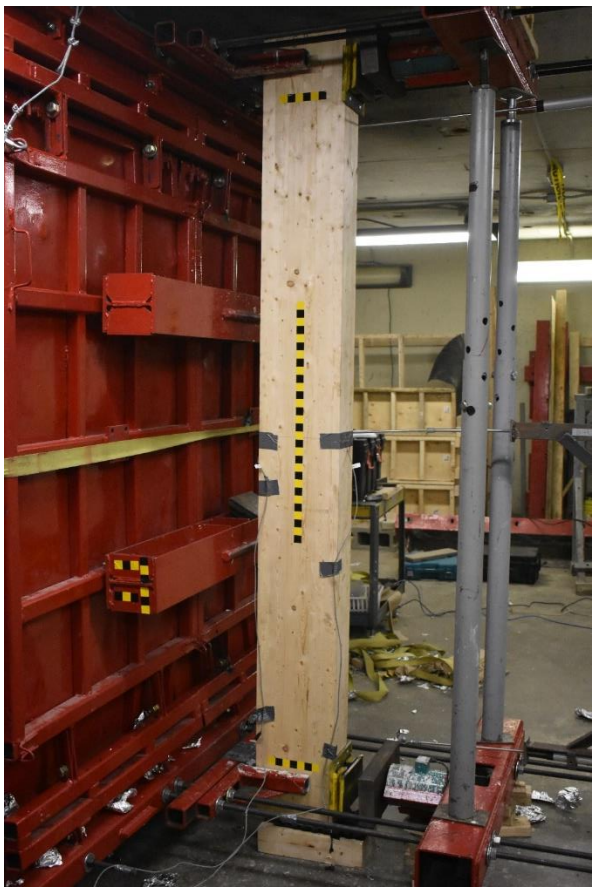


(d) Displacement and Strains

Figure C.43: Dynamic Test Results for Test G16-6



(a) Specimen Prior to Testing



(b) Specimen After Testing



(c) Damage in Bottom EAC

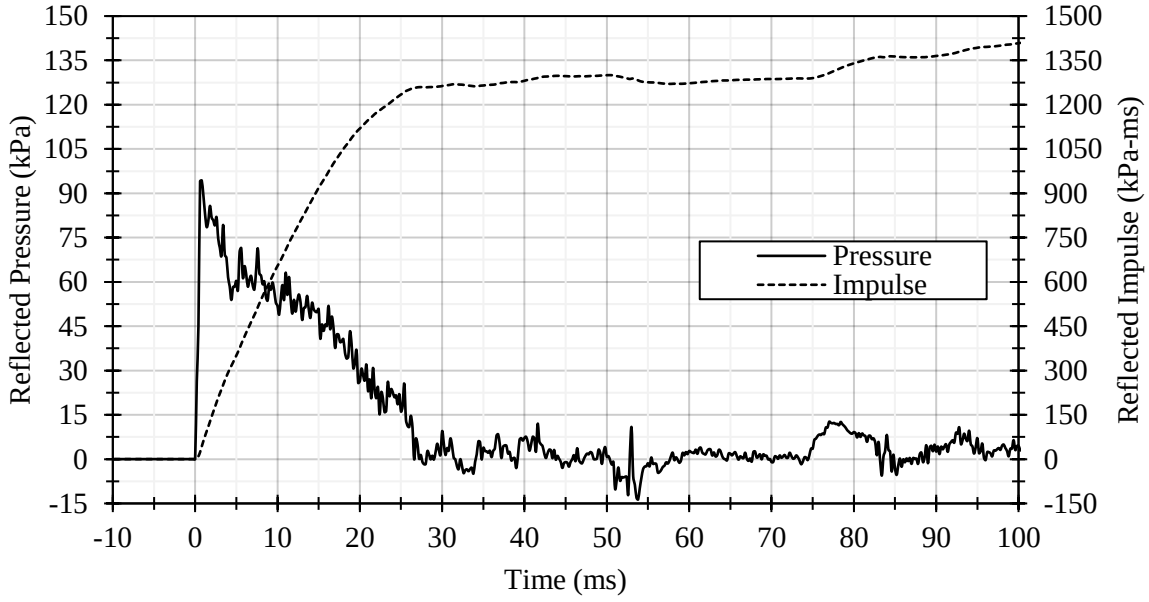


(d) Damage in Top EAC

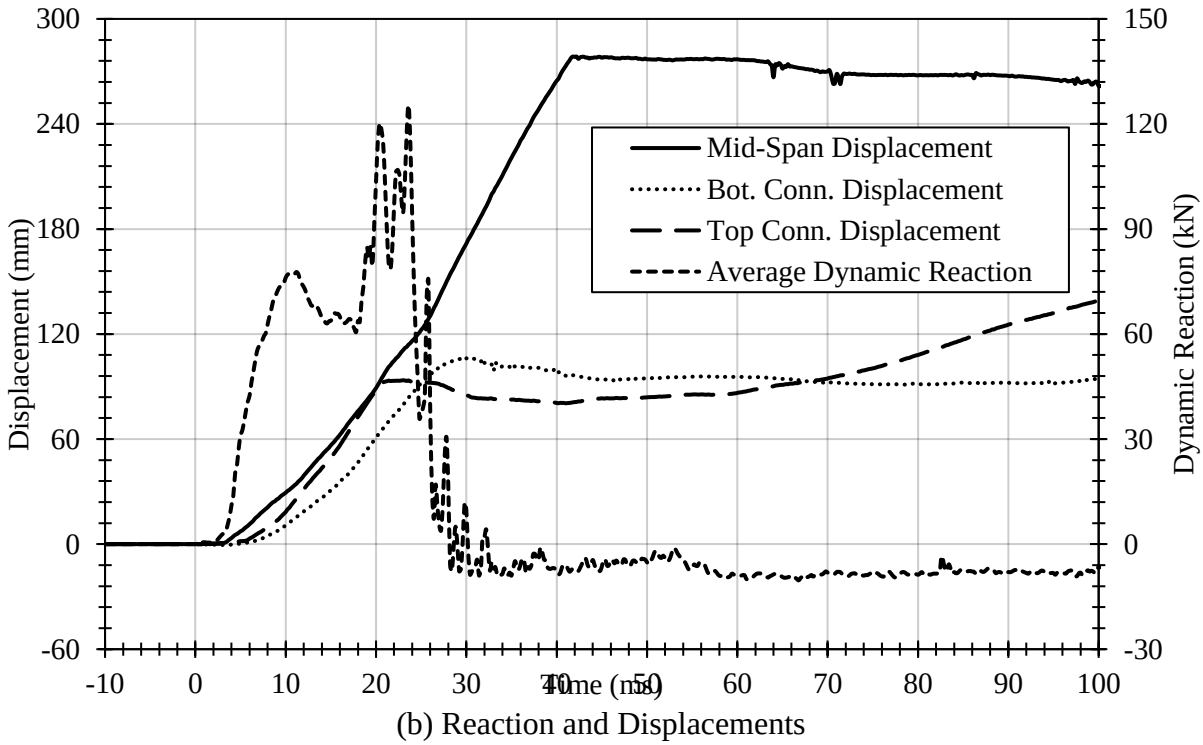
Figure C.44: Documentation of Damage for Test G16-6

Specimen G16 – Shot #7

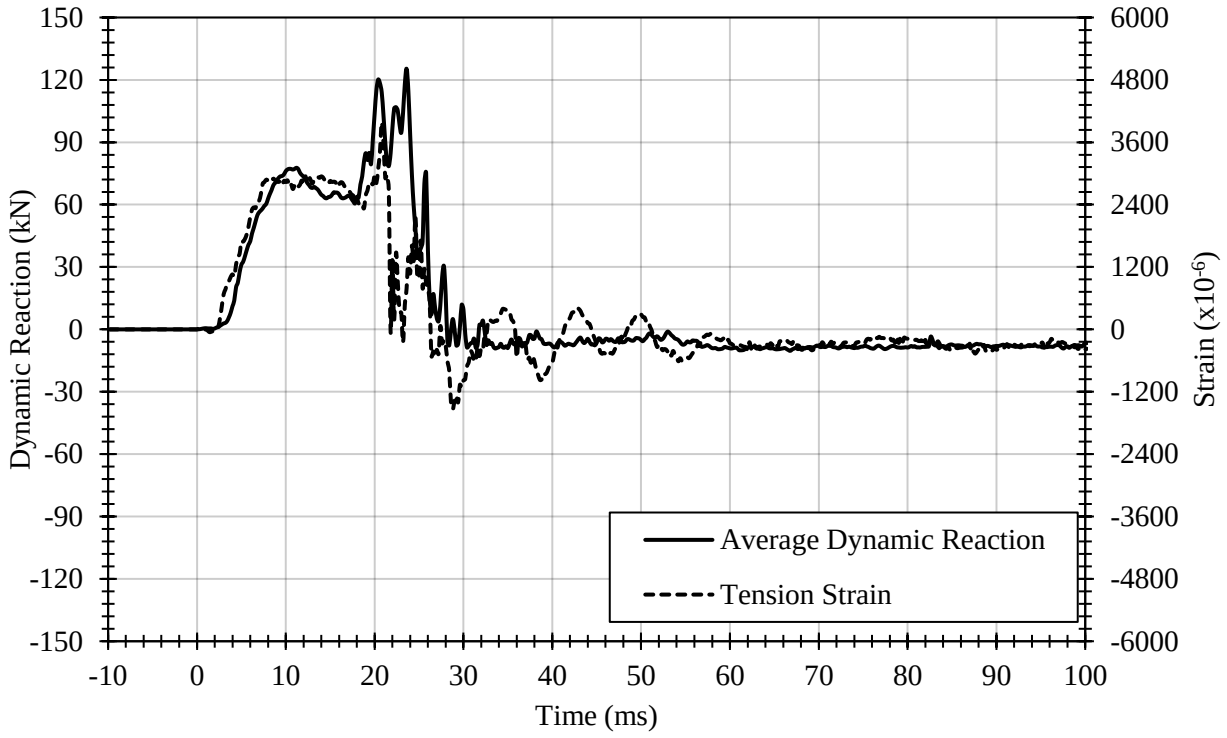
For the seventh and final shot, it was dynamically tested on September 17th 2019 with a 13 ft. driver. A driver pressure of 812.2 kPa was used, which resulted in a positive peak reflected pressure and impulse of 94.4 kPa and 1259.6 kPa-ms, respectively.



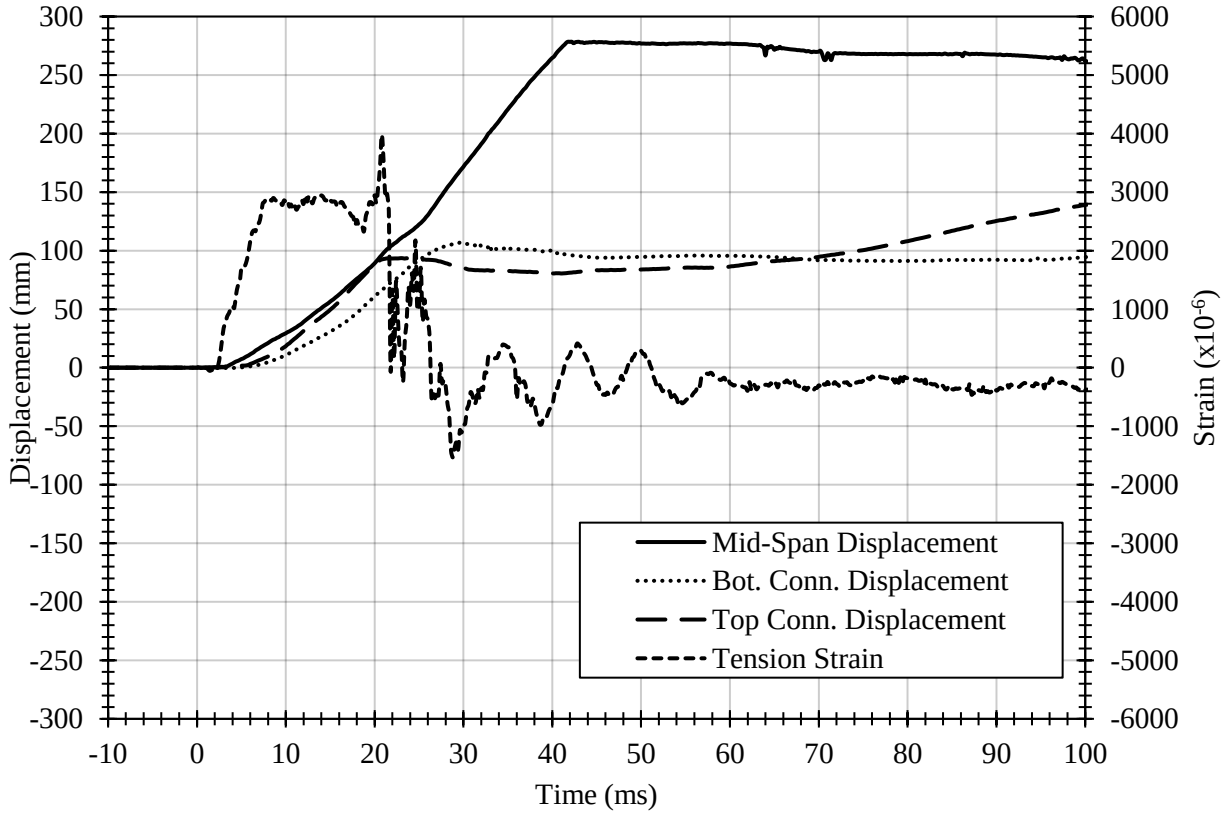
(a) Pressure and Impulse



(b) Reaction and Displacements



(c) Reaction and Strains

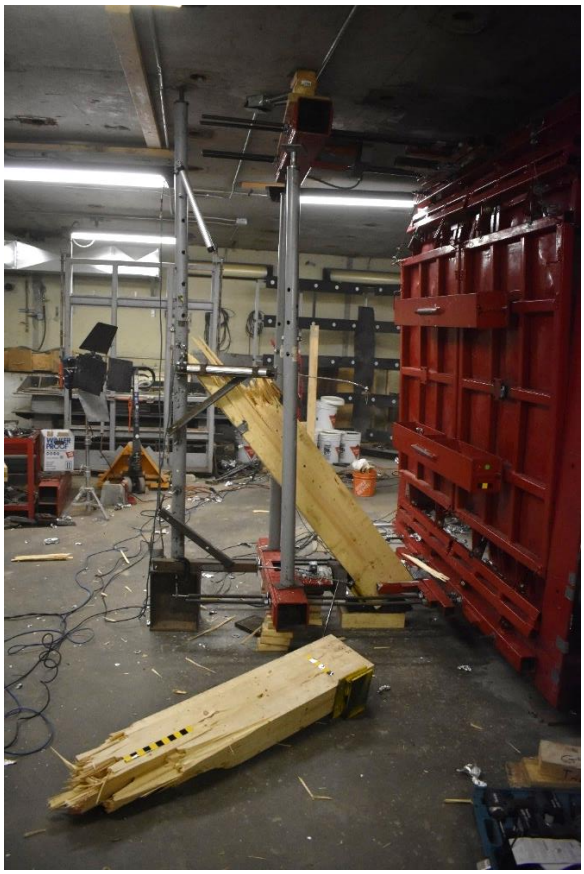


(d) Displacement and Strains

Figure C.45: Dynamic Test Results for Test G16-7



(a) Specimen Prior to Testing



(b) Specimen After Testing



(c) Flexural Failure of Beam



(d) Damage in Bottom EAC

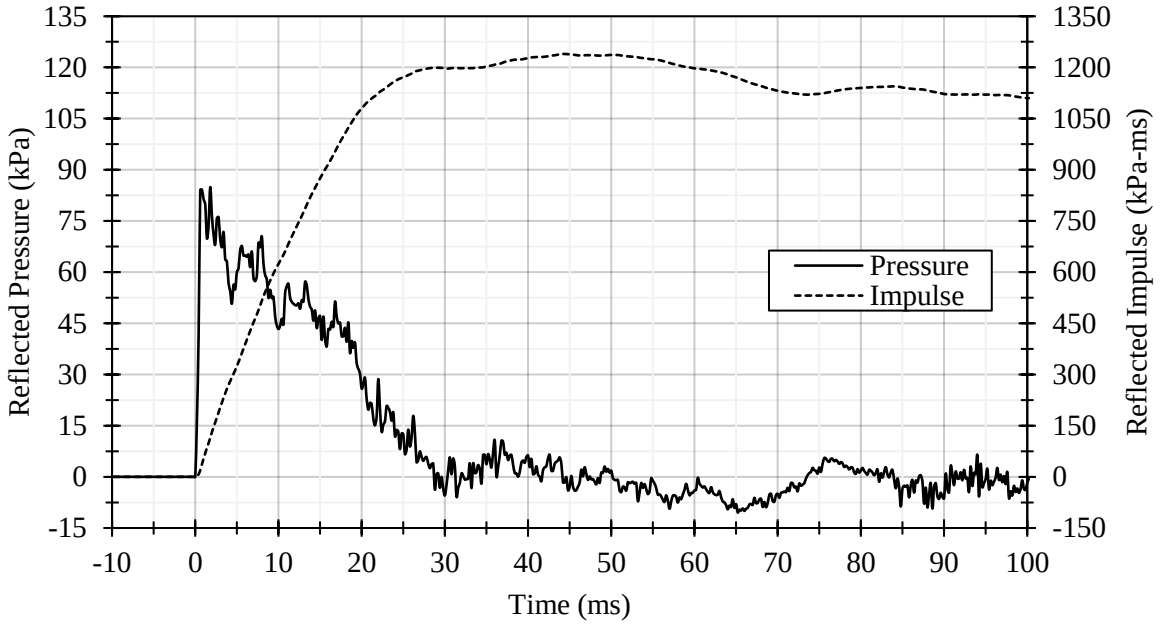


(e) Damage in Top EAC

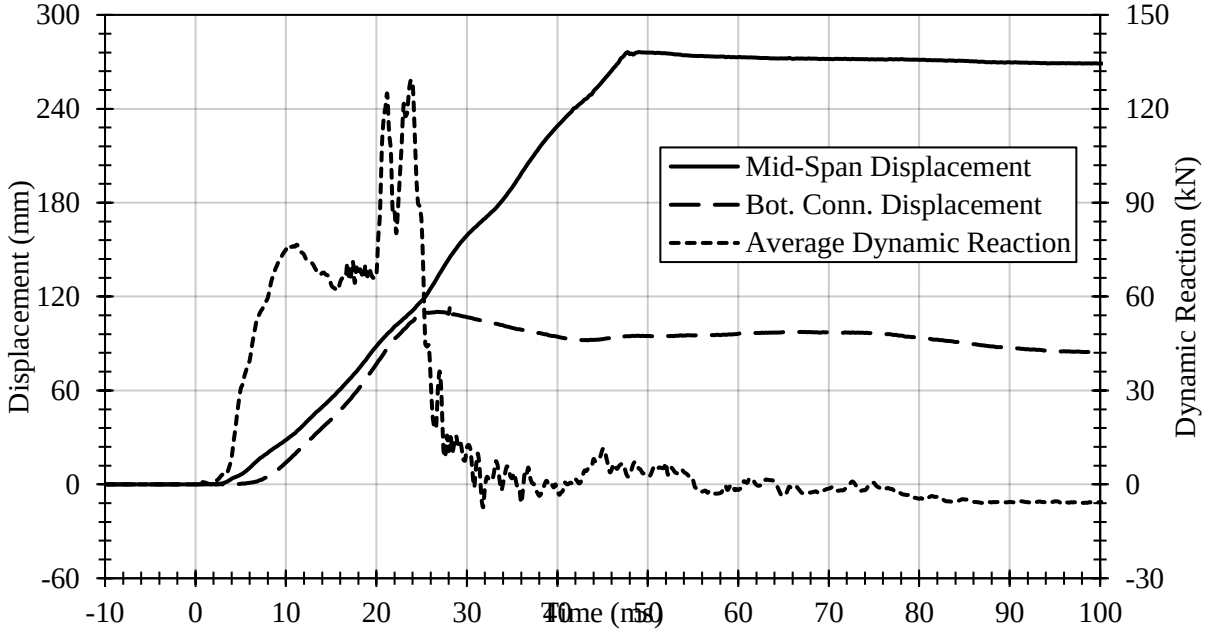
Figure C.46: Documentation of Damage for Test G16-7

Specimen G17

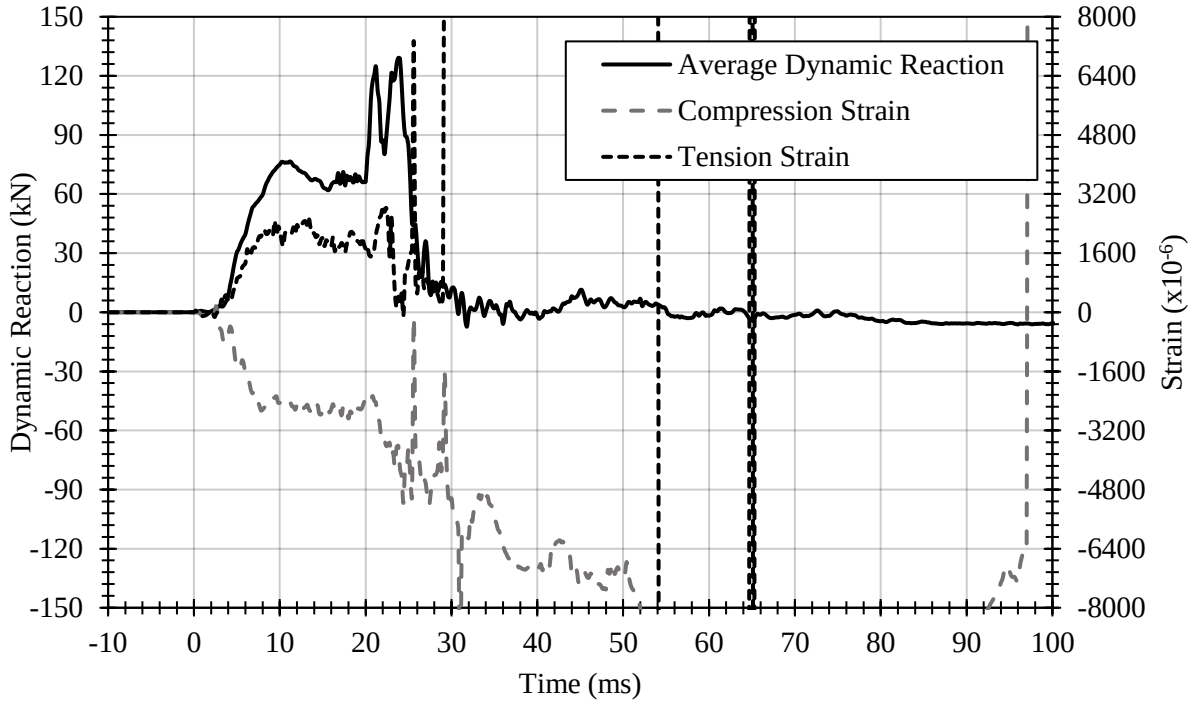
Specimen G17, comprised of a Glulam beam with a 5.0" deep EAC at each end, was dynamically tested on September 18th 2019 with a 13 ft. driver. A driver pressure of 755.7 kPa was used, which resulted in a positive peak reflected pressure and impulse of 84.9 kPa and 1199.4 kPa-ms, respectively.



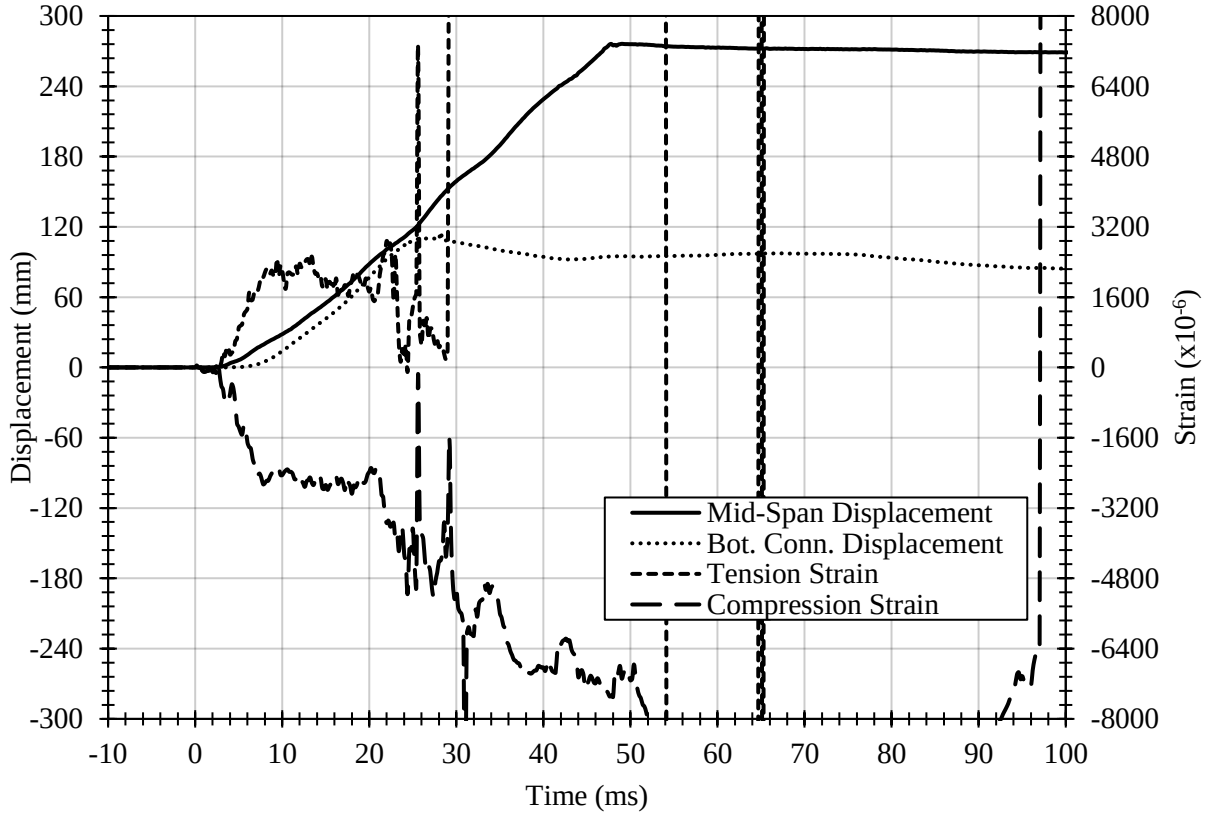
(a) Pressure and Impulse



(b) Reaction and Displacements

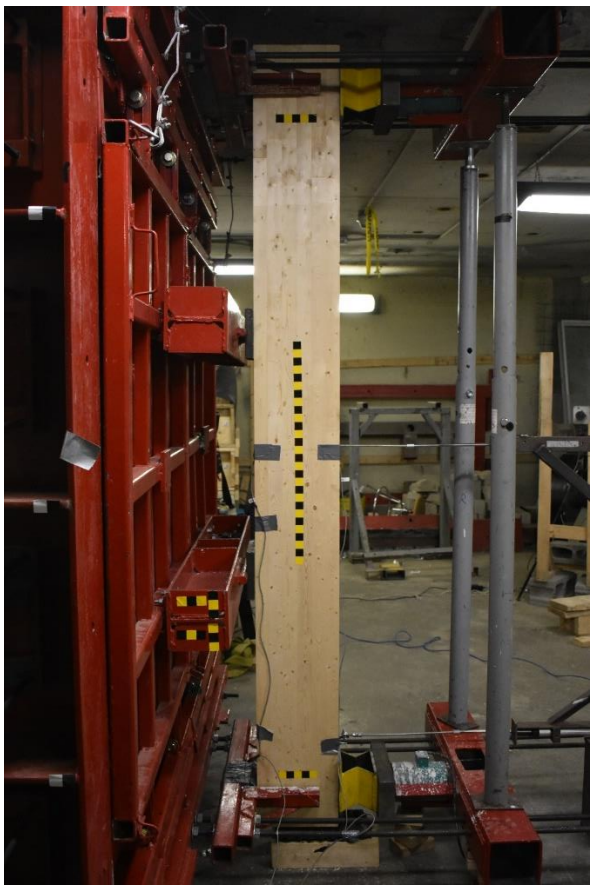


(c) Reaction and Strains

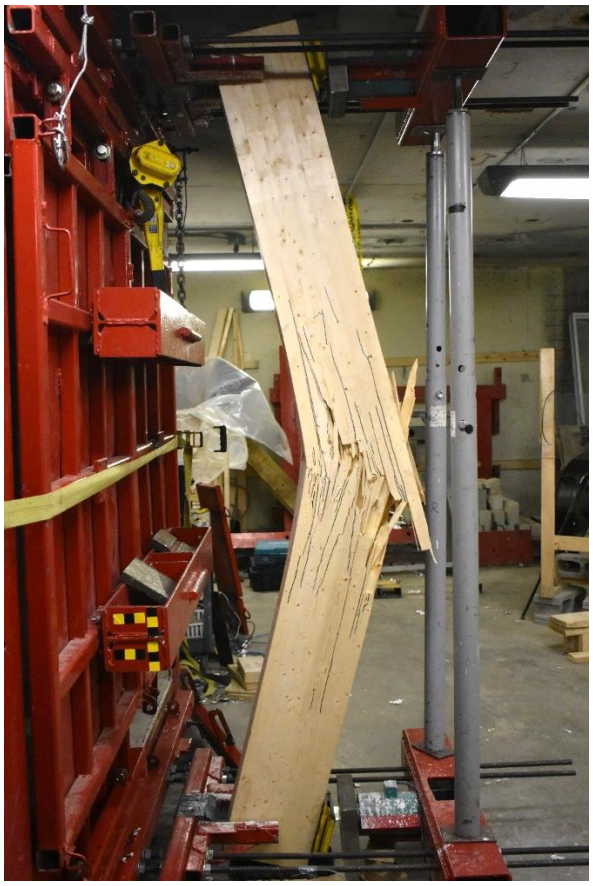


(d) Displacement and Strains

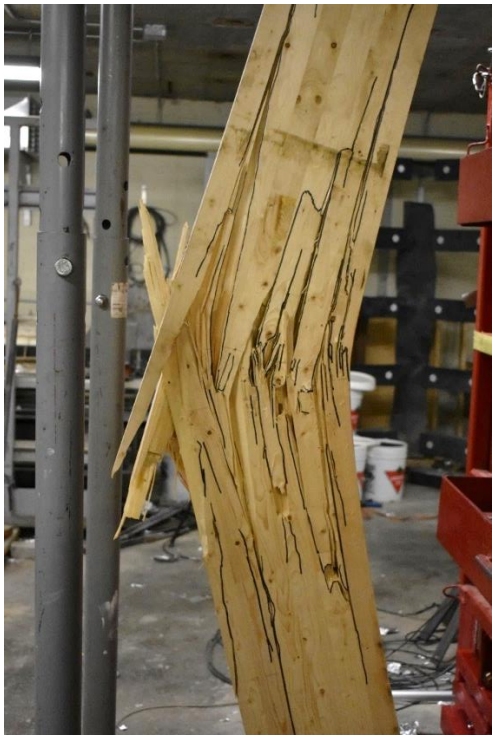
Figure C.47: Dynamic Test Results for Specimen G17



(a) Specimen Prior to Testing



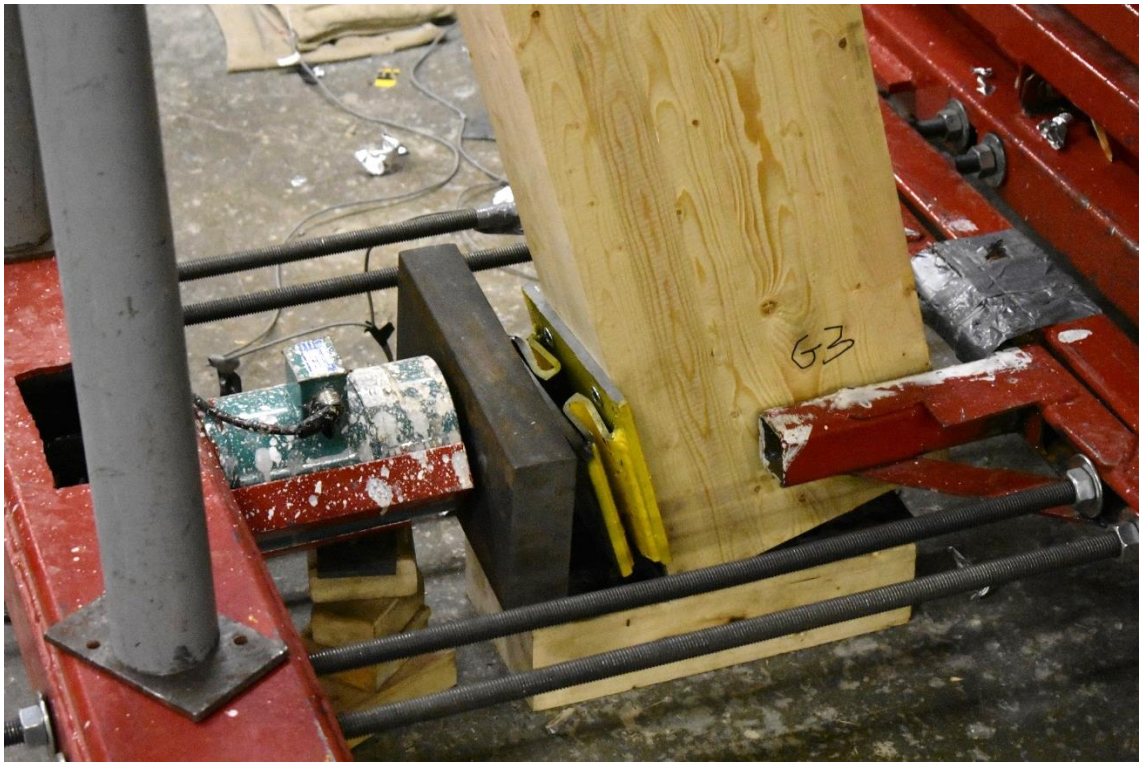
(b) Specimen After Testing



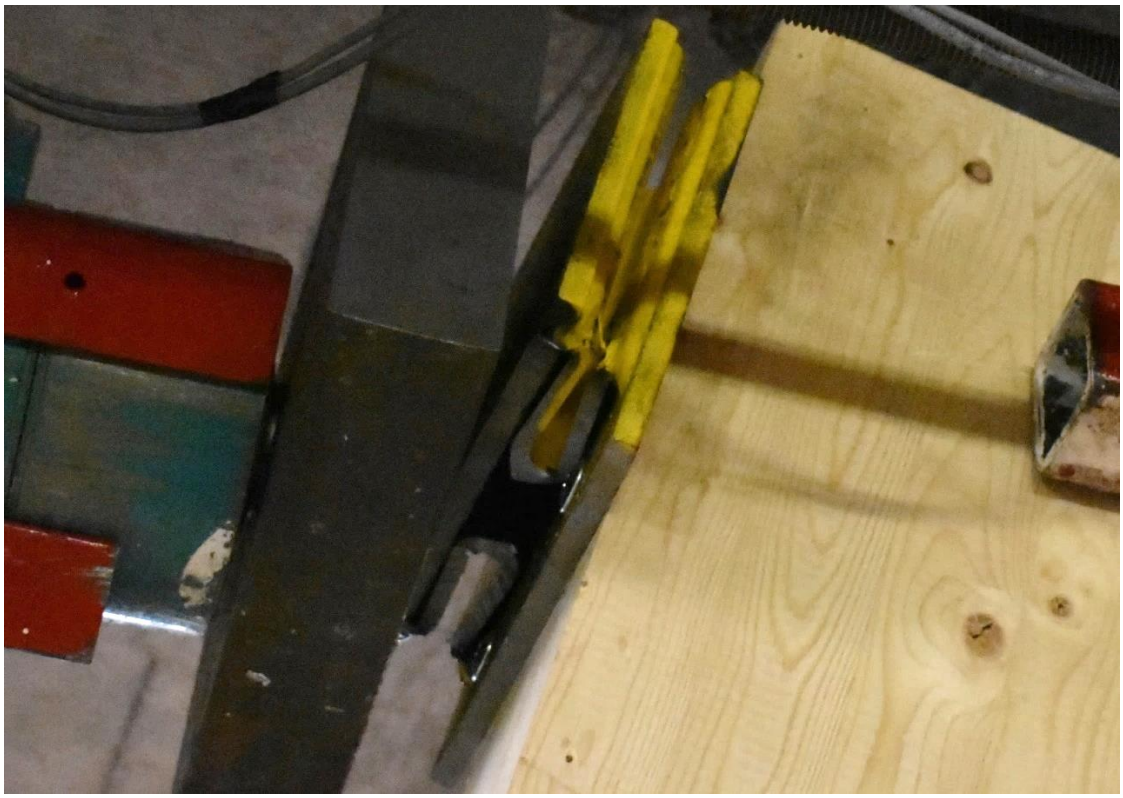
(c) Flexural Failure in Beam



(d) Flexural Failure in Beam (Front)



(e) Damage in Bottom EAC

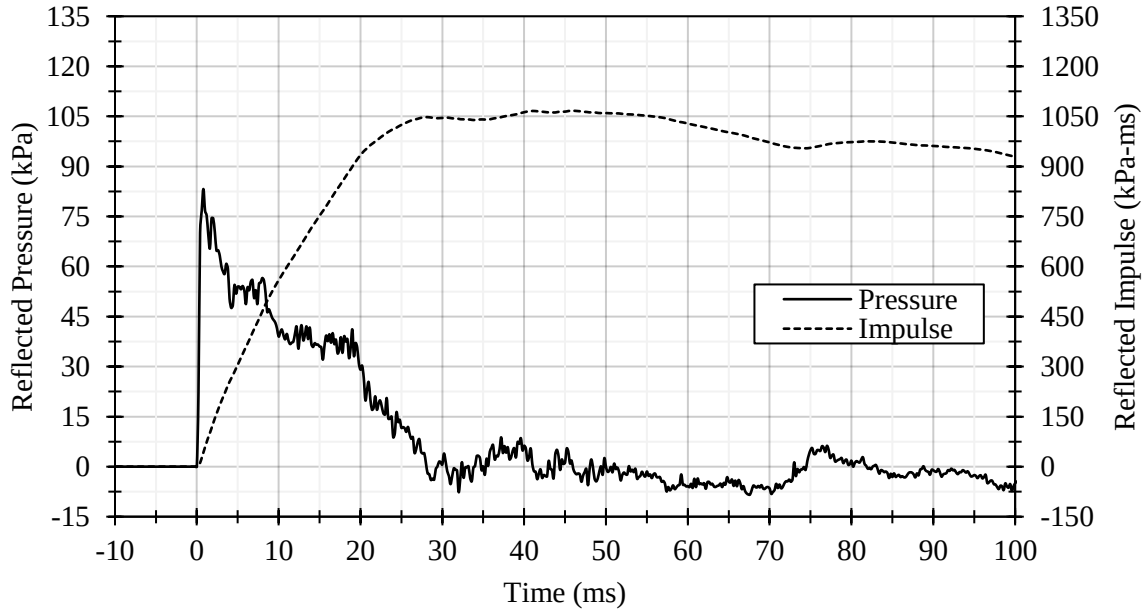


(f) Damage in Top EAC

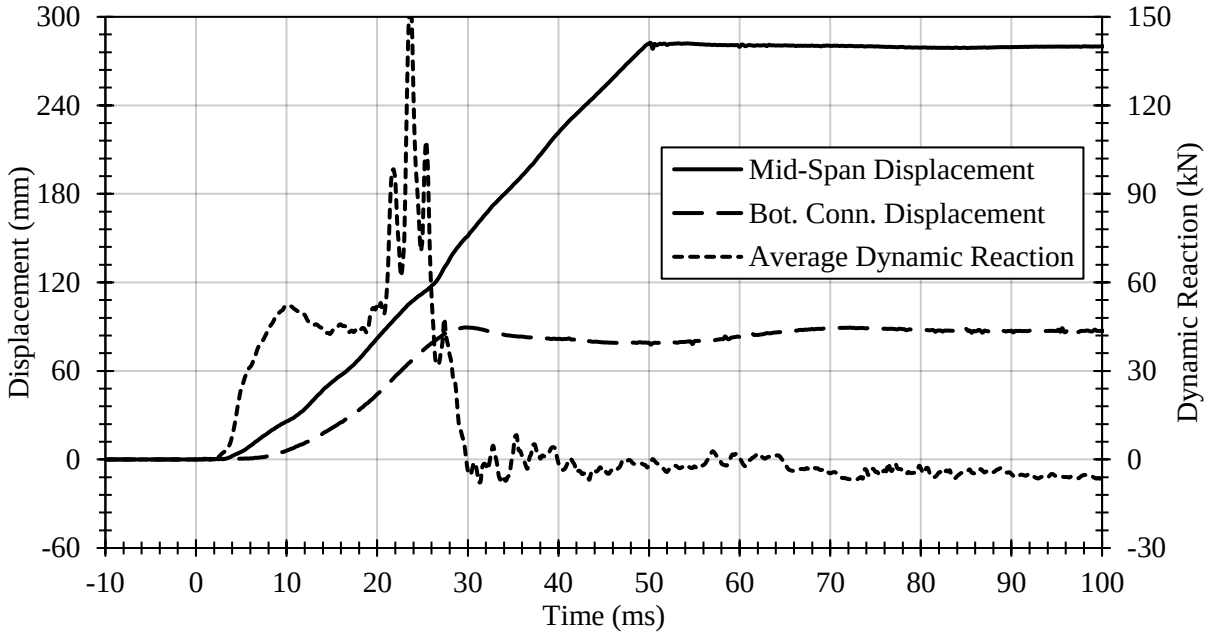
Figure C.48: Documentation of Damage for Specimen G17

Specimen G18

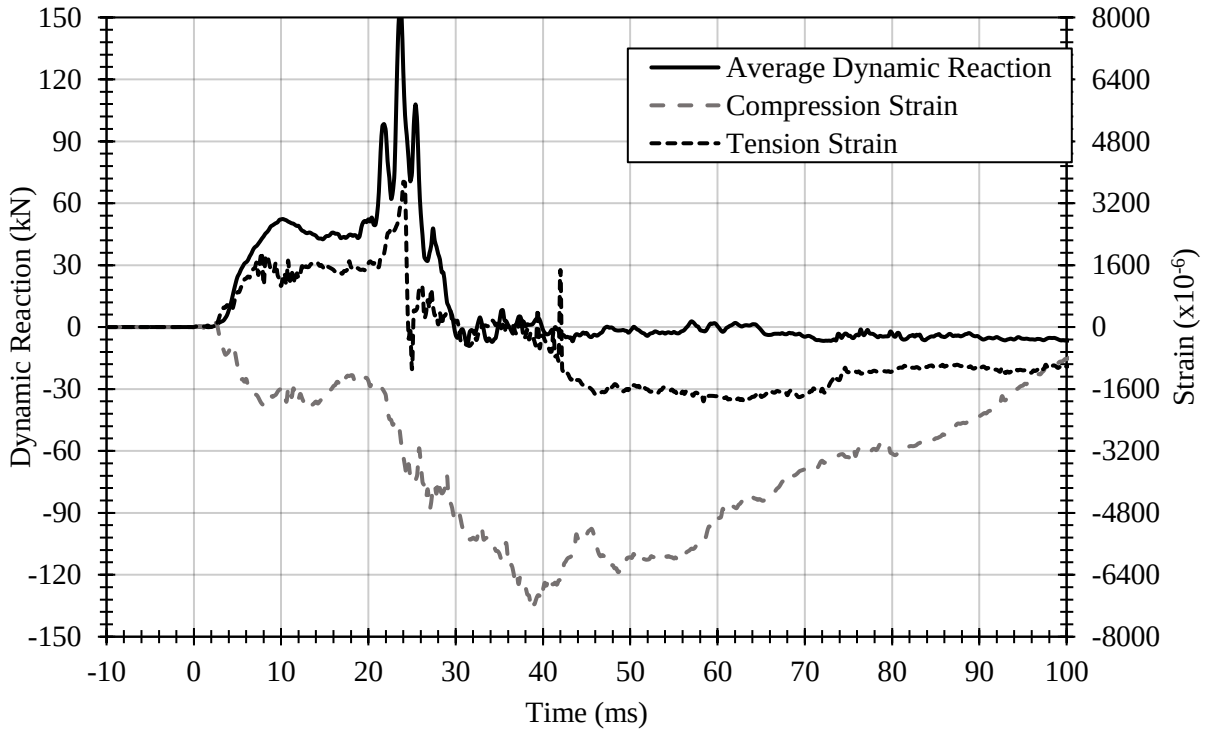
Specimen G18, comprised of a Glulam beam with a 3.75" deep EAC at each end, was dynamically tested on September 18th 2019 with a 13 ft. driver. A driver pressure of 640.5 kPa was used, which resulted in a positive peak reflected pressure and impulse of 83.2 kPa and 1047.7 kPa-ms, respectively.



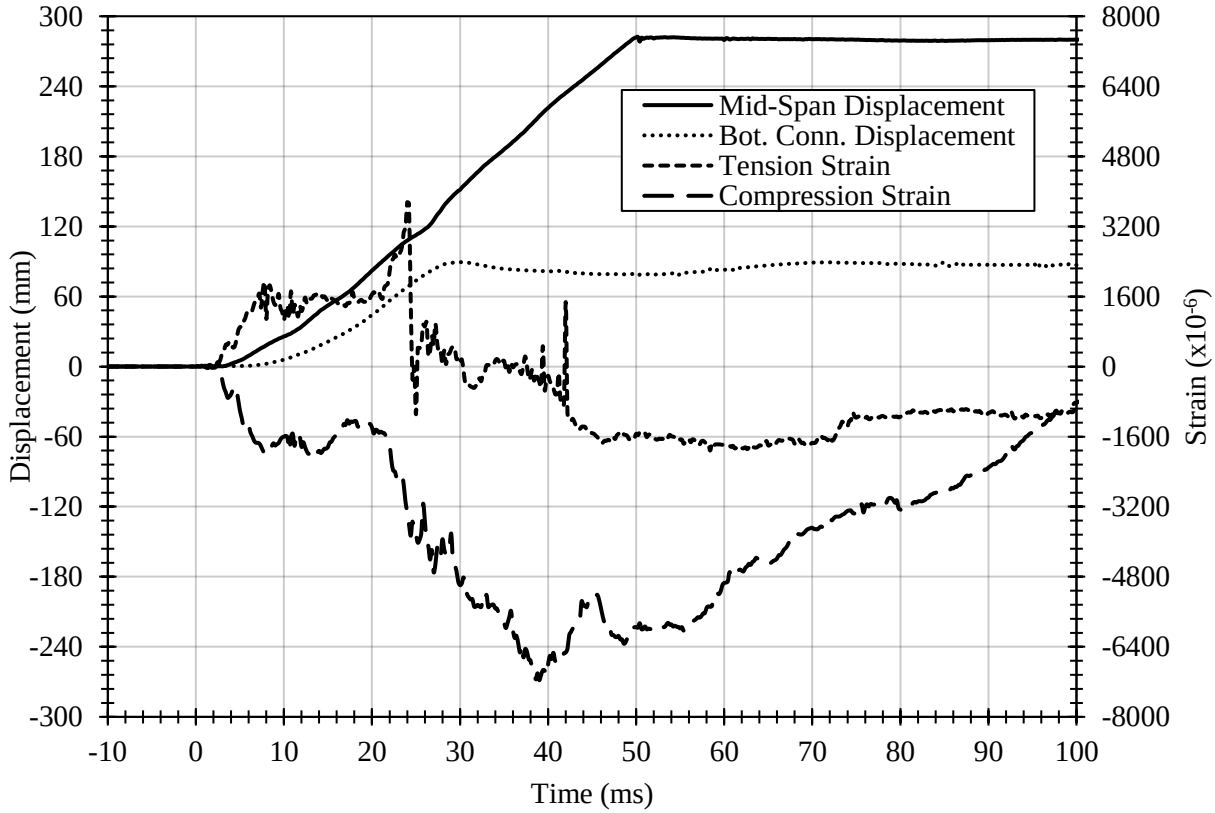
(a) Pressure and Impulse



(b) Reaction and Displacements



(c) Reaction and Strains

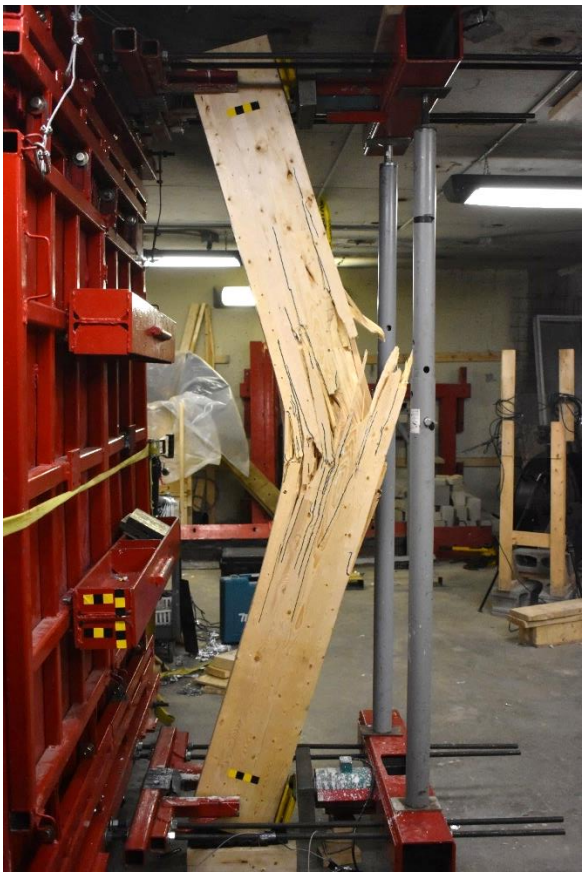


(d) Displacement and Strains

Figure C.49: Dynamic Test Results for Specimen G18



(a) Specimen Prior to Testing



(b) Specimen After Testing



(c) Flexural Failure of Beam



(d) Damage in Bottom EAC

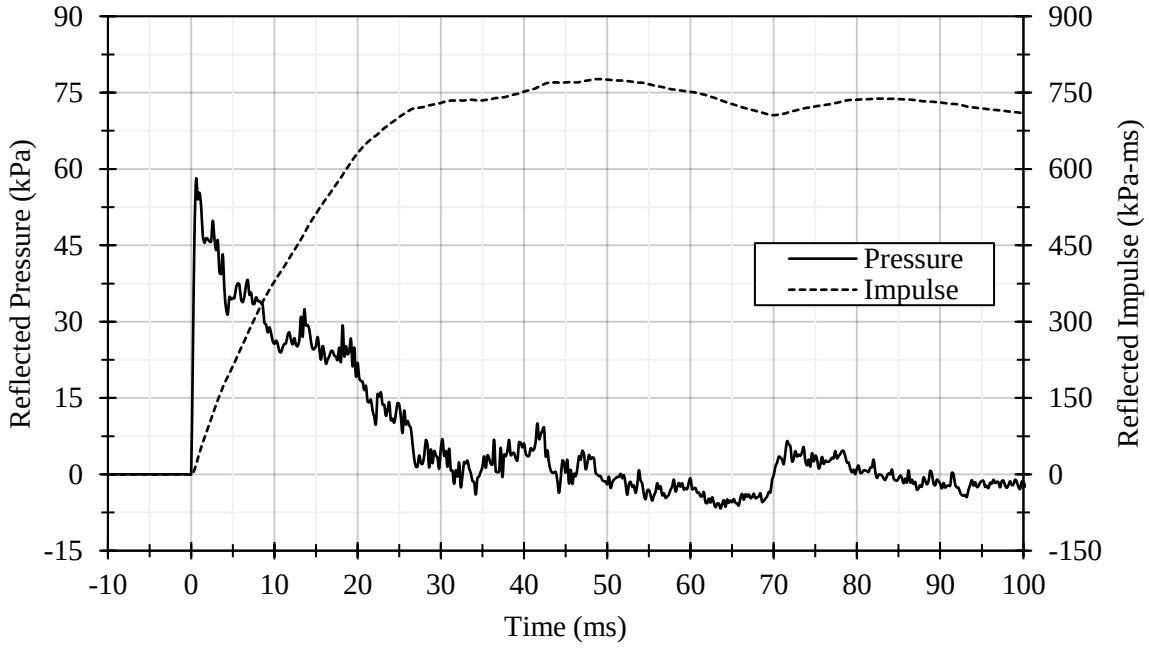


(e) Damage in Top EAC

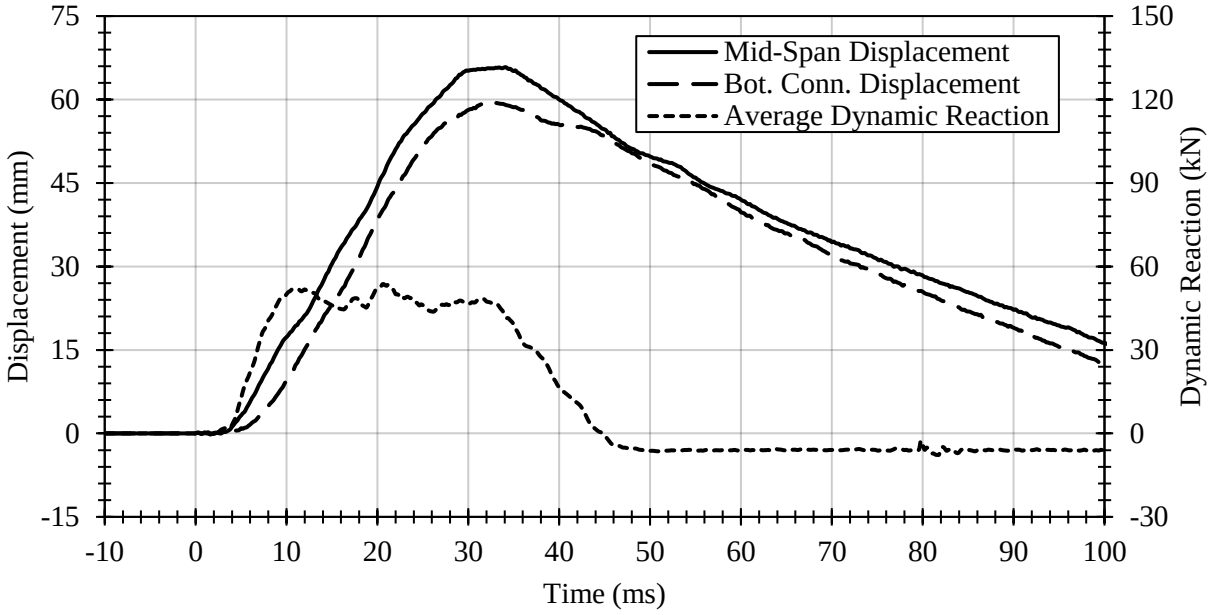
Figure C.50: Documentation of Damage for Specimen G18

Specimen G19 – Shot #1

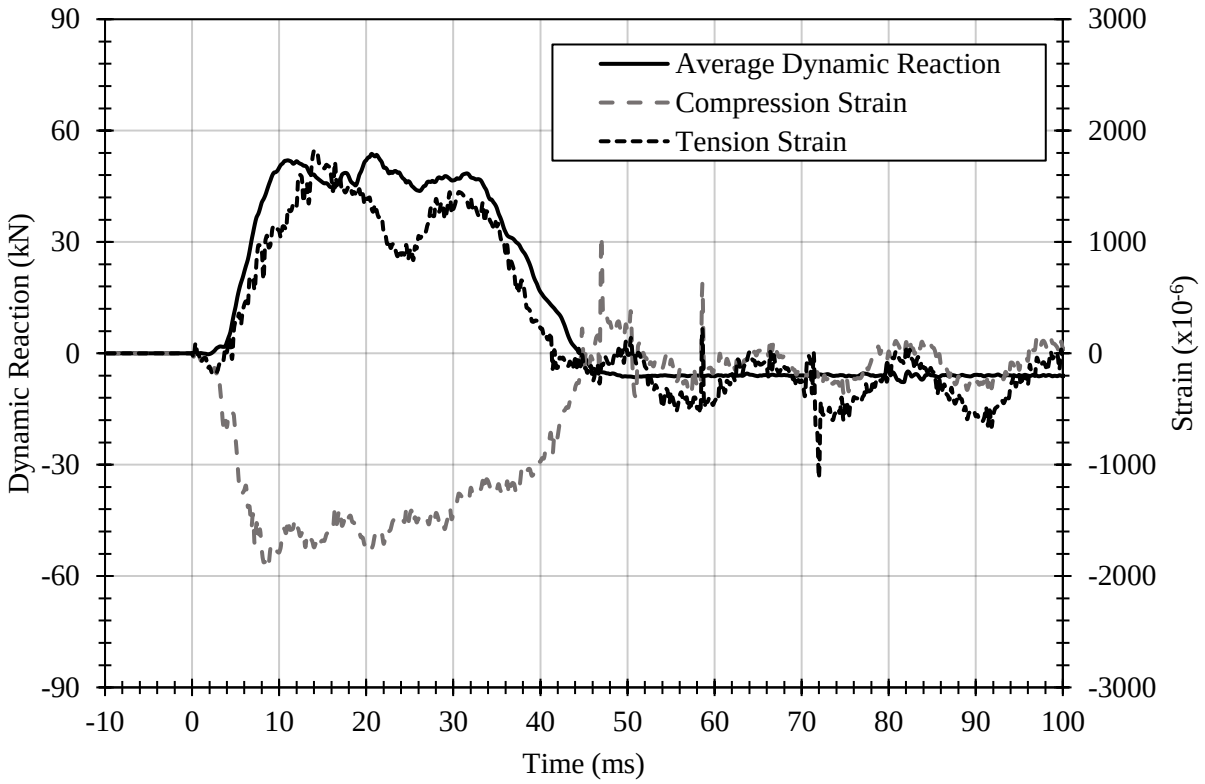
Specimen G19, comprised of a Glulam beam with a 3.75” deep EAC at each end, was subjected to two different pressure-impulse combinations. For the first shot, it was dynamically tested on September 19th 2019 with a 13 ft. driver. A driver pressure of 412.3 kPa was used, which resulted in a positive peak reflected pressure and impulse of 58.0 kPa and 734.6 kPa-ms, respectively.



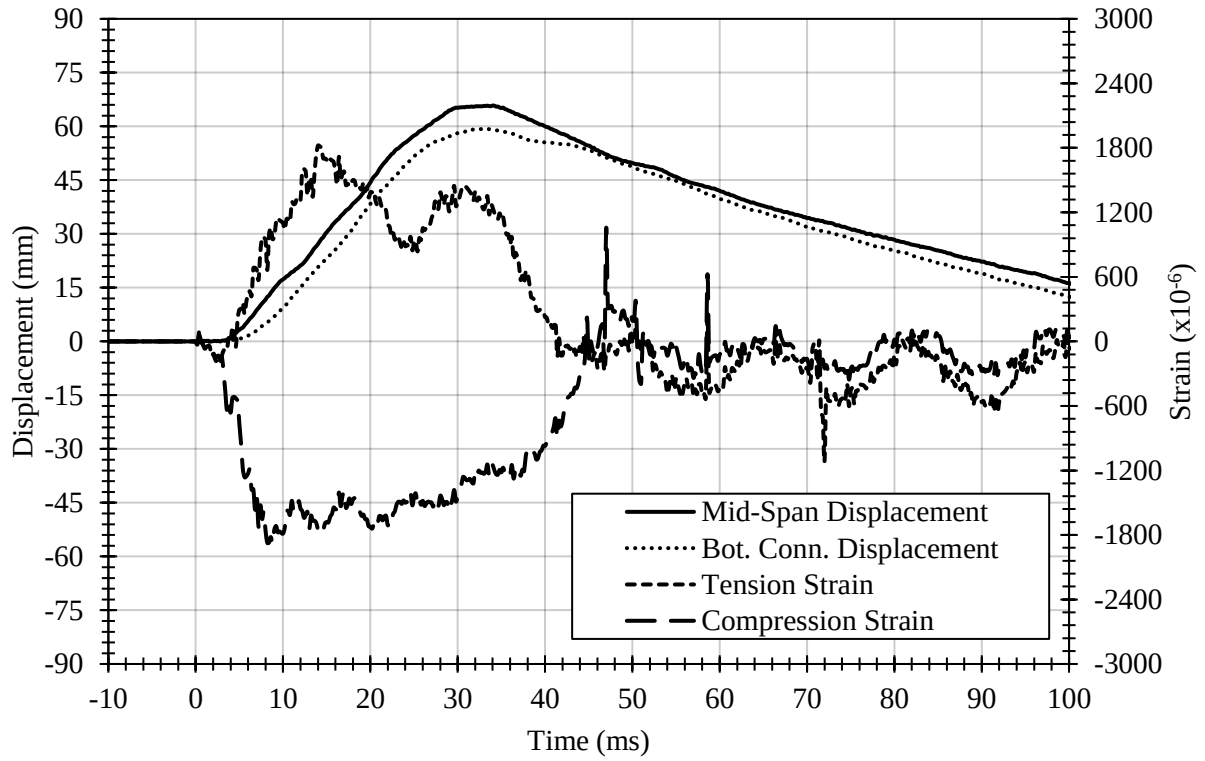
(a) Pressure and Impulse



(b) Reaction and Displacements



(c) Reaction and Strains



(d) Displacement and Strains

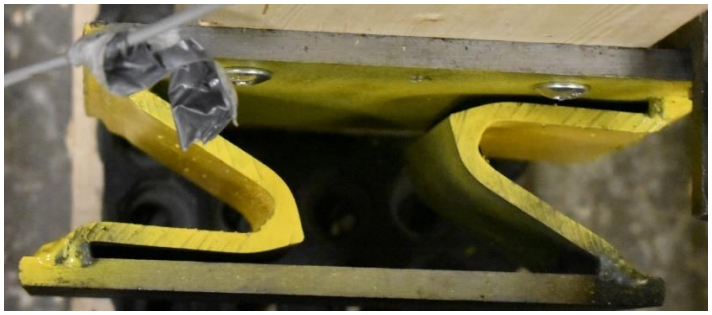
Figure C.51: Dynamic Test Results for Test G19-1



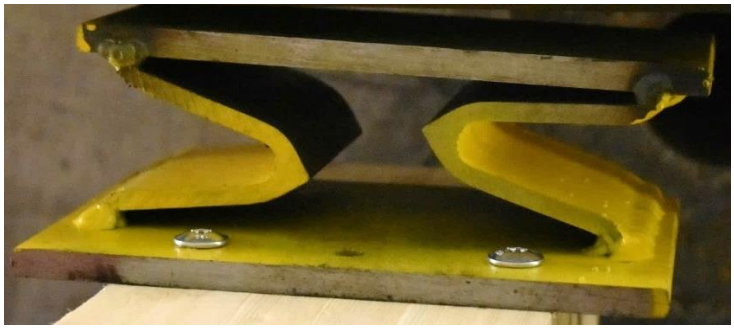
(a) Specimen Prior to Testing



(b) Specimen After Testing



(c) Damage in Bottom EAC

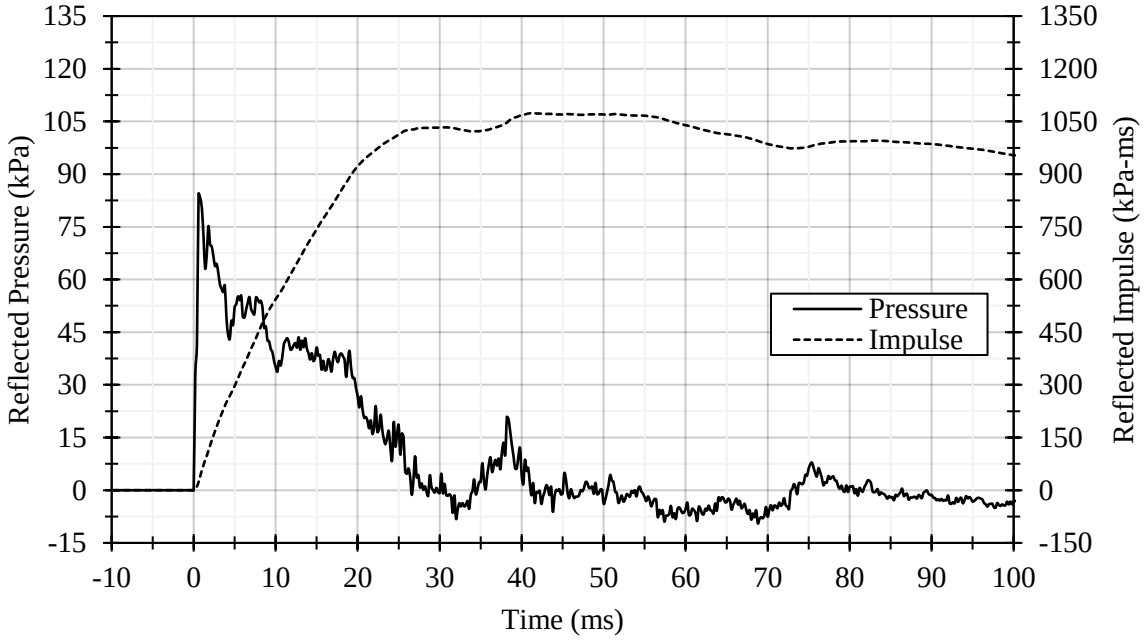


(d) Damage in Top EAC

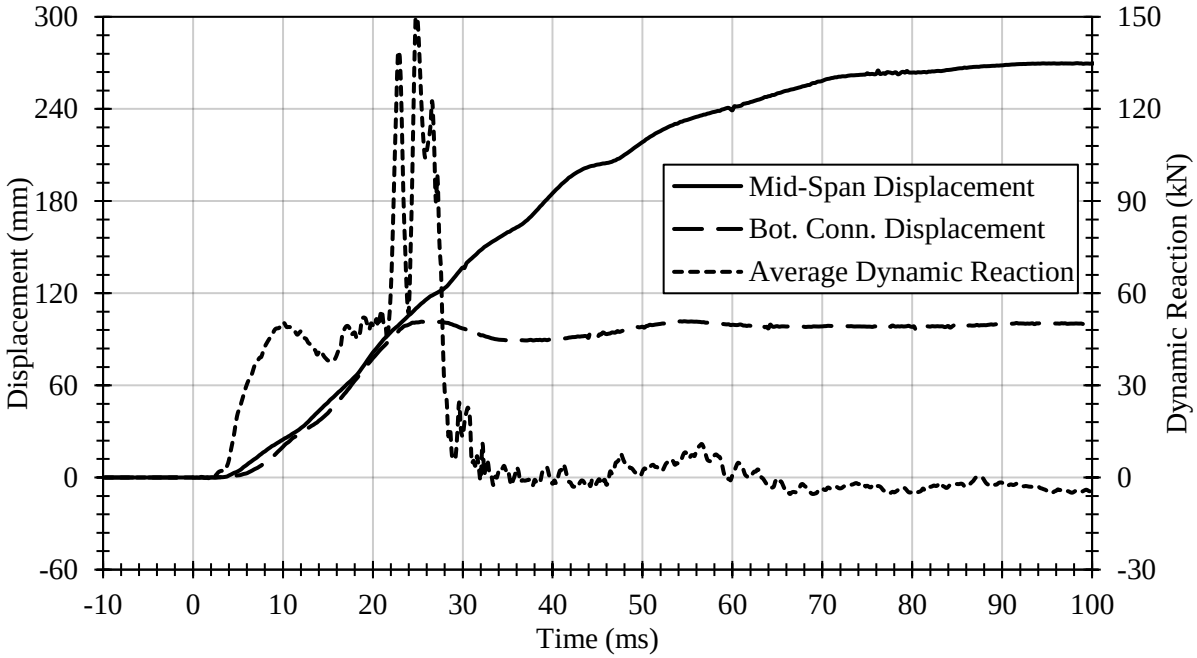
Figure C.52: Documentation of Damage for Test G19-1

Specimen G19 – Shot #2

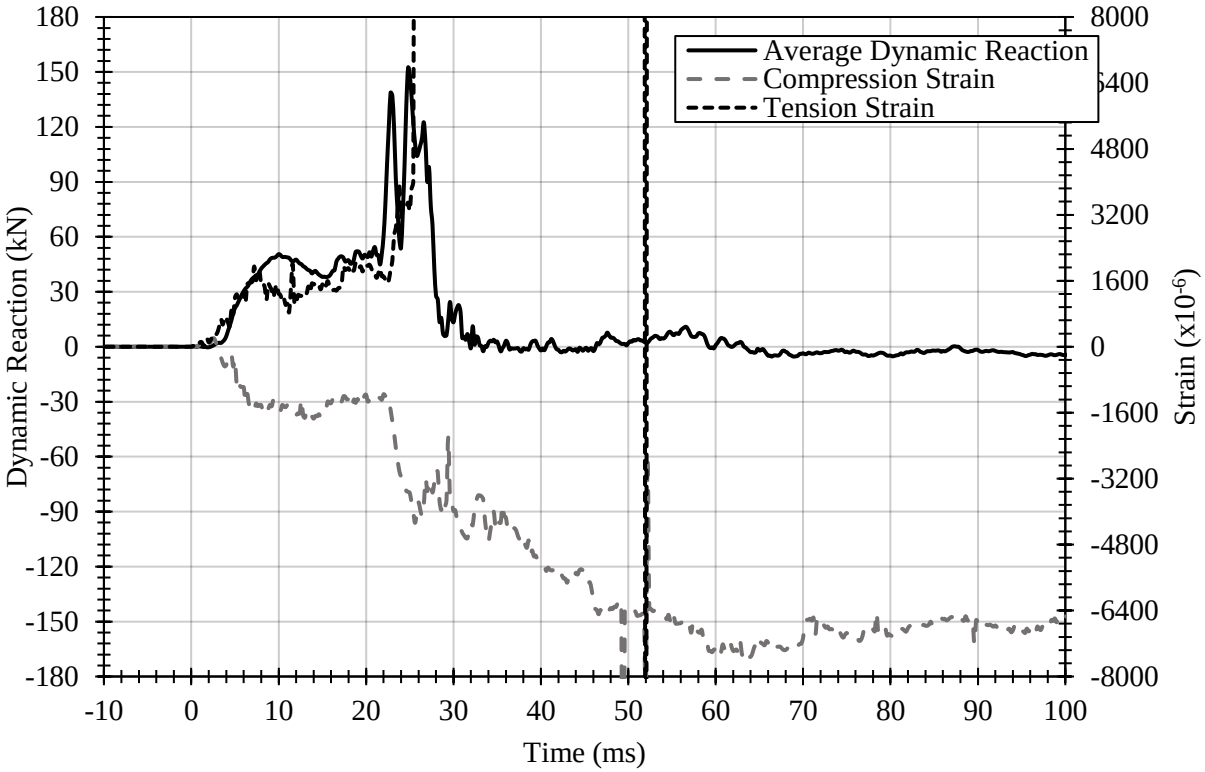
For the second shot, it was dynamically tested on September 20th 2019 with a 13 ft. driver. A driver pressure of 635.7 kPa was used, which resulted in a positive peak reflected pressure and impulse of 84.4 kPa and 1033.1 kPa-ms, respectively.



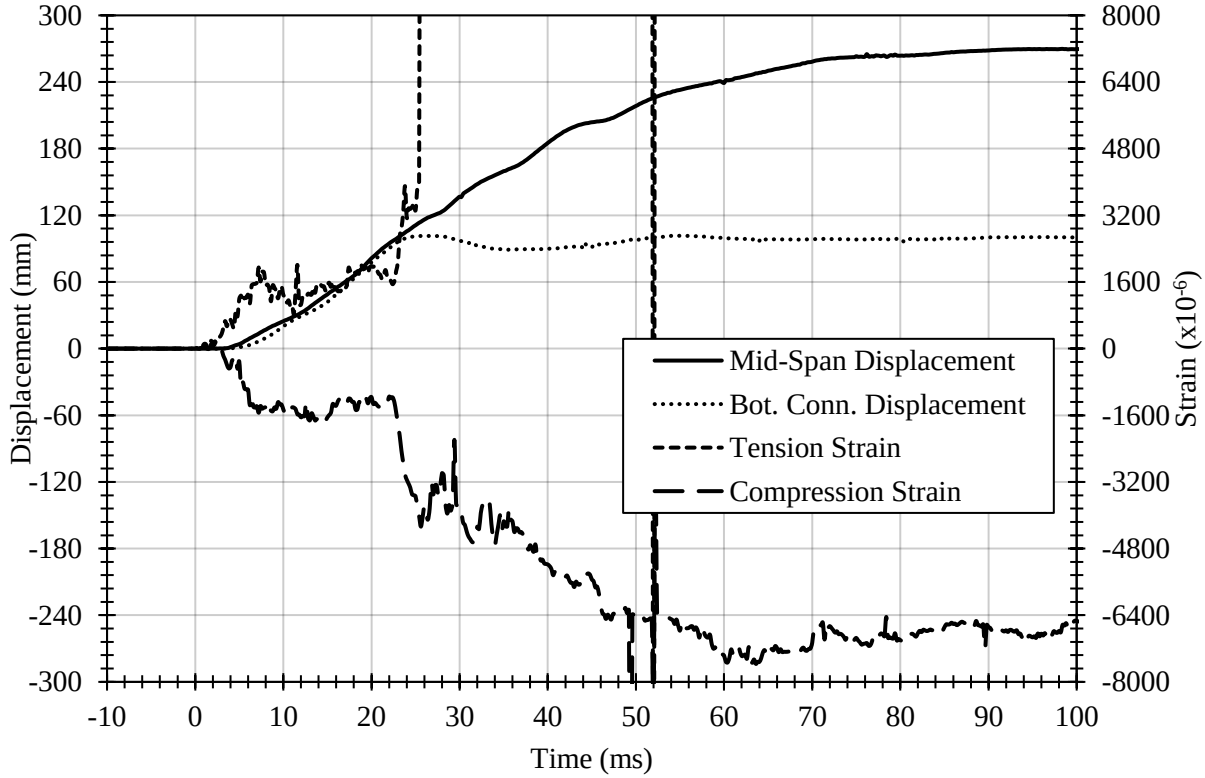
(a) Pressure and Impulse



(b) Reaction and Displacements



(c) Reaction and Strains

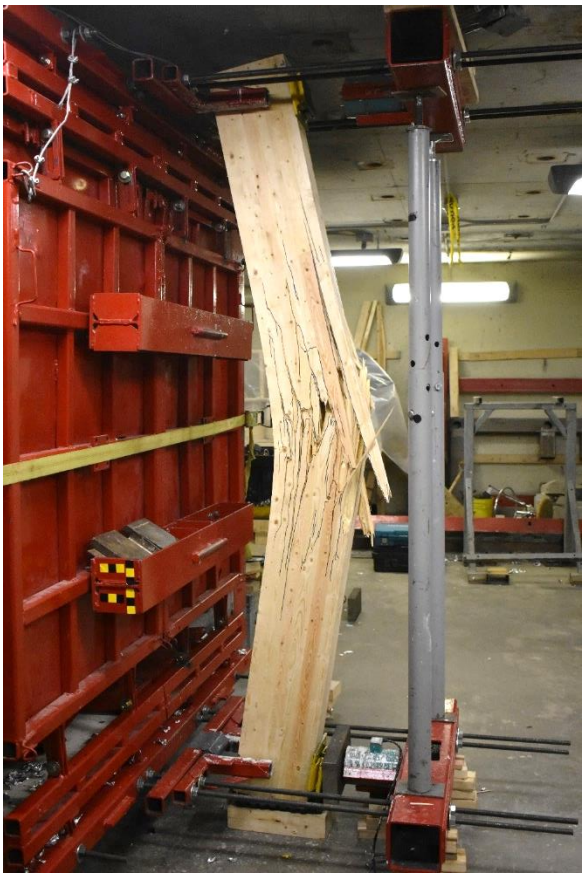


(d) Displacement and Strains

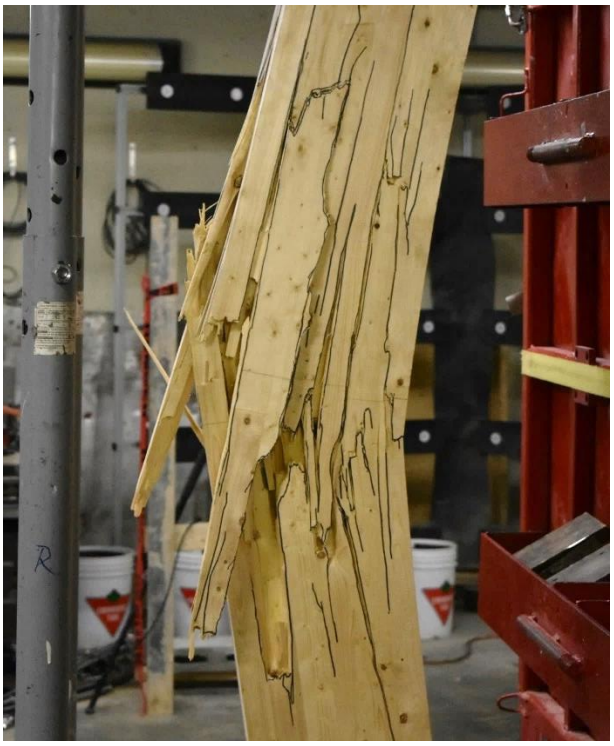
Figure C.53: Dynamic Test Results for Test G19-2



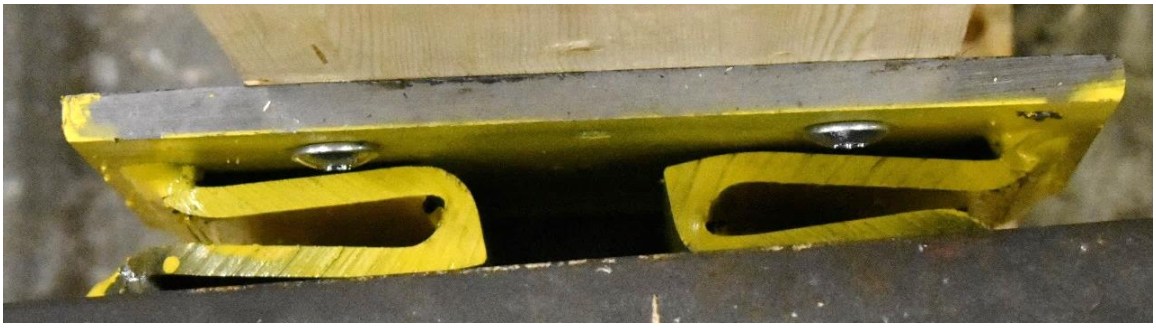
(a) Specimen Prior to Testing



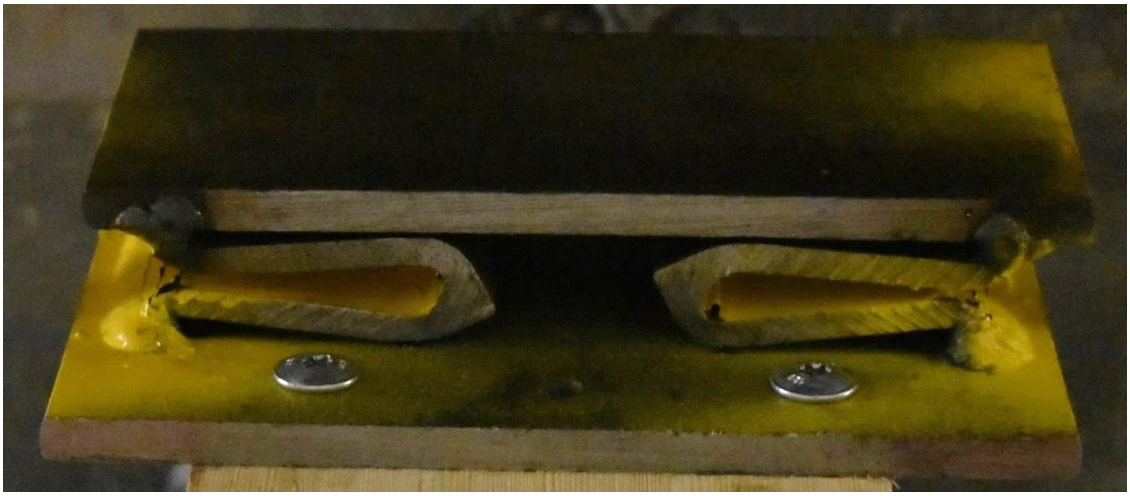
(b) Specimen After Testing



(c) Flexural Failure of Beam



(d) Damage in Bottom EAC

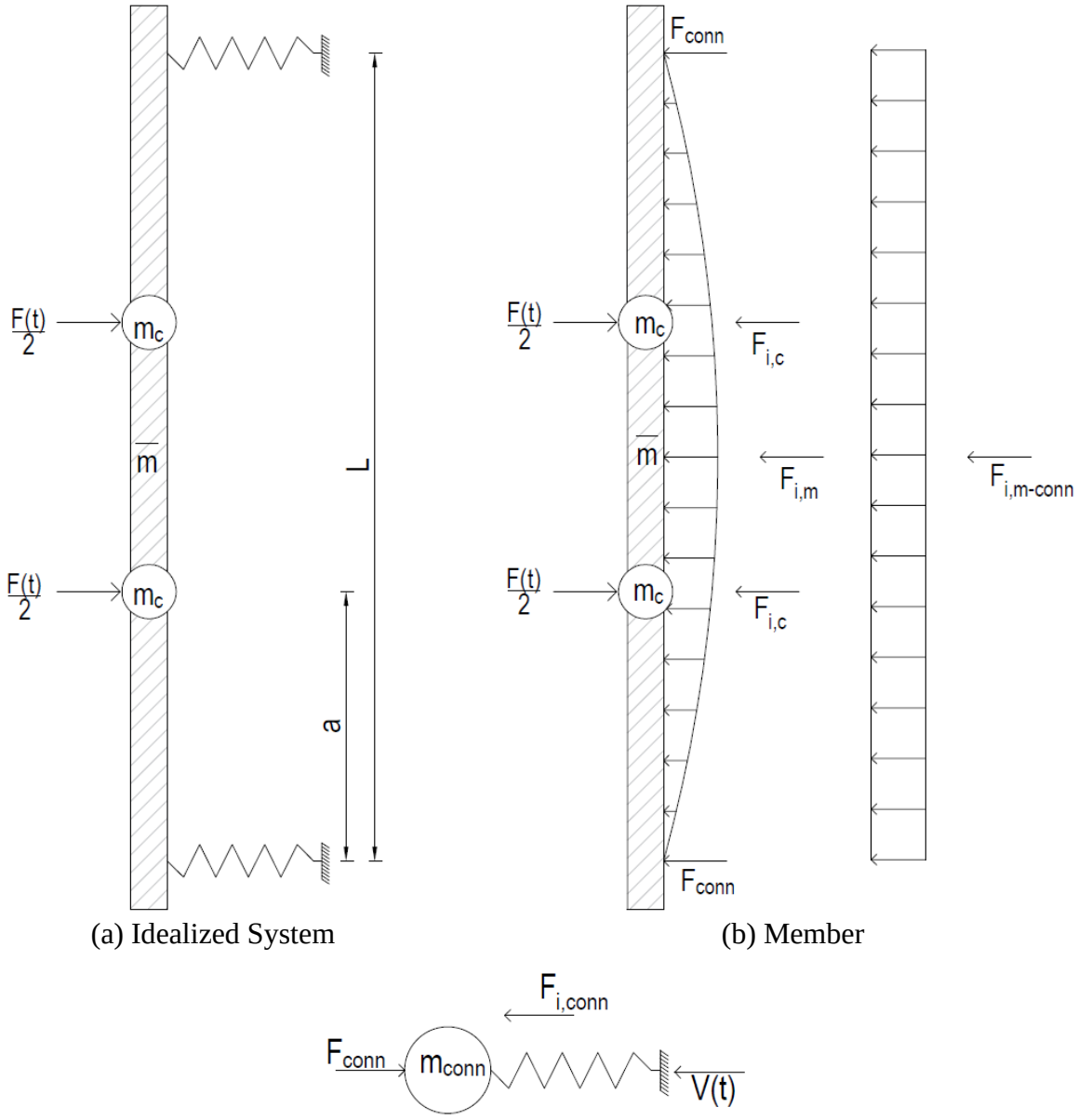


(e) Damage in Top EAC

Figure C.54: Documentation of Damage for Test G19-2

Appendix D – Derivation of Dynamic Resistance

This appendix provides the derivation of the dynamic resistance of a beam with end connections subjected to four-point bending in the elastic and plastic ranges. The system consists of both concentrated (load-transfer device and connections) and distributed (beam specimen) masses. The idealization of the actual dynamic test setup consisting of the load-transfer device, connections, and specimen is shown in Figure D.1.



(a) Idealized System (b) Member

(c) Connections

Figure D.1: Idealized System with External and Internal Forces for the Elastic Range

When subjected to an acceleration, $\ddot{y}$, inertial forces are generated in the system, as shown in Figure D.1b. As a result, the inertial force distribution of the beam follows that of the assumed static deflected shape (Biggs, 1964), whereas the inertial forces resulting from the LTD are assumed to act at the load application points in a direction opposite to that of the acceleration. Uniformly distributed inertial forces generated from the connection accelerations will be generated along the length of the assembly, due to the symmetry of the connections.

The derivation of the dynamic resistance has been done for simply supported beams (Lacroix, 2017). Due to the flexibility of the connections, inertial forces generated by the acceleration of the connections must be considered in the derivation. However, doing so will cause the closed-form solution of the resistance to become tedious to obtain. Additionally, the experimentally measured dynamic reactions, $V(t)$, are in theory affected by these inertial forces, further complicating the matter. As such, two considerations will be used to reduce the complexity of the derivation. The first is an assumption derived from the force balance of the connections (Figure D.1c). This generates the following equation:

$$F_{conn} - F_{i,conn} = V(t) \qquad \text{Equation D.1}$$

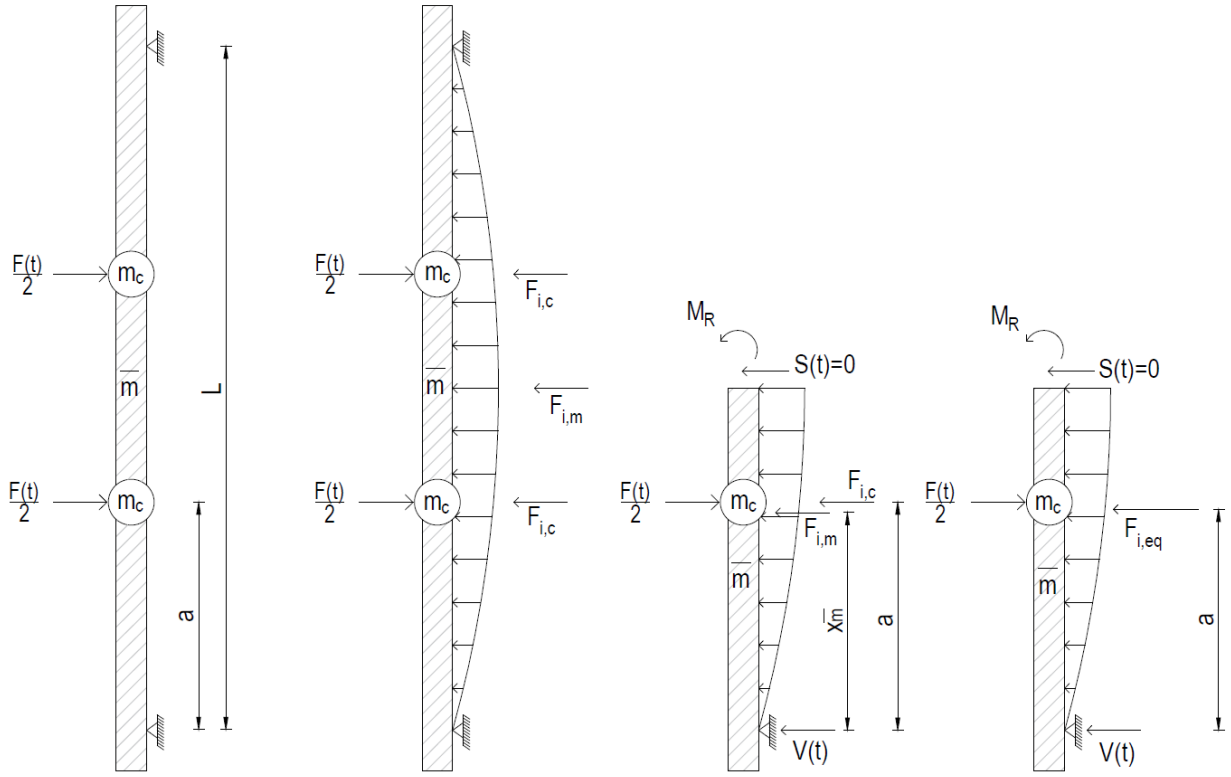
where F_{conn} is the force imposed by the beam, $F_{i,conn}$ is the inertial force caused by the acceleration of the connection mass, m_{conn}, and $V(t)$ is the experimentally measured dynamic reaction. Since typical connections have relatively small masses, thus small inertial forces, one may ignore the contribution of the mass without introducing significant error. The inertial force term in Equation D.1 will disappear and thus:

$$F_{conn} \cong V(t) \qquad \text{Equation D.2}$$

The relationship established in Equation D.2 will allow for the experimentally measured dynamic reactions to be used in the derivation of the resistance term without the need to consider the connections' inertial forces.

Secondly, the distribution of inertial forces presented in Figure D.1b correlates to those observed from a frame of reference being taken from an arbitrary point that is not part of the assembly. By changing this frame of reference to that which is taken from the beam's point of contact with the

connection, the member inertial forces caused by the connections' accelerations will not need be considered, since the observer is now moving along with the beam as a function of the connections' responses. Thus, the derivation for the resistance term may now be based on the simplified idealized system with external and internal forces presented in Figure D.2.



(a) Idealized System (b) Inertial Forces (c) Half-Span Inertial Forces (d) Half-Span Inertial Forces

Figure D.2: Simplified Idealized System with External and Internal Forces for the Elastic Range

The dynamic resistance of the system as a function of time is developed by taking the sum of moments about where the equivalent inertial force acts, as shown in Figure D.2d. Equation D.3 shows the dynamic resistance of the beam as a function of time, $R(t)$, which is obtained by taking the sum of moments about the equivalent inertial force (Figure D.2d) for the idealized system.

$$\sum M_{Fi-eq} = 0$$

$$-V(t)x_{eq} - \frac{F(t)}{2}\left(a - x_{eq}\right) + M_R = 0$$

$$R(t)\left(\frac{a}{2}\right) = V(t)x_{eq} + \frac{F(t)}{2}\left(a - x_{eq}\right)$$

$$R(t) = \left(\frac{2}{a}\right)\left(V(t)x_{eq} + \frac{F(t)}{2}\left(a - x_{eq}\right)\right) \qquad \text{Equation D.3}$$

where $V(t)$ is the measured experimental dynamic reactions as a function of time, $F(t)$ is the applied force at the load point as a function of time, M_R is the dynamic bending capacity of the beam, a is the distance of load application point from the support, and x_{eq} is the distance of the equivalent inertial force from the support.

In the derivation of Equation D.3, M_R is expanded to include the resistance of the beam at mid-span. The location of the equivalent inertial force is directly linked to the ratio of the distributed mass, $\bar{m}$, to the concentrated mass, m_c. The location of the resultant inertial force of the beam for the lower half of the system (Figure D.2c), $x_{\bar{m}}$, can be determined from the assumed deflected shape resulting in the simplified system shown in Figure D.2d. The deflected shape, $\phi(x)$, for concentrated loads at two equally distant points can be obtained from literature and is shown in Equation D.4 and Equation D.5 for the elastic range.

$$\phi(x) = \frac{\Delta x}{\Delta max}$$

$$For\ x \leq a \qquad \phi(x) = \frac{\frac{Fx}{6EI}(3aL - 3a^2 - x^2)}{\frac{Fa}{24EI}(3L^2 - 4a^2)}$$

$$\phi(x) = \frac{12xL - 12ax - \frac{4x^3}{a}}{3L^2 - 4a^2} \qquad \text{Equation D.4}$$

$$For\ a < x \leq (L - a) \qquad \phi(x) = \frac{\frac{Fa}{6EI}(3Lx - 3x^2 - a^2)}{\frac{Fa}{24EI}(3L^2 - 4a^2)}$$

$$\phi(x) = \frac{12xL - 12x^2 - 4a^2}{3L^2 - 4a^2} \qquad \text{Equation D.5}$$

where x is the location along the beam length and L is the span. The acceleration at any point along the span, $\ddot{y}(x)$, can be determined using Equation D.6 assuming once again that the inertial forces' distribution is the same as the deflected shape (Biggs, 1964).

$$\ddot{y}(x) = A\phi(x) \qquad \text{Equation D.6}$$

where A is a constant and $\phi(x)$ is the deflected shape along the beam span. The location of the resultant inertial force of the beam for the lower half of the system, $x_{\bar{m}}$, can be found using Equation D.7 (Biggs, 1964). For the elastic range, $x_{\bar{m}-elastic}$ is shown in Equation D.8.

$$x_{\bar{m}} = \frac{\int_0^{\frac{L}{2}} x\phi(x)dx}{\int_0^{\frac{L}{2}} \phi(x)dx} \qquad \text{Equation D.7}$$

$$x_{\bar{m}-elastic} = \frac{0.0125(4a^2 - 5L^2)^2}{a^3 - 2a^2L + L^3} \qquad \text{Equation D.8}$$

The distance from the support of the equivalent inertial force for the elastic region, $x_{eq-elastic}$, is bounded by the two extremes defined by the absence of distributed mass and concentrated mass as shown in Equation D.9.

$$x_{\bar{m}-elastic} \leq x_{eq-elastic} \leq a \qquad \text{Equation D.9}$$

The inertial forces for the beam and the concentrated mass are obtained using Newton's second law as shown in Equation D.10 and Equation D.11, respectively.

$$F_{i,\bar{m}} = \int_0^{\frac{L}{2}} \bar{m}\ddot{y}(x)\,dx$$

$$F_{i,\bar{m}} = \int_0^{\frac{L}{2}} \bar{m}A\phi(x)\,dx$$

$$F_{i,\bar{m}} = \bar{m}A\int_0^{\frac{L}{2}} \phi(x)\,dx$$

$$F_{i,\bar{m}} = \frac{\bar{m}A(a^3 - 2a^2L + L^3)}{3L^2 - 4a^2} \quad \text{Equation D.10}$$

$$F_{i,c} = m_c\ddot{y}(a)$$

$$F_{i,c} = m_cA\phi(a)$$

$$F_{i,c} = \frac{m_cA(12La - 16a^2)}{3L^2 - 4a^2} \quad \text{Equation D.11}$$

By taking the sum of moments about the support of the system with the two resulting inertial forces ($F_{i,\bar{m}}$ and $F_{i,c}$) and equating it to the sum of moments about the support of the system with an equivalent inertial force ($F_{i,eq}$), it is possible to solve for $x_{eq-elastic}$. The equivalent inertial force for half the beam is shown in Equation D.12 followed by the derivation for $x_{eq-elastic}$ as presented in Equation D.13.

$$F_{i,eq} = F_{i,\bar{m}} + F_{i,c} = \frac{A\left(\bar{m}(a^3 - 2a^2L + L^3) + m_c(12La - 16a^2)\right)}{3L^2 - 4a^2} \quad \text{Equation D.12}$$

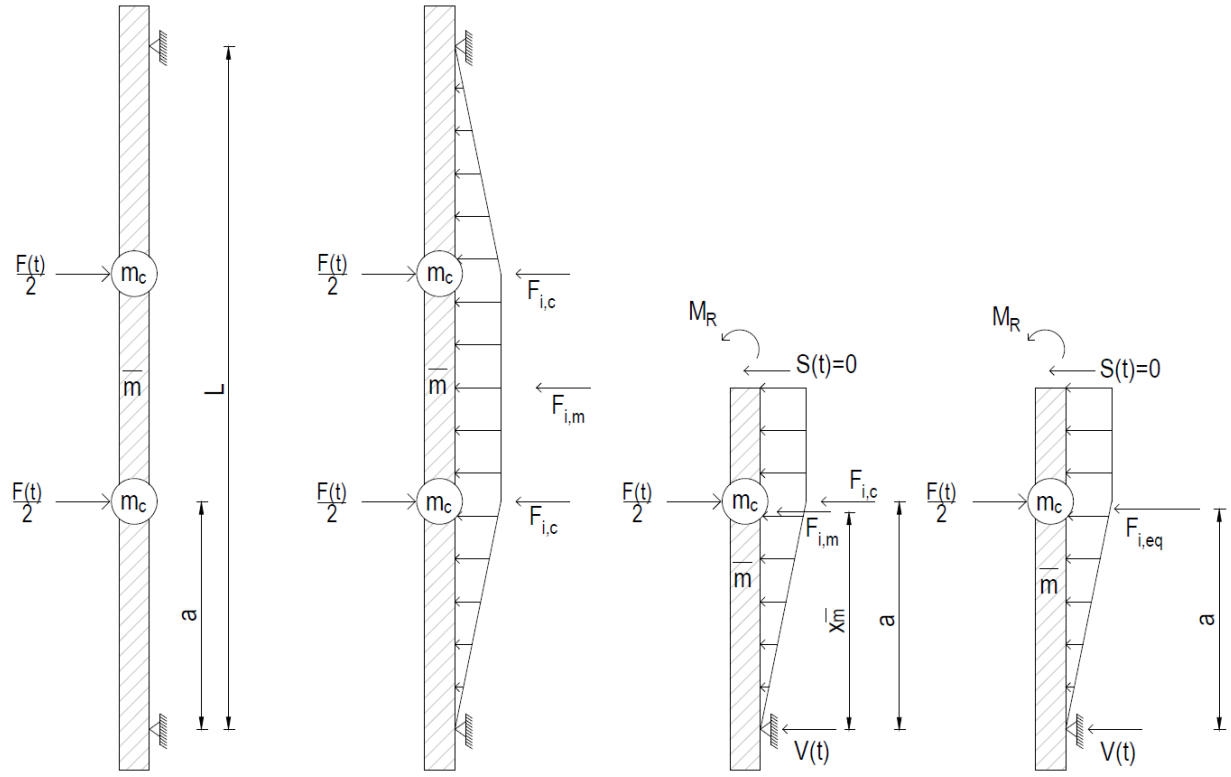
$$\sum M_A = \sum M_{A-eq}$$

$$F_{i,\bar{m}}x_{\bar{m}-elastic} + F_{i,c}a - \frac{F(t)}{2}a + M_R = F_{i,eq}x_{eq-elastic} - \frac{F(t)}{2}a + M_R$$

$$\frac{\bar{m}A0.0125(4a^2 - 5L^2)^2}{3L^2 - 4a^2} + \frac{m_cA(12La^2 - 16a^3)}{3L^2 - 4a^2} = \frac{A\left(\bar{m}(a^3 - 2a^2L + L^3) + m_c(12La - 16a^2)\right)}{3L^2 - 4a^2}x_{eq-elastic}$$

$$x_{eq-elastic} = \frac{0.0125\bar{m}(4a^2 - 5L^2)^2 + m_c(12La^2 - 16a^3)}{\bar{m}(a^3 - 2a^2L + L^3) + m_c(12La - 16a^2)} \quad \text{Equation D.13}$$

where $\bar{m}$ is a distributed mass (i.e. the timber specimen's distributed mass), L is the span length, m_c is the concentrated load (i.e. half of the LTD mass), A is a constant, F is the applied force (i.e. reflected pressure multiplied by effective loaded area of LTD), and M_R is the dynamic bending moment at mid-span.



(a) Idealized System (b) Inertial Forces (c) Half-Span Inertial Forces (d) Half-Span Inertial Forces

Figure D.3: Simplified Idealized System with External and Internal Forces for the Plastic Range

For the plastic range (see Figure D.3), Equation D.4 and Equation D.5 must be modified based on the new assumed deflected shape. These can be obtained from literature and are shown in Equation D.14 and Equation D.15 for the plastic range.

$$For\ x\ \leq a \qquad \phi(x) = \frac{x}{a} \qquad \text{Equation D.14}$$

$$For\ a \leq\ x\ \leq (L-a) \qquad \phi(x) = 1 \qquad \text{Equation D.15}$$

Applying Equation D.7 with the deflected equations for the plastic range (Equation D.14 and Equation D.15), the location of the resultant inertial force of the beam for the lower half of the system, $x_{\bar{m}-plastic}$, can be found, as presented in Equation D.16.

$$x_{\bar{m}-plastic} = \frac{6L^2 - 8a^2}{24(L-a)} \qquad \text{Equation D.16}$$

Reapplying the same procedure outlined for the elastic range, the following inertial forces are obtained:

$$F_{i,\bar{m}} = \frac{\bar{m}A(L-a)}{2} \qquad \text{Equation D.17}$$

$$F_{i,c} = m_c A \qquad \text{Equation D.18}$$

Finally, the equivalent inertial force for half the beam is shown in Equation D.19 followed by the derivation for $x_{eq-plastic}$ as presented in Equation D.20.

$$F_{i,eq} = F_{i,\bar{m}} + F_{i,c} = \frac{\bar{m}A(L-a)}{2} + m_c A \qquad \text{Equation D.19}$$

$$\sum M_A = \sum M_{A-eq}$$

$$F_{i,\bar{m}} x_{m-plastic} + F_{i,c} a - \frac{F(t)}{2} a + M_R = F_{i,eq} x_{eq-plastic} - \frac{F(t)}{2} a + M_R$$

$$\frac{\bar{m}A(L-a)}{2} \frac{(6L^2 - 8a^2)}{24(L-a)} + m_c A a = \left(\frac{\bar{m}A(L-a)}{2} + m_c A \right) x_{eq-plastic}$$

$$x_{eq-plastic} = \frac{\frac{\bar{m}(6L^2 - 8a^2)}{48} + m_c a}{0.5\bar{m}(L-a) + m_c} \qquad \text{Equation D.20}$$

Appendix E – Derivation of Stiffness Expression for Beams with Rotational Springs

This appendix provides the derivation of the modified stiffness equation for a Euler-Bernoulli beam with equal rotational springs at both ends. The expression will be derived based on two possible loading scenarios: uniformly distributed loading (e.g. for a light-frame wood stud wall subjected to uniform blast pressure) and two concentrated point loads at spaced at the third points. Additionally, the derivations will also include the deflected shapes, which can be used in the derivation of the load-mass transformation factor, for lumping beams into an equivalent single-degree-of-freedom system.

Case for Uniformly Distributed Beam

The idealization of a uniformly distributed beam with two end springs represented by rotational springs M_A is shown in Figure E.1.

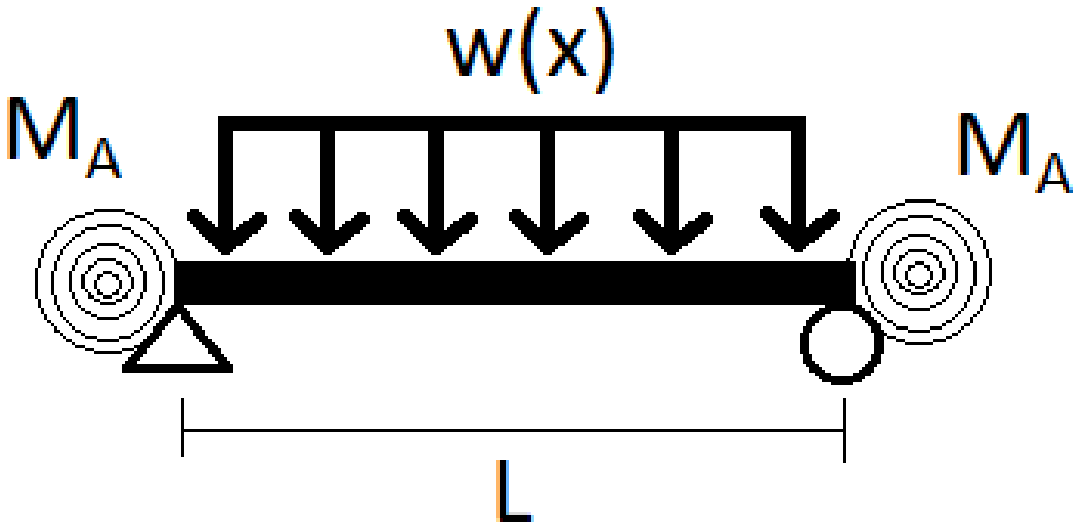
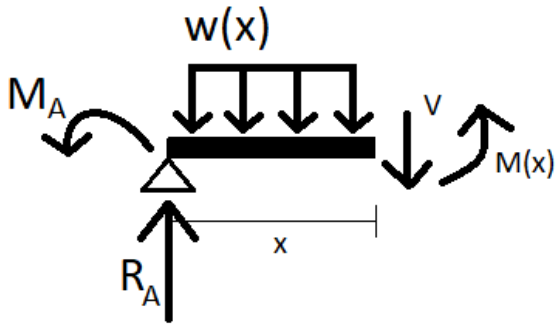


Figure E.1: Uniformly Distributed Beam with Two Rotational End Springs

Drawing a free-body diagram and taking equilibrium from a distance *x* from the left support *A*, we obtain the following:



$$R_A = \frac{wl}{2}$$

$$\sum M = 0$$

$$M(x) + M_A + \frac{wx^2}{2} - \frac{wl}{2}x = 0$$

$$M(x) = -M_A - \frac{wx^2}{2} + \frac{wl}{2}x \qquad \text{Equation E.1}$$

Naturally, we have the following boundary conditions:

$$v(0) = 0 \qquad \text{BC1}$$

$$v'(0) = \theta_a \qquad \text{BC2}$$

For a Euler–Bernoulli beam, the following equation presents the relationship between the beam's deflection and the applied load:

$$M(x) = EIv''(x) \qquad \text{Equation E.2}$$

By sending Equation E.1 into Equation E.2, and integrating twice, we obtain:

$$EIv''(x) = -M_A - \frac{wx^2}{2} + \frac{wl}{2}x$$

$$EIv'(x) = -M_A x - \frac{wx^3}{6} + \frac{wl}{4}x^2 + C_1 \qquad \text{Equation E.3}$$

$$EIv(x) = -\frac{M_A x^2}{2} - \frac{wx^4}{24} + \frac{wl}{12}x^3 + C_1 x + C_2 \qquad \text{Equation E.4}$$

Applying BC1 and BC2 to Equation E.3 and Equation E.4, we find that:

$$C_2 = 0$$

$$C_1 = EIv'(0)$$

$$C_1 = EI\theta_a$$

$$v(x) = \frac{1}{EI}\left(-\frac{M_A x^2}{2} - \frac{wx^4}{24} + \frac{wl}{12}x^3 + EI\theta_a x\right) \qquad \text{Equation E.5}$$

The total rotation at the left support *A* can be calculated by adding the rotations caused by the external loads (θ_{A0}) with the rotations in the beam caused by unit moments applied on both ends of a simply supported beam without end springs. Using the principle of virtual work, this is written as the following:

$$\theta_A = \theta_{A0} + \theta_{AA}M_A + \theta_{AB}M_B \qquad \text{Equation E.6}$$

where

$$\theta_{A0} = -\frac{wl^3}{24EI}$$

$$\theta_{AA} = \frac{L}{3EI}$$

$$\theta_{AB} = -\frac{L}{6EI}$$

Knowing that

$$\theta_A = -\theta_B$$

We can express M_B in terms of M_A

$$M_B = -M_A$$

Since the total rotation at *A* must naturally equal to the rotation in the rotational spring. The moments in the spring will be acted upon the beam, as per the law of action reaction. Therefore, the rotation in the springs can be described as:

$$\theta_A = -\frac{M_A}{K_r} \qquad \text{Equation E.7}$$

With all of this, Equation E.6 becomes:

$$-\frac{M_A}{K_r} = -\frac{wl^3}{24EI} + M_A\frac{L}{3EI} + M_A\frac{L}{6EI}$$

$$\frac{M_A}{K_r} + M_A\frac{L}{2EI} = \frac{wl^3}{24EI}$$

Isolating for M_A, we obtain the following relationship for the moment in the spring at *A:*

$$M_A = \frac{wl^3K_r}{12(K_rl + 2EI)} \qquad \text{Equation E.8}$$

By inserting Equation E.7 and Equation E.8 into Equation E.5, and evaluating at mid-span, we obtain:

$$v\left(\frac{l}{2}\right) = \Delta_{max} = \frac{1}{EI}\left[\frac{3wl^4}{384} - \frac{4wl^5K_r}{384(K_rl + 2EI)} - \frac{16wl^4EI}{384(K_rl + 2EI)}\right]$$

$$\Delta_{max} = \frac{wl^4}{384EI}\left[3 - \frac{4K_rl + 16EI}{K_rl + 2EI}\right] \qquad \text{Equation E.9}$$

We define a nondimensional constant, B, defined as the ratio of the rotational stiffness to that of the beam stiffness:

$$B = \frac{K_rl}{EI} \qquad \text{Equation E.10}$$

Inserting Equation E.10 into Equation E.9, we arrive to

$$\Delta_{max} = \frac{wl^4}{384EI}\left[3 - \frac{4B + 16}{B + 2}\right]$$

$$\Delta_{max} = \frac{-wl^4}{384EI}\left[\frac{B + 10}{B + 2}\right]$$

Inversing the positive direction to downwards positive, we finally get:

$$\Delta_{max} = \frac{wl^4}{384EI}\left[\frac{B + 10}{B + 2}\right] \qquad \text{Equation E.11}$$

Which is the maximum deflection equation for a uniformly distributed beam with end rotational springs. Two extremes exist for Equation E.11:

1. $B = 0$, which corresponds to simply-supported end conditions:

$$B = 0$$

$$\Delta_{max} = \frac{5wl^4}{384EI}$$

2. B tends towards infinity, which corresponds fixed end conditions:

$$\lim_{B \to \infty} \frac{wl^4}{384EI}\left[\frac{B + 10}{B + 2}\right]$$

$$\lim_{B \to \infty} \frac{wl^4}{384EI}\left[\frac{1 + \frac{10}{B}}{1 + \frac{2}{B}}\right] = \frac{wl^4}{384EI}\left[\frac{1 + 0}{1 + 0}\right]$$

$$\Delta_{max} = \frac{wl^4}{384EI}$$

By inserting Equation E.7 and Equation E.8 into Equation E.5, we obtain the expression for the vertical deflection of any point along the beam:

$$v(x) = -\frac{1}{EI}\left(-\frac{wl^3K_rx^2}{24(K_rl+2EI)} - \frac{wx^4}{24} + \frac{wlx^3}{12} - \frac{EIM_A}{K_r}x\right)$$

$$v(x) = \frac{1}{EI}\left(\frac{M_Ax^2}{2} + \frac{wx^4}{24} - \frac{wlx^3}{12} + \frac{EIM_A}{K_r}x\right)$$

$$v(x) = \frac{1}{EI}\left(\frac{w}{12}\left(\frac{x^4}{2} - lx^3\right) + M_A\left(\frac{x^2}{2} + \frac{EIx}{K_r}\right)\right)$$

$$v(x) = \frac{wx}{12EI}\left(\frac{x^3}{2} - lx^2 + \frac{K_rl^3}{K_rl+2EI}\left(\frac{x}{2} + \frac{EI}{K_r}\right)\right)$$

$$v(x) = \frac{wx}{24EI}\left(\frac{x^3(K_rl+2EI) - 2lx^2(K_rl+2EI) + l^3(K_rx+2EI)}{K_rl+2EI}\right)$$

$$v(x) = \frac{wx}{24EI}\left(x^3 - 2lx^2 + \frac{l^3(K_rx+2EI)}{K_rl+2EI}\right) \qquad \text{Equation E.12}$$

The deflected shape for any point along the beam is defined as the following:

$$\varphi(x) = \frac{v(x)}{\Delta_{max}} \qquad \text{Equation E.13}$$

By inserting Equation E.9 and Equation E.12 into Equation E.13, we obtain the following expression:

$$\varphi(x) = \frac{16x}{l^4}\left(x^3 - 2lx^2 + \frac{l^3(K_rx+2EI)}{K_rl+2EI}\right)\left(\frac{K_rl+2EI}{K_rl+10EI}\right) \qquad \text{Equation E.14}$$

Case for a Beam Loaded with Two Equal Concentrated Point Loads at Third Spans

The idealization of a beam loaded by two equal concentrated loads at third points with two end springs represented by rotational springs M_A is shown in Figure E.2.

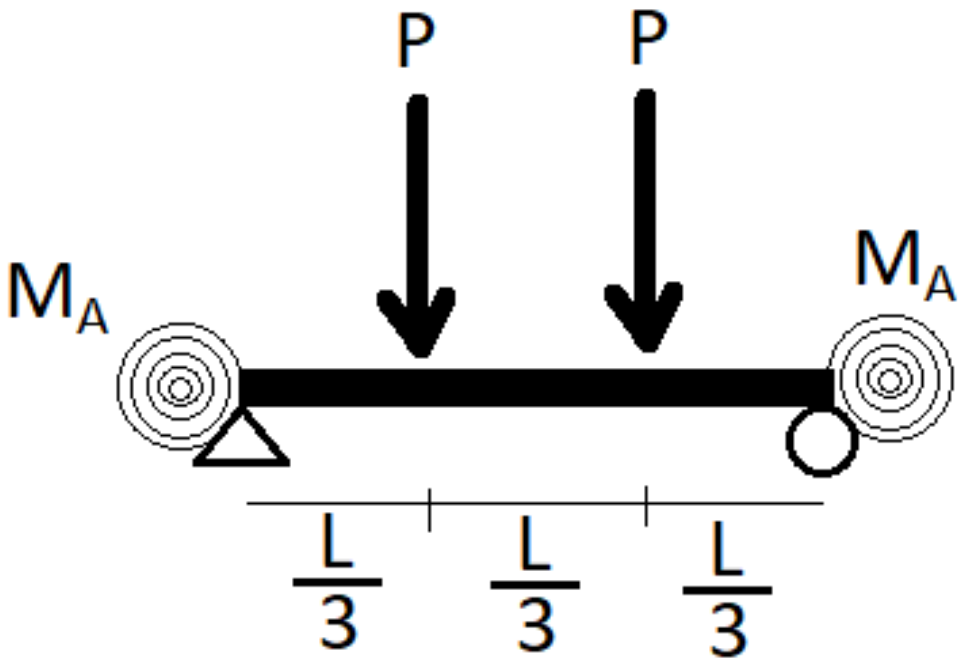
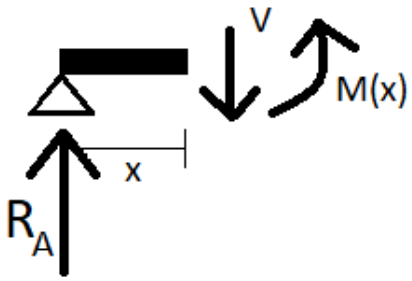


Figure E.2: Beam with Two Equal Concentrated Point Loads at Third Spans with Rotational End Springs

First, in order to obtain a required boundary condition, we consider the case a simply-supported beam (i.e. no rotational springs), and take equilibrium from a distance $x \leq a$ from support *A*, where $a = \frac{L}{3}$. We obtain the following:



$$R_A = P$$

$$\sum M = 0$$

$$M(x) - Px = 0$$

$$M(x) - Px = 0 \qquad \text{Equation E.15}$$

By sending Equation E.15 into Equation E.2, and integrating twice, we obtain:

$$EIv''(x) = Px$$

$$EIv'(x) = \frac{Px^2}{2} + C_1$$

$$EIv(x) = \frac{Px^3}{6} + C_1x + C_2$$

Which resolves into the following known equation for the deflection of a simply-supported beam under two equal point loads at third spans:

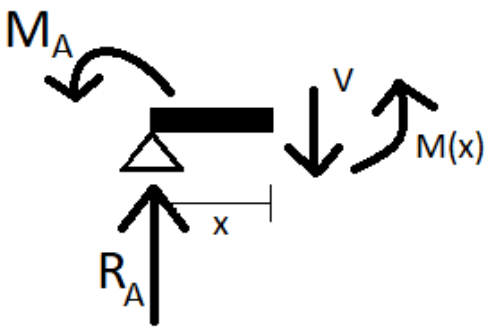
$$v(x) = \frac{-Px}{6EI}\left(\frac{2l^2}{3} - x^2\right) \qquad \text{Equation E.16}$$

Differentiating Equation E.16 once and evaluating at $x = 0$, we obtain the rotation at the left support for the simply supported case, which is needed for the derivation of the same beam with two rotational end springs:

$$v'(x) = -\frac{Pl^2}{9EI} + \frac{Px^2}{2EI}$$

$$v'(0) = \theta_{A0} = -\frac{Pl^2}{9EI} \qquad \text{Equation E.17}$$

Coming back to the case of a beam with two rotational end springs under two equal concentrated loads at third spans, and taking equilibrium from a distance $x \leq a$ from support *A*, where $a = \frac{L}{3}$, we obtain the following:



$$R_A = P$$

$$\sum M = 0$$

$$M(x) + M_A - Px = 0$$

$$M(x) = Px - M_A \qquad \text{Equation E.18}$$

Similar to the case of the uniformly distributed beam, we have the following boundary conditions:

$$v(0) = 0 \qquad \text{BC1}$$

$$v'(0) = \theta_a \qquad \text{BC2}$$

By sending Equation E.18 into Equation E.2, and integrating twice, we obtain:

$$EIv''(x) = Px - M_A$$

$$EIv'(x) = \frac{Px^2}{2} - M_A x + C_1 \qquad \text{Equation E.19}$$

$$EIv(x) = \frac{Px^3}{3} - \frac{M_A x^2}{2} + C_1 x + C_2 \qquad \text{Equation E.20}$$

Applying BC1 and BC2 to Equation E.19 and Equation E.20, and then evaluating Equation E.20 at $x = a$, we find that:

$$C_2 = 0$$

$$C_1 = EIv'(0)$$

$$C_1 = EI\theta_a$$

$$C_1 = -EI\frac{M_A}{K}$$

$$v(a) = \frac{1}{EI}\left(\frac{Pa^3}{6} - \frac{M_A a^2}{2} - \frac{EIM_A a}{K}\right)$$

$$v(a) = \frac{1}{EI}\left(\frac{Pa^3}{6} - M_A\left(\frac{a^2}{2} + \frac{EIa}{K}\right)\right) \qquad \text{Equation E.21}$$

Equation E.21 will be used as one of the required BCs in the next steps of the derivation.

The total rotation can be again calculated by adding the rotations caused by the external loads (θ_{A0}) with the rotations in the beam caused by unit moments applied on both ends of a simply supported beam without end springs.

$$\theta_A = \theta_{A0} + \theta_{AA}M_A + \theta_{AB}M_B \qquad \text{Equation E.6}$$

where

$$\theta_{A0} = -\frac{Pl^2}{9EI}$$

$$\theta_{AA} = \frac{l}{3EI}$$

$$\theta_{AB} = -\frac{l}{6EI}$$

Knowing that

$$\theta_A = -\frac{M_A}{K_r}$$

We can express M_B in terms of M_A

$$M_B = -M_A$$

With all of this, we obtain:

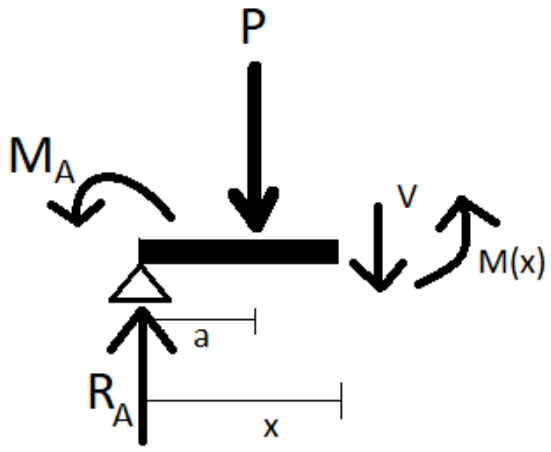
$$-\frac{M_A}{K_r} = -\frac{Pl^2}{9EI} + M_A\frac{l}{3EI} + M_A\frac{l}{6EI}$$

$$\frac{M_A}{K_r} + \frac{M_A l}{2EI} = \frac{Pl^2}{9EI}$$

Isolating for M_A, we obtain the following relationship for the moment in the spring at *A:*

$$M_A = \frac{2Pl^2K_r}{9(K_r l + 2EI)} \qquad \text{Equation E.22}$$

We now establish equilibrium at a new distance: $a \leq x \leq (l-a)$



$$R_A = P$$

$$\sum M = 0$$

$$M(x) + M_A - Pa = 0$$

$$M(x) = Pa - M_A \qquad \text{Equation E.23}$$

We thus have the following boundary conditions

$$v(a) = \frac{1}{EI}\left(\frac{Pa^3}{6} - M_A\left(\frac{a^2}{2} + \frac{EIa}{K}\right)\right) \qquad \text{BC3 (Equation E.21)}$$

$$v'\left(\frac{l}{2}\right) = 0 \qquad \text{BC4}$$

By sending Equation E.23 into Equation E.2, and integrating twice, we obtain:

$$EIv''(x) = Pa - M_A$$

$$EIv'(x) = Pax - M_A x + C_3 \qquad \text{Equation E.24}$$

$$EIv(x) = \frac{Pax^2}{2} - \frac{M_A x^2}{2} + C_3 x + C_4 \qquad \text{Equation E.25}$$

Applying BC3 and BC4 to Equation E.24 and Equation E.25, we find that:

$$EIv'\left(\frac{l}{2}\right) = 0 = \frac{Pal}{2} - \frac{M_A l}{2} + C_3$$

$$C_3 = \frac{M_A l}{2} - \frac{Pal}{2}$$

$$EIv(a) = \left(\frac{Pa^3}{6} - M_A\left(\frac{a^2}{2} + \frac{EIa}{K_r}\right)\right)$$

$$C_4 = \frac{7Pl^3}{162} - M_A\left(\frac{EIa}{K_r} + \frac{l^2}{6}\right)$$

Substituting the value of C_3 and C_4 into Equation E.25 and evaluating for deflection at mid-span ($x = \frac{l}{2}$), we obtain:

$$v\left(\frac{L}{2}\right) = \Delta_{max} = \frac{1}{EI}\left(\frac{Pl^3}{24} - \frac{M_A l^2}{8} + \frac{M_A l^2}{4} - \frac{Pl^3}{12} + \frac{7Pl^3}{162} - M_A\left(\frac{EIa}{K_r} + \frac{l^2}{6}\right)\right)$$

$$\Delta_{max} = \frac{Pl^3}{648EI}\left(1 - \frac{6K_r l + 48EI}{K_r l + 2EI}\right) \qquad \text{Equation E.26}$$

Introducing the nondimensional parameter *B* defined in Equation E.10, Equation E.26 simplifies into:

$$\Delta_{max} = \frac{-Pl^3}{648EI}\left(\frac{5B + 46}{B + 2}\right)$$

Inversing the positive direction to downwards positive, we finally get:

$$\Delta_{max} = \frac{Pl^3}{648EI}\left[\frac{5B+46}{B+2}\right] \qquad \text{Equation E.27}$$

Similar to the case for UDL, two extremes exist:

1. $B = 0$, which corresponds to simply-supported end conditions:

$$B = 0$$

$$\Delta_{max} = \frac{23Pl^3}{648EI}$$

2. B tends towards infinity, which corresponds fixed end conditions:

$$\lim_{B\to\infty} \frac{Pl^3}{648EI}\left[\frac{5B+46}{B+2}\right]$$

$$\lim_{B\to\infty} \frac{Pl^3}{648EI}\left[\frac{5+\frac{46}{B}}{1+\frac{2}{B}}\right] = \frac{Pl^3}{648EI}\left[\frac{5+0}{1+0}\right]$$

$$\Delta_{max} = \frac{5Pl^3}{648EI}$$

The vertical deflection for any point along the beam can be calculated using the following:

For $x \leq \frac{l}{3}$

$$v(x) = \frac{-1}{6EI}\left(\frac{-6EIM_A x}{K_r} - 3M_A x^2 + Px^3\right)$$

$$v(x) = \frac{1}{6EI}\left(\frac{6EIM_A x}{K_r} + 3M_A x^2 - Px^3\right)$$

$$v(x) = \frac{1}{6EI}\left(3M_A\left(\frac{2EIx}{K_r} + x^2\right) - Px^3\right)$$

$$v(x) = \frac{Px}{6EI}\left(\left(\frac{2l^2K_r}{3(K_rl+2EI)}\right)\left(\frac{2EI}{K_r}+x\right)-x^2\right)$$

$$v(x) = \frac{Px}{6EI}\left(\frac{2l^2}{3}\left(\frac{K_rx+2EI}{K_rl+2EI}\right)-x^2\right) \qquad \text{Equation E.28}$$

and for $\frac{l}{3} \le x \le \frac{2}{3}l$

$$v(x) = -\frac{1}{EI}\left(\frac{Pax^2}{2}-\frac{M_Ax^2}{2}+\frac{M_Alx}{2}-\frac{Palx}{2}+\frac{7Pl^3}{162}-M_A\left(\frac{EIa}{K_r}+\frac{l^2}{6}\right)\right)$$

$$v(x) = \frac{1}{EI}\left(M_A\left(\frac{x^2}{2}-\frac{xl}{2}+\frac{EIa}{K_r}+\frac{l^2}{6}\right)+P\left(\frac{alx}{2}-\frac{ax^2}{2}-\frac{7l^3}{162}\right)\right)$$

$$v(x) = \frac{P}{6EI}\left(\frac{2l^2}{9(K_rl+2EI)}(3K_rx^2-3K_rlx+2EIl+K_rl^2)+xl^2-x^2l-\frac{7l^3}{27}\right)$$

$$v(x) = \frac{P}{6EI}\left(\frac{2l^2(3K_rx^2-3K_rlx+2EIl+K_rl^2)}{9(K_rl+2EI)}+xl^2-x^2l-\frac{7l^3}{27}\right) \qquad \text{Equation E.29}$$

The deflected shape for any point along the beam is again defined as the following:

$$\varphi(x) = \frac{v(x)}{\Delta_{max}} \qquad \text{Equation E.13}$$

By entering Equation E.26 and Equation E.28 into Equation E.13, we obtain the following expression for $x \le \frac{l}{3}$:

$$\varphi(x) = \frac{108x}{l^3}\left(\frac{2l^2}{3}\left(\frac{K_rx+2EI}{K_rl+2EI}\right)-x^2\right)\left(\frac{K_rl+2EI}{5K_rl+46EI}\right) \qquad \text{Equation E.30}$$

And by entering Equation E.26 and Equation E.29 into Equation E.13, we obtain the following expression for $\frac{l}{3} \leq x \leq \frac{2}{3}l$:

$$\varphi(x) = \frac{4(-K_r l^3 + 9K_r l^2 x - 2l^2 EI + 54lxEI - 9K_r l x^2 - 54x^2 EI)}{L^2(5K_r l + 46EI)} \quad \text{Equation E.31}$$